STARRA AND TROUGH TANK: IRON-FORMATION-HOSTED GOLD-COPPER DEPOSITS OF NORTH-WEST QUEENSLAND, AUSTRALIA.

James
Garry J. Davidson
B.Sc. (Hons.)

Submitted in fulfillment of the requirements for the degree of Doctor of Philosophy.

conferred 1991

—§—

University of Tasmania
Hobart
1989

This thesis contains no material that has previously formed part of another higher degree or graduate diploma in any tertiary institution, and to the best of the authors knowledge and belief, no material that has been written or published by another person, except where due reference is provided.

Garry James Davidson
December 1989

There is nothing that God hath established in a constant course of nature, and which therefore is done every day, but would seem a Miracle, and exercise our admiration, if it were done but once.

John Donne
1571-1631

ACKNOWLEDGEMENTS

Foremost, I wish to acknowledge the advice, assistance and cheerful patience of my supervisor Dr Ross Large. Thanks are due to the Geology Department of the University of Tasmania for logistical support, and to the Federal Government of Australia for the furnishing of a four year scholarship. I am sincerely grateful to Cyprus Minerals and Placer Pacific for their permission to collect and publish the information on which this thesis is based, and for their generous financial and logistical support in the field. In particular, company geologists Greg Kary, Bryce Roxborough, Rob Harley, Peter Allen, Peter Ruxton and Ian Morrison are warmly thanked for their personal assistance and many useful discussions whilst in the field. John Leishman, although I have never met him, provided invaluable base maps of the Starra area. Bob Osborne, who died suddenly at home on the 9th December 1989, will be remembered not only for his help at Trough Tank, but also for his stubborn confidence and perseverance in the face of pessimism: these attributes will not be forgotten.

A group of long-suffering folk deserving special gratitude are the many critical readers of parts of my thesis: Dr Ron Berry, Dr David Blake, Dr Ian Buick, Dr Tony Crawford, proto-Dr Steve Eggins, Dr Bruce Gemmell, Vanessa Guthrie, Geoff Nicholls, Dr David Huston, Greg Kary, the late Bob Osborne, Dr Mark Rattenbury, Ollie Raymond, Dot Steane, Dr Joe Stolz and Dr Leslie Wyborn. Technical advice and assistance was generously provided by Sharon Adrichem, Stuart Capp, June Pongratz, Fred Koolhoff, Mike Power (senior and junior), Wieslaw Jablonski, the late Dr Ramsay Ford and especially Phil Robinson. I wish too to thank my fellow Ph.D and MS.c students for their kindred spirit over the years, (and for putting up with me); especially John Adam, Baharuddin, Steve Eggins, Trevor Falloon, Vanessa Guthrie, Udi Hartono, Steve Hunns, David Huston, Geoff Nicholls, Ollie Raymond, Nick Odling, Salman Palgundy, Mike Roach, Michael Seitz, Wayne Taylor, Richard Wedekind, Malcolm & Margaret Wallace, Graeme Wheller, Ai Yang, Yuenyong Panjasawatwong and Khin Zaw.

Finally, there can be no substitute or sufficient gratitude for the selfless support provided by my parents, Phyl and Jim Davidson, my siblings Susan, David and Stuart, my close friends in Hobart, and my very special friend Dot.

CONTENTS

4. STRUCTURE AND METAMORPHISM OF THE STARRA AREA

5. STARRA AND TROUGH HOST-ROCK GEOCHEMISTRY MAJOR AND TRACE ELEMENTS

6. THE GEOCHEMISTRY OF STARRA AND TROUGH TANK IRONSTONE

7.THE GEOCHEMISTRY AND ORIGIN OF STARRA MAGNESIAN ROCKS

8. THE RARE EARTH ELEMENT GEOCHEMISTRY OF STARRA IRONSTONES AND WALL-ROCKS

9. TOURMALINITES AND TOURMALINE-BEARING IRON FORMATION IN THE SOUTHERN STAVELEY FORMATION

10. CARBON/OXYGEN ISOTOPE EVIDENCE FROM VEINS AND MATRIXOF THE STARRA IRONSTONES AND HANGINGWALL ROCKS

11. SULFUR ISOTOPE VARIATION OF STARRA, TROUGH TANK, AND SOME CLONCURRY-STYLE CU-AU DEPOSITS.

12. GENESIS OF THE STARRA AND TROUGH TANK GOLD-COPPER ORES

FIGURES

ABSTRACT

Starra and Trough Tank are stratabound Cu-Au deposits hosted by stratiform magnetite-hematite iron formation in the Mount Isa Eastern Succession, Australia. They are part of the rift-related Middle Proterozoic Mary Kathleen Group, deposited in a shallow to evaporitic setting, and subsequently deformed and metamorphosed. The location of Starra (consisting of 4 geographically separate orebodies), on the margin of a major Greenschist facies shear zone (ore metamorphism estimated at 500 – 550° C, 3.5 – 4.5 kbar) has led to a more complex structural history than that experienced by surrounding rocks. Both structural/metamorphic and syngenetic ore genesis models have been proposed for the ores. Trough Tank is far less strained, but was metamorphosed to upper Amphibolite grade (680 – 720° C, ~4 kbar).

Structural events in the Starra region are identified as (1) Starra Shear development during $D1_a$ extension, (2) peak-metamorphic D2(Main Phase) deformation, producing upright, north-trending, isoclinal folds, (3) retrogressional left lateral strike-slip on the Starra Shear, producing adjacent steeply-plunging medium-scale folds (D2(Late Phase)), (4) D3 northwest-trending fold and kink domains, and (5) D4 reverse movement on the Starra Shear and nearby Mount Dore Fault Zone.

A new stratigraphic sub-division for the base of the Staveley Formation is proposed. Lowermost is the Harley Member, a strongly deformed chloritic unit with a tholeiitic tuff component. This is conformably overlain by the low-Nb-Zr-Y felsic Mariposa Creek Member, in turn conformably overlain by the Starra Iron-formation Member, and undifferentiated calcareous metasediments. To the south and east, the mineralised horizon strike-equivalents are massive hematitic ironstones, conglomerate-bearing ironstone, Hamersley-style banded iron formations (BIFs), and tourmalinites, all intercalated with shallow marine and fluvial-marine sediments. The local ore environment is interpreted as a deeper section of the basin.

Starra mineralisation consists of massive to banded quartz-magnetite-chalcopyrite-gold ironstone, grading laterally to magnetite-quartz-hematite-chalcopyrite-pyrite, and thence to poorly mineralised hematite-pyrite ± magnetite ironstone over ~ 250 m. The highest ironstone Cu and Au grades are underlain by either massive chlorite, or intense stringer-style and disseminated magnetite-hematite-chalcopyrite alteration ($Fe_2O_3^{tot}$ average = 43.6 %), amidst pervasively sheared and folded magnetite-albite-pyrite ± chlorite ± sericite network alteration (av. $Fe_2O_3^{tot}$ = 29.9 %), including dominantly hematite and dominantly magnetite-chalcopyrite vein-types. Randomly oriented inclusions in sieve-textured pyrite porphyroblasts in the Starra footwall are evidence of pre-metamorphic sulphide growth in an unlithified medium. The intensity of alteration decreases with depth. Trough Tank alteration is more focussed around flattened, funnel-shaped, quartz-rich "pipes", characterised by Au-Cu enrichment and a ~ 66 % volume

increase compared to the least-altered equivalent. Major and trace element geochemistry indicate similarities between the feldspathic footwall at Starra, and other high field strength (HFS) element-depleted felsic volcanics in the Mount Isa Inlier. However, the footwall rocks are not chemically cogenetic with the underlying Gin Creek Granite, nor could they be chemically altered hangingwall metasediments.

Loss of K, Ba, Sr and Ca, and Na enrichment, characterise the lowest alteration grade at both Trough Tank and Starra. Mn, Zr, Nb and LREE are removed in more intense alteration, with only Ti, Na and Al remaining compared to lower-grade alteration. Cu and Au in mineralised Starra ironstone are positively correlated with W, Sn, Si, Y and Mn, and dramatically depleted in Pb and Zn compared to crustal averages. At Trough Tank Co, $P_2O_5 \pm$ Mo and As are also distinctively anomalous. An unusual HREE enrichment (La/Yb* ~ 0.77) in Starra ironstone is attributed to the dissolution of footwall zircon, and the preservation of feldspar during alteration. A binary plot of (W + Mo) versus chondrite-normalised La/Y, most successfully discriminates proximal from distal barren hematite lenses at Starra. In contrast, Trough Tank ores preserve a typical seafloor volcanogenic fluid REE-pattern with Ce depletion and Eu enrichment.

Carbon isotopes were obtained from carbonate in mineralised ironstone, hangingwall metasediment matrix, and syn to post-D2(LP) veins and shears in the metasediments. Carbonate-hosted fluid inclusions in the latter homogenised between means of 114° and 200° C for individual samples, with salinities of 4.0 to 23.1 wt. % equiv. NaCl. Ironstone carbonate varied between $\delta^{13}C$ = -15.5 – -3.8‰, requiring a source component of oxidised organic carbon. Sediment matrix $\delta^{13}C$ varied between -5.3 and +0.0‰, overlapping with the vein range of -5.1 to 1.4‰. Fluid-rock reactions are interpreted to have altered the sediment matrix $\delta^{13}C$ value towards the vein-fluid composition (reflecting mixing between deep metamorphic and shallow meteoric waters within the Starra Shear). In contrast, $\delta^{13}C$ in ironstone carbonates at Starra and Trough Tank do not converge with the vein-fluid compositions. Instead they form an older unusual trend of increasing $\delta^{18}O$ with decreasing $\delta^{13}C$, which suggests a $\delta^{18}O$-enriched connate water contribution to the the ore fluid.

The $\delta^{34}S$ range of Starra and Trough Tank sulphides are very similar to one another, averaging ~ 0 ‰, ranging from -6 to +5 ‰. The most likely sulphur source is either H_2S formation by inorganic reduction of Mid-Proterozoic seawater (~ 20 ‰) at > 200° C, or leaching/expulsion from magmatic rocks. They preclude an origin from $\delta^{34}S$-rich waters equilibrated with marine sulphate evaporites, although this is a common sulphur source for vein-style and sediment-hosted base-metal ores in the Mount Isa Western Succession. Sulphur isotope values of footwall pyrite cores and later recrystallised pyrite rims, confirm that these are separate pyrite generations.

The many similarities between Starra and Trough Tank permit the formulation of a single genetic model. The stratigraphic, structural, textural, alteration, metal zonation and

geochemical features of the orebodies suggest that features syngenetic processes emplaced much of the mineralisation, whereas deformation produced minor remobilisation of sulphide into boudin necks and hangingwall calc-silicate zones. A coincidence of fold hinges and ore-bodies in three instances at Starra is attributed to preferential ductile slip in areas of higher sulphide content during D2(LP), an observation of clear exploration utility.

In the syngenetic model, the critical features are the ascent of hot, oxidised, low-aH_2S fluids to the seafloor, where ore deposition occurs mainly by cooling in a low-aH_2S water column. Peak ore-formation conditions at Starra were: temperature: 260 – 380° C, log f_{O2} = -27.5 – -30, pH = 3.9 - 6, $\Sigma S \sim 10^{-3}$ M, and salinity ≥ 3 M NaCl. These conditions favour transport of Cu and Au as chloride complexes. The mineralogical effects of fluid-boiling are not apparent at Starra, but can readily explain the subsurface silica and gold enrichment of Trough Tank, which implies the latter was the shallower deposit. Small primary inclusions in the mineralised sub-surface breccias of Area 222 are the best evidence of primary high salinity fluids.

Variation within this genetic model can explain the features of similar ores around the world, which are here termed the time-transgressive "Volcanogenic Copper-bearing Oxide" sub-class (VCO) of exhalative ores. This ore-type is favoured in (but not confined to) shallow continental rift-settings, because these can contain the requisite oxidised sediments or evolved oxidised magmas, which are capable of producing oxidised hydrothermal fluids. Cooling of a VCO fluid during its entry into a more-H_2S-rich aqueous environment could produce Pb-Zn-rich BIFs, such as the Pegmont deposit of the Kuridala Formation, Mount Isa.

POST-SCRIPT

On the seventeenth December 1989, the name "Trough Tank" was altered to "Osborne" in honor of the deposit's discoverer, the late Robert Osborne.

CHAPTER 1

INTRODUCTION

BACKGROUND

Magnetite-rich ironstones ($Fe_2O_3^{tot} + SiO_2 = 96$ %, $Fe_2O_3^{tot} > 60$%) host stratabound Au-Cu mineralisation in an ancient rift-setting of the Mount Isa Eastern Succession, Australia. 'Ironstones' are considered in this thesis to be massive, iron-rich, conformable varieties of iron formation. Banded iron formations (BIFs) are distingiushed from them by the presence of well-defined compositional layering.

The Starra ore deposit is hosted by the Staveley Formation of the Mary Kathleen Group (~1720 Ma; Page (1983)), whereas the stratigraphic affinity of the similar Trough Tank ores is conjectural. The latter is contained in lithologies similar to those which host the well-known Pegmont stratiform Pb-Zn BIF mineralisation, 29 km south-east of Starra (Stanton & Vaughan 1979, Vaughan & Stanton 1986). Both deposits are of international interest, because of the prominent controversy surrounding the genesis of BIF and chemical sediment-hosted gold ores; the studied ores have features which superficially support both an exhalative and an epigenetic origin. They are also significant as a previously unrecognised deposit-style in the Mount Isa area, with implications for similar deposits thoughout the world (Davidson et al. in press).

Starra forms the major mine of the Selwyn Gold-Copper project, (a joint-venture between Cyprus Minerals, Elders Resources and Arimco), consisting of 4 geographically-separate outcropping lodes, totalling 5.3 mt at 5.0 g/t Au, and 1.98 % Cu. It is located 150 km south-east of Mount Isa, in the south-draining catchments of the arid Selwyn Range (latitude 21° 40' S, longitude 140° 28' E; SF-54-6 Duchess 1: 250 000 topographic sheet). "Starra" is a north Australian aboriginal word meaning "ironstone" or "iron hill". The mine and plant are locally referred to as "Selwyn", although this has not been followed in this thesis because of possible confusion with the historical Selwyn township and associated Mount Elliot mine 15 km to the north.

The Australian Bureau of Mineral Resources carried out the first recorded investigations in the Starra region (Kary & Harley, in press) in 1956, when the Selwyn Hematites were assessed as an iron resource. No mineralisation was recognised during the earlier Cloncurry gold-copper rushes of 1907-20, 1928-46, and 1953-71 (Brooks et al. 1975). Anomalous copper and gold were located in the Western Hematites by Enterprise Exploration, Anaconda and Newmont between 1957 and 1974, but because of the low worth of these metals at the time, activity did not persist. Amoco Minerals, which subsequently evolved into Cyprus Minerals, realised the potential of the mineralisation in 1975, commencing mining in 1988, at a planned production of 3,500 kg of Au and 10,000 t of Cu/ year (Kary and Harley, in press).

Trough Tank is a similar, though more metamorphosed orebody, 47 km south-east of Starra (latitude 22° 6' S, longitude 140° 34' E; SF-54-10, Boulia 1: 250 000 topographic sheet), discovered by a CSR Minerals-Billiton exploration venture (CSR Minerals became Placer Pacific N.L. in late-1988). It was discovered beneath 30 m of Mesozoic cover in 1985, and is presently in the evaluation phase.

RATIONALE AND AIMS

Banded iron formations are a common associate of stratiform Pb-Zn ores (Stanton 1976a, 1976b; Westhuizen et al. 1986), disseminated W-ores (Barnes 1983, Appel 1986), and some Au deposits. The latter are the subject of this thesis. In recent years, many such sulphide-rich BIF-hosted Au deposits, which were previously held to be syngenetic (e.g., Ridler 1970, Hutchinson et al. 1971), have been reinterpreted as metamorphic replacement deposits (MacDonald 1983, Phillips et al. 1984, Groves et al. 1987, Foster & Gilligan 1987, Lhotka & Nesbitt 1988), returning in a broad sense to the epigenetic ideas of much earlier works (Tyndale-Biscoe 1940, Woodall 1975). Careful documentation of post-BIF alteration, a spatial relationship to metamorphic fluid conduits, and the revelation that delicate, bedding-parallel sulphide lamination could be formed by replacement, compelled researchers to think of BIFs as chemical traps, rather than chemical sources of gold. Such replacement is characterised by symmetrical carbonate and silica alteration, reduced pyrite-pyrrhotite-arsenopyrite assemblages, a Au-As-Hg-Sb-W elemental association, and metamorphic rather than host-rock mineralisation ages. A key aspect of the model proposed by Phillips et al. (1984) is the reduction of magnetite and Fe-silicates by

Deposit	Syngenetic model	Epigenetic model
Vubachikwe, Zimbabwe	Fripp (1976) Saager et al. (1987)	Phillips et al. (1984) Master et al. (1989)
Passagem de Mariana, Brazil	Fleischer & Routhier (1973)	Vaal et al. (1988)
Montrose and New Consort, South Africa	Maiden (1982)	Anheusser (1976)
Agnico-Eagle, Canada	Barnett et al. (1982)	Wyman et al. (1986)
Dome Mine, Canada	Fryer & Hutchinson (1976), Fryer et al. (1979)	Hodgson (1983), MacDonald (1984)
Dickenson Mine, Canada	Kerrich et al. (1981)	Rigg & Helmstaedt (1981), Mathieson & Hodgson (1984)

Table 1.1 *A compilation of chemical sediment/BIF-hosted gold deposits with divergent genetic interpretations.*

thio-sulphide complexes within reduced, low-salinity metamorphic fluids, to deposit sulphides and gold. Widespread application of the general replacement model has resulted in new hypotheses for many of the previously known chemical-sediment-hosted gold deposits, as summarised in Table 1.1. The lateral-secretion models of Sawkins & Rye (1974), Fripp (1976) and Kerrich & Fryer (1979), in which low grade syngenetic gold is further concentrated by structural remobilisation, are attempts to explain the locally-epigenetic features of many BIF-Au-ores within a syngenetic framework: criteria for their evaluation are suggested by Groves et al. (1987).

Some new models dispute both the synsedimentary nature of the mineralisation, and their host-rocks (e.g., Roberts 1987). For instance, Hodgson (1983) and Mathieson & Hodgson (1984) consider that the ore host-rocks of the Dome and Dickenson mines have been mistakenly identified as chemical sediments by Kerrich et al. (1981) and Fryer et al. (1979). They have reinterpreted them as structurally-laminated shears and vein complexes. A similar controversy over the Starra ironstones is examined within this thesis. Some deposits (summarised in Appendix 11) in fact have low magnetite and sulphide contents, and are hosted by carbonates or cherts, to which the epigenetic sulphidation model of Phillips et al. (1984) appears inapplicable. For the formulation of viable exploration models, it is clearly of fundamental importance to determine whether the host-rocks are chemical sediments, and whether syngenetic or epigenetic processes deposited gold in each case.

The subject of this thesis is a newly-perceived deposit class with features that do not conform to recognised sulphidised oxide-facies BIF deposits, or to oxide-poor chemical sediment Au-ores, such as the giant Homestake deposit (Sawkins & Rye 1974). Disseminated gold and Cu-sulphides are contained in stratiform magnetite or hematite lenses which are associated with volcano-sedimentary sequences, above pervasive and/or focussed oxide stringer systems nested in albitic alteration. The origin of the Starra ores is complicated by an intense deformational history, because of their location on the margin of a major multiply-reactivated shear zone. A motivation in including the Trough Tank ores in this study was their relatively less-deformed state; between Starra and Trough Tank exists an invaluable opportunity to compare two deposits with near-identical chemistry, one strongly deformed and moderately metamorphosed, the other moderately deformed and strongly metamorphosed. A major aim of this thesis is to document the geological, geochemical and isotopic features of these ores. The relative roles of deformational and of syngenetic processes are assessed, with a view to formulating a general genetic model, based on the documented features.

Detailed study has mainly been confined to Starra, and particularly the Area 257 orebody, with subordinate attention to Trough Tank. This has resulted in a topic-by-topic thesis-structure, as distinct from the separate treatment of each orebody. Figure 1.1 summarises the location of the larger maps referred to throughout this thesis.

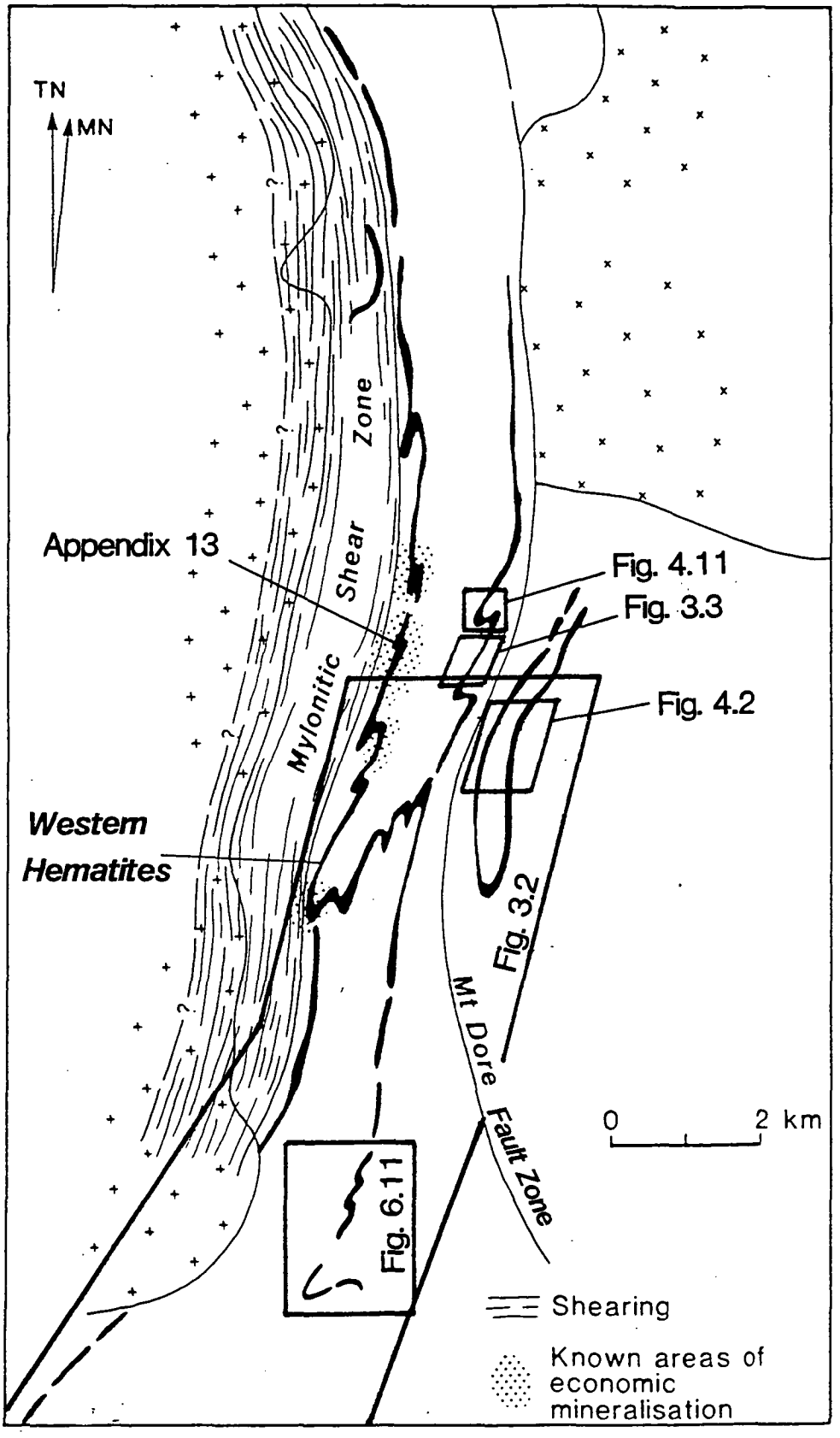

Figure 1.1 *A location diagram of the Starra area for geological maps referred to throughout this thesis.*

CHAPTER 2

REGIONAL GEOLOGY

REGIONAL GEOLOGICAL SETTING OF THE MOUNT ISA INLIER

The Mount Isa Inlier is one of several exposed Proterozoic terrains in northern Australia. Others include the Georgetown and Coen Inliers, the McArthur Basin, and the Tennant Creek Block. Many of these terrains are linked by positive gravity and magnetic anomalies (Tucker et al. 1979, Laing & Beardsmore 1986, Wellman 1988) which supports the view that by the late-Proterozoic they formed a major continent or continental fragment (Etheridge et al. 1987). Amongst these terrains the timing of volcanism, sedimentation, metamorphism and deformation cycles was often synchronous (Page 1988).

The very simple view of Mount Isa Inlier geology is of an older central north-south spine of Amphibolite-grade basement, the Kalkadoon-Leichhardt Block, separating younger eastern and western volcanosedimentary sequences, known as the Eastern and Western Successions (Eastern and Western Fold-belts of Blake (1987))(Fig. 2.1). Beardsmore et al. (1988) have challenged this simple view, proposing much of the Eastern Succession to be a cratonised sediment-filled basin, close to the age of the Kalkadoon-Leichhardt Block. There is no radiometric dating to support this view; it is based entirely on the circumstantial evidence of higher metamorphic grade, and unique lithologies.

A summary of the timing of geological events is presented in Table 2.1.

ROCK-TYPES WITHIN THE MOUNT ISA INLIER

Kalkadoon-Leichhardt Belt

The Kalkadoon-Leichhardt Block is a 2 to 5 km thick sequence of volcanics, minor sediments, felsic intrusions and high-grade gneiss. Metamorphic basement is overlain by Cover Sequences 1, 2 and 3, summarised in Fig. 2.2 (Blake et al. 1984, 1987). Basement is considered by Blake et al. (1984) to include units such as the Plum Mountain Gneiss and undivided Tewinga Group, older than 1850 Ma (Page 1983a). Cover Sequence 1 (1783 to 1740 Ma) includes the Leichhardt Volcanics (comagmatic with the Kalkadoon Batholith), whereas Cover Sequence 2 is represented by the Argylla Formation, Magna Lynn Metabasalt (Tewinga Group members), and parts of the Mary Kathleen Group. Undivided Tewinga Group Amphibolite-grade gneissic to migmatitic rocks (migmatite age: 1870 - 1860 Ma; Blake & Page 1988) are in faulted contact with the little-metamorphosed Leichhardt Volcanics, which therefore post-date the major regional Barramundi metamorphic event (Blake 1982, 1987).

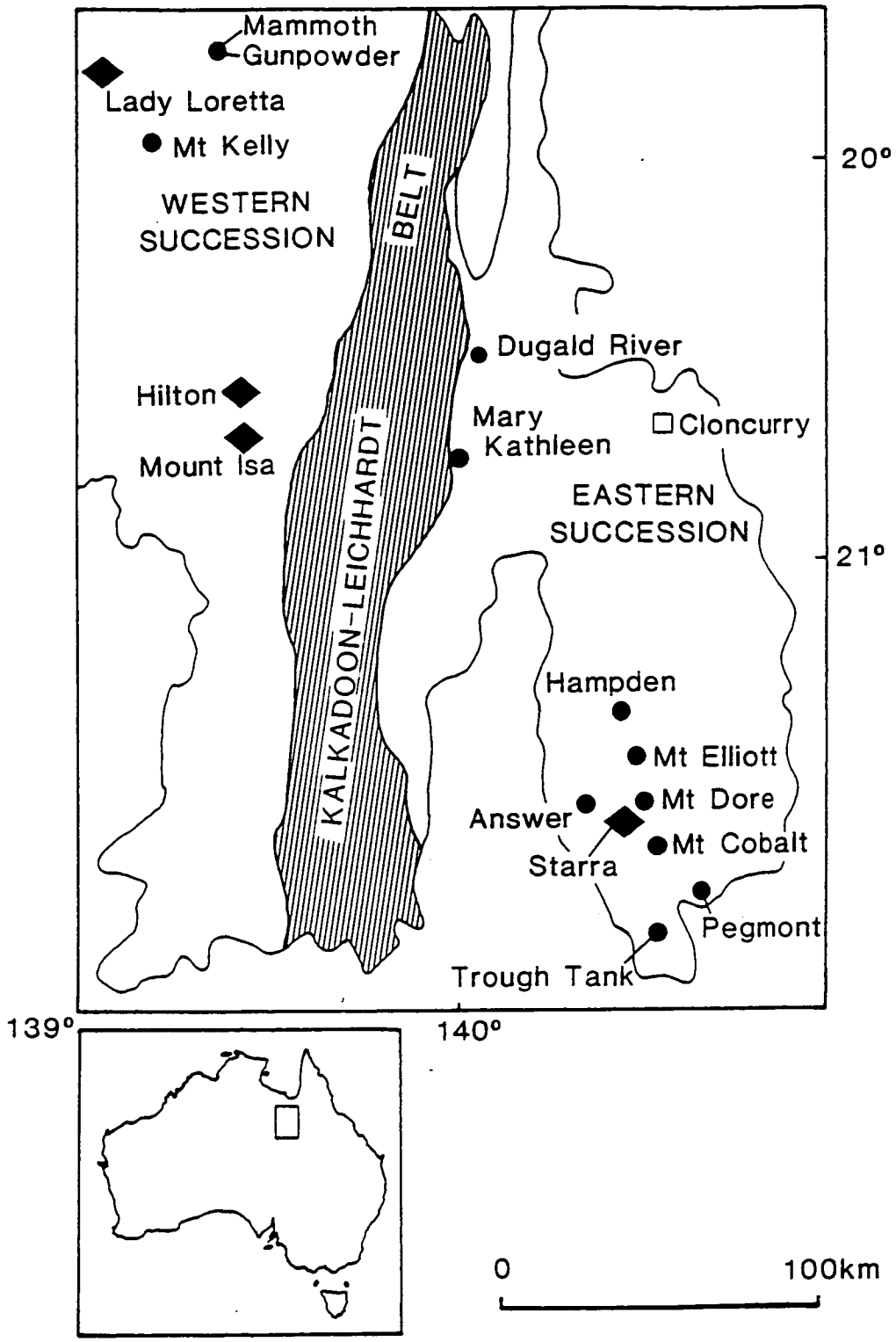

Figure 2.1 *Major geological elements of the Mount Isa Inlier. The Kalkadoon-Leichhardt belt is generally regarded as an older metamorphic basement block separating two complexly deformed volcanosedimentary sequences — the Eastern and Western Successions. Also shown are the operating mines (diamonds), and those prospects with significant historical production or exploration interest (circles).*

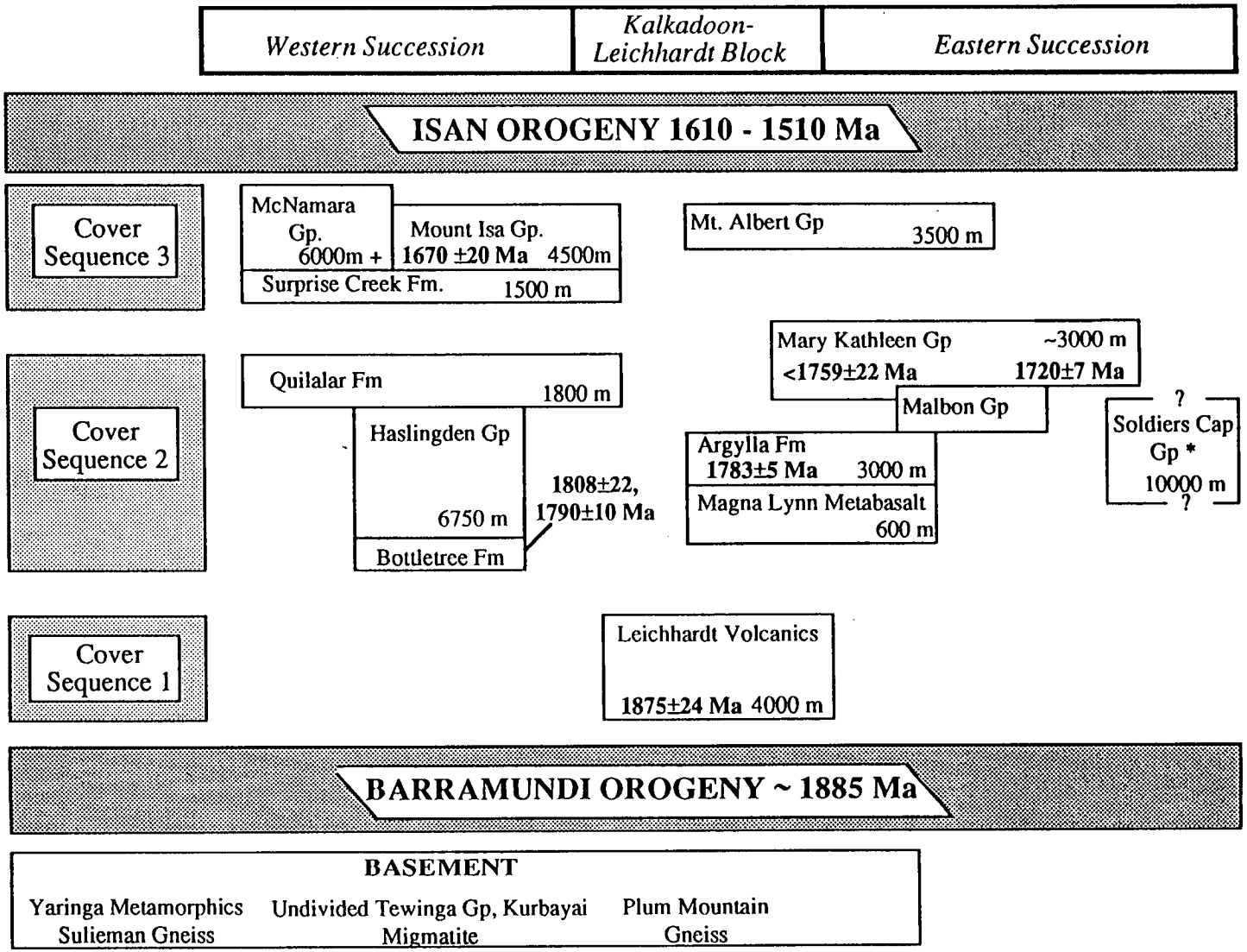

Figure 2.2 *Stratigraphic relationships amongst the major units in the Mount Isa Inlier, after Page(1983a,b), Blake et al.(1984), Blake (1987) and Wyborn et al.(1988). * — for proposed revised Soldiers Cap Group stratigraphy, see Beardsmore et al. (1988).*

Western Succession

Up to eighteen kilometres of shallow water sediments and volcanics in near-equal proportions occupy a linear north-south depocentre, termed the Leichhardt River Fault Trough (LRFT) (Glickson et al. 1976), west of the Kalkadoon-Leichhardt Block. They overly poorly exposed basement west of the Mount Isa Fault, such as the Saint Ronans Metamorphics (~ 2000 Ma; Page et al. 1982), Yaringa Metamorphics and Sulieman Gneiss. Deposition

EVENT	*AGE*
Oldest crust below the Mount Isa region (as indicated by inherited zircons within the Eastern Creek Volcanics)	2700 - 2500 Ma 2100 - 1800 Ma
Felsic volcanism of Cover Sequence 1 (Page 1983a)	1865 - 1852 Ma
Main sedimentation, commencing with widespread basic volcanism,	1808 - 1670 Ma
including: Cover Sequence 2	1808 - 1720 Ma
: Cover Sequence 3	1680 - 1670 Ma
(Page 1978, 1983a, 1983b)	
First appearance of red-beds, carbonates and evaporites throughout the Mount Isa Inlier	1780 - 1740 Ma
Major igneous intrusion episodes (Wyborn et al. 1988)	1870 - 1840 Ma 1820 - 1800 Ma 1760 - 1740 Ma 1700 - 1670 Ma 1560 - 1480 Ma
Major deformations: **Barramundi Orogeny**	1885 ± 10 Ma
: **Isan Orogeny**	
D1: (Page & Bell 1986)	1610 ± 13 Ma
D2: (Page & Bell 1986)	1544 ± 12 Ma
D3: (Page & Bell 1986)	1510 ± 13 Ma

Table 2.1 *A summary of the timing of geological events in the Mount Isa Inlier.*

commenced with the Bottletree Formation of Cover Sequence 2 ($1808\ ^{+27}_{-17}$, 1790^{+10}_{-8} Ma ; Page 1983a), a 3000 m thickness of acid and basic volcanics, conglomerate and graywacke. It was succeeded by the volcanosedimentary Haslingden Group (6750 m; Blake et al. 1984) which contains easterly-sourced quartzites, conglomerate, grits and 2000 m of amygdaloidal metabasalt (Eastern Creek Volcanics), deposited on an "extensive tide-swept shelf" (Jackson 1989) bordered by coalescing deltaic systems (Derrick 1974, Wilson et al. 1977).

Subsequently, calcareous quartzites of the Quilalar Formation and Myally Sub-group transgressed beyond the confines of the LRFT over the Kalkadoon-Leichhardt block.

After a depositional break of approximately 70 Ma, a third sedimentation cycle began (1680 - 1670 Ma; Cover Sequence 3 of Blake 1987, Fig. 2.2), consisting of fine-grained dolomitic sediments of the Mount Isa and equivalent McNamara Groups, and the Surprise Creek Formation, accumulating in fault-bound troughs within the LRFT. The depositional environment was arid, shallow-marine, or lacustrine (Muir 1982, Neudert & Russell 1982). Growth-faulting was a common depositional control (Smith 1969, Mathias & Clark 1975).

Eastern Succession

Tectonic Elements

Areas of strikingly different tectonic style and stratigraphy are juxtaposed across the Eastern Succession, forming the basis for a complex stratigraphic nomenclature seemingly added to by each new worker in the district (Figs. 2.2, 2.3).

The Pilgrim Fault Zone is recognised by Blake (1988) as the fundamental, western, strike-slip boundary with the Kalkadoon-Leichhardt Block. Units are often unmatched on either side, or at least change thickness. This crustal fracture has been active into the Cambrian, and possibly the Mesozoic, faulting and deforming Georgina Basin carbonates in the Burke River Structural Belt. From west to east the other tectonic elements are the Malbon Block of Plumb et al. (1980), and the Staveley and Squirrel Hills Belts, collectively referred to as the Mary Kathleen Fold Belt (Plumb et al. 1980) (Fig. 2.3, 2.4). The term "Cloncurry Fold Belt" (Beardsmore et al. 1988) encompasses the Staveley and Squirrel Hills Belts only, as well as the newly designated Gin Creek Block (Switzer 1987). The Mary Kathleen Shelf is used by Blake et al. (1984) to describe the depositional area of the Mary Kathleen Group.

Stratigraphy

The Malbon Block contains a core of Cover Sequence 2 (Blake 1987) Tewinga Group members, overlain disconformably by the Malbon Group, all folded by the major north-plunging Duck Creek Anticline. The Malbon Group is uniformily regarded as the commencement of a new depositional cycle in the Eastern Succession. It initiates with the metabasalts of the Marraba Volcanics (Derrick et al. 1976), 900 to 2800 m thick. Basalt intervals continue sporadically through the overlying transgressive Mittakoodi Quartzite.

Virtually all of the calcareous sediments in the Eastern Succession are included in the overlying Mary Kathleen Group (Fig. 2.4), some of widely differing ages (Blake et al. 1982). It currently consists of 8 formally-recognised members, total thickness between 1700 and 4000 m (Carter 1959, Carter et al. 1961, Derrick et al. 1977, Blake et al. 1981). It is considered equivalent to the western Quilalar Formation by Derrick et al. (1980) and Beardsmore et al. (1988).

Beyond the Mary Kathleen Group to the east, the Squirrel Hills Belt includes the Kuridala Formation, partly separated from the Doherty Formation by the Williams Batholith. At

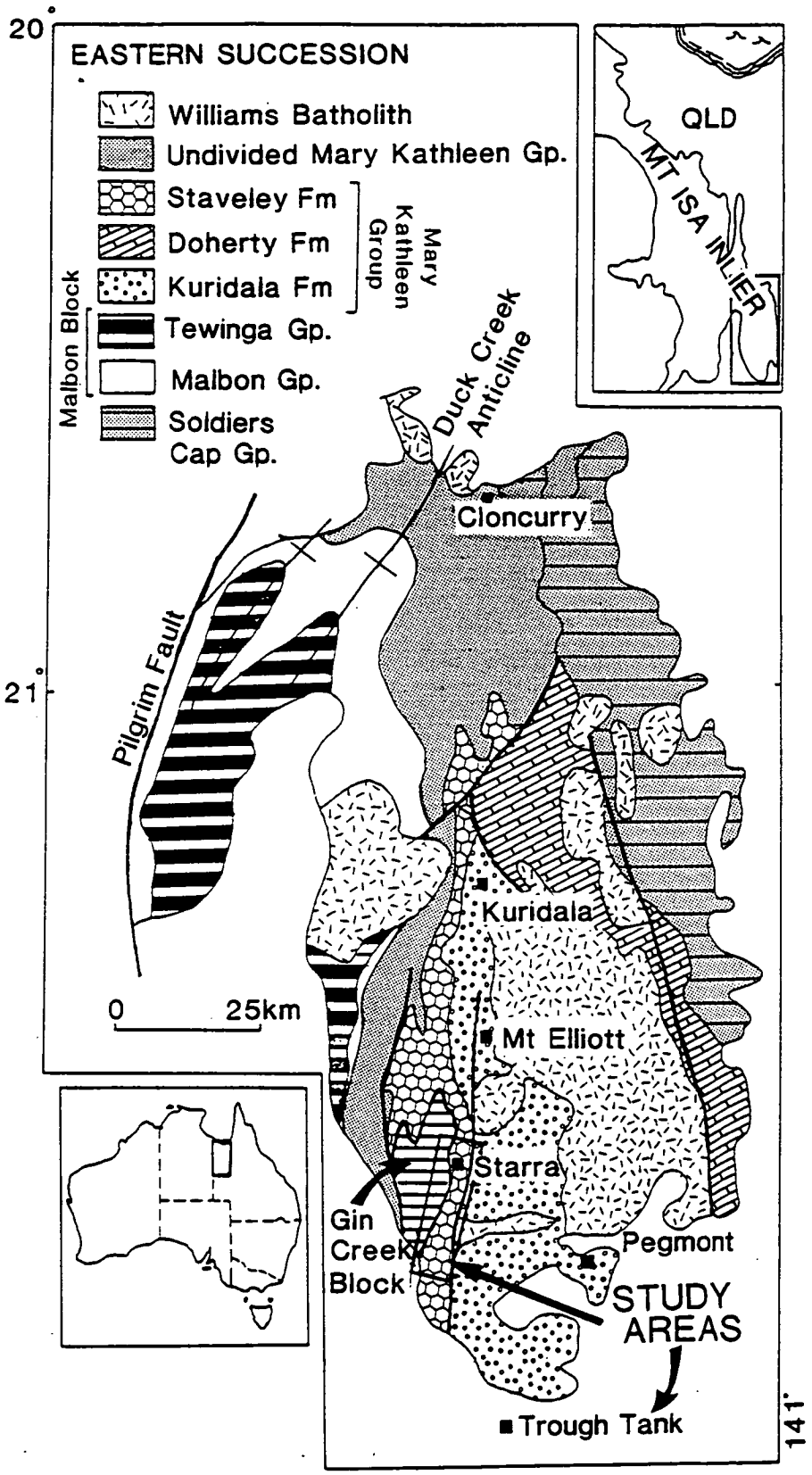

Figure 2.3 *Eastern Succession regional geology, emphasising elements of the Mary Kathleen Group relevant to Starra ore geology.*

the very eastern outcrop limit of the Eastern Succession, the Soldiers Cap Group forms a more highly deformed and metamorphosed strip 120 km long, containing a series of Pb-Zn-rich BIF horizons including Muramungee, Fairmile and Dingo, similar in style to the Pegmont deposit of the Kuridala Formation (Stanton & Vaughan 1979, Loosveld 1989). This is not the only lithological contrast of the Soldiers Cap Group with other Mount Isa units; Beardsmore et al. (1988) describe a 10 km thickness of feldspathic turbiditic sediments deposited in deep water environments, a succession unique within the Mount Isa Inlier.

Status Of Correlations

In the most recent proposal for revision of Mount Isa stratigraphy, Beardsmore et al. (1988) have deleted the Kuridala Formation, replacing it with an expanded Soldiers Cap Group. The Fullarton River Group was created by Beardsmore et al. (1988) to encompass greater than 7000 m of feldspathic gneiss and migmatitic psammite and psammopelite below the Soldiers Cap Group. (The application of these revisions awaits the publishing of formal descriptions). Both of these are placed in a new entity called the Maronan Supergroup, interpreted as an older previously unrecognised cycle of ensialic rifting. This proposal could add a profound new dimension to Mount Isa Inlier geology, if verified. The previous interpretation (Blake et al. 1984, Blake 1987) suggested that the Doherty Formation and Soldiers Cap Group were conformable, and hence not much older than 1720 Ma, because of interfingering on the contact.

It is surprising that Beardsmore et al. (1988) have not addressed the latter evidence in their interpretation. Apart from lithological differences, other evidences for an older age are:

(1) Higher metamorphic grades (up to upper Amphibolite grade)

(2) A decrease in radiogeneiity of $^{206}Pb/^{204}Pb$ in the Pegmont versus Dugald River and Mount Isa deposits

(3) Distinctive incompatible element depletion in mafic lavas of the "Maronan Supergroup" compared to other sequences.

These three arguments cannot conclusively form the basis for the definition of an older Mount Isa rift cycle. High metamorphic grades have affected both the calcareous Doherty Formation (aged at ~1720 Ma), and the supposedly much older underlying Soldiers Cap Group. Radiogenic differences amongst the lead isotope signatures of ore deposits of the region could be due as much to differences in mantle source isotopic signature, as seems apparent for ores in the Mount Read Volcanics of Tasmania (Gulson 1987), as to age differences between the ores. Incompatible element depletion is a feature of basalts and dykes sampled from the Staveley Formation (Chapter 7), and hence is not confined to the Maronan Supergroup: this is also owed to provincial mantle features. On balance, points (1) to (3) are characteristics of the entire Cloncurry Fold Belt, affecting "younger" and "older" cover sequences alike. They are too equivocal to form the evidence used to justify an older volcanosedimentary cycle.

The hypothesis needs to be tested radiometrically, before the stratigraphic revisions of Beardsmore et al. (1988) can be adopted.

Mary Kathleen Group Members of the Eastern Succession

In view of its importance to the Starra ores, the stratigraphy of the Mary Kathleen Group is reviewed here in some detail.

Overhang Jaspilite and Chumvale Breccia

Overhang Jaspilite consists of calcareous to pyritic siltstones, cherts (stromatolitic in part), well-banded manganiferous and barite-bearing iron-formation, and limestone (Derrick et al. 1977). Barite veins up to 5 m thick are a characteristic feature of the 200 - 850 m thick unit. The Chumvale Breccia is the formal name for a breccia unit overlying or forming conformable lenses within the Overhang Jaspilite. Within it jaspilite fragments are orientated irregularly in a siliceous or calcareous matrix. Derrick et al. (1971) suggested the breccia was tectonic, whereas Derrick et al. (1977) preferred a palaeoregolithic origin; if the latter is accepted, the Corella and Staveley Formations overly the Overhang Jaspilite unconformably. Blake et al. (1984) and Derrick (1984) favour a transitional relationship upwards and along strike from the Overhang Jaspilite into the Answer Slate, which in turn may merge laterally with the Kuridala Formation. Marraba Volcanics, Mittakoodi Quartzite and overlying Overhang Jaspilite all thin southward along the eastern limb of the Duck Creek Anticline (Fig. 2.3).

Answer Slate

The Answer Slate forms a coherent north-south belt 72 km long and 6 km wide, comprising cleaved, low-grade, variably pyritic and carbonaceous slates and schists. These are conformable with the overlying Staveley Formation and the underlying Mittakoodi Quartzite in the few instances of non-faulted contact. Leishman (1983) and Blake et al.(1984) correlate the Answer Slate with similar lithologies in the Kuridala Formation, favouring a deeper water distal depositional environment. A growth-fault origin may explain the nature of the northernmost contact with Staveley Formation across the Martin Creek Fault (BMR Duchess-Urandangi 1:250 000 sheet, GR VB430560), where Answer Slate is omitted in the northern section, while the thickness and position of Overhang Jaspilite and Mittakoodi Quartzite is little-changed. Blake et al. (1984) provide evidence that this fault has also been active since D2.

Kuridala Formation

The Kuridala Formation will be discussed as part of the Mary Kathleen Group, despite a proposal for removal by Beardsmore et al. (1988).

Greater than 2000 m of upwardly-fining, turbiditic meta-graywacke, siltstone and shale are present in the Kuridala Formation, derived from an easterly land-mass (Beardsmore et al. 1988). The uppermost sediments exposed in the Starra area are thick transitional intercalations of graphitic schist, micaceous schist and quartzite, tightly folded and metamorphosed to lower Amphibolite facies. Beardsmore et al. (1988) noted the similarity of this assemblage to the Toole Creek Volcanics of the Soldiers Cap Group, correlating them on that basis.

The nature of the upper contact with the Staveley Formation is uncertain: Beardsmore et al. (1988) report it to be a major 75 km-long fault zone (Mount Dore Fault Zone), although concordant bedding and westward younging in both units are also consistent with a conformable relationship. Blake et al.(1984) tentatively ascribe an unconformable relationship because they report finely crenulated and veined Kuridala Formation overlain by little-metamorphosed Staveley Formation sandstone. If this is so, at least one deformation must have interceded prior to Staveley Formation deposition. Alternatively this may be an instance of the divergent mechanical response on different lithologies with the same deformation history. In chapter 3 new evidence is presented favouring an unconformable relationship between the Staveley and Kuridala Formations, although the implied time-break was short.

Staveley Formation, Marimo Slate and Agate Downs Siltstone

The Staveley Formation is thought to be a facies equivalent of the Marimo Slate in the north, whilst the Agate Downs Siltstone forms a finer-grained enclave in the Staveley Range (Fig. 2.4). Staveley Formation stretches at least to the Mort River, southwards along the Gin Creek Block margin, as was originally defined by Carter et al.(1961), beyond the limit shown by Blake et al. (1984). Approximately 2000 m of calcareous arenite, siltstone, conglomerate, minor carbonaceous shale and limestone pods are present, although no upper contacts are exposed. Mapping in the Starra - Mount Elliott region by Leishman (1983), Switzer (1987), Beardsmore et al. (1988), Rob Hartley (pers. comm.) and this work have identified elements of a characteristic basal Staveley Formation association. It includes basic and acid lavas and epiclastics, overlain and intercalated with massive ironstones and BIF. The volcanic units form a previously unrecognised extensive sheet along the exposed western Staveley Formation contact, up to 750 m thick (the basis for a formal sub-division of these units is discussed in greater detail in Chapter 3).

A generally shallow environment of deposition is inferred from cross-bedding, ripple marks, evaporite casts and conglomeratic channels.

Staveley Formation may be the same age as the Doherty Formation (1720 ± 7 Ma ; Page 1983a) as both are calcareous (Blake 1982). However, Blake et al. (1984) prefer a correlation with "young" Corella Formation (~1600 Ma) because of metamorphic grade differences.

Corella and Doherty Formations

Blake (1982) has reviewed the Corella Formation stratigraphy, stressing that dating by Page (1983a, 1983b) indicates a span of at least 140 million years for its accumulation, from >1740 Ma (Burstall Granite intrusion into the Corella Formation) to 1600 Ma — the anomalously young age of Corella Formation in the Tommy Creek area. Considerable stratigraphic revision is recommended by Blake (1982) once knowledge of the distribution of rock-types has improved.

Calcareous lithologies overlying the Overhang Jaspilite are called Corella Formation north, west and east of Cloncurry. Blake (1982) describes the formation as "partly or

predominantly thin-bedded calcareous scapolitic metasediments", deposited in a shallow evaporitic marine setting (Ramsay & Davidson 1971). In the west this uniform succession changes character dramatically to include the 800 m thick Lime Creek Metabasalt Member (Derrick et al. 1978).

Doherty Formation (1720 ± 7 Ma; Page 1983a) is a higher grade lithological Corella Formation-equivalent in the Squirrel Hills Belt south of Cloncurry, with the addition of rhyolitic, cherty, quartz-tourmaline, metabasalt and rare ironstone lenses. It is ~ 1000 m thick, brecciated and granofelsic.

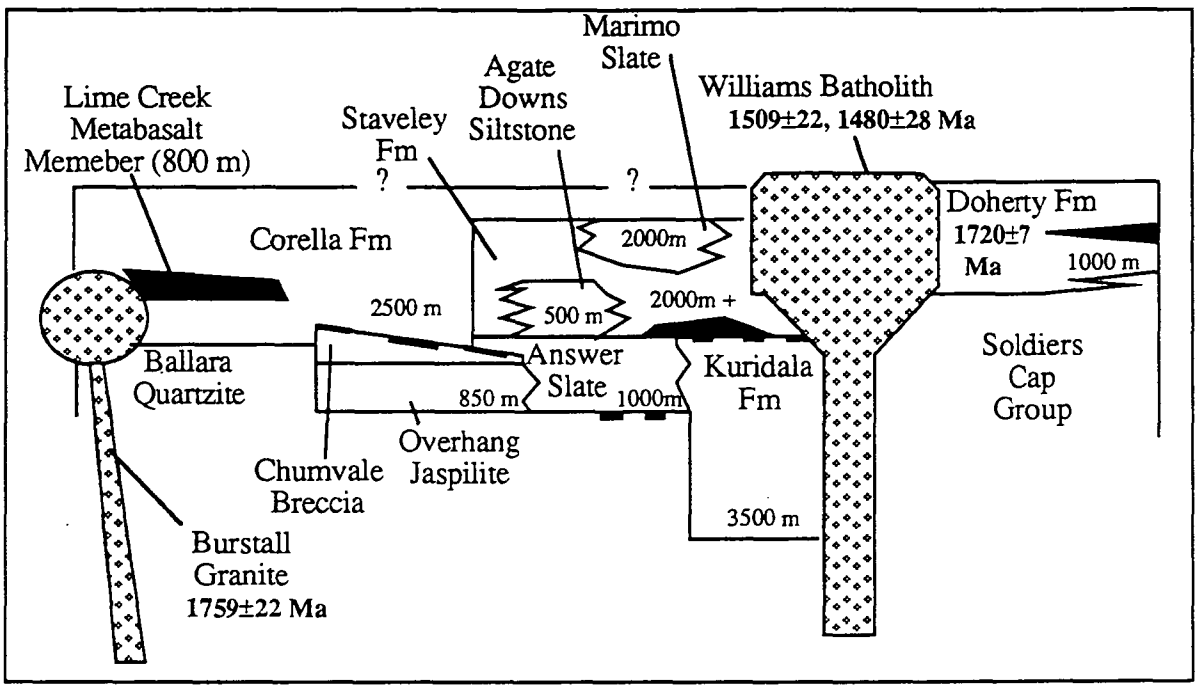

Figure 2.4 *Stratigraphic relationships within the Mary Kathleen Group, Mount Isa Inlier, after Blake et al. (1981), Derrick et al. (1977), and Blake et al. (1984). Unconformities are indicated by thick black dashes; units in black are metabasalts. Jagged contacts infer a transitional facies relationship.*

EVAPORITES IN MOUNT ISA SEDIMENTS

As summarised in Table 2.1, evaporites, carbonates, red-beds and dessication features appear at approximately the same time in the Eastern and Western Successions, between 1780 and 1740 Ma. In the Western Succession minor halite pseudomorphs commence in the Lochness and succeeding Quilalar Formations (Derrick 1982), but the major evaporite-pseudomorph-bearing units are the ~ 1670 Ma old Mount Isa and McNamara Groups. Halite, gypsum and anhydrite pseudomorphs are widespread within these groups (Walter 1978, McClay & Carlisle 1978, Neudert & Russell 1982).

In the Eastern Succession, evaporite-relicts are noted mainly from the calcareous Mary Kathleen Group. The Staveley Formation contains halite and fine gypsum casts (Blake et al. 1984, Davidson et al. 1988, in press). Wells (1980) reports iron-oxide pseudomorphs after gypsum, and common barite, in the Overhang Jaspilite. Muir (1983) describes shortite moulds

(a sodium carbonate characteristic of alkaline lacustrine settings) in the host-rocks to the Dugald River Pb-Zn deposit west of the Pilgrim Fault (Fig. 2.3). Abundant Cl-rich scapolite, thought to recrystallise during the metamorphism of saline calcareous sediments, occurs in the Corella, Staveley, Kuridala and Doherty Formations, as well as the Overhang Jaspilite and Answer Slate (Ramsay & Davidson 1971, Blake et al. 1984). Metamorphosed evaporite-derived magnesian clays are the suggested precursors of cordierite-anthophyllite rocks in the Rosebud Syncline of the Corella Formation (Reinhardt 1987).

Hydrothermal fluids in contact with these formations must have become highly saline, enhancing their metal-carrying capacity. The contrast of common sulphate relicts in the Western Succession, with Cl-rich scapolite in the Eastern Succession, and the potential influence different evaporite assemblages may have had on the ore-types of each region, is discussed in Chapter 11.

IGNEOUS INTRUSIVES

Granites

Seven extensive batholiths occur in the Mount Isa Inlier: the Big Toby, Sybella (Western Succession), Kalkadoon, Ewen (Kalkadoon-Leichhardt Block), Wonga, Williams and Naraku Batholiths (Eastern Succession). Wyborn et al. (1988) identify granite-forming episodes at 1820 - 1800 Ma, 1760 - 1740 Ma, 1700 - 1670 Ma and 1560 - 1480 Ma (also see Table 2.1). The first three episodes formed north-south orientated plutonic belts coeval with major volcanosedimentary sequences, but removed laterally from them. Oldest of these is the Kalkadoon-Ewen batholith, an incompatible-element-depleted suite with I-type granite characteristics, comagmatic with the Leichhardt Volcanics (Wyborn & Page 1983). Volumetrically dominant periods of incompatible-element-enriched, anorogenic, I-type (Chappell & White 1974) magmatism followed, preceded in some instances by small-volume S-type melts, such as the early phases of the Naraku Batholith (Wyborn et al. 1988).

In the Eastern Succession, the Williams Batholith has been a major influence on the geology of the Staveley Belt. It includes in its definition pre-D1 foliated granite within the tectonically emplaced Gin Creek block (Switzer 1987), (i.e., older than 1610 Ma), although younger unfoliated I-type plutons dominate volumetrically, with U-Pb ages between 1560 and 1480 Ma. Joplin & Walker (1961) first noted that deeper levels of the Williams Batholith are exposed in the south, whereas northern plutons are pervasively brecciated and hematitically altered, as is typical in the upper levels of some magma chambers (Wyborn et al. 1988).

The Williams Batholith members in the Starra area are the Mount Dore Granite (Rb/Sr age: 1509 ± 22 Ma; Nisbet et al. 1983), Yellow Waterhole Granite (U/Pb age : 1480 ± 28 Ma; Wyborn et al. 1988) and the Gin Creek Granite, as yet undated.

Mafic Intrusives

Dolerite sills and dykes of at least four generations are recognised by Ellis & Wyborn (1984) (Blake (1987) suggest that there may be many more than this). They have designated

these generations E1 to E4 on geochemical and petrographic characteristics. E1 to E3 are folded by the recognised deformations; the E2-generation Lunch Creek Gabbro is dated at 1740^{+25}_{-20} Ma (Page 1983b). E4 is an east-west post-orogenic dyke suite aged at 1116 ± 12 Ma (Lakeview Dolerite; Page 1983b). Where older dykes intrude calcareous sediments, they are commonly metasomatised to chlorite, biotite or scapolite assemblages.

Folded (E3?) and less-common unfolded (E4) east-west-striking dykes and sills occur throughout the Starra area.

DEFORMATION AND METAMORPHISM

General Features

No major folding or regional metamorphism took place between the Leichhardt volcanism (1865 Ma) and deposition of the Mount Isa Group (~1670 Ma), apart from growth faulting in the major graben systems (Derrick 1982), which is considered to be the probable commencement of the extensional phase of D1 (Etheridge 1987). A poorly understood Amphibolite-grade metamorphic event, correlated with the Barramundi Orogen (Etheridge et al. 1987), affects basement older than ~1865 Ma (e.g. Blake & Page 1988). Beardsmore et al. (1988) suggest that the Soldiers Cap and Fullarton River Groups have experienced as many as six subsequent deformations, of which D1, D2 and D3 are the important dated phases (Bell 1983, Page & Bell 1986, terminology after Bell & Duncan 1978). D1 (1610 Ma) is interpreted to have had an initial extensional phase (D_a of Passchier (1986), D_{1a} in this work), and a subsequent compressional southeast-over-northwest thrusting phase. D2 (1544 Ma) is the major macroscopic folding event, producing regional isoclinal, upright to inclined, north to south shallowly-plunging folds. D3 (1510 Ma) is variably developed along northwest axes, usually as crenulation bands, but also as large shallow to steeply plunging folds, such as those deforming the Mount Isa Pb-Zn ores (Perkins 1981, Beardsmore et al. 1988). They are related by Lister et al. (1986) to transpression along northeast or northwest-trending strike-slip faults. Deformation is discussed in greater detail in chapter 4.

Middle Greenschist to upper Amphibolite grade metamorphism is synchronous with D2 (Blake et al. 1984), commonly retrogressed to lower-middle Greenschist facies close to shears or D3 fold zones. The Eastern Succession metamorphic isograds are unrelated to felsic batholiths (Jaques et al. 1982); the latter have mainly local effects within 100 to 1000 m of their margins.

Gin Creek Block

Switzer (1987) recognised a major D1 extensional zone (Starra Shear) separating the highly deformed and metamorphosed Gin Creek Granite and Double Crossing Metamorphics (Blake 1987), from less-metamorphosed Staveley Formation (Fig. 2.3). He grouped these rocks under the umbrella name "Gin Creek Block" (Fig. 2.2) suggested to be an older terrain tectonically emplaced within the Staveley Formation. In detail the block consists of amphibolite-

grade feldspathic gneiss, biotite and muscovite schist, and two generations of Gin Creek Granite. The boundaries of the granite phases are presently poorly-defined.

Beardsmore et al. (1988) favour a correlation of the Gin Creek Block with pre-Barrumundi orogeny (~1870 Ma) units such as the Plum Mountain Gneiss, on the basis of metamorphic grade.

TECTONIC SETTING

Plumb & Derrick (1975), Glickson et al. (1976) and Wilson (1978) favoured an Andean margin tectonic model for the Mount Isa Inlier, at the edge of a Mid-Proterozoic Australian continent. A continental margin subduction setting explained:

(1) A transition in mafic volcanic geochemistry from continental tholeiites in the east to oceanic tholeiites in the west; felsic volcanics purportedly have K_2O/SiO_2 values which decreased towards the east.

(2) The deeper water environments in which thick turbidite sequences of the Squirrel Hills Belt must have formed, relative to the shallow environments characterising the rest of the Mount Isa Inlier.

(3) Eastward crustal thinning indicated by a predominance of faulting in the east (thick crust) and folding in the west (thin crust); (Dunnet 1976).

With further study, later workers demonstrated some of this evidence to be false. For instance, continental tholeiites are in fact prevalent all over the Mount Isa Inlier (Bultitude & Wyborn 1982). It is unlikely that the inlier was a unique continental margin in the Middle Proterozoic, because rocks of similar age extend eastwards beneath cover to the Georgetown Inlier (Blake 1987). Furthermore, the overall silica distribution in the volcanics is bimodal, most typical of volcanism in extensional settings, with very few rocks in the range of orogenic Andean-type andesite (55 - 63 % SiO_2; Bultitude & Wyborn 1982).

Several workers have now proposed rifting models for the Mount Isa Inlier, including Derrick et al. (1980), Derrick (1982), Wyborn & Blake (1982), Blake (1987), and Beardsmore et al. (1988). (As part of their subduction setting, Glickson et al. (1976) also proposed the extensional Leichhardt River Fault Trough). Blake (1987) subdivided the stratigraphy into Cover Sequence 1, 2 and 3 on the basis of the rifting model of McKenzie (1978), in which each cover sequence has a volcanogenic rift phase overlain by a thermal subsidence or sag-phase. Rift cycles 2 and 3 of Beardsmore et al. (1988) are essentially similar to Blake(1987)'s Cover Sequence 2 and 3.

Current ideas therefore require that the Staveley Formation and other Mary Kathleen Group components formed in an intracratonic setting during regional extension.

REGIONAL METALLOGENESIS

Economically important deposits of Cu, Pb, Zn , Ag, Au, Co, REE and U occur in the region.

Major shale-hosted Pb-Zn-Ag deposits occur in the Mount Isa, McNamara (Hilton, Mount Isa, Lady Loretta) and Mary Kathleen Groups (Dugald River), suggesting at least two episodes of this ore-type in the region, one at 1780 - 1740 Ma, and the other at ~ 1670 Ma (Fig. 2.1). Sub-economic stratiform BIF-hosted Pb-Zn deposits also occur in the Squirrel Hills Belt, including Pegmont (12 mt of ~ 10 % Pb + Zn), Fairmile, Dingo and Muramungee (Stanton & Vaughan 1979, Vaughan & Stanton 1986, Blake et al. 1984).

Epigenetic Cu deposits are common in the Eastern and Western Successions. Cu-sulphides commonly formed by replacement of pre-existing sulphide zones, of which the Mount Isa copper ore body is the grandest example (Perkins 1981, Andrew et al., in press). Others include Mammoth, Paradise Valley, Gunpowder Creek and Mount Kelly (Scott et al. 1985). Beardsmore (1988) has named Eastern Succession shear and vein Cu-deposits "Selwyn"-style ores. Those mines which have produced over 1000 tonnes of Cu in the Eastern Succession were the Answer, Duchess, Hampden Group, Mount Elliott, Saint Mungo, Trekelano and Young Australia (Blake et al. 1984). Historical production in the Starra area is summarised in Table 2.2.

Shear-controlled uranium, and REE have been mined at Mary Kathleen and smaller satellite mines, ~ 80 km west of Cloncurry, hosted by Corella Formation sediments. Page (1983b) estimates that uraninite was concentrated at ~ 1740 Ma, but the present day ore distribution formed at 1550 Ma during deformation and metamorphism.

Minor vein and shear-hosted Co, Mo and W mines occur throughout the Eastern Succession. The largest is the Mount Cobalt mine, with indicated reserves of 60,000 t of 1.25 % Co (see also Chapter 11).

A resurgence of exploration in the Eastern Succession has located interesting new variants of transgressive "Selwyn"-style mineralisation. These include Mt. Dore, Swan, and new mineralisation at Hampden. Mt. Dore is a large, low-grade Cu deposit on the Mt. Dore Fault, overthrust by the Mt. Dore Granite (Ophel 1980, Scott 1986, Beardsmore 1988). Swan is a probable extension of the historically-mined Mount Elliott mineralisation, consisting of a complex Cu-Au-REE element assemblage in a "pipe"-like magnetite zone, hosted by metasomatised Staveley Formation calc-silicates (Nyvlt 1980). A resource of 42 mt grading 0.69 % Cu, and o.4 g/t Au has been outlined (Nisbet 1983). The Hampden Mine has recently been re-evaluated by Metana Minerals, identifying a resource of 2 mt grading 5 % Cu and 2.3 ppm Au (Metals Gazette, February, 1989).

Starra and Trough Tank ironstone-hosted Cu-Au ores are a new variant in the area (Derrick 1984). They possess features of the stratiform BIF-hosted Pb-Zn ores, as well as Selwyn-style vein-Cu deposits, which will ensure discussion of their origin for many years to come.

Mine	Grid reference	Ore (t)	Cu (t)	Au (kg)	Other (kg)
Regional Mines > 1000 t Cu production					
Answer	VB340035	10826	1023	11.1	-
Duchess	UB818374	204865	25155	76.1	61.8 (Ag)
Hampden Group	VB487465	214852	15114	376.1	173.6 (Ag)
Hampden West	VB438479	44	8	-	-
Mount Elliott	VB485178	268201	24862	1054.7	-
Saint Mungo	UB809080	6701	1567	-	-
Trekelano	UB859238	187939	20472	423.2	338.6 (Ag)
Young Australia	VB383403	174333	3911	-	-
Historical mines in the Starra area					
Belgium	VB433765	348	89	-	-
Mt. Dore	VB480045	16	5.9	-	-
Mt. Cobalt	VA490955	20000	-	-	753 t (Co)
Stuart	VA460920	200	?	-	-

Table 2.2 *A summary of the shear and vein-hosted "Selwyn"-style Cu deposits in the Starra region, with production greater than 1000 t Cu, as well as some smaller mines from the Starra area. Locational grid references refer to the BMR 1:250 000 Duchess-Urandangi geological sheet of Blake et al. (1984). Data Sources: Blake et al. (1988), Kary & Harley (in press).*

CHAPTER 3

GEOLOGY OF THE STARRA AND TROUGH TANK AU-CU DEPOSITS AND THEIR ENVIRONS.

INTRODUCTION

The aim of this chapter is to examine the geology of the Starra and Trough Tank ores and their environs to provide a framework of constraints for the conditions of ore formation. Aspects of the structure of the Starra area and its ores are discussed in chapter 4, whereas Trough Tank structure, metamorphism and geology are all combined here because of the more cursory attention they have received in this study.

STARRA

Stratigraphic Overview

A simplified diagram of the local Starra geology is provided in Fig. 3.1. A horizon of BIF and related ironstones, including the mineralised zones, is termed the Starra Iron Formation in this study, although they are more generally known as the Selwyn Hematites (Kary & Harley, in press). It crops out intermittently over 610 km sq. near the base of the Staveley Formation. Like the Staveley Formation, the ironstone distribution forms a confined north-south belt, stretching from beneath Cambrian cover at the Mort River, north 40 km to the tip of the Gin Creek Block, where it widens to include western extensions such as the Limestone Creek ironstones. These are linked magnetically to the main north-south trends.

The strongly magnetic mineralised rocks occur in a 6.5 km long segment of prominent ironstone ridges known as the Western Hematites, separated by the D2(MP) Starra Syncline from a second unmineralised non-magnetic ridge-line, termed the Eastern Hematites (Kary & Harley, in press). The Starra Shear is a 1 km wide north-south zone of high strain commencing immediately east of the Western Hematites. A second important structural element is the Mount Dore Fault Zone (Fig. 3.1; Beardsmore et al. (1988)), which forms the linear western margin of the post-orogenic tourmaline-biotite Mt Dore and Yellow Waterhole Granites. Similar magnetic granite intrudes pre- to syn-orogenic, non-magnetic, muscovite-rich granite to form the composite Gin Creek Granite (Switzer 1987, Wyborn et al. 1988); uncertainty presently surrounds the extent of its boundaries in the Gin Creek Block.

Kuridala Formation

Comment on the Kuridala Formation is restricted to lithologies close to the ore

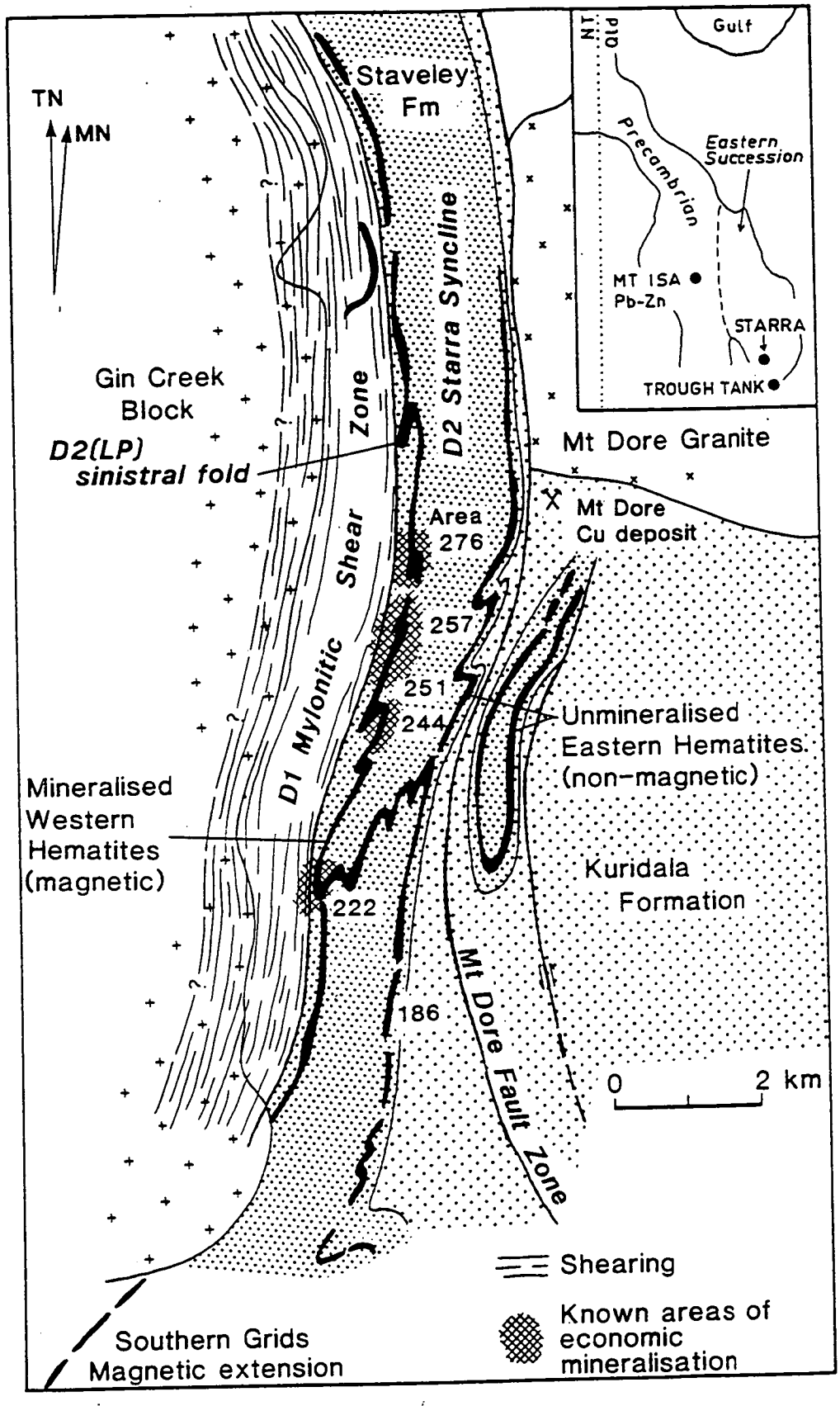

Figure 3.1 *Location and regional geology of the Starra area, with the position of the lodes marked by cross-hatching. An important element of the area is the D1 mylonitic shear (Starra Shear), separating the older high-grade Gin Creek Block from the younger Staveley Formation. The Starra Syncline is a major north-south trending D2(MP) fold separating the Eastern and Western Hematites.*

horizon, and to those marginal to the Starra and Pyramids Synclines (Fig. 3.2). These include micaceous and carbonaceous schist (host to the Mt. Dore copper deposit), and quartzite, recognised by Leishman (1983) as the arbitrarily-defined top of the formation (Pqz: Fig. 3.2). Interfingering and gradational contacts are common between these lithologies. Quartzite mainly occurs within 1 km of the Mt. Dore Fault Zone, whereas variably carbonaceous schist and meta-greywacke occur extensively to the east (Beardsmore et al. 1988).

Quartzite was examined in detail in the Pyramids Syncline and Area 260 of the Eastern Hematites (Fig. 3.3). At its base it is transitional to strongly cleaved carbonaceous schist. Its thickness varies from 0 to ~ 25 m in these areas, elsewhere attaining a maximum fold-thickened width of 100 m (Leishman 1983). It is generally massive and fine-grained, locally carbonaceous, with minor pebbly intervals and bedding-parallel lamination. Conglomerate directly overlying the quartzite in Area 260 (Grid position 25550N,16350E, Fig. 3.3), contains subrounded to angular boulders up to 1 m in diameter, averaging 10 cm (Fig. 3.4A). On Leishmans (1983) definition the 0 to 10 m thick conglomerate is part of the Staveley Formation; however, the boulders commonly are identical to underlying quartzite, are in places enclosed by it, and include a small population of carbonaceous fragments, as well as fragments tectonically folded prior to deposition.

Petrographic analysis of the clasts and matrix of the conglomerate place the top of the Kuridala Formation in a critical new context. Massive quartzite samples and quartzite clasts at Area 260 are identified as silicified carbonates. The most common lithotype is silicified rounded oosparite (classification of Folk (1962)), in which ~ 0.5 mm oolite pseudomorphs comprise greater than 70 % of the rock. The matrix is silicified silty micaceous micrite containing minor oolites and tabular sparry fragments interpreted as flat pebble intraclasts (Fig. 3.4C & E). Silica replacement affects resedimented carbonate clasts and matrix alike, although it is not apparent in stratigraphically higher Staveley carbonates. Metamorphism recrystallised the resulting quartz fabric into sub-polygonal grains ~ 90 μm across, except where a high density of fine original inclusions in the centres of ooliths promoted smaller sub-grains, ~ 30 μm in diameter.

On the basis of the observed textures, an origin for the uppermost Kuridala Formation quartzite as a silicified fault zone is rejected (Nisbet 1983).

Answer Slate/Kuridala Formation

The ore sequence on the western limb of the Starra Syncline is underlain by 50 – 100 m of chlorite-biotite (± cordierite, andalusite) schist (here termed the Harley Member), identified by Leishman (1983) with the carbonaceous Answer Slate. The validity of this correlation is questioned here because of the lack of carbonaceous sediment or graphitic schist, and the basaltic to intermediate character of some rocks (Laing et al. 1988; Davidson et al. 1988): tholeiitic basalt has been mapped in this stratigraphic position to the

Figure 3.2 *A detailed geological map of the area south of Starra, based in part on the mapping of Leishman (1983).*

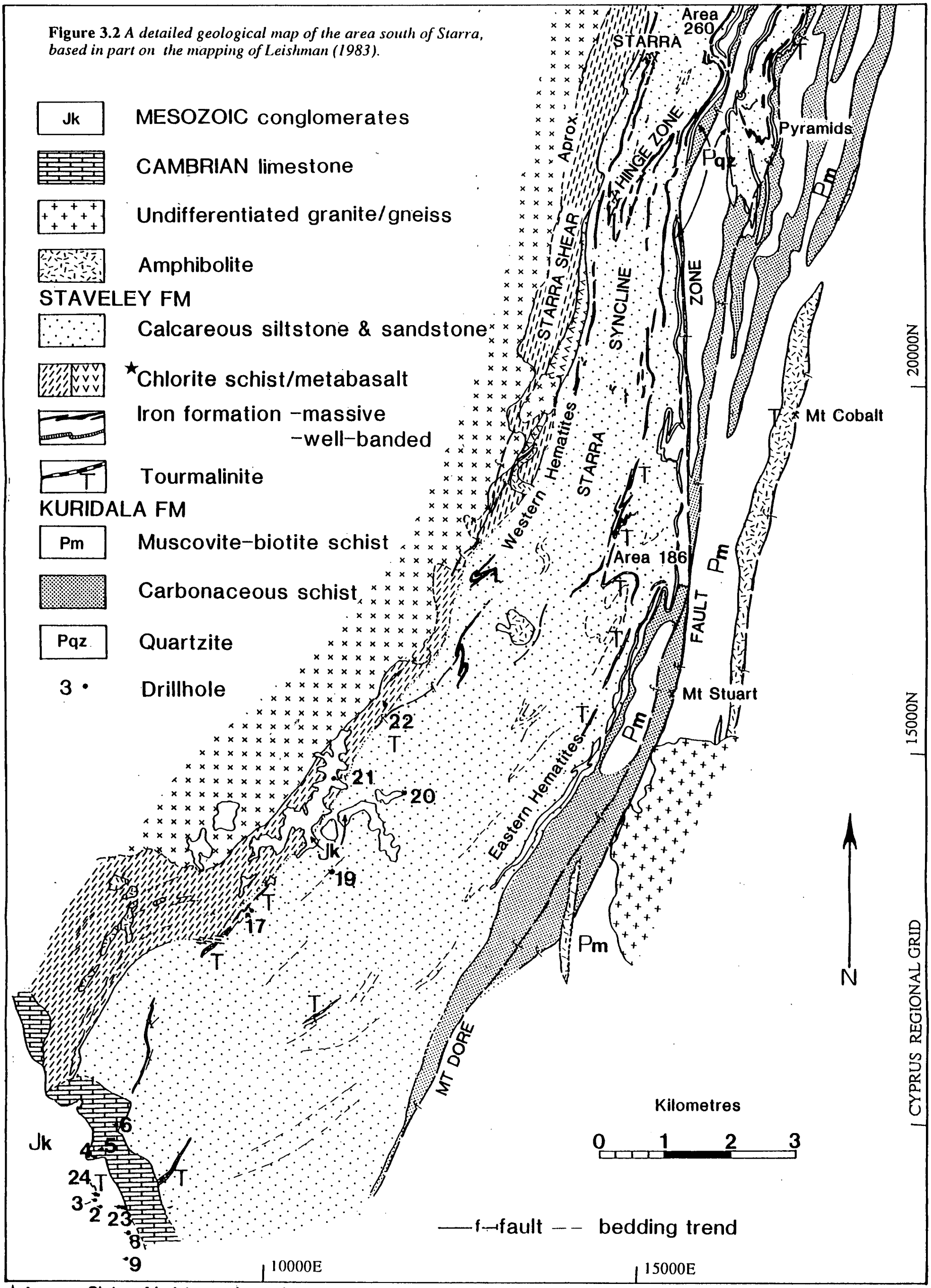

★ Answer Slate of Leishman (1983)

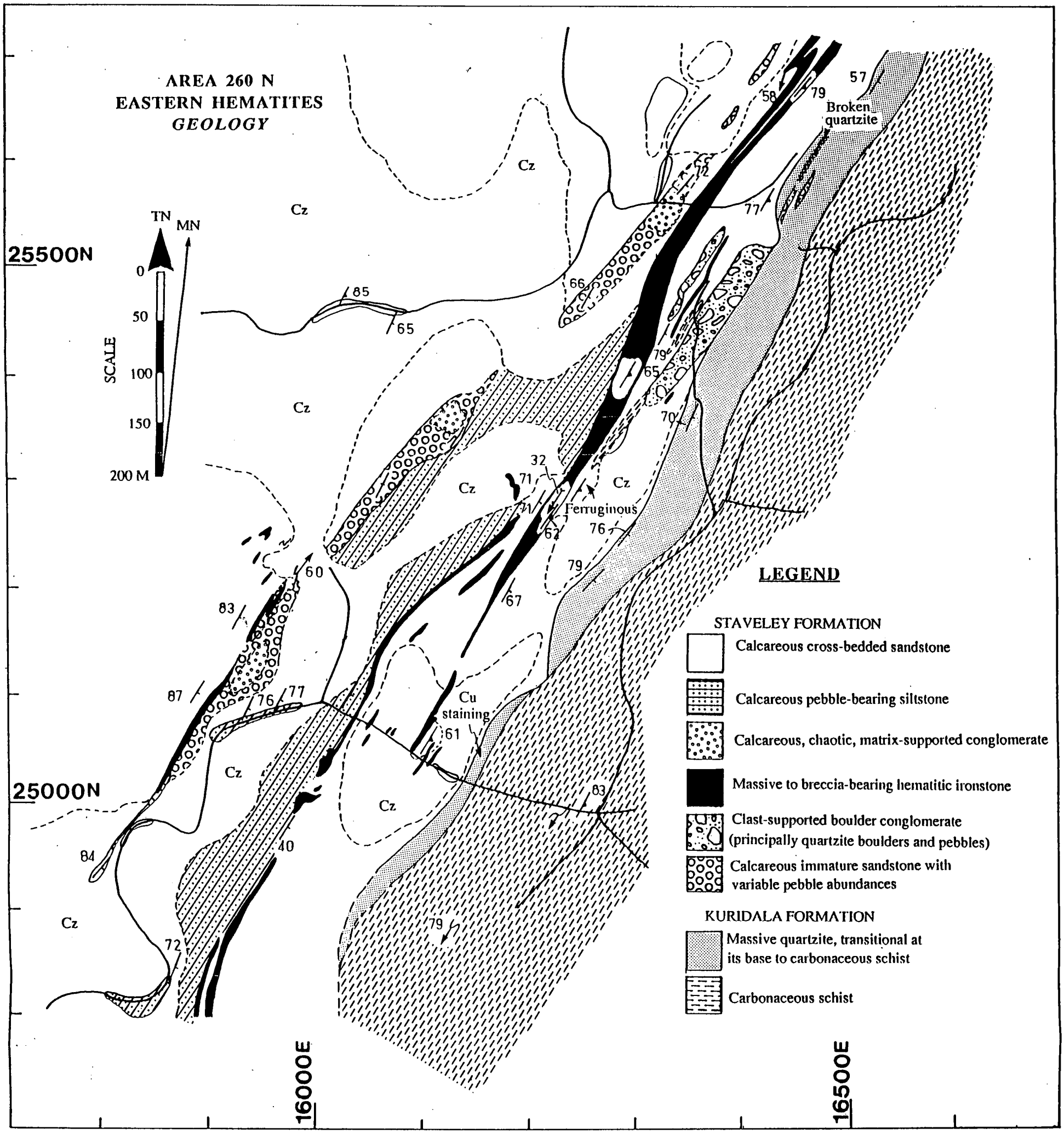

Figure 3.3 *A detailed geological map of Area 260, Eastern Hematites. The map covers the Kuridala-Staveley Formation boundary, Staveley Formation conglomerates, and breccia-hosting hematitic ironstone. The present Selwyn Mine administration block is sited approximately 100 m south-west of the lower left corner of the map; the grid uses Cyprus Minerals regional coordinates.*

north and south. The preferred solution is to place the base of the Staveley Formation below the chloritic interval, and assigning underlying biotite-muscovite and feldspar-quartz schist to the Kuridala Formation.

Staveley Formation

The Dominant Lithologies and their Distribution

Regionally the Staveley Formation consists of shallow-water calcareous cross-bedded psammite and subordinate limestone (also see chapter 2). In the Starra area the exposed basal 500 m sequence contains lithological associations which were derived from a spectrum of depositional settings. Basic and intermediate volcanics/volcanoclastics underlie the ironstones in the Mount Elliott, Limestone Creek and Southern Grids areas (Leishman 1983; Kary & Harley, in press) and are suspected in the mineralised area (Davidson et al. 1988, Laing et al. 1988) (Fig. 3.2). The equivalent seqence below the Eastern Hematites is dominantly clastic, 20 to 100 m thick, including the aforementioned conglomerates, and calcareous siltstones and sandstones. Richly scapolitic beds, mudcracks, and pseudomorphs after the evaporites halite and gypsum (detailed in chapter 8) all support the shallow to subaerial depositional setting identified more widely (Derrick et al. 1977a, Blake et al. 1984) (Fig. 3.4 B, D & F). The east-west distribution of facies is shown schematically in Fig. 3.5. Above the Starra Iron Formation, oxidised sediments are widespread, changing from micritic, silty, massive to banded limestone in the Belgium Mine area (located on Fig. 4.1), to calcareous cross-bedded sandstones in the central and eastern Starra Syncline. South of the Hinge Zone (Fig. 3.2) the main lithology is fine-grained, massive, feldspathic siltstone, overprinted by a strong fracture cleavage. The below-wavebase calcarenites, shales and cherts of the ore hangingwall are a significant facies variant, discussed in more detail under "Ore Sequence".

Conglomerates

A detailed analysis of rock-types close to the eastern Staveley-Kuridala Formation contact was made at Area 260 (Fig. 3.3). Beardsmore (1986) referred to coarse beds above the Kuridala Formation quartzite as "The Basal Conglomerate". In fact at least two conglomeratic levels occur. Lowermost is the conglomerate of quartzite boulders and pebbles described above. This is overlain by 10 to 40 m of pebble-bearing calcareous siltstone and lenses of carbonaceous shale, immediately underlying the main (breccia-bearing) ironstone. A second 50 – 100 m thick sequence of upwardly-fining, 'Red Bed'-style pebble and evaporite-bearing siltstone (Figs. 3.4 D & F) is overlain abruptly by the second conglomerate horizon, consisting of calcareous sub-imbricate chip conglomerate (5 – 30 m thick),in which the clasts are supported by a matrix of quartz-sand and gravel. (These are labelled "Psr" on the maps of Leishman (1983)). Within these lenses, several restricted (5 –10 m wide) zones of very coarse, unstructured, siltstone (Fig. 3.4B)

Figure 3.4

A. *A plain light photomicrograph of a clast-supported conglomerate (SG 65) found at the Kuridala/Staveley Formation boundary. Individual clasts consist mainly of quartzite boulders up to 1 m diameter, which are known to be silicified carbonate fragments of the underlying Kuridala Formation quartzite. The sample was collected at 25500N, 16350E, Fig. 3.3.*

B. *Outcropping poorly-structured conglomerate within the Staveley Formation, interpreted as the product of fluvial debris-flow processes (25130N, 15940E, Fig. 3.3).*

C. *Plain light microphotograph of a "ghosted" oolite-bearing intraclast, a detail from Fig. 3.4A. The silica-replaced carbonate fabric is enhanced by small mineral inclusions.*

D. *A mud-crack breccia in "Red Bed"-facies Staveley Formation, in which small needle-like pits of a former evaporite mineral (gypsum?) are preserved (25100N, 16040E, Fig. 3.3).*

E. *A crossed polars view of (C), illustrating the recrystallised nature of the quartz fabric, and the differential response of former oolites to recrystallisation.*

F. *Gypsum? pseudomorphs in "Red Bed" facies Staveley Formation.*

G. *Plain-light photomicrograph. A hematitised conglomerate, forming part of the Eastern Hematite ironstones (SG 69: 25250N, 16120E, Fig. 3.3). Although the matrix is replaced by hematite, the sub-imbricate clasts remain well-preserved.*

H. *A probable tectonic breccia with a hematite matrix. A tectonic origin is deduced for this example because the clasts are all similar, and could be reassembled to form a uniform lithology. This is not the case for plate G. (Location 22500N, 16000E, Fig. 3.2).*

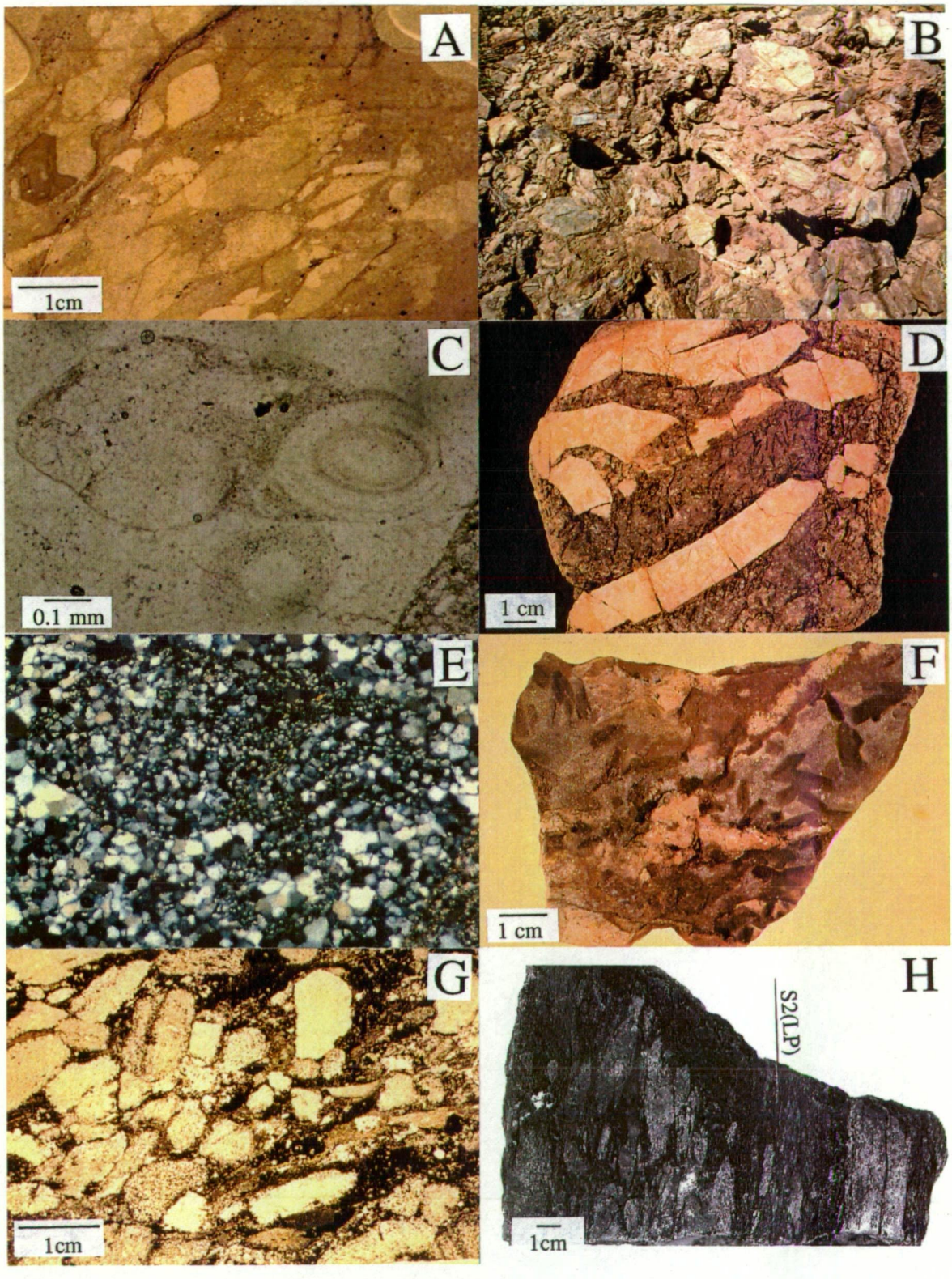
A
1cm
B
C
0.1 mm
D
1 cm
E
F
1 cm
G
1cm
H
S2(LP)
1cm

and quartzite fragments occur (up to 50 cm in diameter).

The upper conglomerate has many of the features of prograding alluvial fans

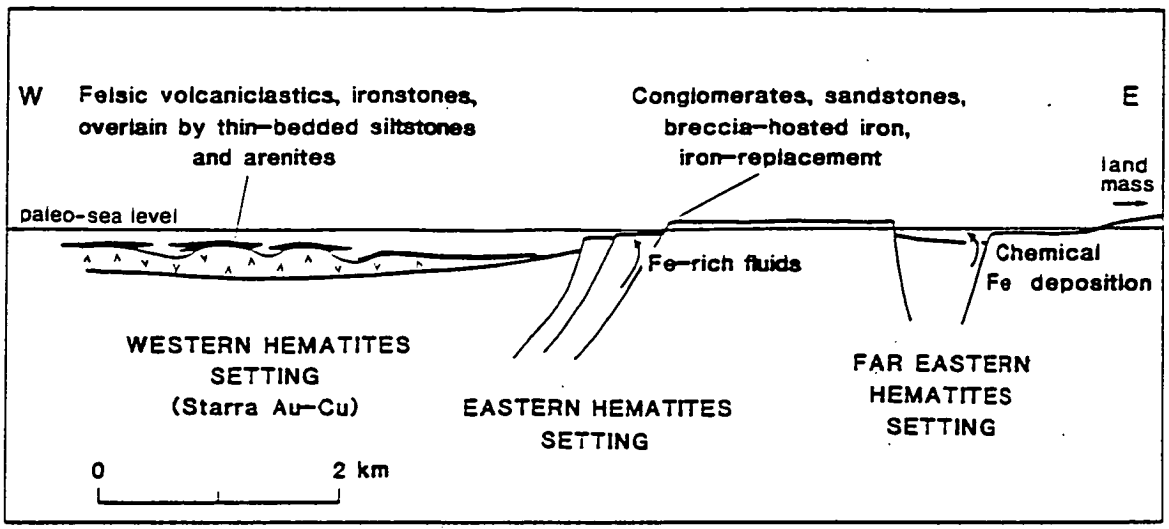

Figure 3.5 *Schematic east-west paleogeographic section at the commencement of Staveley Formation deposition.*

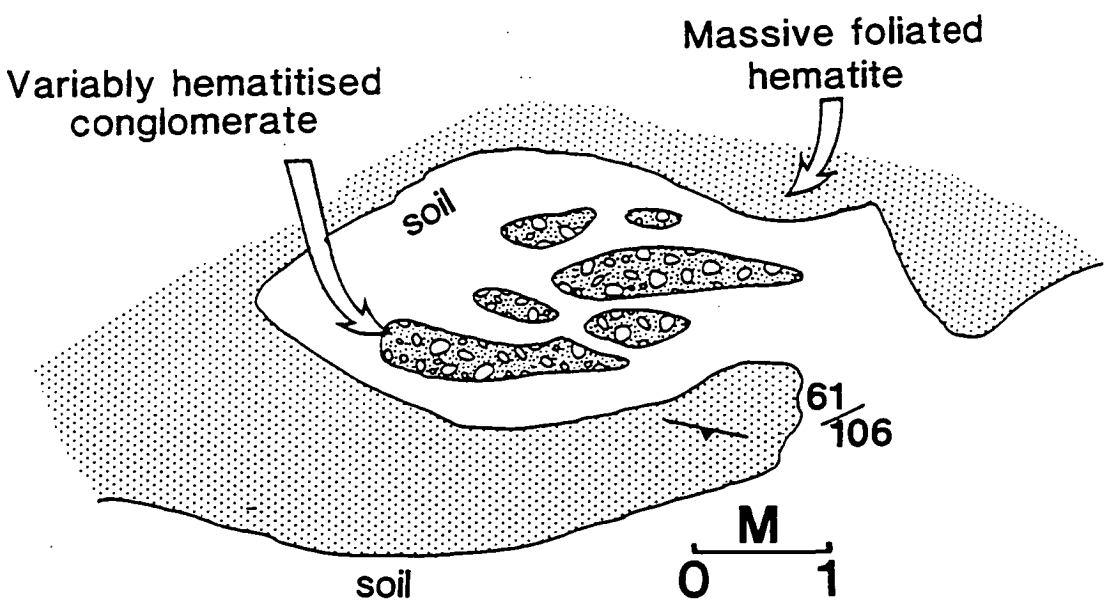

Figure 3.6 *A field sketch of the irregular contact relationships between massive to breccia-bearing hematitic ironstone, and Staveley Formation conglomerate, exposed at 25070N, 16100E, Fig. 3.3, Eastern Hematites.*

(Beardsmore 1986), in which channels were choked by debris flows, represented by the coarser zones. 'Red Bed' pebble-bearing siltstone intercalations could have resulted from periodic reworking of such coastal alluvial fans during marine transgression (e.g., Rust & Koster 1984).

The Staveley-Kuridala Formation Boundary

The above observations bear upon the nature of the Staveley – Kuridala Formation contact, regarded by previous workers as disconformable to unconformable (Blake et al. 1984), or tectonic (Beardsmore et al. 1988). The identification of the underlying quartzite as a probable silicified carbonate closely links the two units as part of one calcareous episode. Carbonate silicification could have developed during either humid Mid-Proterozoic weathering (Fairbridge 1983), or hydrothermal alteration, such as that which characterises Carlin-style epithermal Au deposits of the United States (Berger 1988). The former alternative is preferred because of the regional extent of the silicification (Fig. 3.2). Silica replacement must have accompanied the exposure of the Kuridala Formation, during which time SiO_2-rich meteoric waters interacted with and wholly replaced the carbonate.

Together with conformable bedding and younging, these observations support a disconformity of unknown duration across the Staveley/Kuridala Formation boundary.

Lateral Iron Formation and Tourmalinite

General Features

Along strike from the mineralised segment, the Starra Iron Formation become podiform and hematitic. In the Eastern Hematites, hematitic ironstone is commonly brecciated and breccia-hosting (Leishman, 1983), but south of the hinge becomes massive to well-banded. It is consistently barium-rich (0.1-1.5%). These massive hematitic ironstones grade to well-banded cherty BIF ~5 km south of the mineralised segment (Fig. 3.2). The ironstone categories shown in Fig. 3.8 are based on the presence or absence of banding, the known presence of mineralisation, and the abundance of hematite, quartz and magnetite. They are:

(1) *Mineralised ore environment ironstones* — massive or banded magnetite-quartz-sulphide assemblages; arbitrarily defined as > 0.5 ppm Au.

(2) *Barren ore environment ironstone* — massive stratiform hematite±pyrite within an arbitrary 500 m of an ore zone; arbitrarily defined as having < 0.5 ppm Au.

(3) *Barren and mineralised breccia-bearing ironstones* — variably chloritised polymict fragments in a hematitic matrix.

(4) *Barren, distal, massive ironstones* — stratiform, massive hematite commencing an arbitrary 500 m from ore; Au is generally < 0.3 ppm.

(5) *Barren, distal, cherty BIFs* — stratiform, well-banded, silica-rich units with the textural character of sedimentary iron formations; Au < 0.1 ppm.

The unmineralised ironstone types are detailed below. Note that types (2) and (4) are amalgamated in Fig. 3.8.

Barren, Distal, Massive Ironstone

South of the Hinge Zone in the Eastern and Western Hematites, this rock-type forms up to three semi-continuous, non-magnetic, folded horizons 0.5 to 10 m thick. In outcrop, sharp contacts are made with the conformable host-rocks. Any original banding, or sedimentary features such as ferruginous oolites (which are common in sedimentary hematite iron ores, such as the Minette-type (Maynard 1983)), have usually been destroyed by a strong bedding-parallel foliation, consisting of elongate hematite crystals (50 to 200 μm long), polygonal quartz (~5 to 15 %), minor barite and rutile. Transitional relationships between thick massive ironstone and thinner cherty BIF occur at Area 186 (Eastern Hematites: detailed in chapter 6), the Pyramids Hematites, and the Western Hematites 5 km south of the Hinge Zone.

All of these features are most compatible with aqueous deposition of iron at a sediment/water interface, although there is no compelling evidence that hematite was the primary phase.

Barren, distal, cherty BIF

Cherty BIFs (individually 2 to 5 m thick) are the southernmost iron facies in the Staveley Formation (Fig. 3.8). Several jaspilitic outcrops also occur at Limestone Creek. Hematitic oxide facies is most common (magnetic at depth), but carbonate and manganese facies are also developed, containing Ba-rich feldspar, spessartine garnet, apatite, actinolite and epidote (drillhole STP 24, Fig.3.2). Dravitic tourmaline becomes a constant accessory in iron-formation south of Area 186, additionally forming 1 – 5 m thick banded beds ("tourmalinites") immediately overlying BIF (detailed in chapter 9). In several instances gypsum pseudomorphs occur in the iron-formation, with closely associated scapolite in underlying beds, both taken to indicate the former presence of evaporites.

Cherty BIF is best exposed as a linear ridge 2 km north of the Mort River (Fig. 3.2; iron formation immediately north of hole 6), where it contains many features of classical Hamersley-style BIFs (Trendall 1973a, 1973b, James & Trendall 1982). Nine major hematite-chert macrobands 0.8 to 1.8 m thick occur in a ferruginous 27 m interval, overlain by a further 73 m of hematitic feldspathic sandstone hosting sporadic 10 – 20 cm thick BIFs. Some beds consist of more massive, variably hematitic, feldspathic chert. Mesobands are 0.5 to 2 cm wide alternations of hematite-rich and hematite-poor chert, which at a fine scale contains 1 – 2 mm thick microbands. An early diagenetic origin is ascribed to bedding-parallel chert nodules and pods 5 to 15 cm long, after Gole (1981) and Visser (1985) (Figs. 3.7, 3.9B). The preservation of the delicate lamination indicates these

rocks have not been subjected to high strain.

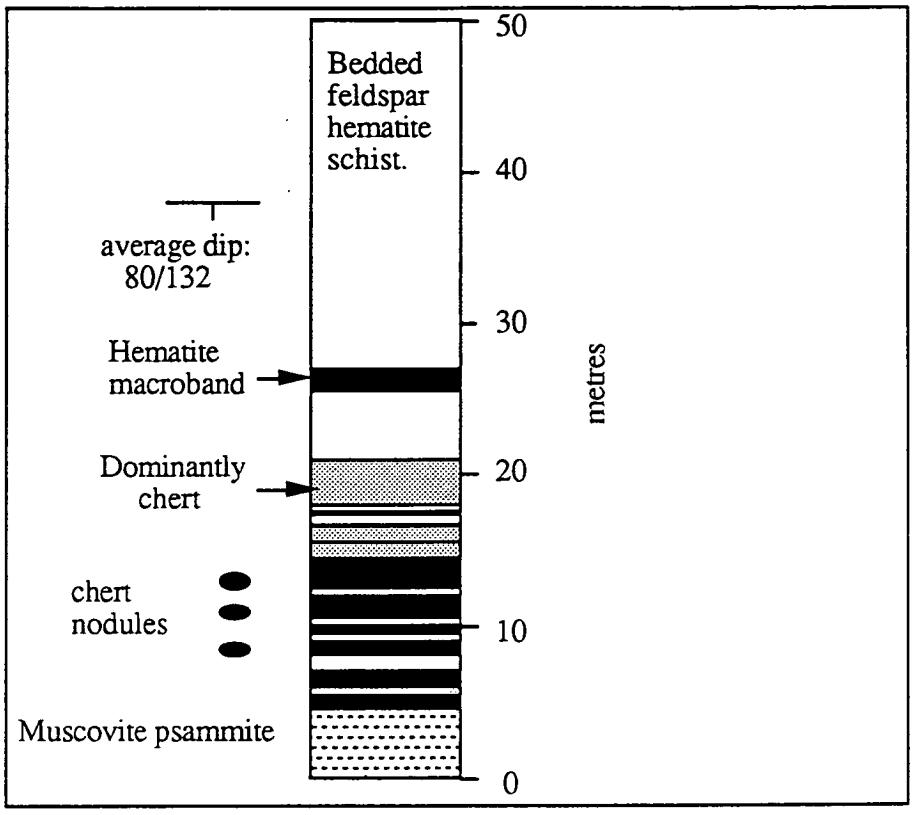

Figure 3.7 *Measured section of Hamersley-style BIF 2 km north of the Mort River, within the Western Hematites.*

Mineralised ironstone away from Starra

Low grade Au-Cu -W±Pb & Zn mineralisation characterises 12 km of thin magnetite-quartz BIF 2 to 10 km northwest of Mount Elliott (Fig. 4.1). The Mobs Lease and Blockbuster prospects contain sub-economic Au in the range 0.5 to 2.0 ppm, at the centre of a more dispersed Au halo, detailed in chapter 6. Significantly the BIFs overlie or occur close to the tops of locally extensive amygdaloidal continental tholeiites (up to 700 m thick) in an area of low strain. Small to medium-scale folds occur, but are not associated with the main mineralised segments (Fig. 3.9H). Hangingwall sediments consist of graphitic to calcareous pelites, psammopelites and psammites typical of the northern Staveley Formation.

Limestone Creek contains a less extensive area of low-grade Au (< 2 ppm Au on average) in massive hematite-magnetite ironstone, characterised by high strain. Some Au occurs in clearly cross-cutting hematite-quartz veins 5 to 15 m thick. In similarity to Starra, the Limestone Creek area contains magnetite-hematite footwall alteration, albitic host rocks (intermediate volcanics?: Beardsmore, pers. comm. (1986)), and tourmaline-rich horizons. Petrographically this tourmaline forms ultrafine crystals in a sheared quartz matrix, interpreted as a metasomatic replacement texture of uncertain timing — several enclosed

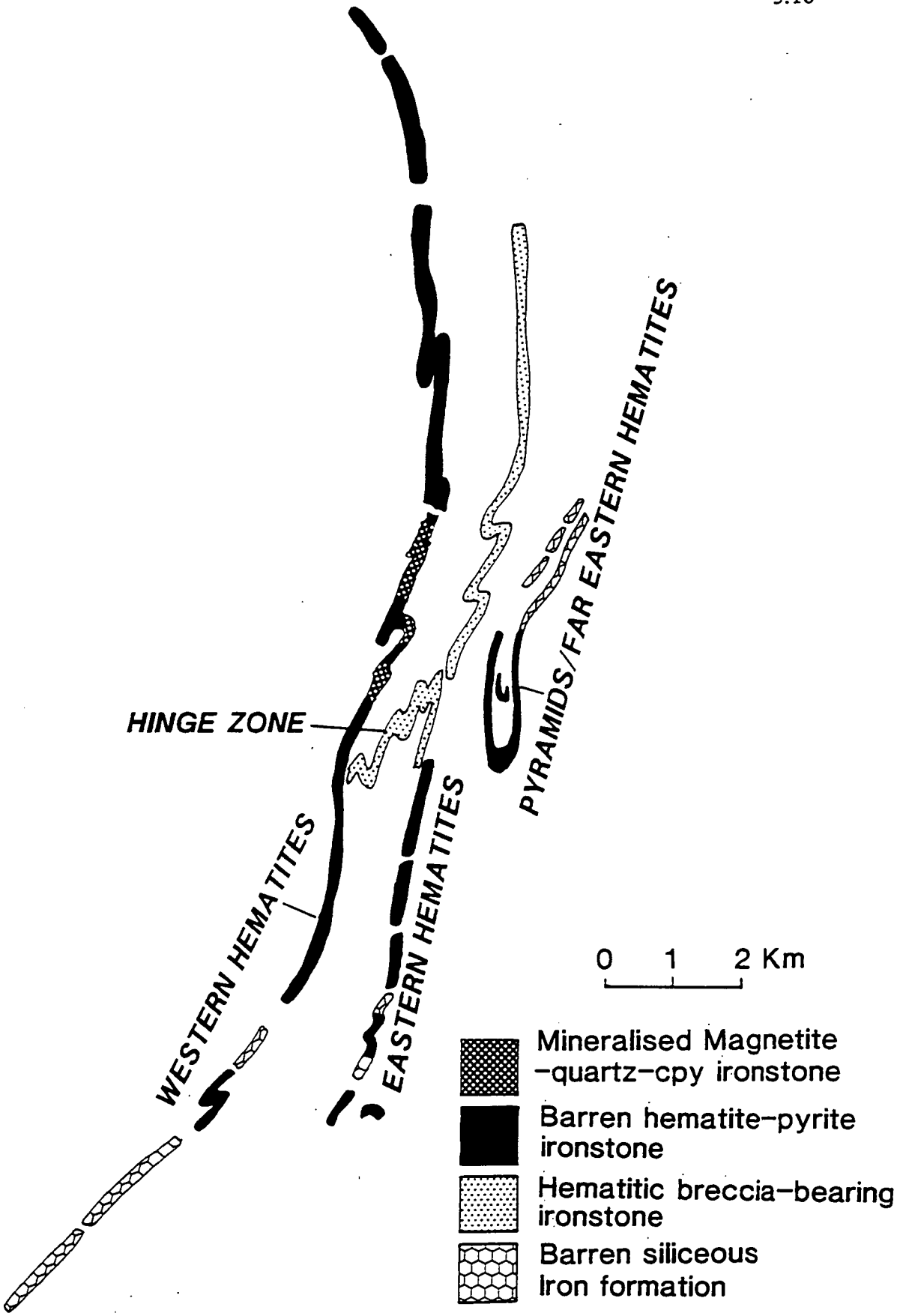

Figure 3.8 *Regional distribution of different ironstone types in the Starra Iron Formation Member of the Staveley Formation.*

Figure 3.9

A. *A drillcore sample (St 239) from the Area 222 mineralised breccia, illustrating the polymictic and relatively unstrained nature of the clasts (location: STQ-200/12 m). Small ironstone fragments are scattered throughout the rock; in other samples some attain a 4 to 5 cm diameter.The 1 m interval from which this rock was obtained contained 5100 ppm Cu, and 0.07 ppm Au.*

B. *A photomicrograph of the margin of an ironstone fragment pictured in "A", illustrating the contrasting hematite textures in the clast (left) compared to the replacive matrix (right). Other phases in the matrix are muscovite (yellowish), and quartz.*

C. *Drillcore sample St 240, Area 222. Some metasediment clasts appear to have fractured within the conglomerate, with the break subsequently filled by matrix. The samples are surprisingly free of the effects of deformation.(Location: STQ-200/18 m).*

D. *Advanced hematite replacement of Area 222 conglomerate, in which the silicate clasts are progressively replaced from their margins inward by hematite, chlorite and muscovite (after sericite). Replacement is particularly well-illustrated by the bleached rim of the largest remaining clast, caused by the early removal of sheet-silicates.(Location: St 243, STQ-200/31 m). The 1 m interval from which this rock was obtained contained 3680 ppm Cu and 0.580 ppm Au.*

E. *Typical surface sample of Area 257 "Western Zone" mineralised magnetite-quartz-chalcopyrite ironstone. Crude banding is commonly present in this area.*

F. *(Top). Hematite-magnetite±pyrite ironstone (barren, STQ 85-119/115.7 m), in sharp contact with veined and deformed albitic footwall, Area 257. Magnetite in hematite ironstones is commonly porphyroblastic, as shown. (Bottom). Poorly layered mineralised ironstone, Area 257 (St 149, STQ-86-243/102m).*

G. *Cherty Banded Iron Formation approximately 20 km south of Starra (11000N, 13000E, Fig. 3.2). The chert mesobands pinch and swell, or form discrete ovoid lenses.*

H. *Cherty BIF from Mobs Lease (for its location see Fig. 4.1). Well-banded iron formation in this area contains anomalously high Cu and Au, immediately above recognisably vesicular basalt.*

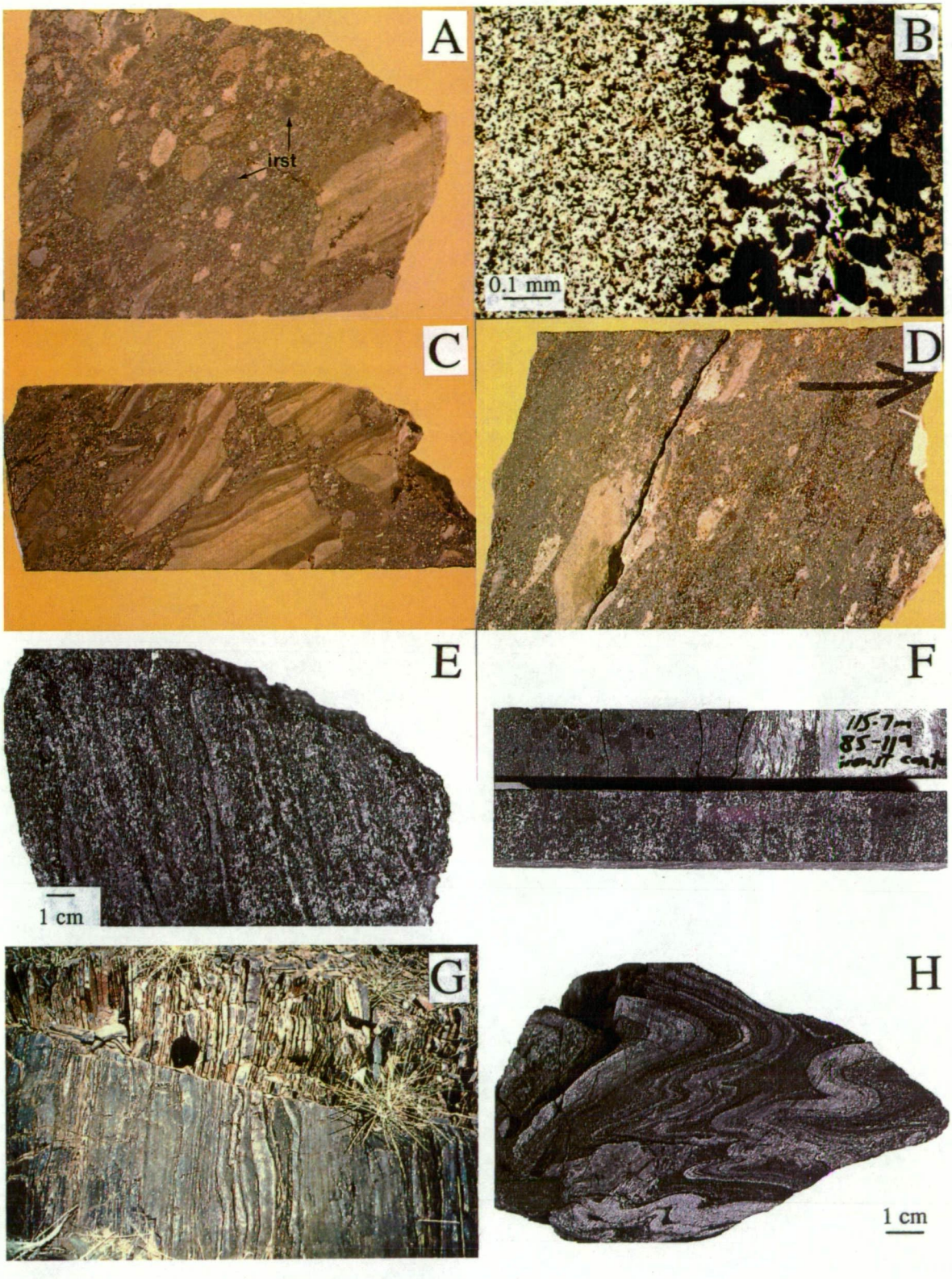
A
irst
B
0.1 mm
C
D
E
1 cm
F
115-7m
85-119
H
1 cm

clasts of rounded metaquartzite suggests a similarity with the polymict ironstone breccias of Area 222, described below.

Breccia-rich hematitic ironstone

Eastern Hematites ironstones north of (and including) the Hinge Zone, (Fig.3.8) differ from the Western Hematites by containing abundant breccia fragments, variably altered to hematite. An understanding of these breccias is central to the origin of the enclosing ironstones. They have previously mainly been regarded as tectonic, developed because of competency contrasts between ironstones and siliceous layers (Leishman 1983, Morrison 1986); the most extreme tectonic interpretation envisages them to be hematite-filled shears (Ransom 1986, Switzer et al. 1988). Kary & Harley (in press) maintained an open mind on genesis, but noted the breccias at Area 222 were polymictic.

Breccia textures do vary in form within the Hinge Zone ironstones, from types which are indisputably tectonically-related (Fig.3.4H)to the dominant texture — that of discrete siliceous clasts in a hematitic matrix, of less determinate origin (Fig. 3.4G). Tectonic breccias in the Eastern Hematites are similar to tectonic transposition zones documented at Areas 251 and 257, commonly associated with the short limb of sinistral F2(LP) folds (chapter 4). Criteria for the assignment of a tectonic origin are (1) a similarity between adjacent clasts, and between the clasts and the host rock; (2) the presence of rootless thickened fold hinges, wedges and lenses, as well as clasts discounted as sedimentary because of their highly irregular shapes; (3) an alignment of clasts with the cleavage. The first point, but not the second and third, could also characterise pre-tectonic intraformational brecciation. Leishman (1983) found that many tectonic breccias in ironstone graded to unbrecciated schist, and hence were difficult to map.

In most ironstone breccias, the tectonic criteria cannot be satisfied. The least deformed of these contain polymict fragments with no obvious elongation; which under high strain are transformed into cleavage-parallel lenses in a cleaved massive hematite matrix.

Further insights into the origin of these breccias has been gained through detailed work at Area 260N (Eastern Hematites) and Area 222, as outlined below.

Area 260N (Eastern Hematites): This area was mapped in detail particularly because major D2(LP) folds are absent, and because three types of sedimentary breccia are well-exposed in the Staveley Formation (see previous discussion and Fig. 3.3).

Polymict hematite breccias (Fig. 3.4G) occur as a major series of 1– 10 m thick pods and semi-continuous horizons commencing ~50 m above the Kuridala Formation quartzite; a second less-significant horizon occurs ~ 120 m above the first, within a pebble-bearing siltstone. In most instances the ironstone-sediment contacts are conformable, but distinctly irregular contacts are also present, in which pebbly ironstone partially encloses conglomeratic quartzite (Fig. 3.6). Rounded to sub-rounded quartzite granules, pebbles

and cobbles are abundant within the ironstones, in some cases forming an imbricate clast-supported fabric. Strongly foliated micaceous clasts are less distinct because of variable hematite replacement inwards from their margins. In one clear instance, (25000N, 15850E, Fig. 3.3), the uppermost massive ironstone can be traced southwards into a conglomerate with a hematite matrix, which merges laterally into a muscovite-rich limonitic pebble-bearing siltstone.

Petrographic examination of these ironstones confirmed that in the least strained examples, polymict clasts occur in an imbricate fabric — the overall texture is very similar to conglomerates found lower in the sequence. Granoblastic quartzite clasts (after oolitic limestone) predominate. These are least altered by hematite; whereas clasts such as micaceous siltstone, are preferentially hematite-altered, in a process resulting in the destruction of the sharp form of the clast boundary, and the development of a marginal zone of silica and dusty hematite, from which mica is absent. Hematite and minor exsolved ilmenite forms irregular needles and nodules, with an average grain-size of 25 μm. At the margins of the upper ironstone, hematite alteration has preferentially altered carbonate and mica-rich clasts.

With increasing deformation, matrix hematite forms a strong cleavage wrapping around quartzite clasts (Fig. 3.9D). Micas remaining in the centres of the clasts, and in the matrix, are aligned to this foliation.

Area 222: Leishman (1983) and Kary & Harley (in press) identified breccias in the Area 222 host rocks and ore, which are texturally and lithologically very different to the other ore zones. The area is strongly folded by both D2(MP) and D2(LP). The ore bodies (Fig.3.13) consist of two folded hematite lenses, amidst a much larger area of variably hematitised breccia — surface exposure is obscured by laterisation. However, at depth, textures within two drillholes (STQ 200 and 207) indicate the breccias are relatively unstrained polymictic rudites, which in company with Area 260 breccias are extensively hematite-altered. The highest Au and Cu grades correlate with the most intense hematite alteration, and with increases in magnetic susceptibility.

Area 222 conglomerates are more polymict than those of Area 260. They contain clasts of cross-bedded calcareous arenite and siltstone (variably scapolitic), with lesser amounts of pink porphyritic rhyolite, chloritised vesicular basalt, milky vein quartz, carbonaceous shale, tourmaline-bearing siltstone, and most significantly, fine-grained barite-bearing hematitic ironstone (Fig. 3.9A). Poor to moderate sorting, sub-angular to angular shapes, and sub-imbricate orientations characterise the clasts, which range in size from a sand matrix to a cobble-framework (maximum ~ 15 cm, average ~ 4 cm). Intraformational fracturing is a feature of some larger arenaceous fragments, indicating their consolidated state at the time of deposition (Fig. 3.9C). Several 5 to 10 m thick bedded calc-arenite intervals separate individual conglomerate beds, and are identical to the

sedimentary hangingwall of the other Starra ore bodies.

At petrographic scales the tectonothermal overprint is surprisingly slight; cleavage is poorly developed, quartz is only mildly undulose. Matrix hematite is coarse-grained (~ 500

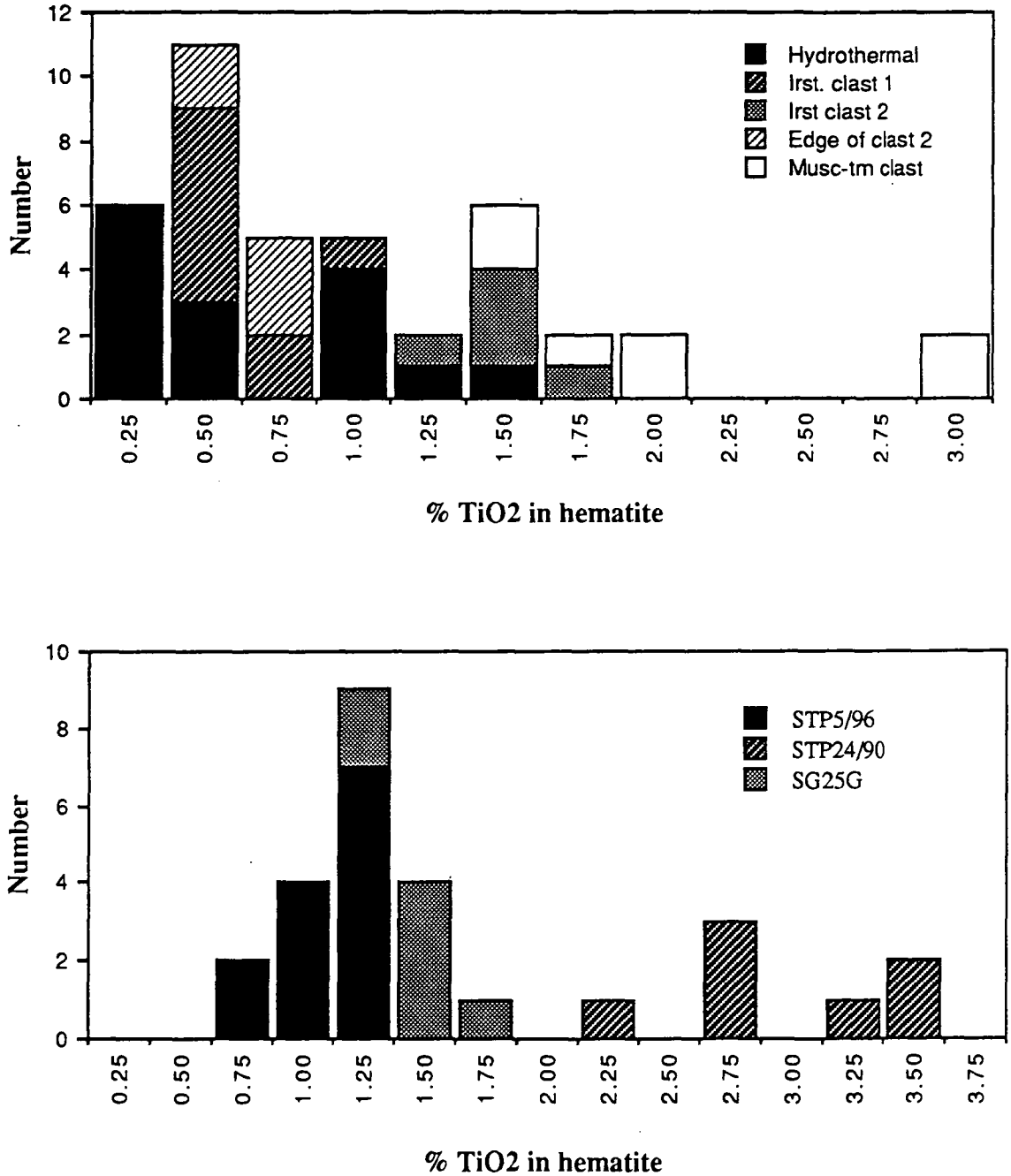

Figure 3.10 Top *TiO_2 in titanhematite crystals from samples St 239 and St 240, STQ200, 12–14 m, Starra Area 222. Hydrothermal hematite occurs as a matrix to the other clast hematite generations, and has the widest compositional range, with the majority below 0.5% TiO_2. Analyses were made on the energy dispersive system of a Jeol microprobe at 15 kV, with analyses normalised to 100 % for this diagram. (0.25 = 0 to 0.25 wt. %; irst. = ironstone).* **Bottom** *TiO_2 in titanhematite from 3 distal ironstone samples south of Starra. Not shown is Sample SG33, in which TiO_2 varied from 5.45 to 6.88 % in 9 grains (this rock is described in detail in chapter 9).*

μm), blocky and commonly twinned: where alteration is least intense hematite concentrates on pebble margins, but with increasing alteration the primary quartz sand (with syntaxial overgrowths) and detrital mica is replaced by widespread anhedral hematite, quartz, and chlorite. (Metamorphic decussate muscovite found mainly in the altered matrix may have either a hydrothermal-sericite or detrital origin). The margins of clasts are progressively bleached with increasing alteration, transitional to massive foliated hematite-chlorite with a ghosted clast fabric (Fig. 3.9D). Small primary fluid inclusions in the hydrothermal quartz contain a small vapour bubble, halite, and an unidentified daughter salt: a minimum salinity of 26.5% NaCl (weight % equivalent) for the introduced fluid is indicated, although the inclusions have proved too small for thermometric analysis.

In view of the stratigraphic importance of ironstone fragments in the Area 222 conglomerates, their textures and geochemistry were examined in detail, to ascertain whether they could be better explained by preferential hematite alteration. They are composed of uniform to banded fine (~ 80 μm) hematite, quartz, rutile and ~ 2 - 4 % barite, in grains which parallel compositional layering. This texture is unlike the matrix hematite generation. Ironstone clast margins meet the surrounding hydrothermal matrix with sharp contact (Fig. 3.9B). In addition to these textural differences, hematite in the clasts and exterior hydrothermal hematite have contrasting chemistry. In 40 hematite crystals the majority of hydrothermal hematites have $TiO_2 < 0.5$ %, whereas fine-grained hematite in clasts are, strictly, titanhematites containing as much as 2.98 % TiO_2 (Fig. 3.10). The latter are comparable to TiO_2 values in hematites in several southern cherty BIFs, which ranged between 0.71 and 6.89 % TiO_2 in ferric iron-corrected analyses. Up to 10 % TiO_2 can exist in limited solid solution in titanhematite, in rocks of appropriate bulk composition (Rumble 1976). Fluid interaction is suggested by the approach of TiO_2 in titanhematite at the edge of ironstone clasts to the hydrothermal hematite composition (Fig. 3.10). These chemical features indicate that hematite clasts were present in the breccias prior to the introduction of hydrothermal fluids — if all hematite was hydrothermally introduced its composition and textures would be expected to be relatively uniform.

Discussion

The excellent preservation of unstrained polymictic fragments compels a sedimentary rather than a tectonic origin for the breccias of Area 222 and the Eastern Hematites. The breccias have the form and structure characteristic of sedimentary conglomerates. On the basis of textures, the deposits originated as pre-tectonic polylithic channel or peidmont-related debris flows, transitional to grain flows, although the three dimensional geometry of the resulting units is not well-known.

Barite-bearing siliceous ironstone fragments are important evidence for the pre-tectonic origin of ironstone in the Starra area, refuting claims that the iron is shear-related

(Laing et al. 1988). They also suggest that Area 222 conglomerates are stratigraphically higher than the main Starra Iron Formation. The clast types recognised to date were sourced from sequences of acid/basic volcanics, immature sediments, and silicified limestone, although some pebbles containing folds in unaltered breccias at Area 260 must derive from a previously deformed terrain.

Hematite is preferentially present in conglomeratic sediments, which were likely to have been permeable during diagenesis. It is not present in overlying or strike-equivalent fine-grained lithologies, or in conglomerates sealed by silicification, such as those at the Kuridala/Staveley Formation boundary. Moreover, the preferential alteration of clast margins is evidence that hematite did not merely fill conglomerate voids, or originate as part of the bedload, but reacted with some components progressively, in many instances culminating in massive hematite through whole-scale replacement. The hydrothermal fluid was highly oxidised, saline, and saturated with respect to silica and iron, and is also the best guide to the fluids which formed the other ironstone types.

An original sub-surface porosity control on iron distribution in these areas is one means of explaining the podiform and disconnected nature of some Eastern Hematites ironstones. Hydrothermal fluids could have ascended along secondary rift faults (sketched in Fig. 3.5), and dispersed into porous conglomerate horizons, possibly experiencing boiling during expansion of the fluid as it entered the aquifer to react with the constituent minerals. A different origin is required to explain the features of all of the other ironstone types, because of their distinct sedimentary banding, and a lack of polymictic fragments.

Ore Sequence

Stratigraphic Revisions

A revision of the Staveley Formation nomenclature to include elements of the Starra mine sequence is proposed and applied generally within this thesis. The revision unifies and formalises the divisions of Leishman (1983) and others, recognising that the sequence contains previously undocumented lithologies with significant strikelengths (Table 3.1). The Staveley Formation has a minimum thickness of 2000 m (Blake et al. 1984); at Area 257 the newly divided Starra mine sequence is 120 m thick, forming the tectonically thinned base of the Staveley Formation. It increases to 250 m at a well-exposed section along Mariposa Creek at Area 236. A formal revision will be submitted for publication using the latter section. The specific comments and textural descriptions cited below are drawn from detailed drill-logging of Area 257.

Harley Member

In the absence of a named topographic feature, "Harley Member" (Fig. 3.11) is named for Robert Harley, a Cyprus geologist who worked extensively in the area. The Harley Member refers to 50 to 100 m of fissile chlorite-biotite (± cordierite, andalusite)

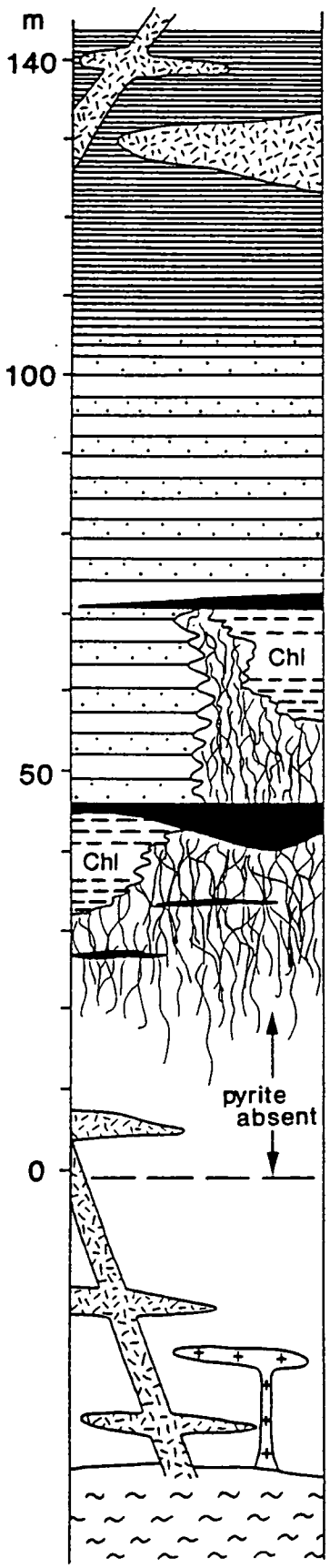

STAVELEY FORMATION

Thin bedded fine lamellar metasiltstone, with minor chert and jaspillite. Intrusive amphibolites

Interbedded graded calc-arenite and scapolitic pelite. Calcite veining increases towards footwall

STARRA IRON FORMATION MEMBER

251 Ironstone: mineralised

Interbedded calcareous sediments and veined feldspar schist. Minor chlorite schist

257 Ironstone: mineralised

MARIPOSA CREEK MEMBER

Magnetite-veined bedded to massive albite-hematite-pyrite schist, weakly mineralised. Occasional thin hematitic BIF, and lenses of chlorite schist immediately beneath ironstone

HARLEY MEMBER

Chlorite-biotite schist, with feldspar-quartz intercalations. Basaltic geochemistry. Intruded by felsic and basic dykes and pegmatites

Undifferentiated schist and felsic gneiss

KURIDALA FORMATION

Figure 3.11 *A local stratigraphic column of the 251 and 257 areas, Starra, showing the positions of the Harley, Mariposa Creek and Starra Iron Formation Members.*

Figure 3.12

A. *(Top). Typical Harley Member chloritic schist (St 53, Area 257, STQ-80-15/165.5 m), with rapid alternations of strongly strained chlorite and albite-rich bands. This particular sample is unusual because it contains 1850 ppm Zn, but low Cu and Au. (Bottom). Folded alteration and bedding in albitic Mariposa Creek Member rocks. The fold generation is D2(LP).(Sample St 216, Area 244, STQ 79-2/187 m).*

B. *A relict fragment of bedded chlorite (1) with a reaction rim of epidote, from a conformable lens of chlorite schist (St 220, Area 236, STQ 85-113/110 m). Porphyroblastic magnetite is intergrown with the epidote. A second chlorite generation (2) occurs in contact with the surrounding albite. The abundant small green crystals within and exterior to the relic are tourmaline.*

C. *A photomicrograph of a minor strongly foliated chlorite schist band within the Mariposa Creek Member. Hematite (needles) and magnetite (blocky crystals) are inhomogeneously distributed. A quartz vein is folded about S2(MP). (St 45, CRQ 78-1/219.3 m, Area 257).*

D. *A sample of intensely iron-oxide-altered Mariposa Creek Member, obtained from level 1275 R.L. underground at Area 251. The fragmental fabric, and the pyrite, are both deformed by D2(MP) (location: Fig. 4.6).*

E. *Typical deformed albitic Mariposa Creek Member. Network veins and disseminated zones of magnetite, hematite and pyrite constitute approximately 20 % of the rock. (St 275, Area 257, STQ-85-127/179 m).*

F. *(Top). Thinly-bedded cherts, siltstones and jaspilites of the uppermost cored Staveley Formation hangingwall (St 89, STQ-80-17/81.5 m, Area 257). (Bottom). Interbedded meta-calcarenite (light) and scapolitic/cordieritic meta-shale (dark). Several thin layers of magnetite occur at the right end of the sample (St 134, Area 276, STQ 85-121/118 m).*

G. *A reflected light photomicrograph of a well-zoned pyrite porphyroblast with associated disseminated magnetite, in the Area 257 footwall. An inner pyrite zone is inclusion-rich with a vaguely radiating form, whereas the outer pyrite zone is free of inclusions, and is euhedral. Its growth was favoured along a NW-SE axis (St 171, SHQ 77-26/280 m).*

H. *A detailed reflected light examination of the margin of a pyrite porphyroblast, illustrating the sieved texture of the silicate and hematite inclusions. Magnetite is only rarely found as an inclusion. Hematite and other inclusions are not aligned to the exterior cleavage. (St 171).*

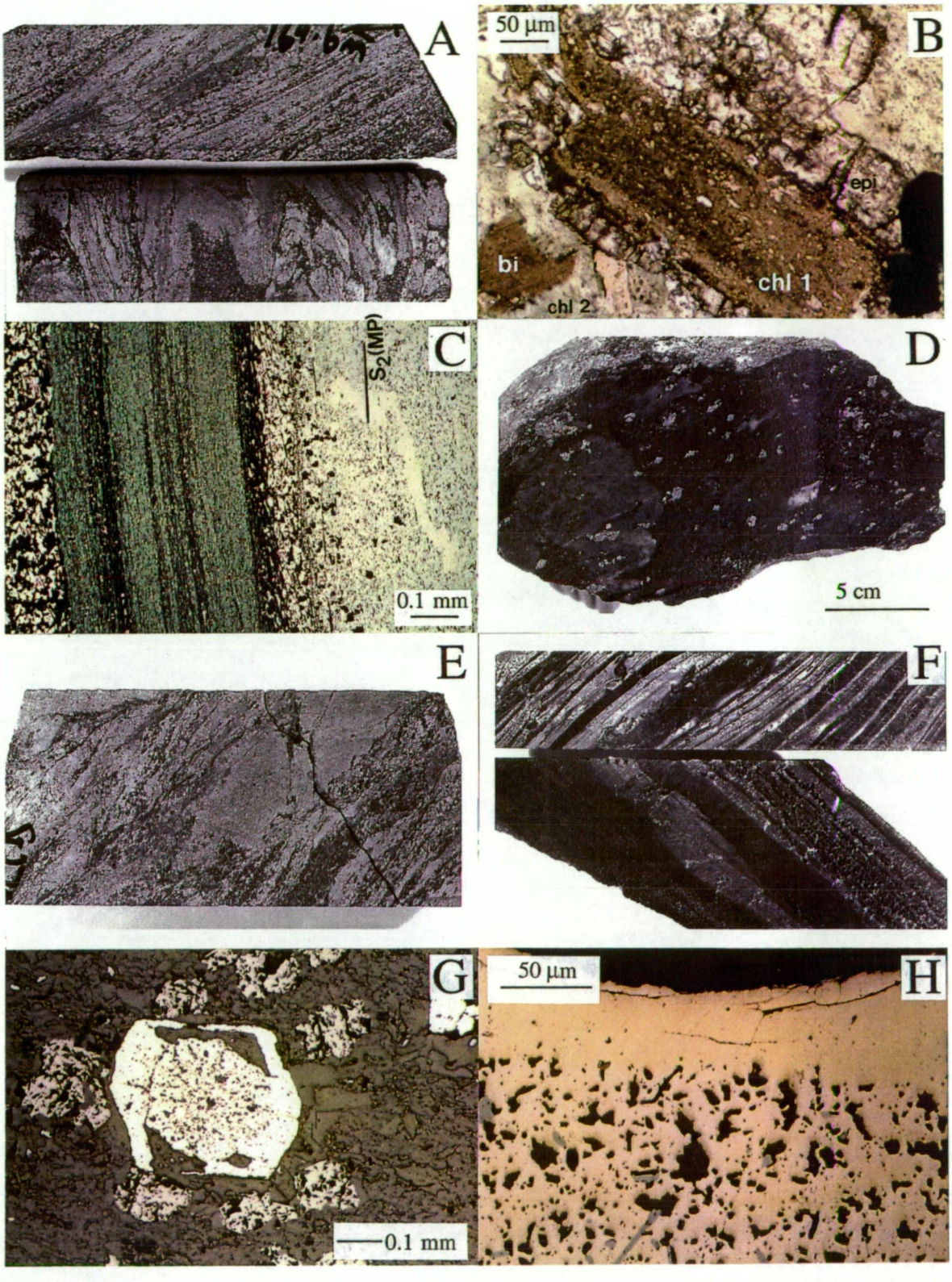
A
50 µm
B
epi
bi
chl 1
chl 2
C
S_2(MP)
0.1 mm
D
5 cm
E
F
G
0.1 mm
50 µm
H

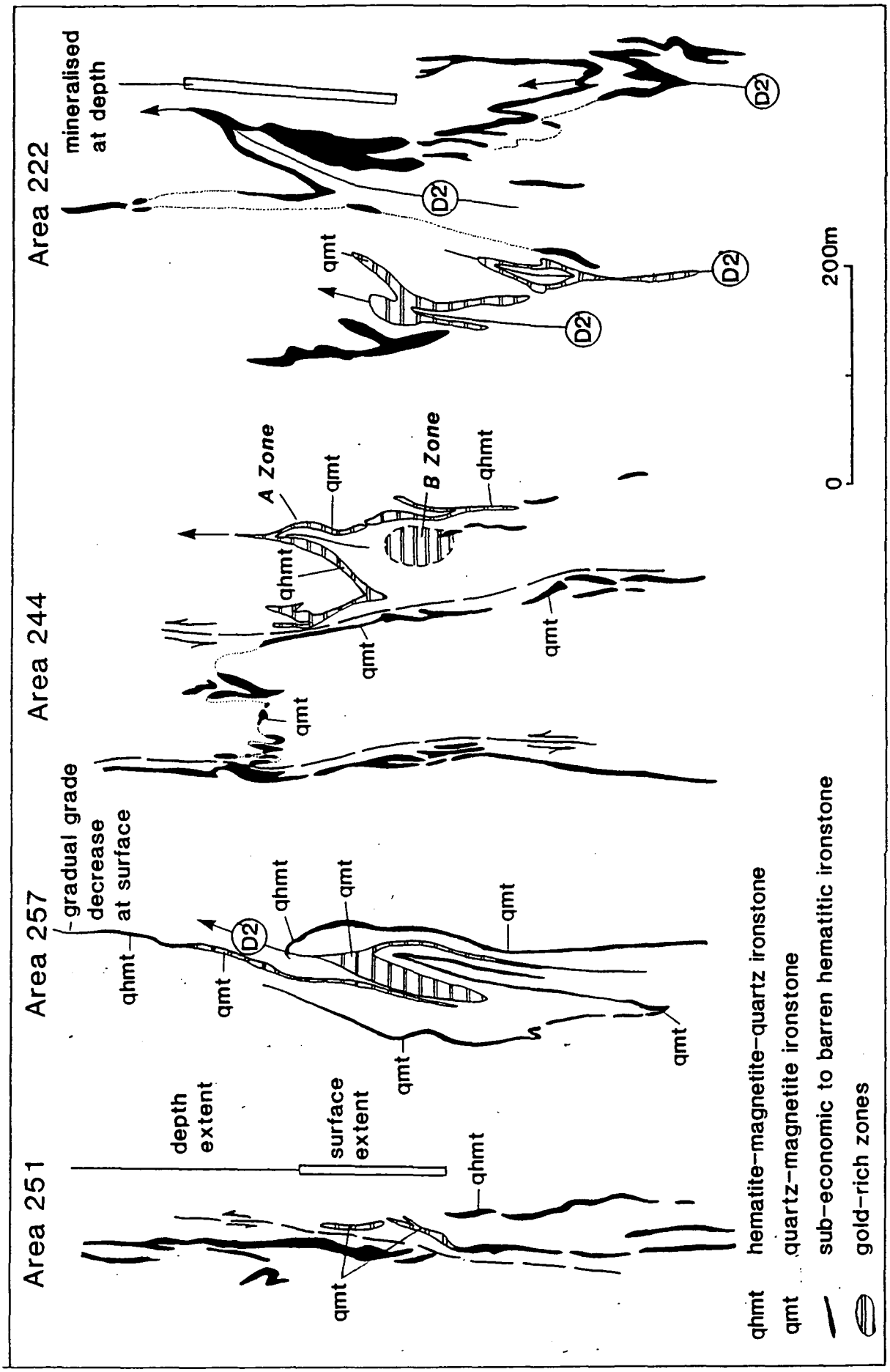

Figure 3.13 *A plan of the geology and structural configuration of the four Starra orebodies. Area 222 ironstones show features of folding about both D2(MP) and D2(LP); Areas 244 and 257 contain D2(LP) anticlines, with faulting of the dextral limb and right lateral displacement. Area 251 is not grossly folded. (D2' = D2(Main Phase), D2* = D2(Later Phase)).*

schist forming an easily identifiable upper contact (gradational over 5 m) with the feldspathic Mariposa Creek Member. The lower contact with biotite-muscovite-andalusite schist of an undifferentiated Kuridala Formation (originally identified as Answer Slate by Leishman (1983), as discussed previously) is more difficult to define, but is based on the recognition of abundant chlorite in handspecimen (Fig. 3.12A). High strain has resulted in a strong L-S fabric, rootless folds, and boudinage of the more feldspathic layers. In drill-core the Harley Member consists of 1 – 2 cm wide alternations of chlorite-rich and albite-rich layering, in part tectonic, with < 5% disseminated hematite and magnetite. The origin of the Harley Member as a probable mixed mafic tuff, felsic volcanoclastic and pelitic sediment sequence is discussed in chapter 7; petrography identifies primary chlorite and chloritised biotite in approximately equal amounts.

The name 'Harley Member' may also be applicable to metabasalts found near or at the base of the Staveley Formation northwest of the Mt. Elliott mine, which (in similarity to the Starra sequence) are footwall to mineralised iron formation.

Mariposa Creek Member

The Mariposa Creek Member (45 – 180 m thick) is a massive to banded albite-quartz-hematite ± chlorite ± muscovite schist, pervasively cut by magnetite-pyrite clots and veinlets (Figs. 3.12A,C,D & E). It is overlain with sharp contact by auriferous magnetite-hematite ironstone, or the more common, poorly mineralised hematite-magnetite variant. Shearing has affected this unit inhomogeneously, permitting the preservation of sedimentary grading in some 0.5 –10 cm thick beds. Fine-grained hematite is concentrated at the the chloritic tops of these, and hence was a likely syn-depositional component, whereas magnetite is not bedded and hence was added post-depositionally. Ten percent of the unit comprises massive medium-grained beds 1 to 4 m thick, petrographically consisting of interlocking albite and quartz.

The average diameter of recrystallised albite at the base of grading cycles is 80 μm, (a maximum of 2.5 mm), passing up to 35 μm grains in a foliated muscovite-chlorite matrix. In the least strained examples, larger grains occur, consisting of subangular to angular quartz and feldspar, and rounded quartzite lithofragments. A description of the more common highly-strained fabric is presented in chapter 4.

It is concluded that turbidite processes transported feldspathic and quartz debris to the depositional site, *whereas hematite was deposited chemically as part of the hemipelagic* deposition characterising the 'E' zone of each Bouma cycle. Most turbidites preserve A, AB-E, or rarely ABC-E Bouma zones, i.e., the ripple and upper parallel-lamination of the standard Bouma sequence is uncommon. The preservation of the lower graded 'A' subdivision is interpreted by Bouma (1962), Walker (1984) and many others as a feature of proximal fan deposition. Overall, a proximal felsic volcanic source or sources best explains the fine-grained, feldspathic and angular nature of the preserved transported

detritus; turbidite transport of vitriclasts and crystals has been widely documented around subaqueous felsic volcanic centres (Niem 1977, Wright & Mutti 1981, Davidson & Dashlooty in press).

Hangingwall Metasediments

Least tectonised Staveley Formation immediately hangingwall to ironstone consists of 60–70 m of well-bedded calcareous psammite and intercalated pelite, giving way transitionally to thinly bedded calc-silicate layers and hematitic cherts (average thickness ~ 5 mm) (Fig. 3.12F). The arenites are graded, 1–20 cm thick, with sharp undulose bases, plane lamination and uncommon load structures. The initial 10 m of sediment above the ironstones contains the thickest arenites, with mainly the 'A' Bouma division preserved; above this combinations of the turbidite zones A, A-E, and ABC-E are all normally present (Bouma 1962), overall constituting a fining-upwards sequence. The 'E' Bouma divisions are 1–5 cm thick cordierite-phlogopite-muscovite-albite-quartz bands (± tourmaline ± hematite, ilmenite), forming wavy to discontinuous drapes between calcareous psammites.

Less common hangingwall lithologies include 0.5 – 3.0 m thick massive calcareous albite-quartz beds, which constitute useful markers. Thin unmineralised hematite beds (at times chert-rich) concentrate at the top of some calcareous pelites. More significant is a lens of intercalated weakly mineralised hematitic ironstone (unusually calcareous) in the Area 257 hangingwall. This Au-Cu anomalous lithology is interpreted as the Area 251 ironstone-equivalent horizon; at ~ 11000N the footwall to this ironstone alters from hangingwall metasediment to albitic footwall along a local angular unconformity (Appendix 13). The shape of its margin is explored in chapter 4 (Fig. 4.13).

Metamorphic parageneses of the metasediments are also tabulated in chapter 4. Briefly, relict calcite is present towards the base of calcarenites, as recrystallised plates interstitial to quartz (average 50 μm diameter), together with metamorphic actinolite and epidote. Pelites possess a strongly foliated phlogopite matrix (Mg/(Mg+Fe) mol. % = 74–78), compressed around 0.25 – 1.50 mm diameter ovoids, comprising 10 to 40 % of any given layer. The ovoids are preferentially replaced by low birefringent (δ ~ 0.06 – 0.010) sheet silicates reflecting two older orthogonal cleavages: these features are consistent with the replacement of tetragonal scapolite, as has been suggested by Leishman (1983), Ransom (1986), Davidson et al. (1988), and Kary & Harley (in press). However, recent petrographic observations are more consistent with an orthorhombic cordierite precursor for some ovoids for the following reasons:

(1) no relict scapolite has been found in the pelite layers despite extensive probing.

(2) the ovoid form and replacement mineralogy of chlorite, muscovite, biotite, quartz, and most commonly, low birefringent kaolinite/nacrite (microprobe identification) accords with the often recorded pinnitisation of cordierite (Chevalier & Dejou 1972).

(3) despite their altered state, some ovoids have a sector twin, which is typical of

cordierite, and also display the sheet-silicate zoning which typifies cordierite retrogression (Deer et al. 1986).

(4) very fine-grained relicts occur in some samples, with the birefringence and relief of cordierite, although these have proved impossible to chemically isolate using microprobe techniques.

On these grounds, the ovoids are identified as cordierite pseudomorphs, most likely developed by the prograde reaction

$$\text{Muscovite} + \text{chlorite} + \text{quartz} = \text{cordierite} + \text{phlogopite} + H_2O$$

which occurs in pelites in the range 500 ° C (1 kbar) to 570° C (4 kbar) and above (Seifert & Schreyer 1970). Alteration during late-D2(LP) retrogression is required because the pinnite is not foliated by S2(MP) or S2(LP) — these foliations are instead compressed around the cordierite relicts.

Amphibolite

Field Character

Magnetic amphibolite bodies ~ 30 m thick occupy a D2(MP) syncline 100 m into the Area 257 hangingwall, and also occur as thin boudinaged lenses with foliated or chilled margins in the footwall (Fig. 3.14). In gross form and at hand-specimen scale the contacts of these are bedding-discordant. Numerous thinner dykes (0.2 – 2.0 m) occur close to the contacts of larger bodies. Very few intrude ironstone, or even the Mariposa Creek Member. Amphibolites immediately east of Area 257 are folded by D2(MP).

In the Starra region, a younger east-west dolerite cuts all foliations in the Pyramids area, correlated by its orientation to the 1160 Ma Burstall Granite (E4 generation of Wyborn & Ellis 1984, Page 1983b). Erosion has preferentially weathered this dyke, developing an east-west valley, in which part of the Selwyn ring-road is sited.

Petrography

All of the examined thin-sections of amphibolite consist of a metamorphosed ophitic assemblage of plagioclase, actinolite, epidote, magnetite, chlorite, calcite, biotite and minor sulphide. Plagioclase forms relict twinned hypidiomorphic, dusty-brown crystals 0.2 – 2.5 mm long, compositionally between $An_{5.5}$ and $An_{31.0}$ (albite to andesine). Relict igneous zoning is preserved in some grains, from cores of An_{30} to rims of An_{20} in two instances. Actinolite is hypidioblastic to xenoblastic, ranging from 0.1 to 2.0 mm long. Magnetite may be an igneous relict also, as it occurs in subhedral to euhedral grains interstitial to plagioclase.

Metasomatic evidence includes the replacement of actinolite by unfoliated biotite and chlorite, pervasive development of biotite microlites, calcite-chlorite veining, and domainal epidote alteration of plagioclase with attendant destruction of the ophitic fabric. Pyrite and

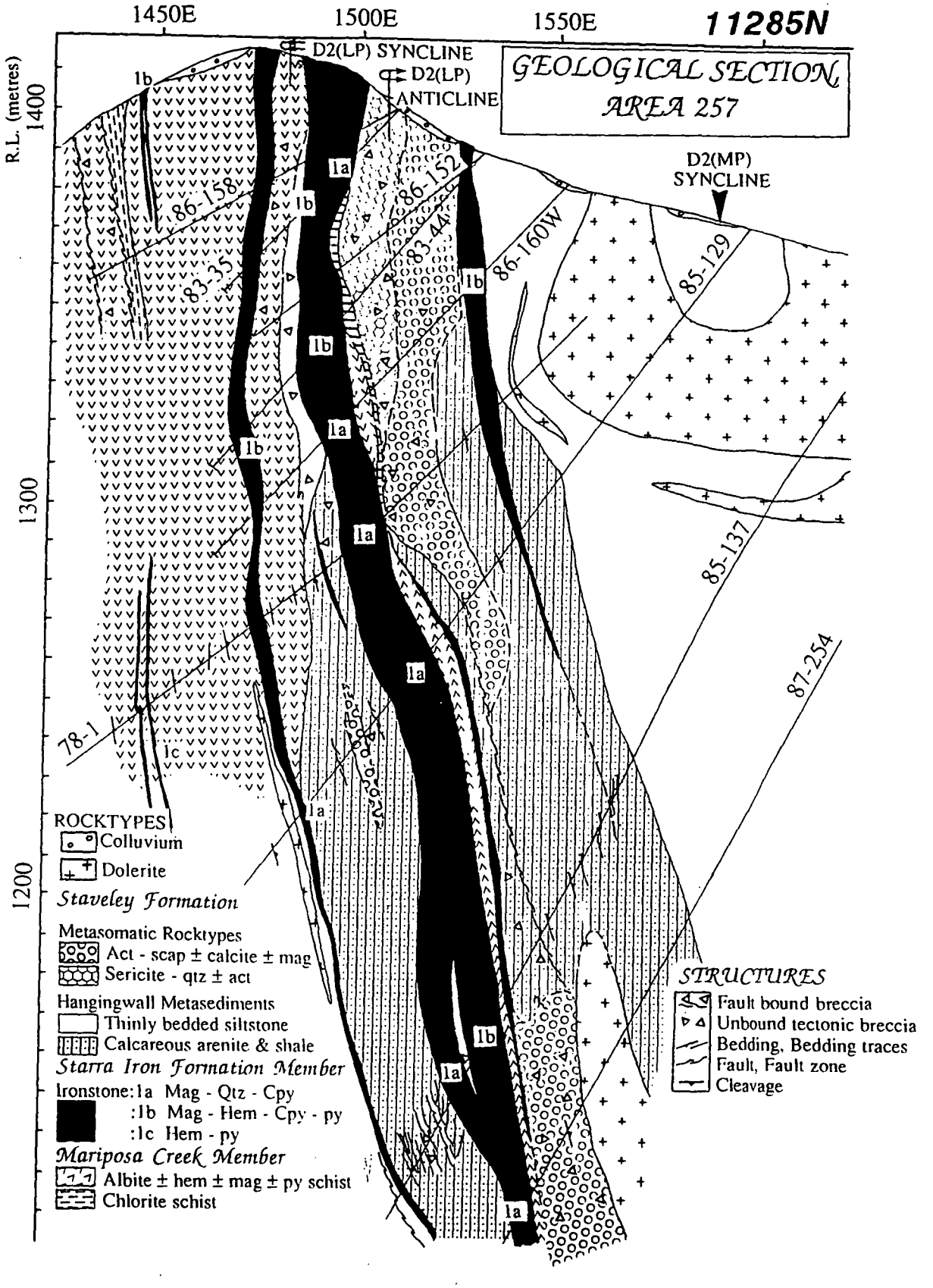

Figure 3.14 *Geological section, line 11285N, Area 257. The section cuts across the "Main Zone" orebody, and in doing so intersects the complex calc-silicates of the orebody hangingwall.*

chalcopyrite can accompany the calcite veining stage, although chalcopyrite also occurs as small primary igneous crystals wholly enclosed by feldspar. Despite the occurrence of scapolite in some hangingwall calc-silicates, the scapolite alteration so prominent in other Mount Isa dyke suites (Ramsay & Davidson 1970, Ellis & Wyborn 1984, Oliver & Wall 1986) suites is absent at Starra.

Footwall amphibolites within the oxide alteration are unmineralised, and therefore post-date the mineralisation.

Hangingwall Skarns

Description

"Skarn" is used here in the non-genetic sense of Einaudi et al. (1981), to describe "calc-silicate rocks that are rich in calcium, iron, magnesium, and aluminium.....that formed by replacement of originally carbonate-rich rocks". The intention of this section is to document the textures and relationships pertinent to the origin of the hangingwall calc-silicates, and any possible links with mineralisation, but not to discuss their petrogenetic evolution in detail. They have emerged as a complex set of parageneses that will surely merit further work.

Coarse-grainsize, loss of original banding, disseminated growth of magnetite, and a dominance of mafic over felsic minerals are the distinguishing features of the calc-silicates, which form up to 20 m thick zones immediately hangingwall to some ironstones. Four important features are:

(1) Calc-silicates are developed hangingwall to mineralised and unmineralised ironstones alike.

(2) Calc-silicates are not a ubiquitous feature of the hangingwall contact; in many instances ironstone is overlain directly by well-banded calcareous metasediments.

(3) Calc-silicate zones above mineralisation are weakly mineralised, never to economic grade, whilst barren skarns overlie barren ironstone.

(4) The thickest calc-silicate zone (Area 257, line 11285 N, Fig. 3.14) is sporadically associated with dolerite at depth.

The mineralogy of skarn is broadly zoned from phlogopite-rich furthest, to actinolite-rich closest to ironstone. The phlogopite zone is extensively chloritised, but consisted of phlogopite (30 – 40%), actinolite (30%), retrogressed cordierite/scapolite, epidote, calcite, albite, magnetite, pyrite and chalcopyrite. Average grainsize is ~ 1–2 mm. Inclusion-rich magnetite blebs enclose embayed pyrite, chalcopyrite and randomly orientated phlogopite.

Closer to ironstone, skarns contain distinct 1–4 cm wide domains dominated by either actinolite, scapolite, or carbonate. The main parageneses are actinolite (~60%)-epidote (~15%) - chlorite (~15 %) ± magnetite, and scapolite (~ 60%)-phlogopite (~ 25 %) ± actinolite - epidote. Marialitic scapolite (Me_{44-46}, with an average composition of

$(Na_{2.0}Ca_{1.7}K_{0.06})Al_4(Si_{7.8}Al_{0.2})O_{24}(Cl)_{0.5}(SO_3)_{0.05}(CO_2)_{0.45})$ occurs as 0.4–1.2 mm subhedral grains altering to muscovite along cleavage traces. A third important paragenesis contains coarse plates (1–5 mm) of anhedral chalcopyrite (replacing pyrite in some sections), partially martitised magnetite, quartz, calcite and baroque dolomite — this zone replaces massive actinolite.

In addition to late carbonate-chalcopyrite deposition, metasomatic replacement textures occur up-dip from dolerite on line 11285 N, Area 257 (Fig. 3.14). Here fine-grained (10–20 μm) alb-act-epi, and in places only quartz, overprint a coarser (100–400 μm) act-alb-mag paragenesis along a sharp but irregular contact (Fig. 4.5G).The resulting atoll fabric of relict calc-silicates is strongly indicative of infiltration replacement.

Genesis and Relationships to Mineralisation

The four genetic skarn types of Einaudi et al. (1981) are:

(1) "Calc-silicate hornfels" — metamorphic recrystallisation with no introduction of chemical components.

(2) "Reaction" or "bimetasomatic diffusion" skarns, which result from a local exchange of components between unlike lithologies during metamorphism as a result of diffusion.

(3) "Primary" skarn, developed by the interaction of magma with intruded carbonate.

(4) Component transfer between a hydrothermal fluid and carbonate, to produce "replacement" or "secondary" skarn, by fluid infiltration. This is the most common skarn-type.

The main criteria in differentiating calc-silicate hornfels from the other types is to demonstrate isochemical change, often requiring careful modal or chemical analysis (Rice & Ferry 1982). In this instance the strongly mafic character of the calc-silicates (as compared to the precursor alb-cc-qtz-act assemblage) eliminates an isochemical origin. Pure "reaction" skarns are only documented within the literature at scales significantly less than those observed at Starra; a maximum of ~ 50 cm is generally accepted for Amphibolite facies,and even less for Greenschist metamorphic grades(Vidale 1969, Hewitt 1973, Einaudi et al.1981, Tracy et al. 1983), resulting most commonly from diffusion between a CO_2-rich fluid produced by mineral buffer reactions in limestone, and an external H_2O-rich fluid. Some reaction skarns are observed at very local scales at Starra: for instance, 5–15 cm wide chloritic margins to some ironstone pods hosted by metasediments. In this zone Fe is presumably contributed from ironstone, and Mg, Al, and Si from metasediment, to form chlorite. Reaction skarn processes are implicated by the overall faithful location of the calc-silicates at the ironstone - metasediment contact, but because of the problem of scale, cannot wholly explain the calc-silicate distribution. A combination of fluid infiltration along bedding/cleavage, and reaction skarn processes, are therefore favoured. Disseminated

sulphide and magnetite growth in the hangingwall is confined to the skarns, and therefore most likely grew from infiltrating metamorphic fluids, rather than recrystallised local assemblages. The infiltrating fluid must have been saline and water-rich (to explain the formation of Cl-bearing marialite and removal of carbonate), although pockets of high X_{CO_2} fluid are required to carbonate earlier calc-silicates. Some possible involvement of magmatic fluid is indicated by the intensification of the metasomatic overprint towards dolerite. However, there is no evidence for "primary" contact magmatic skarns.

Because calc-silicates have no spatial relationship to mineralised ironstone, they are unlikely to be genetically related to it. The observed calc-silicate distribution is best accomodated by the redistribution of pre-existing metals along with other components by reaction and infiltration; sulphur and Cu-bearing ironstone produced Cu-bearing skarns, particularly around zones of shearing and fracturing where metal scavenging was facilitated. Surprisingly Au is only weakly anomalous in calc-silicate, possibly because remobilisation was hindered by preferential retention of Au in chemically resistant magnetite and quartz.

Basin Paleogeography

The east-west distribution of lithologies in the uppermost Kuridala Formation suggests deeper water facies are preserved on the western limb of the Starra Syncline (muscovite-biotite schists) whereas the eastern limb contains elements of a carbonate shore-line, deposited at or near wavebase. Intermittent graphitic schists are interpreted as a euxinic lagoonal facies behind active oolitic carbonate shoals. A period of uplift or marine regression weathered the eastern limb sequence under humid climatic conditions, resulting in carbonate silicification, prior to the recommencement of carbonate/clastic deposition in the Staveley Formation.

The present distribution of ironstone at the base of the Staveley Formation delineates a longitudinal north-south basin, in which shallow water evaporitic and fluviatile conditions prevailed to the east and south (associated with tourmalinite and BIF), bound locally by active faults shedding talus into a deeper trough (Fig. 3.5). Active faulting can explain the reworking of basal lithologies such as basalt and iron formation into the Area 222 conglomerates. The centre of the trough was characterised by accumulating felsic and basic volcaniclastics. At the cessation of volcanism, oxide facies exhalites accumulated at the top of the volcanic pile, followed by deeper water turbidite deposition transporting mainly non-volcanic sediment. The geometries of the resulting fans, and the direction of sediment supply, are not known. Below-wave-base sedimentation in oxidised waters deposited hematite and ilmenite as the stable oxides, and prevented the accumulation of carbonaceous matter. Intercalated massive feldspathic beds in the hangingwall sediments are interpreted as acid pyroclastic flows because of their similar chemistry to the least altered acid footwall samples, as described in chapter 5.

Mineralisation

Ore Environment ironstone

General Geology

This section deals with mineralised and barren ore environment ironstones, as defined under "Lateral Iron Formation and Tourmalinite" previously.

Mineralised magnetite-hematite-quartz-pyrite-chalcopyrite ± siderite ironstones (0.1-20 m thick) occur discontinuously within a 6.5 km long mineralised belt, with individual ore-body strike lengths less than 400 m. These ores are commonly vughy, crumbly and chalcedonic at the surface, oxidised to ~ 200 m depth. The well-defined sequence of copper minerals resulting from weathering is discussed by Kary & Harley (in press).

Areas 251 and 257 are the richest ore zones, averaging 2.6 mt at 6.7 g/t Au, 3.4% Cu (half the total resource) and 1.15 mt at 5.5 g/t Au, 0.8% Cu respectively. Area 251 is 600 m south of 257, and is not macroscopically folded (Fig. 3.13). The zone is lens-like, plunges at ~ 68° to 034° magnetic, with dimensions of 400 m (plunge extent) x 250 m (width) x 20 m (thickness at centre). In contrast Area 257 has been tightly folded around a D2(LP) vertically plunging sinistral anticline (Fig. 3.13). The orebody consists of the 9 m thick Main Zone in the dismembered hinge, with dimensions of 90 x 250 m, and the Western Zone (Kary and Harley, 1988), which is the western detached limb of the fold, 2-3 m thick, and at least 125 m width x 250 m plunge extent. The latter zone plunges approximately 60° north. Area 244 is a peculiar variant of the 251-257 style, with significant footwall ore (the 'B'-zone of Kary & Harley (in press), Fig. 3.13), while Area 222 mineralisation is unlike the other prospects: aspects of its geology have already been discussed.

Mineralised ironstone grades laterally into, and is interbedded with, poorly mineralised massive hematite-magnetite ± pyrite ironstone, which is mineralogically identical to "Barren distal massive ironstone". Isolated instances of well-defined chert and magnetite-hematite banding (0.5-1.5 cm thick) occur in the Area 257 Western Zone (Fig. 3.9E & F), where a transition into hematitic, iron-rich, poorly mineralised ironstone is observed northwards over 300 m (see also chapter 6). In drill-core the recognised mineralogical zonation from mineralised to barren rock is mag-cpy ±bornite, mag-cpy-py, mag-py-hem, to hem-py, coinciding with a general decrease in quartz from 50 % to 10 %.

All of the ore zones are characterised by the close association of a local chlorite schist (with subordinate magnetite and pyrite), immediately footwall or strike-equivalent to mineralisation. At Area 257 two chlorite schist lenses occur: one is prominently exposed at surface beneath the Western Zone (Appendix 13), while the other is associated at depth with the Main Zone. Area 251 chlorite schist thickens in parallel with the ironstone, and may be genetically related to it, although it is usually poorly mineralised. No chlorite schist is associated with barren ironstone, which emphasises the exploration value of this

Figure 3.15

A. *A dual reflected/transmitted light photomicrograph of scheelite within mineralised ironstone. Scheelite, magnetite, chalcopyrite, quartz and chlorite are all metamorphically intergrown. (E8061, Area 251, STQ-76/174.9 m, 12.4 ppm Au & 5.8 % Cu).*

B. *Reflected light photomicrograph of a magnetite porphyroblast within a compact hematite matrix, barren Area 257 ironstone sample St 75 (STQ 80-16/255 m).*

C. *A dual reflected/transmitted light photomicrograph of typically metamorphically intergrown calcite, chalcopyrite, quartz and magnetite, in mineralised ironstone sample St 118, STQ-85-129/150 m, Area 257 Main Zone. Slight grain boundary hematite alteration of magnetite is apparent.*

D. *As shown in this reflected light image, gold in ironstone is commonly hosted by chalcopyrite, in contact with hematite, pyrite, and other minerals such as quartz, siderite, and magnetite. In the lower left hand corner tarnish on pyrite reveals growth zoning. (E 8075, Area 251, STQ 77/155.3 m, in an interval that assayed14.15 ppm Au & 8.65 % Cu).*

E. *Reflected light photomicrograph of a mineralised magnetite-quartz-chalcopyrite ironstone, emphasising the typically disseminated nature of the sulphide component. (St 115, 85-129/135 m, Area 257 Main Zone).*

F. *Trough Tank, near-barren BIF, (HQ 18, lower BIF). The well banded nature of this iron formation contrasts with the massive texture of most Starra ironstones, although they are compositionally similar. Note that a cross-cutting vein has remobilised only the local magnetite, rather than introducing sulphides.*

G. *Trough Tank. "Primary" fluid inclusions in quartz, from siliceous "pipe-like" mineralisation in NQ6/117.7 m (Sample TT41). The inclusions are interpreted as trapped, prograde, saline metamorphic fluids. The large cube is halite, but the identity of the other two daughters is not known.*

H. *Trough Tank. Trails of quartz-hosted fluid inclusions related to retrogression have become trapped during decompression around this pyrite crystal. ("Pipe-like" mineralisation, NQ 6).*

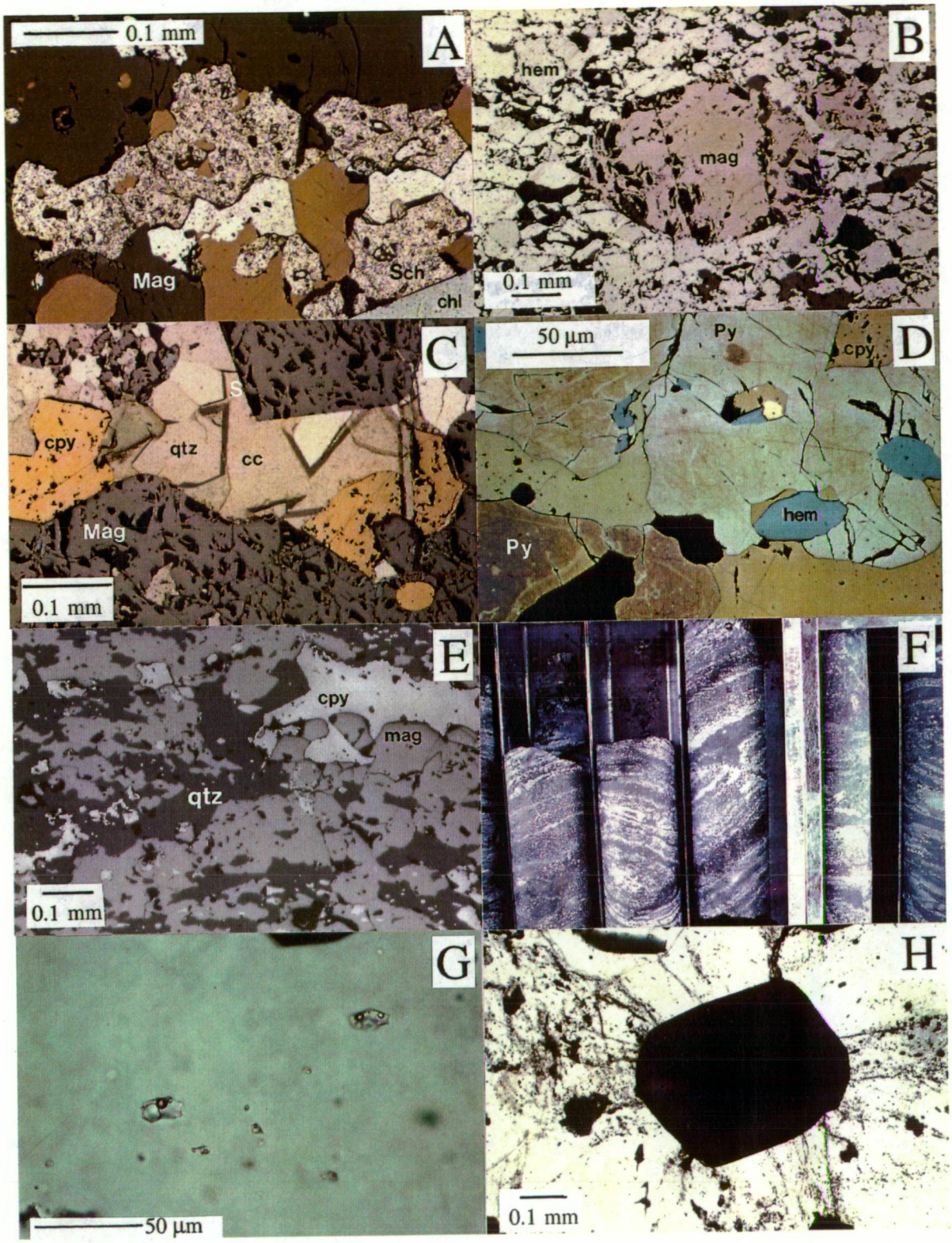
A
0.1 mm
Mag
Sch
chl
B
hem
mag
0.1 mm
C
S
cpy
qtz
cc
Mag
0.1 mm
D
50 µm
Py
cpy
hem
Py
E
cpy
mag
qtz
0.1 mm
F
G
50 µm
H
0.1 mm

lithology. The geology and chemistry of this important rock-type is further investigated in chapter 7.

Petrography

Pyrite, chalcopyrite and minor scheelite comprise 2-5% of mineralised ironstone, either as disseminated subhedral grains 0.2-2 mm long, or as inclusions within porphyritic and non-porphyritic magnetite (Fig. 3.15A & E). Carbonate is a common accessory in mineralised ironstone (Fig. 3.15C), but is absent from barren examples. Trace phases are stannite (Switzer 1987), tellurobismuthinite (Bi_2Te_3) and melonite ($NiTe_2$), identified by microprobe analysis. Magnetite also contains inclusions of quartz, albite, muscovite and chlorite, which are absent from foliation-parallel hematite. Switzer et al. (1988) introduced the concept, based on work at Area 257, that ores in fold hinges were granoblastic, referred to as "granular" ore, grading to finer-grained "foliated" ore in the fold limbs. These observations have been verified for small scale folds, and are in accord with the concept of preservation of peak-metamorphic grain-size in areas of subsequent low D2(LP) strain, such as fold-hinges. However, overall, a comparison of grains in the Main and Western Zones of Area 257 revealed no significant size differences, as shown in Table 3.2. Oxides and quartz are mainly in the range 0.1 to 1.5 mm. Magnetite in barren hematitic ironstone forms porphyroblasts up to 1.5 cm across (Fig. 3.15B).

	Location	Maximum grain size in mm		
		Magnetite	Hematite	Quartz
Hinges				
St 113	Surf.11025N, 1519E	1.5	0.3	0.15
St 115	85-129, 135 m	1.1	0.3	0.13
St 116	85-129, 140 m	0.6	0.4	0.08
St 118	85-129, 150 m	0.4	-	0.10
Limbs				
St 75	80-16, 255 m	0.8	0.12	0.08
St 99	80-17, 163.4 m	1.5	0.9	0.3
St 100	80-17, 166.6 m	0.7	0.7	0.5

Table 3.2 *Grain size comparison in ironstone between Area 257 D2(LP) fold hinges, and fold limbs.*

Gold, 5 to 50 μm in diameter, is commonly hosted by chalcopyrite (Fig. 3.15D), but also occurs within magnetite, pyrite, hematite, quartz and carbonate (I.Pontifex, 1984/86 unpublished data, and personal observation). The coarsest gold is found in boudin-neck zones, and in the weathering profile. Rounded grains dominate over the much rarer crystalline form.

In some samples calcite and siderite fill high-angle fractures invading foliated auriferous ironstone, an event related to late brittle activation of the Starra Shear, discussed in more detail in chapters 4 and 10. The introduced siderite embays pyrite, alters chalcopyrite to chalcocite, and magnetite to hematite, implying the invading fluid was more oxidised than ironstone.

The general textures support contemporaneous recrystallisation of the ore minerals during D2(MP) peak-metamorphism. They do not support extensive sulphidation of magnetite to deposit pyrite, or alteration of pyrite to form chalcopyrite, as concluded by Switzer et al. (1988), unless the evidence of the latter processes has been annealed.

Alteration

General Geology

Pervasive oxide-sulphide-albite ± chlorite alteration is developed within the Mariposa Creek Member, footwall to both mineralised and barren ironstone. This alteration is so widespread that it has not been possible to obtain unaltered material from any of the numerous drillholes in the 6.5 km long mineralised segment. However, the intensity of alteration decreases markedly with depth. At the Harley/Mariposa Creek Member contact, magnetite blebs 0.5–2.0 mm wide comprise only ~ 5–10 % of the rock, while ~20 m above this, coarse pyrite porphyroblasts appear, coinciding with a gradual increase of disseminated magnetite, and mag-hem-py-cpy gash and network veining (Ultraviolet study has shown scheelite to concentrate in these). Restricted footwall zones of intense iron enrichment have been mapped underground beneath the Area 251 ironstone (see Figs. 3.12 & 4.6). These consist of distinct, irregular, reddened albitite fragments in a matrix of network-veined (mag-hem-cpy-py-bornite) albite-hem-quartz rock, interpreted as a brecciation and progressive replacement fabric. In many instances irregularly-shaped pods and veins of intense oxide alteration are folded and lineated, attesting to a pre or syn-deformational alteration chronology. Nevertheless, the prevailing fabric consists of loose strings of oxides and sulphides 2–20 mm wide, oriented parallel to S2(LP) foliation. The hangingwall sequence is often tectonically transposed adjacent to the ironstone, but is not veined by oxides or sulphides, giving rise to a marked asymmetry in the geometry of host-rock alteration about the lodes.

Pyrite Morphology

Description:The morphology of pyrite porphyroblasts within the footwall alteration indicates a protracted structural history, with early sulphide introduction.

Pyrite occurs as euhedral grains with clear rims and 'poikilitic' cores in schists containing the D2(MP) schistosity (Fig. 3.12G & H). Sulphur isotope analysis of the two types shows them to be distinct (chapter 11, Davidson et al.(in press)). In samples also deformed by D2(LP), these recrystallised grains are sheared and elongate, chalcopyrite has

concentrated in pyrite pressure shadows (Fig. 4.5E), and poikilitic blocks are separated by new inclusion-free pyrite, suggesting that cataclasis was followed by annealing and dislocation flow. Cox et al. (1981) found that dislocation flow in pyrite is thermally activated only above 450° C at geologically realistic strain rates.

The inclusions are mainly randomly oriented, rather than aligned, and may therefore represent a predeformational fabric; hematite, chlorite, albite, quartz and carbonate are common inclusions, whereas muscovite and biotite are rare. Albite has the same composition within and exterior to pyrite (pure albite, with 0.4 – 0.6 % FeO, determined by microprobe analysis), meaning that albite alteration must have preceded or accompanied pyrite growth (similarly for magnetite). The textures preserved in footwall pyrite are in sharp contrast to pyrite in the deformed footwall veins, and in ironstone, which are inclusion-free.

Interpretation: Studies of pyrite in the thermotectonised rocks of other terrains show it to commonly form idioblastic porphyroblasts preserving pre and post-depositional fabrics, depending on the timing and speed of its growth (Ramdohr 1980). Relict early fabrics are noted by Briggs et al. (1977), Frater (1985) and Brooker et al. (1987) in metamorphosed syngenetic deposits, while Deb (1979) and Brooker et al. (1987) record the preservation of cleavage in pyrite. Frater (1985) in particular attributed pyrite sieve-textures in the Golden Grove massive sulphide ore (Western Australia) to "rapid growth from supersaturated solutions in unconsolidated ash or mud". The observations of these authors imply that if sieved pyrites at Starra had grown in deformed rocks, they would have preserved cleavage. This is not the case. These pyrites must therefore have grown rapidly in a (possibly unconsolidated) rock matrix prior to deformation, whereas the enclosing idioblastic rims grew by diffusion slowly in areas of low mean deformational stress (Mookherjee 1971, McClay & Ellis 1984), embaying the older cores, and growing across cleavage and transposition-slip boundaries to form epigenetic pyrite morphologies (Amaro et al. 1988). Strong diffusion has partially destroyed some older pyrite cores.

Overall, poikilitic pyrite constitutes firm evidence of predeformational alteration in the Starra footwall.

TROUGH TANK

Broad Geological Setting

Trough Tank lies in an area of no outcrop ~ 40 km south of Starra, along strike from Kuridala Formation metasediments (Fig. 2.3). It is overlain everywhere by ~ 30 m of Mesozoic cover, which necessitated a reliance on aeromagnetics in the early phases of exploration, followed by percussion and diamond-drilling (over 90 holes to date) by the joint venture partners Placer Minerals (83 %) and Billiton Australia (17 %). The known mineralised zone, referred to as the"Keel Anomaly", is ~ 500 m long, occurring as the northern, most magnetic end (16000 nT above reference) of a 7 km long north-south

aeromagnetic trend (detailed in part in Fig. 3.16, hole locations in Fig. 6.20). This trend (termed the "Central Anomaly") repeats 800 m west of Trough Tank ("Western Anomaly"). At present the main anomaly is believed to be a large D2 synform, dislocated by northwest-trending strike-slip faults.

Stratigraphy

Cu-Au-Co mineralisation is hosted mainly within three concordant banded magnetite-rich units (BIFs) (Fig. 3.15F), in a sequence of quartzites, feldspathic quartzites, phlogopitic and feldspathic schists at least 120 m thick (Fig. 3.17). In addition, some holes contain a second discordant style of coarse-grained silica-hosted mineralisation, with the greatest promise of economic tonnage. BIFs 2 and 3 (Fig.3.17) are usually underlain by a massive pink feldspathic schist, and overlain by quartzite (coarsening upward to isolated pebble-bearing grits), whilst the uppermost BIF 1 is hosted by all of these lithologies. Of these, BIF 2 is most consistently mineralised, with an average of 0.55 ppm Au and 0.53 % Cu, (n=216), ranging up to 52 ppm Au (an indication of 'nuggeting' in the analyses caused by coarse gold). Beds of biotite-anthophyllite-cordierite schist are not abundant, but are most common near the base of the prospect.

Broad lithological trends indicate an increase in sediment maturity upwards, with a change from aluminous and feldspathic beds to cross-bedded (up to 1 m long, low-angle foresets), quartzite-dominated beds, interpreted as a coarsening-upward cycle. These features argue for a shallow clastic-hosted sedimentary environment. An origin of the massive feldspathic intervals as acid volcanics or pyroclastics is discussed with the chemical affinities of the sediments in chapter 5.

A lack of outcrop lends uncertainty to the stratigraphic position of Trough Tank. Minor primary carbonate in the sediments, acid volcanism, and the strong similarity of the mineralisation-style to Starra, favour a position close to the Kuridala/Staveley Formation boundary. However, Trough Tank BIFs could also represent a continuant of Pegmont BIFs exposed ~ 32 km NNE of Trough Tank, assigned to the upper Kuridala Formation by Stanton & Vaughan (1979) and Blake et al. (1984). Beardsmore et al. (1988) place Pegmont at least 2000 m below the base of the Staveley Formation.

Metamorphic Conditions

The following prograde parageneses have been recognised, with an average coarse-grain size of 0.6 mm (numbers in brackets refer to the Mg number, calculated in mole % as Mg/(Mg+Fe)):

Feldspathic Schist

Albite - biotite (50.5–54.2) - muscovite (41.8–43.6) - K-feldspar ± quartz.

Albite - sillimanite - muscovite.

Albite - quartz.

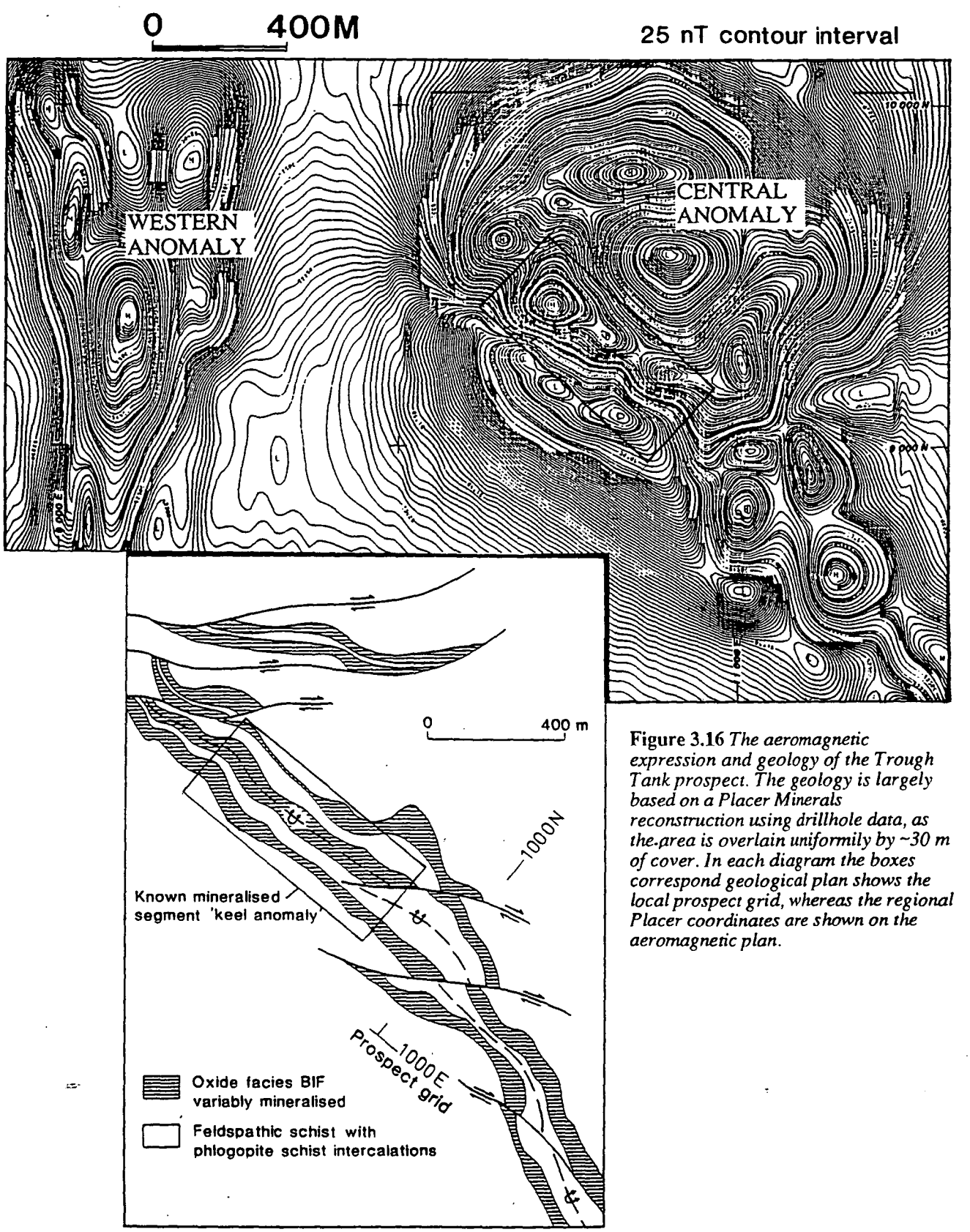

Figure 3.16 *The aeromagnetic expression and geology of the Trough Tank prospect. The geology is largely based on a Placer Minerals reconstruction using drillhole data, as the area is overlain uniformly by ~30 m of cover. In each diagram the boxes correspond geological plan shows the local prospect grid, whereas the regional Placer coordinates are shown on the aeromagnetic plan.*

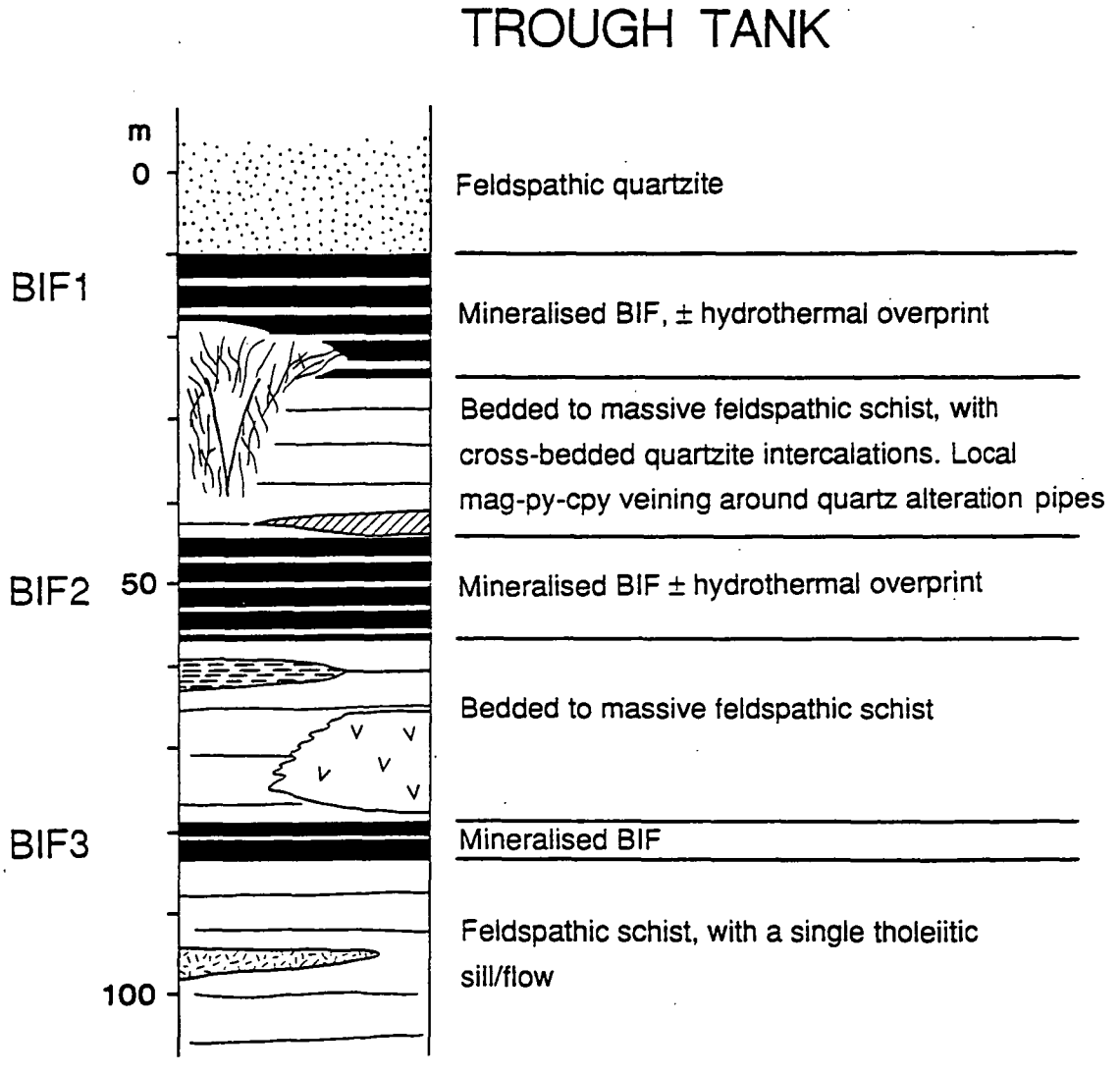

Figure 3.17 *Generalised stratigraphy of the Trough Tank sequence.*

Corundum - muscovite (23.2–28.4)

Magnesian Schist

Phlogopite (68.3–71.6) - anthophyllite (retrogressed) - cordierite (80.2–82.0) ± monazite

Anthophyllite (70.2–72.2) - apatite (0.15–0.62 % Cl) - magnetite ± pyrite

Anthophyllite - chrysotile - muscovite

Amphibolite

Andesine (An 36–42) - pargasitic hornblende - sphene - ilmenite ± zoisite

The albitic schist is by far the most common rock-type, and shows signs of the anatexic breakdown of biotite and muscovite, such as migmatitic feldspathic veins and quartzofeldspathic leucosomes transitional to larger bodies of pegmatite. This implies a minimum temperature of ~ 650 - 680° C over the 2 – 5 kbar range (Merrill et al. 1970), close to the highest in the Eastern Succession, near the top of Zone C of Jaques et al. (1982). To further define the metamorphic temperature, the plagioclase-hornblende thermometer of Spear (1980) was employed. The method is detailed in chapter 4, with typical amphibole and plagioclase compositions presented in Table 3.3. Average compositions provide an estimate (incorporating the recalibration suggested by Jaques et al. (1982)), of 694 ± 25° C, which substantially exceeds an earlier estimate of Davidson et al.(in press) using the method of Plyusnina (1982), but accords with the observed anatexis.

Further constraints on temperature are the minimum stability of sillimanite, ~ 510° C (Holdaway 1971), and the presence of cordierite-anthophyllite rocks; Reinhardt (1987) estimates a temperature range of 620–650° C and 4 kbar for the assemblage Cord + Anth + Bi + Qtz ± Plag found in the Rosebud Syncline (west of Mary Kathleen, Mount Isa area), while James et al. (1978) estimate ~ 630° C for the same assemblage at ~ 6 kbar. This paragenesis, strongly retrogressed, occurs in sample TT29 (TNQ3, 174 m). Pressure is not well constrained, relying on the estimate of ~4 kbar for Zone C provided by Jaques et al. (1982).

Strong retrogression is an important feature of Trough Tank. It is expressed by dolomitic veining and replacement of anthophyllite and cordierite, with new growth of muscovite, biotite and magnesian chlorite. The source of the CO_2 is problematic, but may relate to anatexis, because dolomitic calcite (Mg/Mg+Ca mol % = 0.42–0.48) is a common component of the albite-dominated segregations; high water activities are also suggested by the alteration of biotite and muscovite to chlorite close to leucosomes.

Further knowledge of the composition and temperature of circulating metamorphic fluids was provided by thermometric analysis of fluid inclusions trapped in annealled quartz close to the ore zones . Entrapment as isolated inclusions within annealled grains, rather than along fractures, suggests these fluids evolved during prograde metamorphism.

These "primary" inclusions are highly saline, 42–57 wt. % equiv. NaCl, with $T_{h\ vapour}$ = 186–466° C, a distinct $T_{h\ vapour}$ maximum at ~ 235° C, and $T_{h\ crystals}$ = 416–483° C, uncorrected for pressure (Fig. 3.18, Appendix 1). They occur as 3–15 μm liquid-vapour inclusions consistently containing 3 daughter salts, of which only halite is identified with certainty, and are associated with 5–15 μm high density CO_2 inclusions (Fig. 3.15G). The depression of T_m to -36.8° C suggests that $CaCl_2$ was a brine component. The

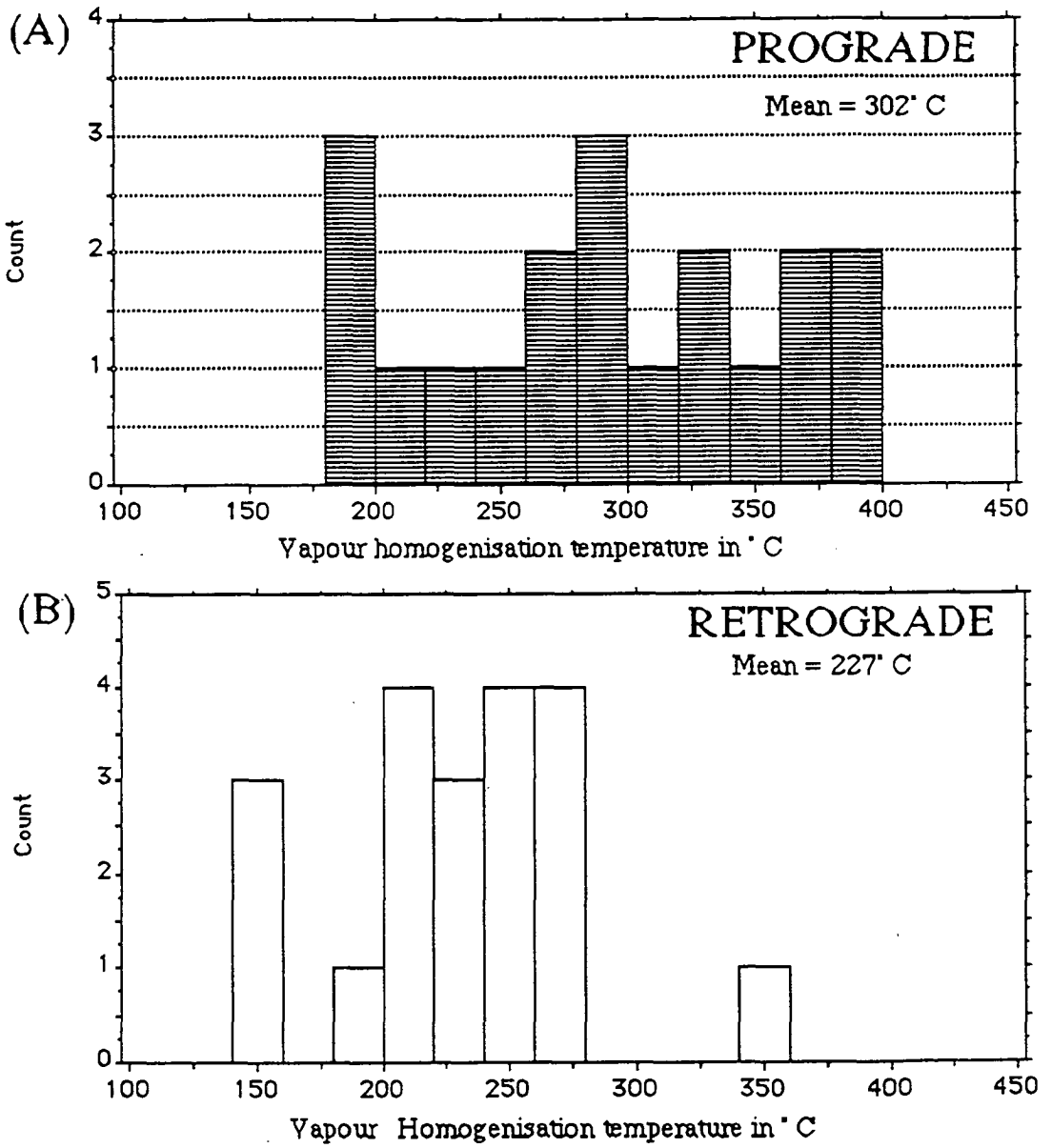

Figure 3.18 *Fluid inclusion vapour homogenisation temperatures within the silica alteration at Trough Tank. Prograde inclusions are isolated within annealled quartz crystals, whereas retrograde inclusions occur in radial decompression cracks around magnetites. Daughter crystal homogenisation temperatures for both groups are in the range 416–513 °C.The inclusion conditions do not necessarily indicate the conditions of ore formation, as other criteria suggest the ores are premetamorphic.*

inclusion-types observed are similar to those from other high-grade meta-evaporite terrains, in which entrapment is thought to have occurred from an immiscible fluid consisting of a saline aqueous phase, and a low salinity CO_2-rich phase (Gehrig et al. 1979, Sisson 1981). Given the upper amphibolite facies metamorphic conditions, it is unlikely that these are relict ore-related inclusions, as thought by Davidson et al. (1988), but instead were trapped during quartz recovery near peak metamorphism; most authors agree that inclusions can only survive 100 – 150° C and 1–2 kb above their entrapment conditions (Hollister et al. 1979, Ohmoto & Rye 1979, Woods et al. 1982).

A second inclusion group is identified as retrogressional because it commonly occupies radial decompression cracks (Van der Molen & Roermun 1986) around magnetites and pyrites (Fig. 3.15H) : salinities between 31 and 50 wt. % equiv. NaCl and $T_{h\ vapour}$ = 148 –345° C, and $T_{h\ crystals}$ = 457 – 513° C, are the indicated conditions of entrapment. Thus, high

	HORNBLENDE				PLAGIOCLASE		
	1.	2.	3.		1.	2.	3.
SiO_2	41.34	41.12	41.91	SiO_2	57.76	58.45	58.88
TiO_2	1.22	1.21	1.15	Al_2O_3	26.70	26.28	25.36
Al_2O_3	11.86	11.87	11.55	CaO	8.12	8.01	7.15
Fe_2O_3	17.74	16.74	17.68	Na_2O	6.11	6.80	6.95
FeO	6.78	7.23	6.61	K_2O	-	-	0.10
MnO	0.27	-	0.30	**Total**	**99.33**	**99.51**	**98.44**
MgO	6.23	5.98	6.40				
CaO	11.18	11.00	11.37				
K_2O	0.46	0.47	0.46				
Na_2O	1.61	1.66	1.69				
Cl	0.19	0.20	0.15				
Total	**98.88**	**97.49**	**99.30**				
Cations per 23 oxygens				Cations per 8 oxygens			
Si	6.153	6.198	6.203	Si	2.596	2.619	2.660
Ti	0.137	0.137	0.128	Al	1.414	1.388	1.351
Al	2.080	2.109	2.015	Ca	0.406	0.384	0.346
Fe^{3+}	1.987	1.899	1.969	Na	0.561	0.591	0.608
Fe^{2+}	0.845	0.912	0.822	K	-	-	0.006
Mn	0.033	-	0.038	**Total**	**4.977**	**4.982**	**4.971**
Mg	1.382	1.343	1.412				
Ca	1.783	1.777	1.803				
K	0.087	0.090	0.087				
Na	0.465	0.484	0.486				
Cl	0.048	0.052	0.037				
Total	**15.000**	**15.000**	**15.000**				

Table 3.3 *Microprobe analyses used for temperature estimation, from sample TT61, (NQ1, 156.3 m), a plagioclase-hornblende amphibolite with tholeiitic chemistry.*

salinity, high temperature fluids were present in the area of the ores during the heating and cooling phases of metamorphism, most likely derived from evaporitic sediments rather than granites, because of the high $CaCl_2$ contents (Behr & Horn 1982, Schmidt-Mumm et al. 1987, McKibben et al. 1988). Granite-derived fluids become $CaCl_2$-rich only in the instance of large-scale carbonate wall-rock-reaction (e.g., Kwak & Tan 1981).

Structure

The regional fold terminology of the Mount Isa area (Page & Bell 1986) is applicable to Trough Tank structure (although D1 features are not apparent), as distinct from nomenclature used within this thesis to describe additional events confined to the Starra area. The main folds and cleavage are of similar style and orientation to those of the regionally identified D2 deformation.

The detailed structure of the Keel Anomaly is dominated by a single, SSE-plunging, tight to isoclinal D2 syncline, minimum wavelength 300 m, using the evidence of the geometry of iron formation, and minor fold vergences deduced by orienting drill-core with respect to cleavage (~ 60° east). Sparsely distributed grading and cross-bedding indicate the fold is upward-facing. Hinge thickening is inferred from drillholes intersecting the upper BIF unit (Figs. 3.19, 6.16). Both limbs dip at between 55° to 65° east. Vergence fold-widths range from 10 cm to 20 m, exhibiting moderate degrees of layer transposition. A mild strain increase west of the main fold hinge has resulted in asymmetric porphyroclasts, alignment of pre-existing veins to the foliation, and a weak L-S fabric (intensifying with depth), associated with thin (1–2 cm wide) mylonite zones within feldspathic schist. The regional significance or extent of this zone of increasing strain is uncertain. Elsewhere in the syncline the random orientation of peak metamorphic minerals suggests that peak metamorphism post-dated the peak of D2 deformation.

Mineralisation

Iron Formation-hosted Mineralisation

Bands of magnetite averaging 1 cm, but at times attaining 1 m in thickness, alternate with either quartz-magnetite beds, or thin (1-5 cm) bands of metasediment (mineralogically similar to adjacent clastic units). Banded and massive anthophyllite + chrysotile schist also occurs as 10-30 cm thick bands which are strike-equivalent and intercalated with BIF, mainly in the northern 250 m of the lower BIF, associated with lower Au grades (0.1-0.5 g/t). They are interpreted as metamorphosed magnesian carbonate - silica iron formations, featuring low Al_2O_3 contents (eliminating origins such as metamorphosed magnesian clays, suggested by Reinhardt (1987) for similar lithologies in the Rosebud Syncline). A more detailed study of thickness variation and the chemistry of BIF is presented in chapter 6.

The main sulphide minerals are pyrite and chalcopyrite, occurring as disseminated

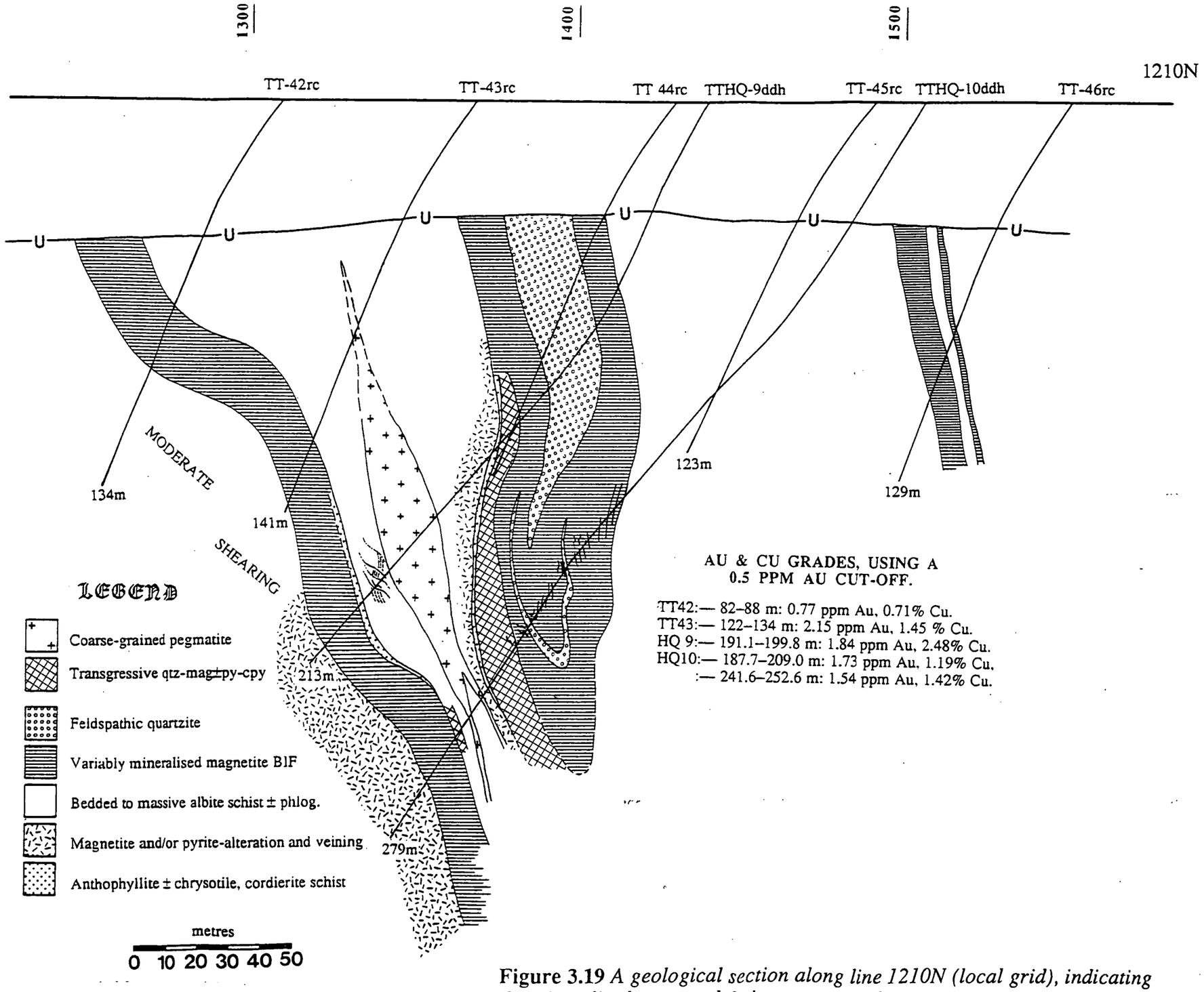

Figure 3.19 *A geological section along line 1210N (local grid), indicating the mineralised areas and their average grade.*

grains in magnetite ± hematite bands, with similar grainsize to the other recrystallised components (magnetite averages 20 μm diameter in quartz layers, and 0.4 mm in massive magnetite bands). The ore rarely contains more than 5% disseminated sulphides. Quartz and sediment bands do not normally contain sulphide. Apatite and siderite are constant accessories in magnetite bands, whereas tourmaline and bornite are uncommon. Magnetite is the dominant prograde oxide in quartz bands, whereas hematite forms randomly-oriented retrograde blades overgrowing some magnetite.

In thin-section pyrite and chalcopyrite are intergrown, but not replacive; inclusions of both occur in annealled magnetite, and vice versa. Some magnetites preserve lines of quartz and sulphide inclusions paralleling the larger-scale compositional layering, suggesting the overgrown layering is relict bedding.

Gold has not been observed in thin section.

Discordant Mineralisation

Two types occur:

(a) *Structural Remobilisation:* Within concordant ores the deformational effects include (1) cleavage-parallel recrystallisation of sulphides (2) Sulphide movement into poorly-defined magnetite-quartz veins sub-parallel to foliation (3) Coarsening of sulphide patches to clots 2-3 cm across in fold hinges, without change in Cu grade from limb areas (4) 10-30 cm scale layer transposition in some hinges (5) Rotation and recrystallisation into shear planes where mineralisation is within a ductile unit (for instance, anthophyllite schist) (6) Alteration of chalcopyrite to chalcocite at the intersection of retrogressive carbonate-chlorite veins with older sulphides.

The confinement of these features to BIF is evidence for only local movement of sulphides and gold. Features such as injection or Durchbewegung textures (Maiden, 1986) are not apparent because of the low sulphide content of the BIFs. The mineralogy of cross-cutting veins reflects the mineralogy of the surrounding rock. For instance, veins in a virtually barren BIF hinge in drillhole HQ19 (1930N, 1450E, prospect grid, Fig. 3.16) contain only remobilised magnetite (Fig. 3.15F), whereas chalcopyrite-pyrite BIF is cut by chalcopyrite-bearing veins. Specific drilling of D2 fold hinges has failed to demonstrate enrichment in these sites.

(b)*Ore zones that cut bedding, but predate folding*: These are discrete massive silica and magnetite zones which underlie concordant BIF mineralisation, in places overprinting it, recognised by coarsening grain-size (2-10 mm, annealled in thin section) and cross-cutting folded mineralised veinlets. The dominant feature of this style is a clear quartz matrix, which hosts fine euhedra of magnetite, pyrite, chalcopyrite and carbonate, and is folded by D2. One to five centimetre-wide irregular blocks of feldspathic schist contained within the quartz matrix have chloritised rims and are infiltrated by fine pyrite. They are thought to

represent remnants of the pre-existing lithology.

A relatively sharp 0.1–2.0 m wide chloritic selvedge occurs on the margin of each zone, cross-cutting recognised bedding at moderate angles. For instance, the subtended angle between bedding and epigenetic mineralisation in HQ13 (1520N, Fig. 6.20), is 55°. This selvedge in thin-section contains peak-metamorphic anthophyllite retrogressed to chlorite and talc. The overall geometry of the silica-pipe alteration is believed to be an upwardly-opening funnel, characterised by bedding-parallel incursions away from the main discordant zone, and in which the top is so wide as to be easily mistaken as a stratigraphic unit. The surrounding feldspathic gneiss contains a 10 to 30 m wide zone of pyrite-magnetite veins, blebs and strings, some folded, frequently parallel to but also cross-cutting compositional layering (this alteration is most similar to the pervasive oxide alteration of Starra). Beyond this a disseminated cobalt-rich pyrite zone extends 50 m or more along strike, with variable carbonate alteration.

SUMMARY AND CONCLUSIONS

The following critical observations are relevant to the genesis of Starra-style BIF-hosted Cu-Au deposits.

(1) Economic mineralisation is confined to massive and banded iron-rich units which are conformable with the host rocks, and are strike-equivalent to barren Hamersley-style iron formation, and tourmalinite. Taken in company with the evidence of sedimentary reworking of ironstone into polymict conglomerates, a synsedimentary origin for ironstones is strongly advocated.

(2) Alteration at Starra and Trough Tank is mainly confined to the footwall, and hence is markedly asymmetric. Starra alteration consists of mag-hem-py-cpy veins, whereas that at Trough Tank is more confined and pipe-like, zoned from py-carbonate to mag-py-cpy to the most intense qtz-mag-py-cpy assemblage.

(3) Starra ores coincide with the edge of a major shear zone, contrasting with the mainly low strain environment of Trough Tank.

(4) Starra mineralised ironstone occurs at a rock-type change, believed to correspond with a change from volcanosedimentary to sedimentary deposition, in a basinal environment deeper than that prevailing to the east and south during Staveley Formation deposition. In contrast, Trough Tank BIFs do not conspicuously occur at a rock-type change, although acid and basic volcanics are recognised within the host sequence.

(5) The features of Area 222 Cu-Au mineralisation differ from the other Starra prospects. Ore is confined to the matrix of polymict conglomerates, but is absent from finer intercalated calcareous sandstones and siltstones, suggesting that fluid-paths were controlled by diagenetic porosity, rather than zones of structurally-prepared brecciation.

(6) The annealled microstructures of Starra and Trough Tank ores indicate that the sulphides were present in ironstone prior to D2 deformation and metamorphism. Footwall pyrite at Starra contain internal structures which favour their pre-cleavage origin.

CHAPTER 4

STRUCTURE AND METAMORPHISM OF THE STARRA AREA

INTRODUCTION

By virtue of its proximity to the Starra Shear, the Starra area is more deformed than much of the Cloncurry Fold Belt, although metamorphic grade is comparatively low. The Kuridala and Staveley Formations participated in the regional Mount Isa Inlier deformations. Reactivation of the shear during these episodes imposed high strains, resulting in strong L/S fabrics, transposition of layering and brecciation. Ductile deformation is most intense west of the Western Hematites, and decreases east to the Eastern Hematites, before increasing again in the "Central Zone" of Nisbet et al. 1983, east to Mt. Cobalt (Fig. 13).

The purpose of this study is to review the structural history of the area between the Mort River (south of the Yellow Waterhole Granite) and the Mt Elliott Mine, to determine the timing of Starra mineralisation with respect to deformation. With this aim, detailed maps have been prepared of Area 257 (Appendix 4.1), level 1275 R.L. at Area 251 (underground), Eastern Hematites Area 260 (presented in the "Geology" section), and a part of the Pyramids Syncline.

A REVIEW OF PREVIOUS WORK ON THE STRUCTURE OF THE MORT RIVER TO MT. ELLIOTT AREA

$D1_a$ and D1— Extension Followed by Compression

Regional Evidence

An extensional episode prior to the compressional phase of D1 has been identified in the Cloncurry Fold Belt (Passchier 1986, Holcombe et al. 1987), termed the "Alligator Phase" or D_a by Passchier & Williams (in press). Williams (1989) assigned high degrees of south to south-west extension (57 - 81 %) to D_a during the formation of the Cover Sequence 2 rift-basin in the period 1730 - 1670 Ma, using structures close to the Pilgrim Fault area of the Duck Creek Anticline. To distinguish between the extensional and compressive phases of D1, the extension event is termed '$D1_a$' within the text, whereas D1 is retained to describe the earliest compressional event.

Throughout the Mount Isa Inlier, the evidence for D1 compressive deformation preceding the main D2 shortening event includes folded cleavage, downward facing F2 folds, and strata repetition (Bell 1983, Lister et al. 1986, Beardsmore et al. 1988, Loosveld

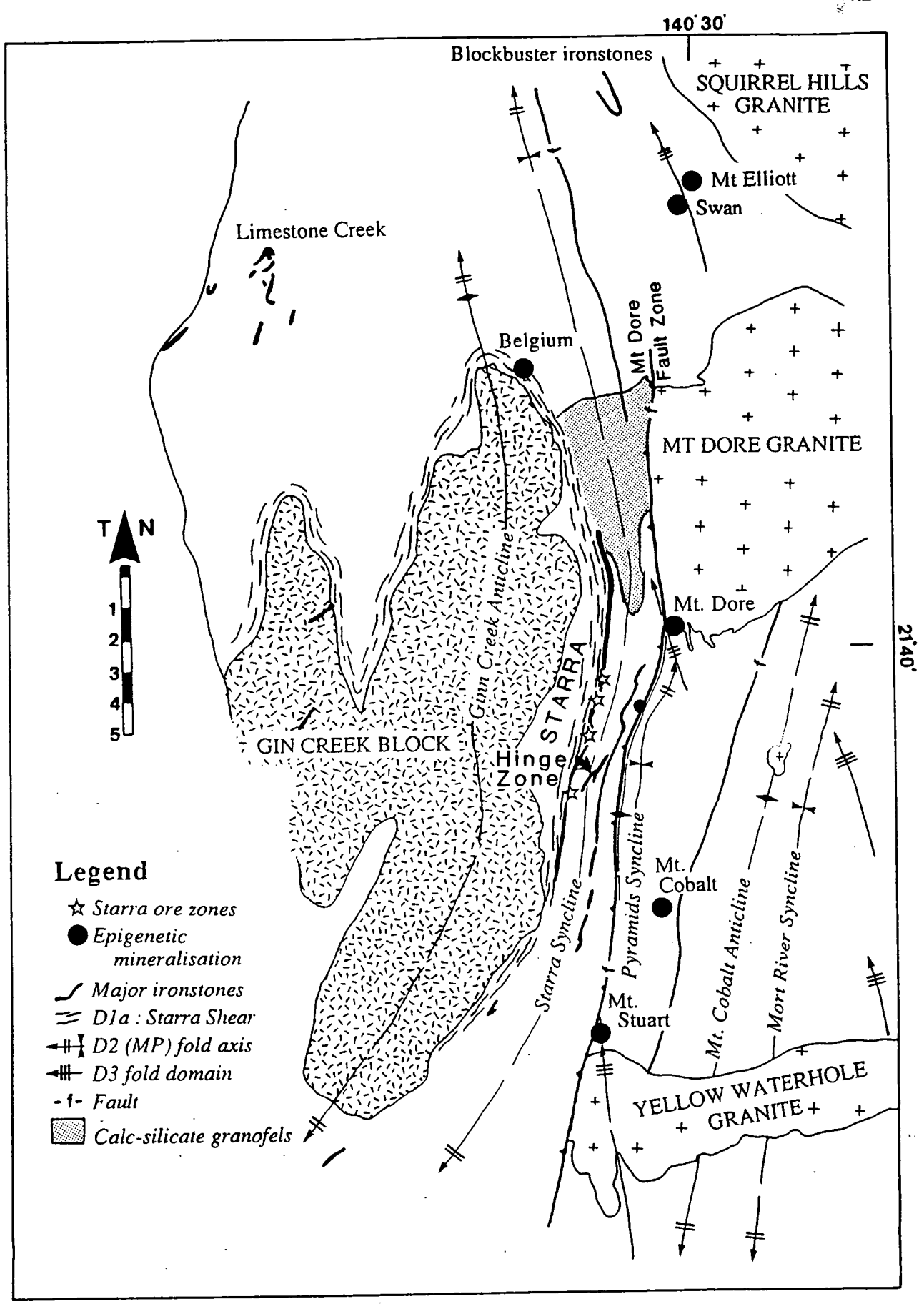

Figure 4.1 *Tectonic elements of the Starra region. The boundary of the Gin Creek Block includes the Double Crossing Metamorphics (Blake et al. 1984) and all Gin Creek Granite types.*

1989). The deformation style responsible for these features is inferred to be ductile thrusting and associated recumbent "nappe" formation, with at least two tectonic movement directions. Thrusts in the Leichhardt River Fault Trough and Tommy Creek areas moved southward (Bell 1983), whilst those in the Deighton area moved westward to northwestward (Loosveld & Schreurs 1987).

Staveley Belt Evidence

Switzer (1987), Laing et al. (1988) and Switzer et al. (1988) identified the Starra Shear (a 1 km wide zone of high strain immediately west of the Western Hematites), as an extensional pre-D2 shear with an upper block-to-the-north movement sense (i.e., lineations in the hinge of the Gin Creek Anticline are near-vertical). The zone separates middle to upper greenschist facies Staveley Formation from the upper amphibolite facies Gin Creek Block. Folding of the shear around the D2 Gin Creek Anticline (Fig. 4.1), and the normal sense of movement suggested by the juxtaposition of Staveley Formation and the Gin Creek Block, are the best evidence for a $D1_a$ timing. Switzer et al. (1988) concluded the Starra Shear was a "major crustal detachment fault" during the Alligator Phase "with the Gin Creek Block representing a metamorphic core complex". The identified sense of extension is similar to that of Williams (1989).

Compressive D1 deformation is also postulated in the area. D1 nappe formation with westward movement was suggested by Beardsmore (1986), to explain downward-facing F2 folds in the Belgium and Mariposa Mine areas (Fig. 4.1), and mylonitic textures in Kuridala Formation quartzite (postulated as the highly strained sole of a large recumbent structure). (The validity of the downward-facing fold in the Mariposa Mine area is examined later in the chapter). Beardsmore (1986) further suggested that the "Hinge Zone" (Fig. 4.1) of Leishman (1983) could be interpreted as a series of parasitic D1 folds refolded during D2 to produce small to medium-scale domes and basins.

D2 — Kilometre-scale Isoclinal Folding

D2 deformation was a major, penetrative, east-west shortening event, producing upright, tight to isoclinal, shallowly doubly-plunging, kilometre-scale folds. Nisbet et al. (1983), Leishman (1983), Beardsmore (1986) and Beardsmore et al. (1988) have documented the important D2 folds in the region, summarised in Fig. 4.1. Westernmost is the Gin Creek Anticline (wavelength 5 to 6 km), adjacent to the Starra Syncline, which separates Eastern and Western Hematites of the Staveley Formation (Kary & Harley , in press). Ironstone-bearing Staveley Formation is infolded again east of the Mt. Dore Fault Zone in the Pyramids Syncline (a name based on a prominent outcrop of ironstone known as "Pyramids" in the core of the structure.). Further east, the Kuridala Formation is folded about the regional Mort River Anticline (not figured), which has a 40 km long axis (Beardsmore et al. (1988).

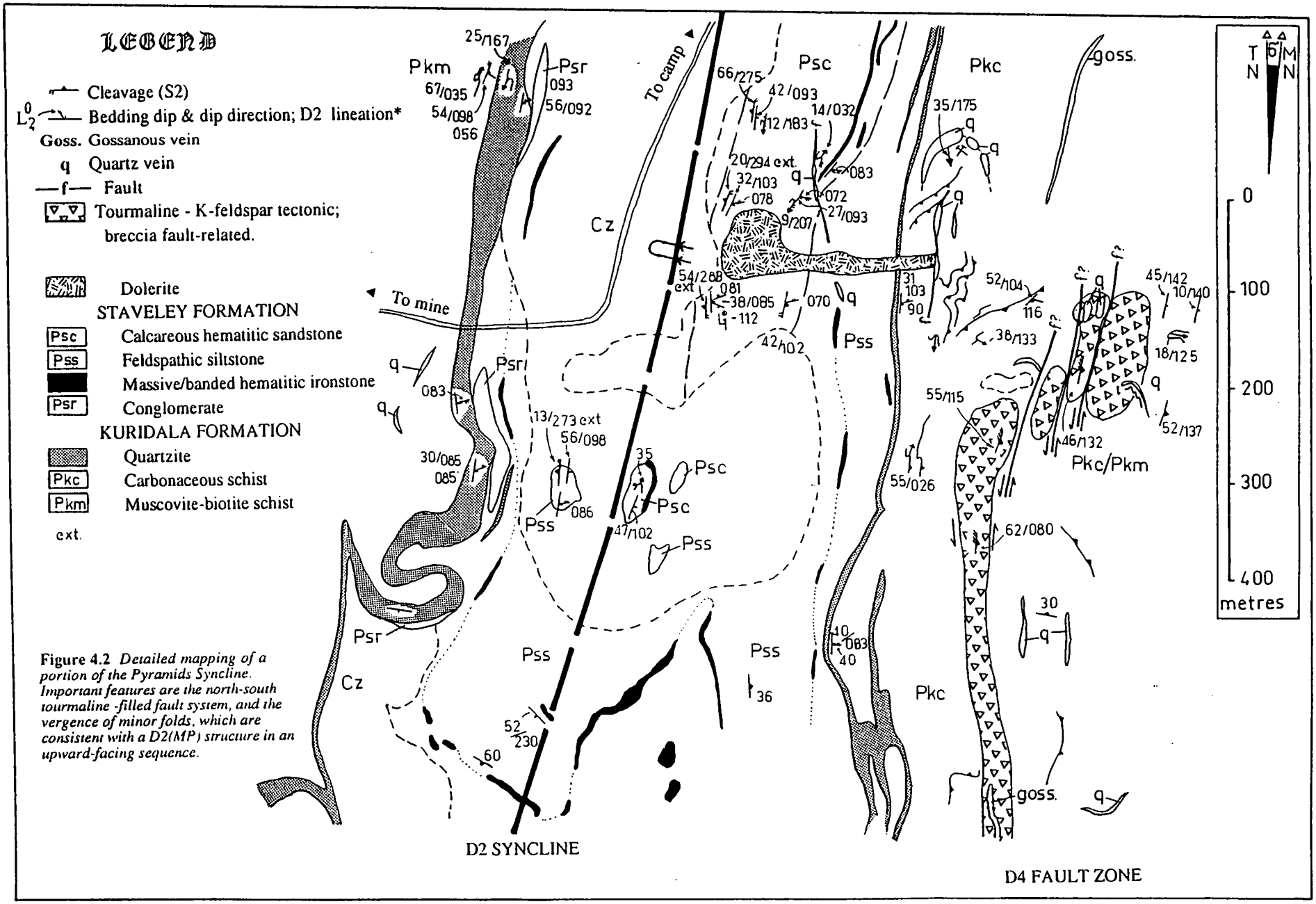

Figure 4.2 *Detailed mapping of a portion of the Pyramids Syncline. Important features are the north-south tourmaline -filled fault system, and the vergence of minor folds, which are consistent with a D2(MP) structure in an upward-facing sequence.*

S2 forms a near-vertical to east-dipping slaty to differentiated cleavage sub-parallel to bedding, best reflected in pelitic lithologies. It is associated with a pronounced steeply north-plunging stretching lineation defined variously by peak metamorphic mica, amphibole, feldspar, sillimanite, staurolite, hematite and magnetite (Jaques et al. 1982, Nisbet et al. 1983, Switzer et al. 1988; D1 of Jaques et al. 1982 corresponds to the regional D2.). An early D2 timing was identified for peak metamorphism in the Soldiers Cap Group by Loosveld (1989), because S1 is crenulated to a lesser degree by S2 within staurolite than outside of it.

D3 — Restricted Bands of Small to Medium-scale Folding and Kinking

D3 folding is not a pervasive feature in the Selwyn-Starra area, but where present it can be associated with significant structurally-controlled Cu-Au mineralisation, such as the Mt. Elliott, Swan, Mt. Dore and Mt. Stuart prospects (Nisbet 1983, Beardsmore 1988). Beardsmore (1988) describes D3 as a series of northwest-trending, 1 km-wide "corridors" of small to medium-scale folding, kinking and crenulation. Individual F3 folds are tight to isoclinal, moderate to steeply plunging, with an axial surface dipping at 45 - 60 °/~075°. Nisbet (1983) found that F3 folds at Mt. Dore verge westward, whereas domains to the east of here verge to the east. The "Hinge Zone" is identified by Nisbet (1983) as a boundary between upward and downward-facing F3 domains, and hence predates F3.

Apart from minor northwest-trending kink-bands, D3 folding is absent from the mineralised Western Hematites, eliminating the need for further discussion of this generation.

Other Deformation

Both Nisbet (1983) and Leishman (1983) recognised a series of steeply north-plunging medium-scale sinistral folds which verge west. These folds tighten westwards from open styles in the Eastern Hematites, to isoclinal folds in the mineralised Western Hematites, with abundant shear fabrics, transposition breccias and faulting. Several of the Starra ore zones are associated with this fold generation. Switzer (1987) and Switzer et al. (1988) regard these as D2-folds in which the F2 axes rotated towards the L2 stretching direction. The validity of this argument will be examined in a later section.

A second important deformation feature is the brittle to brittle-ductile Mt. Dore Fault Zone (Fig. 4.1). This is an east-dipping, north-trending, breccia-bearing reverse fault zone ~ 250 m wide, which because of its truncation of the Mt. Dore and Yellow Waterhole Granites must be younger than ~ 1480 Ma (Nisbet 1983, Scott 1986, Beardsmore 1988). The Mt. Dore copper ores occur at the intersection between a D3 fold-band and the Mt. Dore Fault Zone, hosted within a breccia of previously folded and crenulated clasts (Beardsmore 1988). The fault zone assumes great regional importance in the tectonic model of Beardsmore et al. (1988), where it is identified as the tectonic western boundary of the Maronan Supergroup.

PROSPECT-SCALE STRUCTURAL ENVIRONMENT

Terminology

Regionally applied deformation names have been used to describe ore prospect structures, with the following exceptions:

D2(MAIN PHASE), abbreviated to D2(MP), is used to describe the widely recognised, shallowly plunging, kilometre-scale folds such as the Gin Creek Anticline and Starra Syncline.

D2(LATE PHASE), abbreviated to D2(LP), is used to describe the sinistral, steeply-plunging, medium-scale folds which most obviously deform the Eastern and Western Hematites. The evidence for the view that D2(LP) followed D2(MP) and preceded D3 is discussed in a subsequent section.

D4 describes brittle-ductile deformation akin to the Mt. Dore Fault Zone, occurring around the Williams Batholith, possibly related to the intrusion. The "Cloncurry Overthrust" is a similar feature to the Mt. Dore Fault Zone, separating the Doherty Formation and Williams Batholith in the Squirrel Hills Belt (Loosveld 1989).

$D1_a$ Extension

F2(MP) has folded east-west trending lineations in the Gin Creek Anticline hinge (Switzer 1987); the same folds possess well-developed L^2_2 lineations.

Within the Starra Shear, a 400 m thick domain of shallowly north and south plunging lineations on the S1/S2 surface is also likely to reflect $D1_a$ deformation. The lineation is defined by quartz rodding and elongate aggregates of biotite or feldspar. This domain, identified on two transects of the Starra Shear, commences 250 m west of Area 257 (Fig. 4.3 A & B), persisting to the first extensive outcrops of deformed Gin Creek Granite. It can occur on the same surface as steeply-plunging lineations characterising the Mariposa Creek Member, Western Hematites, and hangingwall metasediments.

The orientation of the older lineation-domain could correspond to Switzers (1987) $D1_a$ stretching direction which he obtained from the Gin Creek Anticline hinge. The inhomogeneous preservation of the older lineation domain through D2(MP) is evidence that later reactivation of the Starra Shear was not penetrative.

D2 (Main Phase)

General Fold Forms

The orientation of minor and major D2(MP) folds away from the Starra Shear is plotted in Fig. 4.4B. They plunge north and south; 17 southern plunges have a mean vector of 42°/182°, while less common northern plunges have a mean vector of 22°/006°. The Starra Syncline, separating the Eastern and Western Hematites, is a tight to isoclinal fold with an axial plane dipping approximately 75°/115°. It contains several smaller south-plunging "M" folds (Nisbet 1983). The axial plane of D2 folds east of the Starra Syncline dip more shallowly, resulting in an average axial plane of ~ 40°/100° in the Pyramids Syncline.

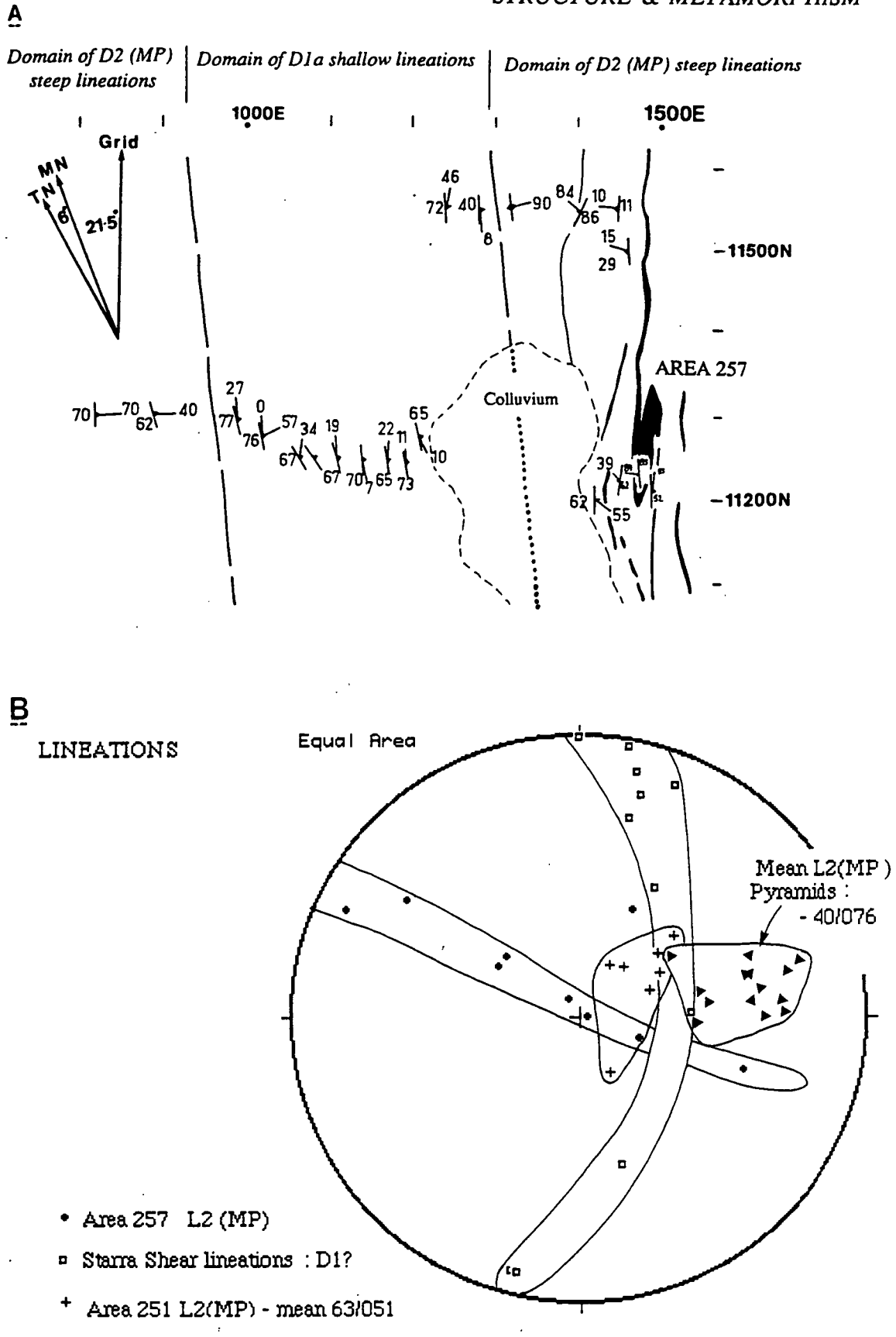

Figure 4.3(A) *A lineation map constructed from two transects across the Starra Shear at Area 257. A domain of shallowly plunging lineations encountered 200 m west of the ironstones is attributed to D1, whereas lineations on S2(MP) are generally steeply north plunging.* **(B)** *An equal area stereoplot of lineations illustrates that the L2(MP) and the D1 lineations are co-planar, L2(MP) in the Pyramids Syncline plunges more shallowly east than Starra Shear lineations, and L2(MP) lineations at Area 257 have been reorientated by a late shallowly-south-plunging D4 folding.*

Detailed mapping (Fig. 4.2) does not support the downward-facing nature of the Pyramids Syncline (Fig. 4.1) proposed by Beardsmore (1986), who refers to the fold as the Mariposa Antiform. This structure is cored by calcareous Staveley Formation and so youngs towards the D2 fold axis. South-plunging D2(MP) vergence folds on either side of the fold-axis indicate a moderately-overturned syncline, rather than an antiform. In addition, quartzites on the eastern limb are more intensely lineated than those of the western limb, which is evidence that the lineations were the product of differential D2(MP) strain, rather than homogeneous D1 strain.

Cleavage

D2(MP) cleavage is present in all rocks, best defined by alignment of the peak metamorphic minerals. The Starra Shear contains an andalusite-defined or slaty biotite-defined plane at a low angle to S1 close to the edge of the Gin Creek Block, whereas close to the Western Hematites, two slaty cleavages are identified (probably S2(MP) and S2(LP), on the basis of their mineral associations). In many instances the latter cleavages are difficult to distinguish. Starra hangingwall metasediments contain prograde scapolite/cordierite pseudomorphs and actinolite in drill-core, defining a steeply east-dipping S2(MP) surface. In outcrops of Staveley Formation limestone, D2(MP) has a strongly developed spaced cleavage accentuated by carbonate dissolution during weathering.

Lineations

S2(MP) foliations possess a well-developed steeply north-plunging lineation, defined by the long axes of peak metamorphic minerals (Fig. 4.3B). Pyramids Syncline L2(MP) lineations plunge to 40°/076°, while Area 251 ore zone lineations (away from D2(LP) folds) plunge to an average of 63°/051°, defined by hematite and biotite elongation.

Asymmetric pyrite porphyroclasts (σ-type of Passchier & Simpson (1986)) indicate a uniform east-block-up sense of shear during D2(MP) (~ 70 ° southerly plunge to the pyrite lineation): these are widely developed in feldspathic footwall rocks. The "tails" of the sigmoids parallel the hematite D2(MP) lineation, and are defined by recrystallised inclusion-free pyrite, chalcopyrite, chlorite and quartz (Fig. 4.5C & E). Such well-developed asymmetry suggests that D2(MP) was characterised by non-coaxial laminar flow (Lister & Snoke 1984) at the edge of the Starra Shear, associated with S-C cleavages. More importantly, the pyrite shear sense indicates that uplift of the Staveley Formation east of the Starra Shear was a part of general D2 (MP) east-west shortening.

Boudinage

Boudinage of relatively competent ironstone, quartzite, and psammitic layers within metasediments occurred during D2(MP). The scale of boudinage varies greatly, but the plunge of boudin necklines is always similar — shallowly north and south, plotting with D2(MP) fold plunges on an equal area stereonet (Fig. 4.4). This orientation is the same for

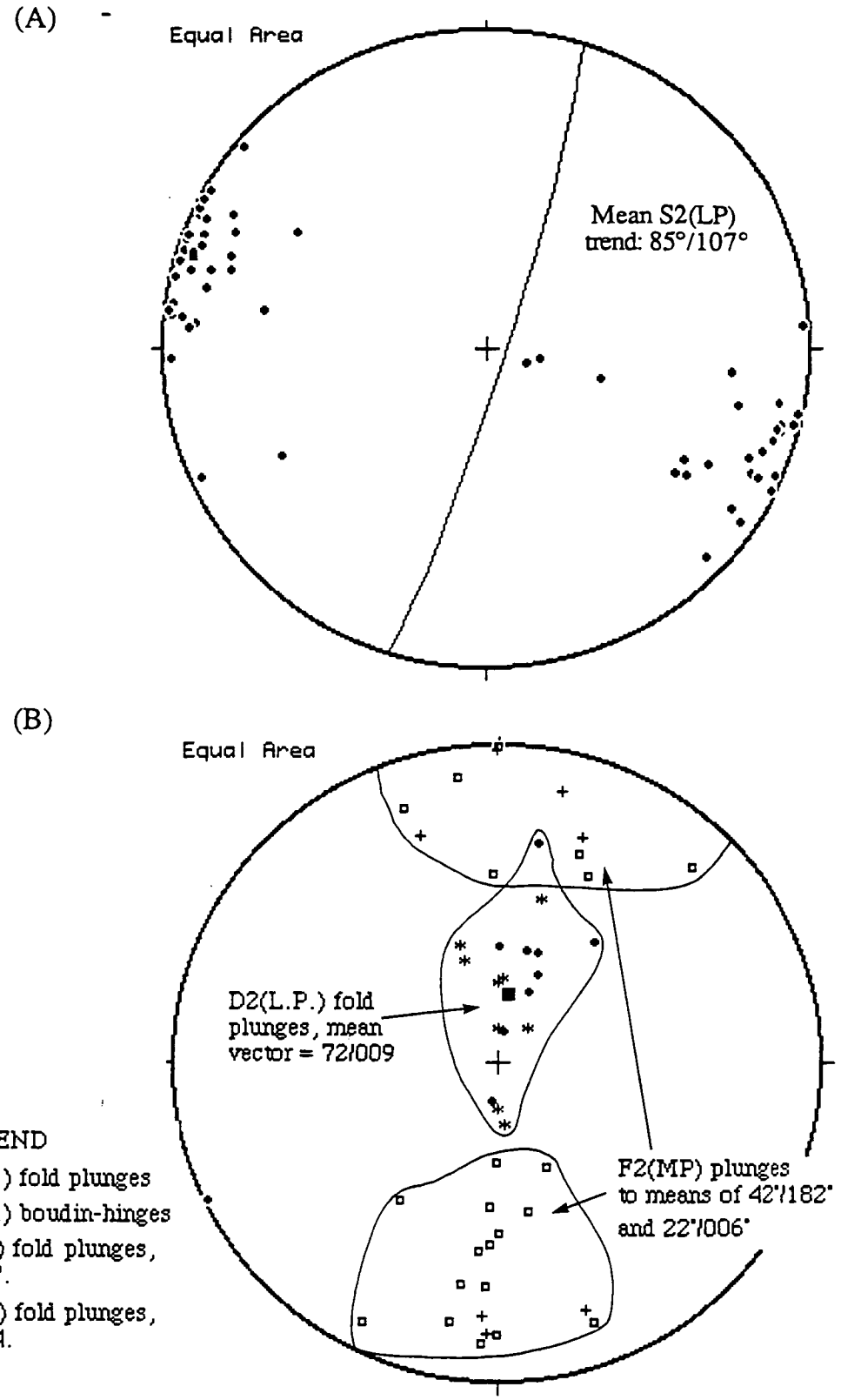

Figure 4.4(A) *Equal area steronet presentation of Area 257 S2(LP).*
(B) *Fold and boudin neckline plunge data for F2(MP) and F2(LP).*

Figure 4.5

A. *A reflected light photomicrograph of an unstrained pyrite porphyroblast, containing an early sieve-textured pyrite generation, and a later euhedral pyrite overgrowth (St 200, 81-19/250 m, Area 257).*

B. *A transposed fabric in barren ironstone, Area 244 surface. The block is not in place. The transposing cleavage is S2(LP).*

C. *An asymmetrically sheared pyrite porphyroclast, St 140 (Area 276, 85-121/155m), indicating left lateral movement at the scale of the thin-section. Many such pyrites also show the two growth generations pictured in "A".*

D. *Folded compositional sulphide bands in mineralised ironstone, Area 251, 85-119/114.8 m.*

E. *Reflected light photomicrograph. A clear pyrite overgrowth on a corroded sieve-textured pyrite core, within albite schist. Chalcopyrite occupies the pressure-shadow area of the pyrite. Hematite defines the D2(Later Phase) foliation, and also occurs as randomly oriented blades within the pyrite. The latter fabric is considered predeformational, and is evidence for the very early development of pyrite in the sediments. (St 201, Area 257, 81-19/262 m).*

F. *Reflected light photomicrograph. A magnetite porphyroblast (**mag**) rims a corroded pyrite grain (**py**) in auriferous ironstone, in the Western Zone of Area 257. The sample contains less than 2% sulfide but carries 8 ppm Au.The photo is typical of pyrite-magnetite relationships in the footwall and ore, and therefore is unlikely to be a function of a particular thin-section orientation. (St 116, Area 257, 85-129/140 m).*

G. *A metasomatic reaction front developed during D2(MP) deformation of the hangingwall metasediments, in which biotite-quartz-albite-actinolite-calcite was replaced by fine quartz-actinolite. (St 160, Area 257, CRQ 77-26/136 m).*

H. *A D2(LP) transposition fabric within well-bedded feldspathic sediment of the Mariposa Creek Member, Area 257.*

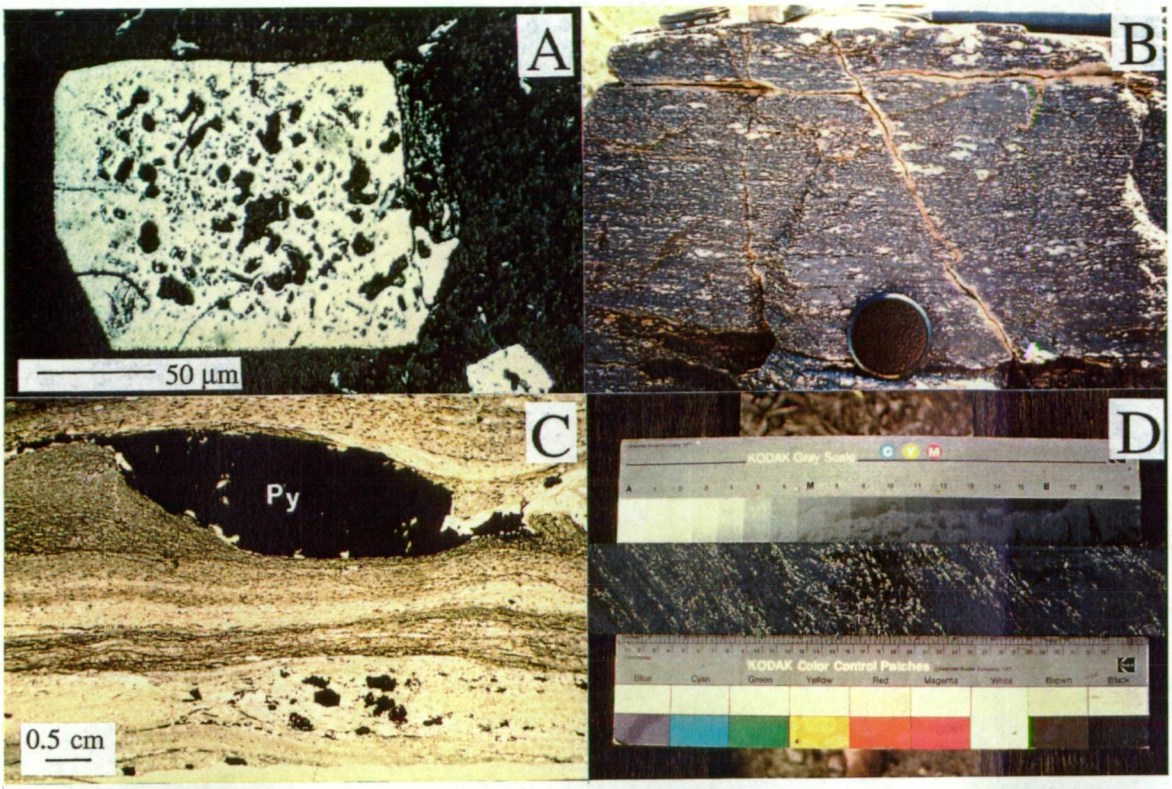
A
50 µm
B
C
Py
0.5 cm
D
KODAK Gray Scale
KODAK Color Control Patches
E
50 µm
cpy
py
hem
F
Py
mag
100 µm
G
qtz-act
0.5 cm
H
S2 LP
2 cm

Figure 4.6

A. *An atypical replacement texture, in which chalcopyrite replaces pyrite in ironstone adjacent to calc-silicate skarn development. (St 100, Area 257, 80-17/166.3 m).*

B. *Deformation twinning in a footwall chalcopyrite vein, Area 257 (St 38, CRQ 78-1/163.0 m).*

C. *Typical expression of S2(LP) at thin-section scale. This cleavage anastomes, wrapping around phacoids, and develops an S-C fabric in places. Magnetite clearly overgrows the cleavage in this slide.(St 40b, Area 257, CRQ 78-1/183.1 m).*

D. *Late chlorite-filled fracturing in an elongated magnetite porpyroblast, St 110, Area 257 (85-129/124 m).*

E. *Recrystallised calcite at the base of a gravel-bearing calcarenite bed, Starra hangingwall. The calcite has been stained purple for ease-of-recognition.*

F. *(Left) A recrystallised fault zone filled with calcite, Area 257 hangingwall (St 267b, 85-127/78m). (Middle) Evidence of continued shearing after the development of carbonate veins. Here carbonate vein fragments have been transposed and are rotating in a hangingwall shear zone (St 252, CRQ 78-3/93 m). (Right) Evidence of carbonate veining after the development of D2(LP) phacoidal breccias (St 276a, 85-127/189 m).*

G. *A polarised light image of cross-cutting late calcite gash-veins in St 219 (85-113/103 m), Area 236 hangingwall. Graded bedding in the calcarenite is also present.*

H. *Detail of a thick carbonate gash vein, on which fluid inclusion work was carried out. The outer zone is a rhombic dolomite containing abundant fluid inclusions (detailed in the insert). A thin band of euhedral red siderite (black in the photo) has been brecciated by subsequent fluid flow in the vein. The vein was sealed by low temperature calcite containing few fluid inclusions. (St 263a, Area 257, 80-13/126 m).*

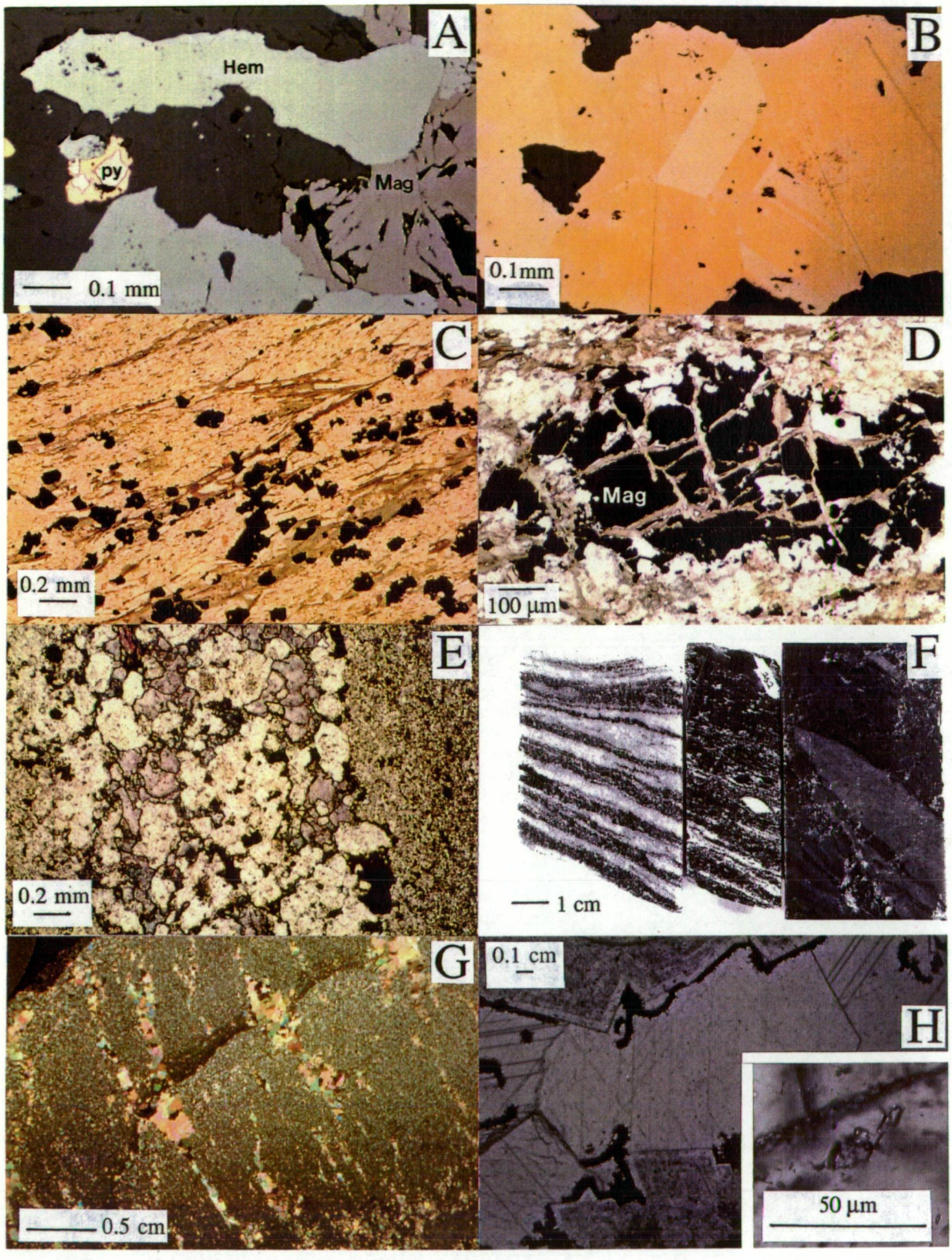
A
Hem
py
Mag
0.1 mm
B
0.1mm
C
0.2 mm
D
Mag
100 µm
E
0.2 mm
F
1 cm
G
0.5 cm
0.1 cm
H
50 µm

boudins close to the Starra Shear (e.g., Fig. 4.7), as for those removed from it. The important implications of this to ore zone deformation models will be discussed subsequently.

The development of boudins in psammite, quartzite and ironstone resulted in irregular neck-point quartz veins. They are accompanied by apparent isoclinal closures, so called "scar folds" of Hobbs et al. (1976); these and other features are illustrated in Fig. 4.8. In most cases boudin axes are sub-perpendicular or markedly oblique to the principal axis of extension, identified by mineral lineations.

D2 (Late Phase)

General Fold Forms

D2(LP) deformation consists of sinistral reclined folds at small to medium scales, confined to a north-south belt extending from the Mort River to ~ Area 290 (Fig. 4.9), bounded to the west by the Gin Creek Block, and to the east by the Mt. Dore Fault. The northern boundary to the fold domain corresponds to a change in orientation of the Staveley Belt from a north to a northwesterly trend. Significantly, D2(LP) folds have the same vergence on either side of the Starra Syncline, and therefore post-date D2(MP).

D2(LP) folds have a maximum wavelength of 400 m, and many smaller parasitic folds. Forms vary from tight in the Eastern Hematites, to isoclinal in the Western Hematites, with a mean plunge of 72°/009° (overlapping with the field of L2(MP) lineations at Area 251) (Figs. 4.3B & 4.4B). Eastern Hematite F2(LP) plunges vary from 46° to 80°. Individual folds in competent layers approach similar fold geometry.

Increasing strain towards the Starra Shear, measured by tightening fold forms, suggests that the deformation was a product of reactivation on the shear. In the Western Hematites increased strain resulted in fold-hinge faulting, severe layer transposition, "phacoidal" breccias, and left-lateral S-C fabrics. Area 244 is an example of severe fold disruption by transposition, with the result that the ironstone now constitutes a "complex of lenses and north-plunging rootless folds" (Leishman 1983). Shearing here relates in part to ~ 420 m of left lateral strike-slip displacement along a plane immediately east of the most western ironstone (Fig. 4.10). Sub-horizontal left-lateral movement senses can be inferred in other instances from the geometry of small scale faulted fold hinges (Fig. 4.12, Appendix 4.1).

Leishman (1983) highlighted the interference effects between F2(MP) and F2(LP). These produced complex strata repetitions and closures, with variable patterns which are dependent on the orientation of the intersecting topographic surface. An example drawn from Leishman (1983) is provided in Fig. 4.11. The "Hinge Zone" (Fig. 4.1) is regarded by some authors as a large-scale example of fold interference (Leishman 1983; Kary & Harley, in press).

Cleavage and Transposition Brecciation

Severe transposition is a distinctive aspect of D2(LP) in the Starra Shear . It is usually difficult to separate the S2(MP) and S2(LP) cleavages, except in S2(LP) fold-hinges within the hangingwall metasediments, because S2(LP) has a pervasively overprinting character. In general the surface associated with remobilised hematite, transposition, and retrograde chlorite is S2(LP), with a moderate to weak lineation parallel to F2(LP) plunges. Chloritic schists such as the Harley Member exhibit proto-mylonitic fabrics, feldspathic rocks are inhomogeneously sheared (5 - 10 m wide shears separate less-deformed 'corridors' of well-bedded rocks), while ironstones possess a strong foliation defined by aligned hematite grains. Transposition zones probably represent the hinge and "short-limb" of sinistral closures, containing elongate phacoids with long axes perpendicular to fold axes, separated by hematite-chlorite-bearing anastomosing cleavage strands. The latter contain a mild down-dip lineation defined by the long axes of hematite grains.

Although ironstones have deformed more coherently than other rock-types, internal competency-contrasts lead to the common destruction of internal primary layering. Relict banding has, however, been preserved in the long-limbs of some sinistral folds, such as the Western Zone of Area 257. It is thus impossible to infer the original extent of ironstone banding.

Cross-cutting Faults and Veins

D2(LP) north-east striking faults and veins occur at several scales in the Starra Shear. Leishman (1983) recognised several large quartz-filled north-east oriented faults within the Gin Creek Block, which swing northward into the axial zones of transposed D2(LP) folds (e.g., Area 282, Fig. 4.10). Leishman (1983) suggested a transitional relationship between the quartz-filled faults and massive foliated ironstone.

Check-mapping at Area 282 (2.5 km north of Area 257) showed that one such fault zone:

(1) cuts across the ore sequence

(2) consists of strongly transposed lithologies, including ironstone

(3) contains a north-easterly cleavage at an angle to the Starra Shear foliation

(4) does not pass immediately along strike from massive hematite schist to quartz veining, as inferred from the map of Leishman (1983).

Ransom (1986) also analysed these faults, concluding they were Reidel Shears produced during dextral movement, on the basis of cleavage orientation. The view of the author is that the faults were dilatant reverse or pressure-shears (Roberts 1987), which normally form late in the fracturing history of shear zones (Tchalenko 1968). They became fault splays with sinistral movement, as indicated by accompanying anticlinal drag-folds (Fig. 4.10), consistent with other movement evidence.

At a smaller scale, the Area 257 footwall contains 1 - 30 cm wide magnetite-pyrite ± chalcopyrite veins at 5 to 20 m spacings, with a similar orientation to the larger faults (015 -

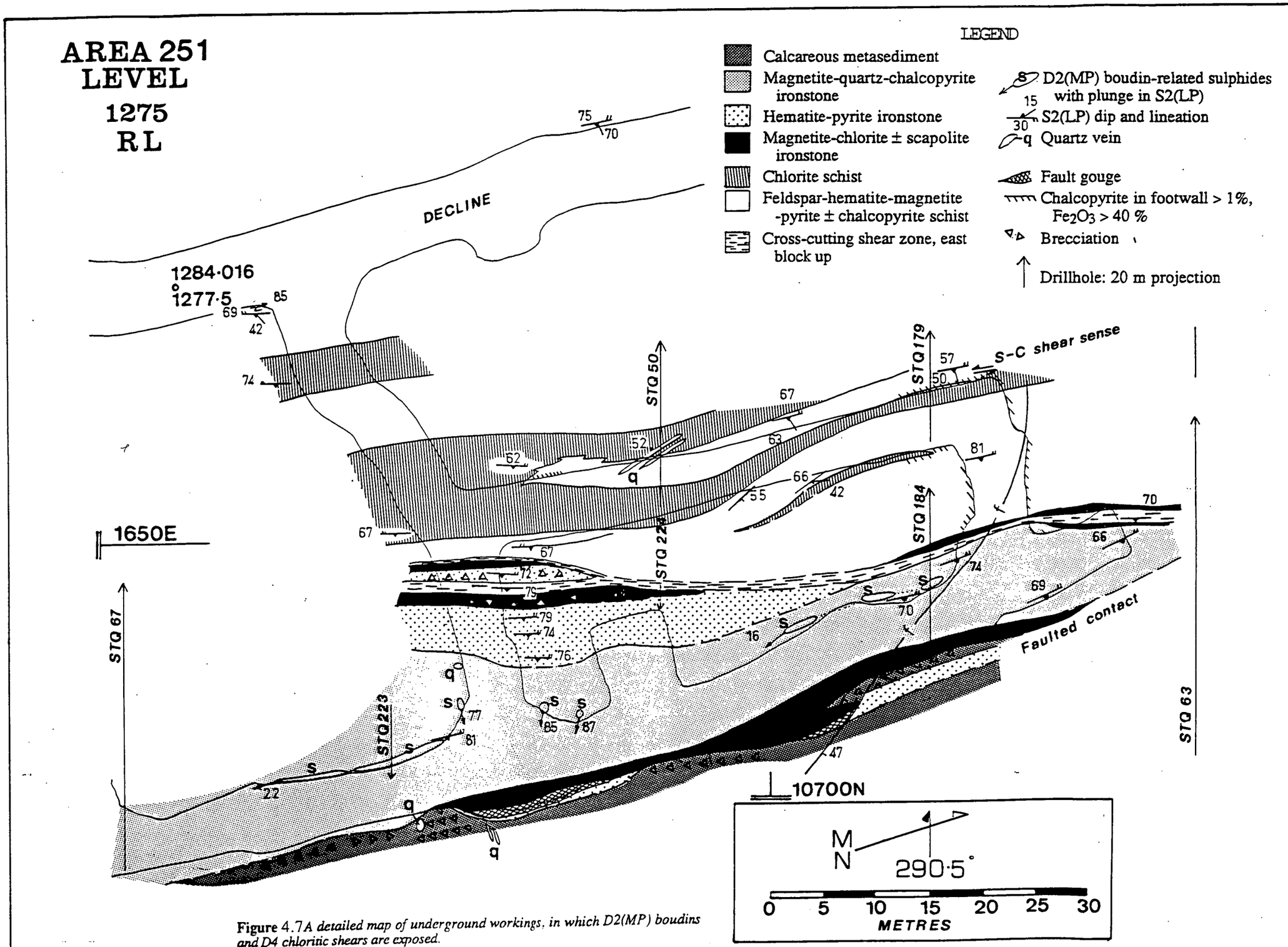

Figure 4.7 *A detailed map of underground workings, in which D2(MP) boudins and D4 chloritic shears are exposed.*

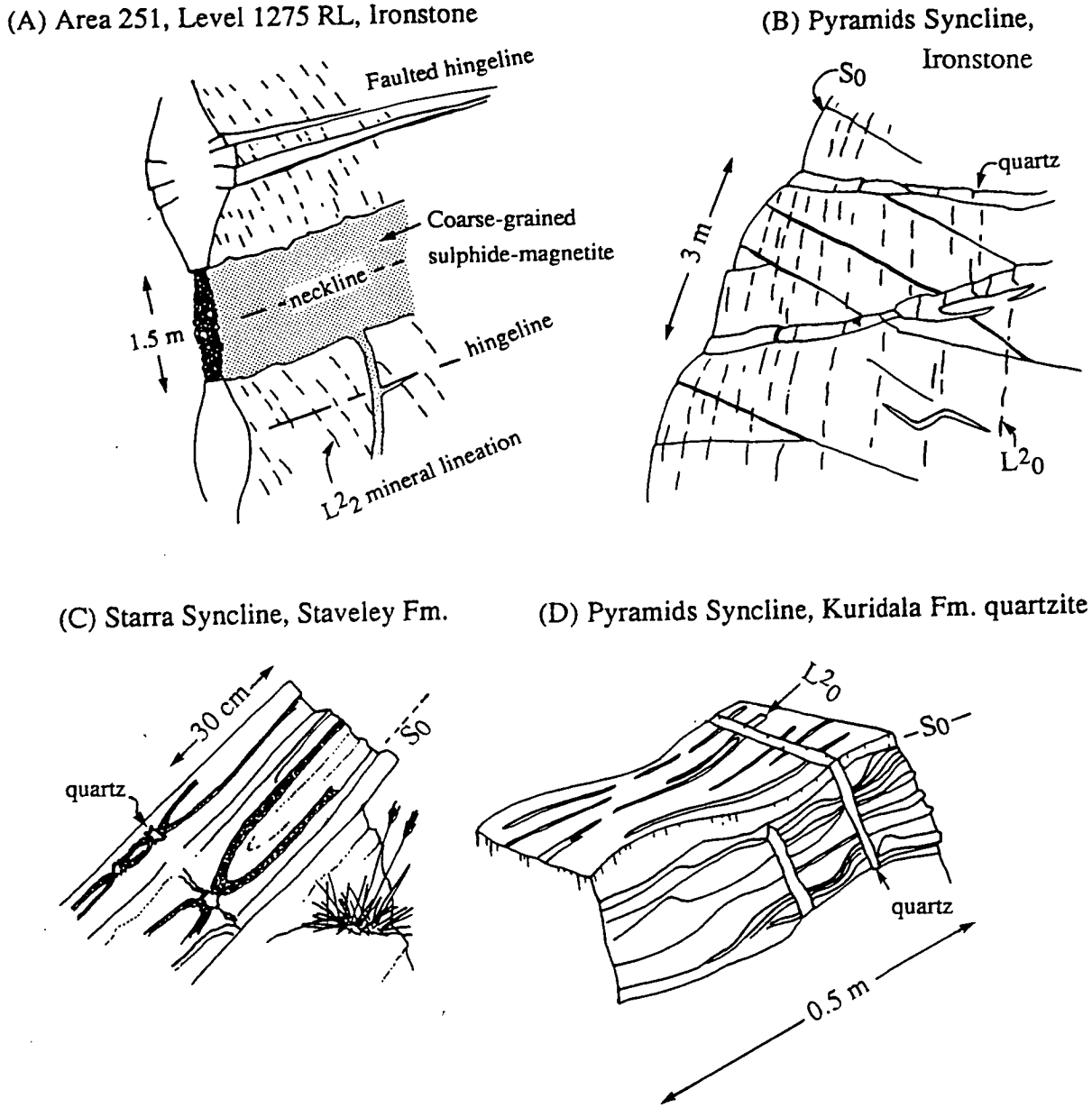

Figure 4.8 *Examples of D2(MP) boudinage in the Starra area. (A) Boudins within mineralised ironstone have necklines and secondary fractures filled with coarse-grained magnetite-chalcopyrite-quartz. (B) An ironstone/host-rock contact is boudinaged in the Pyramids Syncline, illustrating the variability of neckline plunges within a single outcrop. (C) 'Scar fold' boudinage, Area 236. (D) progressive boudinage in strongly lineated quartzite, with extensional fractures developing along older hingelines.*

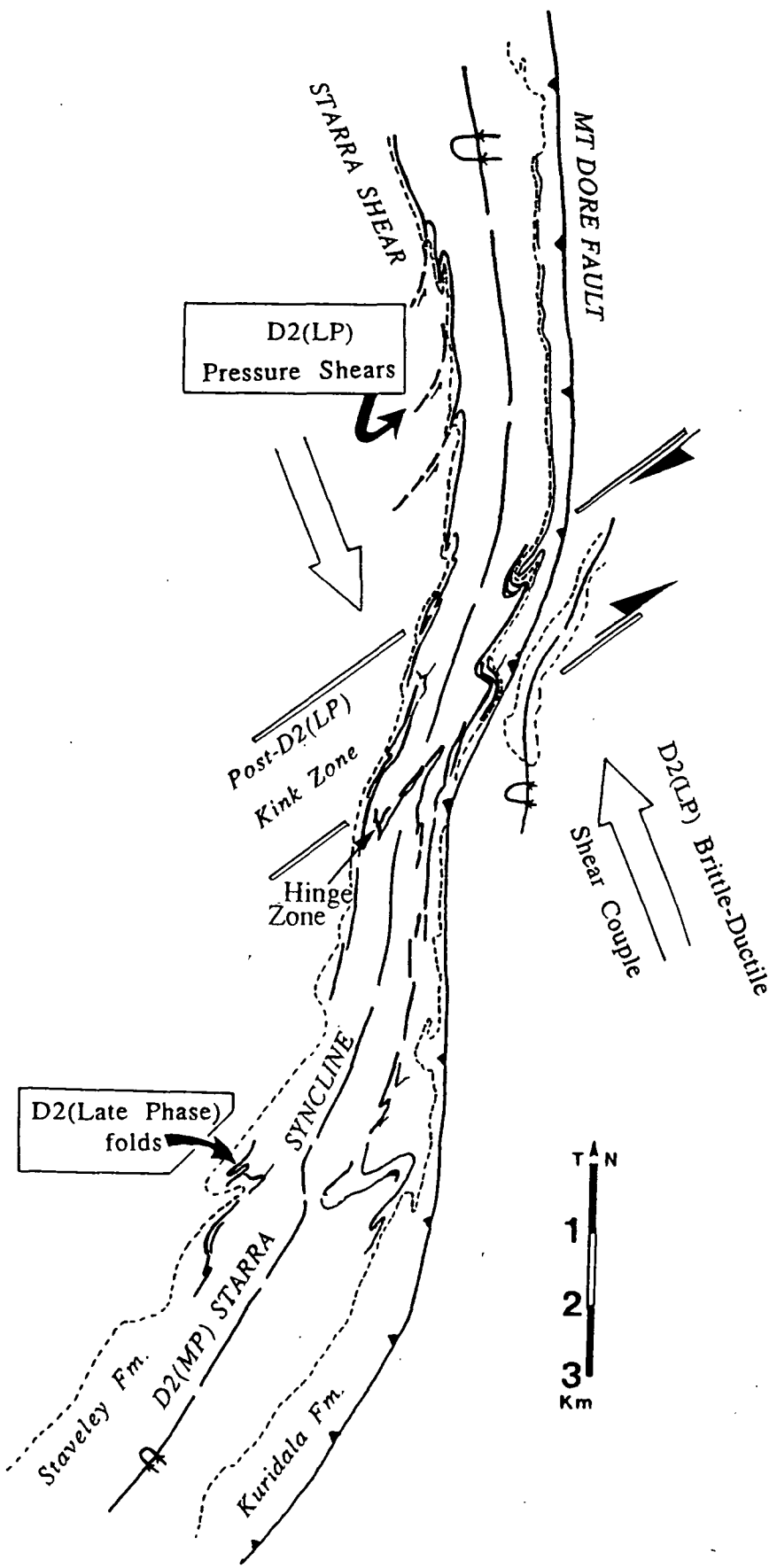

Figure 4.9 *Geographic distribution of D2(LP) deformation, additionally showing the post-D2(LP) megakink of Ransom (1986).*

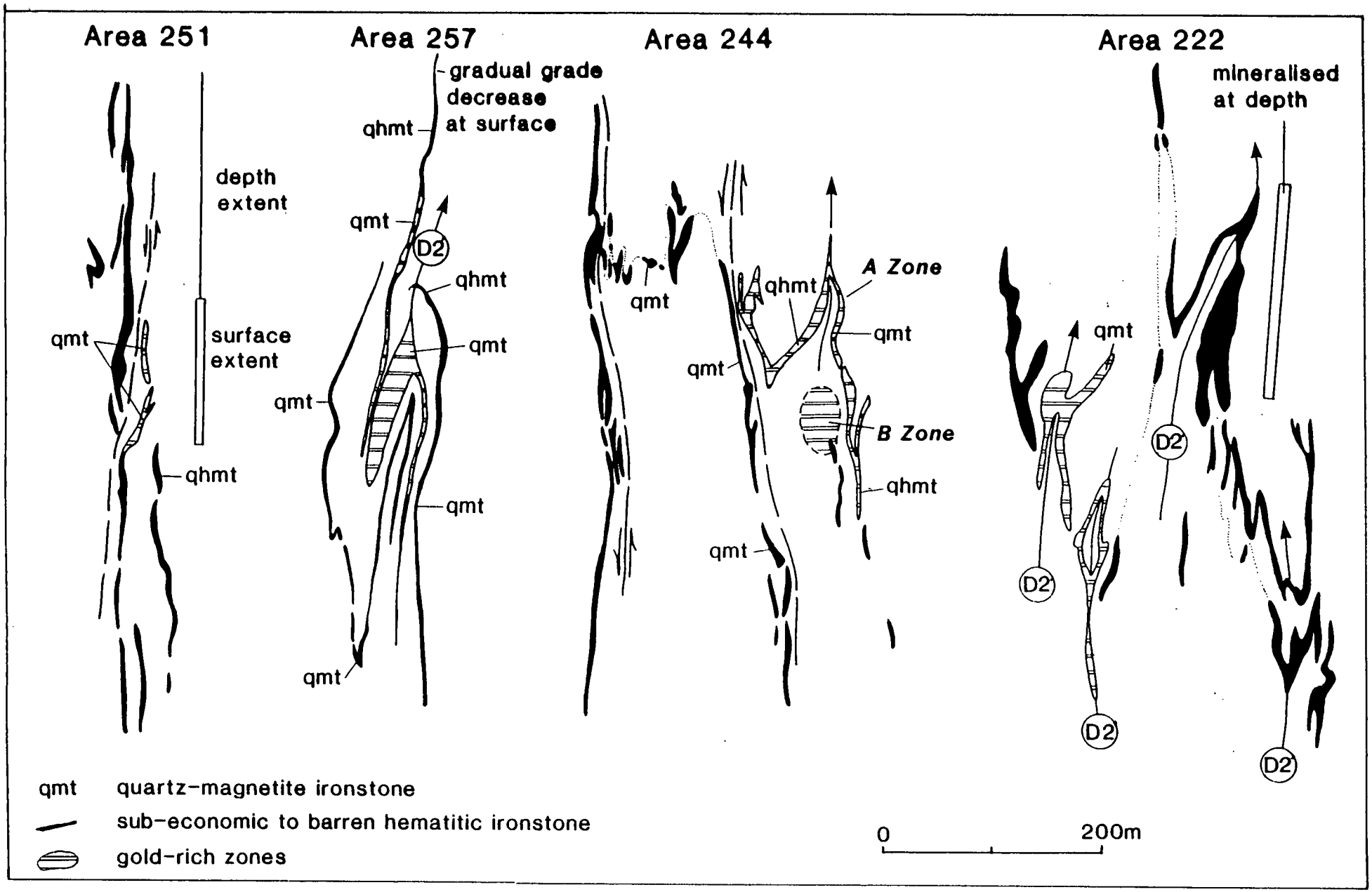

Figure 4.10 *Plan structural geology of the four mineralised areas of the Western Hematites. D2* = D2(MP) fold, D2' = D2(LP) fold.*

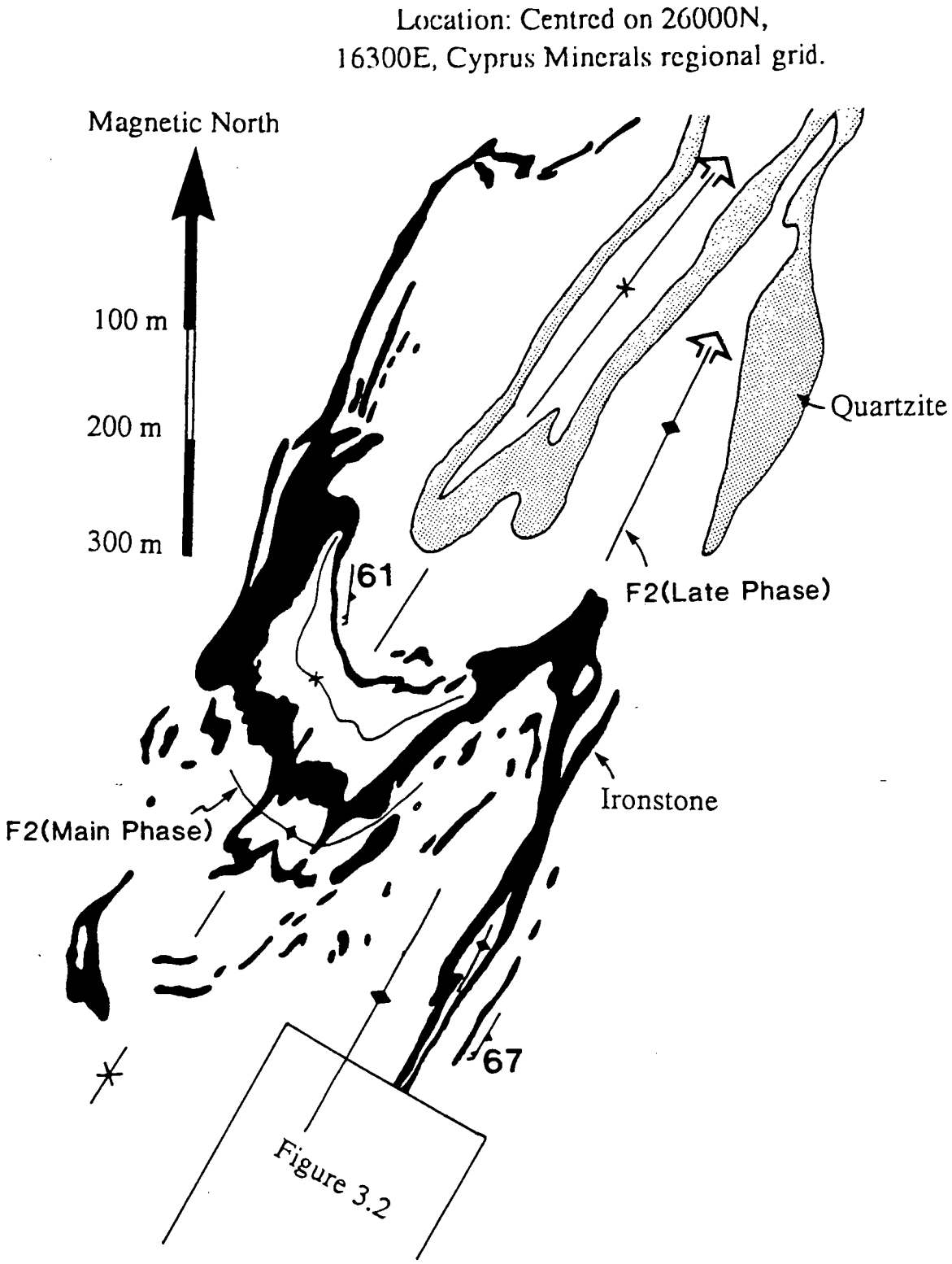

Figure 4.11 *Refolded fold geometries at Area 260, Eastern Hematites, after Leishman (1983). A large, steeply north-plunging, sinistral D2(LP) fold refolds shallowly doubly-plungingD2(MP) structures.*

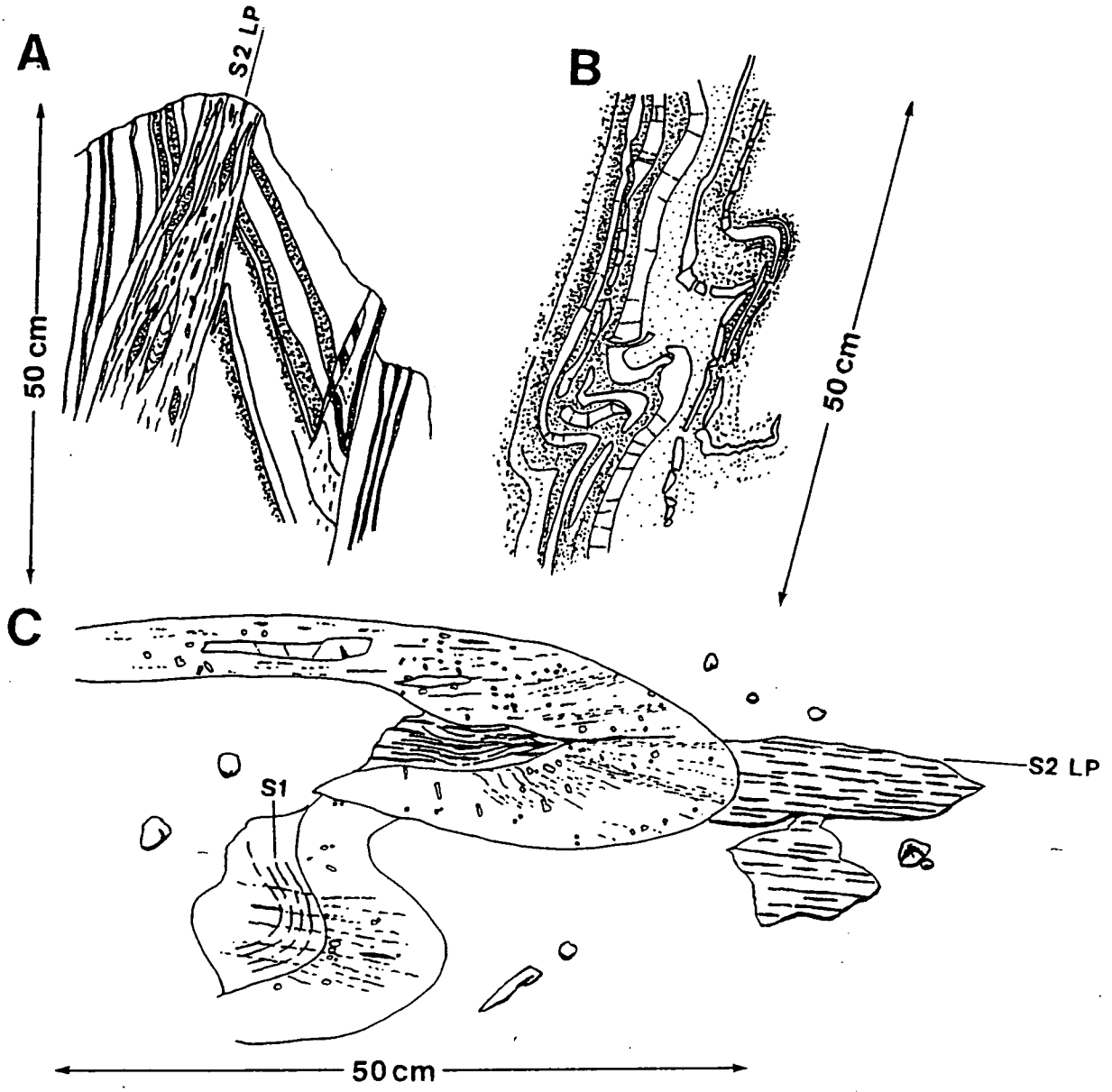

Figure 4.12 *Examples of D2(LP) deformation from the ore environs, all viewed in plan. (A) Area 257 (11500N, 1480E); transposition of the short limbs of D2(LP) folds in feldspathic shist — a small scale example of a common phenomenon footwall to Area 257 ironstone. (B) Chert-band disruption in a steeply-plunging, concentric, sinistral fold in hematitic BIF, Mistake Creek area.(C) Quartz-veined granite folded and cleaved by D2(LP), approaches a similar geometry, but was intruded parallel to* $S1_a$.

032° Magnetic, i.e. east of the S2(LP) foliation. They are interpreted as tensile segregations developed during transcurrent left-lateral shearing.

Timing and Fold Orientation Controls

A sinistral strike-slip movement for D2(LP) is inferred from the orientations of folds, and from offsets in ironstones (e.g., Area 244, Fig. 4.10). The folding was induced by brittle-ductile transpression, with the shear couple aproximately oriented as shown in Fig. 4.9. This movement direction, and the prevailing rheological field, were quite different to those inferred for D2(MP) from assymetric pyrites and other evidence . Refolding of F2(MP) by F2(LP) (e.g, Fig. 4.11) is the best evidence that D2(MP) predated D2(LP). It is not certain what relationship D2(LP) had to the regional D3 brittle-ductile event, but a distinct difference in fold orientation (NE-trending versus NW-trending) suggests the two were separate events. More-ductile fold styles are the basis for presuming D2(LP) to be older than D3. In general, Mount Isa deformation evolved from ductile to brittle with time, suggesting that it was accompanied by regional uplift and erosion.

Switzer (1987) and Switzer et al. (1988) arrived at a different structural history to explain F2(LP) orientations. They viewed these sinistral folds as congruent to the D2(MP) Gin Creek Anticline, rotated non-coaxially into the L2-stretching direction. In fact, the similar vergence of F2(LP) east and west of the F2(MP) Starra Syncline requires a later origin for these folds, and fold-axis rotation is argued against because major D2(MP) boudin hingelines and fold-hinges have the same orientation in the Starra Shear as elsewhere.

There remains the conundrum of the near-parallelism of L2(MP), F2(LP) axes, and L2(LP), considering that the reactivated shear movements for these events was so different. Parallelism of lineations and fold axes is a common phenomenon in folded rocks (for instance see Sanderson (1974), Hobbs et al. (1976), Skwarnecki (1987)), but is nevertheless perceived as a problem in structural geology, because it implies that strain is accommodated during shortening by horizontal extension parallel to fold axes, rather than in the vertical direction (Hobbs et al. 1976). Models of rotational non-coaxial deformation have resolved the matter for many shear zones (e.g., Bell 1978, Skjernaa 1980, Cobbold & Quinquis 1980, Ridley 1986), but given the above arguments, non-coaxial deformation is not relevant to the genesis of F2(LP).

The preferred solution arises from the work of Watkinson & Cobbold (1981), who examined the effects of pre-existing linear anisotropy on subsequent fold attitudes. These authors tendered the analogy of folding in a layered rubber medium which contains oriented steel rods — fold axes in orientations other than near-parallel to the rods would be unlikely, no matter the direction of exterior stresses. Natural examples of anisotropic control of subsequent deformation are provided by Ramsay (1967, p. 220), Hossack (1968), Quinquis (1980), Watkinson & Cobbold (1981) and Cobbold & Watkinson (1981). It follows that D2(LP) folds may have paralleled L2(MP) because this direction most readily enabled

folding. A similar conclusion can be reached for D2(MP) from Switzer et als. (1988) observation that F2(MP) is coaxial with the $L1_a$ stretching lineation.

D4

D4 brittle-ductile reverse motion late in the history of the Starra Shear was identified underground at Area 251, but has not been recognised at surface (Fig. 4.7). It is mainly confined to 2 to 5 m wide near-vertical chloritic shears faulting mineralised ironstone at a low angle, containing excellent mylonitic S-C fabrics with an east-block-up movement sense (Passchier & Simpson 1986). The trend of these faults, and cleavage within them, truncates S2(MP). Similar, as yet unidentified faults may explain some thickening, thinning, and termination of ironstones elsewhere in the Western Hematites — the common faulting of ironstone - metasediment contacts may also relate to this event.

Small to medium-scale kinking along horizontal axes are tentatively identified as part of D4. At Area 257 this kinking has a 50 m wavelength generating unusual westerly dips in ironstone (Appendix 13), illustrated by the folding of D2(LP) lineations about an axis plunging at 8° to 217° (Fig. 4.3B). Smaller scale, open, chevron folds with sub-horizontal fold axes were mapped at Area 257 (Appendix 13).

Other Deformation

Calcite Gash-veining

A prominent set of pervasive calcite-chlorite gash veins (Fig. 4.6F & G) cut hangingwall metasediments, dolerites and ironstones with an average vein pole of 35°/029°. The vein intensity decreases markedly away from the Starra Shear. A detailed structural interpretation is provided in Chapter 10, where it is concluded that the veins originated as tensile pinnate fractures during sinistral transcurrent fault reactivation. Although the calcite veins cross-cut D2(LP) fabrics and are mainly brittle, the sense of movement accords with that deduced for D2(LP). Some veins were clearly sheared and broken after their formation (Fig. 4.6F). Notably the sense of movement also accords with that deduced for a major fault immediately east of the Pyramids Syncline (Fig. 4.2). This fault is filled with brecciated tourmaline – K-feldspar, which may have emanated from the Mt. Dore Granite late in its crystallisation history.

Regional Kinking

A regional mega-kink was identified by Ransom (1986), which he related to the ore-forming event. The kink (Fig. 4.9) is a zone in which the strike of all stratigraphic and structural elements are altered sharply from north to north-east, and offset. Kinking of the Mt. Dore Fault dates the event as post-1500 Ma, well after other deformation events affecting Starra mineralisation. D2(LP) folds occur within and outside of the mega-kink, with no change in fold trend.

The "Hinge Zone"

No attempt has been made to unravel the structural history of the complex "Hinge Zone" (Fig. 4.9), which comprises multiple or repeated breccia-rich ironstones (e.g. Area 222, Fig. 4.10), forming a south-veeing link between the Eastern and Western Hematites. Despite the probable structural complexity, many of the ironstones are virtually unstrained, as explored in detail in chapter 3. Textures of these ironstones are more consistent with pre-deformational oxide alteration, than with the syn-deformational shear-fill proposal of Ransom (1986). The Hinge Zone contains both F2(MP) and F2(LP) folds, supporting a consensus view of an origin through large-scale D2 fold interference. However, another possibility is an origin as a D1 imbricate thrust stack, similar to those proposed by (Bell (1986) and Lossveld & Schreurs (1987), in which the Hinge Zone is part of a duplex with southward movement. This could explain (1) why the ironstone outcrops only once, rather than twice, as would be expected if it had developed due to F2(MP) plunge reversal; (2) why the ironstones are not connected to the main Hematites trends at either end of the Hinge Zone — each would be separated by an early floor thrust. This option is tendered not as a definitive conclusion, but as a possibility for evaluation by future workers.

THE TIMING OF ORE DEVELOPMENT WITH RESPECT TO THERMOTECTONISM

Field Observations

No relationship between mineralisation and the extensional $D1_a$ of Switzer (1987) was observed; indeed, the only reliable evidence of this event within the Starra Shear does not impinge on ore mineralogies.

At small to medium scales, mineralised ironstone is folded by D2(MP). Sheared and transposed medium-scale D2(LP) folds are associated with Areas 257, 244, and 222; detailed geochemistry at Area 257 (Fig. 6.2A) illustrates that Au grades in ironstone are continuous within folded ironstones. Folded, compositionally-banded sulphide-rich ironstone, as well as hematite-magnetite alteration, occur at drill-core scales (Fig. 4.5D). Although Area 251 is the largest and most sulphide-rich ore zone, it is not associated with medium scale folds of any generation.

The four orebodies vary significantly in plunge, on the basis of Cyprus Minerals metal-factor-based long-sections (average grade multiplied by the intersection width; Fig. 4.13). Area 257 Main Zone plunges vertically, Area 251 plunges northward to ~ 70°, "A" zone of Area 244 plunges ~28° north, "B" zone plunges 65° north, while individual high grade pods at Area 251 plunge 44° north and 40° south. Overall, there is a strong elongation sub-parallel to the D2(MP) elongation direction, with some significant departures.

As part of the examination of the shape of mineralised areas, the edge of the Area 251 ironstone was analysed to assess its similarity to the overall Area 251 geometry. Numerous drill-holes have intersected this horizon while drilling the deeper levels of Area 257. Figure 4.14 shows that the ironstone contact lenses out along both sub-horizontal and steep contacts, which are discordant to the gross form of the 251 orebody.

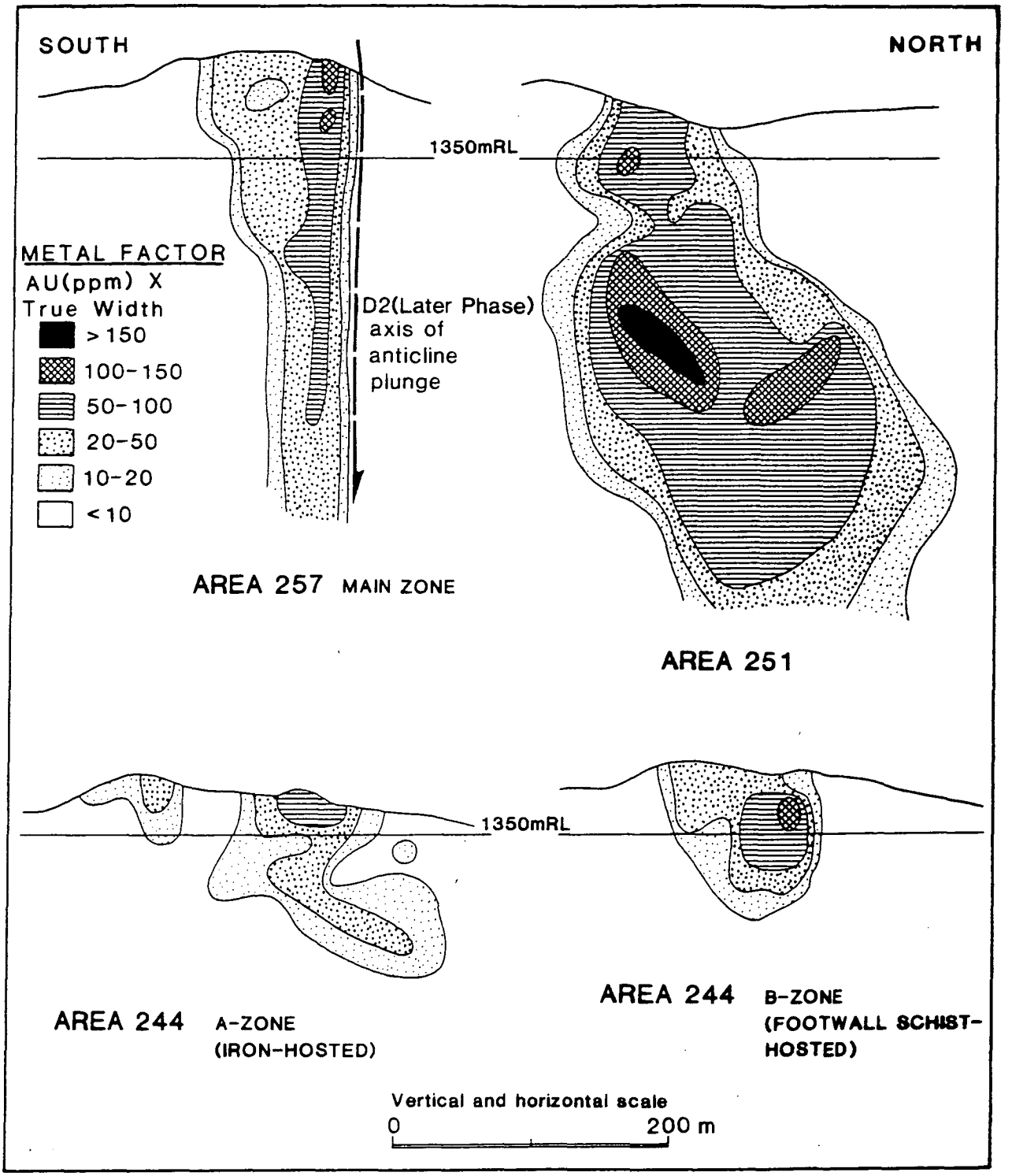

Figure 4.13 *Long section geometry of the Starra ore zones, based on metal factor analysis (average true width X average Au grade in ppm).*

Geometry and grade of the youngest ironstone, Area 257

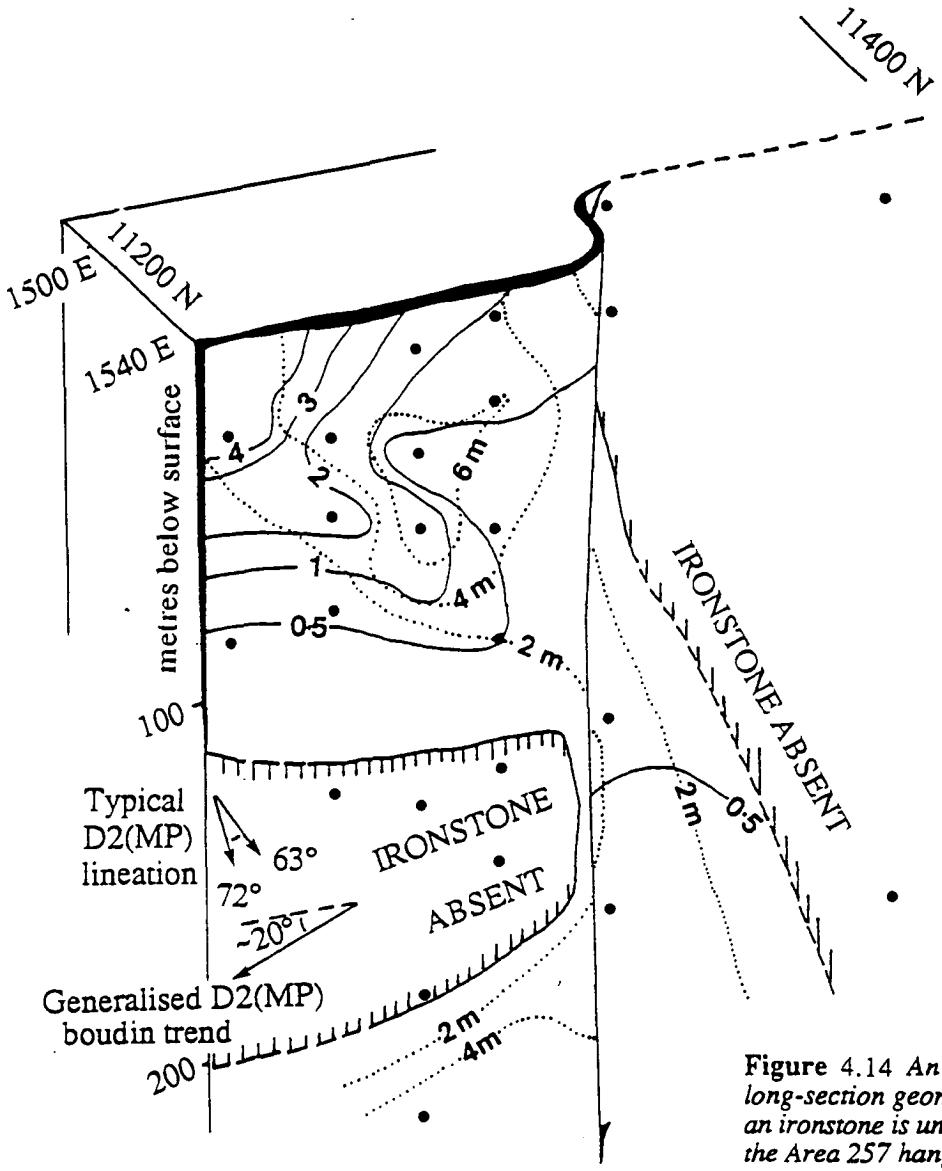

LEGEND

- DDH intercept

Average Au grade in ppm

Contours of Au grade

Contours of ironstone thickness

Figure 4.14 *An analysis of the long-section geometry of the edge of an ironstone is uniquely available in the Area 257 hangingwall. This particular ironstone horizon is wholly enclosed by calcareous metasediment, and is a likely strike-equivalent to the Area 251 mineralisation. An analysis of ironstone thickness, and its presence or absence, suggests the margin is sub-horizontal at depth, and sub-vertical to the north. Average Au grades increase systematically upwards and southward, so defining a shallowly north-plunging ridge with no clear correlation with ironstone thickness. There is also no clear alignment of these elements with the D2(LP) fold plunge, D2(MP) lineation or direction of boudinage.*

Underground exposures of Area 251 provide clear evidence that ore existed prior to, or during early D2(MP). Incompletely-necked boudins were mapped on RL 1275 (Fig. 4.7 & 4.8), in which individual boudin-axes are at least 60 m long, with wavelengths of ~ 2 - 5 m, and amplitudes of 0.5 to 2.0 m. Shallowly-plunging necklines in mineralised ironstone are filled with coarse-grained chalcopyrite-magnetite-quartz (no scheelite was located despite close inspection with a UV lamp). Several smaller vein-like masses cut transversely across the ironstone boudins, close to parallelism with the D2(MP) mineral elongation. These are identified as secondary zones of necking, "chocolate tablet" boudinage of Weggman (1932). The orientation of the secondary boudinage direction accords with the view of Ghosh (1988), who states that " irrespective of the the direction of principal extension....the second generation extension fractures are likely to form approximately perpendicular to the first generation boudin axes". Neck-line and secondary fracture sulphides were deposited from metamorphic fluids close to peak metamorphism — they are volumetrically minor compared to the overall volume of fine-grained mineralisation within ironstone, and logically were derived by local solution of in-situ sulphides and oxides during D2(MP), because similar boudins away from ironstone are not mineralised.

Chalcopyrite, magnetite, scheelite and minor gold also occur in previously

Sample	Location	(ppm) Au	Cu	W	% Fe_2O_3
Veins folded by D2(LP)					
St95	80-17,136.5 m	-	2.06%	456	36.65
St129	78-2, 87-109 m	-	6521	1034	86.11
St266	80-13, 158.1 m	1.140	9470	-	-
St273	85-127, 110-130 m	3.28	8100	-	-
D2(LP) tensile veins					
D7	Area 251, 1320 RL 10965N, 1570E	0.660	5500	-	-
St258	78-2, 90 - 113 m	1.560	1.51%	-	-
231793	(surf.)11500N, 1460E	0.075	297	48	80.60
Matrix hematite in D2(LP) transposition zones					
St64	(surf.)11360N, 1420E	-	39	26.5	45.17
St271	85-127, 80 - 100 m	<0.005	1090	-	-

Table 4.1 *Chemical analyses of 3 different transgressive oxide-rich vein styles in the Area 257 footwall. Veins predating D2(LP) are Au, Cu and W enriched; tensile veins related to D2(LP) are variably Au-Cu enriched, while two samples of D2(LP) transposition matrix material contained low to anomalous grades. Notably none of the samples above are as high as grades in the average mineralised ironstone. (Au was fire assayed at Tetchem Laboratories, Brisbane).*

described low-angle tectonic D2(LP) fractures footwall to ironstone (analyses of Area 251 and 257 samples are provided in Table 4.1). However, the equivalent larger-scale faults at Area 282 and elsewhere are unmineralised.

Reverse D4 shears faulting Area 251 ironstone are inconsistently mineralised; some samples have returned up to 22 ppm Au, but most are below 1 ppm (G.Kary, pers. comm. 1988).

Critical Petrographic Evidence

General Textures

Annealed textures dominate the petrography of the ore minerals. Pyrite, and to a lesser extent magnetite, are important exceptions, betraying an ore history which preceded D2 metamorphism (Figs. 3.15A, B, C & D).

Evidence of the pre-metamorphic history has been gathered from the footwall feldspathic and chloritic schists, and some from ironstone (additional descriptions of these rock-types are presented in chapter 3). D2(MP) is characterised by prograde metamorphic minerals, such as epidote, pressure shadow quartz, muscovite, biotite, magnetite and at times chlorite; D2(LP) has a strongly developed fabric, with strong asymmetry, transposition, and coarse chlorite-hematite assemblages.

Magnetite

Within the Mariposa Creek Member feldspathic and chlorite-biotite host-rocks, magnetite commonly forms fine to medium-grained inclusion-poor euhedra, averaging 500 μm diameter. Chlorite-filled fractures cut most magnetites (but not the surrounding minerals) at ~70° to the dominant S2(LP) foliation, an orientation paralleling late (post-D4) calcite fractures (Fig. 4.6D). Pressure shadows parallel to S2(MP) and S2(LP) extend approximately a half-grains width from magnetite contacts; polygonal quartz, subhedral muscovite or anhedral chlorite, chalcopyrite and hematite commonly are recrystallised within them. Epidote and tourmaline project into magnetite. In severely D2(LP)-strained areas, euhedral magnetite is deformed plastically into elongate or sigmoidal shapes.

Ironstone magnetite takes two forms — in gold-rich ores it forms elongate anhedral strings defining a foliation parallel to weakly developed compositional banding (Fig. 3.15E), whereas in hematitic ironstone it is coarse (0.5 - 1.8 cm diameter), euhedral, with abundant silicate inclusions and hints of old grain boundaries (Fig. 3.15B).

Overall, magnetite morphologies are metamorphic. Evidence for the reaction of other minerals to produce magnetite is absent. It is concluded that most magnetite recrystallised from premetamorphic precursor grains, or was deposited from a metamorphic fluid early in D2(MP).

Hematite

Two main hematite generations are documented: (1) Primary layers in which the abundance of hematite parallels sedimentary layering (2) Epigenetic hematite associated with S2(LP).

Primary hematite occurs as fine elongate euhedra in hangingwall metasediment and footwall feldspathic beds, and as medium to coarse, compact, elongate-grains in strike-equivalents to auriferous ironstone. Distal cherty ironstones are dominated by fine hematite, which in its least deformed state forms blocky crystals, weakly aligned with bedding. With increasing strain and metamorphism, coarser hematite (40 - 100 μm) defines the S2(MP) cleavage.

S2(LP) hematite martitises euhedral magnetite, crystallises in coarse blades in the pressure shadows of asymmetric porphyroclasts, reorientates domainally into S2(LP), and most prominently crystallises with chlorite in fine fractures and shears separating transposed clasts.

Pyrite

Pyrite morphology has been discussed in some detail in chapter 3. Salient points are:

(1) In footwall lithologies, older pyrite cores, which overgrew an isotropic fabric, are rimmed by a clear euhedral pyrite generation attributed to late D2(MP) (Fig. 4.5A). Isotopic analysis (chapter 11) found that the former grew from more oxidised fluids than the latter. In samples affected by S2(LP), further recrystallisation produced asymmetrically sheared grains indicating a large component of reverse shear (Fig. 4.5C). The regrowth of pyrite in areas of low mean stress is a general feature indicating local diffusion (McClay & Ellis 1984, Brooker et al. 1987).

(2) In ironstones, pyrite commonly forms blebs and corroded grains rimmed by magnetite and hematite. The texture is annealed, without inference for premetamorphic parageneses. No evidence of sulphidation of magnetite or hematite to form pyrite was observed: a sulphidation mechanism (Switzer et al. 1988) is unlikely given the highly disseminated nature of sulphides in Starra ironstones.

Chalcopyrite

Chalcopyrite is strongly affected by deformation, and hence occurs in the pressure shadows of magnetite and pyrite, or as rounded inclusions in these minerals. As argued for pyrite, the latter texture is likely to be an effect of metamorphism and deformation, rather than replacement. Chalcopyrite which has not obviously seen remobilisation contains deformation twins, as shown in Fig. 4.6B. Replacement of pyrite by chalcopyrite was observed in some ironstones close to major hangingwall skarn occurrences (Fig. 4.6A).

Discussion

The evidence reported in this chapter provides critical constraints to the ore genesis models of Chapter 12. The preferred model must explain clear evidence that ore existed prior

to or during early D2(MP), and the lack of evidence for epigenetic processes such as sulphidation..

The coincidence of three Starra orebodies with D2(LP) folding is one strong argument for a tectonothermal genesis. However, a consideration of the likely rheological behavior of pre-deformational sulphide zones during folding, suggests another possible explanation. These areas may have constituted foci for preferential flexural slip, because of competency contrasts between sulphides and adjacent ironstone during deformation. This hypothesis would be consistent with the strong preference of ore zones for the D2(MP) stretching direction. Such a model advocates the continued exploration of fold zones, because sulphides instrumental in fold initiation may be present at some point along the fold axis, although not necessarily at surface.

METAMORPHIC GRADE

Previous Work

The variance of pressure and temperature during peak metamorphism was examined by Jaques et al. (1982) for the Selwyn region. They found the province varied in grade from middle Greenschist in the Staveley Belt, to upper Amphibolite facies in the Squirrel Hills Belt. "Zone A" mainly includes Staveley Formation, which equilibrated at 3 to 4 kbar, and 450 - 550° C. Quartz, muscovite, andalusite and biotite predominate in the pelitic rocks, epidote and tremolitic amphibole appear with the addition of carbonate, and mafic rocks contain albite, epidote, chlorite, actinolite ± blue/green hornblende and sphene. "Zone B" is defined on the first incidence of almandine or staurolite in pelitic rocks, diopside in calcareous rocks, and coexistence of green hornblende and oligoclase (>An_{17}) in mafic rocks; conditions of 3 to 4 kbar and 550 - 600° C are estimated. "Zone C" pelites contain sillimanite, the metabasites green-brown pargasitic hornblende, clinopyroxene or garnet, with common local anatectic melting ascribed to muscovite breakdown. These rocks experienced ~4 kbar pressure and 600 - 680° C temperature.

It is apparent that "Zone B" metamorphic grade rocks surround a thin south-trending strip of lower grade Staveley Formation in the Starra area. "The Zone B" isograd intersects the Staveley Formation calc-silicates approximately 2 km north of Mt. Dore, and hence is not coincident with stratigraphy: it coincides with the calc-silicate granofels lithology of Leishman (1983), a zone in which sedimentary structures have been destroyed (Fig. 4.1). Nyvlt (1980) suggested amphibolite facies conditions for this lithology at the Mt. Elliott mine, where calc-silicates contain diopside and An_{55} plagioclase in amphibolites. East of the Mount Dore Fault Zone the grade increases rapidly to "Zone B", suggested by hornblende-oligoclase in Mt. Cobalt amphibolites (Nisbet 1983, Beardsmore et al. 1988). Still further south, "Zone C" anatectic melting is observed in the Trough Tank area, and in outcrops along the Mort River. Metamorphic grade also increases from the Starra Shear westwards, where foliation and bedding-parallel isograds are compressed across the shear, rising from

middle-upper Greenschist to upper Amphibolite grade in the Gin Creek Block (Switzer 1987, Laing et al. 1988).

Western Hematites Metamorphic Grade

General

The immediate host-rocks to the Western Hematites record a peak metamorphism within "Zone A" on the basis of mineralogical comparison, preservation of sedimentary structures, and independent geothermometry and barometry.

A summary of parageneses is presented in Table 4.2. Metamorphic assemblages useful for P-T estimation are actinolite-andesine-epidote in amphibolites, scapolite-biotite-actinolite in calcareous metasediments, actinolite-biotite-scapolite-epidote-calcite-magnetite± chalcopyrite in reaction skarns, and biotite-chlorite-muscovite-albite-quartz ± epidote in footwall Harley Member schists. Some magnetite may have formed by the reaction hematite + carbonate in hematitic ironstone.

Temperature

Temperature was estimated using plagioclase-amphibole pairs preserved in

Hangingwall metasediment
Act - biot - calcite - albite - hem
Scap - biot ± hem ± ilmenite ± tourm
(late) Calcite - dol - qtz - chl - hem
Reaction skarns
Act - epi - chl - calcite - mag
Scap - biot ± act ± epi
Act - plag
Ironstone
Hem - mag - qtz ± cpy ± musc ± chl
Mag - calcite - qtz - cpy - py
(late) siderite - hem - chl ± chalcocite ± covellite
Amphibolite
Act - plag - epi - mag
Mariposa Creek Formation
Alb - qtz - biot - chl ± K-spar, tourm, calcite, epi
Chloritic schist
Biot - qtz - chl - hem -alb
Musc - alb - qtz - chl ± hem, mag
Py - epi - hem - qtz
Py - calcite - hem - mag

Table 4.2 *Metamorphic assemblages of Starra rock-types.*

amphibolites 100 to 200 m east of Area 257. Sample St 154 contained well-preserved sub-

ophitic dolerite textures, devoid of epidote: this is important because epidote increases the anorthite content of plagioclase (Winkler 1979, p. 174).

Method 1: Experimental Thermometer of Plyusnina (1982). The anorthite component of plagioclase varies regularly with the Al - content of Ca-amphiboles as temperature rises in orthoamphibolites (Wenk & Keller 1969). Plyusnina (1982) provided an experimentally calibrated geothermometer for tholeiitic compositions using the variation of anorthite in plagioclase, found to be invariant with pressure in the range 2 - 8 kbar. In amphibolite St 154, plagioclase varied from An_5 to An_{31}, corresponding to a temperature range of 490 - 530° C, and notably spanning the An_5 to An_{17} transition advocated by Winkler (1979) as a useful marker to a point 20 – 30 ° C below the low to medium grade metamorphic boundary.

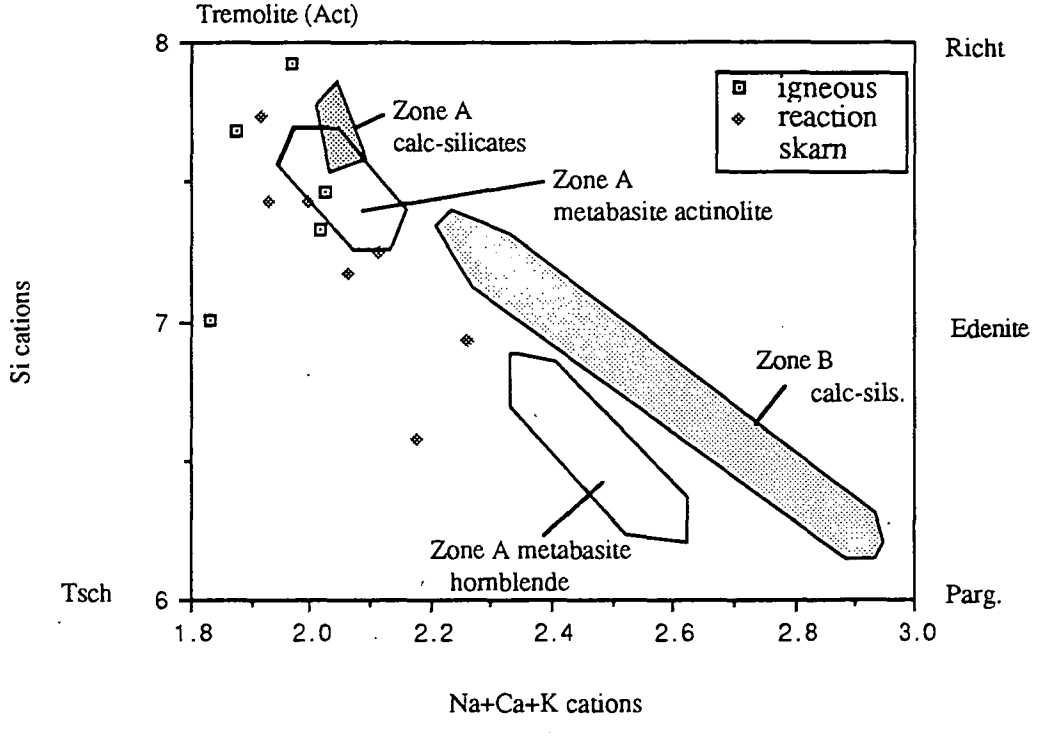

Figure 4.15 *Variation of amphibole composition (per 23 O) in Starra meta-dolerite and calc-silicate reaction skarns. The data is compared to amphiboles from Zone A and Zone B of Jaques et al. (1982) for the Selwyn area: Zone A recrystallised at 450 - 550 °C, and Zone B at 550 - 600 °C, with pressures of 3 to 4 kb.*

Method 2: Empirical Thermometer of Spear (1980), modified after Jaques et al. (1982).
Spear (1980) empirically calibrated the NaSi-CaAl exchange between plagioclase and the amphibole M4 cation site, to use as a geothermometer. Compositional data for Starra amphiboles is presented in Table 4.3, summarised in Fig. 4.15. The method of Jaques et al. (1982) was followed, involving assignment of all Ca to the M4 site, followed by enough Na to bring the cation total to 2. K_D for the reaction is expressed as

$$K_D = X_{Ca}/X_{Na,plag.} \cdot X_{Na}/X_{Ca\ M4,\ Amph}$$

,where X is the mole fraction.

Jaques et al. (1982) found that the empirical calibration of Spear (1980) provided temperature estimates significantly lower than the range recorded by the garnet-biotite geothermometer of Ferry & Spear (1978) for Selwyn metabasites.

	St 154:1	St 154:1a	St 154:2	St 148:3	St 148:3a	St 148:1
SiO_2	48.56	52.13	54.42	53.06	46.38	49.93
TiO_2	-	0.17	-	0.19	0.39	-
Al_2O_3	6.99	5.41	3.16	5.02	10.81	8.61
Fe_2O_3	9.36	5.75	0.95	3.58	12.66	6.74
FeO	4.46	6.21	9.22	8.49	4.08	7.02
MnO	0.38	0.49	0.41	-	-	-
MgO	15.69	15.96	17.46	16.4	12.07	13.6
CaO	10.44	12.08	12.39	12.21	12.09	11.62
K_2O	0.11	-	-	-	0.36	0.3
Na_2O	0.7	0.72	-	0.37	1.01	0.8
Sum	96.7	98.93	97.99	99.33	99.91	98.71
Cations per 23 oxygens						
Si	7.01	7.33	7.69	7.43	6.57	7.17
Ti	-	0.02	-	0.02	0.04	-
Al	1.19	0.9	0.53	0.83	1.81	1.46
Fe^{3+}	1.02	0.61	0.1	0.38	1.35	0.72
Fe^{2+}	0.54	0.73	1.09	0.99	0.48	0.93
Mn	0.05	0.06	0.05	-	-	-
Mg	3.37	3.34	3.68	3.42	2.55	2.91
Ca	1.61	1.82	1.87	1.83	1.84	1.79
K	0.02	-	-	-	0.07	0.06
Na	0.2	0.2	-	0.1	0.28	0.22
Sum	15.0	15.0	15.0	15.0	15.0	15.0
	dolerite	dolerite	dolerite	reaction skarn	reaction skarn	reaction skarn

Table 4.3 *Selected amphibole analyses from orthoamphibolite St 154 (CRQ 77-26, 53.1 m), and reaction skarn St 148 (STQ 86-243, 83.1 m).*

They accordingly formulated the regression

$$\ln K_D = (-9752/T^\circ K) + 7.407 \qquad (r = 0.925)$$

which provided temperatures more consistent with those of other methods. This modification was adopted for analysis of metabasite sample St 154, with compositional data for co-existing amphibole-plagioclase pairs presented in Table 4.4.

	XCa	XNa	Na(M4)	Ca(M4)	In K	T° C
St 154a	10.08	89.92	0.165	1.845	-4.603	539°
St 154b	16.63	83.37	0.123	1.876	-4.337	557°

Table 4.4 *Compositional data for amphibole-plagioclase pairs, analysed by microprobe, using a clinopyroxene standard.*

The resulting temperatures were slightly higher than those of method 1, in the range 540° to 560° C. The near overlap of the methods is the preferred temperature range, 520 - 550° C, with a conventional accuracy of ± 25° C (e.g., Ferry & Spear 1978).

Pressure

The celadonite (Mg-end-member: $KFe^{3+}(Mg,Fe^{2+})Si_4O_{10}(OH)_2$) of muscovite in low-grade assemblages is sensitive to temperature, pressure, bulk chemistry and a_{H2O}. With increasing pressure, Si substitutes for Al in four-fold coordination, and Mg and Fe^{2+} substitutes for Al in six-fold coordination (Sassi & Scolari 1974). Velde (1965) suggested that Si content of muscovite might therefore be a useful geobarometer, which has subsequently been formulated and widely employed (Velde 1965, Guidotti & Sassi 1976, Massonne & Schreyer 1987, Bucher-Nurminen 1987, Brill 1988).

The geobarometer of Sassi & Scolari (1974) is based on the non-limiting assemblage qtz-plag-musc-chl, with the proviso that quartz and chlorite-rich samples are avoided because they are celadonite-enriched. The phengite-chl-alb-qtz paragenesis of sample St 60, within the Harley Member footwall to Area 257, is suitable for analysis, because the chlorite is in textural equilibrium with muscovite. Selected muscovite analyses are provided in Table 4.5.

The Si number used in the Massonne & Schreyer (1987) adaption of the Sassi & Scolari (1974) geobarometer represents half the value for the number of Si atoms per structural unit: St 60 muscovites had Si contents ranging from 3.14 to 3.17 per half cell unit. However, the experiments of Massone & Schreyer (1987) were based on a limiting K-feldspar assemblage, which fixes the Si content of white mica; Brill (1988) recommended using the highest Si value of a group of analysed muscovites to allow for this. Assuming a temperature average of 520 to 550° C, a pressure range of 4 - 5 kbar is determined (Fig. 4.16). Brill (1988) found the method overestimated pressure by ~ 0.5 kbar, and accordingly a range of 3.5 to 4.5 ± 1 kbar is most likely.

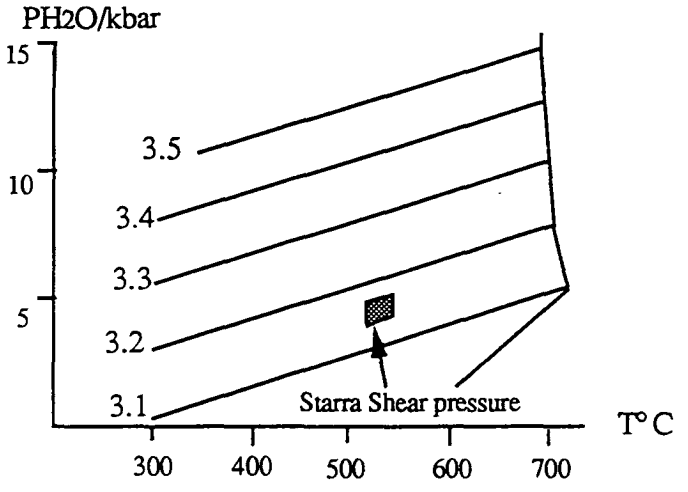

Figure 4.16 *Si isopleths with respect to pressure and temperature in phengitic muscovite, after Massone & Schreyer (1987). The estimated P-T conditions for sample St 60 are shown, calculated from data compiled in Table 4.6.*

	St 60.1	St 60.2	St 60.3	St 60.4
SiO_2	46.37	46.97	46.94	45.99
TiO_2	1.10	1.18	0.63	1.02
Al_2O_3	30.93	31.33	31.31	31.71
FeO	4.25	4.50	4.80	4.07
MgO	1.20	1.32	1.34	0.93
K_2O	9.82	10.59	10.69	10.46
sum	93.66	95.89	95.72	94.19
cations per 22 oxygens				
Si	6.350	6.317	6.335	6.283
Ti	0.113	0.119	0.064	0.110
Al	4.991	4.966	4.980	5.106
Fe	0.487	0.506	0.542	0.465
Mg	0.244	0.265	0.270	0.189
K	1.714	1.817	1.841	1.823
sum	13.900	13.990	14.031	13.971

Table 4.5 *Selected analyses of footwall phengitic muscovite from sample St 60, in equlibrium with chlorite, quartz and albite.*

Metamorphic Fluid Conditions

A brief study of fluid inclusions was made to infer the fluid compositions prevailing during metamorphism and deformation: a very diverse group of fluids has emerged, as might be expected along a zone of recurrent shearing. Firstly, as discussed in chapter 3, very small (~ 3 μm) pre-metamorphic hydrothermal inclusions occur within the Area 222 ore, consisting of 3 phases. Their diminutive state has prevented thermometric measurement,

	T_{h}- v to l	T_{h} - NaCl	T_{e}- first melting
Primary: CO_2 -rich, (melting at ~ -55.3 ° C)	-3.4		
	-0.7		
	1.6		
	1.7		
	1.8		
	4.3		
	-8.2		
	-7.8		
	0.0		
	-0.6		
	-0.5		
	4.8		
	6.8		
	10.0		
	16.2		
	17.9		
Saline secondary inclusions (l/v ratio ~ 10 %)	114.1	206.8	-44.6
	116.7	204.1	-40
	114.4	-	-
	126	-	-
	130	226.5	-
	123.8	233.2	-
	123.7	235.7	-43.1
	118.9	210.9	-
	121.6	204.6	-

Table 4.6 *Fluid inclusion thermometric data from D2(MP) boudin veins, Area 251, 1275 R.L., underground (Fig. 4.7).*

although a minimum salinity of 26.2 wt. % NaCl-equivalent is indicated by halite and two other daughters, which form 25 - 50 % of the inclusion volume.

The fluids associated with D2(MP) quartz-sulphide boudin-neck veins (Area 251, level 1275 R.L. ; Fig. 4.7, samples from 7 m north of STQ 223) are very different to those of Area 222. Quartz within the boudins (Table 4.6) contains numerous negative-relief, high density CO_2 inclusions, up to 15 μm in diameter, (density variation of 0.90 - 0.97 g/cc), with an average X_{CO2} of 0.98 (derived by the method of Hollister & Crawford (1981), p. 61). Trains of larger secondary inclusions (related to D2 (LP) or later deformation) with small vapour to liquid ratios cut the boudins, and have $T_{h\ vapour}$ between 114° and 125° C, $T_{h\ NaCl}$ = 206.8 – 235.7° C, and salinities of 30.7 – 33.8° C (Potter et al. 1978), uncorrected for pressure. T_e (first melting) of ~ -43° C requires that $CaCl_2$ was a brine component. Thus, the earliest preserved metamorphic fluid was dense and CO_2-rich, while later retrogressive fluids were CO_2-poor and saline (see chapter 10). Switzer et al. (1988) document metamorphic inclusions containing CO_2, KCl crystals and Fe+Ca chlorides, dissolving KCl when heated to ~ 400° C. The context and timing are uncertain. By

comparison with the CO_2-dominated fluids identified in D2(MP) boudin-necks, they are most likely retrogressive. Switzer et al. (1988) identify them as the primary mineralising fluid.

Although further work is required to specifically isolate the fluids characterising D2(LP), data has been obtained for the tensile calcite-chlorite veins which developed late in this event. Fluid inclusion had a T_h of 100° to 365° C (see chapter 10). The cataclastic nature of the late deformation provides a lithostatic pressure range of 0.5 to 2.5 kbar (Scholz 1988). In view of this large pressure uncertainty, it is not possible to pressure-correct the fluid inclusion temperatures.

Discussion

The above peak metamorphic D2(MP) conditions are immediately below the Greenschist-Amphibolite facies boundary, and accord with uppermost "Zone A" of Jaques et al. (1982). At these temperatures, the style of D2(MP) was ductile; retrograde conditions which produced chlorite-hematite assemblages during D2(LP) were associated with brittle-ductile deformation, and hence most likely ranged between 300° and 450° C, the respective lower limits of quartz and feldspar plasticity (Scholz 1988). Pervasive biotite replacement of hangingwall cordierite and scapolite is attributed to this event.

CONCLUSIONS

1. The Starra Shear in the vicinity of the Starra orebodies was produced during $D1_a$, and reactivated during D2(MP), D2(LP) and D4. These events progressed from ductile pervasive deformation, through brittle-ductile, to brittle highly localised deformation. On the evidence of Switzer (1987), $D1_a$ was an extensional event in which the Staveley Formation moved northward on a low-angle detachment surface. D2(MP) corresponds to the regionally recognised shortening event, manifested as large-wavelength, upright, shallowly-plunging, isoclinal folds. D2(LP) steeply-plunging folds form a sinistrally-verging domain between the Mt. Dore Fault Zone and the Starra Shear, attributed to transpression during strike-slip movements on the Starra Shear. The resulting folds were near-coaxial with the early D2(MP) lineation. Fold interference, transposition and reverse faulting were the important influences on ironstone geometry at a local scale.

2. At outcrop and petrographic scales the magnetite-Cu-Au ironstones and the underlying alteration are folded and boudinaged by D2(MP) and D2(LP); the ore-forming event therefore predated or formed early in D2(MP). Further strengthening the evidence for a predeformational origin, pyrite porphyroblasts contain cores of randomly oriented silicate inclusions. There is little petrographic evidence for oxide sulphidation, or chalcopyrite replacement of pyrite, as argued by Switzer et al. (1988).

3. The coincidence of three Starra orebodies with portions of D2(LP) folds has been a major argument for their deformational origin. In the light of petrographic evidence for a pre-tectonic history, it is suggested these fold zones formed by preferential ductile slip in areas of higher sulphide content. Such a model advocates a continued exploration focus on fold zones, in which mineralisation may be present at some point along the fold axis, although not necessarily at surface.

4. Peak syn-D2(MP) metamorphism is estimated at 520 - 550° ± 25° C, and 3.5 - 4.5 ± 1 kbar, using the plagioclase – amphibole chemistry of amphibolite, and the celadonite content of phengite.

CHAPTER 5

MAJOR AND TRACE ELEMENT GEOCHEMISTRY OF THE STARRA AND TROUGH TANK HOST-ROCKS.

PARENT ROCKS OF THE FELSIC HOST ROCKS

Introduction

Aims

The aim of this chapter is to document and advance interpretations to explain the chemistry of the ore deposit wall-rocks, excluding magnesian varieties. The latter are dealt with in Chapter 7. The methods of analysis, and the analyses themselves, are available in Appendices 2 and 3.

The Problem of the Origin of Sodic Schists

The origin of sodic quartzofeldspathic schist, such as the Starra footwall, and Trough Tank host-rocks, has long been a problem (Coombs 1965, Shaw 1972, Dougan 1976, Stanton 1976, Plimer 1977, Whitney & Olsted 1988). Such rocks commonly have compositions isochemical with known variants of graywacke, arkose, altered felsic volcanics/epiclastics, and intrusive/extrusive trondhjemitic magmas. The often-equivocal field relations of metamorphosed and deformed rocks has led to a great reliance on geochemistry to distinguish between such sedimentary and igneous rocks. The geochemical approach is based on the fractionation of alkali and alkali earth elements into seawater during physical and chemical weathering. This results in the preferential partitioning of Na, Mg, B, K, Sr, Li, Ca, Se, Au, Mo, U, Pb, Ni, and V into seawater. Elements in resistate minerals (Zr, Hf, Nb, Ta, Sn) tend to concentrate in high silica sediments and hence are also useful; unfortunately these incompatable elements are also enriched in siliceous melts, in some cases to very high levels (topaz rhyolite and alkaline varieties, Christiansen et al. (1986)), which limits their application. Elements of less use in discrimination are those transported during weathering with little fractionation into sediments, such as Ti, Y, Sc, Al, Ga, Th, Co and the rare earths. They are nevertheless helpful in characterising sediment provenance (e.g., Bhatia 1983, Maynard et al. 1982, Bhatia & Crook 1986), or petrogenetic history.

Shaw (1972) developed a discriminatory analysis technique for feldspathic rocks based on previous attempts by Moine & de la Roche (1968), Weisbrod (1969) and Dennen & Moore (1969) with binary scatter diagrams. Shaw's method gives quantitative values to the premise that with increasing maturity sediments become silicic, and that alkalis in sandstones are depleted compared to felsic igneous rocks at similar silica levels. K_2O/Na_2O ratios also change with sediment maturity, from <1 for modern arc settings, to >1 for

trailing margin settings (Maynard et al. 1983). In a very general fashion, unaltered igneous rocks have a ratio less than 1.

Field criteria at Starra and Trough Tank eliminate an intrusive origin, but cannot uniquely differentiate between immature feldspathic sediment accumulation, and volcanics/volcaniclastics which could be evidence of contemporaneous volcanism. If the sodic character was imposed after deposition, then it is important to determine whether this was a regional diagenetic/metamorphic effect, or one related to gold mineralisation localised around the ores. An additional factor at Trough Tank is the geochemical effect of limited partial melting which resulted in the formation of sporadic albitic leucosomes. Such rocks were excluded from the data set.

Trough Tank

Field Evidence

The high metamorphic grade (Chapter 3) has recrystallised most original textures in the feldspathic host rocks. However, they still divide into those which are biotite-poor and massive (~20 % overall), characterised by occasional chloritised angular clasts 1–2.5 cm long (conceivably a volcanic texture), and those consisting of foliated coarse albite and biotite (~ 60 %). In the latter, biotite variation crudely defines compositional layering, but otherwise an origin is indeterminate. Grading and occasional cross-bedding occur, but are uncommon. Perhaps 20% of the sequence is undeniable sediment, consisting of very micaceous intervals or cross-bedded gravel-rich quartzite.

Low Temperature Alkali Alteration

Both altered and unaltered lithologies occur at Trough Tank, but because alteration is so extensive at Starra, few unaltered rocks have been cored there. Thus the only opportunity to distinguish between host-rock chemistry associated with mineralisation, and that related to other processes, is at Trough Tank.

The Trough Tank sampling has shown that feldspathic rocks with high Na, but low levels of ore elements, extend hundreds of metres beyond the obvious alteration haloes. Figure 5.1 (a plot of all host-rock samples) illustrates that Fe-altered rocks close to mineralisation are characterised by Na_2O levels between 1 and 5.2%, whereas rocks further from ore (averaging 3.3% $Fe_2O_3^{tot}$) range between 4.6 and 8.5 % Na_2O i.e. markedly more sodic. The spread of altered rock data can be approximated by simple Fe-dilution from a minimum pre-alteration value of 5.5% Na_2O. Rocks which contain no anomalous levels of ore elements, but are nevertheless very sodic, are likely to represent background compositions unrelated to ore. This group of compositions has been used to identify the protoliths for the Trough Tank host rocks.

'Background' alkali alteration is a common diagenetic feature of acid fragmentals and feldspathic sediments deposited under evaporitic conditions. Sodic diagenetic alteration is less common than potassic alteration (Kastner & Siever 1979), and in the specific instance

of evaporitic diagenesis (applicable to many Mount Isa sequences) relates to the evolution of interstitial brines within the sediments. In studying tuff-bearing alkaline basins, Sheppard & Gude (1968, 1969) found that a central potassium feldspar facies is flanked by a zone of analcime, and finally a zeolite facies, representing interaction with increasingly evolved saline waters. These changes decouple Na and K from Ba, Rb, Sr and Pb, because authigenic feldspars do not incorporate the latter trace elements, although authigenic K-feldspar does concentrate B (Kastner & Siever 1979).

The consideration of these processes leads to greater reliance on discrimination techniques which use the immobile elements Ti, Zr, Y, Nb, Ce, Ga and Sc (Floyd & Winchester 1978). For instance, the pitfalls Na and Fe alteration poses to the Shaw (1972) sediment/volcanic discrimination technique are illustrated in Fig. 5.2.

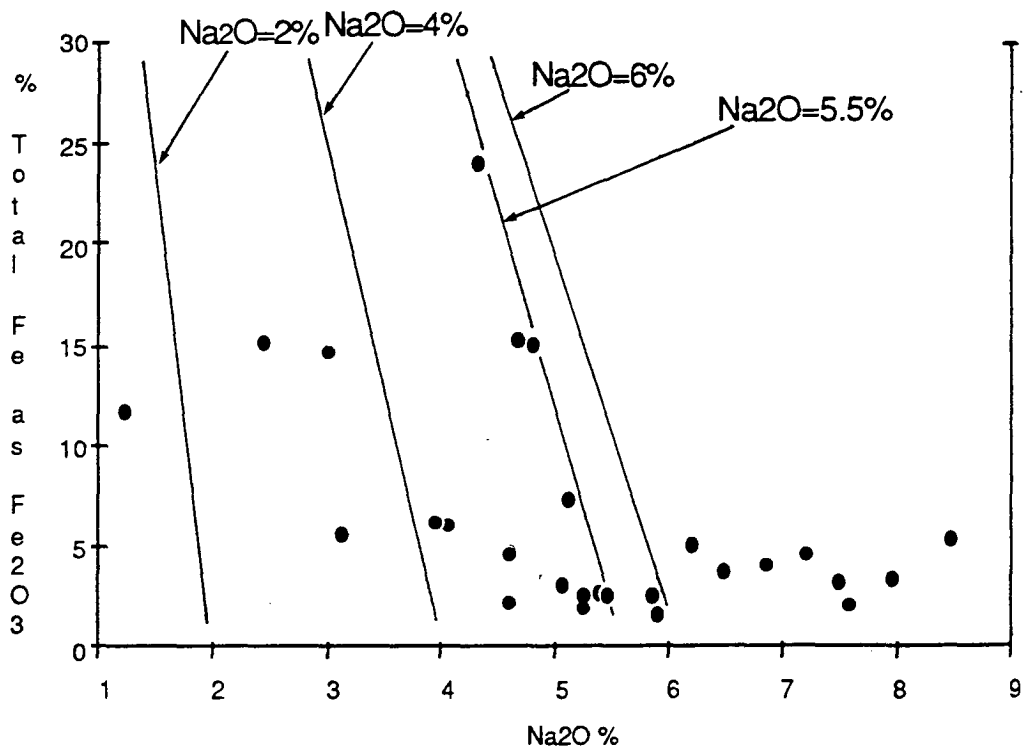

Figure 5.1. *A plot of weight % Na_2O versus $Fe_2O_3^{tot}$ for unaltered and altered lithologies of Trough Tank host rocks. The data indicates that rocks with no hydrothermal Fe addition nevertheless have elevated Na_2O levels, suggesting sodium alteration to be a feature of the unaltered host-rocks. The lines of Fe addition assume no volume change during Fe alteration. They show that an original value of 5.5 % Na_2O would explain most of the data, and that values in excess of this are 'primary', or at least pre-Fe addition.*

The Ti/Zr ratio has therefore been used here for comparison with other elements (see results section). It is a good index of igneous differentiation, remains relatively constant during low temperature alteration, and its sedimentary trend differs to its igneous behavior (Floyd & Winchester 1978, Bhatia & Crook 1986).

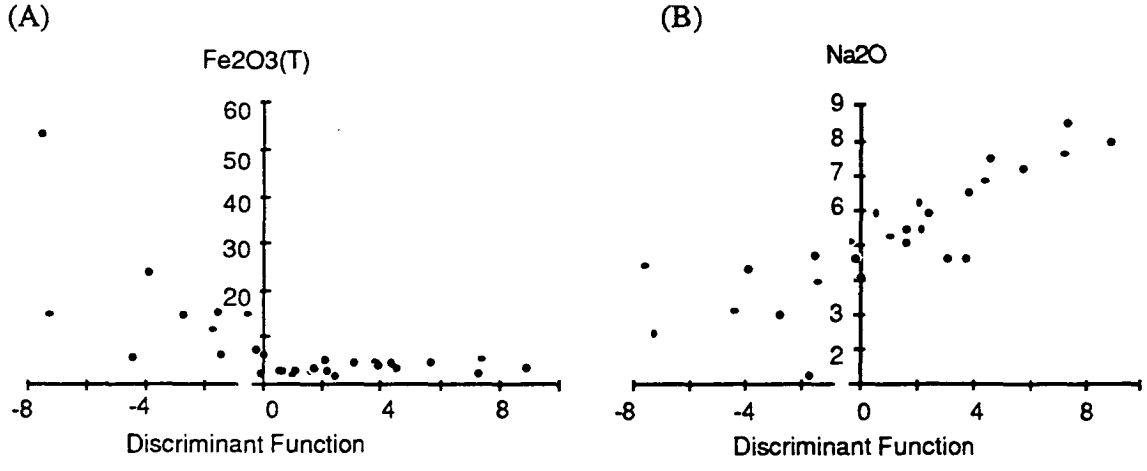

Figure 5.2. *All Trough Tank host-rock data for Fe_2O3 and Na_2O, plotted as a function of the Discriminant Function DF=10.44 - 0.21SiO_2 - 0.32Fe_2O3 - 0.98MgO + 0.55CaO + 1.46Na_2O + 0.54K_2O (after Shaw 1972). A positive value indicates igneous parentage, a negative one a sedimentary origin. In (A) the effect of Fe alteration clearly biases DF towards negative values, whilst Na enrichment (B) imparts a strong positive (igneous) signature. The example illustrates that functions using elements liable to alteration are inappropriate.*

Geochemistry

Given the clear alkali alteration history of the Trough Tank rocks, two approaches have been used:

(1) A selected comparison of absolute levels of elements in the samples with those of possible precursors.

(2) Comparison of Ti/Zr trends in all least-altered samples, with those expected from either igneous differentiation or sediment maturation.

(1) Absolute element levels. Sample 236616 (Table 5.1) has been selected for this comparison because it shows minimal evidence of alkali alteration, and its field characters are most typical of a massive acid volcanic. Chemical analysis has shown this sample to be a 4 m wide fresh pocket amidst strong alkali alteration (Samples TT137, 138, 139, 140; Appendix 3). Table 5.1 illustrates that this unit is similar to nearby recognised acid volcanics, such as parts of the Doherty Formation (Bultitude & Wyborn 1982), and close to unaltered global rhyolite averages (Ewart & Stipp 1968, Ewart 1979). Only K, Ba, Rb, and Ca show depletion, interpreted as the effect of weak albitisation. Interestingly the average of all 14 'least altered' host-rock samples also have SiO_2, Al_2O_3 and immobile element similarities with acid volcanics.

Some basic constraints to the identification of sediments are given by the limits to igneous fractionation. For instance, SiO_2 in unaltered volcanics cannot exceed ~77 %, the composition of minimum melts in the SiO_2-Al_2O_3-Na_2O-CaO-K_2O system, at pressures appropriate for magma generation. Very few igneous rocks have Al_2O_3 exceeding 22%, and most are less than 18%, although peraluminous varieties such as phonolites, syenites and

mugearites may attain 25%. This 'rule of thumb' approach identifies samples TT18 and TT60 as sedimentary.

(2) Element trends. Some major and trace elements of the least-altered sample group were plotted as a function of Ti/Zr (Fig. 5.3), and compared to sediment compositions in the literature, and to acid volcanic compositions from the Eastern Succession (Bultitude & Wyborn 1982).

	Trough Tank acid volcanic TT236616	Average Trough Tank host rock, n=14	Starra volcaniclastic n=2	Doherty Fm acid volc.* 1 n=1	Rhyolite—bimodal *2	Average calc-alk. rhyolite *3
SiO_2	75.18	72.47	73.13	75	73.49	73.85
TiO_2	0.47	0.44	0.28	0.13	0.27	0.23
Al_2O_3	12.59	12.74	9.89	13.1	13.93	13.55
$Fe_2O_3^{tot}$	3.15	3.3	2.04	0.82	2.7	1.25
MnO	0.01	0.03	0.04	0.02	0.02	0.05
MgO	0.64	1.35	1.07	0.19	0.35	0.3
CaO	0.66	1.17	3.88	0.6	1.45	1.53
Na_2O	5.07	5.91	7.49	5.04	4	3.71
K_2O	1.61	0.64	0.08	4.05	4.15	3.6
P_2O_5	0.18	0.13	0.15	0.05	0.05	0.05
loss	0.5	1.26	3.57	-	-	0.97
Total	100.06	99.45	99.60	99.05	100.41	99.69
Rb	73	35	<2	90	156	95
Sr	29	21	22.2	17	27	169
Ba	345	88	6	250	849	880
Zr	204	201	222	130	203	185
Y	27	26	15	38	30	33
Nb	14.6	13	7.8	15	5	-
Cu	18	26	<6	-	15	9.4
Pb	8	7	-	<2	20	-
Zn	7	8	<2	-	25	-
Ni	8.3	27	4.6	-	3	-
V	-	-	22	-	9	21
Al/Al+alk	63.17	62.27	46.34	57.48	59.20	60.52

Table 5.1 *A comparison between the geochemistry of probable acid volcanics amongst the Trough Tank and Starra host rocks, acid volcanics from the Doherty Formation and some fresh average rhyolites. *1. Bultitude & Wyborn (1982) *2. Ewart (1979)*3. Ewart & Stipp (1968). Al/Al+alk = $Al_2O_3/(Al_2O_3+Na_2O+K_2O+CaO)$.*

This exercise shows that while Trough Tank host-rocks overlap with the volcanic samples, their distinct trends cross the series at an angle for the elements examined. The trends are, however, sub-parallel to (and in the cases of Al_2O_3 and SiO_2 contained within) the sediment trends (data from Bhatia & Crook 1986, McLennan & Taylor 1985). These angular trends are unlikely to be due to alteration, because this would produce a vertical spread at a fixed Ti/Zr value (e.g., Whitford et al. 1983). The trends strongly suggest Trough Tank host-rocks to lie on a mixing line between low Nb/high silica acid volcanics (Ti/Zr ~ 10), and an aluminous sediment. The latter component has enriched Nb (>18 ppm),

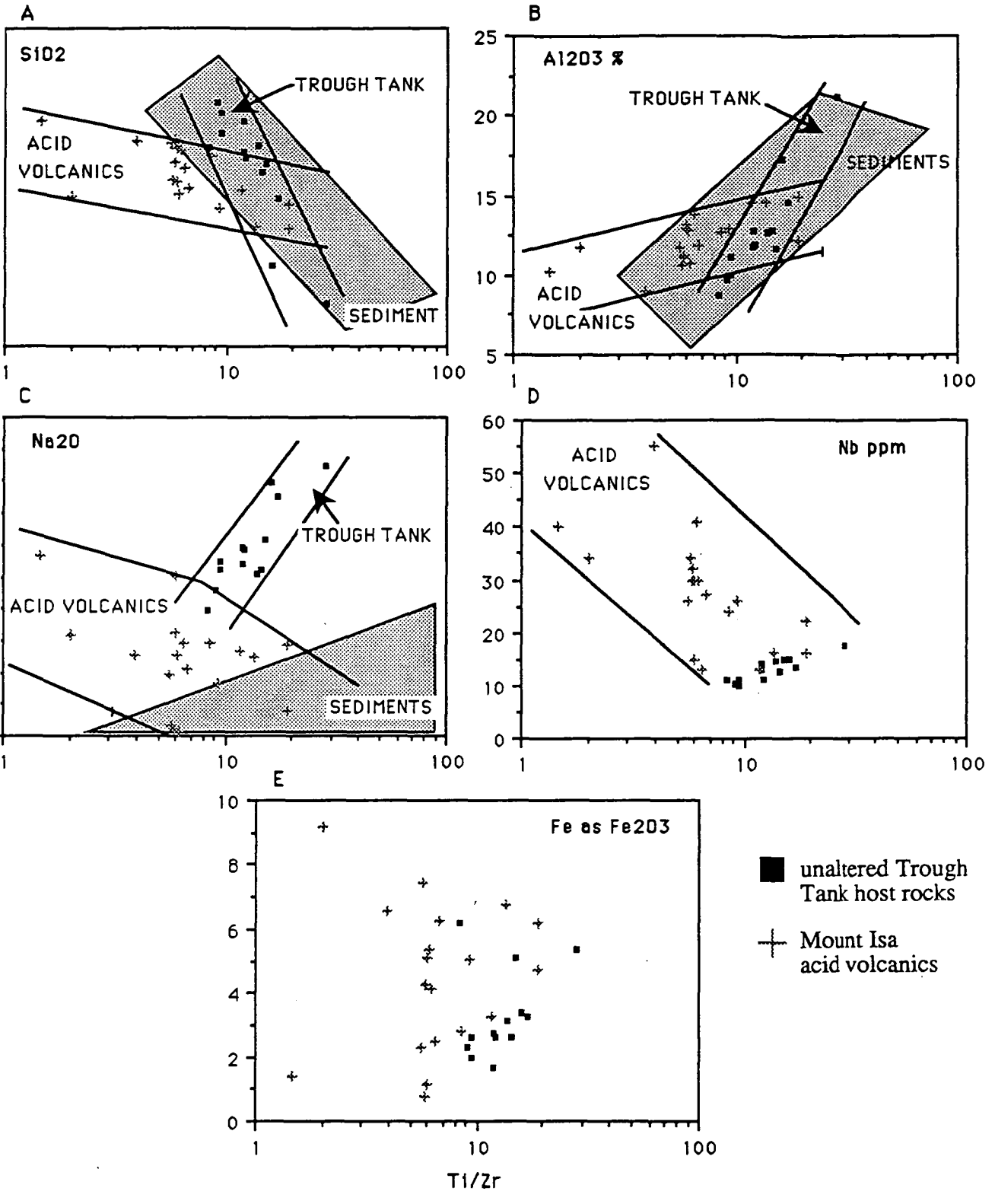

Figure 5.3A-E. *The relationship of Ti/Zr to SiO2, Al2O3, Na2O, Fe2O3 and Nb is illustrated for Trough Tank host rocks, and for the comparison suites of Eastern Succession acid volcanics (after Bultitude & Wyborn 1982) and selected average sediment compositions (after Bhatia & Crook 1986, McLennan & Taylor 1985). The latter is only shown as a field.*

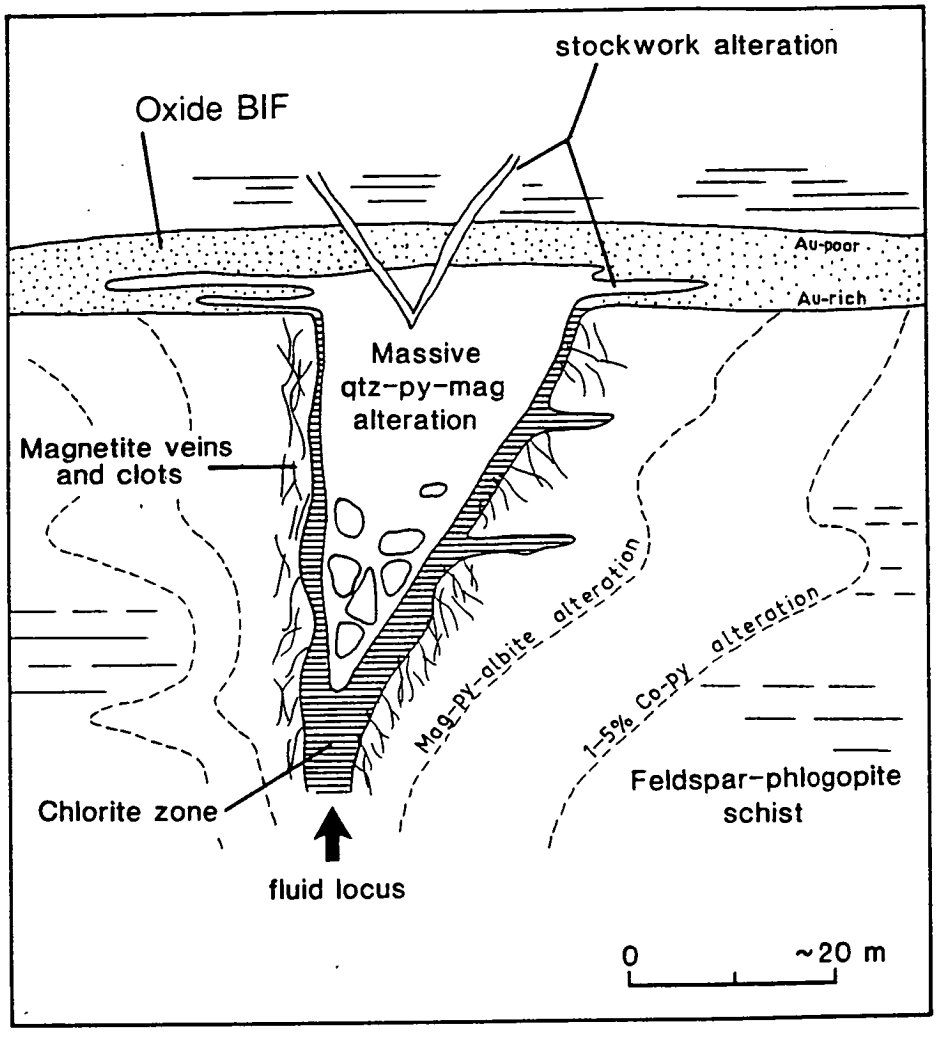

Figure 5.4 *A schematic diagram of the alteration zones identified below Trough Tank BIF mineralisation. A central silica 'pipe' zone is characterised by vein networks of magnetite, pyrite and chalcopyrite cutting a quartz matrix. Shown as a cone in the diagram, in some cases the 'funnel' of the top of the zone meets the overlying layers at very low angles. The pipe is surrounded successively by a sharp, thin, chlorite selvedge, diffuse magnetite ± cpy-py alteration, and pyrite - carbonate alteration hosted by albite schist.*

high Ti/Zr (> 20), high Nb/Y (> 0.8) and low SiO_2 (< 54 %). These elevated incompatible element levels are consistent with the weathering of alkalic volcanics, which contain varieties such as mugearites enriched in Na, Al, Ti, and Nb. The Trough Tank volcanic end-member was a rhyolite with no alkalic features, possessing lower Nb levels than most of the Mount Isa samples in Figure 5.3D.

Na_2O in the Trough Tank sample set (Fig. 5.3C) clearly diverges from either the global sediment or the Mount Isa volcanic trend. This is interpreted as post-depositional addition of sodium to the sequence by replacement of other alkali elements: this is why values of 8 to 9 % Na_2O coincide with the most SiO_2-poor and alkali-enriched lithologies.

Starra

Field evidence

The features of the albitic Mariposa Creek Member, which forms the Starra footwall, were documented in Chapter 3. The important features relevant to the origin of the unit are compositional layering, 1 cm high cross-beds, and well-developed grading (in which the phyllitic tops of beds are markedly enriched in fine hematite). The last suggests that mass-flow processes were important during formation. Another common texture is massive albite, variably silicified and hematitised.

Several 0.5 - 2 m thick, conformable, feldspathic beds also occur within the hangingwall metasediments, distinctly more albite-rich than their host calcarenites. They have sharp boundaries, and contain 5 to 10 % carbonate, but internal microtextures are too recrystallised to identify diagnostic features. The intervention of beds which are not typical of the hangingwall metasediments suggests these beds had a special source: the bed thickness, feldspathic mineralogy and abrupt contacts are most consistent with an origin as a felsic pyroclastic flow (e.g., Fisher & Schmincke 1984; Davidson & Dashlooty, in press). A similar origin can be inferred for massive feldspathic beds in the footwall. A depositional environment close to a felsic volcanic centre is anticipated, where turbiditic epiclastics and massive volcaniclastic beds accumulated together.

Geochemistry

Methods

Twenty seven samples of variably altered footwall schist, and 21 samples of fresh and altered hangingwall metasediments were analysed (Tables 5.2, 5.6, Appendix 3). All samples are representative of drill-intercepts 1 to 25 m long, except for Area 251 underground samples which were chipped in fresh rock over 10 m widths along drives. These are discussed in more detail under "Alteration Geochemistry". All hangingwall samples derive from Area 257, mainly close to line 11285 N, whereas the footwall samples come from Areas 276, 257, 251 and 244 (Area 257 sampling concentrated on line 11285 N). Sample locations are provided in Appendix 3, and for line 11285 N are shown on Fig. 5.14.

Are the Footwall Schists Altered Hangingwall Sediments?

The proposal is examined that lithologies footwall to tabular ironstones in fact are metasomatised hangingwall metasediments. This is likely, for instance, if the ironstones formed as metamorphic/igneous skarns replacing calcareous layers.

Firstly, field evidence does not support this proposal, if the remnant primary footwall textures described above are compared to the well-preserved sedimentary textures of the hangingwall (described in detail in Chapter 2). Hangingwall metasediments consist of couplets of 1 - 5 cm thick graded calcarenite, and 1 - 3 cm thick scapolite/cordierite-biotite layers (after calcareous shale). The two layer types are distinctive, in places grading into one another. Such distinctive compositional layering is not observed in the footwall.

wt. %	Least altered sediment n=11	Altered sediment n=7	Shale layer n=2	calcarenite layer n=2
SiO_2	50.23	53.40	49.28	55.97
TiO_2	0.48	0.54	0.90	0.49
Al_2O_3	11.54	12.66	18.08	12.69
$Fe_2O_3^{tot}$	8.63	7.02	9.43	4.92
MnO	0.12	0.12	0.06	0.10
MgO	4.70	3.59	7.90	3.40
CaO	9.54	9.68	2.47	8.49
Na_2O	3.70	6.78	3.96	6.09
K_2O	1.59	0.22	3.97	1.23
P_2O_5	0.14	0.14	0.14	0.17
ppm				
Cu	11	33	8	<2
Zn	9	28	29	7
Ba	154	69	433	102
Ni	28	30	128	27
Rb	72	11	210	61
Sr	37	54	65	49
Zr	135	178	219	169
Y	26	25	26	21
W	13	11	10	11
Sc	10	14	30	12
V	64	88	175	75
Nb	12	12	21	11
La	31	39	36	32
Ce	64	82	76	64
Nd	26	32	29	26
U	8	7	9	5
Th	14	15	24	12

Table 5.2 *Average Starra hangingwall sediment compositions, including least altered sediments, the coarse and fine components of these, and sediments altered because of their proximity to shear zones and dolerites.*

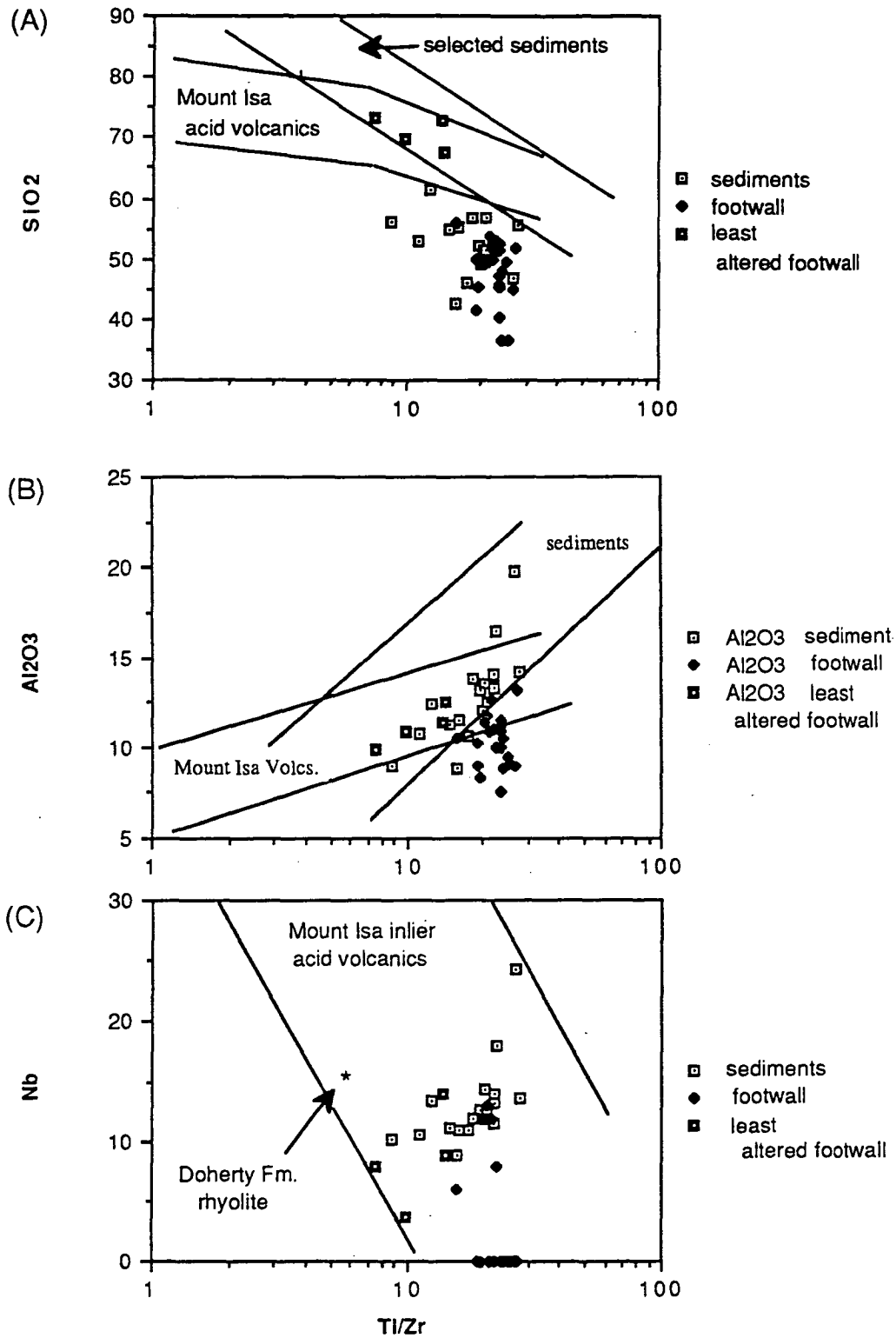

Figure 5.5 *A SiO_2 weight % versus Ti/Zr for hangingwall metasediments, footwall alteration, and 'least altered' footwall (made up of albitic samples from above and below the ironstone). For comparison, the fields of Mount Isa Inlier acid volcanics, and typical sediments are shown. Starra sediments fall below the sediment field because of their high carbonate content. B. Al_2O_3 versus Ti/Zr for the aforementioned sample groups. Although not shown, the Trough Tank host-rocks are coincident with Starra sediments on this plot. C. Nb versus Ti/Zr. All sample groups fall at the HFS element-depleted end of the Mount Isa volcanics field, suggesting that they ultimately are all volcanic-derived materials.*

In addition, where metamorphic albitic alteration occurs in the hangingwall (around dolerites, shears and local skarns) it preserved pre-existing layering, and is accompanied by calc-silicate assemblages such as epidote-actinolite — assemblages not commonly observed in the footwall.

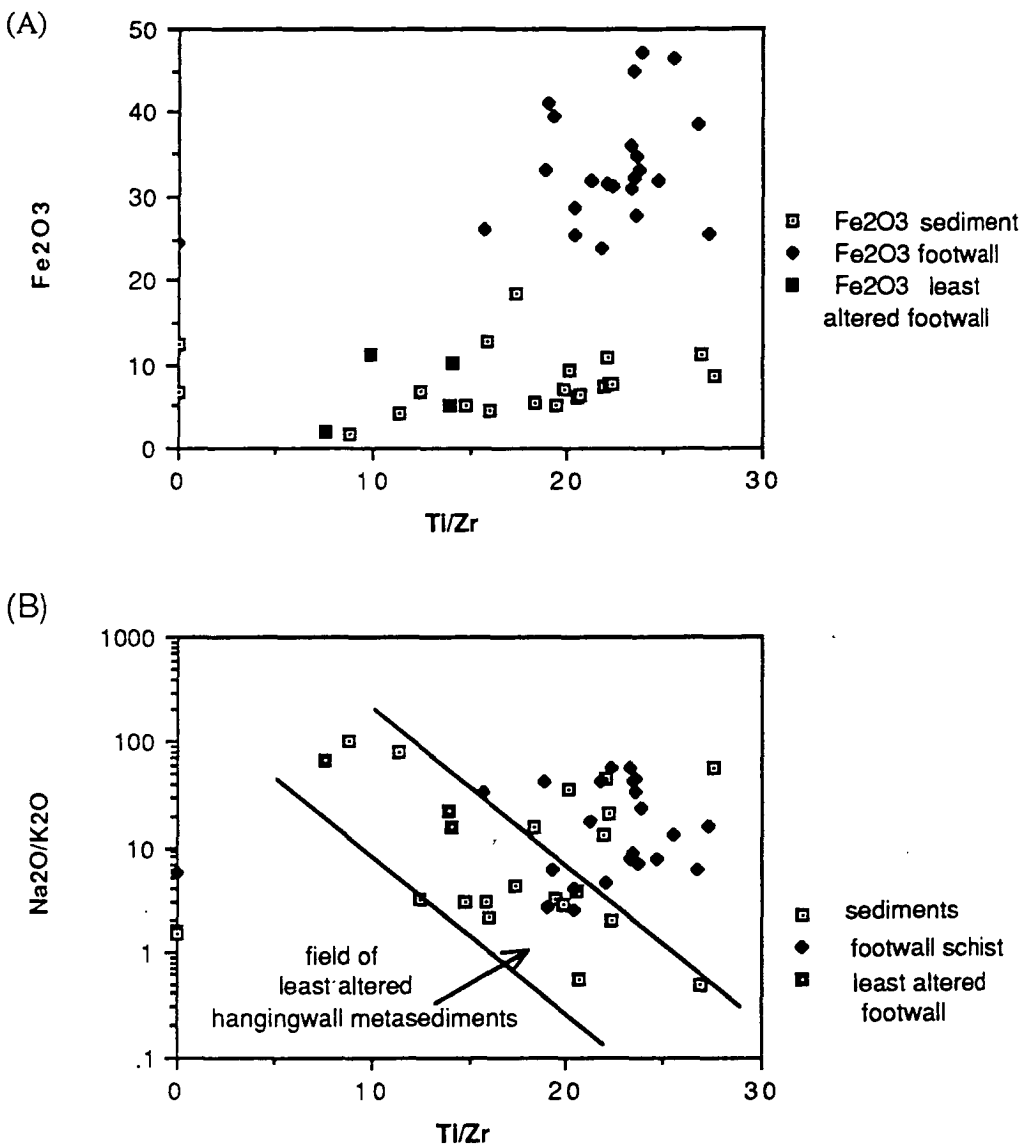

Figure 5.6 A *$Fe_2O_3^{tot}$ versus Ti/Zr for the sample groups in Fig. 5.5. Hangingwall metasediments do not show the characteristic Fe-enrichment of the footwall.* **B.** *Na_2O/K_2O versus Ti/Zr, illustrating the complex effects of alkali alteration. Firstly, fresh sediments show a linear trend towards higher Na at lower Ti/Zr (opposite to Trough Tank sediments) with 'least altered' footwall as an end-member.*

The geochemistry of the hangingwall metasediments, the least altered footwall, and the typical altered footwall were graphically compared (Figs. 5.5, 5.6). Ti/Zr ratios were mainly used as a category axis in the binary plots because both elements are generally immobile through low grade alteration (Floyd & Winchester 1977, Winchester & Floyd 1978).

In terms of SiO_2 (Fig. 5.5 A), the four least-altered felsic samples plot within the known variation of Mount Isa volcanics (data from Bultitude & Wyborn 1982, and Wilson 1983), as well as coinciding with 'normal' sediment trends. Fresh hangingwall sediments are substantially silica-depleted because of their high primary carbonate contents, and do not overlap the least altered felsic field, or 'normal' sediments. In terms of other selected elements, the 'least altered' group forms an end-member to the hangingwall sediment trend, as well as being wholly enclosed by Mount Isa volcanic variation; for instance Nb and Al_2O_3 versus Ti/Zr (Fig. 5.5 B, C). From this there is the implication that felsic least-altered material was one component contributing to the overall sediment composition of the Starra hangingwall.

The sediment composition is otherwise primarily controlled by the overall ratio of pelitic to arenitic layers. Two fresh examples of each layer-type were analysed, with averaged results reported in Table 5.2. The pelitic layers are enriched in Al, Ti, Fe, Mg, K, P, Zn, Ba, Ni, Rb, Sr, Zr, Sc, V, Nb, U and Th over the arenite beds, and depleted in Si, Mn, Ca, and Na. Pelitic layers have Ti/Zr = 24.6 (average), arenites Ti/Zr = 17.2. However, a significant number of points in the whole-rock sediment array stray below the arenite value, to Ti/Zr = ~ 10 or lower, which is the value of the least altered felsic material. This is additional evidence that felsic material contributed to sedimentation in the hangingwall (far more than is evident from the obvious distribution of albite beds), and that this material had a separate source.

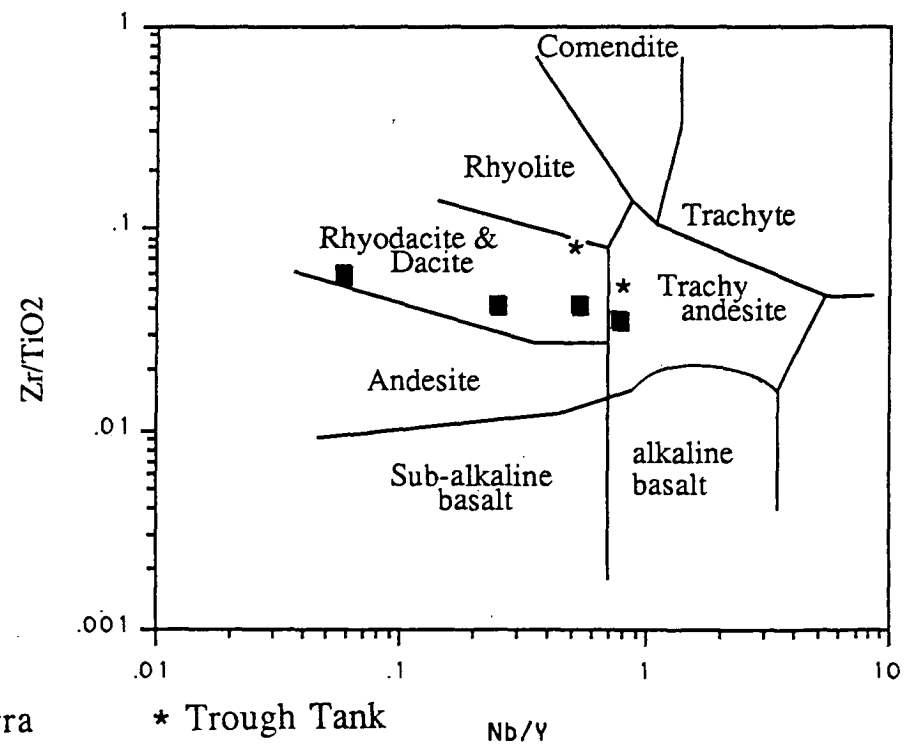

Figure 5.7A *An immobile element plot after Floyd & Winchester (1978), showing the affinities of the felsic compositions from Starra and Trough Tank.*

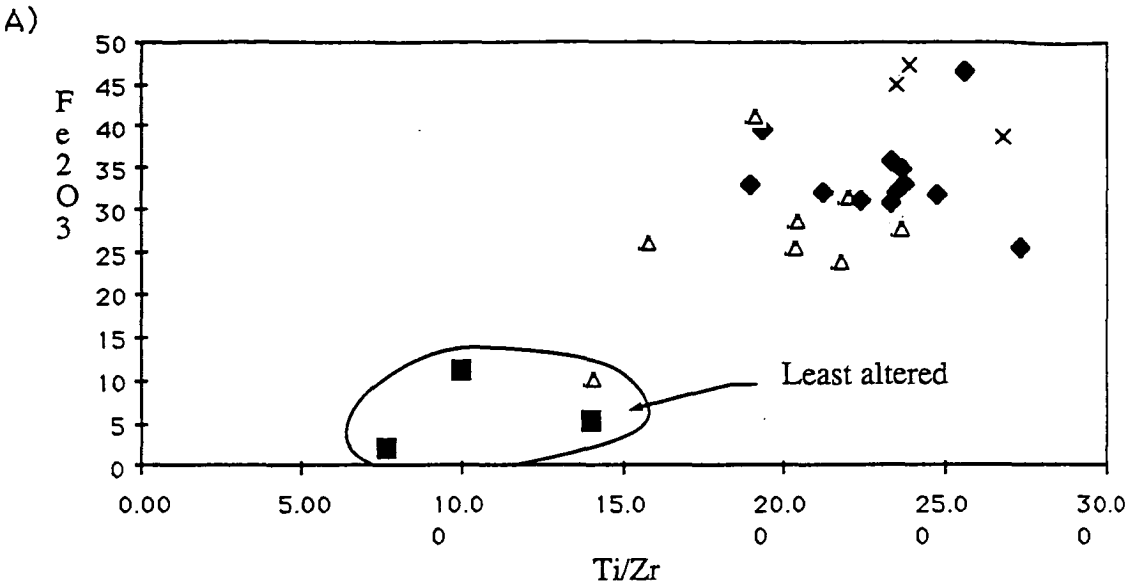

Figure 5.7B *Total Fe2O3 plotted as a function of Ti/Zr ratio, illustrating the mobility of some high field strength elements with increasing alteration (inferred from increasing Fe2O3.* ***Crosses:*** *Area 251 proximal alteration;* ***Filled diamonds:*** *Area 251 footwall schist;* ***Triangles:*** *Area 257 and 244 footwall;* ***Squares:*** *hangingwall volcaniclastics.*

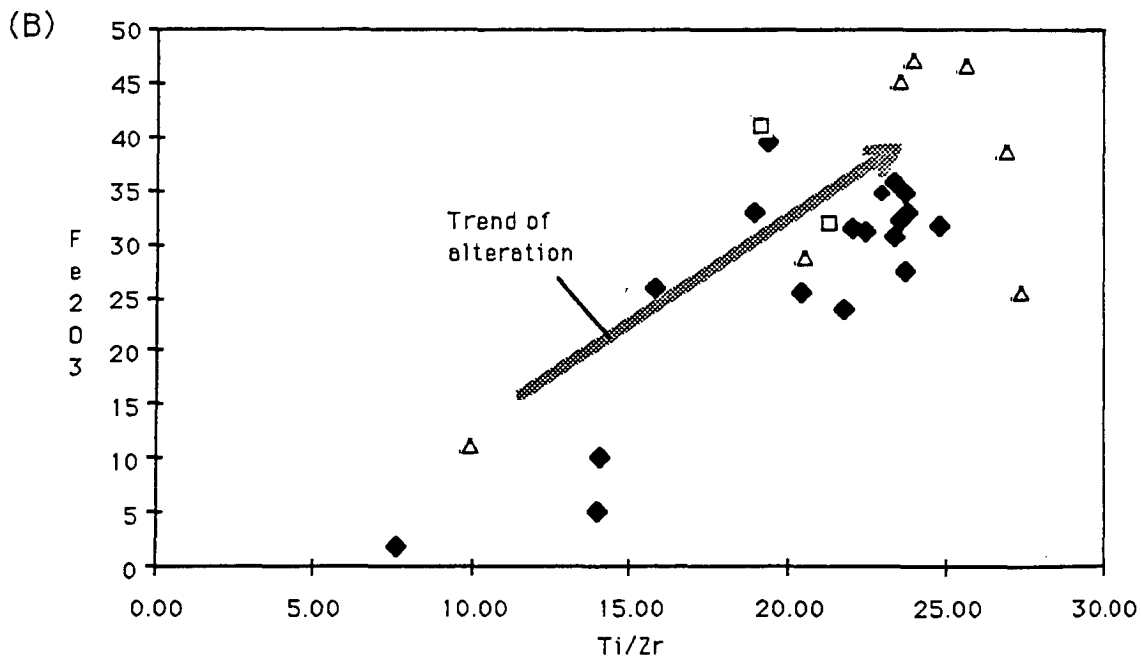

Figure 5.7C *As for Fig.5.7B, but the points are indexed to show gold content of the footwall with respect to total Fe2O3 and Ti/Zr.* ***Triangles*** *: > 0.5 ppm Au,* ***Squares:*** *0.1 - 0.5 ppm Au,* ***Diamonds:*** *< 0.1 ppm Au.*

The question of footwall-hangingwall equivalence can be further examined via consideration of the field of altered felsic footwall rocks. In terms of SiO_2 – Ti/Zr (Fig. 5.5A), there is a large overlap between fresh hangingwall and altered footwall samples. This overlap betrays their genetic non-equivalence. If fresh hangingwall was subjected to the same alteration processes as observed in the footwall, the addition of an average 29.9% $Fe_2O_3^{tot}$ (assuming constant volume) would move the average hangingwall silica value from ~50% to ~20%, or perhaps more reasonably to ~30% if the carbonate component was replaced volumetrically. This hypothetical field of altered hangingwall would not coincide with the present altered footwall. A similar exercise can be conducted for many of the other elements.

Alteration of the hangingwall did not commonly include the addition of iron, except in some metamorphic skarn zones exhibiting strong recrystallisation and veining. This is illustrated in Fig. 5.6A, in which altered sediments have at most 18% $Fe_2O_3^{tot}$, versus a normal altered footwall range of 24 – 48 % $Fe_2O_3^{tot}$.

The above chemical evidence suggests that (a) footwall and hangingwall rocks are not genetically equivalent, and (b) the most likely altered footwall protoliths are alkali-altered albitic layers in the hangingwall and footwall, collectively referred to as 'least altered footwall' samples. Apart from the alkali elements, these samples exhibit chemical similarities to acid volcanics (Table 5.1), and lie within the known field of Mount Isa Inlier acid volcanics (Figs. 5.5 A–C). In terms of immobile elements (Winchester & Floyd 1978) they are identified as dacitic to rhyodacitic in composition (Fig. 5.7A). The entire Starra footwall set cannot be used in such analysis because of probable Zr and P_2O_5 mobility imposed by the Starra-style alteration. This is examined in detail under "Average footwall alteration". Hangingwall sediments with Ti/Zr < 15 are likely to contain a significant acid tuff component.

Affinities of the Felsic Protoliths

Bultitude & Wyborn (1982) examined the known volcanic rocks of the Mount Isa Inlier, and considered that the felsic units should be broken into 5 suites, on the basis of their geochemistry. They demonstrated chemical equivalence of some member units despite major variations in structural style and metamorphism, such as the affinities existing between the rhyolites of the Bottletree and Argylla Formations, and the Mitakoodi Quartzite, supported by the U-Pb dating of Page (1983a). They suggested that units with similar volcanic geochemistry might correspond to successive melting of the same portion of lower crust; the units could therefore be regarded as broad levels of time-equivalence.

The suites recognised by Bultitude & Wyborn (1982) are:

(1) **Leichhardt Suite**: defined by low Zr, Y, Nb, Ti, Th, U and high Al, Pb, Sr, Na and Ca. The main member is the Plum Mountain Gneiss. Age bracket is 1852 ± 7 to $1875 \pm {}^{24}_{19}$ Ma (Page 1983a).

(2) **Argylla Suite**: high Zr, Nb, Y, Ti, K, Th, U; low Na, Al, Pb, Sr. Members include the Mitakoodi Quartzite and the Double Crossing Metamorphics. Cogenetic with the Kalkadoon Batholith. Age — $1766\pm^{23}_{19}$ to 1783 ± 5 Ma (Page 1983a).

(3) **Duchess - Corella Suite**: high Nb and Y but lower Ti, Zr and Fe compared to the Argylla Formation. It has a cogenetic relationship with the Wonga Batholith. Ages vary between 1603 ± 6 and 1720 ± 7 Ma (Page 1983a).

(4) **Bottletree Suite**: Geochemically similar to the Argylla Suite, apart from Ca, Sr and Pb differences. Age: 1790 ± 10 to $1808 \pm ^{22}_{17}$ Ma.

(5) **Carters Bore Suite**: Very high K, Nb, Zr, Y; low Ba, Pb, Sr, Na. Age: 1678 ± 1 Ma (Page 1983a).

Bultitude & Wyborn (1982) found they could not assign the rhyolites within the Soldiers Cap Group and the Doherty Formation to any of these suites, because inadequate sampling did not sufficiently describe each unit's probable chemical variation.

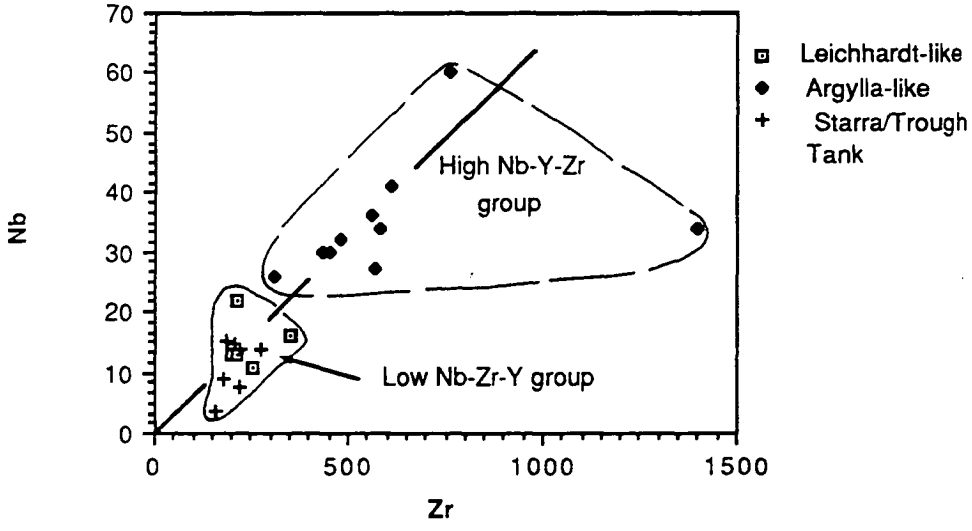

Figure 5.8 *A compilation of the averages of Mount Isa Inlier acid volcanic units, from Bultitude & Wyborn (1982). On the basis of Nb, Y and Zr, the units fall into a depleted (Leichhardt-like) and an enriched group (Argylla-like). The line joining the two groups is likely to be a partial melting trend. Starra and Trough Tank felsic volcanic samples plot together, distinctively with the depleted group.*

More generally, the above suites can be grouped on the basis of their incompatable high field strength (HFS) elements — generally accepted as good indicators of petrogenetic affinity. Only the Leichhardt Suite contains low levels of Nb, Zr and Y, whereas the other 4 suites are comparitively enriched in these (Fig. 5.8). The Plum Mountain Gneiss, Soldiers Cap Group, and samples within the Doherty Formation are all included in the depleted group on the basis of data from Bultitude & Wyborn (1982). All are older than the enriched suites,

except for the Doherty Formation, aged at 1720 ±7 Ma (Page 1983a). In very broad terms therefore, the oldest recognised volcanic cycle (>1840 Ma) mainly produced rocks depleted in HFS elements, whereas the subsequent cycle (1800 - 1750 Ma) produced enriched suites such as the Argylla, interpreted by Wyborn & Page (1983) as the product of melting of an already-depleted lower crust. (This is supported by the basically linear trend between the two groups, Fig. 5.8). Later volcanics associated with the 'sag' phase of Cover Sequence 2, and the 'rift' phase of Cover Sequence 3 (Wyborn et al. 1988; see Chapter 2) contain both depleted (such as some parts of the Doherty Formation) and enriched members (e.g. Carters Bore Rhyolite).

The least altered Trough Tank and Starra felsic volcanic products are also plotted in Fig. 5.8. They all have low HFS element levels, although Ti varies between 0.28 and 0.64 wt. % (Appendix 3). These results (a) support the notion of time-equivalence between Starra and Trough Tank (b) support a cogenetic link between least altered albitic samples above and below ironstone at Starra, and (c) suggests a link with either the Leichhardt Volcanic cycle, or with the younger cycle which includes the Doherty Formation. The latter alternative is favoured on the basis of the established stratigraphic framework.

The recognition of the relatively unusual HFS element depletion of the felsic host rocks constitutes a useful exploration guide for Starra-style ores, at least in establishing the broad stratigraphic ore level, and conceptually as a possible precondition for ore formation.

Are the Starra Felsic Compositions Cogenetic with the Gin Creek Granite?

The four least altered footwall samples exhibiting no demonstrable mobility of the high field strength elements, were compared to the chemistry of the Gin Creek Granite and other nearby members of the Williams Batholith. The levels and ratios of these elements can determine if a particular volcanic rock is relatable to a particular intrusive, as both should show similar fractionation trends derived from a common parent magma, or be related by partial melting to a common source. The assumptions of the method are (1) compositions of both represent liquids, and (2) that the trace elements selected for analysis co-vary consistently, i.e.no 'special' mechanism operates to alter their relative values, such as zircon inheritance.

Nb, Zr and Y were selected on the basis that they normally show consistent enrichment with increasing fractional crystallisation or smaller degrees of partial melting (Cox et al. 1979). Related liquids should lie along lines that basically increase away from the origin in binary plots. The HFS elements are also least affected by post-depositional alteration (Floyd & Winchester 1977).

An example of a cogenetic relationship is plotted in Fig. 5.9. This is the comagmatic Leichhardt Metamorphics and Kalkadoon Batholith (Wyborn & Page 1983). The example illustrates that cogenetic felsic intrusives and extrusives do lie along the same fractionation/partial melting Nb-Zr trend. In this unusual example Zr decreases linearly with SiO_2, whilst Nb shows only subtle change. Wyborn & Page (1983) attribute the decreasing

incompatable element levels with increasing fractional crystallisation, to strong incompatable element enrichment in the Kalkadoon Batholith source region.

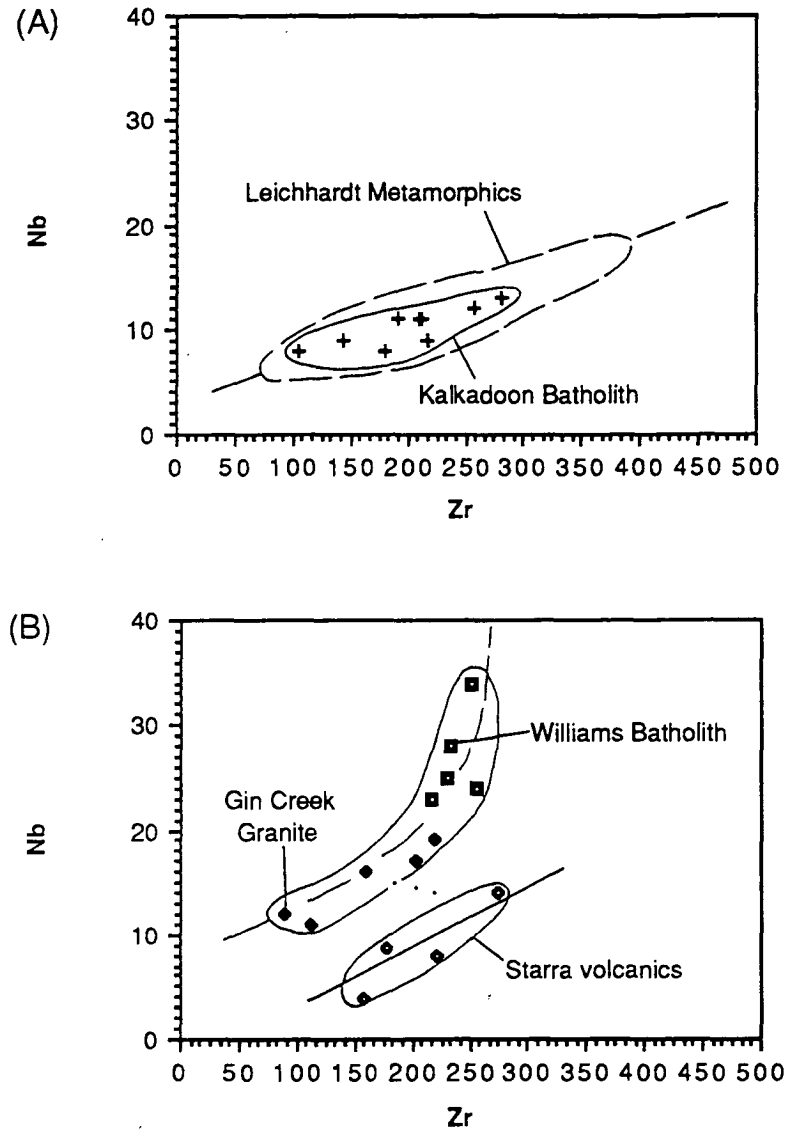

Figure 5.9 A *In terms of Nb and Zr, the Kalkadoon Batholith and the felsic volcanic members of the Leichhardt Metamorphics lie along the same linear fractionation trend (shown as a dashed line). The data was compiled from Wyborn & Page (1983), and Wilson (1983). B. The Starra felsic volcanics do not show a cogenetic relationship with the Gin Creek Granite, or any of the members of the Williams Batholith. (Gin Creek granite data are individual sample points from L.A.I. Wyborn (pers. comm.), while the other Williams Batholith points are average values for pluton members, compiled from Wyborn et al.(1988)). Trough Tank volcanic members are shown as dots.*

In similarly plotting Nb versus Zr for the Starra acid igneous rocks, the Starra extrusive compositions plot on a linear trend markedly displaced from the field of Williams Batholith plutons. In particular the sampled phases of the Gin Creek Granite cannot be related to the Starra felsic volcanics by fractional crystallisation or partial melting. From the existing data it is possible that the younger biotite-rich Gin Creek Granite phase is cogenetic with the older, foliated, muscovite granite phase. (However, the collection and interpretation

of the additional data needed to substantiate this possibility is beyond the scope of this thesis).

The non-cogenetic relationship implies that the intrusive source of the Starra felsic volcanics is no longer present in the immediate 2 km of footwall beneath the Starra ironstones (or has not yet been sampled). This is not unexpected given that the Gin Creek Granite and the proposed felsic volcanics are separated by the Starra Shear (Switzer 1987, Laing et al. 1988), a zone of potentially great movement: the intrusive source is most likely displaced or eroded. While the Gin Creek Granite could not have been a contending source for the volcanics, or for syngenetically deposited Fe, Au or Cu, it remains a potential metals source in any epigenetic theory of ore formation.

ALTERATION GEOCHEMISTRY

Rationale

In many previous studies of alteration in different environments, quantitative analyses of chemical change have relied on the assumptions of either constant mass or constant volume (e.g. Gibson et al. 1983, Roberts & Reardon 1978, Riverin & Hodgson 1980). However, it is now recognised that such assumptions are often too simple to realistically model alteration processes such as hydration, in which (for instance) changes of mass are demanded. Consequently recent approaches rely on the assumption of constant immobile element levels (Ti, Zr, P, Nb, Y, REE, Ta, Th, and to a lesser extent Al) after pioneering work on these elements by Floyd & Winchester (1977), Winchester & Floyd (1978) and others. Using such an approach Grant (1986) modified the equations of Gresens (1967) to describe element gains and losses during metasomatism, producing a simple graphical means of assessing which elements do not move during alteration, and the amount of variation of those which do move (resulting in the so-called "Isocon" diagram). The technique permits the quantification of mass/volume changes and hence the gains or losses of individual elements.

This approach has been employed in analysing the Trough Tank and Starra alteration zones. It involves the initial construction of isocon diagrams, and assessing which of the assumptions of constant mass, volume or immobile element concentration is appropriate. The basic relationship employed is

$$C^{A}_{i} = M^{\circ}/M^{A} \, (C^{\circ}_{i} + \Delta C_{i}) \qquad (5.1)$$

where C°_{i} is the original concentration of an element 'i', C^{A}_{i} is i's altered concentration, ΔC_{i} is the difference between them , and M°/M^{A} is the ratio of the original rock mass to its final altered mass. If M° is assumed to be 100 g, C is conveniently expressed in weight percent.

M°/M^{A} is calculated graphically for the immobile components (for which $\Delta C_{i} = 0$), by plotting C^{A}_{i} against C°_{i} — the slope of the isocon (a line connecting points of equal geochemical concentration (Grant 1986)) is M°/M^{A}. i.e.

$$C^A = (M^\circ/M^A)C^\circ \quad (5.2)$$

or if constant volume is assumed,

$$C^A = (g^\circ/g^A)C^\circ \quad (5.3)$$

where g = density of the rock.

For ease of interpretation the modification employed by Huston (1989) was used in the isocon diagram construction. In this approach the concentrations are scaled by normalising to an arbitrary sequence of integers, and plotted against these integers. Each integer is assigned to an element e.g. Cu = 1, Ni = 2, Co = 3 etc. This overcomes the unwieldy aspect of Grant (1986)s diagram, in which he specifically scaled each element differently to fit within the diagram (such as multiplying TiO_2 by 10). In both diagrams, if the 'immobile' elements form a linear array commencing at the point of origin, distinct from that expected for constant volume or mass, then rock density varied during alteration. If an element plots above the error limits of the isocon, it has been added, and if below, it has been physically removed during alteration (e.g. Fig. 5.11). The error limits were established empirically using the variation of immobile elements away from the isocon.

The actual gain or loss of an element 'i' has been plotted in barchart form for ease of interpretation (Fig. 5.12), and is expressed as a percentage in the relationship

$$\Delta C^A_i(\%) = 100\{[C^A_i/(mC^\circ_i)] - 1\} \quad (5.4)$$

where $m = M^\circ/M^A$.

Trough Tank

The host rocks were separated into four groups based on alteration assemblages, which are encountered progressively away (both with depth and laterally) from a central silicified zone usually found beneath auriferous BIF . The maximum extent of each zone is given in Table 5.3, but is most likely dependent on the size of the original hydrothermal system — for instance, the Starra systems are far more extensive and pervasively developed than those located at Trough Tank to date. Alteration mineralogy has been discussed in more detail in Chapter 3.

A problem encountered in the chemical characterisation of alteration at Trough Tank is the diverse spectrum of initial chemistries forming the mostly sedimentary host-rocks, as outlined previously. In the pyrite and magnetite zones respectively, this has been overcome by only using samples with similar Ti/Zr levels, to insure that the original chemistries were comparable. This unfortunately has meant that only one typical sample of magnetite zone material, and only two averaged pyrite zone samples were compared. The analysis of the central silicic zone is only semi-quantitative because of excellent evidence for "immobile"

element mobility here. In this zone Zr particularly is strongly leached. An isocon with a large error in this zone is formed by the alignment of Y, Al, Nb and Ti. Hence, while a volume

Mineralogy	Description	Maximum observed width	Volume change (relative to unaltered host rock)
Central core or pipe zone: Quartz-mag.±cpy,py, dol.	Coarse-grained aggregates (0.5-3cm) of mag., py., cpy, & carb., all in a clear qtz matrix. Occasional breccia frags. of chloritised albite rk.	20 - 110 m. Pipes have a funnel-like geometry, very wide at the top.	66 %
Magnetite-cpy-py -biotite	Sulphides & oxides form 1-5cm long strings and blebs, and veins up to 2cm wide. Sulphides/oxides comprise 10-40% of the rock. Matrix is albite.	12 - 90 m.	35 %
Pyrite-carbonate	Pyrite and carbonate are disseminated in small clusters throughout the albitic host, varying from 1-5%. This facies may include pockets of anth.-cordierite rock.	10 - 32 m, inferred to be greater, of the order of 50 - 200 m.	23 %
Albite ± phlogopite	Sulphides and oxides are absent, although sporadic carb. blebs occur. The regional extent of this facies suggests it may be diagenetic rather than hydrothermal in origin.	—	—

Table 5.3 *Trough Tank alteration types.*

increase of ~66 % is identified, it may not be accurate because the chemistry of the unaltered protolith is in this case poorly constrained. The alteration in this area is so severe, and so inhomogeneous, that the variations within the protolith are a secondary consideration.

Prior to performing the isocon analysis, the so-called "immobile" elements were examined as a function of SiO_2 (Fig. 5.10). This diagram illustrates that the unaltered rock Ti/Zr range is 0.6 - 2.9, and that all pyrite zone alteration lies within this, clustering between 0.08-1.30. Magnetite zone alteration is also mainly confined to this range. Ti and Zr was very likely immobile within these alteration zones. Conversely the severely altered silica zone has a Ti/Zr variation between 0.41 and 119.9, indicating substantial HFS element mobility.

(%)	Least altered footwall n=13	S.D.	Pyrite Alteration n=10	S.D.	Magnetite alteration n=6	S.D.	Silica Zone n=12	S.D.
SiO_2	72.47	7.04	68.5	7.52	58.5	16.6	51.69	15.16
TiO_2	0.44	0.09	0.33	0.13	0.23	0.11	0.029	0.029
Al_2O_3	12.74	3.2	9.82	3.4	9.17	1.9	1.3	1.37
$Fe_2O_3^{tot}$	3.3	1.3	6.2	3.8	21.7	16.4	36.33	5.42
MnO	0.03	0.018	0.11	0.18	0.06	0.03	0.08	0.05
MgO	1.35	1.14	1.29	1.55	1.68	2.69	1.04	1.25
CaO	1.17	0.75	3.4	2.4	1.1	1.27	0.86	1.15
Na_2O	5.91	1.27	4.87	2.1	4.29	0.95	0.62	1.17
K_2O	0.64	0.69	0.21	0.32	0.12	0.14	0.15	0.17
P_2O_5	0.13	0.04	0.09	0.03	0.07	0.05	0.34	0.26
LOI	1.25	0.84	4.42	4.25	2.41	2.92	4.04	3.89
Total	99.43		99.24		99.33		96.479	
(ppm)								
Ni	27	20	27	30	54	29	64	65
Co	66	85	289	169	456	219	1010	1121
Sc	11	15	-	-	-	-	13	16
Cu	26	39	140	331	346	282	1.54%	1.29%
Pb	7	4	10	5	12	4	18	17
Zn	8	4	6	3	12	6	35	40
Au	0.008	0.005	0.009	0.010	0.057	0.069	0.690	0.81
Rb	35	47	10	19	10	8	19	19
Ba	88	139	17	11	23	114	25	24
Sr	21	10	20	6	12	3	4	4
Nb	12.9	2.1	13.3	4.0	22.1	16.8	2.3	2.4
Zr	201	26	163	49	133	49	13	20
Y	26.3	11.6	23.1	15.5	18	15.9	7.7	11.6

Table 5.4 *Trough Tank averaged alteration types, and their standard deviations. (S.D. = standard deviation.)*

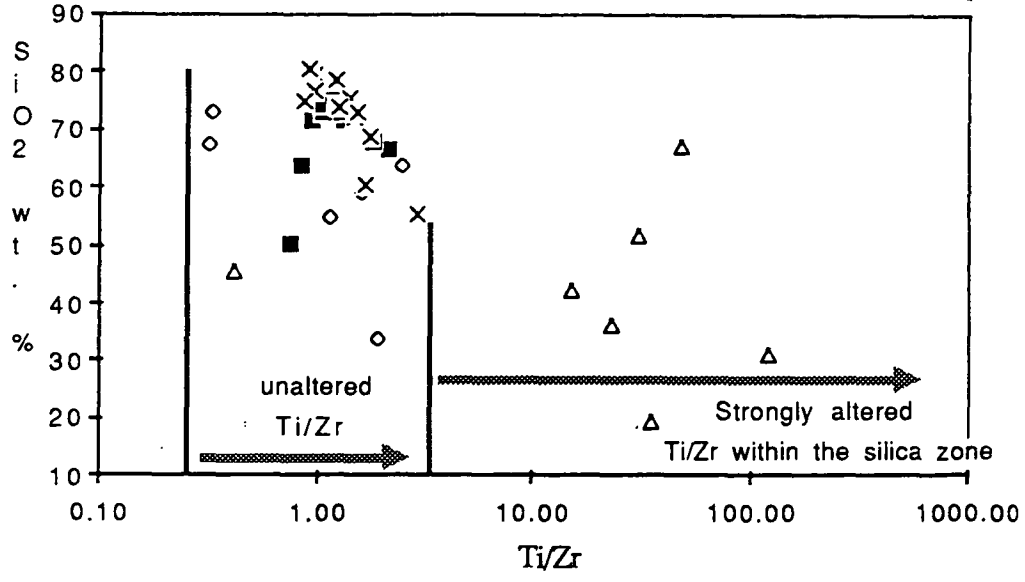

Figure 5.10 *A comparison of log Ti/Zr ratios in the groups of altered rocks at Trough Tank, illustrating that the silica 'pipe' zone is the only area of significant change in this ratio,*

*due to the almost complete removal of Zr. **Crosses: least altered rocks, Filled squares: pyrite zone, Diamonds: magnetite zone, Triangles: silica zone.***

The least altered protolith composition used is provided in Table 5.1, being a probable metavolcanic exhibiting only mild alkali element loss, low levels of the ore elements (Cu = 18 ppm, Au = 0.005 ppm), and a Ti/Zr ratio of 1.38.

Pyrite Zone

Isocon analysis (Figs. 5.11 & 5.12) indicates that the pyrite zone experienced a 23 % increase in mass or volume compared to the least altered protolith. Of the "immobile" elements, only Nb showed a real increase, and therefore was not used for the isocon fit. The other elements showing significant increases in real concentration were Cu, Ni, Co, Mn, Ca, Fe, and Au. Significant depletions occurred in Mg, K, P, Rb and Ba, while Si and Al remained immobile. A major alteration influence was the hydrothermal growth of carbonate, illustrated by the change in average CaO in the protolith from 1.17 % to 3.44 % in the pyrite zone (ranging as high as 8.39 %).

Magnetite Zone

Mass or volume increased by 35 % in the magnetite zone compared to the least altered protolith (Figs. 5.11 & 5.12), recorded by considerable dilution of the immobile elements Ti, Y, and Zr (Nb shows a significant increase). Cu, Ni, Co, Au, Mg, Mn, Zn, Ca, and Fe all show substantial gains. Real losses are sustained by Na, K, Rb and Ba, while Si, Al and P altered only slightly, but within the indicated errors. A probable shift in alteration mineralogy from calcite to dolomite, or to calcite + chlorite, is recorded by a change from MgO/CaO = 0.38 in the pyrite zone to MgO/CaO = 1.5 in the magnetite zone. The major factors contributing to density changes are increasing magnetite and pyrite.

Silica 'pipe' Zones

An increase in volume of 66% from the protolith is indicated by the fit of Y, Ti , Al, and Nb to the isocon — regarded as imprecise because of reasons outlined above (Figs. 5.11 & 5.12). The semi-quantitative changes in this area are large increases in Cu, Ni, Co, Mg, Mn, Ca, Fe, Au and P. Decreases occur in Ti, Na, Zr, and Ba. A small amount of Si has also been added, but in view of the texture of the alteration, it is probable that hydrothermal quartz replaced former siliceous phases. Averages for ore-anomalous elements (analysed within the silica zone, but regrettably not elsewhere; n = 10) are Sn (9.8 ppm), Mo (75.4 ppm), As (31.1 ppm), and Bi (22.4 ppm), W and Sb were generally undetectable.

Correlation Coefficient Analysis

Linear relationships between elements were examined via the construction of correlation matrices, using the "Correlation Coefficient" application of 'Statview', a Macintosh statistical package. Prior to using this statistical technique, the frequency

distribution of each element was examined graphically. Most Major elements follow Normal distributions, whereas MgO, CaO K_2O, Zr, Y, Nb, Ba, Sr, Cu, Au and Bi are negatively skewed, approximating a log-Normal distribution. The populations of the latter elements were log-transformed prior to their use in the Correlation Coefficient

Alteration Zone	Positive Correlations	Negative Correlations
Pyrite-carbonate n=10	Al - P, Na, Nb, Y, Ti LOI - Mg, Ca, Mn, Sr Cu -Ni, Zn, Mn, Pb, Zn	Si -Mn, K, LOI, Ni, Cu Na - Fe, Ni, Rb Co -Y,P
Magnetite-pyrite -chalcopyrite, n = 6	Ca - Mg, LOI, Co Fe -Zn Cu -Ti Nb - Y Au -K, Al (weak) Rb - P	Na - Mg, Ca, Co, Fe Si - Fe, Zn Cu -Y, Nb
Silica - apatite ± chalcopyrite, pyrite n =12	Au - Na, Fe, Co, Zn, Mo, Sn, As Si - Al, Mn, K, Sc, Nb, Y, Ti, P, Ba, Ca. P - Zr, Ca, Y, Nb, Si.	Au, Cu, Co - Mn, Sr, Y, Ti, K P, Zr, Ca, Si. Fe - Si, Al, Mn, K, Ba, Sr, Nb Y, Ca. P, Ca, Zr - Fe, Ni, Co, Sn, Cu Mo, As, Zn.

Table 5.5 *Summarised relationships from the correlation coefficient matrices in Appendix 4 for the different Trough Tank alteration zones, mainly using those correlations with a 99% significance or greater.*

Matrix. The coefficient quantifies the degree of dependence of one element upon another, via the least squares method, after estimating a regression line for the data. The reliability of the coefficient in identifying real dependence is a function of the number of samples in a given sample-set. Statistical significance at the 99 and 95% levels were estimated using tables from Freund (1976), based on the Students T-test. The correlation coefficient matrices are available in Appendix 4, but the relationships are summarised in Table 5.5.

Pyrite Zone

Positive correlations in this zone separate into two distinct groups, identified as relationships inherited from the host rocks, and those attributed to alteration. The host rock signature is essentially that identified from primary rock analysis previously, an incompatable element association possibly linked to alkaline rocks; Al-Nb-Y-Na-P-Ti. The second association is a function of trace element substitution into sulphides (Pb, Zn, Ni, Cu). Negative correlations are evidence for both dilution due to increasing ore minerals, and possible leaching of components during hydrothermal reactions.

Gold displays only a very weak positive relationship with Co in this zone.

Magnetite Zone

Due to an increase in hydrothermal leaching, the host-rock signature observed in the pyrite zone is absent here, apart from the maintenance of a Nb-Y correlation. Carbonate components Ca, Mg and LOI (also a function of lost H_2O and S) all show a negative relationship with Na, suggesting that carbonate addition in this zone proceeded via albite replacement. The ore elements display interesting trends: Co is well correlated with Ca and Mg, but not with Fe or Cu as would be expected if Co was substituting into pyrite or chalcopyrite. Cu is positively correlated with Ti and negatively with Y, an unexplained relationship given the demonstrated immobility of the latter elements.

Au correlates weakly with K, Rb, Ti, Al, and Cu, but shows no relationship to Co, Fe or the carbonate alteration components.

Silica Zone

Within this zone chalcophile elements, all co-vary with Mo and Sn, suggesting that inclusions of molybdenite and cassiterite are deposited with the sulphides in the 'pipe' zone. Au is positively related to Fe, Na, Co, Zn, Mo, Sn and weakly to As; negatively to the elements associated with quartz and host-rock relics, such as Si, P, Ti, Mn, K, Ca, Zr, Sr and Y. Magnetite-rich portions of the silica zones have concentrated gold and sulphides, rather than the siliceous sections. Apatite components P, Zr, Ca and Sr co-vary positively, but are inversely correlated to the chalcophile group and poorly related to Au. Sulphide zones are therefore likely to be apatite-poor.

Starra

The Starra footwall lithologies were divided into three groups for the purposes of alteration analysis — least altered, average altered, and intensely altered or 'pipe'-like zones. The data for this analysis comprised 12 complete analyses from the 257 ore zone, carried out at the University of Tasmania, and 15 analyses from the 251 ore zone, analysed by Comlabs Pty.Ltd. for Cyprus Minerals. All gold analyses were prepared by geochemical contractors.

Starra 'least altered' samples (n=2) are from feldspathic beds hosted by calcareous hangingwall metasediments, using the arbitrary criteria of $Fe_2O_3^{tot} < 5\%$ (Table 5.1). They are distinctly sodically altered, depleted in K, Ba, Rb, and enriched in Ca compared to fresh rhyolites or near-equivalents such as the Doherty Formation rhyolites (Table 5.1), and hence represent a good 'background' to the immediate ore footwall, but not to fresh rock.

Starra "average altered footwall" comprises 22 samples with a spectrum of iron contents ($Fe_2O_3^{tot}$: 10.15 - 46.5 %, av. = 29.88%; Table 5.6). It is not possible to accurately differentiate between magnetite-pyrite and pyrite-only alteration groups, as at Trough Tank. In general, $Fe_2O_3^{tot}$ increases towards the ironstone (Fig. 5.18), but discrete zones of strong iron enrichment also exist immediately beneath the ironstone, such as those identified at Area 251 and the 244 'B'-zone. These have been treated separately in the alteration analysis, as the 'pipe'-like cross-cutting zones. Unlike analogous zones at Trough

Tank, they contain very little hydrothermal quartz, and are instead dominated by magnetite, hematite and chalcopyrite.

Extent and Distribution of Alteration

The absolute limits to alteration have not been established beneath the Starra ore zones. Although alteration decreases markedly downhole, occasional pyrite blebs are still present, and disseminated magnetite comprises ~ 5-10% by volume even at the chloritic Answer Slate transition, where most drill-holes terminate.

	Least Altered	S.D.	Average Footwall	S.D.	'Pipe' alteration	S.D.
wt. %						
SiO_2	73.06	0.09	50.55	7.18	40.63	4.26
Al_2O_3	10.61	1.02	10.8	1.23	8.43	0.75
TiO_2	0.46	0.26	0.44	0.07	0.38	0.03
$Fe_2O_3^{tot}$	3.64	2.26	29.88	8.3	43.57	4.4
MgO	1.31	0.34	1.14	0.01	0.61	0.14
MnO	0.03	0.02	0.01	1.7	0.01	0.002
Na_2O	5.28	0.28	4.75	0.7	3.7	0.64
K_2O	0.16	0.11	0.58	0.2	0.38	0.2
CaO	2.49	1.97	0.25	0.04	0.17	0.04
P_2O_5	0.16	0.01	0.14	0.9	0.13	0.03
LOI	2.57	1.42	1.29	0.28	1.12	0.05
ppm						
Au	0.005	-	0.16	0.9	2.35	2.4
Cu	5	6	1200	2481	7683	835
Pb	0	-	0.2	3.1	0	-
Zn	0	-	3	36	5	0
Ba	16	14	48	14	31	17
Ni	9	6	22	41	14	3
Rb	3	4	31	5	12	7
Sr	29	9	6	34	3	-
Zr	248	38	121	16	93	3
Y	20.5	7.8	17.2	7.9	11.7	2.1
Sn	0	-	9	62	33	7.6
W	0	-	44	4	267	74
Sc	6	4	3	29	-	-
V	38	22	18	5	-	-
Nb	10.9	4.4	3.4	1.7	-	-
	n=2		n=22		n=3	

Table 5.6 *Average values and standard deviations for the probable footwall protolith, the average footwall and the Fe-oxide-rich 'pipe'-like alteration in the Starra footwall rocks.*

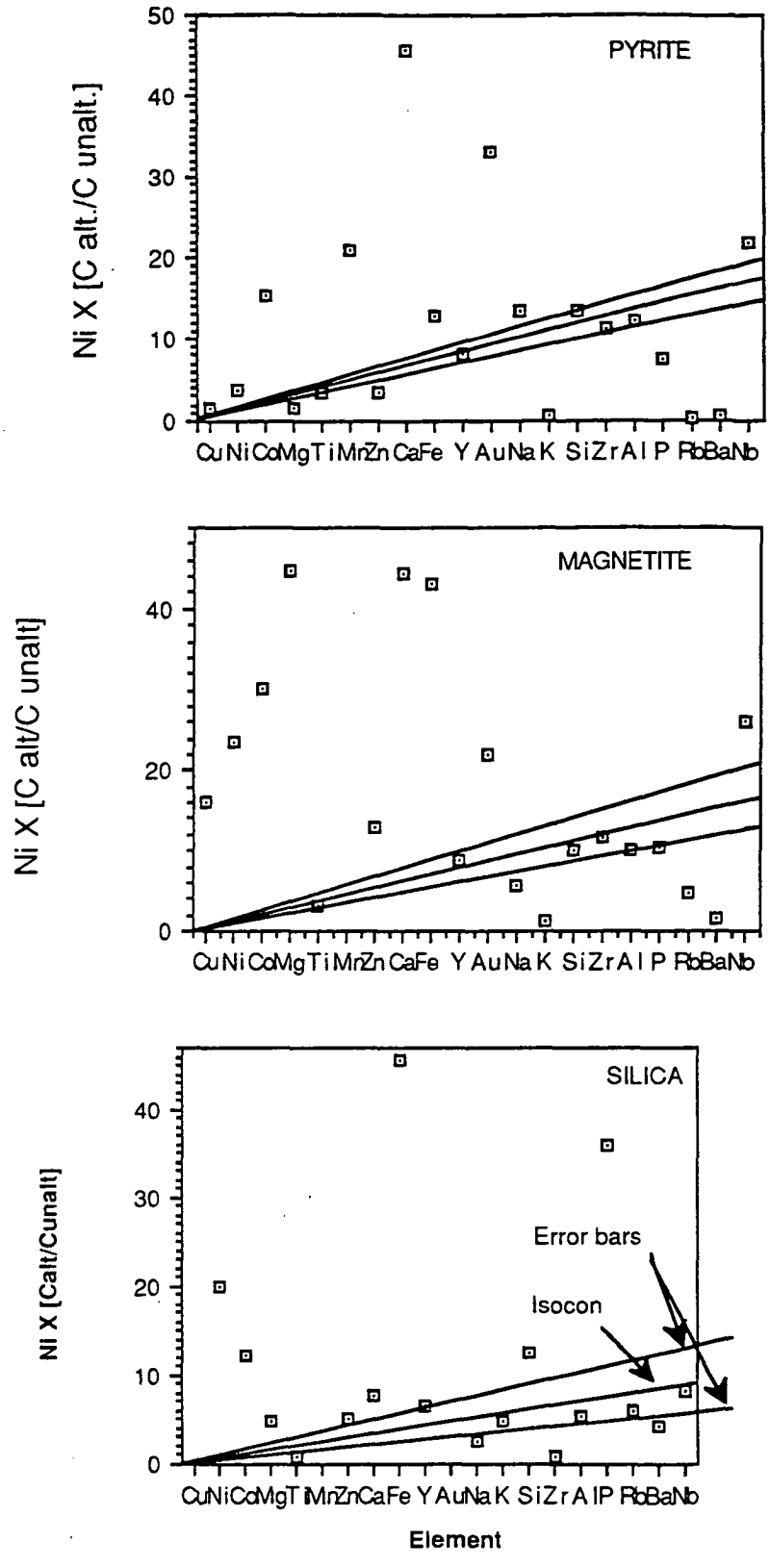

Figure 5.11 *Isocon analysis of the three main alteration types at Trough Tank. The gradient of the isocon indicates the change in mass/volume, and in these cases was fitted to the immobile elements Ti, Al, Zr and Y. Nb and P show clear mobility compared to the other high field strength elements. Elements within the indicated error bars are close to isochemical, while those above and below show real change compared to the least altered protolith.*

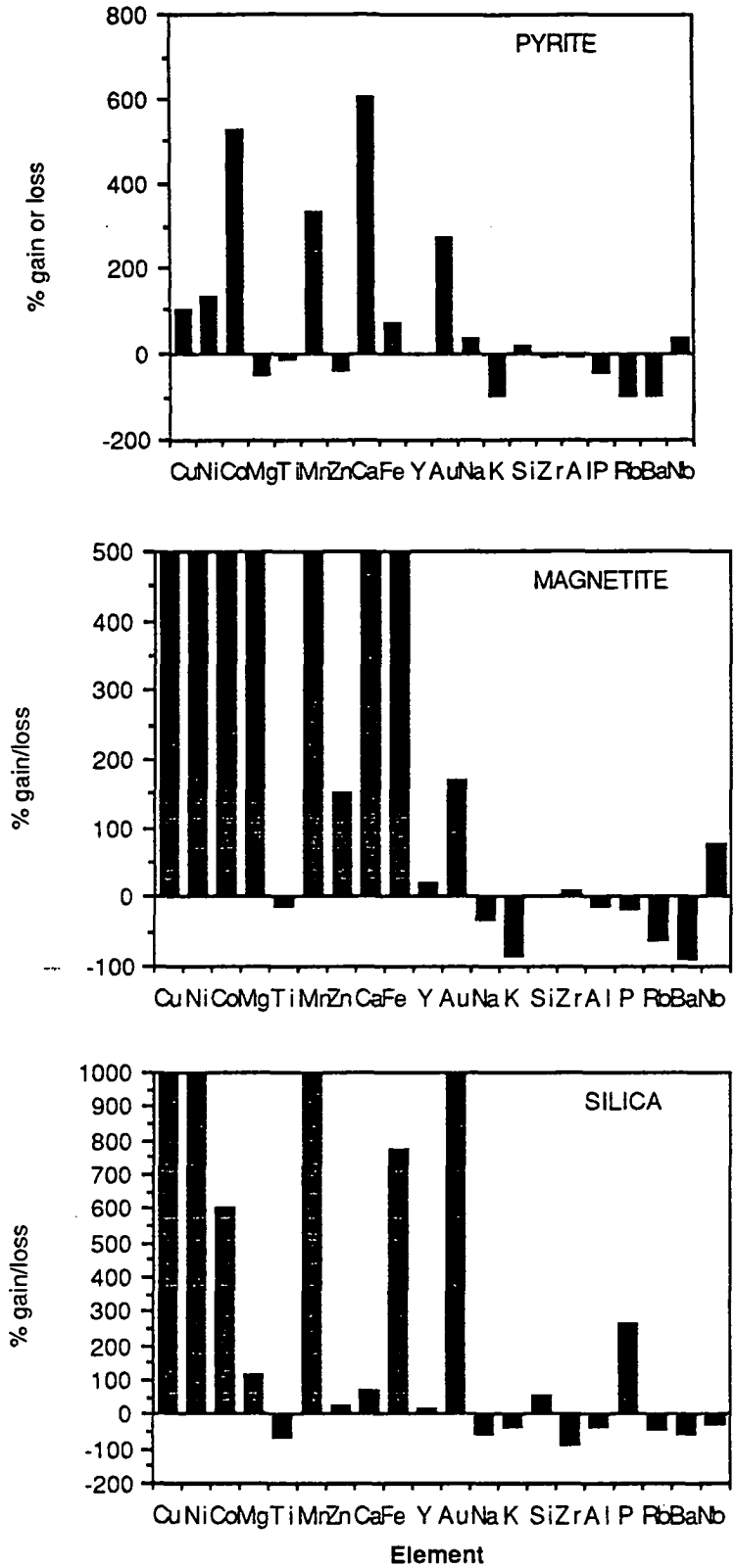

Figure 5.12 *Percentage gains and losses in the three different Trough Tank alteration zones. In the magnetite and silica diagrams the gains in Cu, Au, Co etc. are too great to express here.*

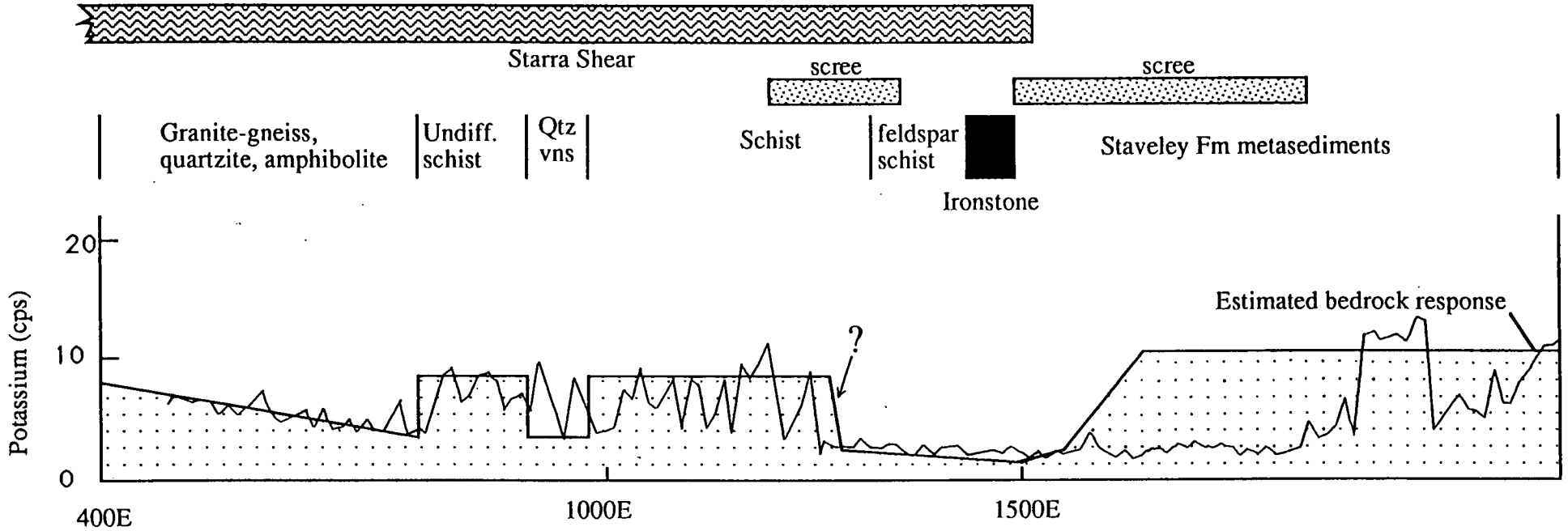

Figure 5.13 *A ground radiometrics transect measured at 10m intervals on line 11275 N , Area 257. The Potassium channel in counts per second is shown here, compared to the estimated bedrock response, with the surface geology for reference. The limited area of outcrop in the immediate footwall displayed extremely low counts, but the point of return to higher counts was obscured by ironstone-bearing scree, and is therefore uncertain. The entire hangingwall response is also obscured for some 350 m east of the ironstone by scree. Where reliably measured, the Staveley Fm is on average 5 cps higher than elements within the Starra Shear foowall sequence.*

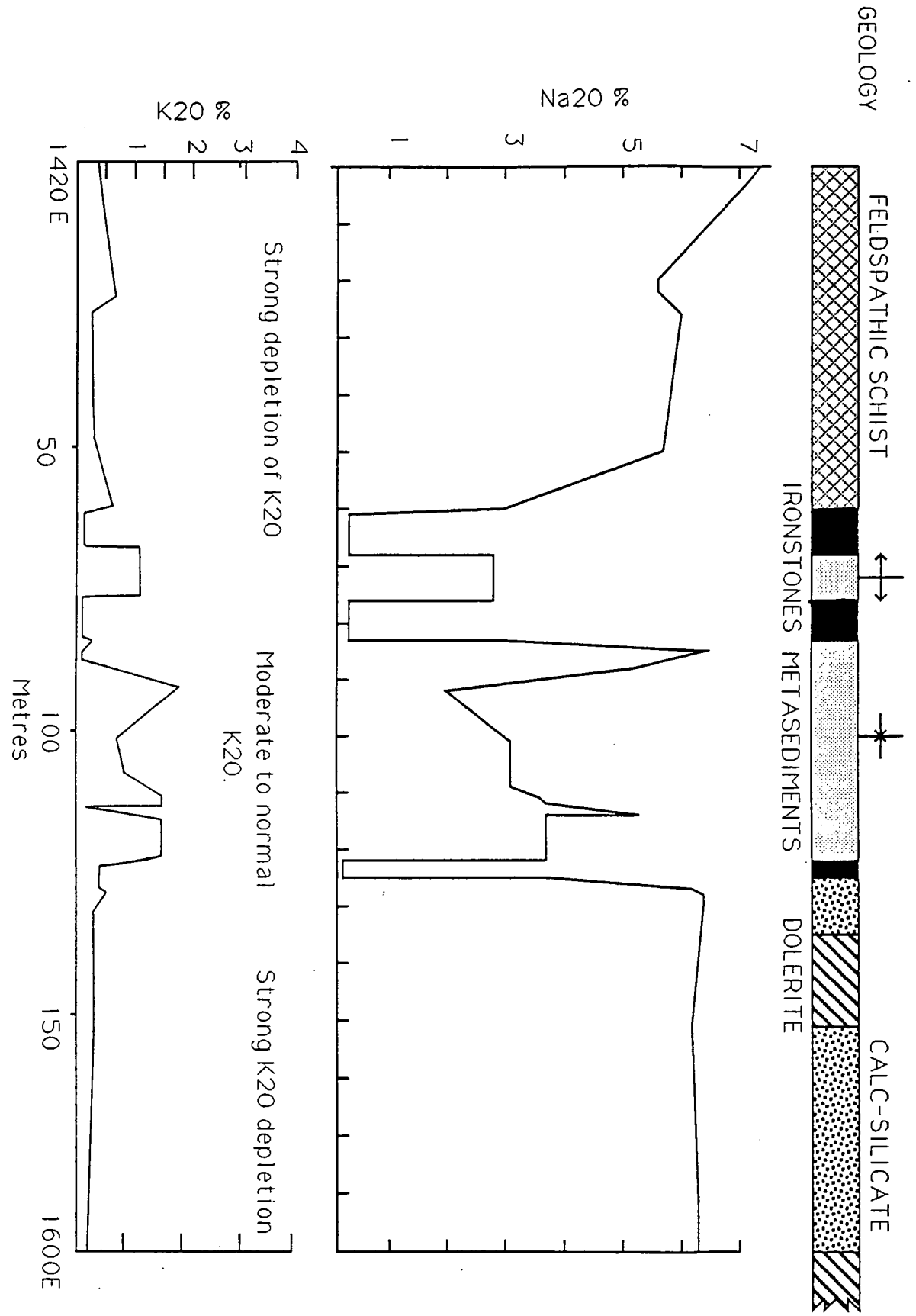

Figure 5.14 *K2O and Na2O variation in DDH STQ 78-1, 11285N, Area 257. Sodium is strongly enriched in footwall samples, (with consequent K depletion), and also in calc-silicate zones around amphibolites. Ironstones contain very low amounts of both elements. Replacement of albite by magnetite has caused the footwall decrease over 50 m in Na2Otowards ironstone.*

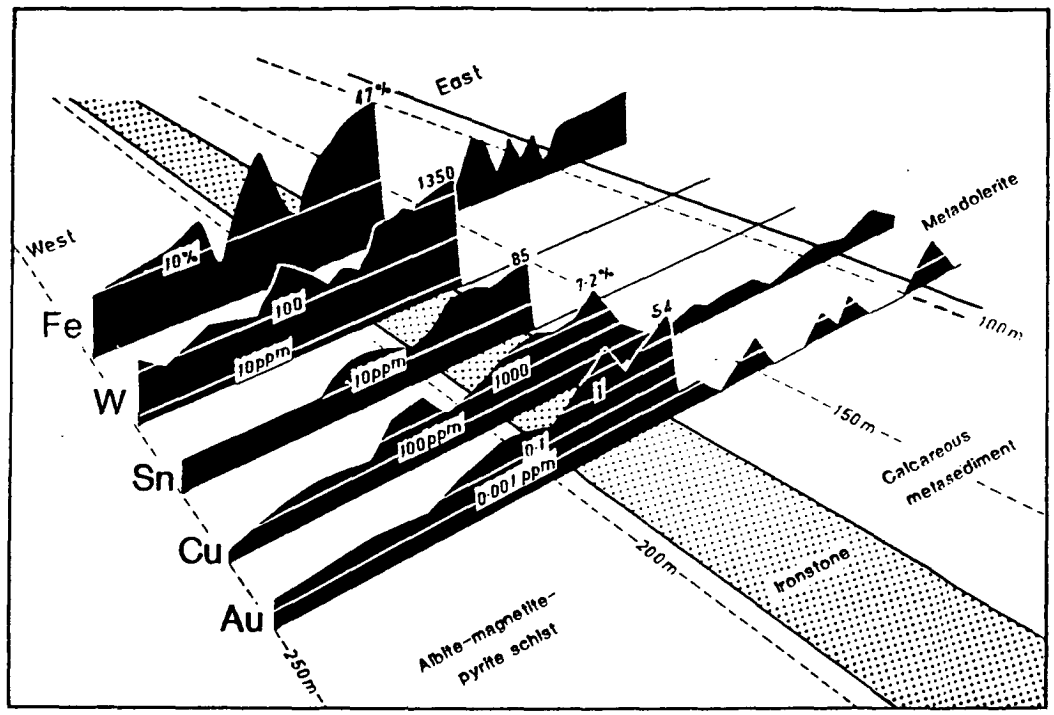

Figure 5.15 *Zoning of the ore elements beneath Area 251, DDH STQ 84-76, after Wall (1986). There is a general increase in concentration of these elements eastwards, culminating in the highest footwall values immediately below the ironstone. Hangingwall metasediments show an abrupt decrease in these elements, with sporadic highs attributed to occasional ferruginous beds, shears, and remobilisation associated with dolerite.*

One approach to establishing the depth of footwall alteration has been the analysis of the potassium channel of a Cyprus Minerals ground radiometric survey, across strike on line 11300N, Area 257. Unfortunately even thin overburden masks the radiometric response (> 6 cm, S. Collins pers. comm. 1988); the 257 transect was mapped for areas of overburden versus outcrop, which are indicated on Fig. 5.13. In this figure potassium levels increase to a maximum 200 m west of the main ironstone, after exhibiting very low levels footwall to the ore. This can be considered the maximum extent of albite alteration in the footwall.

Sodic enrichment is present in the hangingwall at a variety of locations (Fig.5.14). Enrichment is apparent adjacent to the ironstone, within chloritised fold-zones, and integral to metamorphic skarns which lie adjacent to some ironstones and occur as haloes around dolerites. While these are at times extensive, wide zones of unaltered metasediments are also present (e.g. the immediate 75 m above ironstone in STQ 80-16 has a Na_2O/K_2O ratio averaging 3.17, whereas sodically-altered zones average ~30). This is not the case in the footwall, where sodic alteration is ubiquitous.

The behaviour of the ore elements through the entire sequence is summarised in Fig. 5.15, adapted from Wall (1986). The elements Sn, W, Au, Fe, and Cu increase rapidly from 60 m below the 257 ironstone, by 3-4 times for Fe, Sn and W, to 140–160 times for Au and Cu. Above the ironstone these elements return abruptly to very low levels, with sporadic kicks corresponding to small iron formations and dolerite.

Average Footwall Alteration

Isocon analysis (see "Rationale", this chapter) of the average footwall composition shows that in comparison to the least altered protolith, alteration was virtually isovolumetric, with $C^A/C^\circ = 1.02 \pm 0.15$, using Ti, Y, and Al as the basis of the isocon fit (Fig. 5.16 and Fig. 5.17). As at Trough Tank, the "immobile" elements Nb and Zr show significant mobility, that is, they lie well below the chosen isocon 'point of origin'-Ti-Y-Al. The surprising constancy of Al_2O_3 in such severe alteration, and the isovolumetric alteration in general, may be related to the stability of albite; indeed Na also lies close to the isocon and in comparison to the chosen protolith has not changed. Mn, Ca, Si, Zr and Nb exhibit losses, whilst Cu, Au, Sn, W, Zn, Fe, K, Ba and Rb show gains.

"Pipe"-like Alteration

An isocon fit of Ti, Na, Al and Y indicates $C^A/C^\circ = 0.81 \pm 0.24$, corresponding to a mass or volume increase of ~23% in this zone. Addition of magnetite and sulphide is the most likely cause of this change. Losses occur in Mn, Ca, Zr, and Mg (Nb was not analysed), whilst gains characterise Cu, Fe, Au, Sn, W, Zn and the alkalis K, Ba and Rb. The latter suggests that compared to weakly altered feldspathic tuff, K, Ba and Rb are subtly added.

Correlation Coefficient Analysis

A correlation coefficient matrix was constructed for 24 samples using Mg, Ca, Si, Ti, Al, Fe, Mn, Na, P, Loss on Ignition (LOI), Ba, Pb, Zr, and Y as well as log transformed values of K, Ca, Cu, Au, W, Sn, Rb, Sr, Zn, and Ni. The sample group represents the combined data sets for "average altered" and "pipe-like" footwall alteration. The method was summarised previously in this chapter. The full matrix is appended (Appendix 4), but the broad relationships are summarised in Table 5.7. Note that mainly correlations with $r_{0.005} > 0.517$ (the 99% significance level for $n = 24$) have been considered.

Positive correlations reflect the different substitutions within the component minerals of the footwall. Fe is positively correlated with Sn, W, Au and Cu, although below the 95% significance level. The weak correlation of Mg with LOI, Mn, Zn and Ni suggests these elements depend on the presence of chlorite and biotite (which chlorite commonly pseudomorphs). A significant Ca-P correlation, and antipathy between Ca and LOI, is evidence that Ca mostly resides in disseminated apatite, rather than carbonate. Correlations between K and Zr+Y, and between Ti and P, are at present unexplained.

Negative correlations resolve to two associations signalling replacement processes in the footwall. The replacement of K-feldspar by albite is recorded by a negative correlation of Na with K, LOI, Ba and Rb, whereas the replacement of albite, quartz and K-feldspar is suggested by negative correlations of Fe, W, Sn, Au and Cu with Al, Y, Sr, Rb, and Si. Dissolution of zircon with increasing alteration is evidenced by a negative correlation of Zr with Au, Cu, Sn, W and weakly with Fe.

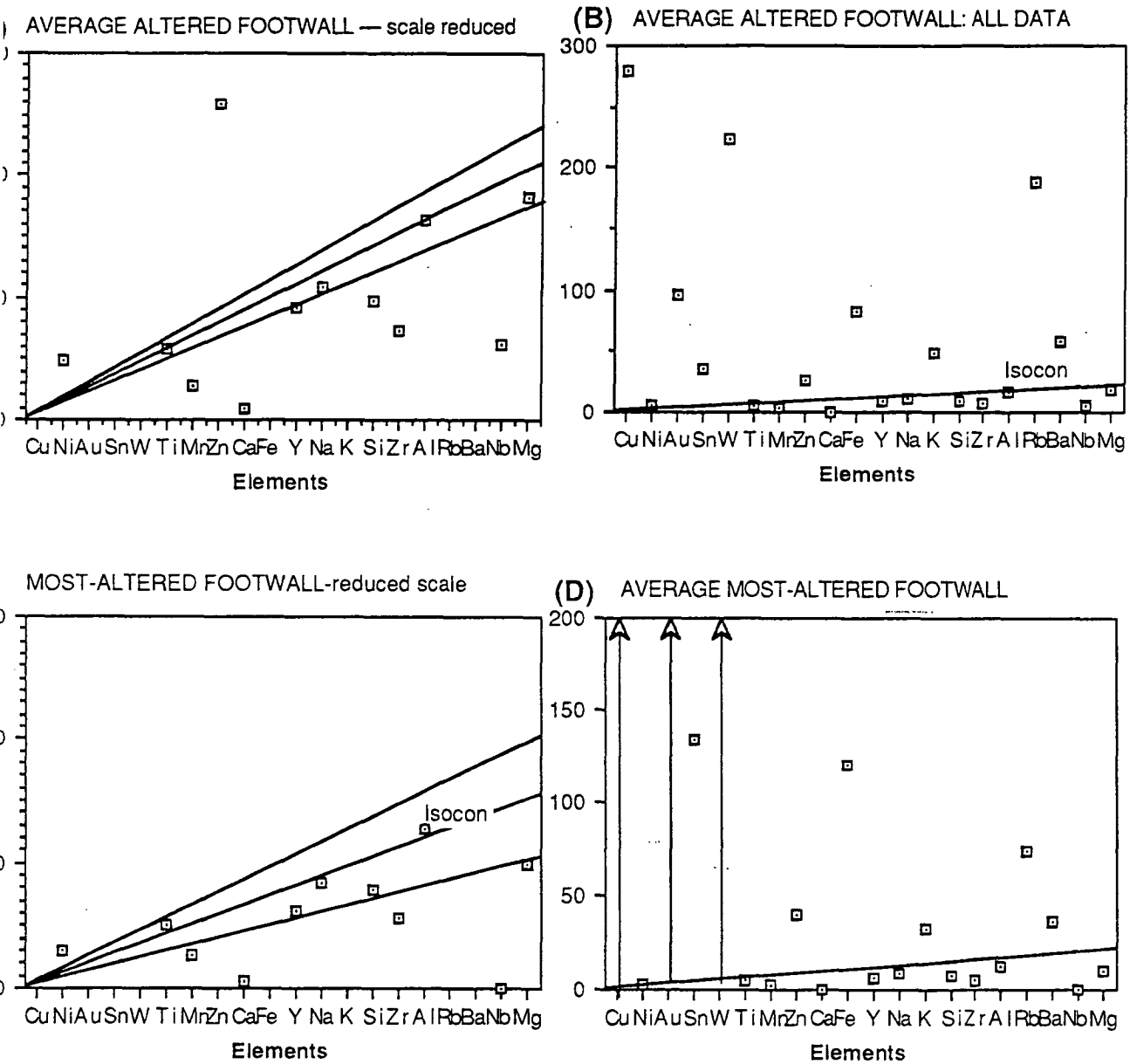

Figure 5.16 *Isocon analysis of the Starra footwall samples, (A) Average altered footwall — plotted at a reduced scale to define the isocon; (B) as for 'A', all data shown; (C) most-altered or 'pipe'-like alteration, reduced scale ; (D) as for 'C', full-scale. In reading the diagrams points above the isocon have been added, and those below subtracted in real terms. Errors inherent in the fit are shown by the cone around the isocon. Ni X CalCo = position of the element 'i' multiplied by the ratio of the altered to the original concentration of 'i'.*

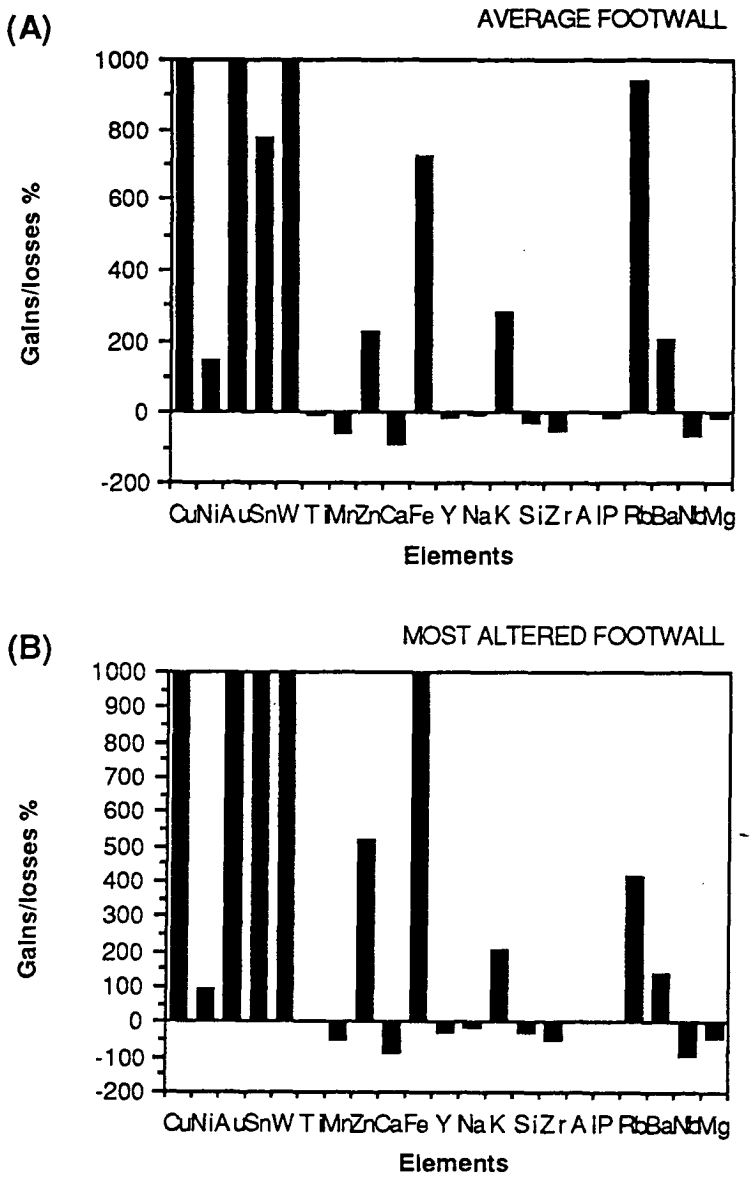

Figure 5.17 *Gains/losses diagrams comparing the least altered footwall (feldspathic beds which overly the ore horizon) to the average magnetite altered footwall (A), and the intense alteration zones which underlie the 251 orebody (B). Apparent enrichments of K, Ba and Rb are due to weak alteration in the comparison beds.*

Positive Correlations	Negative Correlations
Fe — Au (wk), Cu (wk), Sn (wk) oxides and sulphides	Na — K, LOI, Ba, Rb albite replacing K-spar
Mg - LOI - Mn - Zn - Ni chlorite substitution	Au — Zr, Sr
K - Ba - Rb - Zr - Y Biotite and K-spar	Fe, Sn , W — Si, Al, Y, Sr, Rb Sulphide/oxide replacement of albite, K-spar and quartz.
Al — Na Albite components	
Al — Ti, P Uncertain	
Au — Zn, Cu, Sn, W, Fe. Metals deposited from the ore fluid.	

Table 5.7 *A summary of significant correlations for 24 average and 'pipe'-like footwall samples, (Areas 257 and 251), and their probable explanation.*

DISCUSSION

Starra Footwall Geochemistry

Wall (1986) studied 137 footwall, ironstone and hangingwall samples in a report to Cyprus Minerals. In this statistical study he did not differentiate between the different unit-types, as the objective was to identify elements systematically associated with gold in the whole sequence. The elements analysed were Au, Sn, W, Sb, As, Bi, Zn, Co, Ni, Cr, V, La, Fe, P, Mn and Ca. He found, in company with the present work, that Au was positively

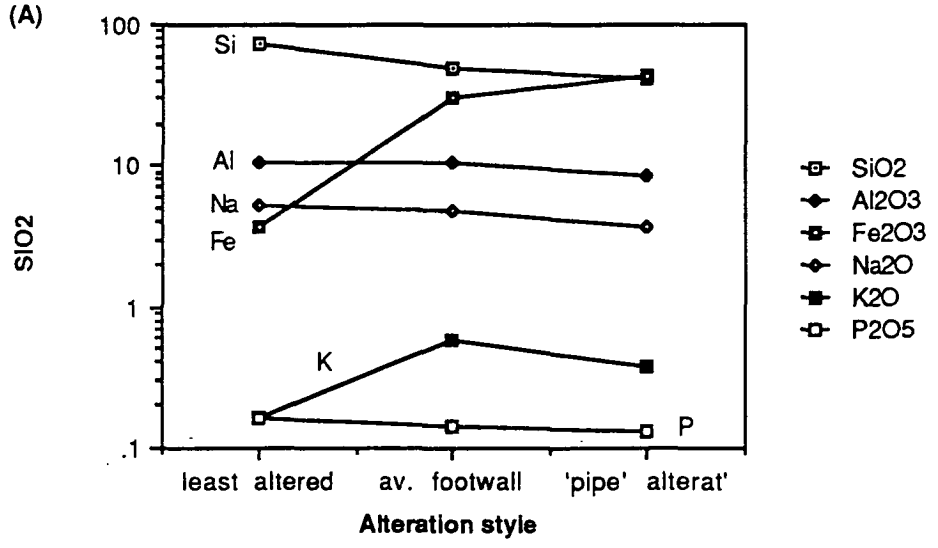

Figure 5.18A *Average major element trends between the Starra least altered, average footwall, and most altered or 'pipe'-like alteration. The spacing of the sample points on the diagram is schematic.*

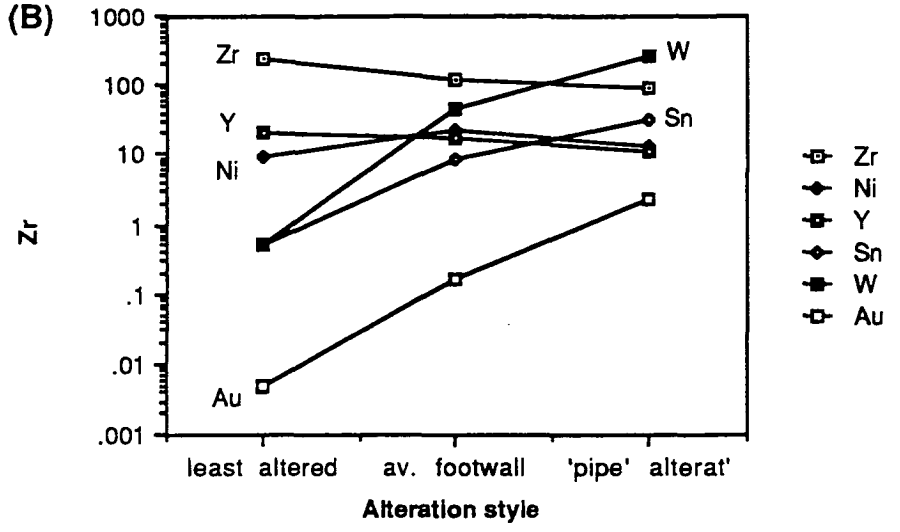

Figure 5.18B *Average trace element trends for the Starra alteration zones. Ore elements such as Sn, W, and Cu show systematic increases, whereas Zr is depleted.*

correlated with Cu, Sn, W, Fe and weakly with Sb and Bi. The present study has only analysed Sb and Bi sporadically, hence they were excluded from the correlation matrix. Wall (1986) also found that V, Ni, P, As and Ca were significantly inversely associated with Au, using log transformed data.

The present study has added Zn to the list of Au-correlated elements defined by Wall (1986), and has identified an inverse correlation of Au with Zr, Y and Sr. A study has also been made of the footwall patterns of Rare Earth Elements (REE), reported in detail in Chapter 8. Briefly, this indicated significant mobility of the HREEs with respect to the LREE in the most intense alteration zones.

Trough Tank Host-rock Alteration

Figures 5.19 A & B graphically summarise the changes in absolute average abundance of selected elements through increasing alteration. An important feature is high CaO (≈ 3%) in the pyrite zone, but not in the adjacent magnetite zone. This could form a useful guide to ore. As Cu-Au mineralisation is approached elevated Fe (>10 %), Cu (> 140 ppm), Co (> 280 ppm) and Ni (> 40 ppm) are observed in the host rocks. Anomalous levels of elements enriched in the silica zones, such as Zn, P, Mo, As, Bi and Sn are also likely to be good exploration guides.

Correlation analysis has distinguished new relationships in the alteration zones. In particular the correlation of Co with carbonate minerals rather than with Fe is intriguing, and presently unexplained. Within the silica 'pipe' zone such analysis suggests that apatite was mainly deposited with quartz, not magnetite, whereas the ore elements show a distinct preference for magnetite zones.

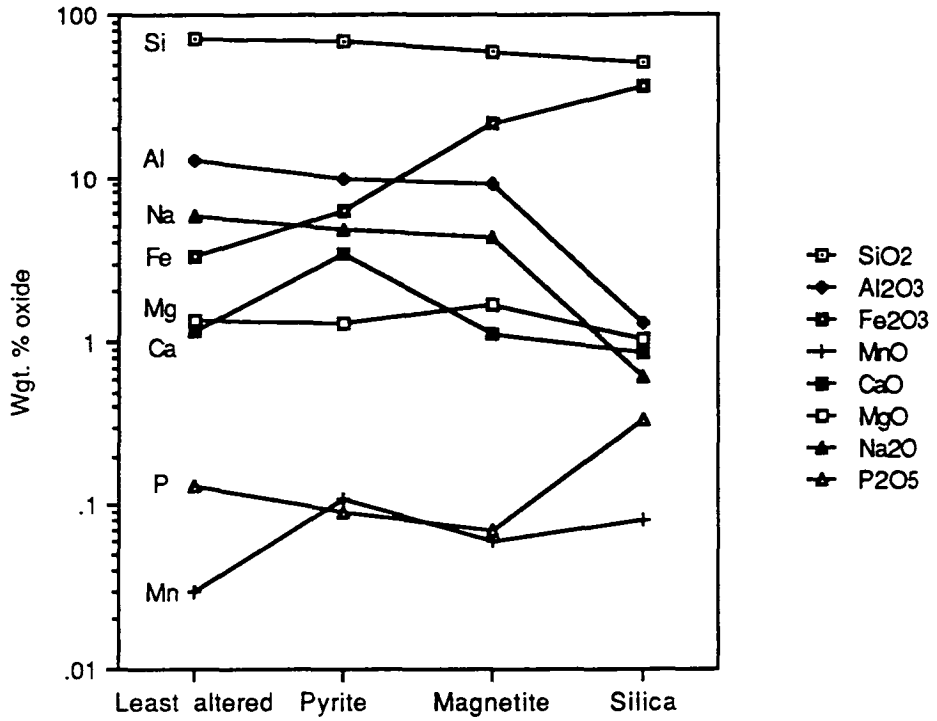

Figure 5.19A. *Average major element comparisons between the different alteration zones at Trough Tank.*

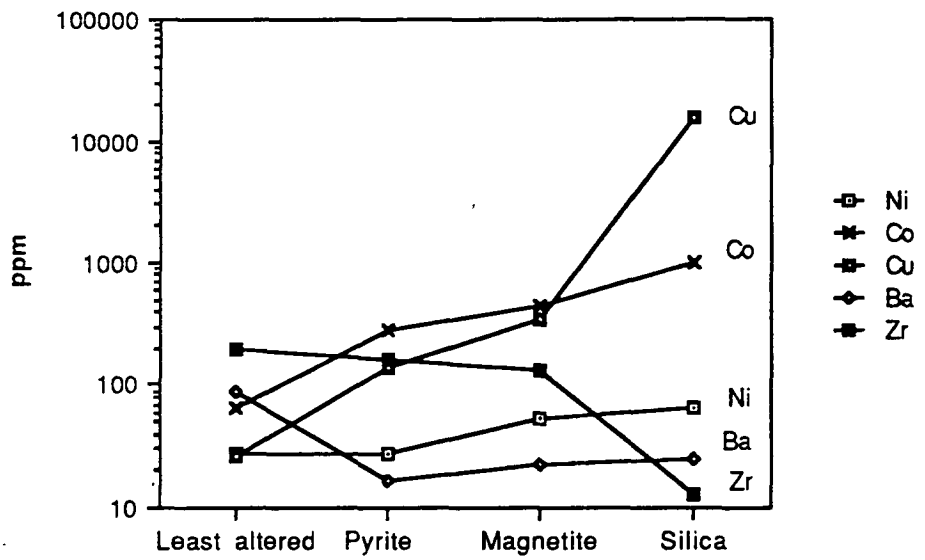

Figure 5.19B *Average trace element comparisons between the different alteration zones at Trough Tank.*

Comparisons Between Trough Tank and Starra Alteration

Starra and Trough Tank display similar element trends and associations in their alteration haloes. In both, the footwall is characterised by an enrichment in Fe, Na, Cu, Au and weakly in Zn, and a depletion of K, Mn, Ca, Zr, Nb, Ba and Sr (Figs. 5.18, 5.19), in

mineralogies dominated by albite, magnetite, pyrite, chalcopyrite and chlorite. Trough Tank haloes are much smaller than those beneath Starra, and exhibit marked zoning from pyrite-carbonate to magnetite-pyrite-chalcopyrite surrounding a discrete quartz-mag-cpy-py discordant pipe. Carbonate and the consequent Ca-Mg-Mn element association has not been recognised in the Starra footwall, although drilling to date has remained within the magnetite envelope. A further contrast is the dominance of magnetite in the most intense alteration at Starra, whereas analogous zones at Trough Tank are quartz-rich.

While there is a common thread in the footwall geochemistry, there are also significant chemical differences, such as an enrichment in Ni, P, Mo and Co at Trough Tank, and in W and Sn at Starra (Co at Starra ranges to 230 ppm, over a background of 20 ppm, but this enrichment is apparently confined to the Area 244 chloritic schists (Wall 1986)). These differences may be due to variations in the physicochemical conditions of the ore fluids, but in view of the similar mineral assemblages, are more likely to reflect differences in the chemistry of the hydrothermally-leached source. This is particularly so in the case of P at Trough Tank, where the pyrite and magnetite zones show real P depletion, but substantial enrichment in the pipe (as apatite). Phosphorous-enrichment has been detected in the host rocks of Trough Tank and linked to the alkaline volcanic chemistry of one of the sediment components. Such a hypothesis has implications for other deposits, such as the phosphatic Kiruna iron ores of Sweden (Parak 1985) and Roxby Downs (average transgressive chalcocite-bornite zone = 0.8 % P_2O_5, Roberts & Hudson 1983), although melt fractionation is also an explanation for these ores (Lyons 1988). An enrichment of W and Sn at Starra suggests a granitic contribution for these components, despite a non-cogenetic relationship established between volcanics in the Starra footwall, and the Gin Creek Granite. Co-enrichment in ores is often used to infer basaltic rocks within the source area. Two examples in the Mount Isa block are the Mount Isa copper orebody (in which an average of > 0.1% Co (Robertson 1982) was presumably sourced from the basaltic Eastern Creek Volcanics), and the Mt. Cobalt mine (chapter 2, a shear zone Co-As occurrence within metamorphosed dolerite; Nisbet et al. (1983)). The Co-enrichment of Trough Tank may therefore also be owed to basic lithologies deep in the footwall.

Both Starra and Trough Tank share a Na-rich/K-Ba-Rb-poor association in albitic schist. That this Na enrichment precedes the main hydrothermal event is evidenced by:

1) The presence of albitic rocks at Trough Tank and Starra, well removed from mineralisation, with low levels of the ore elements. At Starra, K, Ba, and Rb actually increase again subtly within the most altered areas.

2) Absolute levels of Na decrease towards ironstone in the footwall (Fig. 5.14), and Na is negatively correlated with Fe. Both of these facts would be expected if albite was replaced by magnetite during alteration, although a component of dilution must also be present.

3) Microprobe analysis has shown that predeformational pyrite (Davidson et al. 1989) contains inclusions of pure albite similar to albites exterior to pyrite. It follows that the included albite preceded the replacive pyrite.

Bultitude & Wyborn (1982) record a markedly sodic rhyolite composition in the Doherty Formation (underlying the Kuridala Formation regionally) whilst other workers have recorded sodic-altered tuff in some northern Australian Proterozoic sequences (Davidson & Dashlooty 1989, Plumb et al., in press). Globally, diagenetic hypersaline alteration of tuff has been invoked to explain extensive areas of either strongly sodic or strongly potassic feldspathic rocks. For instance Whitney & Olsted (1988) describe widespread Na-altered gneiss containing "numerous magnetite iron ore bodies" in the Adirondack Mountains, New York, and distinguished them from primary trondhjemitic compositions. These instances support the idea that a hypersaline diagenetic history could have given rise to widespread sodic alteration in the Staveley Formation, prior to hydrothermal mineralisation.

Nevertheless, albite was a stable silicate during the mineralising events at Trough Tank and Starra. It was also stable during fluid movement around dolerites and within shear and skarn zones, and has been noted from similar shear zones and tectonic breccias throughout the Mount Isa area (e.g., Blake et al. 1982, Oliver and Wall 1987).

In summary, the high temperature alteration at Starra and Trough Tank was preceded by low temperature alkaline diagenesis which began to enrich the sequence in Na and deplete it in K, Ba and Rb, probably via the development of analcime (favoured by high alkali and silica activities, and low hydrogen ion levels; Sheppard & Gude (1973)). With the onset of alteration albite replaced analcime. The most intense alteration was characterised by magnetite, chalcopyrite, and chlorite focussed in discrete zones at both deposits, but at Trough Tank the result was quartz-magnetite-apatite deposition, rather than magnetite-hematite as at Starra. There is excellent evidence in the focussed alteration zones of the movement of the high field strength elements Zr and Nb at both prospects.

CHAPTER 6

THE GEOCHEMISTRY OF THE STARRA AND TROUGH TANK IRON FORMATIONS

INTRODUCTION

A detailed geochemical study of Starra and Trough Tank iron formations was undertaken to: (1) describe the variation between different types in the Starra and Trough Tank areas, (2) formulate chemical discriminants to differentiate barren and mineralised ironstone, and (3) determine the most likely origin of the iron formations by combining geochemical data with the established geological framework.

'Ironstones' are considered in this thesis to be massive, iron-rich, conformable varieties of iron formation. Banded iron formations (BIFs) are distinguished from them by the presence of well-defined compositional layering.

STARRA

Ironstone types

Starra iron formations were grouped in chapter 3 (also Fig. 3.8) into

(1) **Mineralised ore environment ironstones** — : magnetite-quartz-chalcopyrite assemblages, arbitrarily containing greater than 0.5 ppm Au.

(2) **Barren ore environment ironstones**, sometimes termed "proximal massive hematitic" ironstones, consisting of hematite-pyrite assemblages within an arbitrary 500 m of an ore zone, and containing less than 0.5 ppm Au.

(3) **Barren distal massive ironstones**: stratiform massive hematite commencing an arbitrary 500 m from ore. They are texturally identical to type (2).

(4) **Barren distal cherty BIFs** — < 0.1 ppm Au: stratiform, well-banded, silica-rich units with the textural character of sedimentary iron-formation, normally containing < 0.1 ppm.

(5) **Barren and mineralised breccia-bearing ironstones**, which have not been examined geochemically.

Sampling and Analytical Techniques

All of the ore environment samples were obtained from Area 257 drill-core, comprising complete quarter-core 2 -10 m intercepts (n = 18). Cherty BIFs were obtained from fresh percussion drill-chips, which were washed and sieved to retain the +5 mm fraction. Contaminants were removed by hand. Barren distal massive ironstones could only be reliably sampled in outcrop (n=5).

The geochemical effects of weathering have not been studied in detail here, but a comparison of the fresh and weathered composites produced by Cyprus Minerals shows that sulphide and carbonate-rich ironstone changes chemically during weathering. Losses of Cu, Pb, Zn and Ca accompany increases in Ba and the REE. Extensive reprecipitation of Fe, Si and Au was observed by Pontifex (1986) in gossanous ironstones of the Starra "leached zone", which are therefore unreliable indicators of primary geochemistry. In contrast, all elements with the exception of the chalcophiles have not changed during the weathering of non-gossanous ironstone (types 2, 3 and 4 above).

The general methods and specific preparations required for the analysis of very iron-rich rocks are described in Appendix 2.

Spatial Distribution of Copper and Gold

Background Gold Values

The Starra Iron-formation Member has been sampled in detail along its 60 km length by Cyprus Minerals, who found gold to be enriched relative to crustal averages in many ironstones. Mineralised ironstones contain a common range of 2 to 15 ppm Au (maximum of 120 ppm), ore environment hematite lenses contain 0.05 and 0.5 ppm, and all distal ironstones have 0.001 to 0.2 ppm.

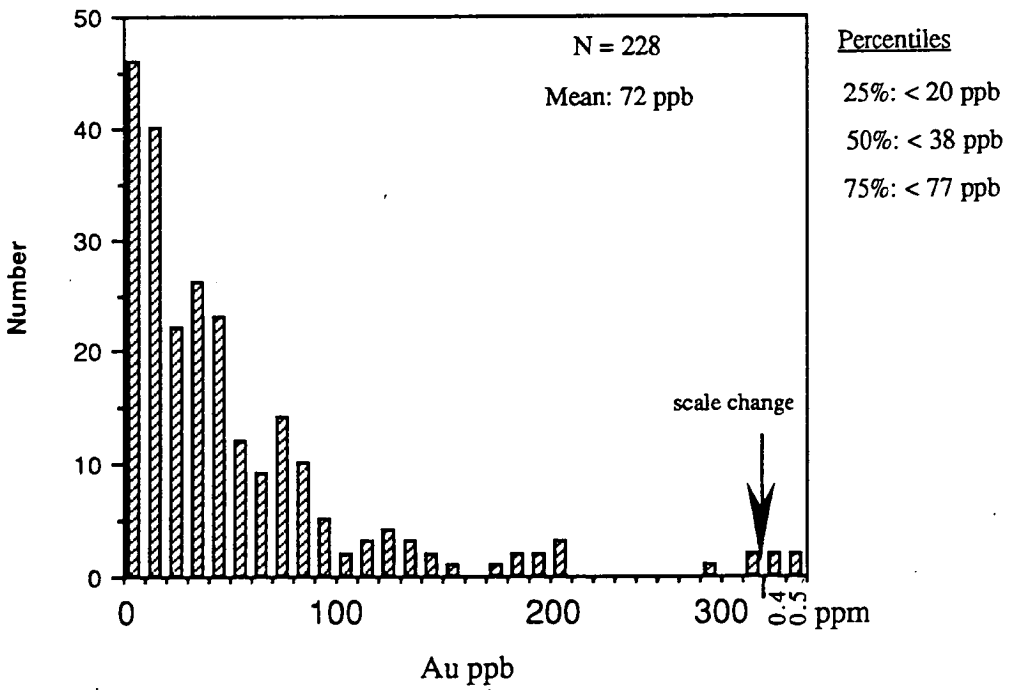

Figure 6.1 *A histogram of Au values (fire-assay-carbon rod detection limit of 1 ppb) in 12 km of Blockbuster/Mobs Lease BIF. They are Au-enriched compared to the major iron formation types, e.g. Groves et al. (1987).*

The most reliable detailed chemical survey in the area has been carried out in the Blockbuster/Mobs Lease region (for location see Fig. 4.1), where distal barren and weakly

mineralised ironstone varieties outcrop. These iron formations are well-banded, directly overlying basalt, and are strike-equivalents of the Starra ores, possessing a similar enrichment of Cu and W, but an uncharacteristic enrichment in Pb and Zn. A 12 km strike-length was sampled at 50 m intervals, using a 2 kg sample size, commencing 2 km west of the historical Selwyn township. The gold analyses were performed by Tetchem Laboratories of Brisbane in 1986, using a fire assay–carbon rod technique with a 1 ppb detection limit. In 228 samples, the gold values of Mobs Lease BIFs ranged between 1 ppb and 1.2 ppm, average 72 ±17 ppb (95% sigma level), with 50% of the data greater than 38 ppb (Fig. 6.1). A significant level of regional gold enrichment is indicated by these results.

Ore Environment Gold and Copper Values

Gold and copper in ore environment ironstones was examined in detail for the Area 257 orebody (10900N - 11500N, Mine grid; Appendix 13), using only intercepts from below the 1350 m R.L., 60 m below the 257 hilltop (Figs. 6.2A & B, 6.3A & B, 6.4A & B). This selective sampling minimised the influence of weathering observed by Pontifex (1986), illustrated by the fragmentation of linear Au-Cu contours in Figs. 6.3B & C. Very high erratic Au and Cu values occur sporadically in the leached zone, and in inter-boudin pockets of sulphide ore. Preferential sulphide oxidation has been observed in ironstones down to 250 m depth along contacts.

Most Au and Cu is confined to ironstone, as illustrated for the 1300 m RL in Figs. 6.2A & B. The 1 ppm Au contour in most instances delineates ironstone, with some minor pockets of 1 - 4 ppm Au extending into the hangingwall actinolite-scapolite-magnetite breccias (Fig. 6.3B), notably only above the 1350 m R.L. Along the Western Zone, surface ironstone Au values decline northward, corresponding to a transition from magnetite-quartz to hematite ironstones (Fig. 6.5). There is a notable positive anomaly in this behaviour in a 70 m long segment, centred on 11400N, averaging 10 ppm Au, coinciding with a marked thickening.

At Area 257, multiple ironstone horizons are mineralised, differing to the general pattern noted by Kary & Harley (in press), of confinement of ore grades to the most eastern ironstone. Across individual mineralised ironstones, Au and Cu commonly increase to peak adjacent to the metasediment contact (Kary & Harley in press). Au and Cu in ironstone show a linear relationship

$$(\log Cu\ \%) = 0.70(\log Au\ ppm) - 0.69$$

with a correlation coefficient of 0.402 (n = 182; significant at the 99 % level). Binary Au-Cu (Fig. 6.6) shows a distinct scatter of points away from the main linear trend, towards higher Au at lower Cu values. This may be a primary feature, or reflect leaching of Cu from weathered samples along the ironstone contacts. There is no similar trend towards higher Cu values at low Au levels. Au is log-normally distributed, with a mean of 3.71 ppm, and a mode of 0.4 ppm. Cu is also log-normally distributed with a mean of 0.86 % and a mode of 0.60 %. Cu %/Au ppm has a mean of 0.44, and a range of 0.005 to 11.67 (Fig. 6.7A & B).

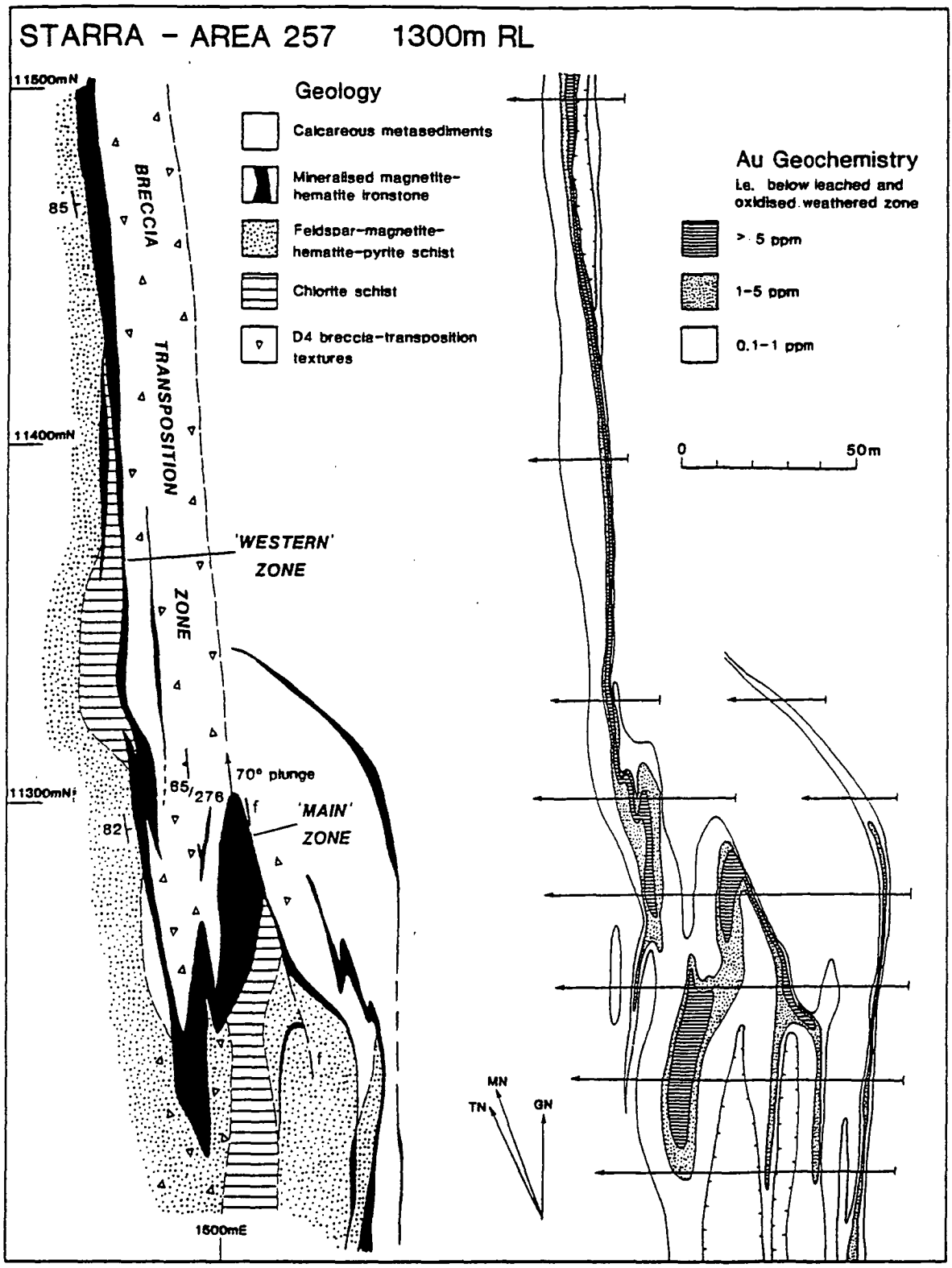

Figure 6.2A *Contoured Au geochemistry, primary ore, Area 257. The contouring illustrates the concordance of grades greater than 1 ppm with ironstone, even in the strongly folded and transposed areas. The geochemistry supports the idea of faulting of the syncline hinge with consequent left-lateral motion of the anticline northwards during D2(LP). The data on which this plot is based is taken from 1 m intercepts projected from no more than 20 m either side of the 1300m R.L., aproximately 120 m below surface.*

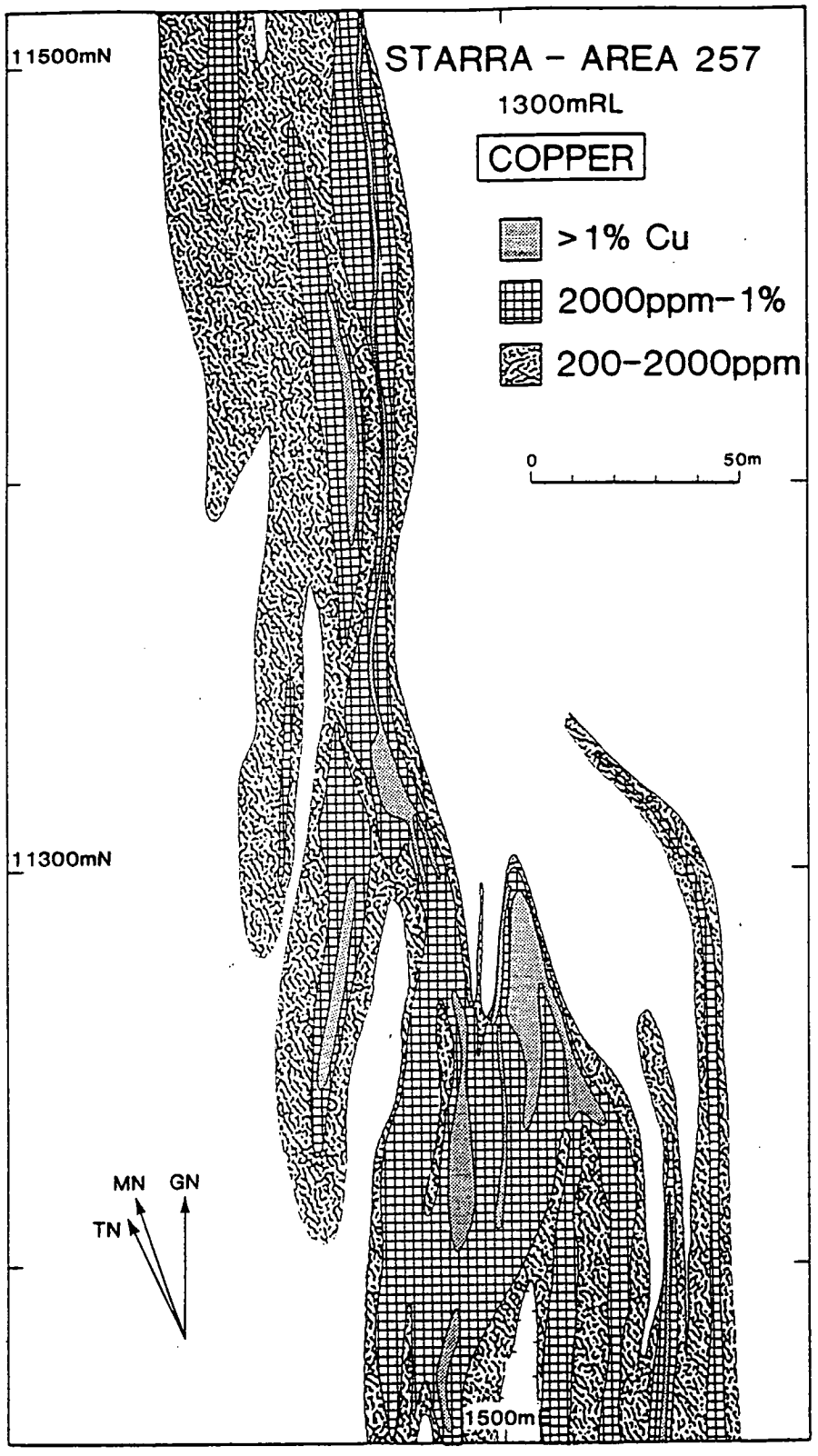

Figure 6.2b *Cu geochemistry of the 1300 R.L., Area 257, using the same sampling parameters as specified in Fig. 6.2a.*

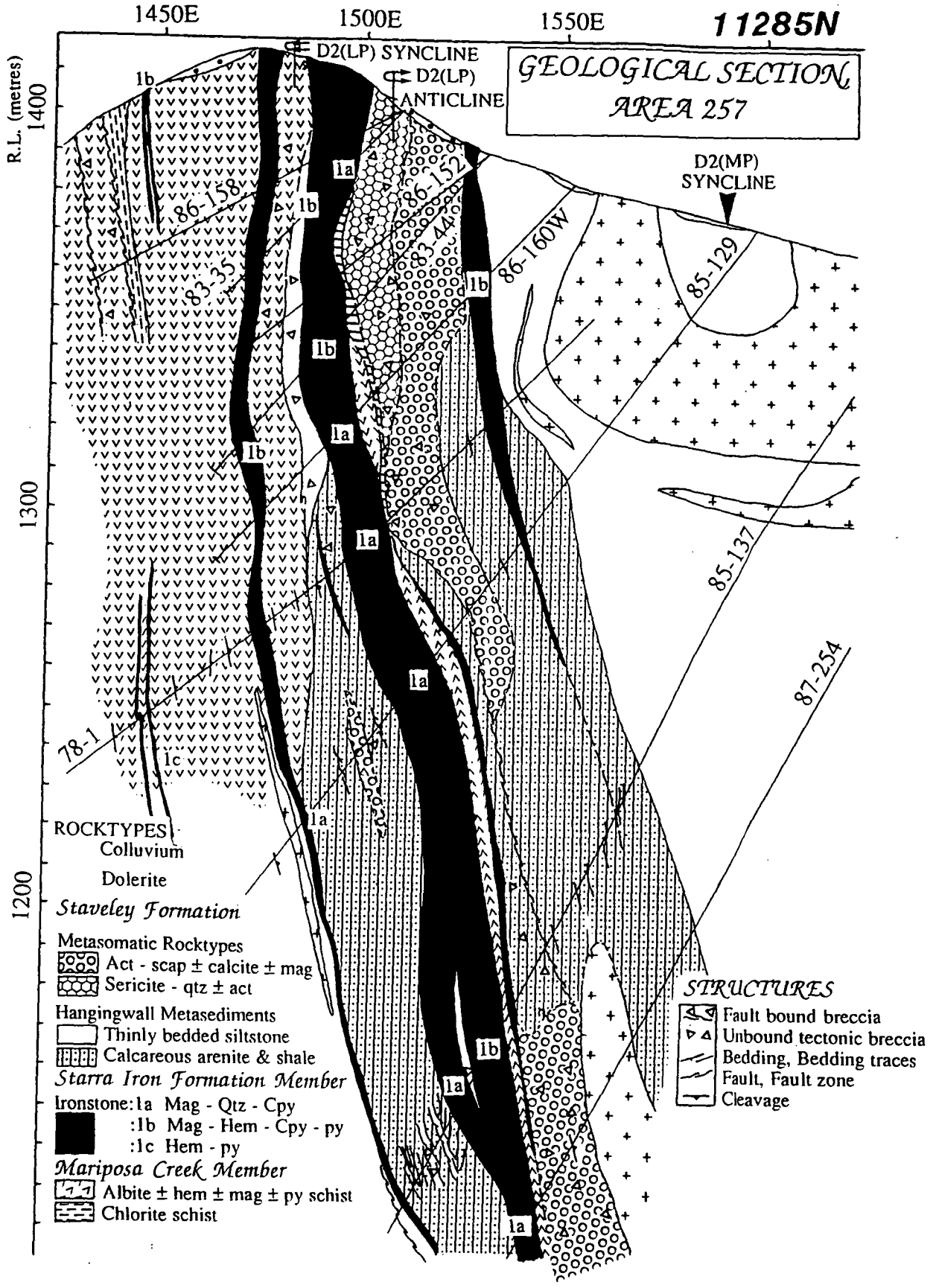

Figure 6.3a *A geological section along line 11285N, Area 257.*

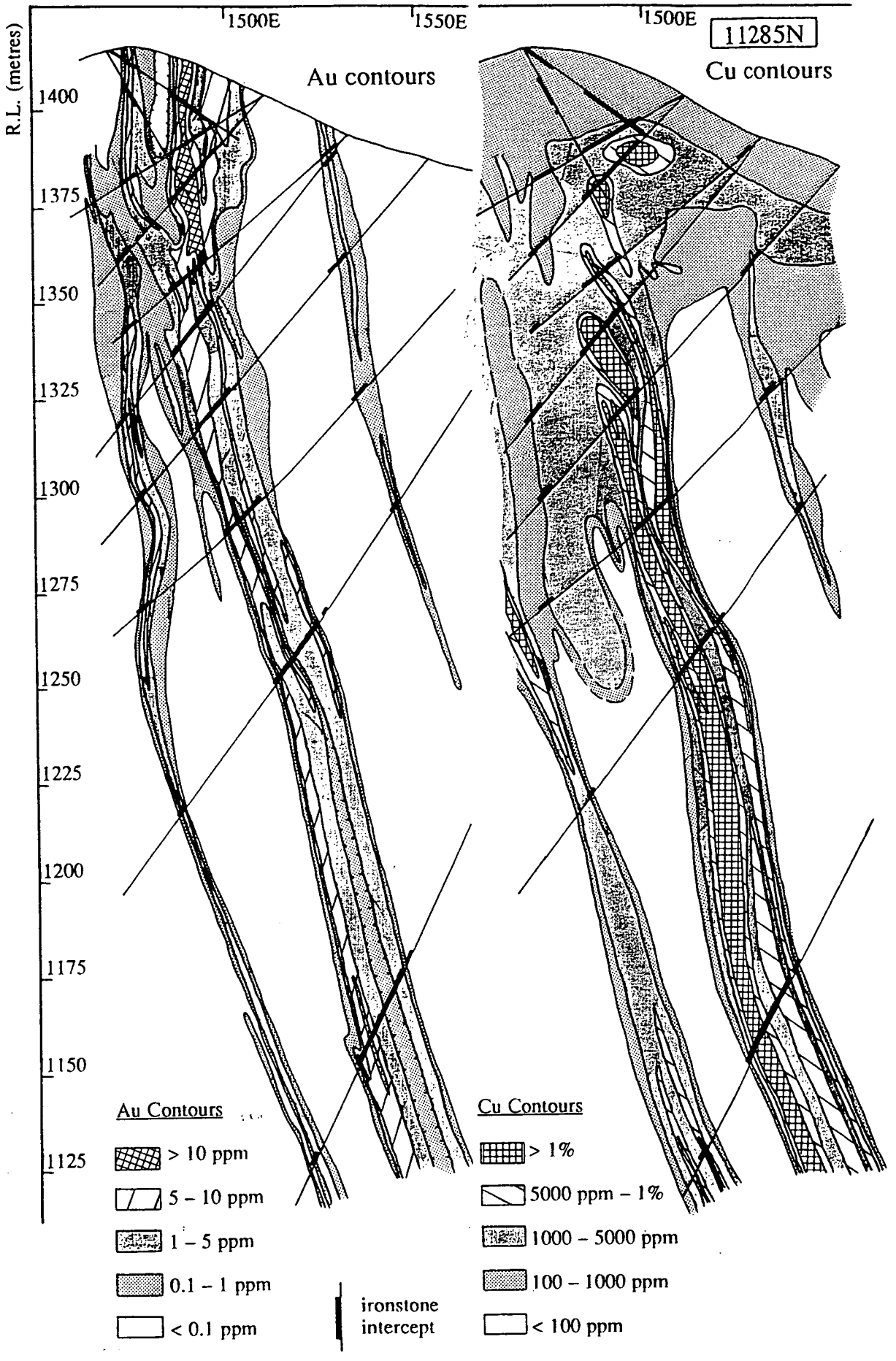

Figure 6.3b *Au and Cu geochemistry contours, employing no more than a 20 m projection, for section 11285N, Area 257. Ironstone intercepts are shown in black bars. The drillhole details are available in Fig. 6.3a.*

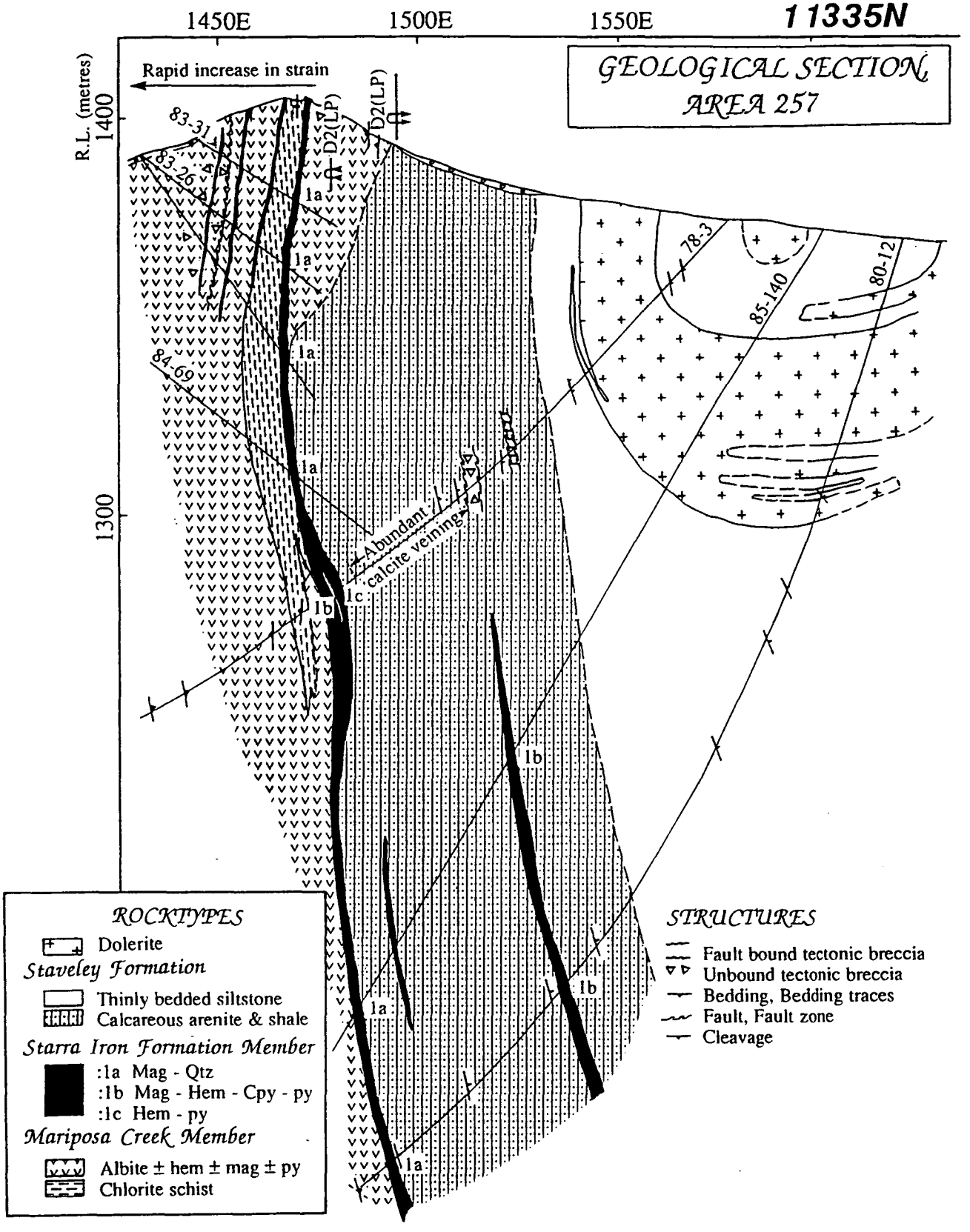

Figure 6.4a *A geological section along line 11335N, Area 257.*

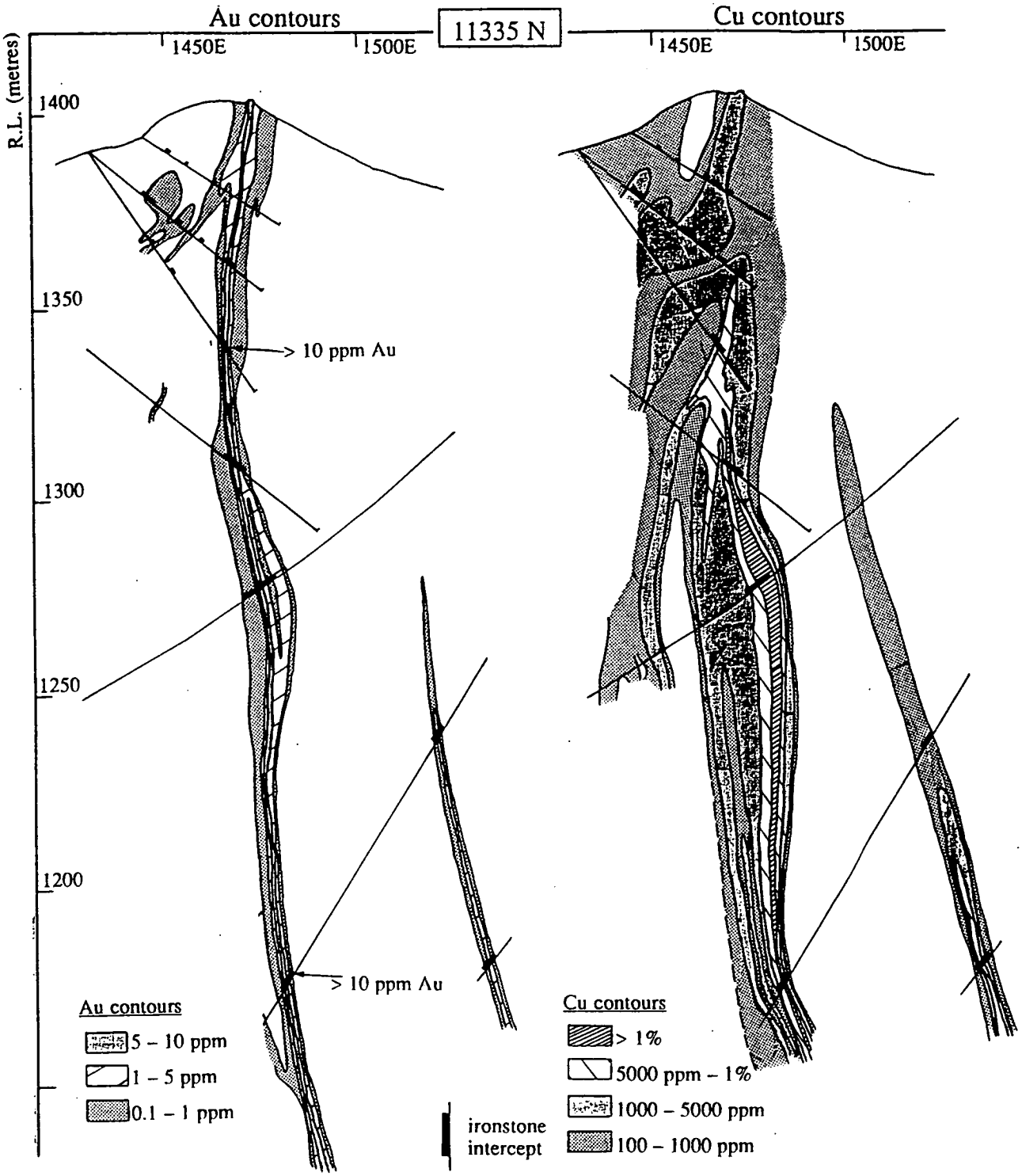

Figure 6.4b *Au and Cu geochemistry contours, employing no more than a 20 m projection, for section 11335N, Area 257. Ironstone intercepts are shown in black bars. The drillhole details are available in Fig. 6.4a.*

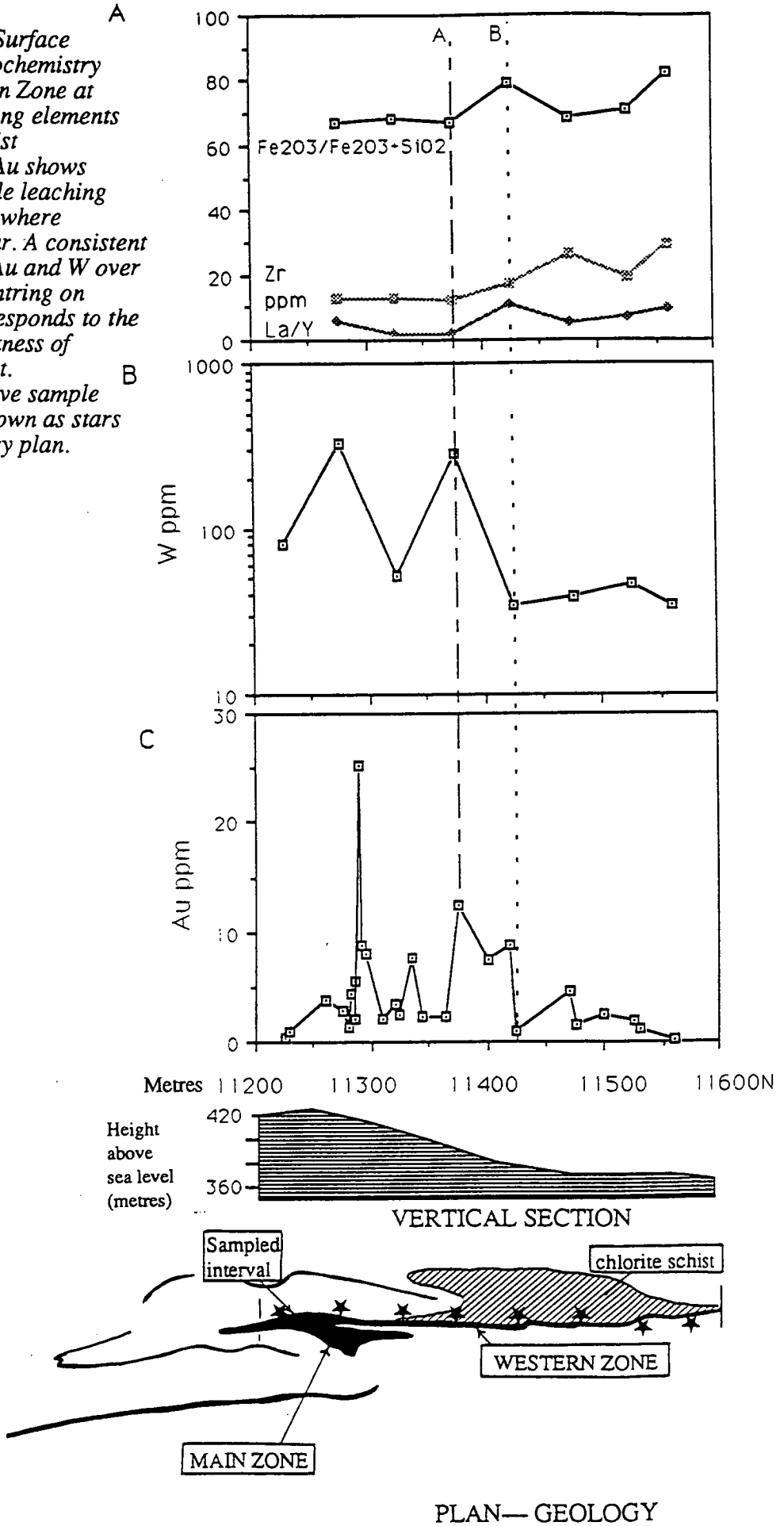

Figure 6. 5 *Surface ironstone geochemistry of the Western Zone at Area 257, using elements known to resist weathering. Au shows some probable leaching above 417m, where laterites occur. A consistent elevation of Au and W over 50 metres centring on 11400N corresponds to the greatest thickness of chlorite schist. Comprehensive sample points are shown as stars on the geology plan.*

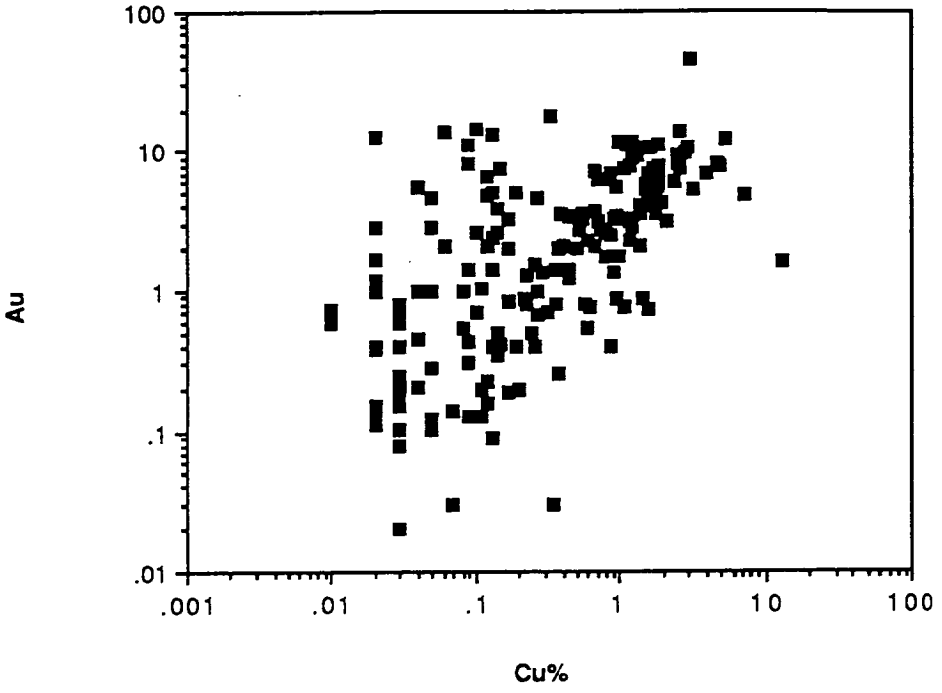

Figure 6.6 *Au versus Cu geochemistry for the Area 257 ore environment ironstones, sampling only below the 1350 m R.L.*

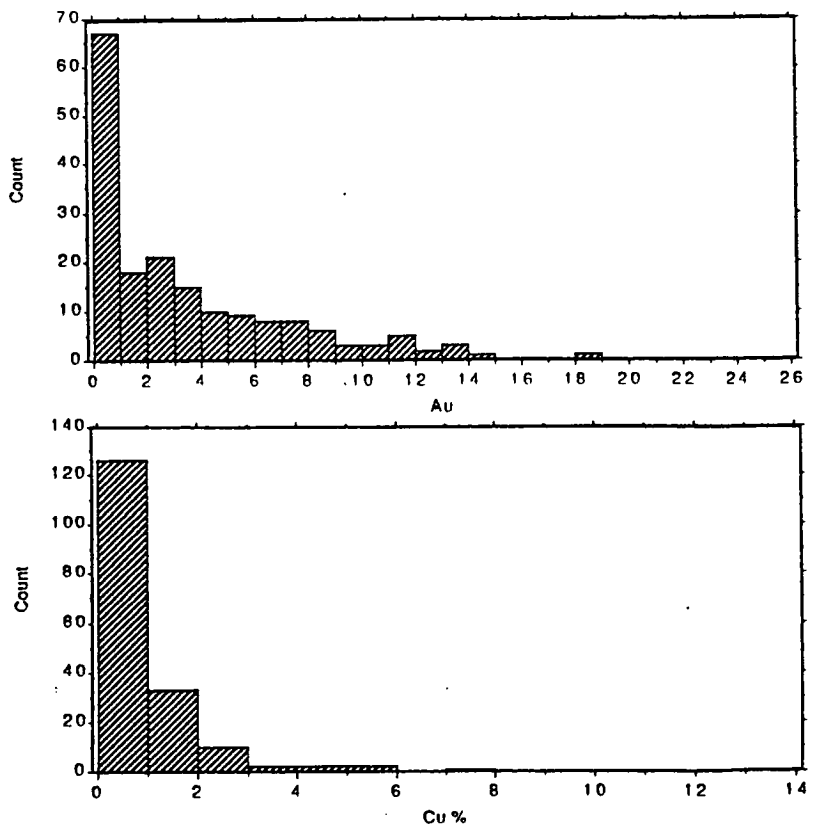

Figure 6.7 *Histograms of Au and Cu. All samples were selected from below the 1350 m R.L., in Area 257 ironstone (11100N - 11500N). Each sample is a 2 m diamond-drillhole intercept, in which Au was analysed in triplicate by fire assay, and averaged. A log normal distribution is indicated for all parameters.*

Mineral Chemistry of Gold

Gold is hosted most commonly by chalcopyrite, and to a lesser extent by magnetite, hematite, siderite and quartz. The minor telluride phases Tellurobismuthinite (Bi_2Te_3) and Melonite ($NiTe_2$), identified from microprobe analysis, also contain small amounts of Au (< 1.0 wt. %).

Microprobe analysis of 19 gold grains (6 – 60 μm across) from Areas 251 and 257 found the gold fineness (=1000 Au wt. %/(Ag + Au) wt. %) to be very high and uniform, averaging 930.5, with a range of 836 - 996 (Fig. 6.8). Margins of grains are subtly more Ag-rich than their centres (Table 6.1). No obvious correlation exists between the size of grains and their fineness.

Sample No.	Grain No.	Location	Host	Size μm	Fineness	
E8078, A251	1	STQ77,168.8m	chalcopyrite	6	945	
	2		chalcopyrite		996	(crystalline)
E8074, A251	3	STQ77,154.7m	chalcopyrite	10	933	centre
			chalcopyrite		920	rim
	4		chalcopyrite	30	929	centre
			chalcopyrite		929	rim
	5		chalcopyrite	8	929	
	6		chalcopyrite	7	925	
	7		chalcopyrite	20	924	centre
	8		chalcopyrite	60	943	centre
			chalcopyrite		836	rim
			chalcopyrite		914	rim
E8072, A251	9	STQ77,144.8m	quartz	10	943	centre
			quartz		929	rim
	10		quartz	10	933	centre
	11		quartz	20	940	centre
			quartz		937	rim
			quartz		936	rim of 10
	12		quartz	20	935	centre
			quartz		923	rim
	13		quartz	7	935	centre
			quartz		927	rim
	14		quartz	10	931	centre
			quartz		932	rim
St115, A257	15	STQ129	chalcopyrite	8	942	centre
			chalcopyrite		928	rim
E8080, A251	16	STQ84,193.6m	chalcopyrite	23	926	centre
	17		chalcopyrite	22	934	rim
	18		chalcopyrite	18	933	centre
	19		chalcopyrite	7	928	centre

Table 6.1 *Details of grains analysed for gold fineness, mainly from Area 251.*

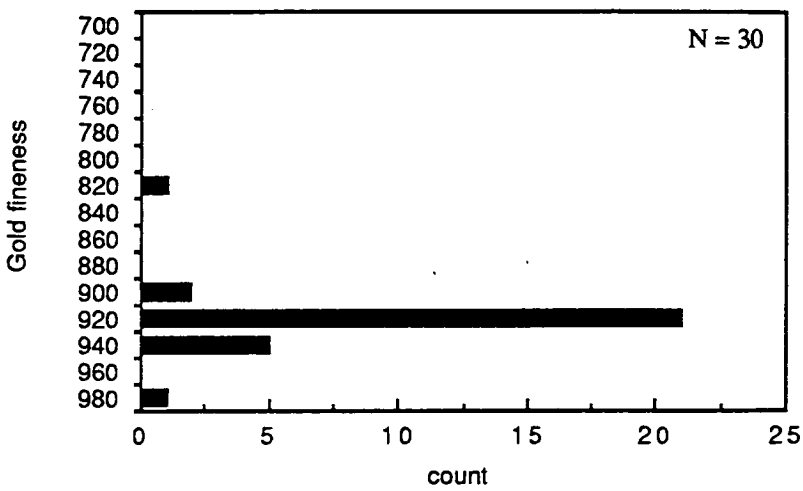

Figure 6.8 *Gold fineness for 19 grains from the Area 251 and 257 ironstones (primary zone), including core and rim analyses. Sample details are listed in Table 6.1.*

Major and Trace Element Variations

Ore Environment Ironstones

In mineralised and barren ironstones in the Western Hematites ($Fe_2O_3^{tot}$ + SiO_2) wt. % is ~ 96 % (Appendix 5). The remaining important components commonly at percent levels are Al_2O_3, MgO , CaO and Na_2O, whereas TiO_2, MnO, K_2O and P_2O_5 are all less than 0.20 % (Table 6.2). Both ironstone types are depleted in Pb, Zn, Ba, Sc, Rb, Sr and Zr compared to crustal averages. Total organic carbon, evaluated on 14 surface samples by Leishman (1983), lies between 0.020 and 0.055 wt. %.

Mineralised ironstones show distinct and transitional chemical differences to barren examples. They are quartz-rich, with SiO_2 between 22 - 41.4 % (and even higher in Area 251 ironstones — Wall (1986)). Conversely, weakly mineralised to barren hematitic ironstones (Au < 0.5 ppm) are silica depleted, SiO_2 = 7.98 - 32.69 %. Ba in surface ore is commonly greater than that of adjacent barren ironstone, but this is not the case at depth, where they are approximately equivalent. This phenomenon may be due to Ba adsorption during the formation of gossan, as has been noted by Orridge (1980) for the nearby Pegmont deposit. At Area 257, Au is positively correlated at the 90 % significance level with Cu, W, Y, SiO_2 and MnO (e.g., Fig. 6.9) , and negatively correlated with TiO_2, $Fe_2O_3^{tot}$, P_2O_5 and Zr (e.g., Fig. 6.9 , Appendix 4). Mineralised ironstones have unusual LREE-depleted patterns, whereas nearby barren ironstones have flat to LREE-enriched patterns (see also chapter 8).

Along-strike Trends: Some systematic trends are evident in the 6.5 km mineralised segment of the Western Hematites, using surface sample data from Leishman (1983) and the Cyprus Minerals geochemical files. There is a southward trend of increasing Ba (average 222 ore =

670 ppm) and total REE (158.3 ppm) compared to Areas 251 and 257 (Ba = 22 ppm, ΣREE = 30.7 ppm) (Fig. 6.10).

	Mineralised Ironstone (257)	S.D.	Proximal barren ironstone	S.D.	Distal massive ironstone	S.D.	Distal cherty BIF	S.D.
%								
SiO_2	27.63	4.40	16.05	7.92	15.93	8.23	50.64	4.56
TiO_2	0.06	0.05	0.14	0.07	0.23	0.11	0.4	0.23
Al_2O_3	0.48	0.39	1.23	1.88	0.83	0.93	7.16	3.94
$Fe_2O_3^{tot}$	69.57	3.46	81.69	11.29	81.84	9.98	32.61	10.84
MnO	0.05	0.03	0.04	0.02	0.03	0.01	0.11	0.14
MgO	0.42	0.33	0.54	0.53	0.11	0.02	2.67	2.02
CaO	0.06	0.04	0.3	0.47	<0.02	-	1.41	1.45
Na_2O	0.32	0.55	0.43	0.68	<0.3	-	0.75	0.59
K_2O	0.05	0.03	0.11	0.11	0.16	0.19	2.13	2.23
P_2O_5	0.01	0.01	0.12	0.24	0.06	0.02	0.28	0.2
loss	0.38	1.99	-0.19	1.25	0.66	0.39	2.04	0.94
ppm								
Au	4.63	3.7	0.18	0.12	0.1	-	<0.1	-
Cu	9666	6498	1551	2036	15.7	7	121	227
Pb	1	1.7	6	8.8	<2	-	1	0.4
Zn	3	3.9	5.9	8.4	5.7	-	19	12.9
Ba	14	18.2	11	6.3	451	411.6	2215	2686.0
Sc	2	2.5	4	4.5	6	3.1	10	5.6
Ni	15	10.3	14	10.9	7	2.6	35	17.9
V	15	5.4	45	32	59.5	40	130	68.2
Rb	12	17.1	7	12	17.0	5	83	90.3
Sr	2	0.1	3	1.4	19	10.8	56	75.6
W	191	287.3	56	51.1	5	4.4	7	3.3
Mo	15	16.7	75	142.9	1	0.6	1	0.4
Zr	12	17.0	30	28.3	49	20.7	91	49.0
Y	39.7	41.9	19.6	13.1	17.0	13.7	19.5	15.3
Nb	4.0	3.7	3.0	2.6	<2	-	8.0	3.6
Bi	2	2.4	2	1.9	<1		2	0.4
La	5.6	-	6.4	-	7.7	-	47.9	-
U	7	-	4	-	-	-	-	-
Th	<3	-	<3	-	-	-	-	-
La/Y(chond.)	1.13	-	4.68	-	5.37	-	22.61	
n	8		10		5		17	

Table 6.2 *Geochemical averages for four ironstone types in the Starra area (n = number of analyses).*

Regionally Developed Ironstones

Distal, barren, massive ironstones: These are chemically similar to the ore environment hematitic ironstones. They are iron-rich, with $Fe_2O_3^{tot}/(Fe_2O_3^{tot}+SiO_2)$ (referred to hereafter as the "**Fe Number**") ranging from 0.72 - 0.95. MnO, MgO, CaO, Na_2O, K_2O and P_2O_5 are all close to the detection limits in the five weathered samples analysed. Weathering precludes an analysis of Cu, Pb and Zn. Resistate ore elements W and Mo are depleted

relative to ore environment ironstones. All other trace elements are at comparable levels, with the exception of Ba and the REE. Ba is enriched relative to barren ironstone north of Area 244, but similar to values in barren ironstones south of this area (Fig. 6.10). Chondritic La/Y ratios partly overlap with barren ore environment ironstones, ranging from ~2 to 7.

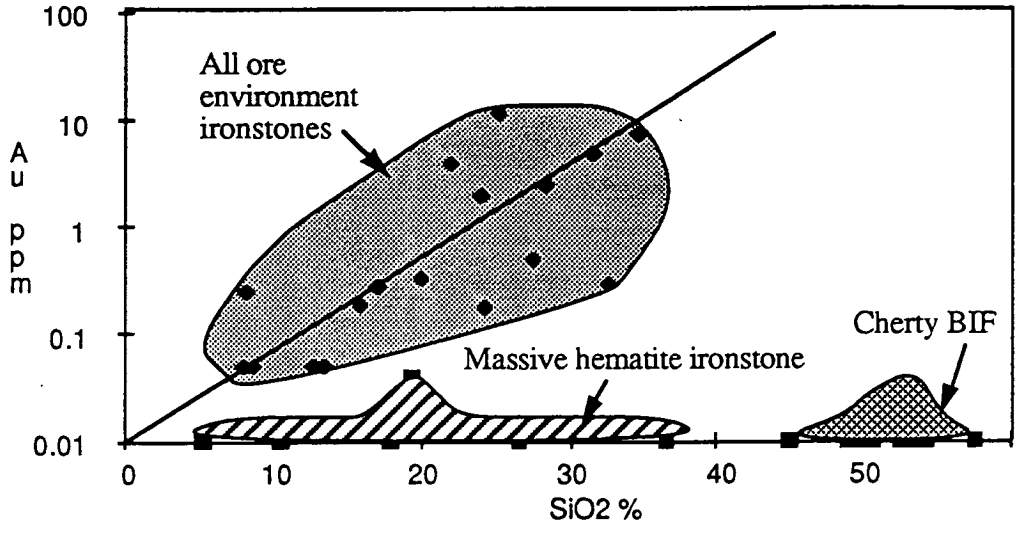

Figure 6.9 *Au plotted against SiO_2 for the major groups of ironstone: a strong positive correlation is evident for the ore environment ironstones.*

Cherty BIFs: Distal, barren, massive, hematitic ironstones grade texturally and chemically in to cherty BIF, a sample group with distinctive chemistry. The dominance of quartz banding in the latter is reflected in increased SiO_2 (44.95 - 57.52 %), and Fe Numbers between 0.47 and 0.62. Al_2O_3, TiO_2 and Zr are markedly enriched over all other ironstones. ΣREE and chondritic La/Y increase in proportion to Al_2O_3. Other distinctive features are erratically high P_2O_5 (0.02 - 0.65 %), MnO (0.01 - 0.58%), CaO (0.04 - 4.65%), Ni (8 - 70 ppm) and V (35.3 - 316 ppm). Alkali elements are strongly enriched over the other ironstone groups, e.g., K_2O (0.15 - 8.86 %), Rb (4 - 351 ppm) and particularly Ba (244 - 10551 ppm).

Along-strike Trends: Changes in chemistry are transitional between hematitic ironstone and cherty BIF, demonstrated in the systematic surface sampling of Area 186 (Figs. 6.11 & 6.12). The term "Area 186" describes a discrete 2 km length of the Eastern Hematites, sinistrally folded about a steeply plunging D2(LP) fold. A central 5 – 10 m thick hematite facies thins along strike north and south in to meso-banded cherty BIF and tourmalinite, before lensing out completely in a sequence of siltstone and cross-bedded sandstone (in places scapolitic).

Fig. 6.12 illustrates that Au in the Area 186 sub-basin is elevated but erratic. SiO_2, Ba, Zr, chondritic La/Y and K_2O all increase towards the cherty facies, whereas Fe_2O_3 decreases and MnO shows no change. The prevalence of tourmalinites and disseminated

tourmaline in cherty iron formation suggests that boron is also enriched towards the edge of iron deposition, although this element was not analysed.

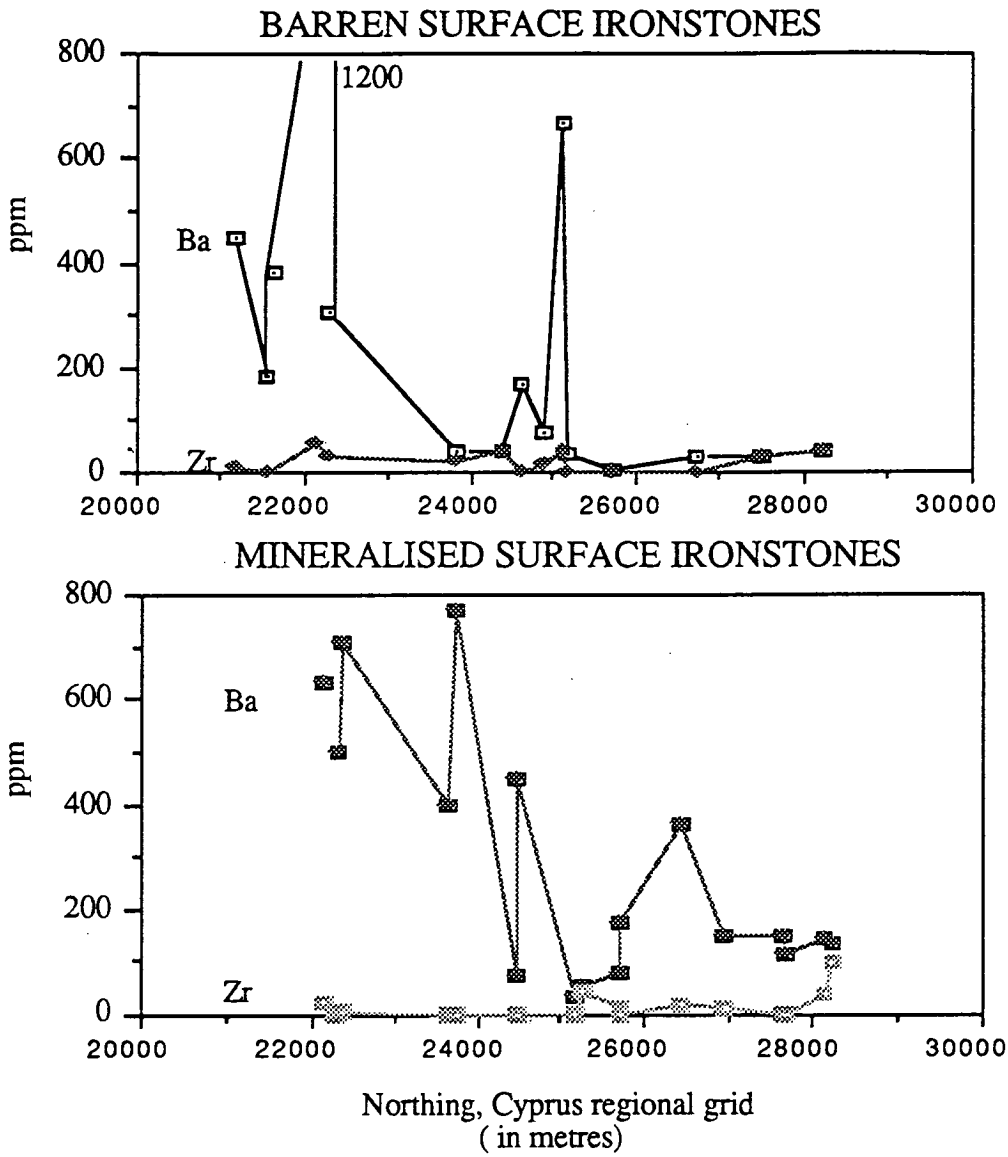

Figure 6.10 *Ba and Zr variation in surface ironstones, from data within Cyprus Minerals geochemical files. The samples have been separated into mineralised (> 0.5 ppm) and non-mineralised groups. Both groups display a distinct southward increase in Ba, with no corresponding increase in the clastic sediment indicator Zr.*

Chemical Discrimination of Ironstone Types

The previous discussion has demonstrated that subtle but significant differences exist amongst the four analysed ironstone types in the Starra area. W, Mo, La, Y, Fe, Si, Zr, Ba, Al, Ti and Au are the most useful elements for chemical discrimination. Elements which do not resist weathering are not useful for this study, eliminating Cu, Pb, Zn ± Co, Ni and Mg (which have carbonate and sulphide hosts). The discriminants assume that the ironstones are sedimentary, or sedimentary-hydrothermal, but do not rely on a similar origin for mineralisation: this approach to discrimination is intended to be non-genetic.

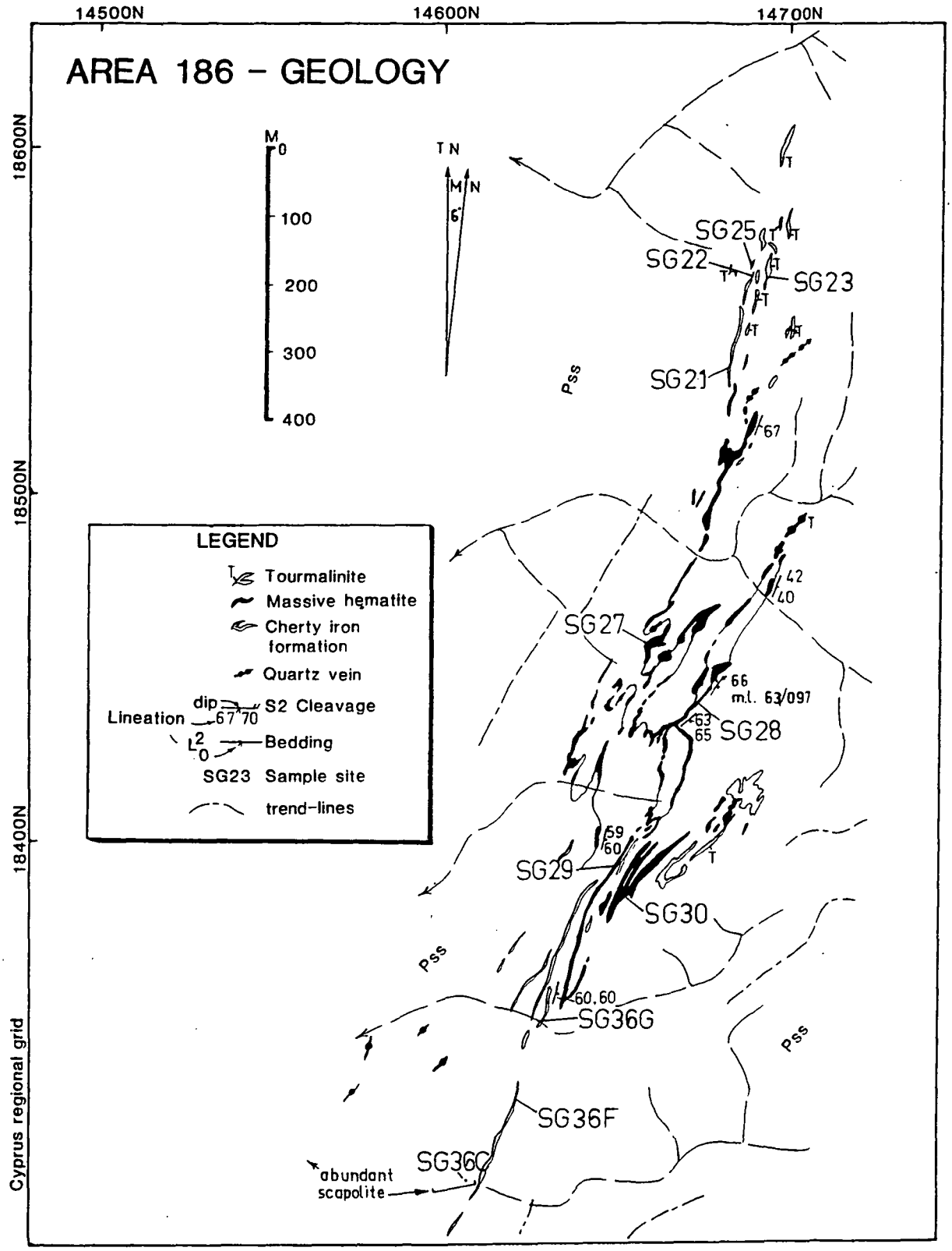

Figure 6.11 *Geology of Area 186, Eastern Hematites, aproximately 3.5 km south east of Area 222. A discrete segment of iron formation occurs, which is zoned from cherty banded margins to a massive hematitic centre. Sample locations are also shown. The map is based on outcrop mapping by Leishman(1983), modified by additional mapping.*

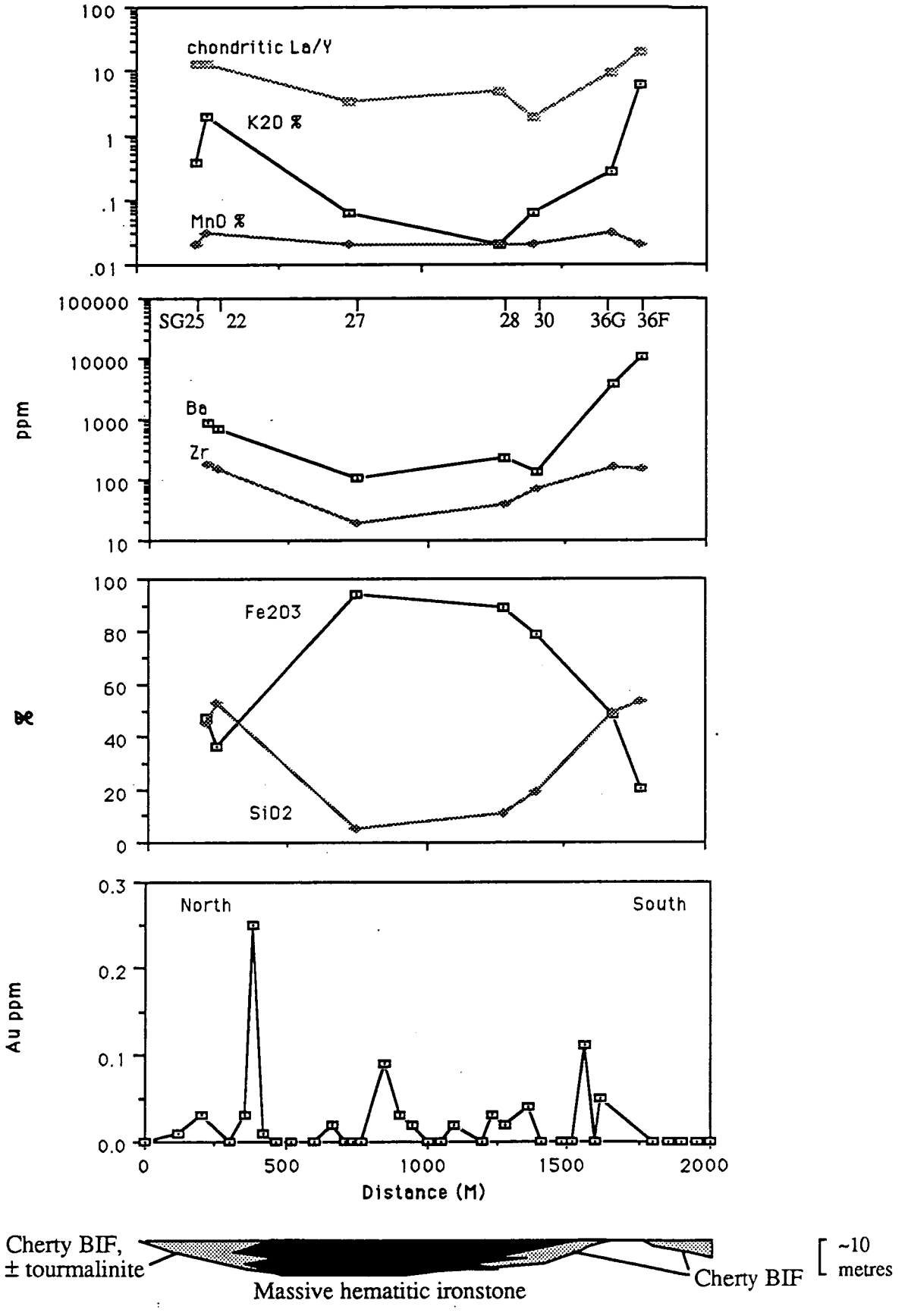

Figure 6.12 *Geochemical profiles of ironstone at Area 186, measured as if unfolded, illustrating the distinct changes between massive continuous hematitic ironstone, and the cherty lateral equivalents. The latter contain strongly enriched Ba, K, Zr and SiO2 over the former. Au is more consistently enriched in the massive zone, whilst Mn shows no difference between the two facies. These elemental changes cannot be a function of dilution by increasing Fe, because the amount of change is too great; for instance, K increases 200 times, whereas Fe only doubles. See Fig. 6.11 for detailed geology and sample locations.*

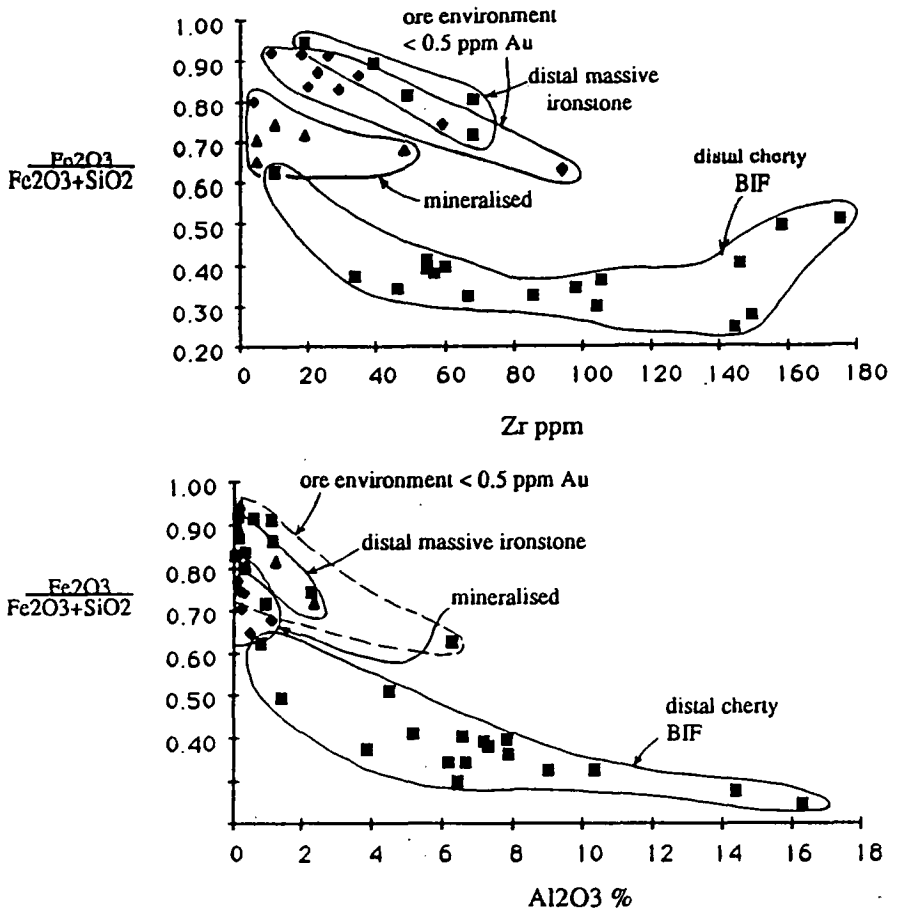

Figure 6.13 *A comparison amongst the four Starra iron formation types, using Zr and Al2O3, elements which reflect the chemical effects of clastic sediment addition. Plotted against Fe2O3/(Fe2O3+SiO2) they indicate that (1) most ore environment ironstones have low clastic sediment contributions (2) massive barren hematitic ironstones, distal to ore, have low to intermediate contributions, and (3) cherty BIFs form an array trending away from ore ironstones to very high sediment levels (e.g., to 16 % Al2O3 and 180 ppm Zr). These patterns can be used to infer the paleo-basin geometry, as decreasing clastic sediment is found towards the centre of most sedimentary basins.*

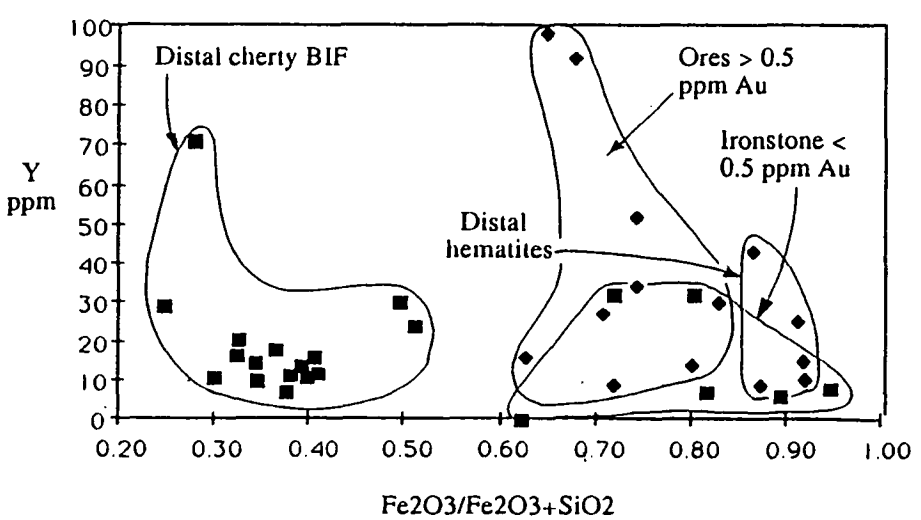

Figure 6.14 *Cherty distal BIFs are clearly differentiated from the other ironstone types on the basis of their Y - Fe2O3/Fe2O3+SiO2 patterns. Many mineralised ironstones are Y-enriched at lower Fe numbers than the massive hematitic varieties, but this is not a reliable discriminant.*

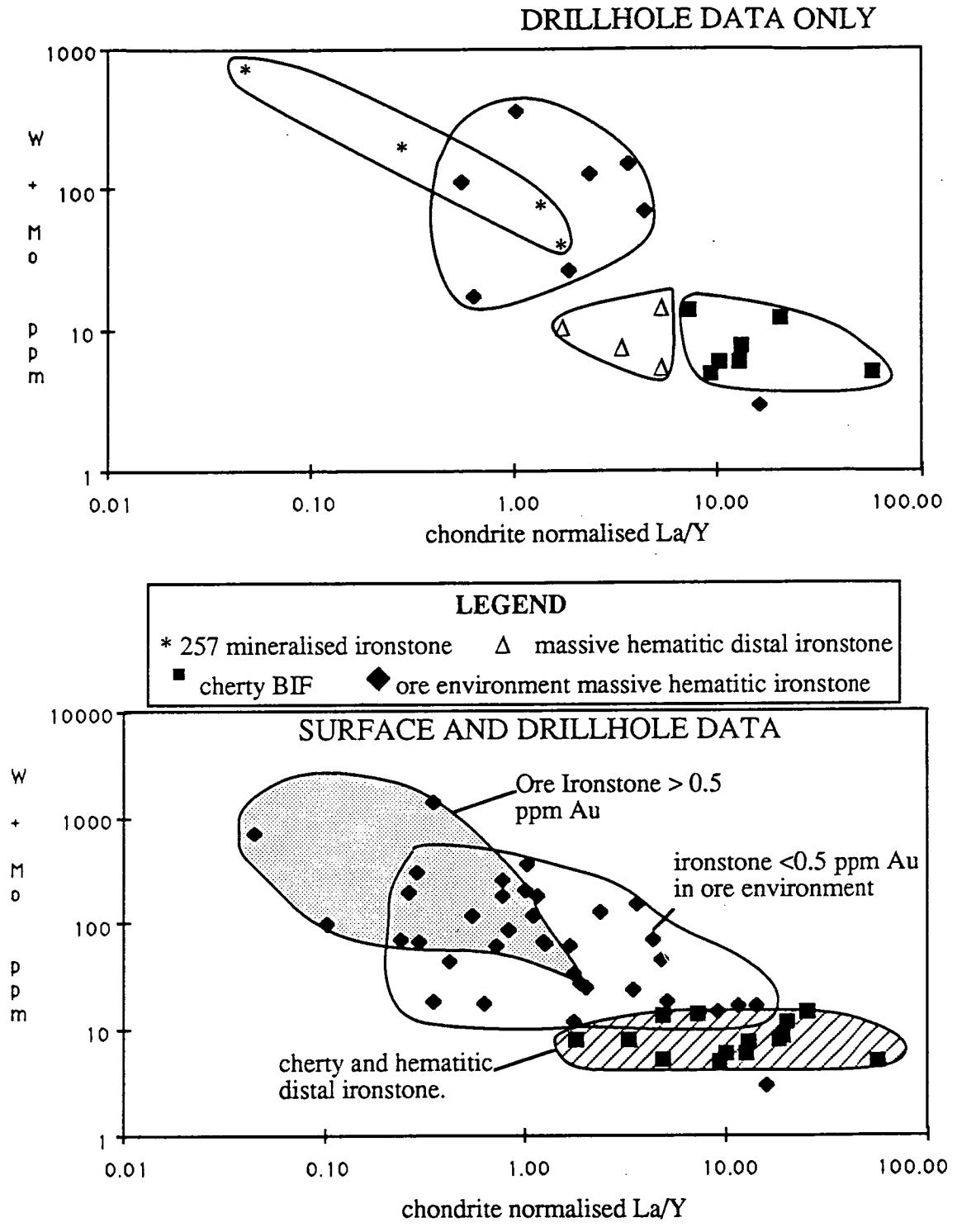

Figure 6.15 *(W+Mo) versus chondritic La/Y is the most successful plot for discrimination of Starra iron formation types. Initially the fields were formulated using only diamond-drilling and percussion samples (top). The groupings were tested by subsequently plotting surface data from the Eastern and Western Hematites, obtained from Cyprus Minerals geochemical files (bottom). In particular barren ironstones (<0.5 ppm Au) in the ore environment can be distinguished from barren ironstones well-removed from ore, although they are geochemically very similar in other regards.*

The virtues of element ratios which were employed to highlight the differences between competing chemical influences are discussed below:

Fe Number versus Zr and Al_2O_3 (Chemical-Clastic Influences): Zr, Al, Ti, La and chondritic La/Y should increase with increasing clastic content in ironstones. Elevated Fe is a feature of gold-poor, hematitic ironstones deposited away from the Fe-basin margin. Distal cherty BIF is discriminated from the other ironstone groups using combinations of these elements because of its high clastic element content (Fig. 6.13). Mineralised ironstones have the consistently lowest Zr and Al_2O_3 values.

(W+Mo) versus La/Y (Variable Dispersion of Elements Associated With Mineralisation): The elevation of Y differentiates mineralised ironstones and distal cherty BIFs from the massive ironstone groups (Fig. 6.14).This feature has been combined with W and Mo to successfully discriminate the four ironstone types (Fig. 6.15). Both W and Mo are used because they occur in solid solution in the ores in the scheelite-powellite series (Sn could also be added to this index given enough data, as it is anomalous in the ores (Wall 1986), and is commonly associated with W in hydrothermal systems). The applicability of Fig. 6.15A to weathered ironstones was tested by including 26 barren and mineralised surface ironstones from the Cyprus Minerals geochemical files, analysed for a large suite of elements by Analabs in March 1985. This test confirmed the usefulness of the diagram for discrimination (Fig. 6.15B). Mineralised and "barren" samples from the ore environment partly overlap because 0.5 ppm Au was an arbitrary economically-imposed means of separation. In fact the diagram indicates that chemical change is transitional between the two groups. All ore environment ironstones contain (W+Mo) > 15 ppm, and extend to very low La/Y, whereas cherty and hematitic distal ironstones have (W+Mo) < 15 ppm, and La/Y > 2.0. Even ore environment ironstones with Au < 0.1 ppm, which would be ignored in an exploration program, possess elevated W, Mo and Y, suggesting that the latter elements disperse beyond Au in the Starra hydrothermal system. Au should not be the only element on which the prospectivity of a given ironstone is judged.

TROUGH TANK

General

Two distinct ironstone types are distinguished at Trough Tank: (1) Mineralised to barren magnetite-quartz-apatite BIF: oxide facies (2) Weakly mineralised, anthophyllite-cordierite-magnetite-apatite±chrysotile BIF: magnesian carbonate-silicate facies.

Spatial Distribution of Gold and Copper

Trough Tank ironstones contain primary sulphides below an average depth of 35 m, unlike the deeply weathered Starra ores. This has permitted a detailed study of Cu versus Au behaviour in three dimensions, impossible at Starra.

UNIT	WEIGHTED MEAN	Cu%/Au ppm
BIF 1 (n = 184) Au	0.17 ppm	1.24
Cu	0.21%	
BIF2 (n = 216) Au	0.55 ppm	0.96
Cu	0.53 %	
Silicic alteration (n=22)		
Au	0.74 ppm	1.35
Cu	1.46 %	

Table 6.3 *Cu and Au statistics for the Trough Tank "Central Anomaly", compiled from CSR drill-logs. Refer to Fig. 6.16 for the definitions of BIFs 1 and 2.*

Cu and Au are directly correlated, although the degree of dependence varies between the three major BIF horizons. The thickest BIF (BIF 2 on Fig.6.16) has the lowest average Cu %/Au ppm ratio (0.90, compared to 1.22 in BIF 1) and therefore has attracted more exploration interest (Mr Bob Osborne, Placer Minerals, pers. comm.1987). Au and Cu grades are lower at Trough Tank than at Starra (Table 6.3).

A useful illustration of Cu-Au variance is found in BIF 1, hole TNQ6 (Figs.6.16 & 6.17), where the ratio varies according to distance from a "pipe-like" zone of discordant mineralisation. The "pipe" contains the highest and most uniform Au values (mean Cu/Au = 0.35, ranging between 0.28 - 0.44). Altered BIF above the "pipe" has a mean of 0.90, while that of unaltered overlying BIF is 0.85, i.e., identical. 8 samples from the eastern BIF limb, interpreted as distal to the "pipe", average 3.92. In summary, the greatest proportion of Au to unit Cu is deposited in the discordant pipe, less in BIF above it, and even less in the distal BIF.

Cu/Au ratios were assessed in detail for BIF 2, where an enormous variation occurs, even at one stratigraphic level. The ratio varies between ~ 0.5 and as high as 12.5 in BIF 2, although most values are below 4.0. Assay intervals of 2 m were composited and averaged for each BIF intercept, and plotted (using the interpreted structure) as points on the original BIF surface, rotated to horizontal (Fig. 6.18). For simplicity only holes penetrating the western limb of the syncline were used. In all figures, the depth from the Mesozoic unconformity to the top of the BIF unit increases eastwards. The average Au value and metal factor (averaged grade times true width) for each intercept were treated similarly, to gauge the total Au volume at any place (Figs. 6.19 & 6.20).

A systematic Cu-Au pattern resulted. Two Au-loci are apparent in Fig. 6.19, separated by a less-mineralised area. The northern zone is larger with lower Cu/Au averages. In both areas Au, Au metal factor and Cu/Au have a linear northwest-trending distribution, suggesting a fracture control to gold deposition. This direction is at a marked angle to the D2 fold axis and stretching orientation, drawn in Fig. 6.18.

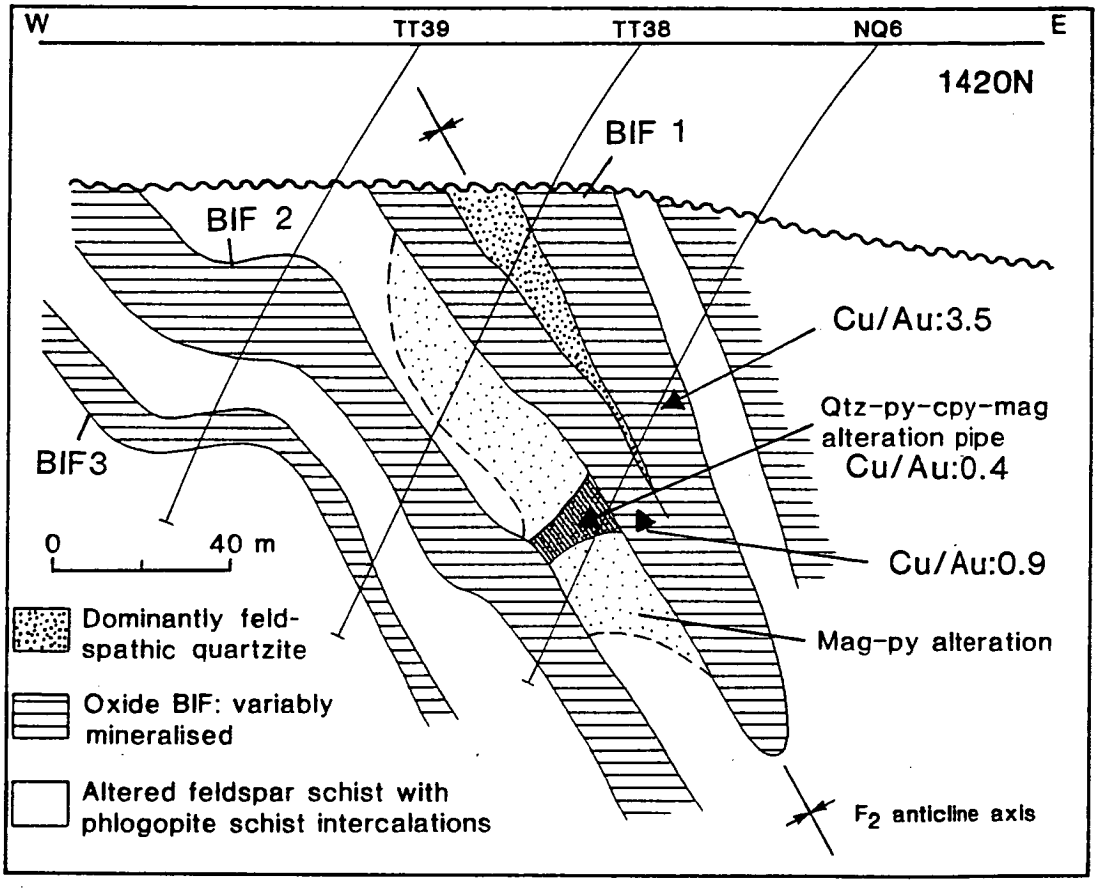

Figure 6.16 *A geological section along line 1420N, Trough Tank. Cu%/Au ppm ratios are also shown for selected BIF and discordant or pipe-like mineralisation intercepts. Discordant zones have the lowest Cu/Au ratios, BIF close to these zones have low values, which increase in BIF with distance from the pipe.*

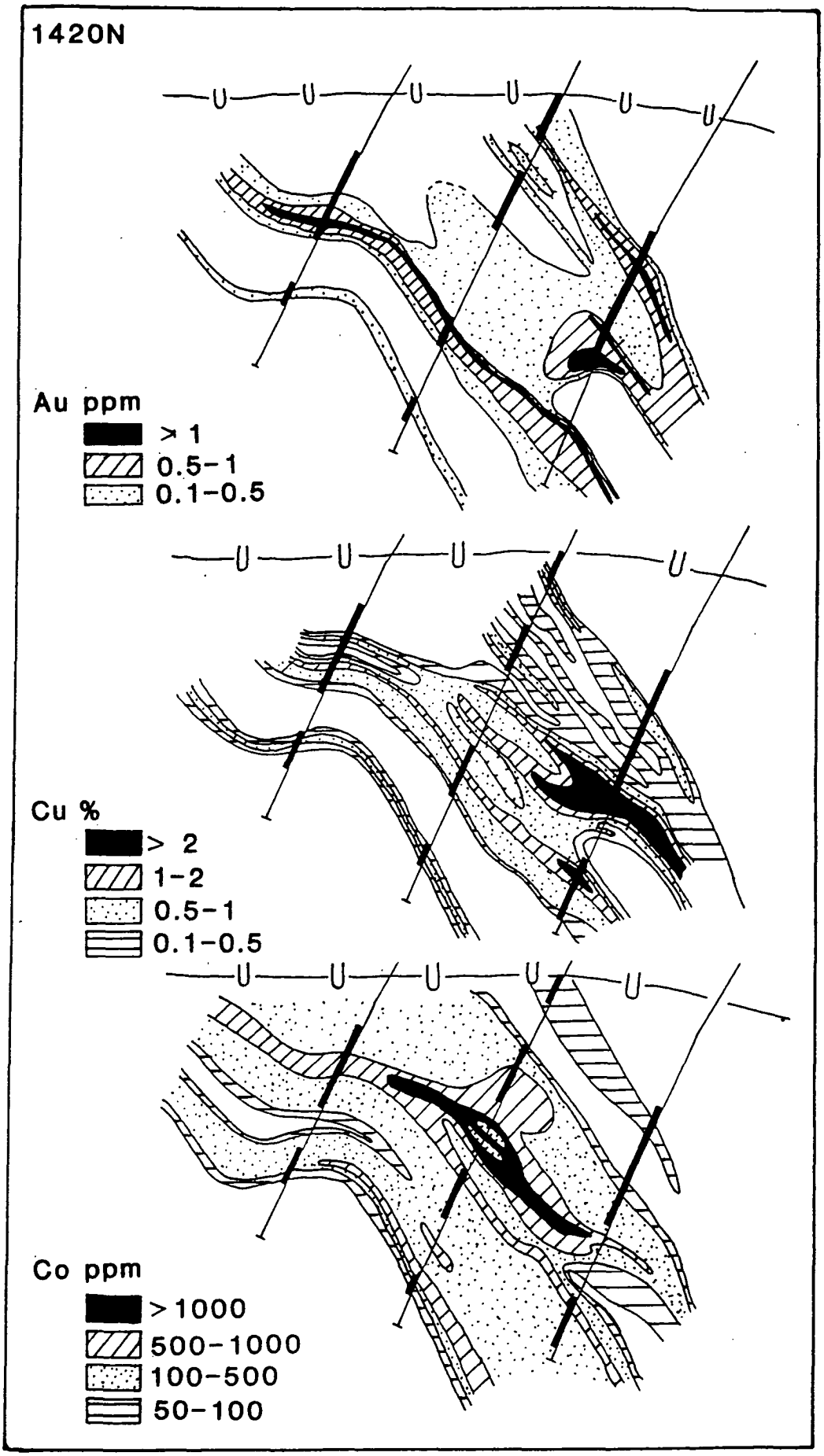

Figure 6.17 *(1420N) Contoured geochemical sections of Au, Cu and Co for Trough Tank. The intercepts of ironstone are shown by thick black lines on the drillholes. Highest grades of gold are strongly linear within the iron-formations, as well as concentrating within the discordant pipe. Cu is most strongly enriched in the discordant pipe. Co enrichment forms a broad haloe with the highest values between BIFs 1 and 2, interpreted as a thick zone of alteration-related pyrite and carbonate.*

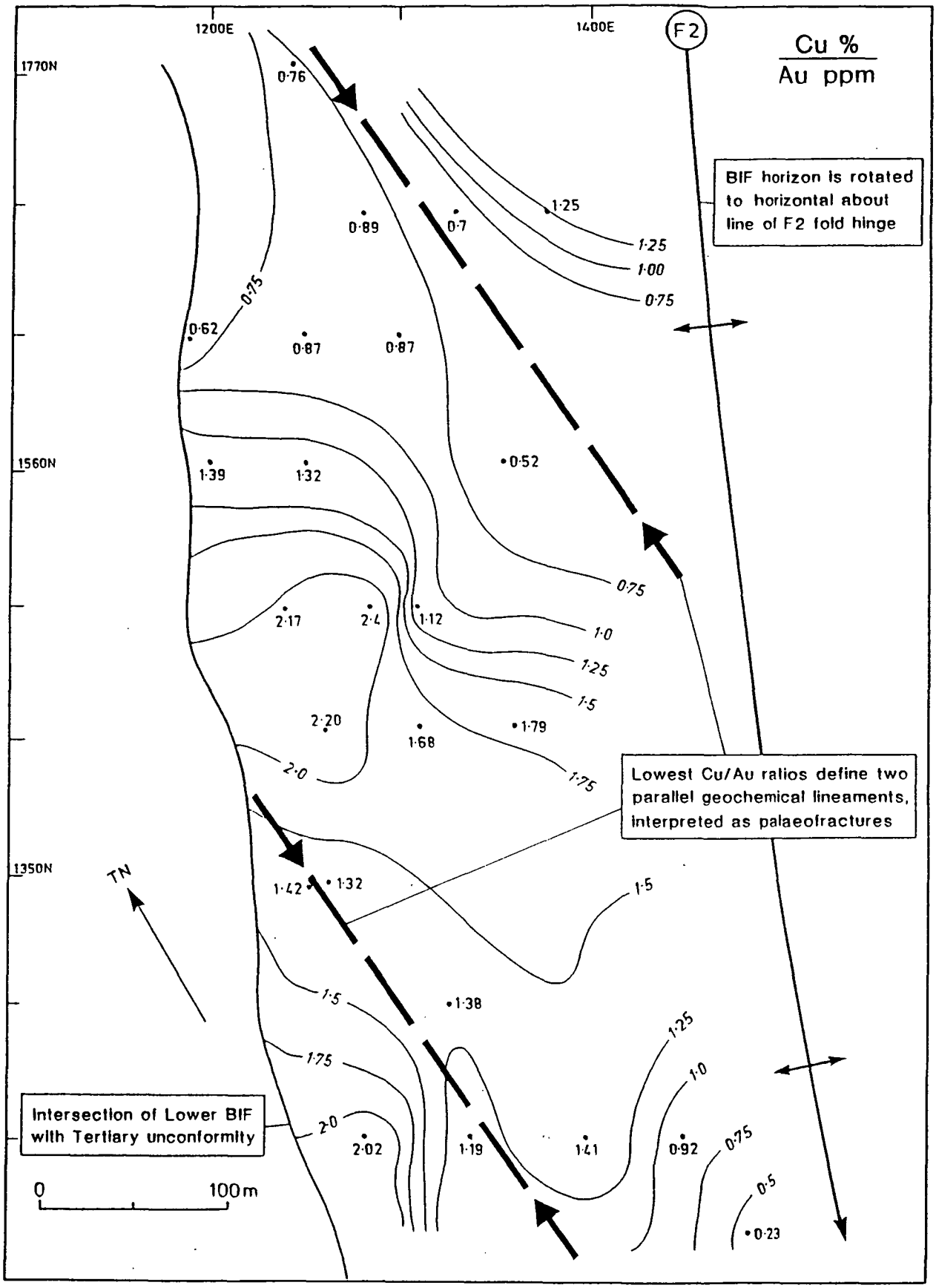

Figure 6.18 *Cu%/Au ppm, averaged for BIF 2, Trough Tank. The diagram covers the western limb of the major syncline, here rotated to the horizontal. Two centres with the lowest Cu/Au ratios are interpreted as proximal to the hydrothermal fluid source. Notably the contoured trends do not align with the D2 fold axis or the stretching direction. 2 m wide diamond and reverse circulation drill intercepts were used to construct this plot.*

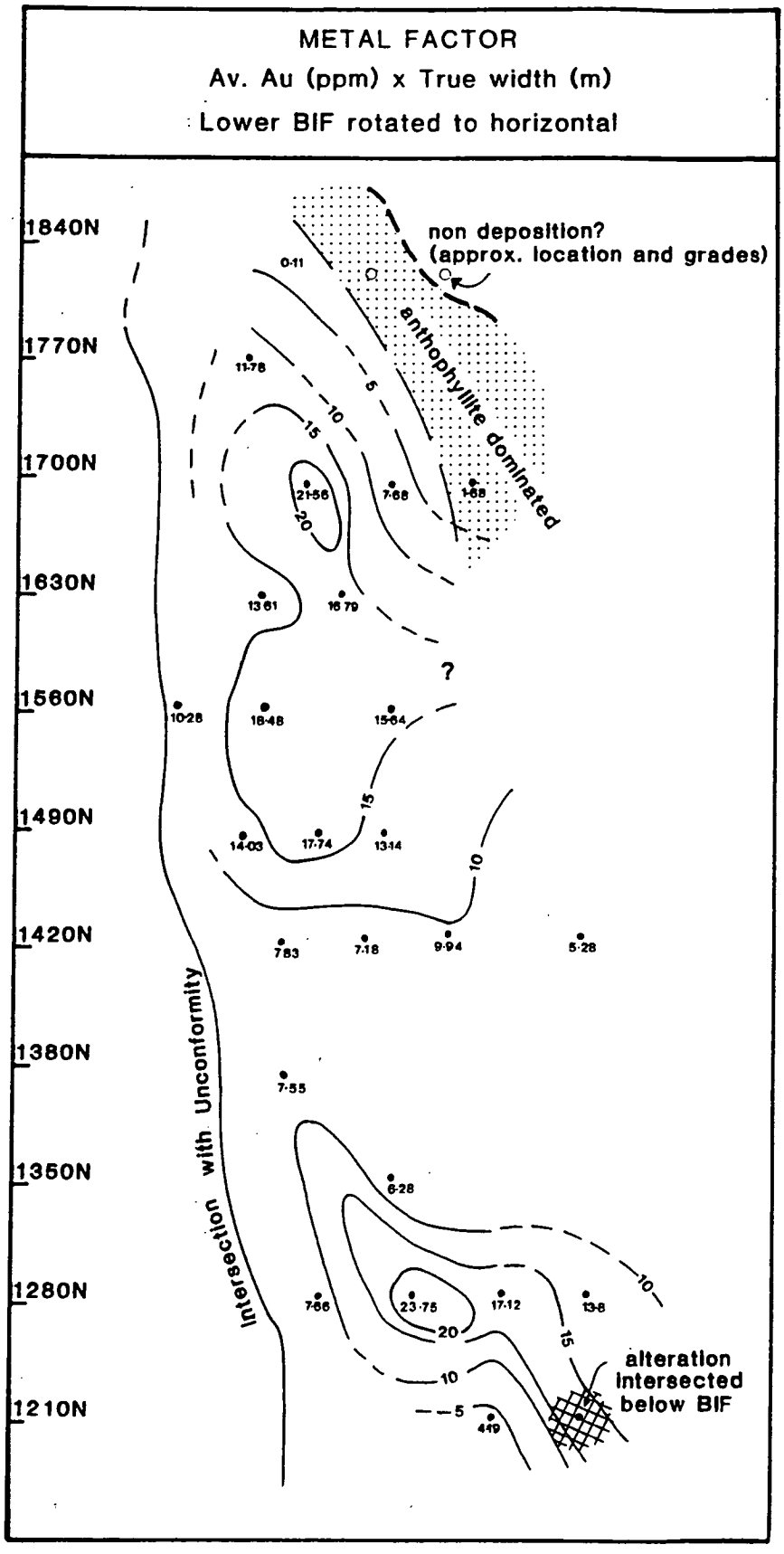

Figure 6.19 *Au metal factor plan (average grade in ppm X true width in metres) of BIF 2, delineating two mineralisatrion centres. Metamorphic Mg-silicate facies BIF occurs at the edge of the oxide facies metal factor anomalies in the north. This change may represent an original carbonate enrichment zone in the BIF.*

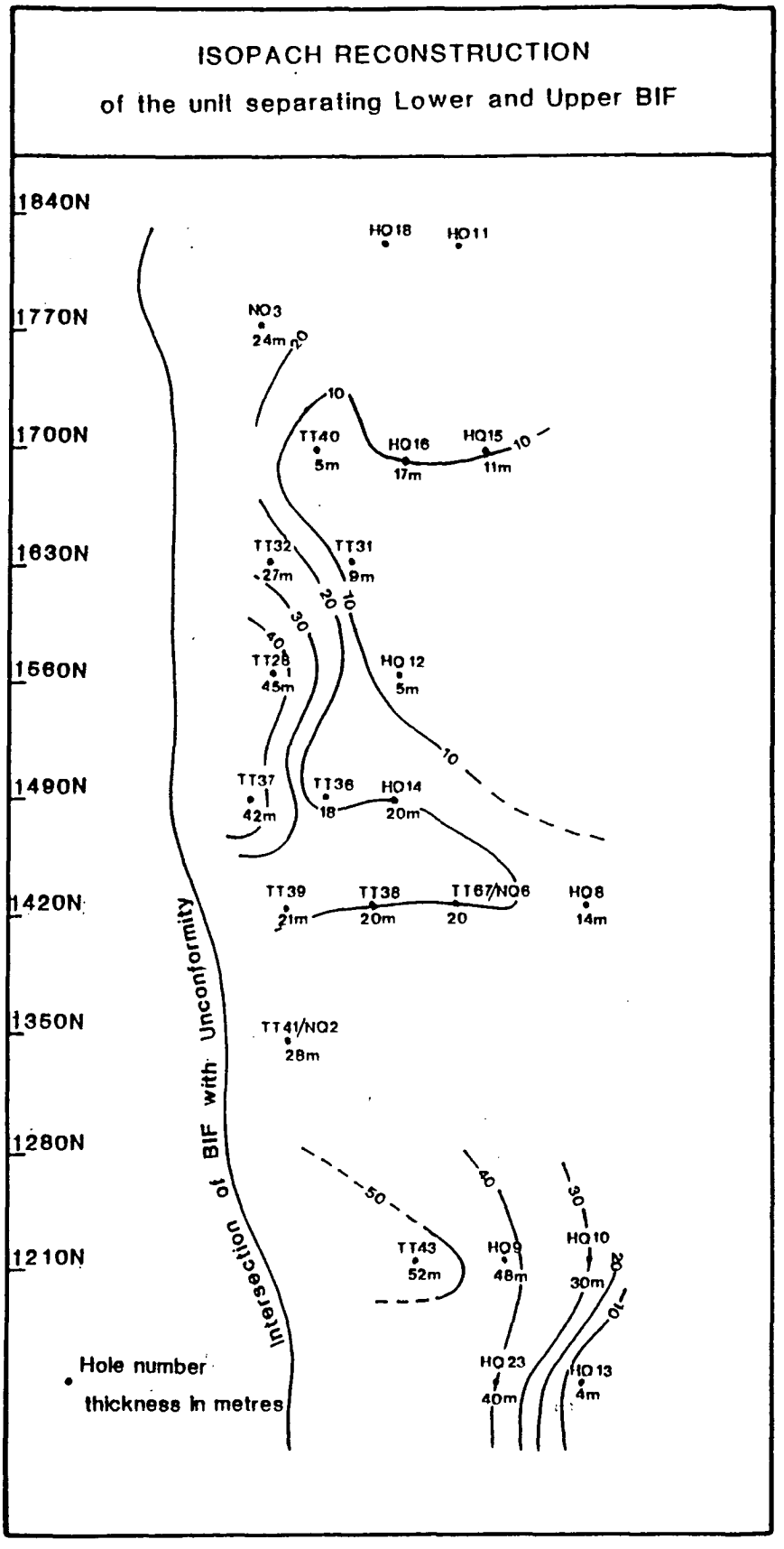

Figure 6.20 *An isopach reconstruction of the feldspathic schist which separates BIFs 1 and 2 (see Fig. 6.16). Thickness changes are surprisingly great. They suggest that BIF deposition took place in north-westerly orientated steep-sided (faulted?) troughs.*

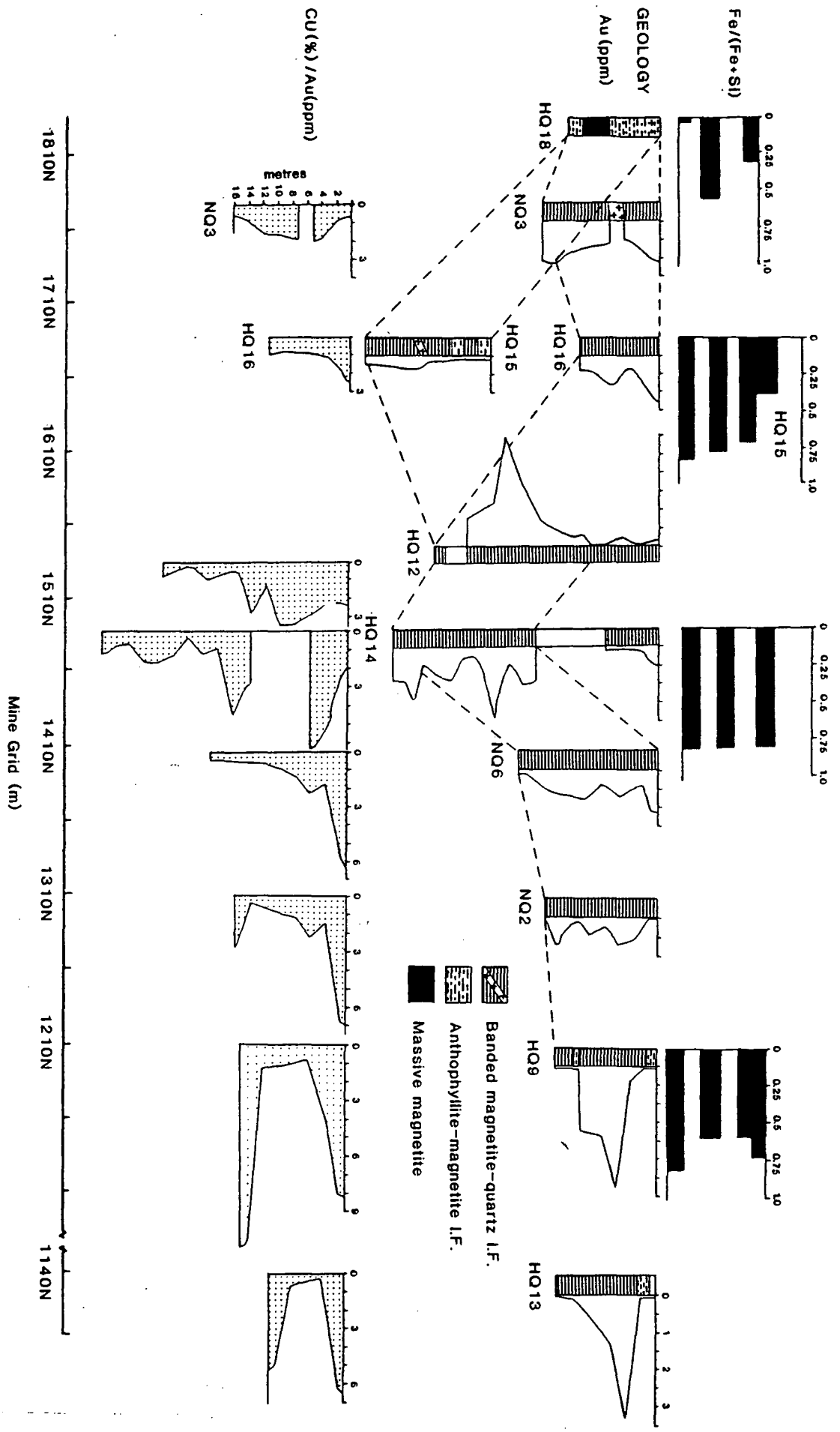

Figure 6.21 *A long section north-south along BIF horizon 2, Trough Tank. Regular patterns occur in Cu %/Au ppm acoss the width of individual BIF intercepts. These patterns evolve from south to north.* $Fe_2O_3/(Fe_2O_3+SiO_2)$ *values are also shown, but have little correlation with Au.*

Large changes in thickness are evident in the sediment package separating BIFs 1 and 2 (Fig. 6.20). The changes parallel the geochemical northwest fabric, and are considered too large and random to be explained by subsequent deformation. Their near-coincidence with the highest Au and Cu grades supports a synsedimentary fault control on BIF and ore deposition.

A comparison of Cu/Au ratios across individual BIF intercepts reveals reoccurring patterns (Fig. 6.21). In particular, holes south of 1490N (Trough Tank prospect grid) have tops which are commonly enriched in Cu relative to Au, grading to Au-rich centres. These features are evidence for two dominant and competing loci, each with its own metallogenic history. Between the two centres the BIFs have interfingered, imparting the characteristics of

	Oxide facies BIF	S.D.	Mg-silicate BIF	range of Mg-BIF**
%				
SiO_2	24.31	15.08	46.76	25.3-69.7
TiO_2	0.06	0.06	0.04	0.01-0.09
Al_2O_3	1.22	1.99	3.79	0.19-15
$Fe_2O_3^{tot}$	70.26	17.18	39.04	3.14-59.4
MgO	0.73	0.61	3.69	0.77-8.8
MnO	0.05	0.03	0.09	0.04-0.18
CaO	1.12	0.57	1.62	0.66-4.06
K_2O	0.11	0.12	0.64	0.01-2.68
Na_2O	0.7	1.17	1.18	0.1-5.15
P_2O_5	0.78	0.35	0.4	0.02-0.61
LOI	-0.48	-	1.64	0.01-2.66
ppm				
Au	0.5	0.65	0.02	0.005-0.08
Cu	3564	4252	1319	12-6416
Co	106	98	185	18-480
Pb	9	8.2	9	0-16
Zn	14	8.1	21	6.0-42
V	93	51.9	237*	-
Ni	19	21.9	42	2-125
Sc	3	3.33	5	2.0-20
W	8	6.5	-	-
Mo	3	4.2	-	-
Sn	2	3.8	-	-
Ba	9	10.68	31	2.0-90
Rb	27	19.6	45	8-115
Sr	9	5.1	9	0.0-22
Zr	22	36.9	11	2.0-18
Y	11	10	4	0.5-18
Nb	4	1.5	8	1.0-16.0
As	7	8.5	-	
n	24		5	

Table 6.4 *Average geochemistry of Trough Tank oxide and silicate-rich BIFs. All analyses represent half or quarter core composites over a minimum of 2 m of diamond drill core. * One sample only.** Ranges are provided, rather than standard deviations, because the sample population of this heterogeneous rock-type is small.*

both sources to the one BIF interval.

Major and Trace Element Variation

Oxide Facies BIF

The oxide facies iron formations have a mean ($Fe_2O_3^{tot}$ + SiO_2) of 94.5 %, (85.11 – 99.72 %), and an Fe Number averaging 0.74. These features are very similar to mineralised Starra ironstone.

The remaining 5.5 % includes percent values of Al_2O_3, CaO, MgO and Na_2O, with TiO_2, MnO and K_2O all less than 0.15 % (Table 6.4). A major contrast with Starra ironstone is the presence of an average 0.78 % P_2O_5 (range 0.11 - 1.48 %). Individual analysis of mesobands in sample TT1 (Appendix 5) revealed that 88 % of this occurs in magnetite bands. Elevated P_2O_5 has also been noted from the "pipe-like" siliceous zones below some BIFs (see chapter 5). Au, Cu, Co and V are enriched over their crustal abundances, while Pb, Zn, Zr, Ba, Rb and Sr are depleted.

Magnesian-silicate Facies BIF

Mg-silicate facies BIFs form thinner lateral equivalents to the oxide facies. They are uniformily low in Au (0.01 - 0.08 ppm), but vary in Cu enrichment (12 - 6416 ppm) in the five averaged intercepts of Appendix 5.

The major element geochemistry (Table 6.4) is more variable than that of adjacent oxide facies, with ($Fe_2O_3^{tot}$ + SiO_2) = 72.84 - 95 70 %, Fe Number = 0.04 - 0.70. MgO-enrichment (0.77 - 8.88 %) is a key feature, accompanied by elevated V, Mn, Sc and Nb. Very low Al_2O_3 contents set these Mg-rich rocks apart from other magnesian lithologies in the Starra area (dealt with in detail in chapter 7), a feature responsible for the common dominance of anthophyllite in the metamorphic assemblage.

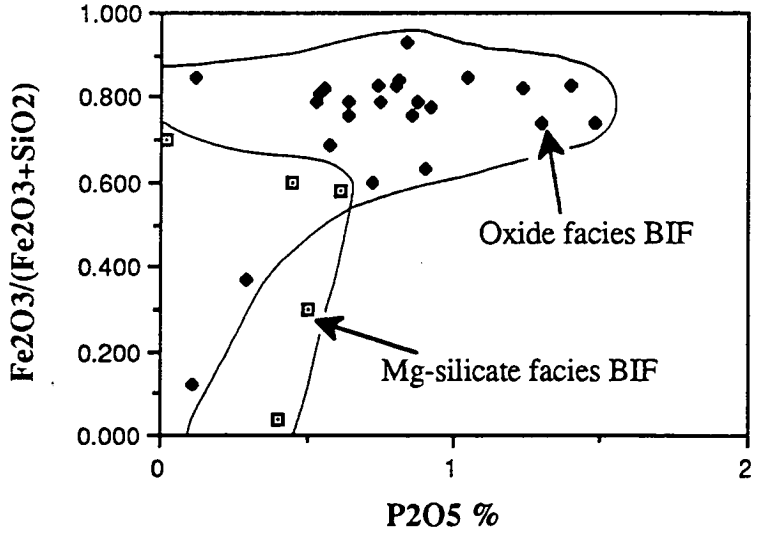

Figure 6.22 *P_2O_5 is enriched in oxide facies BIFs relative to anthophyllite-bearing Mg-silicate BIF.*

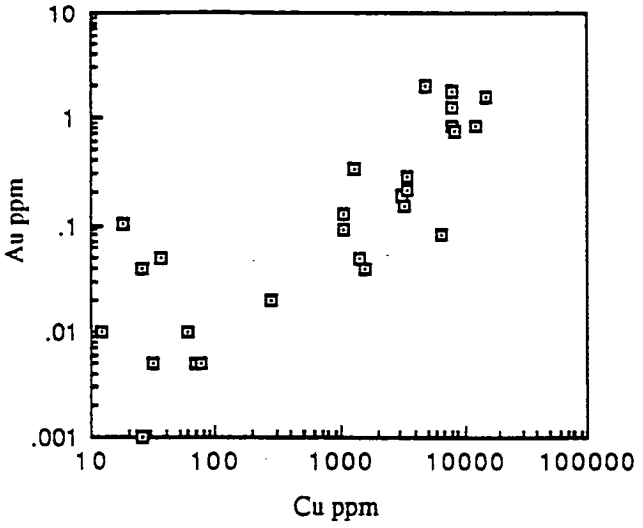

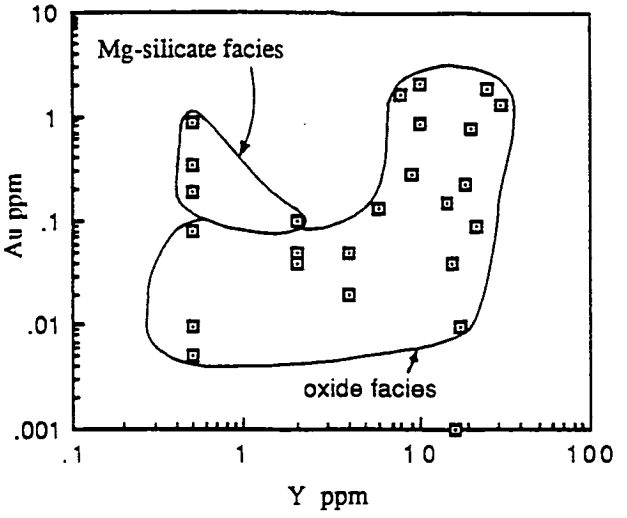

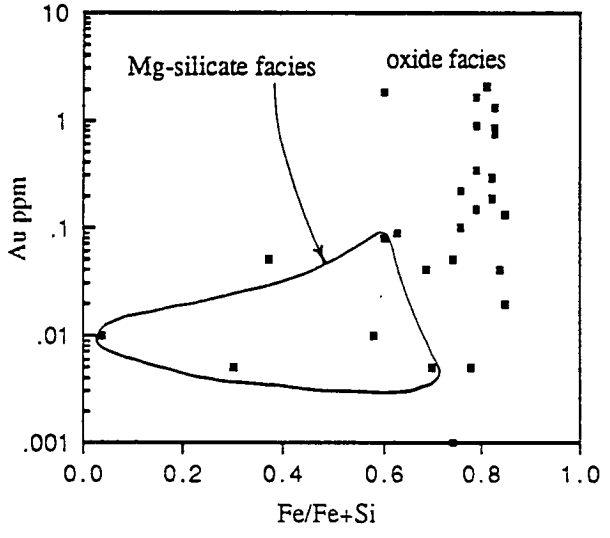

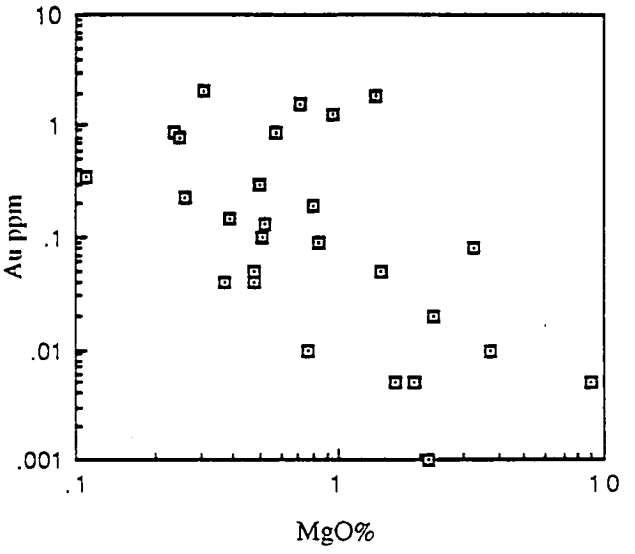

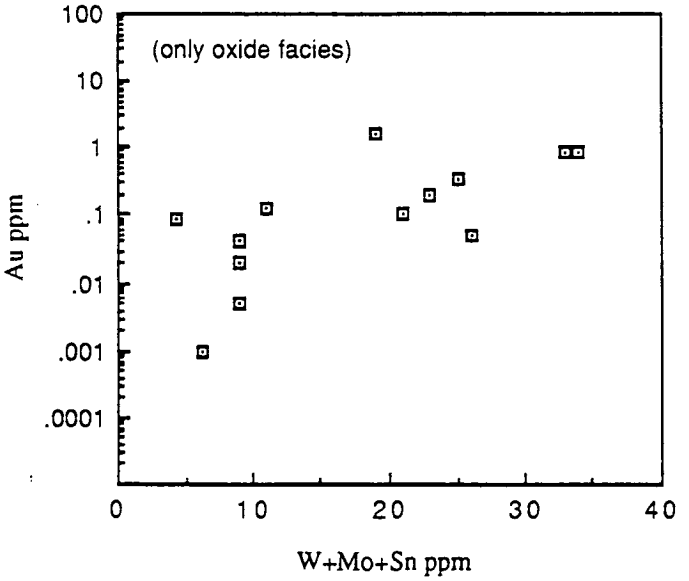

Figure 6.23 Variation of Au with other elements in Trough Tank BIFs.

Chemical Discrimination of Barren from Mineralised Oxide-facies BIF

Unlike Starra auriferous ironstone, Au-rich BIF is not consistently SiO_2-enriched. Fig. 6.23 illustrates that, while the Fe Number and Au show no statistically significant correlation, the best Au grades occur over a narrow Fe Number range of 0.79 to 0.83. Correlation analysis of oxide BIF (Table 6.5) indicated log-normalised Au to be positively correlated with Cu, Y and Mn (Ba, Sr, Pb, Ni, Nb, Zr, W, Mo and Sn were excluded because of omissions in the data set). A positive linear relationship is evident graphically (on limited data) between (W+Mo+Sn) ppm and Au (Fig.6.23), in parallel with Starra ironstone. Correlation analysis also found Co to be only weakly dependent on Au or Cu (Appendix 4), despite the anomalous levels in mineralised BIF and altered pyritic footwall. Unlike many hydrothermal systems, arsenic is correlated with Co, rather than Au, at the 95 % significance level.

Positive Correlations		
log(Au) —	log(Cu)	+0.95 (Fig.6.23)
—	Y	+0.37 (Fig. 6.23)
—	Mn	+0.54
Negative Correlations		
log(Au) —	TiO_2	- 0.42
—	MgO	- 0.62 (Fig. 6.23)
—	V	- 0.69
—	Sc	- 0.63

Table 6.5 *Element correlation of Au in oxide facies Trough Tank BIF (90 % significance level = 0.38, for n = 25).*

DISCUSSION

Previous Work

Leishman (1983) analysed a suite of surface ironstones from the Western Hematites and concluded that they were chemically unlike known iron formations of the world. He noted that "total iron oxides ranging from 48 to 98.5 % are uncharacteristically high for unenriched iron formations (usually 30 - 60%)", and concluded that the ironstones were metasomatically modified sedimentary BIFs. Laing et al. (1988) and Switzer et al. (1988) have argued (without chemical basis), that the ironstones are skarns, produced by the interaction of metamorphic/igneous fluids with the basal calcareous units of the Staveley Formation. Davidson et al. (1988), (in press), suggest that the ironstones are chemically-unmodified deformed exhalative precipitates.

Did the Starra Ironstones Form by Replacement?: Geochemical Evidence

Al_2O_3/TiO_2 ratios were examined for the different Starra rock-types (Table 6.6). Isocon analysis in chapter 5 demonstrated that of all elements in the footwall alteration,

Al_2O_3 and TiO_2 were least mobile, whereas Zr, Nb and Y were significantly leached. There is a very clear difference in Al_2O_3/TiO_2 ratio between ironstones (8 – 18) and all other lithologies (20 – 24.5). Under a replacement hypothesis the ratio in ironstones should be the same as in the replaced units, given that TiO_2 and Al_2O_3 have remained immobile. If mobility was occurring, a gradual change in the ratio with increasing alteration would be expected, measured at Starra by increasing $Fe_2O_3^{tot}$. Table 6.6 (also refer to Fig. 7.10) illustrates that there is no change in Al_2O_3/TiO_2 in altered rocks up to ~48% $Fe_2O_3^{tot}$. The uniformly low Al_2O_3/TiO_2 ratios of ironstones are therefore inconsistent with a replacement origin.

Averages	*Al_2O_3/TiO_2*		
	Footwall	Hangingwall	Ironstone
Least altered volcaniclastic (n=4)	23.06		
Altered feldspathic footwall (n=26)	24.54		
Most-altered footwall, $Fe_2O_3^{tot}$ > 40% (n=3)	22.18		
Fresh metasediment (n=11)		24.04	
Altered metasediment (n=7)		23.44	
Shale component (n=2)		20.09	
Calcarenite component (n=2)		25.90	
Mineralised ironstone (n=8)			8.00
Ore environment barren ironstone (n=10)			9.79
Distal barren massive ironstone (n=5)			3.61
Distal Cherty BIF (n=17)			17.9

Table 6.6 *Average Al_2O_3/TiO_2 ratios for Starra rock-types.*

Replacement is also discounted on geological grounds:

(1) Starra ironstones pass along strike to recognisable sedimentary BIF.

(2) Reworked ironstone pebbles occur within and above some Starra ironstones, which require a pre-metamorphic origin.

(3) Minerals such as garnet and pyroxene typically found in metamorphic/igneous skarns (Einaudi et al. 1981) are not present.

Deformation/Metamorphism-related Changes in Ironstone Chemistry

Klein (1973), Stanton (1976d) Gole (1981) and others emphasise that oxide facies BIF shows only small chemical and textural changes up to very high metamorphic grades. However, textural changes accompany progressive imposition of strain. Gole (1981) and Chadwick et al. (1986) have documented the destruction of original micro and mesobanding, via solution transfer of silica from high stress sites to dilatant zones. Gole (1981) noted that deformation produced massive 1 m thick beds from delicately laminated BIF, with no chemical changes in the process.

Where deformation proceeds to mylonitic strains, Drury (1974), Sinha et al. (1986) and Owen (1988) have documented chemical changes in felsic and basic lithologies, K_2O and SiO_2 loss, and gains in FeO and CaO, enhanced by the presence of a fluid. This work is relevant to BIFs by analogy only, because comparable studies on BIFs are not available. Hence the presence of mylonitic textures requires the consideration of chemical change.

Starra and Trough Tank ironstones regionally display the style of fabric destruction described by Gole (1981), particularly in the short limbs of sinistral folds. Nevertheless, some mineralised zones are finely banded (chapter 3, Fig. 3.9E). Gross SiO_2 mass transfer to dilatant fold zones, as discussed by Chadwick et al. (1986), could explain the siliceous nature of mineralised ironstone in the folded Main Zone of Area 257, but is inapplicable to the unfolded Area 251 ore.

All of the ore zones lie on the edge of the major Starra Shear (Switzer 1987), and are highly strained, requiring consideration of chemical change. But are they mylonites? Thin-section observations shows that while the grain-size of matrix hematite is smaller than in the pressure shadows of magnetite, it is still very coarse, rather that mylonitic. As discussed in chapter 3, mylonites are developed preferentially in adjacent ductile chlorite and feldspar schist, but not in ironstone. Chemical change due to mylonitisation is therefore not relevant, except where fluid infiltration was facilitated by transposition brecciation. In support of this conclusion, hematite lenses within the relatively unstrained hangingwall, and those of the more distal Eastern Hematites, have similar compositions to highly strained lenses within the Starra Shear.

In conclusion, the chemical modification of sedimentary BIF during deformation is discounted to explain the major element variation of Starra ironstone. Textural modification during tectonism nevertheless best explains the massive nature of Starra ores, which may originally have been finely banded.

Implications of Gold Fineness for Epigenetic/Syngenetic Models

The use of gold fineness as an ore deposit classification tool was initially suggested by Fisher (1945). Many authors have subsequently analysed specific deposits in detail, with results summarised by Rose & Morrison (1988).

Archean veins and shears, "Slate belt" veins, porphyry Cu-Au-Mo bodies, and epithermal Au-Te-Se ores all typically concentrate in the same fineness range as Starra ores, between 800 and 1000. Tennant Creek-style magnetite ores also have exceptionally high fineness, > 980 (Garrett 1989). Volcanogenic massive sulphide deposits are reported by Huston & Zaw (1988) to divide into two fineness categories: those dominated by Pb-Zn-Au-Ag assemblages, with widely variable fineness (320 - 820), and Cu-Au assemblages, which exhibit only high fineness (> 700). They relate the latter behaviour to the dominance of Au-chloride complexing in saline fluids.

There are conflicting claims on the effects of deformation and metamorphism on the fineness of gold. Oberthur & Saager (1986) promote a view of compositional

homogenisation with increasing grade, whereas Reid et al. (1988) suggest this to be a local rather than regional phenomenon.

Since the Starra gold fineness overlaps with many ore-types, it is not possible to differentiate between the competing syngenetic and epigenetic models for ore formation. Starra fineness values are in general consistent with the model of Huston & Zaw (1988) for chloride-dominated ore fluids, if it is assumed that the Au/Ag ratio has not been significantly altered by deformation.

A review of the Global Chemistry of Iron Formations

Global iron formation chemistry is reviewed here to assess the overlap of Starra ironstone compositions with the known BIF types.

James (1966) used 15 % Fe, or 21.5 % $Fe_2O_3^{tot}$, to distinguish iron formations from other sedimentary rock-types. He recognised the four facies of BIFs which are still used today: oxide, carbonate, silicate and sulphide. Gross (1980) formulated the well-known sub-division of BIFs into Algoman types (small, thin deposits with a clear volcanic association) and Superior/Hamersley types (typical of clastic-dominated shallow shelf environments, interdigitated with carbonate, shale, sandstone and siltstone). Whereas these are mainly Precambrian (older than ~ 1900 Ma (James & Trendall 1980)), oolitic Minette ironstones dominate the Phanerozoic, distinguished from the other types by an absence of chert and a formation under very shallow to subaerial, often brackish conditions (Maynard 1983). A fourth, largely unrecognised type are the "Lahn-Dill" hematite-magnetite ± melnicovite ± chlorite ± siderite ores (Quade 1976), and the equivalent carbonate-rich Teliuc-Ghelar type (Krautner 1977). Both are considered to have formed proximal to exhalative vents in volcanic terrains, but at different oxidation states. Lahn-Dill iron formations are associated with carbonate reef-complexes in well-oxygenated waters around volcanic rises, whereas Teliuc-Ghelar ores formed in deeper more-reduced waters permitting Mn-transport (see also Appendix 11). In this regard they are transitional to Algoman iron formations, differing mainly in the sense of proximality — alteration zones are readily identified beneath Lahn-Dill ores, but not Algoman BIFs.

Gole & Klein (1981) and Gole (1981), using a large sample population, determined that Algoman and Hamersley BIFs are chemically very similar. The main differences are higher average P_2O_5, S, Al_2O_3, K_2O, TiO_2, V, ΣREE, Cu, Pb and Zn in Algoman BIF, and lower MnO (Table 6.7). In contrast, Lahn-Dill iron-formations show enormous variation in Fe, from pure SiO_2 to 99% $Fe_2O_3^{tot}$ (data from Quade 1976, Krautner 1977, and Kimberly 1979), with a large proportion substantially exceeding the average Fe content of the common Precambrian BIFs. Trace element compositions of Lahn-Dill ores are poorly documented; available analyses indicate highly variable P_2O_5, MnO, CaO, B, Ba and alkalis (Kimberly 1979).

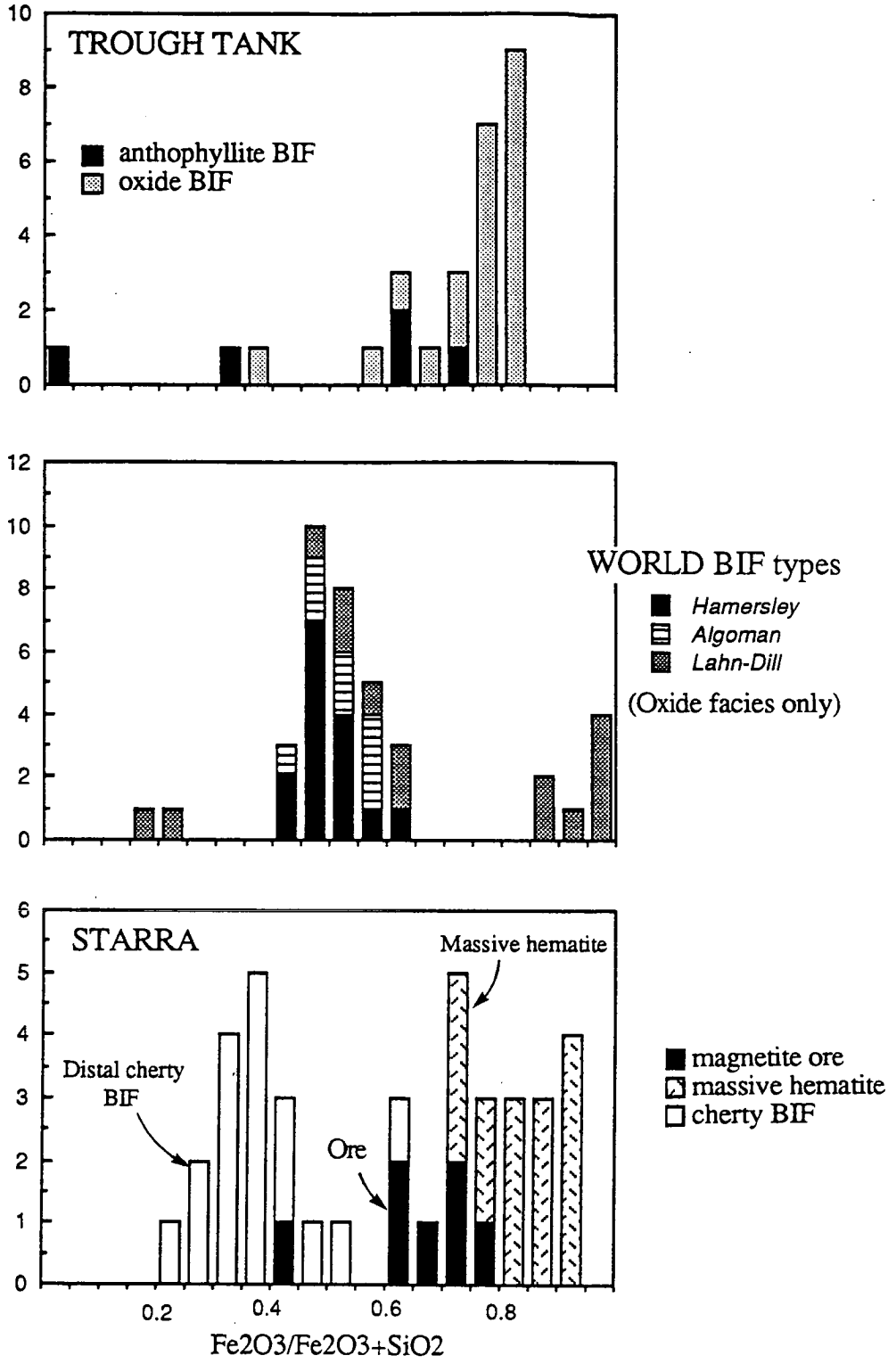

Figure 6.24 *A comparison of Fe Numbers of the Starra and Trough Tank iron-formations with those of three globally-documented BIF-types: Hamersley, Algoman, and Lahn-Dill ores.*

A comparison of the chemistry of these iron ore types leads to the conclusion that Starra ores are most like Lahn-Dill iron formations (Table 6.7, Fig. 6.24). A similar conclusion was reached by Stanton (1976a,b) for the iron formations close to the Broken Hill ore body. Both exhibit variable chemistry, with a tendency towards iron enrichment.

	A	B	C	D	E	F
%						
SiO_2	27.63	15.92	24.31	47.2	5.04	50.5
TiO_2	0.06	0.23	0.06	0.02	-	0.2
Al_2O_3	0.48	0.83	1.22	1.15	0.34	3.0
Fe_2O_3	69.57	81.84	70.26	44.40	89.38	45.49
MnO	0.05	0.03	0.06	0.59	0.11	0.2
MgO	0.42	0.11	0.73	1.24	-	1.53
CaO	0.06	<0.02	1.12	1.58	0.80	1.51
Na_2O	0.32	<0.3	0.7	0.12	-	0.31
K_2O	0.05	0.16	0.11	0.14	-	0.58
P_2O_5	0.01	0.06	0.78	0.06	0.06	0.21
ppm						
Cu	9666	16	3564	10	-	96
Pb	1	<2	14.7	30.3	-	-
Zn	2.9	5.7	13.7	51.1	-	330
Co	8	-	106	27	-	38
Au	4.63	0.1	0.51	-	-	<0.1
Ba	12	451	17.9	180	-	170
W	191	5	8.2	-	-	-
Sn	60*	-	5.3	9.3	-	-
As	7.0	<3	6.9	9.3	-	-
Ni	15	6.5	19.1	32	-	-

A: Average Area 257 magnetite-quartz Cu-Au ironstone, n=8.
B: Average barren, massive BIF south of Starra, surface samples, n=5.
C: Average oxide facies Trough Tank BIF, n=24.
D: Average Hamersley BIF (Maynard (1983), after Gross (1980)), n=148.
E: Fortuna Mine, Lahn-Dill volcanogenic oxide ore, n=5.(Quade 1976).
F: Average Algoman BIF (Maynard (1983), after Gross (1980)).
* Kary & Harley (in press).

Table 6.7: *Geochemistry of iron-rich rocks at Starra and Trough Tank, with data from possible progenitors for comparison. Of these progenitors, Lahn-Dill volcanogenic oxide ore compares best with the iron ores of Starra, although to date the precious and base-metal contents of this type have been poorly documented.*

A Syn-sedimentary Model for Starra Ironstone Chemistry

The Major Influences

As reviewed above, the chemistry of the two classic BIF types show differences to Starra ironstones. The overlap of the chemical range of Lahn-Dill ores with Starra compositions offers an alternative origin on the basis of empirical comparison.

A general chemical model for Starra is suggested, involving the hydrothermal supply of Fe and Si to proximal Lahn-Dill-style ironstones, with chemical-clastic iron formation

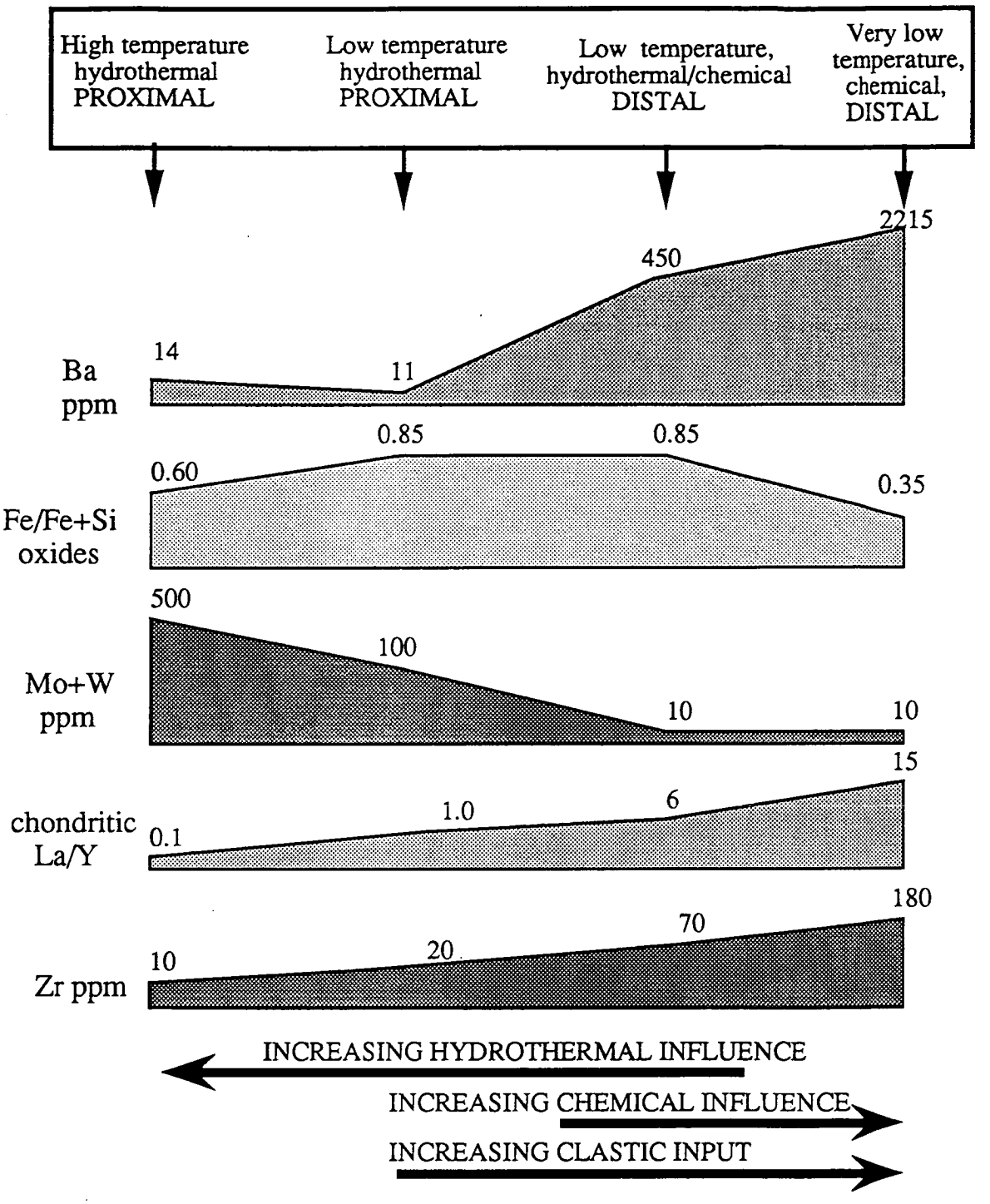

Figure 6.25 *A schematic portrayal of the important changes in geochemistry through the four ironstone groups at Starra. The influences on chemistry are the proximity to high and low temperature hydrothermal vents, clastic sediment supply, and the contribution of evaporitically induced chemical precipitation in shallow waters.*

deposition at a shallow basin margin. Elements which are depleted in the altered Starra footwall are likely to have contributed to the exhaling hydrothermal fluid, together with Fe and Si. These include K, Ba, Ca, Rb, Sr, Zr, Nb, Pb, Zn, REE and B. (It is likely that alkali elements were also significantly leached from the footwall prior to the mineralising event by diagenetic reaction with saline waters, as discussed in chapter 5). If unusually-high concentrations of a particular element were present in the footwall, the same enrichment is likely to occur in exhalites produced through alteration of that footwall. For instance, the leaching of P_2O_5 from P_2O_5-rich parent-rocks in the Trough Tank footwall (chapter 5), has resulted in high P_2O_5 values in Trough Tank BIF. A biogenic origin for this P_2O_5 is discounted because the silicic alteration pipes below BIF are also phosphate-bearing. P_2O_5 is virtually absent from the proximal ironstones at Starra.

Iron formation chemistry is also argued to be a function of the amount of clastic material accumulating during chemical sedimentation, in turn related to the distance from the basin margin. Zr, Al_2O_3, SiO_2 and LREE were mainly contributed clastically to the Starra Iron-formation Member (Fig. 6.25), whereas Mo and W abundances were controlled by hydrothermal input. Sporadic enrichment of Mn and Ca in distal cherty BIF are attributed to locally more reduced chemical conditions, and may be particularly important because these elements are enriched in many Proterozoic Pb-Zn-rich BIFs, such as the nearby Pegmont deposit (Orridge 1980, Vaughan & Stanton 1986). They contribute to a theme developed in chapter 12, that Starra-style BIFs, and the more thoroughly studied Pb-Zn BIF varieties, are part of a transitional chemical spectrum.

Deposition of Alkali Elements and Distal Cherty BIF

One hypothesis which could explain the southward increase of alkali elements in Starra ironstones is a systematic increase in the amount of clastic sediment, i.e., that Ba was contained in feldspar, which was transported to the basin with other detritus. This notion was tested by analysing the variation of Zr (commonly used as an index of clastic maturity in sediments), as shown in Fig. 6.10. No parallel change of Zr with Ba was found in the Western Hematites. Additionally, an average 154 ppm Ba and 1.54 % K_2O in fresh Staveley Formation sediments (Table 5.2) proves that detritus entering the iron formation basin was not necessarily alkali-enriched.

The Ba enrichment may alternatively have originated diagenetically in areas of shallow sedimentation and evaporite accumulation. High Ba (~3400 ppm) and K_2O (~5.4 %) levels found in evaporite-pseudomorph-bearing sediment close to Area 186 support this hypothesis. Wavelength-dispersive microprobe analysis found up to 2.5 wt. % Ba in potassium feldspar in these rocks. Alkalic diagenesis of evaporites and shallow sediments is therefore the favoured mechanism of K, Ba, Rb, Sr and B deposition at the basin margin. This alkali enrichment occurs above and below, as well as within the distal iron formations, and is therefore not related simply to the mineralising event, as concluded in chapter 5. The most probable hypothesis is the precipitation of Ba at or below the sediment surface with

other evaporites from Ba-enriched waters, because both Ba-carbonate and Ba-sulphate have a very low solubility (22 g/m^3 of carbonate and 2.22 g/m^3 of sulphate in water at 18 ° C; Sonnenfield 1984). Barite can precipitate during the mixing of fresh water and brine at evaporite basin margins, commonly replacing shallow water gypsum (Lambert et al. 1978, Mossman & Brown 1986). At Area 186, the replacement of gypsum by Ba-rich K-feldspar supports such an origin.

Microbanded cherty iron formation deposition can also be explained by evaporitically induced mineral solubility changes at the basin margin, following the models of Trendall (1973), Birnbaum & Wireman (1985) and Garrels (1987). Gypsum pseudomorphs documented within boron-rich iron formation at Area 186 (chapters 3 and 9) are consistent with this explanation.

In summary, the diverse chemistry of the iron formation types at Starra can be explained by combinations of proximal hydrothermal precipitation and shallower evaporitically-controlled chemical-clastic deposition.

CONCLUSIONS

(1) Ironstone compositions at Starra cannot be explained by the replacement of wall rocks or by the tectonic/metasomatic modification of sedimentary iron formation.

(2) Starra ore environment ironstone compositions are not similar to the chemistry of the classical BIF-types, but compare favourably with volcanogenic Lahn-Dill ores.

(3) The chemistry of the four ironstone types at Starra can be explained by a combination of proximal exhalative ore precipitation, diagenetic/hydrothermal enrichment of basin waters with elements depleted in the Starra footwall, and chemical deposition through evaporitically-induced solubility changes at the basin margin.

(4) Au-poor hematite lenses close to Starra ore can be distinguished from distal lenses on the basis of their La, Y, W, Mo, Sn, Fe, Si, Zr and Al concentrations. The dispersion of W, Mo, Cu and Y is greater than Au in a given ironstone.

(5) The fineness of gold in Areas 251 and 257 is 836 - 996, within the range of gold from a spectrum of ore deposit types in which metal-chloride complexes are important.

(6) BIFs in the Starra area are regionally enriched in Au, with 50 % of the population of samples from a 12 km ironstone segment containing > 38 ppb Au.

(7) BIF Cu/Au ratios at Trough Tank vary systematically along strike and across individual BIF intercepts. The northwest-oriented trends are not parallel to the recognised fold hinge or stretching direction.

CHAPTER 7

THE GEOCHEMISTRY AND ORIGIN OF THE MAGNESIAN ROCKS AT STARRA AND TROUGH TANK

INTRODUCTION

A discussion of the magnesian rocks in the Starra area has not been included in any other section because their affinities are ambiguous. The lithologies studied in this chapter are:

(1) basalts and dolerites
(2) chloritic Harley Member
(3) chloritic lenses within the Mariposa Creek Member, associated with ore.

The origin of unusual Mg-rich rocks in hydrothermally-altered settings has long been a controversial subject, due to the paucity of modern igneous and sedimentary equivalents (e.g., Eskola 1914, Schemerhorn 1978, Tuominen & Mikkola 1950, Reed 1983). Lithologies which are isochemical with magnesian chlorite-quartz assemblages at low metamorphic grade form cordierite-anthophyllite (Eskola 1914, Vallance 1974, Hudson & Harte 1985, Reinhardt 1987), cordierite-orthopyroxene, or sapphirine-rich (Schreyer 1977, Warren & Shaw 1985) assemblages at higher metamorphic grades. A review of the features of different Mg-rich-precursors is available in Reinhardt (1987).

The least ambiguous Mg-rich lithology at Starra is basalt. Amygdaloidal basalt commonly occurs at the base of the Staveley Formation in the Mt. Elliott area, and south of Starra in the Southern Grids (Figs. 3.2 & 4.1). The volcanism was significant, forming a basalt unit up to 650 m thick north and west of Mount Elliott, in the Blockbuster/Mobs Lease area. Iron formation commonly directly overlies it. Magnesian rocks of less-certain affinity occur in the footwall of the Western Hematites, firstly as an extensive stratiform chlorite-biotite unit, here termed the Harley Member, and secondly as chlorite-magnetite lenses and pods beneath or along strike from auriferous ironstone. Chlorite also occurs as a common retrogression product in reaction/metasomatic skarns hangingwall to ironstone.

The chloritic rocks of the Western Hematites are compared in this study to the chemistry of Staveley Formation basalt. Other possible precursors, such as deformational retrogression products, predeformational hydrothermal alteration zones, evaporitic clays, and syn-metamorphic metasomatic alteration zones, are all considered.

CHEMISTRY OF THE MAFIC IGNEOUS ROCKS

Mafic Igneous Groups

Seven samples of Staveley Formation basalt from north (Mobs Lease area) and south (Southern Grids area) of Starra were obtained, mainly from percussion drill-holes. They consist mainly of actinolite-plagioclase-sphene assemblages. Detailed geochemistry and metreages are available in Appendix 6, with hole locations in Fig. 3.2. Two Amphibolite-grade samples (hornblende-plagioclase-magnetite assemblages) from Trough Tank were also compared. They are tentatively identified as basalts, rather than dolerites, because of their conformable, gradational contact with feldspathic metasediment.

Three samples of ophitic dolerite from the Starra hangingwall have also been included. The dolerites are folded by D2(MP), a feature of the regional E1, E2 and E3 dyke generations (Ellis & Wyborn 1984). The details of regional dolerite generations are outlined in chapter 2.

Petrogenetic Classification

Average bulk-rock chemistry and selected examples are compiled in Table 7.1. All three sample groups (Staveley Formation basalts, dykes and Trough Tank basalts) are remarkably similar despite the differences in the timing of their emplacement. They are transitional between sub-alkaline basalts and tholeiites on the basis of SiO_2, Na_2O and K_2O concentrations, and Nb/Y ratios universally less than 0.65 (Winchester & Floyd 1977). Tholeiitic, rather than calc-alkaline affinities, are assigned using the AFM diagram of Irvine & Baragar (1971) (Fig. 7.1). This diagram is applicable because the samples are mainly not metasomatised. The exception to this are several basalts from the Southern Grids with anomalous K_2O, which is attributed to low-grade biotite-metasomatism, commonly encountered in Mount Isa Inlier mafic rocks (Ellis & Wyborn 1984). The metasomatic addition of K_2O or Na_2O (e.g., St 145, Table 7.1) tends to push these samples artificially into the calc-alkaline field of the AFM diagram. In general all samples have low incompatible element levels (e.g, Zr: 40 – 115 ppm, Y: 13.3 – 41 ppm), moderate TiO_2 (0.6 - 1.83 %), and high $Fe_2O_3^{tot}$ (12.5 – 17.6 %, compared to an average MORB value of 9.67%; Engel et al. 1965). A tholeiitic rather than alkalic affinity is suggested by these low incompatible element levels, as illustrated in Fig. 7.3.

Figure 7.4 is a plot designed by Meschede (1986) to specifically distinguish ocean floor from continental tholeiites. Holm (1982), Meschede (1986) and others maintain that these affinities cannot be separated using the now-standard Ti-Zr-Y plot devised by Pearce & Cann (1973). Meschede (1986)s revised diagram is relevant to strongly altered rocks, because it employs relatively immobile high-field-strength elements (Winchester & Floyd 1978). Staveley Formation basalts and Starra dolerites plot transitionally between ocean floor and continental tholeiites, whilst Trough Tank basalt plots wholly within the continental tholeiite field. Seven samples of basalt from the Eastern Succession (Doherty and Kuridala Formations, Soldiers Cap Group, and Marraba Volcanics) plot similarly, with some creep

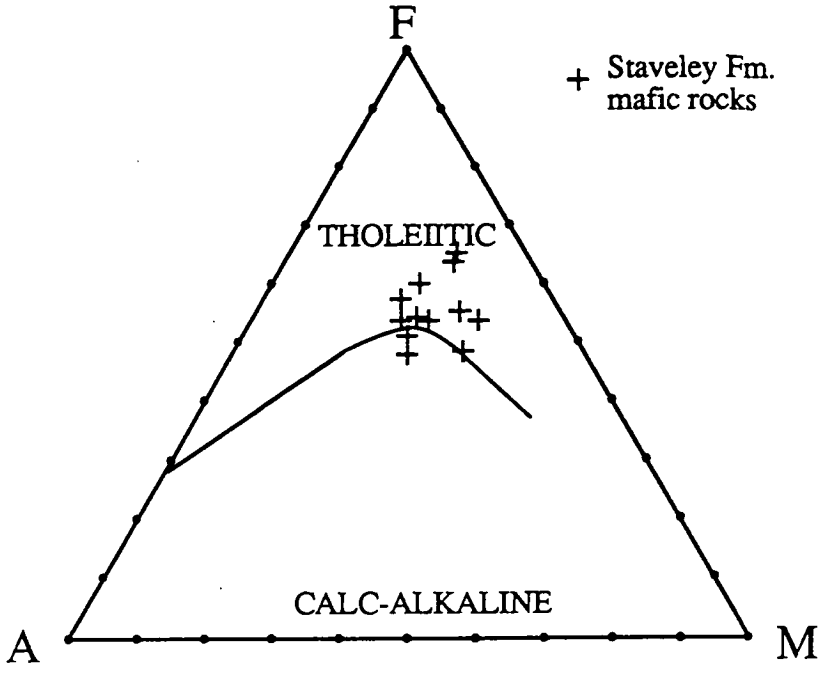

Figure 7.1 *AFM plot of mafic igneous compositions in the Staveley Fm. A tholeiitic rather than calc-alkaline origin is indicated (A = Na2O + K2O, F = Total Fe as FeO, M = MgO %; Irvine & Baragar (1971))*

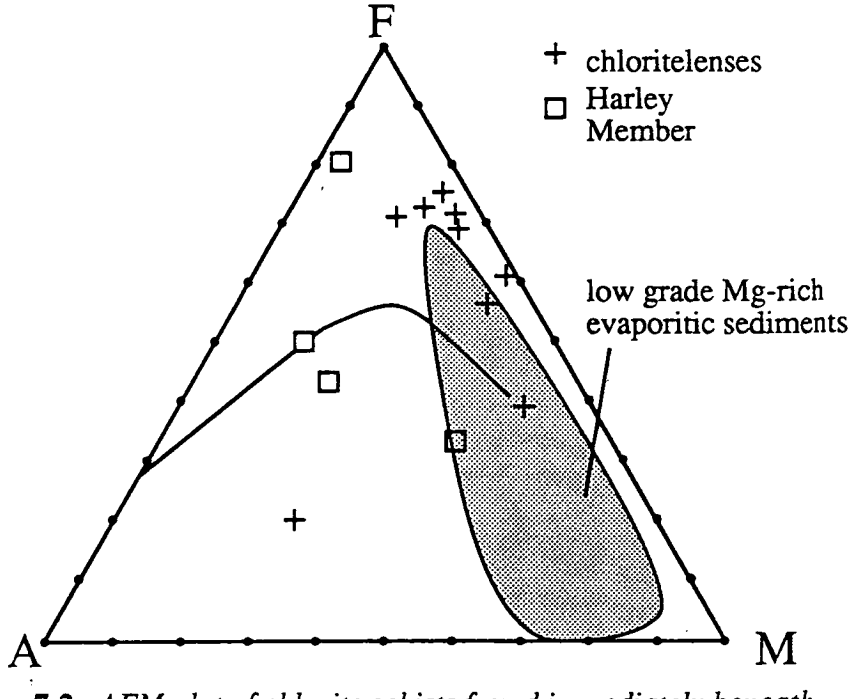

Figure 7.2 *AFM plot of chlorite schists found immediately beneath Starra ironstone, and Harley Member The field of Mg-clays related to evaporitic sediments is shown for comparison, data from Reinhardt (1987), compiled after Fontes et al. (1972). The line separating calc-alkaline from tholeiitic basalts is shown for reference.*

into the field of Plume-type MORB, characterising ocean island volcanism (data from Bultitude & Wyborn 1982).

%	Starra chl. lenses (average)	S.D. (n=10)	Harley Member St172	Harley Member St202	Trough basalt 236620	Staveley Fm. basalt (average)	S.D. (n=7)	Starra dolerite St145
SiO_2	48.99	6	57.87	48.01	48	51.04	2.35	50.71
TiO_2	0.49	0.09	0.71	1.96	1.73	1.12	0.37	1.55
Al_2O_3	11.51	2.54	15.82	13.12	12.0	14.3	0.84	14.43
$Fe_2O_3^{tot}$	21.75	8.46	10.68	11.74	16.9	14.57	1.58	14.04
MnO	0.06	0.04	0.02	0.03	0.25	0.17	0.1	0.14
MgO	8.41	3.21	4.47	13.85	5.9	6.86	1.27	6.02
CaO	1.25	0.91	0.79	0.5	9.15	5.1	2.05	6.2
Na_20	1.95	2.18	6.52	0.83	1.78	2.93	1.12	5.41
K_2O	1.09	0.45	1.52	6.37	0.75	1.6	5.6	0.53
P_2O_5	0.14	0.02	0.2	0.31	0.15	0.11	0.04	0.15
Loss	4.55	1.59	1.33	2.02	1.66	2.38	1.61	1.19
SUM	100.19	-	99.93	98.74	98.27	100.18	-	100.37
ppm								
Au	0.22	-	<0.05	-	<0.01	-		-
Cu	954	1570	23	838	175	61	43.5	48
Pb	<2	-	<2	8	15	<2	-	<2
Zn	14	11.9	6	14	40	49	18.9	45
Ba	287	275	87	270	155	459	278	233
Rb	51	26.3	91	388	38	69	26.2	18
Sr	17	24.7	51	9	115	66	33.3	133
Zr	151	52.3	138	147	115	84	25.3	111
Y	40.6	15.9	22.4	41.1	28	25.5	8.7	32
Nb	11.6	3.2	13.7	9.5	9	4.6	1.6	7.5
W	34	24.1	12	29	10	<5	-	6.5
Sc	12	3.6	20	31	70	41	6.6	40.5
V	83	37.1	144.7	468	-	331	107	425
Cr	29	47.3	79	103	24	43	-	43
Ni	52	36.2	47	127	22	86	30.1	53
As	<3	-	<3	<3	7	-	-	5
Bi	<3	-	<3	<3	<3	-	-	<2
Ti/Zr	20.1	3.7	30.96	79.77	90.19	81.1	12.2	83.72

Table 7.1 *Averages and selected analyses of magnesian lithologies in the Starra and Trough Tank ore sequences. Selected analyses are provided if the sample population of an inhomogeneous rock-type is small. Standard deviations (S.D.) are provided for the averaged analyses. All individual analyses are available in Appendix 6. (Abbreviations: '-' — not analysed).*

Another important geochemical feature is a general Fe enrichment in the analysed mafic rocks, paralleling that of other mafic rocks in the Eastern Succession (Ellis & Wyborn 1984). This is typical of the end-products of tholeiitic fractionation. Examining the available data on Eastern Succession basalts (Bultitude & Wyborn 1982), including this work, two distinct primary melt trends can be identified on the basis of $Fe_2O_3^{tot}$ versus MgO weight % (Fig. 7.5). The Eastern Succession dolerites sampled by Ellis & Wyborn (1984) mainly

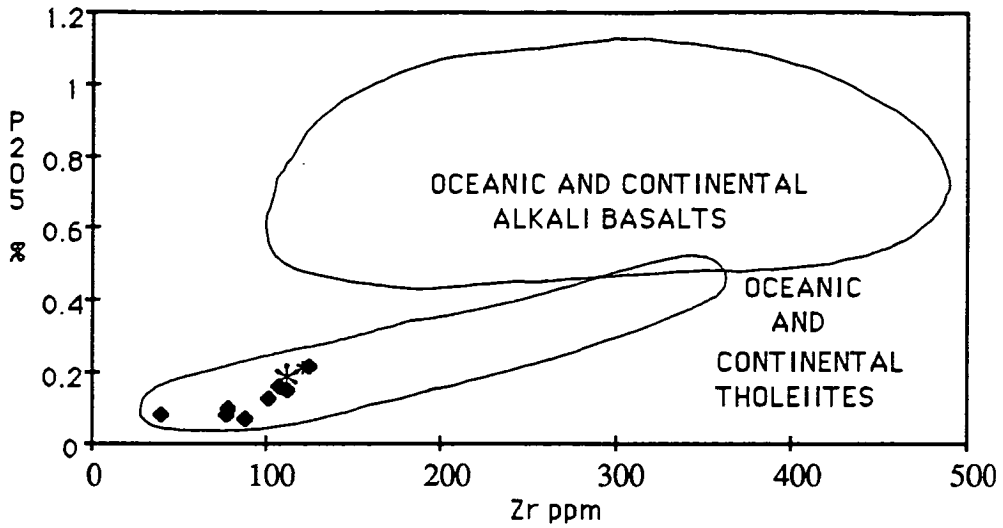

Figure 7.3 *A classification of basalt compositions after Floyd & Winchester (1975). This plot readily distinguishes alkalic basalts from tholeiites, but cannot separate the oceanic or continental affinities within these types. Stavely Fm. basalts are classified as tholeiitic using this diagram.* ***Diamonds:*** *Staveley Fm. basalt,* ***Asterisks:*** *Trough Tank basalt.*

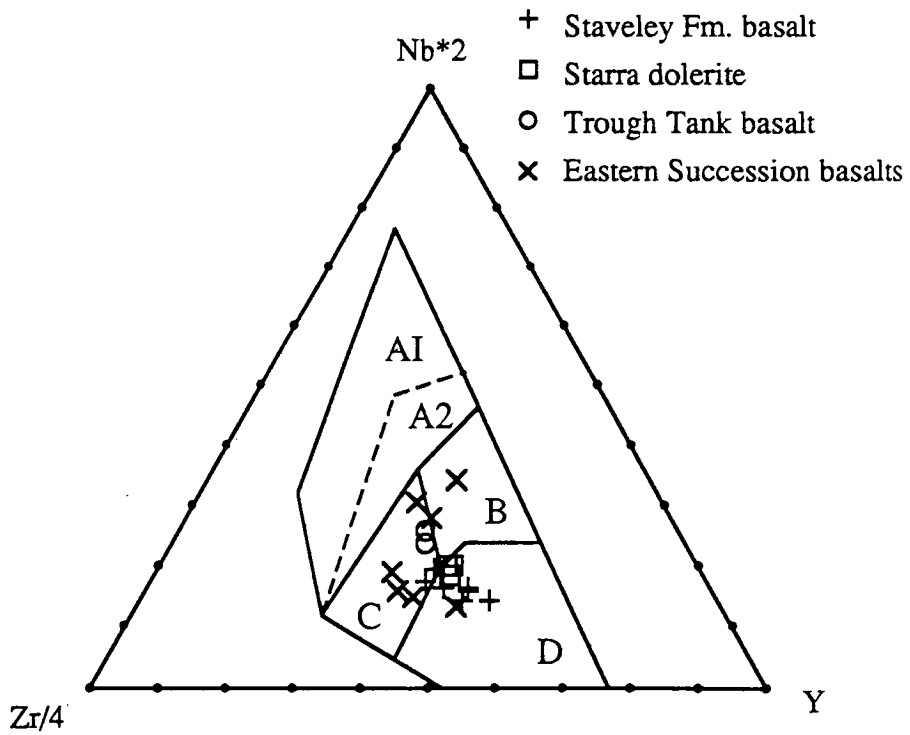

Figure 7.4 *An immobile element classification using Zr, Nb and Y abundances in basalts, formulated by Meschede (1986). The plot specifically deals with the problem of differentiating continental from ocean floor tholeiites.* ***A1:*** *Within Plate alkaline basalt.* ***A2:*** *Within Plate tholeiite.* ***B:*** *"Plume"-type MORB.* ***C:*** *Within Plate basalt, arc basalt.* ***D:*** *N-MORB, arc basalt. Almost all mafic rocks in the Eastern Succession, including those sampled here from the Staveley Fm., are classified as transitional between continental and ocean floor basalt. Regional samples were obtained from Bultitude & Wyborn (1982).*

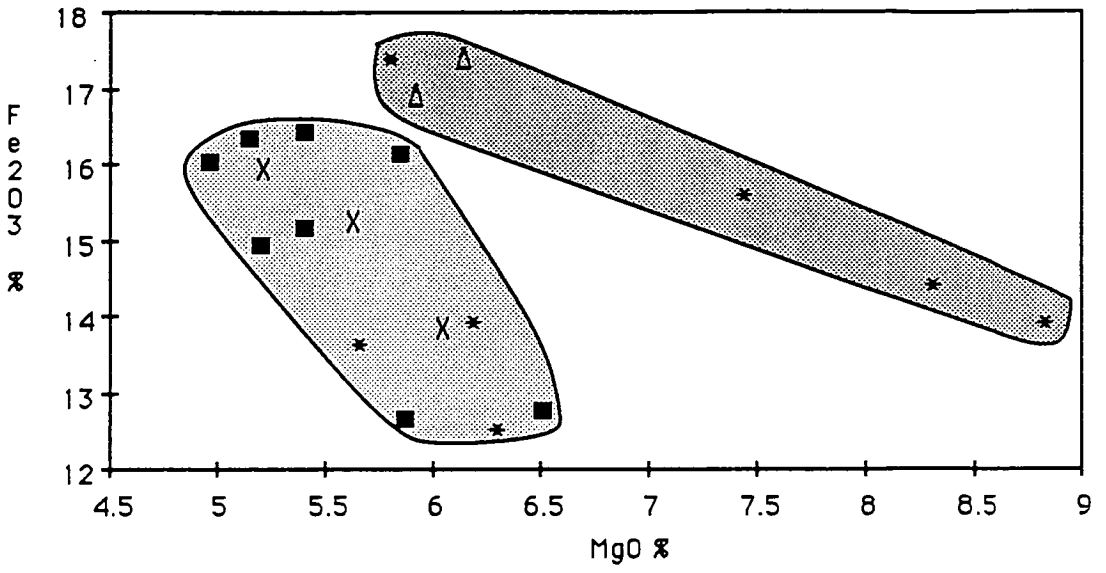

Figure 7.5 *The fractionation of Fe with respect to Mg is a characteristic of tholeiitic melts. In this diagram only basalt data from the Eastern Succession is presented, together with the three Starra dolerite samples. Southern Grids and Trough Tank samples are separated from the main Eastern Succession trend, suggesting different primary magmas for these rocktypes.* *: *Staveley Fm. basalt.* X *: Starra dolerite.* ■*:Eastern Succession basalt (data from Bultitude & Wyborn (1982).* Δ*:Trough Tank basalt.*

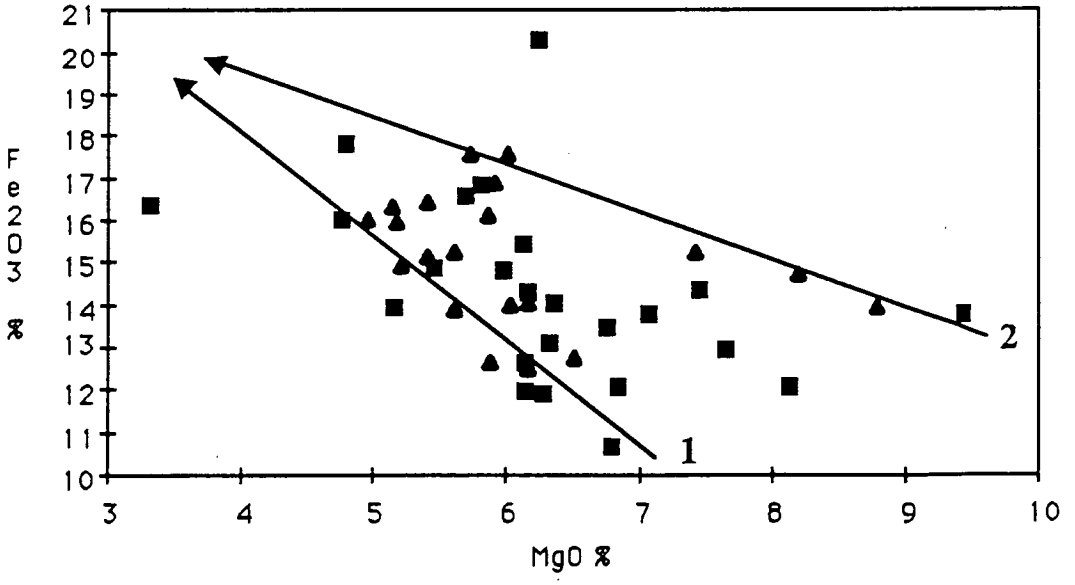

Figure 7.6 *Dolerites from the Eastern Succession, sampled by Ellis & Wyborn (1984) are here compared with Eastern Succession basalt, including those from this study. Dolerites plot along the main primary magma lineage (1) indicated in Fig. 7.5. All three lineages seemingly are differentiating towards a common high Fe-low Mg composition.(* ■ *dolerite,* ▲*basalt. Fe2O3 is an expression of total Fe.)*

conform to the low-Mg differentiation trend in Figure 7.6, with some scatter. Two primary melt compositions were also suggested by the LREE patterns of Southern Grids basalts and Starra dolerites (see chapter 8).

Tectonic Implications

Continental flood tholeiites such as those of the South African Karoo Province (Richardson 1979) and Southern Brazil (Fodor 1987) characterise the initial volcanism of many rifting events. They can commonly be matched across opened ocean basins. The recognition of thick continental tholeiites in many places at the base of the Staveley Formation suggests an origin through aborted rifting, or within a discrete strike-slip pull-apart basin, during the evolution of regional structures such as the Leichhardt River Fault Trough (LRFT) (Derrick et al. 1980). Rather than being a post-rift sag-phase setting (Beardsmore et al. 1988), the renewed basic and acid volcanism suggests a rejuvenated rift basin, which was subsequently filled by Staveley Formation sediments. Basalts were derived from at least two primary sources, which continued to supply magma during and after the D2(MP) deformation event.

Glickson & Derrick (1978) proposed that Mount Isa Inlier basalts grade from continental tholeiites in the west to oceanic tholeiites in the east, supporting a broad continental subduction margin tectonic-setting. Bultitude & Wyborn (1982) opposed this setting because it cannot explain the bimodal character of Eastern Succession volcanism. Bimodal volcanism is commonly encountered in tensional, rift-related, tectonic regimes. The transitional ocean floor tholeiites identified in this study do lend some support to the assertion of Glickson & Derrick (1978). However, in kind with Bultitude & Wyborn (1982), a collisional tectonic-model is rejected because of its inability to explain many aspects of the Eastern Succession (chapter 2). Ocean floor tholeiites in the Staveley Formation more likely imply that the rifting proposed by Bultitude & Wyborn (1982) and others, proceeded to an advanced stage on the Mary Kathleen Shelf (Blake et al. 1984), prior to its termination.

AFFINITIES OF MAGNESIAN ROCKS IN THE IMMEDIATE STARRA SEQUENCE.

Harley Member

Inferences From Geology

Lithologies mapped as Answer Slate by Leishman (1983), here referred to as the Harley Member, commonly occur in the succession below the Western Hematites along the western limb of the Starra Syncline. The Harley Member, commencing 50 - 100 m west of the Western Hematites, is considered to be the base of the Staveley Formation, transitional to undifferentiated schist. The upper contact is sharper and hence easier to define, characterised by a rapid increase over 5 m of foliated chlorite bands 1 – 5 cm thick, interbedded with albite ± hematite beds. The latter exhibit well-developed graded bedding in places, with the implication that sedimentary reworking occurred during deposition.

Inferences From Geochemistry

The four samples of Harley Member analysed (Appendix 6) exhibit large chemical variation. (Two examples are provided in Table 7.1, rather than an average). St172, St199 and St202 were composites of 10 to 15 m of drillcore, whereas sample Answer 1 was a 3kg composite of rock-chips obtained over 20 m close to the upper unit boundary, along line 11400N, Area 257.

Major Elements: The major element heterogeneiity of the Harley Member is exemplified by the wide scatter of data across the calc-alkaline-tholeiitic boundary of Irvine & Baragar (1971) in the AFM ternary (Fig. 7.2). Iron alteration, which characterises the overlying Mariposa Creek Member, is also present sporadically in the Harley Member. MgO varies between 1.08 and 13.85%, and K_2O between 0.25 and 6.37 %. TiO_2 (0.38 - 1.96 %) is generally higher than in the overlying units. These features hinder the assignment of a specific precursor, although the universal enrichment of TiO_2 requires a contribution from a moderately TiO_2-enriched precursor, such as the Staveley Formation basalts.

Trace Elements: Trace element concentrations reflect the same alteration which is associated with the ironstone-mineralising event. Cu varies between 6 and 838 ppm, and W between 12 – 56 ppm. The depletion of alkali elements so prevalent close to mineralisation in the Mariposa Creek Member is not as evident in these samples. For instance Ba (14 – 270 ppm), Rb (13 – 388 ppm) and Sr (4 – 63 ppm) are all at moderate levels.

A consideration of the highly variable trace element concentrations supports the idea that the protoliths were a lithologically heterogeneous group. Post-depositional (ore-related) metasomatic alteration must also have contributed to chemical variation.

"Immobile" Elements: In chapter 5, Ti and Al were identified as only locally mobile under the alteration regime characterising the mineralising event, whereas Nb, Zr and Y were all variably mobile. In the Harley Member, more moderate retention of alkali elements is evidence that the same alteration was not as severe, and hence elements such as Zr, Y, and Nb may have been retained. On this basis the ratios TiO_2/Al_2O_3, Nb/Y, and Ti/Zr have been examined to determine the origin of the Harley Member (Figs. 7.7 & 7.8).

Sample St 202 (Table 7.1) consistently plots with other Starra basalts in these diagrams, and additionally exhibits similarly high levels of Sc, V and Ni. It is identified as K-metasomatised basalt. Two of the other samples plot close to, but at higher Ti/Zr, than any of the altered rocks of the Mariposa Creek Member, suggestive of a small basaltic component, or of depletion of Zr relative to TiO_2. The remaining sample plots wholly within the altered feldspathic footwall field, and may represent a chloritised equivalent.

Possible Harley Member Protoliths

One Harley Member sample clearly has continental tholeiite affinities, but has been extensively K-metasomatised. The origin of the others relies both on the geological and geochemical data. Compositional banding characterising the Harley Member is interpreted as

structurally-modified bedding, because of the associated sedimentary structures in some layers. Sedimentary reworking and mixing of felsic pyroclastics with basaltic detritus could explain the "immobile" element features of some Harley Member samples. Elevated MgO and TiO_2 are a feature of the basaltic component.

An origin as evaporitic Mg-clays (Reinhardt 1987), (Fig. 7.2), is also capable of explaining sedimentary structures and the Mg enrichment, but not the high TiO_2, Sc, V and Ni values in some samples. In addition, the sedimentary facies changes associated with evaporitic Mg-clays, such as a transition from clays to carbonate-rich rocks (Moine et al. 1981, Reinhardt 1987), are not observed in the Harley Member. In fact the rocks observed at the same stratigraphic position along strike are basalts (for instance, Mobs Lease, Blockbuster, Southern Grids).

In conclusion, admittedly on limited geochemical data, the Harley Member protolith was a mixed mafic/acid pyroclastic/epiclastic sediment sequence, which was subsequently metasomatised. Some metasomatism (oxide alteration) occurred during the mineralising event, but the timing of the potassic alteration is uncertain.

Massive Chlorite Lenses

Inferences From Geology

Massive chlorite, sometimes referred to in the literature as "chloritite", occurs as lenses and pods associated with gold-rich ironstone. Lenses are noted at all the major prospects along the Western Hematites, but not below barren ironstones, and hence they are a direct exploration indicator. The geometry of some of these bodies is illustrated in Fig. 6.9. Those at Areas 244, 251 and 257 form lozenge-like bodies 50 – 100 m long, footwall to ironstone, whereas Area 236 chloritite also occurs along strike to ore, as an ironstone-equivalent. At Area 251 detailed underground mapping demonstrated that massive chlorite thickens in parallel with Au-rich ironstone, although the two are separated by ~5 m of feldspathic schist. The thickest part of this lens is also coincident with severe oxide alteration in the Mariposa Creek Member, studied chemically in chapter 5.

Mineral assemblages consist of chlorite, quartz, biotite, disseminated magnetite and pyrite, as well as accessory epidote, sphene, bornite, chalcopyrite and tourmaline. Unlike the feldspathic schist of the Mariposa Creek Member, magnetite-sulphide veins are uncommon. This may be due to their destruction during the accommodation of very high strains by these incompetent units during deformation. Some highly folded oxide-veins have been observed in massive chlorite beneath the "Western Zone" of Area 257.

Chlorite lenses are developed irrespective of the distribution of large D2(LP) folds. For instance, massive chlorite occurs on long "limb" sections of sinistral D2(LP) folds at

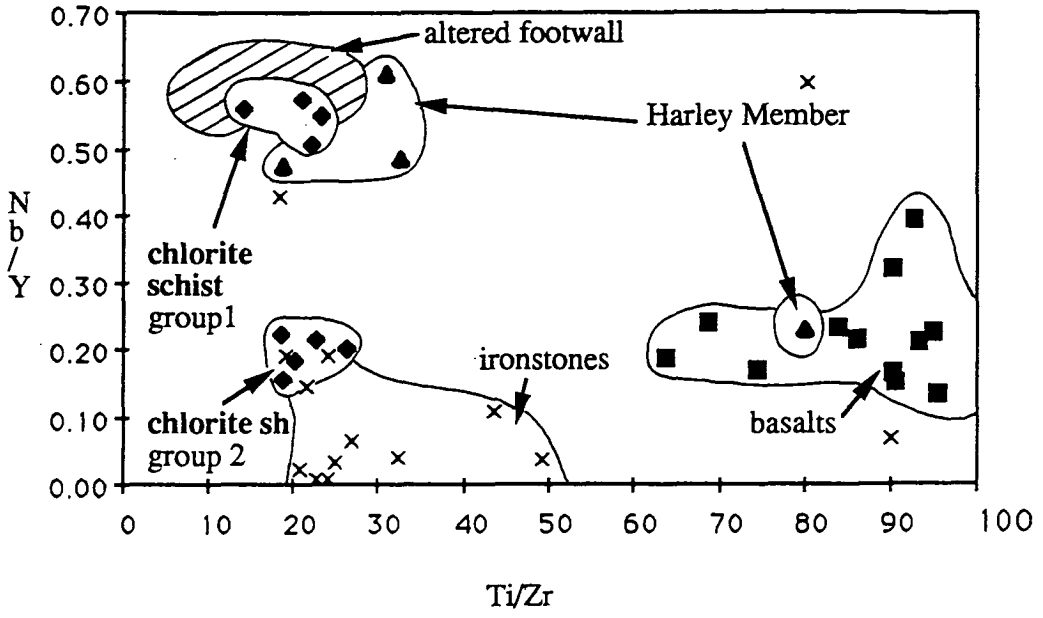

Figure 7.7 *Although mobility of Zr, Y and Nb has been demonstrated in the Starra ore environment, ratios of the elements still differ for the major rocktypes. In this diagram chlorite schists split into two very distinct fields. One of these overlaps the field of altered feldspathic schist, while the other has similar ratios to ore environment ironstones. Chloritites in the latter group are notably mostly stratiform. The Harley Member is also plotted, exhibiting affinity with either Staveley mafic igneous rocks, or feldspathic schist. (× ore environment ironstone, ◆ chloritite, ▲Harley Member, ■basalts & Starra dolerites.)*

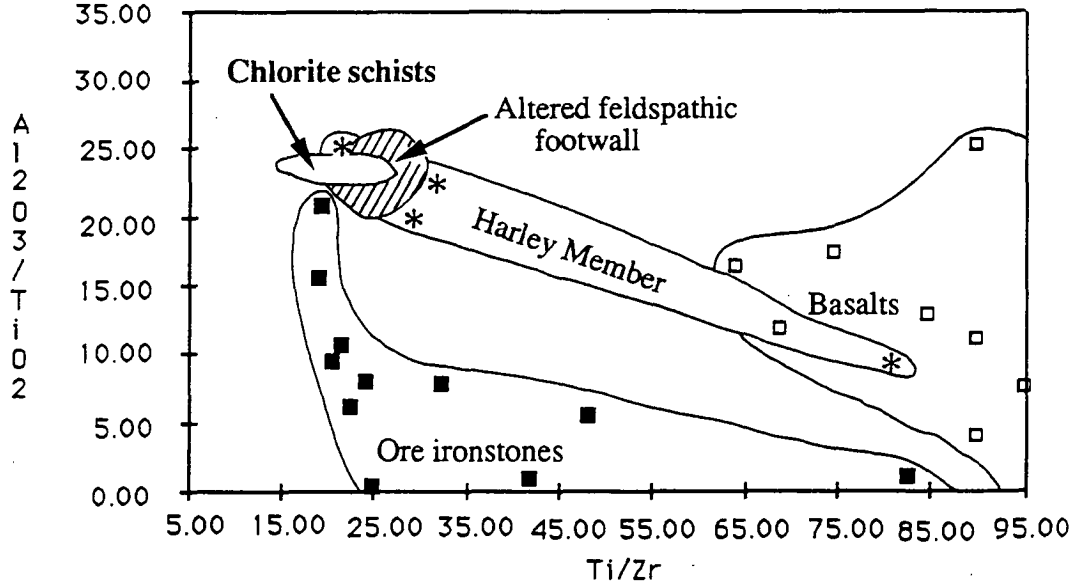

Figure 7.8 *On the basis of their Al2O3/TiO2 ratios, chloritite schists have strong affinities with altered feldspathic footwall rather than ironstone or basalt. Chlorite schist and feldspathic footwall are indicated only as fields, whereas the other groups are represented by points and fields i.e., □ Basalts and Starra dolerites, ■ ore enviroment ironstone, * Harley Member schists.*

Areas 236, 251 and 257, but in anticlinal fold hinges at Areas 222 and 244. They are absent from the major sinistral anticlines documented by Leishman (1983) at Areas 232, 264, 281, 284, 312 and other sites along the Western Hematites.

Inferences From Geochemistry

Major Elements: In company with the enclosing feldspathic schist, massive chlorite lenses are strongly enriched in $Fe_2O_3^{tot}$ (3.57 – 31.04 %, average 21.75%). They also have similar average TiO_2 (0.49%), P_2O_5 (0.14 %), Al_2O_3 (11.51 %) and SiO_2 (48.89 %) concentrations. The major contrast is the higher MgO (av. 8.41%), K_2O (av. 1.09 %) and CaO (av. 1.25 %), and lower Na_2O (1.95 %) of massive chlorite.

Trace Elements: Chlorite lenses are anomalous in (averages, n = 9), Au (0.22 ppm), Cu (954 ppm), W (33.8 ppm) and Y (40.6 ppm). Sc, Ni and V are enriched above concentrations within feldspathic schist, but are 3-fold below typical Staveley Formation basalt values. As detailed in chapter 8, chlorite schists exhibit similar HREE enrichment to mineralised ironstone and feldspathic schist.

"Immobile" Elements: Figure 7.7, a plot of Nb/Y versus Ti/Zr, shows an intriguing separation of the chlorite lenses into two distinct groups, both with constant Ti/Zr: the groupings are due primarily to variable Y concentrations. They are notably clearly distinguished from Staveley Formation basalt. Altered feldspathic schist samples are mainly coincident with group 1 (Fig. 7.7) whereas ore environment ironstones have an affinity with the low Nb group 2, extending to very low Nb/Y ratios. The latter group is dominated by stratiform massive chlorite from Area 236 and 244, a common denominator in the separation.

Figure 7.8, Al_2O_3/TiO_2 versus Ti/Zr, again demonstrates the chemical similarities between chlorite schists and altered feldspathic schist. Al_2O_3 and TiO_2 are interpreted as the least mobile of all elements in Starra-style alteration (Chapter 5), as demonstrated in Fig. 7.10, in which Al_2O_3/TiO_2 in chloritites and feldspathic schist show no change with increasing $Fe_2O_3^{tot}$ (an alteration index).

Chlorite lenses cannot have originated as altered basalt on the basis of these plots. Rather, they have a strong affinity with "immobile element" levels in the enclosing and underlying feldspathic schists. The clear split of chlorite lenses into low and high Nb/Y groups is evidence for a link on the one hand with feldspathic schists, and on the other with ironstones. This link will be explored in more detail below.

Chemical Changes Along Strike: Of all the elements examined, only Ba regularly changes with distance from chlorite lens to chlorite lens. There is no obvious relationship between the modal abundance of chlorite and the level of Ba. Ba content increases markedly from north (Area 257: 25 - 142 ppm) to south (Area 236: 553 - 824 ppm), mimicking a similar trend in mineralised and unmineralised ironstones (Figs. 7.11 & 6.10). In chapter 6 the ironstone trend was interpreted as a product of shallowing sedimentation in an evaporitic environment, unrelated to mineralisation. The application of this conclusion to the analogous

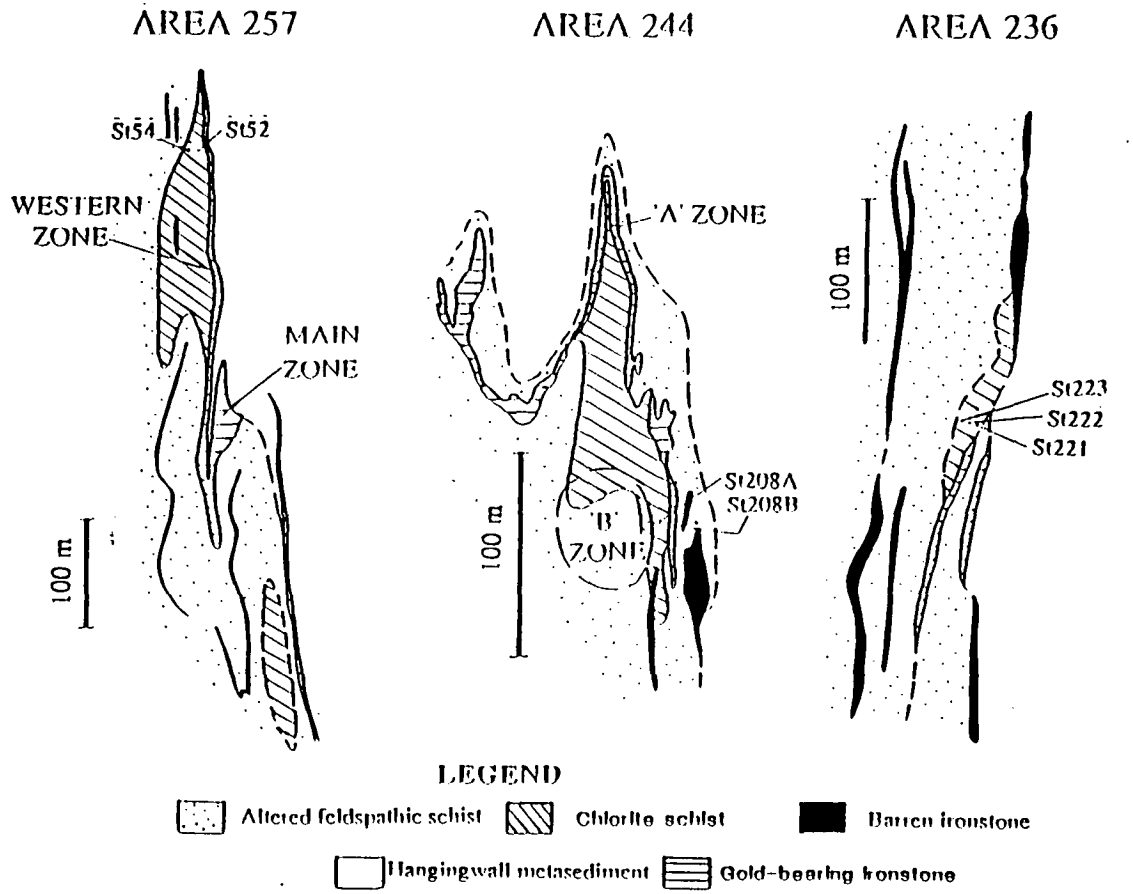

Figure 7.9 *Surface geological summary maps for three chloritite zones discussed in Chapter 7. At Area 257 chlorite schists forms a large zone below the highest grades in the "Western Zone" ironstone (see also Fig. 6.5). Chlorite schist also occurs at depth close to the "Main Zone". Area 244 chloritite is folded around a D2(LP) anticline beneath the auriferous "A zone". Area 236 chlorite lenses occurs on an unfolded ironstone segment, but is likewise associated with ore-grade (and notably magnetic) ironstone. This particular lens passes along strike to ironstone, as well as underlying it. These maps were compiled from Leishman (1983), and modified using additional mapping data. The approximate sample locations of rocks referred to in the text are projected to surface.*

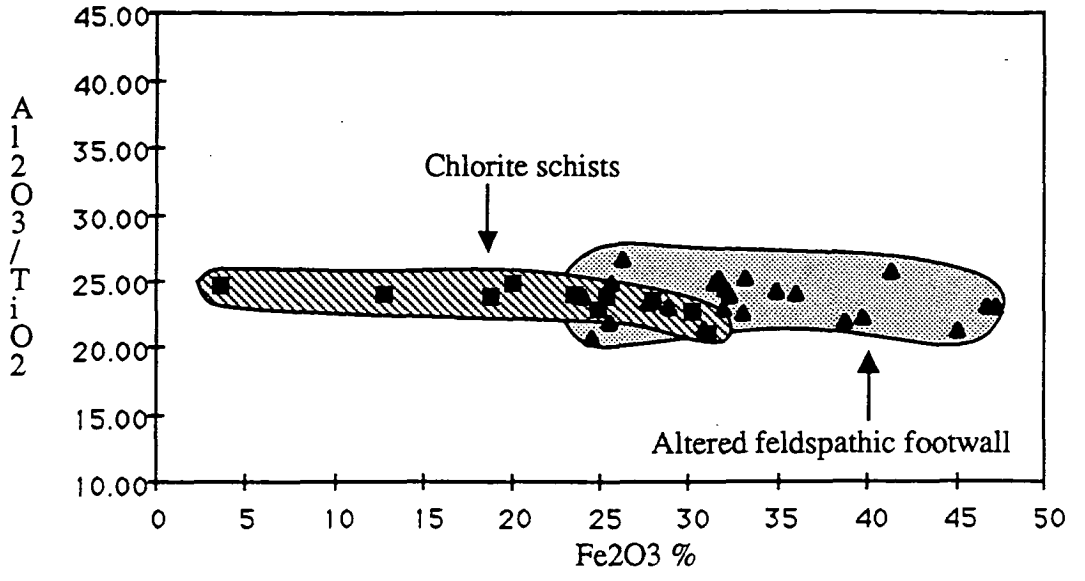

Figure 7.10 *A plot of Al2O3/TiO2 versus Fe2O3 illustrates the immobility of this ratio through the oxide alteration. The fields of chloritite and feldspathic alteration closely overlap along Al2O3/TiO2 ~ 24.5.*

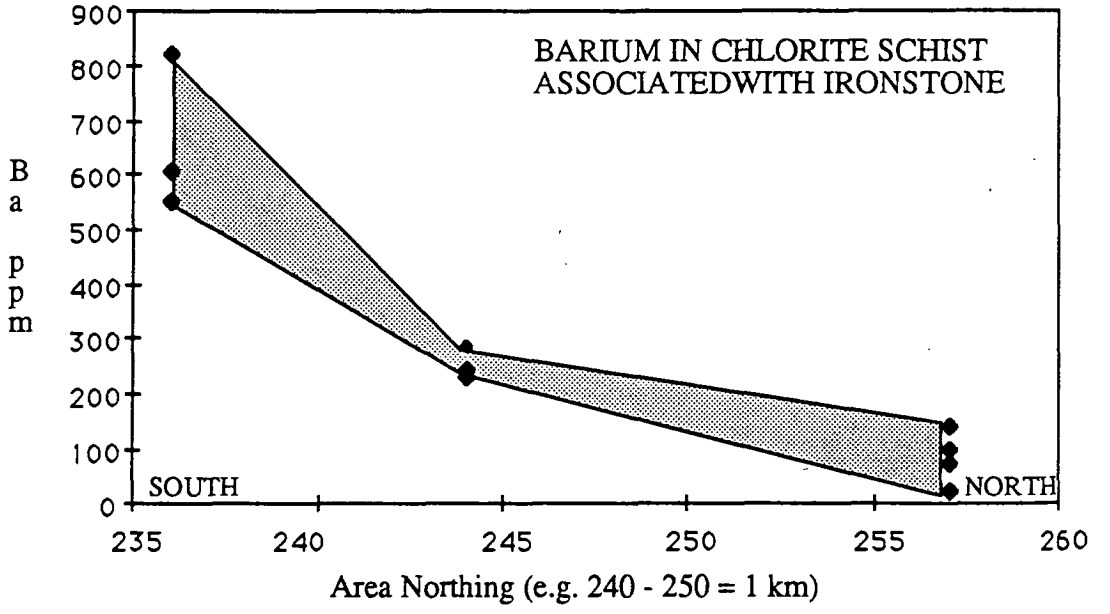

Figure 7.11 *The Ba content of chlorite schists increases with distance southwards. As indicated in Chapter 6, Ba in ironstone behaves similarly. Ba in the underlying feldspathic schist does not show regular changes with distance. It has a relatively uniform average of 48 ppm Ba, (maximum 130 ppm), much lower than in ironstone and chlorite schist (see Chapter 5).*

stratiform chlorite lens-trend provides an important genetic constraint. It requires that the chlorite formed at or near a sediment/water interface under similar conditions to ironstone, rather than developing later during alteration, metamorphism or deformation.

Chlorite Mineral Chemistry

Microprobe analysis of chlorite from the Starra ore environment was undertaken with the aim of chemically distinguishing different petrographic generations. A data compilation is presented in Appendix 7, with selected analyses in Table 7.2. Chlorites were analysed from the following settings:

1. Epidote-armoured chlorite: dark green non-pleochroic — **chlorite lenses.**
2. Massive foliated chlorite: light green-yellow pleochroic, intergrown with biotite — **chlorite lenses.**
3. Biotite replacive: light green-yellow chlorite — **chlorite lenses.**
4. Ironstone-hosted: green-yellow pleochroic.
5. Chlorite in reaction skarns adjacent to ironstone: description as above.
6. Chlorite in hangingwall veins: as above.

Weight %	1.Earliest chlorite generation St222	2.Massive chlorite St153	3.Chlorite after biotite in chlorite schist St202	4.Chlorite, ironstone St115	5.Chlorite in reaction skarns St40c	6.Chlorite in hangingwall metamorphic veins St203
SiO_2	31.32	27.27	30.99	27.64	26.67	28.21
Al_2O_3	15.69	21.87	17.06	21.55	23.18	20.77
FeO	19.07	14.59	14.66	12.23	10.88	11.88
Fe_2O_3	-	-	-	1.78	2.04	-
MgO	21.05	25.51	26.09	25.44	25.57	25.86
CaO	-	-	-	-	-	0.35
Sum	87.13	89.69	86.84	88.64	88.34	87.08
No. of cations on the basis of 14 oxygens						
SiO_2	3.19	2.69	3.08	2.70	2.60	2.78
Al_2O_3	1.88	2.50	2.00	2.48	2.66	2.41
FeO	1.62	1.18	1.22	1.00	0.89	0.98
MgO	3.19	3.69	3.86	3.70	3.71	3.80
CaO	-	-	-	-	-	0.04
Sum	9.88	10.06	10.15	9.87	9.85	9.98

Table 7.2 *Microprobe analyses of selected chlorites from the Starra ore sequence. The numbers in the table match the sample-types listed above.*

Of the above, the earliest chlorite generation is contained in massive chlorite lenses, rimmed by epidote. (Fig. 3.12B). These armoured chlorite relicts form layering which is not

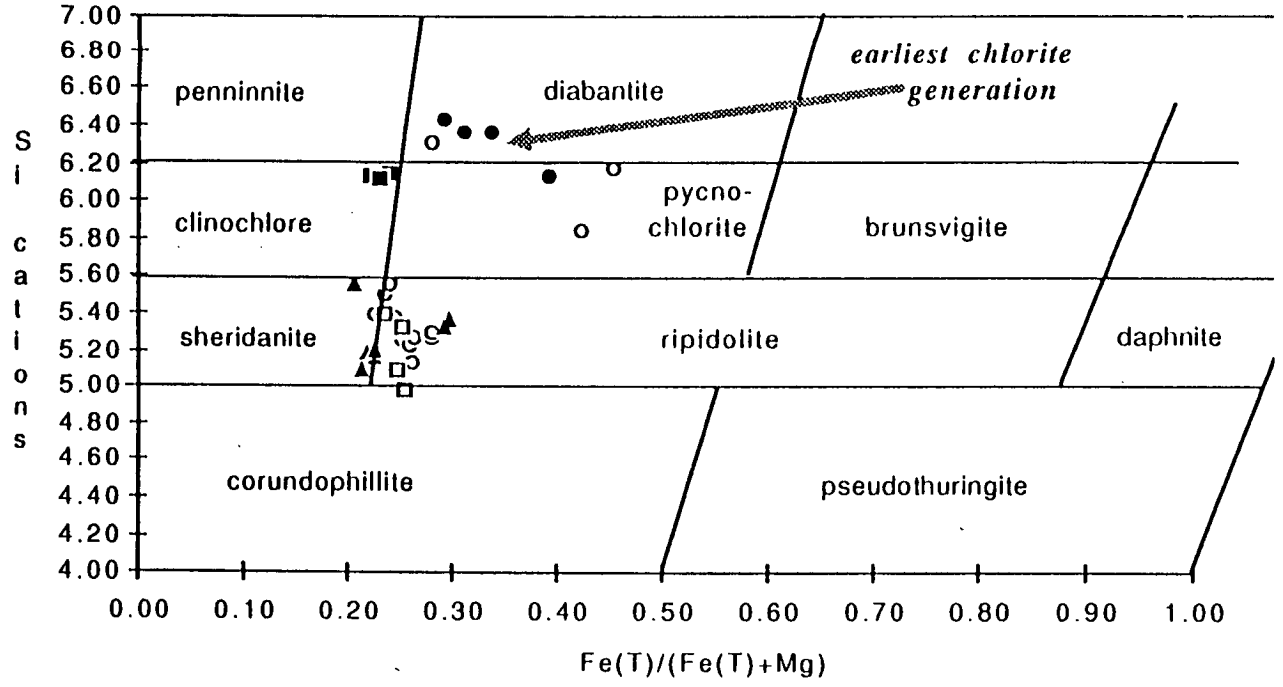

Figure 7.12 *Starra chlorite mineral chemistry, classified after Hey (1954). The earliest chlorite generation is Fe and Si-rich, and may be pre-deformational. All other chlorite groups are in some way related to deformation or metamorphism : chlorites are foliated, occur in veins, or clearly replace metamorphic minerals. Most of these chlorites are lower in Si and Fe than the earliest generation.* (**Filled circles**: *early chlorite*. **Unfilled circles**: *foliated chlorite*. **Filled squares** *chlorite after biotite*. **Unfilled squares**: *ironstone chlorite*. **Triangles**: *reaction skarns, late-carbonate veins.*)

aligned with the exterior foliation, contain many small randomly orientated inclusions (including tourmaline), and are finer-grained than the surrounding assemblage. They are interpreted as pre-metamorphic pre-deformational chlorite, which did not equilibrate with the surrounding minerals because of the prior hydrothermal or metamorphic growth of epidote. Chemically these early chlorites are more iron and silica-rich than the surrounding foliated chlorites (Fig. 3.12C), and are classified as the unoxidised chlorites diabantite and pycnochlorite (< 4 % Fe_2O_3; Hey (1954), Fig. 7.12). Surrounding chlorites are sheridanites and low-Fe ripidolites, or overlap with the earliest chlorite generation. Chloritic alteration products of biotite within massive chlorite lenses reflect the biotite chemistry closely, plotting as clinochlore (Fig. 7.12). Foliated chlorite in ironstone, and those retrogressively altering actinolite, albite and biotite in reaction skarns around ironstone, are all chemically similar.

The above chemical and petrographic evidence suggests that some chlorite in the massive chlorite lenses had a pre-metamorphic origin. These chlorites contain more Fe and Si than succeeding chlorite generations. The latter have on the basis of their chemistry probably equilibrated with chemically homogeneous metamorphic fluids.

The Origin of the Massive Chlorite Lenses

On the basis of the above evidence, the only relevant genetic precursors for Starra chlorite schists are:

(1) Metasomatic zones formed by a focus of metamorphic fluids.

(2) Reaction skarns formed by chemical diffusion away from ironstone.

(3) Isochemical metamorphic products of basaltic or Mg-evaporitic precursors.

(4) Hydrothermal alteration of host-rock during the exhalative growth of ironstones (chapter 6).

Field relations effectively rule out the first three alternatives. Chloritites show no preference for fold hinges, or cross-cutting shears, and are therefore unlikely to have formed at metamorphic fluid focal points. Their occurrence as discrete lenses eliminates an origin as metamorphic skarns around ironstones, developed during channelised metamorphic fluid flow, because ironstones occur over a much larger area than chlorite schists. Lens-like shapes also eliminate basaltic or Mg-evaporitic precursors, which are likely to be stratiform (e.g., Reinhardt 1987). As previously dicussed, a basaltic precursor is also not supported by the geochemistry.

Magnesian chemistry can be explained by Mg-K-Ca alteration of feldspathic schist. However, the gross distribution of Ba in stratiform chloritite is best explained by an interaction between chlorite and the sedimentary environment, by analogy with Starra ironstone. Petrographic and chemical evidence requires that some Fe-rich chlorite was present prior to the metamorphic growth of epidote.

The fourth alternative, that of pre-deformational hydrothermal alteration during exhalative ironstone formation, best explains these features. Under this model, the observed coincidence of massive chlorite and Au-rich ores is likely to be genetic.

On the modern seafloor (Helkinian et al. 1978, Rona 1988), and in numerous ancient examples (e.g., Rui 1973, Shimozo 1974, Riverin & Hodgson 1980, Kalogeropoulos & Scott 1983, Large et al. 1988, Schmidt 1988), chloritic alteration is observed to underlie massive sulphide exhalative vents. It is also a common feature of volcanogenic oxide deposits (Quade 1976, Bhajwar 1985). The alteration forms network-veined funnel-shapes immediately beneath conformable polymetallic ore. Stratiform lenses within, along strike and above sulphide ore also occur, but are not common (Quade 1976, Bernard et al. 1982, Schmidt 1988). They are, however, a variant of "tetsusekiei" (hematite-quartz-chlorite) layers overlying Kuroko ores (Kalogeropoulos & Scott 1983). Many chemical studies have shown that the footwall chlorite alteration originates as one of successive alteration shells produced when cool Mg-rich seawater mixes with the ascending hydrothermal fluid (e.g., Shimozo 1974, Riverin & Hodgson 1980, Schmidt 1988).

At Starra the trends in Ba in lenses of chlorite, and their stratiform character, are evidence that at least some chlorite accumulated on the seafloor. These units possess the same Nb/Y ratio as associated ironstones (~0.20 or less), yet also have chemical features of the feldspathic host rock, such as constant Al_2O_3/TiO_2 ~ 24. They cannot have developed as true chemical exhalites deposited from solution, because the latter would possess low Al_2O_3/TiO_2 ratios, and low levels of other clastic elements such as Zr. One possibility is that they represent alteration products initially formed below the sea-floor, which were subsequently physically eroded by turbulent hydrothermal fluids (Schemerhorn 1978). Such chloritites are interpreted to be the result of changes in permeability and stability of convective cells within alteration zones (Bernard et al. 1982). By analogy with the well-preserved Kuroko ores (Kalogeropoulos & Scott 1983), a more likely origin is that chlorite lenses below iron formation represent sub-surface alteration zones, experiencing some hydrothermal addition of Y, whereas the stratiform examples represent conformable layers of porous clastic and volcaniclastic detritus altered by low temperature exhaled fluids (< 200° C; Ohmoto et al. (1983)). Nb and Y concentrations in the latter were mainly controlled by the fluid chemistry.

CONCLUSIONS

1. The Staveley Formation basalts which regionally underlie the Starra Iron-formation Member are chemically transitional between continental and ocean floor tholeiites. Their widespread occurrence at the base of the Staveley Formation is evidence that sedimentation was preceded by rejuvenated rifting within the Mary Kathleen Shelf (Blake et al. 1984).

2. The Harley Member contains samples chemically transitional between Staveley Formation basalt, and Mariposa Creek Member feldspathic schist. A mixed acid/basic volcanic - sedimentary origin is suggested, with possible subsequent K-metasomatism during the development of the Starra Shear.

3. The physical and chemical aspects of massive chlorite lenses found close to gold-rich ironstones cannot be explained by metamorphic or deformational processes. They are interpreted as Mg-alteration zones formed by the interaction of seawater with feldspathic host-rocks beneath exhalative vents. The chemistry of stratiform chloritite has some similarities to the associated ironstones (Ba, Nb/Y levels), but the variation of Al_2O_3/TiO_2 and Ti/Zr cannot be explained if these rocks formed as chemical sediments. One solution to this dilemma is their origin via the low temperature sub-surface alteration of porous clastic/volcaniclastic sediment.

CHAPTER 8

THE RARE EARTH ELEMENT GEOCHEMISTRY OF STARRA IRONSTONES AND WALL-ROCKS.

INTRODUCTION

The coherent behaviour of the lanthanides, caused by their common +3 oxidation state and gradually changing ionic radii, renders them useful elements in the study of geological processes. The aim of the present study is to

(a) examine Rare Earth Element (REE) behaviour at Starra,

(b) assess whether mineralised ironstone has a unique REE signature useful for exploration, and determine if it is preserved in the weathered equivalent,

(c) compare the Starra patterns to known signatures of epigenetic and exhalative magnetite-Au-Cu ores of the world, to discriminate between these contrasting origins.

METHODS

In this study, only selected samples were analysed for all the lanthanides, but all lithologies were analysed for La, Ce, Nd and Y by XRF techniques. These values are tabulated in Appendix 8, with selected analyses in Table 8.1. Analytical techniques are discussed in detail in Appendix 2. Mineralised and barren ore-environment, and barren-distal ironstones were examined in detail, as were stratiform tourmalinites, stratiform chlorite schist lenses, albitic footwall and basalts. Averaged mineralised ironstone compositions were obtained for each Starra prospect from metallurgical composites compiled by Cyprus Minerals, analysed by an ICP process at Perth Metallurgical Laboratories (see Appendix 2). Sm values in these results were consistently low and have been estimated in the plots from the La-Ce-Nd slopes (Fig. 8.1A). The composites were originally selected by Cyprus on the basis of the overall gold grade of the drill intercept, a method which did not prevent the inclusion of thin intervals of barren ironstone. These samples are nevertheless useful for the study of REE changes during weathering.

Unless otherwise stated, the REE presented graphically have been normalised to the chondrite values of Evensen (1978). The practice of normalisation to shales for some chemical sediments (e.g. Barrett et al. 1988) is not seen as useful here because of the variety of rock-types which host the iron formations: chondrite normalisation permits a wider comparison with the literature. The term La/Yb* used throughout is the ratio of the chondrite-normalised abundances of these elements. Eu/Eu* is a term which describes the extent of Eu depletion or enrichment relative to Sm and Nd, its nearest neighbours: $Eu/Eu^* = Eu_N/\{Sm_N+(|Sm_N-Nd_N|/2)\}$, where "$_N$" indicates the chondritically-normalised value of a particular element. Values of Eu/Eu* less than 0.95 indicate europium depletion,

and greater than 1.05, enrichment. Other abbreviations used in this chapter are HREE, MREE, and LREE, which are acronyms for heavy, middle and light rare earth elements.

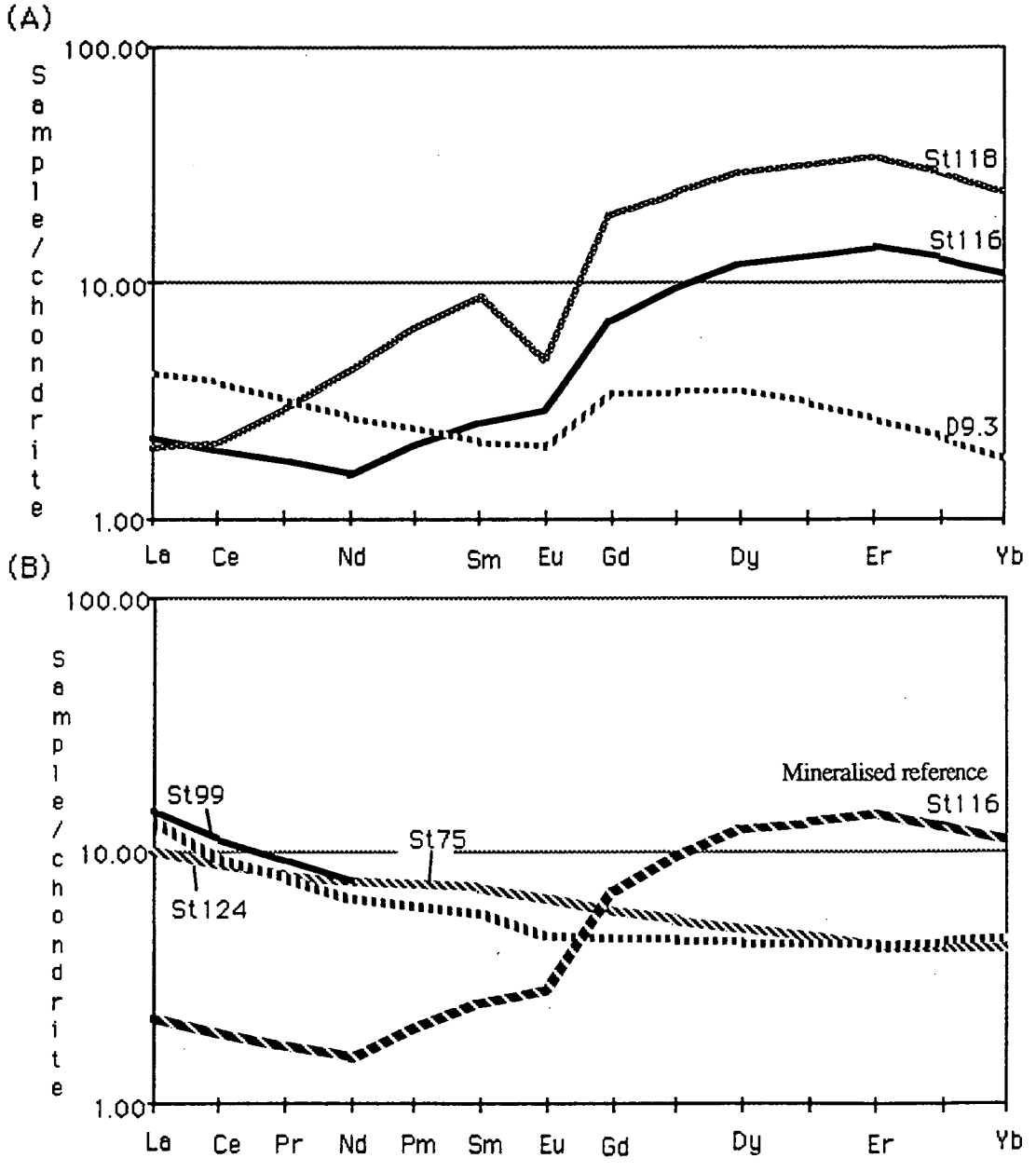

Figure 8.1A *Detailed REE analyses of mineralised ironstones from Areas 257 and 251.* **Figure 8.1B** *Barren ore-environment ironstones from Area 257.They are characterised by low REE levels and slight LREE enrichment relative to mineralised ironstone, such as St 116.*

RESULTS

Proximal Mineralised and Barren Ironstones

A comparison of primary rock composites for each Starra ore zone (obtained by Cyprus Minerals), indicates that the abundance of REE increases southwards from Area 257 (Σ= 25.9 ppm) Area 244 (Σ = 71.9 ppm) and thence to Area 222 (Σ = 160.1 ppm).

	La	Ce	Pr	Nd	Sm	Eu	Gd	Dy	Er	Yb	Y
BIFS & IRONSTONES											
Barren, well-banded, distal											
A7	46	88	-	47.5	6.69	1.55	4.04	2.73	1.33	0.4	7
24/92	13.2	28.8	3.05	12.1	2.25	0.72	1.88	2.24	1.37	1.23	11.5
Barren, massive, distal											
SG28	3.3	<5	-	<3	-	-	-	-	-	-	6
SG30	6.6	<5	-	<3	-	-	-	-	-	-	32
Barren, massive, ore environment											
St75	3.68	8.51	1.1	-	1.64	-	1.76		1.03	0.99	9
St124	4.89	8.93	-	4.64	1.3	0.4	1.37	1.64	1.05	1.11	10
Mineralised ironstones											
St116(257)	0.81	1.85	-	1.08	0.58	0.25	2.09	4.61	3.54	2.68	27
St118(257)	<0.5	2	0.4	3	2	0.4	6	11	8.5	6	98
D9.3 (251)	1.51	3.54	0.44	1.93	0.48	<0.22	1.05	1.32	0.66	0.45	-
Primary 257*	3.7	9.9	1.2	3.9	1.1	0.3	1.5	2	1.2	1.1	11
257oxidised*	6.1	15	1.7	6.8	1.3	0.4	2.4	2.1	1.5	1.3	12
257leached*	42	110	12	42	5.6	1.7	6.8	4.9	2.6	3.3	28
Primary 251*	4.5	9.3	1.1	4.4	0.8	0.3	1.3	1.1	0.8	0.4	7.5
251oxidised*	11	23	2.5	9.8	1.3	0.4	2.1	1.9	1.1	0.9	9.1
251leached*	40	50	11	40	7.2	1.5	8.4	5.7	3	3	31
OTHER LITHOLOGIES											
Tourmalinite											
SG43	3.41	7.11	0.9	4.2	1.59	0.6	2.37	3.63	2.61	2.79	-
SG45F	5.12	8.09	0.83	3.53	1.37	0.48	1.93	3.02	2.19	2.69	18
Least Altered Footwall											
St152	11.8	25.1	2.97	12.8	2.82	0.45	3.27	4.5	3.29	3.41	35
St109	13	24.9	2.88	11.6	2.53	0.4	2.16	2.11	1.37	1.42	15
Most Altered Footwall											
GD110	5.86	12.8	1.51	6.23	2.02	0.67	4.79	8.7	6.29	5.17	12
GD111.	10.4	20.2	2.31	9.12	2.62	0.65	4.29	6.94	4.54	4.23	-
Chlorite schist											
St221	10.3	21.3	2.64	11.8	3.58	1.09	5.22	6.58	3.69	2.28	-
Basalt											
STP5/90	12.6	27.1	3.11	12.2	2.61	0.82	2.85	3.39	1.97	1.86	21
Dolerite											
St154	26.9	15.5	-	12	-	-	-	-	-	-	33
Footwall veins, and hangingwall skarn											
St95.vein	4.4	6.4	-	8.1	-	-	-	-	-	-	7
St64.vein	8.6	17.2	-	6.8	-	-	-	-	-	-	14
St148.skarn	112.2	49.5	-	51	-	-	-	-	-	-	20
St165.skarn	38.8	16.7	-	23	-	-	-	-	-	-	36

Table 8.1 *Selected rare earth element analyses of Starra lithologies. Elements not analysed are shown by "-". All values are in ppm. * Cyprus Minerals composites, representing average REE compositions of the ores.*

Sampling of individual mineralised mag - cpy - qtz ironstones was carried out at Areas 257 and 251. The REE patterns are strikingly different to those of most hydrothermal rocks, in being LREE poor, HREE rich ($La/Yb^* = 0.06 - 2.26$), with a variably negative Eu anomaly ($Eu/Eu^* = 0.35 - 0.94$) (Fig. 8.1B), and ΣREE averaging 21.5 ppm. In two

of the samples HREE and MREE enrichment commences with Nd, tailing off slightly in all samples over Er - Yb (Fig.8.1a).

In contrast, two samples of ore-environment hematitic iron formation (Au < 0.1 ppm), obtained from less than 100 m along strike from ironstone mineralisation, and in one case immediately overlying it, have flat to slightly LREE-enriched patterns (La/Yb* = 2.51 - 2.98), no Eu anomaly, but ΣREE similar to mineralised samples. La, Ce and Nd in transitional weakly mineralised samples (Cu = 4250 - 7800 ppm, Au < 0.3 ppm) have higher LREE than both mineralised and barren ironstones (Appendix 8).

This detailed analysis readily discriminates mineralised from barren ore environment ironstones on the basis of their REE patterns.

Weathering Effects

Observations

The Cyprus Minerals metallurgical composites were used to determine changes in the lanthanide pattern of ironstone during weathering (Fig. 8.2). For metallurgical purposes the uppermost weathered ironstone was classified as "leached" to a depth of 41.5 m at Area 251, and "oxidised" down to 98 m (Pontifex 1986).

ΣREE increase dramatically in the leached zone of Areas 257 and 251 (only Area 257 is shown in Fig. 8.2), accompanied by a relative increase in LREE, and a decrease in the magnitude of the negative Eu anomaly. An increase of between 5.7 to 8.9-fold occurs in ΣREE between the primary and leached zones, whereas the oxidized zone shows increases of between 1.5 and 2.3-fold over the primary rock. The LREE exhibit proportionaly greater increases: for instance, Ce at Area 257 increases 11.1-fold from the primary to the leached zones. In summary, REE clearly accumulated steadily but disproportionately in the Starra weathering zones, and hence the values of the leached composites cannot be used to infer the values of the primary rock. This may explain why Switzer et al. (1988) claim that Starra ores are REE-enriched, when in fact they are well below average crustal abundances.

Interpretation

Mobility of the lanthanides during intense chemical weathering has been documented by Burkov & Podporina (1967), Maksimovic & Roaldset (1976) and Nesbitt (1979), among others, emphasising that acidic pH is a major controlling factor under humid conditions. All of these authors have shown a successive enrichment of the lanthanides with prolonged weathering, by clay adsorption. Nesbitt (1979) noted that bicarbonate complexing of HREE can enrich them disproportionately to LREE in the weathered profile. Rankin & Childs (1976) found that Fe-Mn concretions in New Zealand soils particularly concentrated all the REE; by analogy weathering Starra ironstones would have reacted similarly.

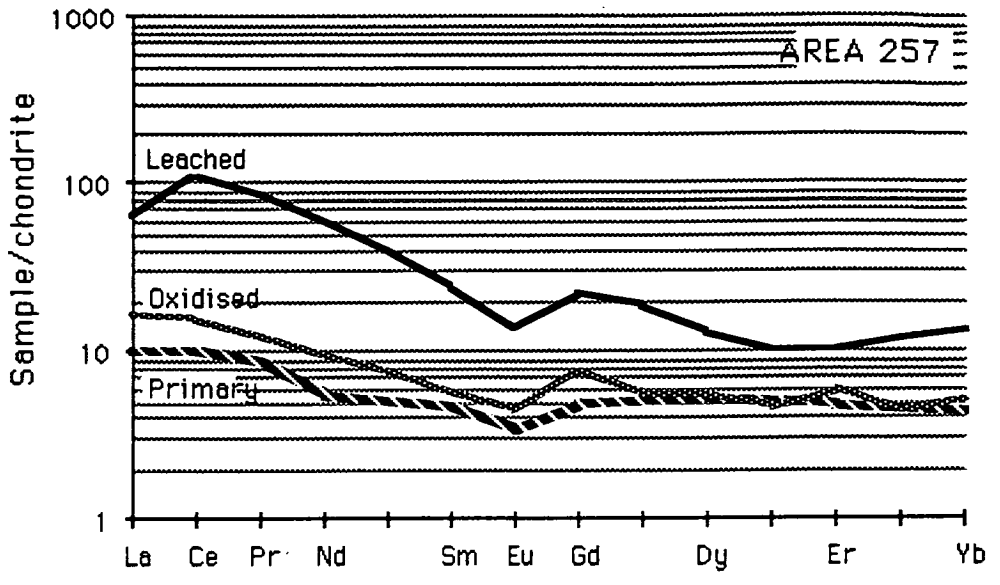

Figure 8.2 *A comparison between the REE distribution in the primary, oxidised, and leached zones of Area 257 mineralised ironstone. In each case diamond-drillhole material was composited from a large number of holes, and analysed by ICP methods for the REE by Cyprus Minerals.The results show a gradual change in the composite pattern through weathering, and an absolute REE increase of 5 to 8-fold.*

Areas 257 and 222 have well-developed 1 – 2m thick layers of laterite at ~ 420 m above sea level, indicating that the ironstones were exposed to the Tertiary-age tropical weathering episode experienced by much of northern Australia. In addition, dissolution of sulphides during weathering would have promoted acidic ground-water conditions, and hence accelerated the leaching of lanthanides, with probable reprecipitation at the top of the water-table by mixing with meteoric water. REE must have been leached from LREE-enriched wall-rock as well as the underlying ironstone, to account for the LREE-enriched weathered values of the leached zone. However, individual (as distinct from composite) signatures of barren and mineralised ironstones are likely to have been preserved if the amount of original sulphide was not great. This is certainly the case for many non-gossanous mineralised ironstones at Area 257, as was confirmed in chapter 6 for yttrium, a REE analog.

Distal Barren Massive Ironstones, and Cherty BIFs

All distal barren ironstones were chip-sampled several kilometres from known mineralisation, apart from STP 24/92, which was obtained from a percussion hole at 92 m (location available on Fig. 3.2). While caution suggests that Starra-style weathering processes, discussed above, may have acted on these surface samples, the low sulphide contents of distal BIFs would not have promoted the low pH conditions which favour REE mobility. This is supported by a comparison of the one deep sample and the surface samples, in Figure 8.3.

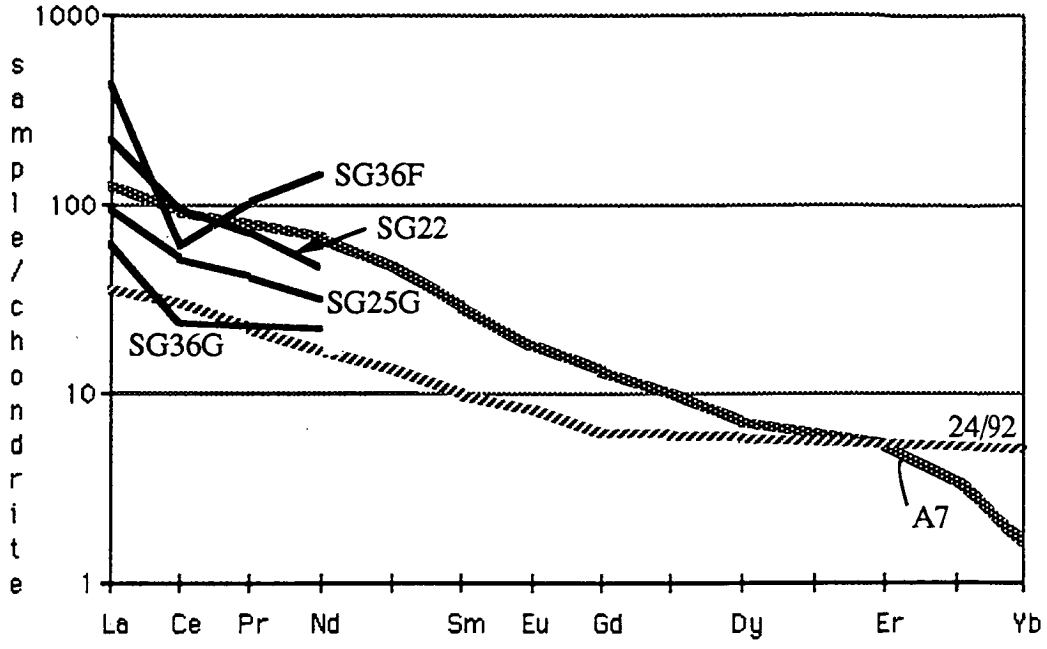

Figure 8.3 *Distal, barren, cherty iron formation. Samples shown in black were analysed only for La, Ce and Nd. As a group the samples are uniformly LREE-enriched over all other iron formation styles in the basin, a fact attributed both to the influence of apatite, and to the contribution of clastic sediment(see discussion). Variable Ce depletion is evident, but Eu does not deviate from the other lanthanides.*

The barren iron-rich rocks are divided texturally into cherty well-banded, and massive, hematitic varieties, as previously discussed. Each contains different concentrations of REE. Hematitic massive ironstones, with $Fe_2O_3 > 75$ %, have only been analysed for La, Ce, Nd and Y. In all instances the REE results of these were below detection for Ce (5 ppm) and Nd (3 ppm), whereas La ranged between < 3 and 6.6 ppm. Where La was detectable, plotting of chondrite-normalised Y after Ho (closest to Y in ionic radius) in the pattern indicates a slight LREE enrichment, a pattern distinct from that of mineralised ironstone, but similar to proximal barren hematitic ironstone.

In contrast, cherty BIFs contain moderate to high ΣREE, are LREE-enriched (La/Yb* = 6.9 – 74.4), and have no perceptible Eu anomaly (Fig. 8.3). Some samples analysed only for LREE, contain up to 325.3 ppm of La, Ce and Nd alone, and hence are probably strongly REE-enriched overall. A feature of several samples (e.g. SG22, SG36F, SG41B; Appendix 8 and Fig. 8.3) is a distinct Ce depletion, although this is not present in all the cherty BIFs. The very high REE levels are atypical of banded iron formations in general (Fryer 1977), but are similar to the concentrations in apatite-rich varieties.

Tourmalinites

The REE analyses of stratiform tourmalinites SG43, SG45F and SG49 are the first known for this rock-type from the literature. SG43 is a tourmaline concentrate; the similarity of its pattern to that of the other samples suggests that their REE trends are also tourmaline-dominated, with quartz acting as a dilutant.

The patterns are skewed and "dish"-like, with the concave-down apex occurring at Nd (Fig. 8.4). Eu and Ce anomalies are absent. La is distinctive because of its sharply higher concentration. Two out of the three analyses have chondrite-normalised HREE > LREE, with La/Yb* of 0.51, 0.83 and 1.29. ΣREE are low, between 12.5 - 29.3 ppm. Few comparable patterns have been located in other sediments or volcanics of the literature, although Hamersley iron formation possesses similarities which will be subsequently discussed. Iron formation closely interbedded with Starra tourmalinite differs markedly to the adjacent tourmalinites by having higher ΣREE and strong LREE enrichment (Fig. 8.4).

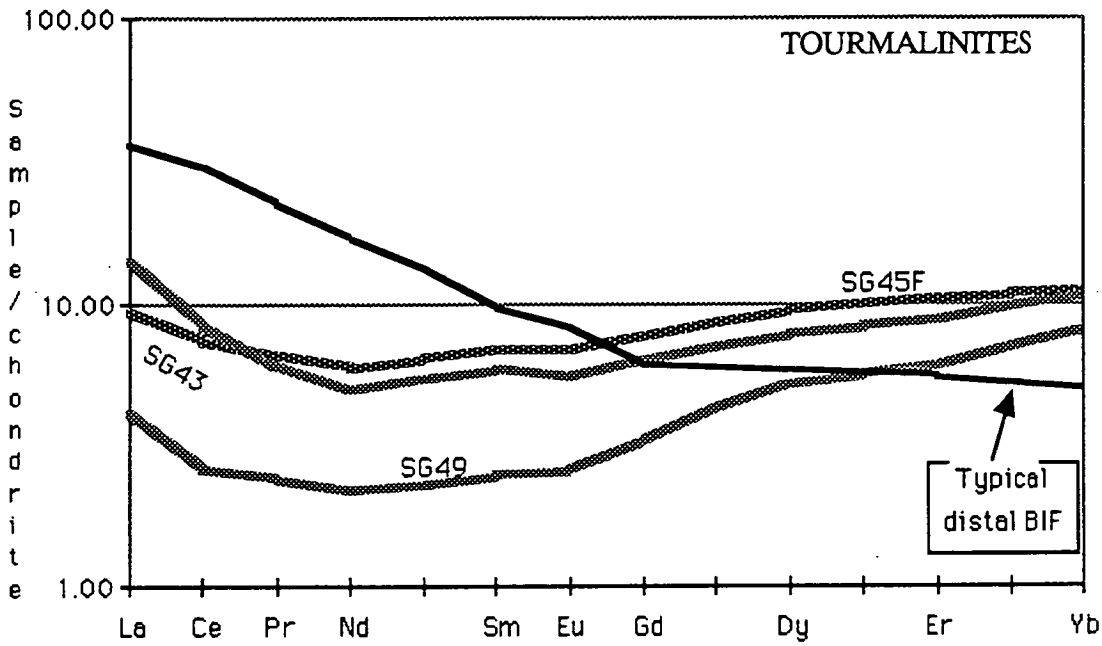

Figure 8.4 *Stratiform and shear-related tourmalinites, compared to a typical distal silicic BIF, a lithology which is a common companion to tourmalinite. SG43 is a tourmaline concentrate, emphasising that the patterns observed in tourmalinites are caused by REE contained within tourmaline.*

Mafic Lithologies

Fe-rich basalt and stratiform chlorite schist were sampled for all the REE (Table 8.1), while dolerites, and the Harley Member ("Answer Schist" of Leishman (1983)) were sampled only for La, Ce, Nd and Y.

The basalt patterns obtained from percussion drill-holes 10 – 25 km south of Starra below iron formation (see Chapter 7), are typical of evolved tholeiites, with LREE enrichment (La/Yb* = 4.58), intermediate ΣREE (68.5 ppm), and no Eu anomaly. The range of LREE values, up to 95 X chondrite, is well within the tholeiite spectrum (Cullers & Graf 1984a) and is explicable in terms of limited differences in the degree of fractional crystallisation of the parent magma. Using only the REE patterns, it is not possible to differentiate between a continental, island arc or back-arc origin for these tholeiites.

Samples of chlorite-biotite-feldspar schist (Harley Member), fall in a narrow band at the top of the observed range of tholeiites (Fig. 8.5), and have similar slopes for the LREE.

The LREE patterns are compatable with an origin as evolved tholeiitic basalts. In contrast, two samples of dolerite, identified as continental tholeiites on other chemical grounds (Chapter 7), have consistently higher LREE slopes. They are unlikely to have originated from the same parent magma as any of the analysed basalts. This supports the conclusions of chapter 7 made on major element grounds, that the parent magmas of some Staveley Formation basalts were chemically distinct from those of the majority of Eastern Succession basalts and dolerites (e.g., Fig. 7.6).

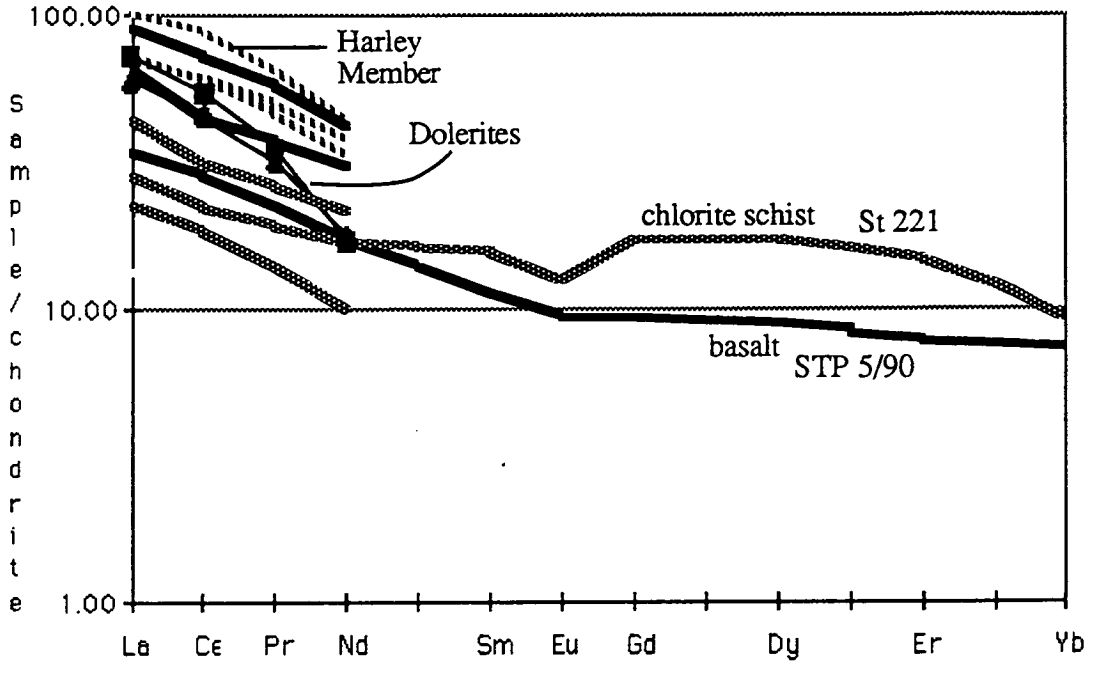

Figure 8.5 *Mafic lithologies in the Starra area. These include regionally-developed basalt (black), probable basalt/mixed sediment from the lower Starra footwall (Harley Member, dashed lines), dolerites (thin black lines and squares), and stratiform chlorite schist developed close to mineralisation (grey). The latter shows the distinct MREE - HREE enrichment which characterises the mineralised ironstone.*

Chlorite lenses close to mineralisation within the Mariposa Creek Member, have a LREE character similar to the least-evolved of the sampled basalts (however, absolute REE levels are also likely to have been reduced by dilution during alteration). The single ion-exchange REE pattern obtained for stratiform chlorite schist (taken from Area 236) displays HREE enrichment similar to that found in mineralised ironstone, and altered feldspathic footwall. On the basis of the REE patterns alone, it is therefore not possible to differentiate these chlorite schists within the alternatives of altered basalt, altered feldspathic footwall, or exhalative sediments. It is only clear that they participated in the HREE enrichment characterising the mineralising event.

Feldspathic Footwall Schist

The least altered equivalents of the altered feldspathic footwall were analysed to further constrain the affinities of the protolith. The resulting patterns (Fig. 8.6a) are

variably enriched (La/Yb* = 2.34 - 6.19), with very distinct negative Eu anomalies (Eu/Eu* = 0.45) slopes that differ between the LREE and HREE segments (hinging around Eu), and ΣREE between 62.4 and 67.6. They are compatible with the rhyodacitic parentage suggested from major element geochemistry and rock-textures. However, it is uncertain whether the Eu anomaly, and the slight HREE enrichment in St 152, are primary igneous features. This is because even the "least altered" footwall rocks at Starra have suffered strong diagenetic albitisation, with the consequent loss of K, Ba, Rb and Sr (Chapter 5). As Sr^{2+} and Eu^{2+} have almost identical radii, it is probable that Eu was also excluded from secondary albite, prior to the main hydrothermal event. Hence hydrothermal fluids in the Starra footwall are likely to have leached an already Eu-depleted protolith.

One certainty from the "least altered" footwall patterns is that they cannot be cogenetic with the underlying evolved tholeiites of the Harley Member, or other along-strike basalts. The REE concentrations of the freshest felsic footwall samples are lower than those of the tholeiites, and could therefore not be the result of either increased fractional crystallisation, or smaller degrees of partial melting of the same source material. This is in accord with the model of Wyborn et al. (1988) for the evolution of the Mount Isa Inlier and other rifted Proterozoic terrains, in which the acid volcanics mainly derive from melting of the lower crust during the underplating of mafic magmas.

Footwall Alteration Effects

Although several altered footwall samples were analysed for LREE, only one complete REE spectrum was obtained. This sample was taken from 5 m below mineralised ironstone, in the centre of a severely altered "pipe-like" zone identified at Area 251 (location shown on Figs. 4.7 & 12.8). It consists of a matrix of hematite, magnetite and chalcopyrite, surrounding relict kernels of reddened, silicified, pyritic albite schist. Matrix and fragments were originally compositionally identical. The zone is interpreted as a focal area for the hydrothermal fluids which supplied metals to overlying ironstone.

The REE pattern of this zone is similar to mineralised ironstone, with LREE depletion and strong MREE-HREE enrichment commencing from Gd. La/Yb* is 0.77, although the most enriched element in these patterns is Er. ΣREE = 54.2 ppm, and a moderate negative Eu anomaly occurs (Fig. 8.6b).

A separate analysis of the albite schist 'kernels' identified LREE abundances close to the "least altered" rhyodacitic precursor, but less HREE enrichment than the altered whole rock. The La/Sm* ratio, a measure of LREE enrichment, was reduced from 2.50 in the albitic kernels (2.63 in "least altered" tuff), to 1.83 in the most altered whole rock, which is evidence of the mobility of LREE with respect to the MREE.

It is therefore suggested that alteration in the pipe-like zones proceeds first by the addition of HREE to an albite-pyrite rock (commencing with Eu). Then, with the alteration of this assemblage to iron oxides via the breakdown of LREE-enriched albite, LREE are leached relative to Sm and Eu, accompanied by further HREE addition. The process is not

related to simple volume change, which would change ΣREE without affecting the shape of the spectrum. A logical extension of future study will be to explore the deeper sections of the alteration to seek areas of REE depletion, which must logically exist, and have been located in other hydrothermal systems (e.g., Campbell et al. (1984) and Palacios et al. (1986)).

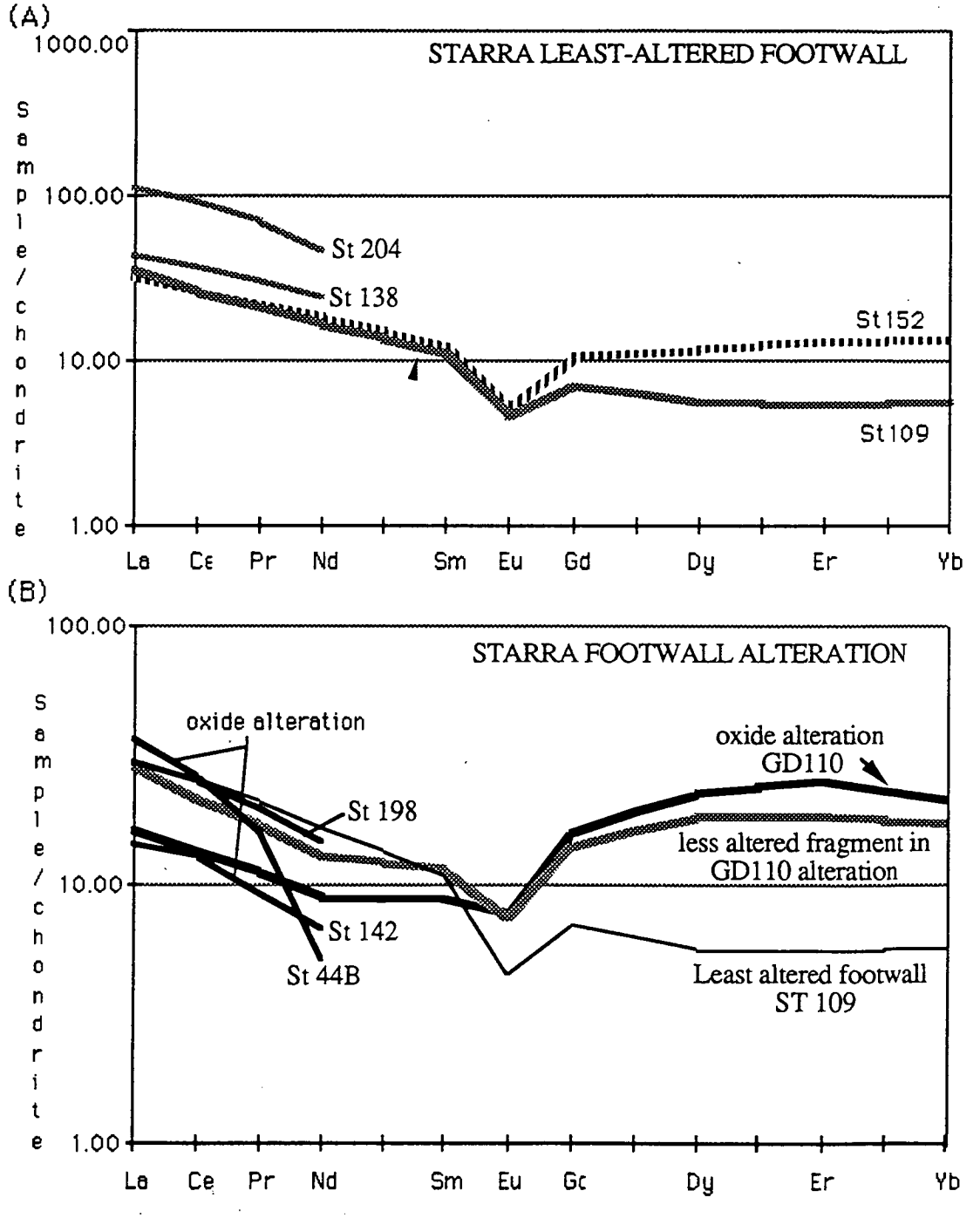

Figure 8.6A *The least altered footwall lithologies (grey and striped) show typical features of felsic volcanics — the hinging of two variably-sloping segments around Eu . These patterns indicate that the felsic volcanics did not share a common source with the underlying basalts.* **Figure 8.6B** *Alteration signatures of the most-altered footwall (black), compared to least altered sample St 109. Features of alteration LREE depletion and HREE enrichment .*

Fresh and Alkali-altered Sediments, and Skarns

Samples of biotite-actinolite-scapolite-magnetite skarn, analysed only for La, Ce, Nd and Y only, were compared to fresh and alkali-altered Staveley Formation

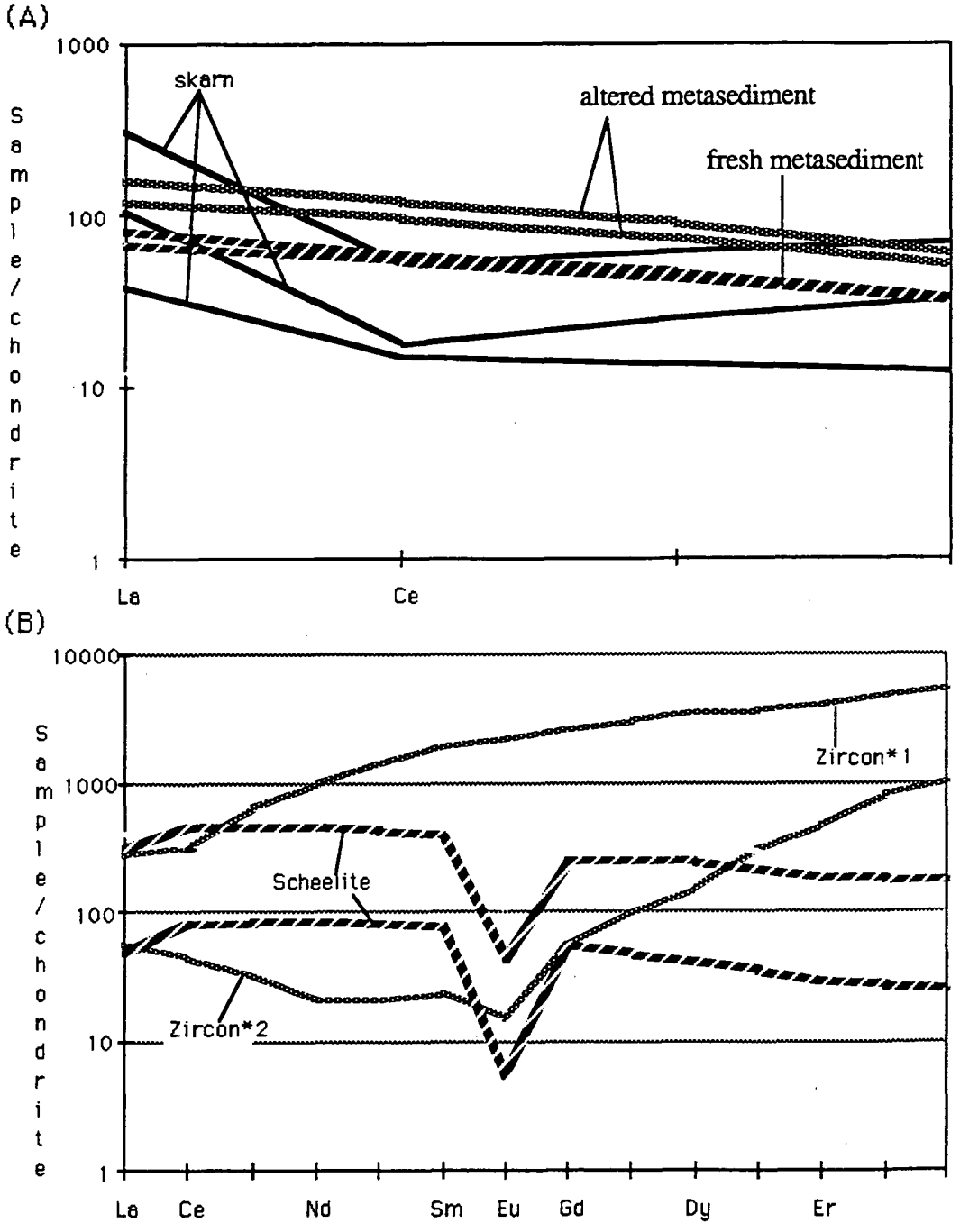

Figure 8.7A *Metamorphic skarn samples (black) occurring at the ironstone-hangingwall contact have a distinctive negative Ce anomaly, compared to fresh (diagonal striped) and altered metasediments(grey stiple).* **Figure 8.7B Two** *possible host/source minerals for REE in the Starra ore deposit. The scheelite separates were obtained by Guiliani et al. (1987), whereas the zircon patterns are typical examples gleaned from Taylor & Mclennan (1985){1} and Exley (1980){2}.*

metasediments. The skarns occur above the ironstone-hangingwall contact in places, contain up to 1% copper but little gold, and have replaced calcareous metasediments.

The average of fresh sediments for ∑(La, Ce, Nd) (see Appendices 3 and 8 for data), is 121.03 ppm, range 97.1 - 155.3 ppm, compared to an average "least altered" volcanic footwall value of 82.6 ppm. Alkali-altered metasediments (average ∑REE = 148.3 ppm, range of 80.8 - 213.7) are enriched over fresh metasediments. In the latter group the highest values occur in calcite-veined metasediment, with very high Na_2O (7.19 %) and low K_2O (0.13 %), and hence adsorption on to biotite or other sheet silicates is an unlikely enrichment mechanism. However, the similarity of pattern slopes between the two suggests that the differences were caused by volume changes, not differential LREE deposition. In contrast, three skarn samples are significantly depleted in Ce compared to the parent metasediments (Fig. 8.7A.). Although this skarn REE study is not intended to be definitive, early indications are that calc-silicate skarn development is accompanied by (1) redistribution of REE, and (2) no HREE enrichment, as indicated by the behaviour of Y. (On the contrary, LREE-enrichment is supported by La/Y* ratios in the range 4.8 to 13.9).

DISCUSSION

REE Behaviour In Hydrothermal Systems

This topic has been reviewed by Cullers & Graf (1984b).

Rare earth elements are known to be carried as chloride, fluoride, carbonate and sulphate complexes (Bandurkin 1961, Mineyev et al. 1961, Flynn & Burnham 1978, Sanjuan et al. 1988), but in most hydrothermal systems carbonate and chloride anions dominate (Cullers & Graf 1984b, Michard & Albarede 1986). Many studies emphasise the immobility of REE during weathering, low temperature metamorphism, and low temperature - low Water to Rock (W/R) ratios under hydrothermal conditions (Staudigel et al. 1979, Menzies et al. 1977, Campbell et al. 1984, Cullers & Graf 1984b, Whitford et al. 1988). Michard & Albarede (1986) have demonstrated that the common water to rock (W/R) ratios of 1 - 5 which characterise hydrothermal fluids from the East Pacific Rise (EPR), are well below those required ($>10^6$) to alter the REE rock concentrations, although they are sufficient to hugely enrich the fluid in REE relative to seawater. Nevertheless, some massive sulphide alteration zones, and other hydrothermal systems, show distinct REE mobility, diagnostically indicated by changing ratios of REE. For instance, Campbell et al. (1984) and Maclean (1988) noted the loss of LREE and Eu at Kidd Creek, Canada, and suggested that losses in general were a function of the size of hydrothermal systems. Exley (1980), Alderton et al. (1980), Palacios et al. (1986), and Guiliani et al. (1987) also have documented significant mobility of the LREE in granite-related chloride-dominated hydrothermal systems. Kerrich & Fryer (1979) invoked leaching under high W/R conditions, and carbonate complexing, to explain large HREE depletions in basalts and komatiites at the Dome Mine, Canada.

While REE complexing is one control on the REE composition of the hydrothermal fluid, another is the stability of mineral phases in the hydrothermal reservoir. Most commonly, Eu and LREE are readily contributed to hydrothermal fluids via the breakdown

of glass, plagioclase and K-feldspar, which are LREE and Eu-enriched. For this reason EPR hydrothermal fluids are enriched in LREE and Eu compared to their parent basalts (Michard & Albarede 1986). The effect of the breakdown of a particular phase on the fluid will be in proportion to the abundance of that phase in the source, and its particular REE profile. The fluid REE pattern should therefore approach that of the rock with increasing severity of alteration (high W/R).

The ability of hydrothermal precipitates to reflect the fluid-REE composition has been another subject of controversy. Morgan & Wandless (1980), and Alderton et al. (1981) endorse a crystallographic control, such that the REE pattern of a precipitated mineral will only be a function of the crystallographic ability of that particular phase to accommodate REE. While this appears to be the case for many igneous minerals and simple hydrothermal phases, regardless of the original fluid composition, several empirical studies (Kerrich & Fryer 1979, Palacios et al. 1986, Baker & Hellingwerf 1988), have found some REE whole-rock patterns to be independent of the constituent mineralogy. Illustrating the same point, studies of some mineral separates (e.g., Fryer & Taylor (1987) on uraninite), also show that the REE spectra of a single phase can vary considerably from location to location. Studies of modern and ancient seafloor exhalative systems corroborate the view that some precipitates reflect the REE-composition of the parent fluid. Bence (1983) found that sulfide - anhydrite chimneys growing around hydrothermal vents on the EPR have similar LREE-enriched patterns to the discharging fluid. A positive Eu anomaly, extends only a few hundred metres above and along strike from vents, but is otherwise absent from the hydrothermal plume (Ruhlin & Owen 1986). As the plume ascends, a seawater REE pattern is imparted to the suspended Mn-Fe particles, which eventually accumulate to form distal metalliferous sediments, with seawater rather than hydrothermal REE profiles.

One mechanism to account for this general behaviour may be the adsorption of REE on to minerals with a large number of surface sorption sites, such as clays, or the above iron-hydroxides. Phases which possess a variety of cation-exchange sites in the crystal lattice may also be important. The latter are suggested by Khomyakov (1963) to have fixed unit cell dimensions, better able to accommodate a larger atomic radii range of the substituting REE atoms. A third alternative is that some hydrothermal minerals have very high mineral/fluid partition coefficients for REE, and hence will reflect the full spectra of REE in the fluid (e.g., Guiliani et al. 1987).

HREE Enrichment of the Starra Ironstones

Identification of the REE-host

The very strong HREE enrichment with respect to chondrites and to the acid and basic footwall rocks of Starra mineralisation is atypical of most known hydrothermal systems (Fig. 8.8). Hydrothermal fluids must have leached the latter lithologies, but the exact REE contribution from each remains uncertain.

There is evidence that HREE-enrichment in the mineralised ironstone reflects an enrichment of HREE in the mineralising fluid, rather than a crystallographic control. This evidence is the similarity between the patterns of chlorite schist, uppermost altered footwall, and mineralised ironstone, despite very different mineralogies. Chlorite in particular is recognised as a mineral capable of diverse fluid-derived REE patterns, from HREE-rich with a positive Eu anomaly (Alderton et al. 1980), flat (similar to precursor basalts; Copeland et al. 1971), to LREE-enriched as in the Auriat Granite (Arniaud et al. 1984). Similarly, Palacios et al. (1986) commended sericite and epidote as hydrothermal minerals which could similarly reflect the hydrothermal composition of the fluid. It is concluded that the Starra hydrothermal fluid was HREE-enriched.

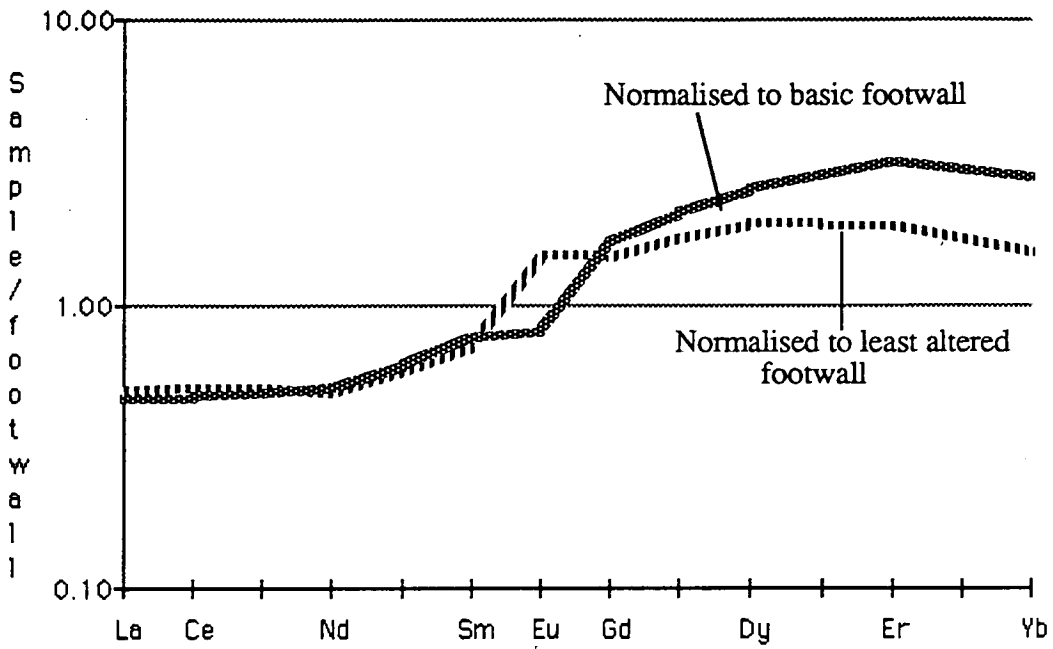

Figure 8.8 *Starra 'Most altered' footwall (GD 110) normalised to the basic footwall (using sample STP 5190), and to the least-altered felsic protolith, represented by St152. In both instances the alteration is strongly LREE-depleted, and HREE-enriched, as it was in comparison to chondrite. Footwall alteration is depleted in Eu compared to the felsic protolith, suggesting Eu is actually gained during alteration.*

Correlation coefficient analysis of ironstone geochemistry (Appendix 4) was used to identify the elemental relationships of Y, an element generally considered to vary coherently with the HREE. Yttrium showed significant positive relationships with SiO_2, Cu, Au, and W, but no relationship to Zr, Nb or Ti, its frequent companion elements in igneous systems. If these relationships can be interpreted to identify a single host phase, that phase is likely to be scheelite ($CaWO_4$); quartz and the sulphides are unlikely hosts because of their well documented low REE retention (Kerrich & Fryer 1979, Morgan & Wandless 1980, Whitford et al. 1988). However, this implies that scheelite will have a HREE-enriched profile, which would be very different to the MREE-enriched "birds-wing" pattern obtained by Guiliani et al. (1987) for igneous scheelite (Fig. 8.7B). These workers

observed REE levels 100 - 500 X chondrite in scheelite, and suggested that where W was greater than 1000 ppm, the scheelite signature should dominate the whole rock REE pattern. This difference between Guilianis' data and the observed Starra profile, supports the hypothesis that scheelite is a mineral capable of reflecting differing REE hydrothermal input. Guiliani et al. (1987) also assert this for fluid temperatures of between 400 - 600° C, because the very high scheelite/fluid partition coefficients of 4400 for Lu and 28000 for La (Raimbault 1985) imply almost total extraction of the REE from hydrothermal fluids by scheelite crystals.

Identification of the HREE source

Three possible explanations exist for HREE-enrichment of the Starra fluids:

(1) selective complexing of these elements by carbonate anions in the fluid,

(2) selective dissolution of a HREE-rich mineral in the hydrothermal source region,

(3) selective leaching of LREE from a protolith during the formation of ironstone and related mineralisation.

A lack of abundant carbonate tends to rule out the destabilising of carbonate complexes as a mechanism for HREE deposition (possibility 1), leaving chlorides as the most probable REE-transporting complex (high salinity ore-fluids are also inferred from other evidence in Chapter 12). Possibility(3) is unlikely because comparative analysis of the profiles of less-altered fragments within alteration indicates that HREE are added prior to the loss of LREE.

Alternative (2) is most attractive, because of the observed footwall mobility of Zr (Chapter 5). Zircon ($ZrSiO_4$) is an important HREE-hosting phase in the continental crust (Fig. 8.7B), containing 100 – 1000 X chondritic levels (garnet is a major HREE phase in metamorphic rocks). A loss of 52 % zirconium is calculated between the protolith and the altered footwall from data in Chapter 5; zircon-dissolution was therefore a very likely source of the HREE which now resides in mineralised ironstone.

Wider Importance of Zircon Dissolution

A corollary of alternative(2) is the wider implication for high field strength element mobility in hydrothermal systems. The ubiquitous immobility of Ti and Zr has been questioned recently by Murphy (1986), Rubin et al. (1989) and others, although there is a large body of evidence which supports the concept during metamorphism and low W/R hydrothermal activity (Pearce & Cann 1973, Floyd & Winchester 1975, Winchester & Floyd 1978, Finlow-Bates & Stumpfl 1981, Speer 1982). The best evidence for the mobility of Zr is the documentation of hydrothermal zircons and zircon overgrowths by Ludington et al. (1980), Johnson & McIntyre (1983), Jackson et al. (1985), Gates (1987), Rubin et al. (1989) and Claoue-Long & Clout (in press). Good indirect evidence of mobility

in exhalative systems is the presence of up to ~800 ppm Zr in some ores, despite a lack of clastic detritus (Kalogeropoulos 1983). What remains to be investigated are the conditions which affect Zr solubility, because high fluorine concentrations, advocated by Dietrich (1968), Ludington et al. (1980) and Rubin et al. (1989), are insufficient to account for the full span of environments in which mobility is observed.

The present study strengthens the claim that Zr can be leached by hydrothermal fluids. It further suggests that if Zr is removed during alteration, HREE will also be released, perceptibly altering the hydrothermal REE budget. This will be enhanced if LREE-bearing phases such as feldspar are preserved in the hydrothermal reservoir, as is the case at Starra. Essentially, a claim of Zr mobility in the reservoir can be tested by the occurrence of HREE enrichment in precipitates, unless these elements are accommodated by a replacement phase in-situ, and are not released to the fluid. Notably however, systems which are dominated by carbonate-complexing will also be HREE-enriched (e.g. Kerrich & Fryer 1979).

Implications for Epigenetic Versus Syngenetic Hypotheses

Dissimilarity between Starra skarn and Starra ironstone patterns, particularly higher REE levels and the distinctive negative Ce anomalies of the former, are evidence that these lithologies were deposited by separate — possibly unrelated — fluids. On a strictly empirical basis, mineralised ironstone is also unlike the magnetite-Cu-Au skarns of the nearby Mount Elliot area, which have ΣREE as high as 2.9 %, strong LREE enrichment (La/Yb^* ~ 430) and large negative Eu anomalies (Fig. 8.9). High concentrations of REE accompany many exoskarns, with LREE characteristically transported further into wall rocks than HREE (Exley 1980, Baker & Hellingwerf 1988). These features are unlike those of Starra ironstones.

The Starra patterns are also dissimilar to known exhalative iron formations, with the exception of some broad features. These are total REE in the range 20 - 100 ppm, and rapid pattern changes away from the mineralised site (Graf 1977, Bence 1983, Barrett et al. 1988). The inferred dissolution of zircon by a hot oxidised saline fluid invoked for Starra could explain unusual features of the ironstone patterns in an exhalative framework, such as HREE enrichment, but do not in themselves constitute empirical evidence in favour of an exhalative origin. Negative Eu is attributed to the oxidised nature of the fluid, which would maintain Eu in a +3 state where it would have a similar solubility to the other trivalent REE. A second important factor explaining negative Eu is its probable initial depletion during the proposed footwall diagenesis (Chapter 5).

The Trough Tank deposit, mineralogically closely analogous to Starra, has REE patterns more similar to VMS exhalites spectra (Fig. 8.10). In this deposit however, Zr only shows footwall mobility very locally beneath the ores, and hence the HREE enrichment inferred for zircon dissolution is not likely to be apparent. By analogy, the presence of a positive Eu anomaly in Trough Tank BIF implies that the hydrothermal fluids here

interacted with footwall rocks not depleted in Eu, as is the case for VMS deposits (Graf 1978, Michard & Albarede 1986).

Distal cherty BIFs south of Starra exhibit REE patterns with similarities to classical Superior-type Iron Formations. They are in accord with the time-dependence model for Eu

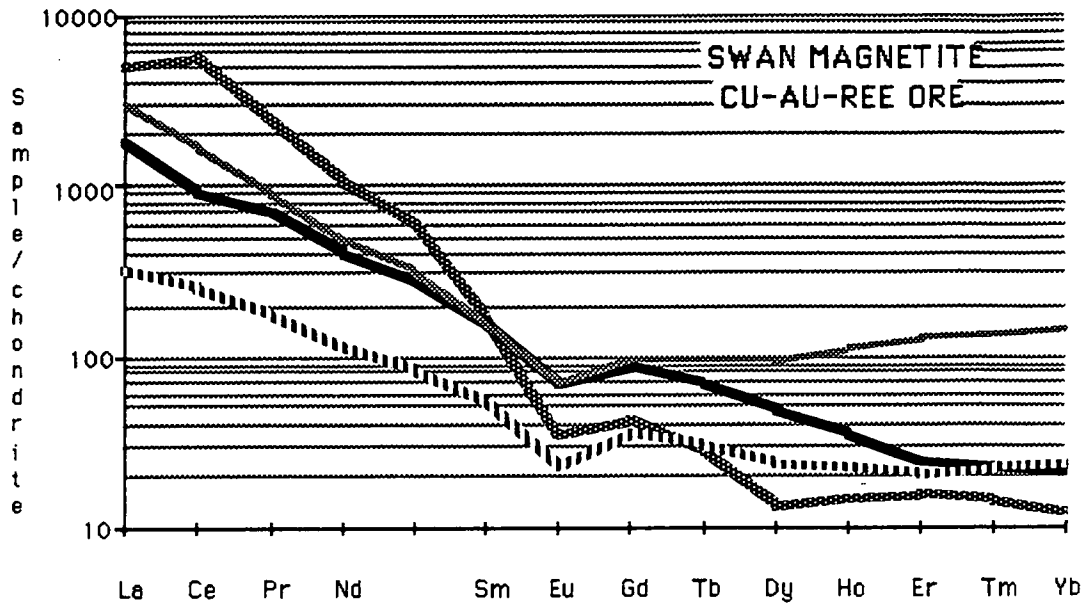

Figure 8.9 *A range of REE patterns are shown from the Swan-Mt. Elliot Cu-Au-magnetite deposit , ~ 15 km north of Starra. They are distinctly LREE-enriched, with well-developed negative Eu anomalies, in contrast to the Starra ironstones.*

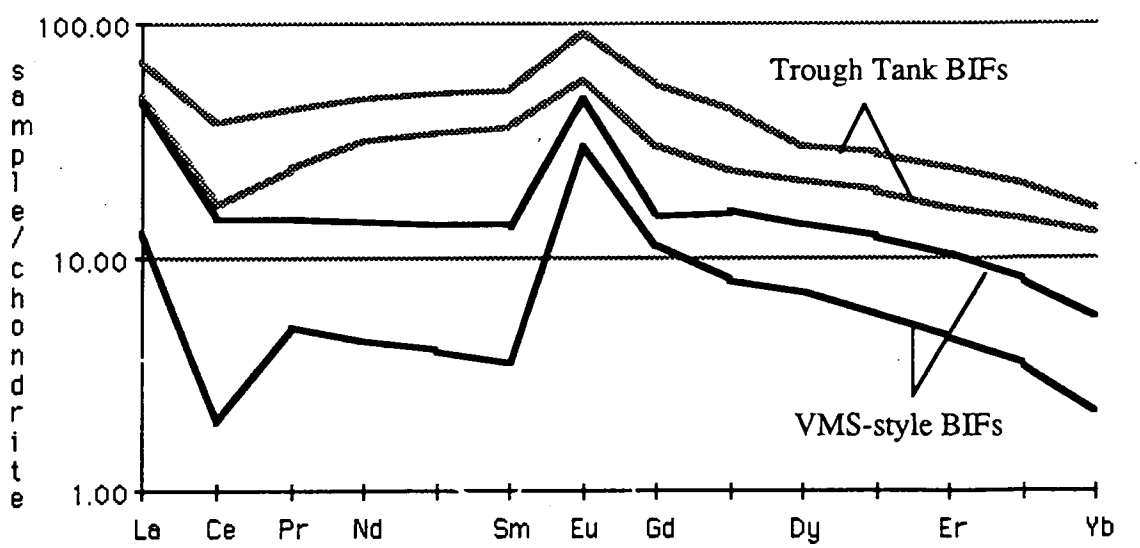

Figure 8.10 *The Trough Tank magnetite BIFs (grey, upper: NQ3/121.7 m, lower: NQ2/92 m) are strikingly similar to patterns obtained by Graf (1978) for BIFs around the New Brunswick VMS deposit (shown in black , upper: JG346, lower: JG77BM). Barrett et al. (1988) suggest that positive La and Eu anomalies are signatures of the hydrothermal fluid, which disappear with distance away from a vent. If the Starra ores had a similar origin, the fluid must have been HREE-enriched, a characteristic inherited from the unusual dissolution of zircon or other HREE-bearing phases in the footwall. In company with classic VMS-related BIFs, the mineralised pattern at Starra gives way over a small distance to a different LREE-enriched pattern in barren hematitic ironstone, possibly more like the ambient basin waters.*

proposed by Fryer (1977), who found that no positive Eu anomaly is present in BIFs younger than 1900 Ma, (excepting those adjacent to hydrothermal vents; (Graf 1978)), due to an increase in the oxidation state of seawater. Mineralogy supports a high oxidation state for the Staveley Formation basin waters.

Starra cherty BIF is unusual in having elevated total REE levels, which is attributed to chemically precipitated apatite, and to a probable detrital component, evidenced by elevated Zr (> 100 ppm) and TiO_2 (> 0.3 %). An important implication of negative Ce in some distal samples is that it implies deposition from oxidised present-day-like seawater

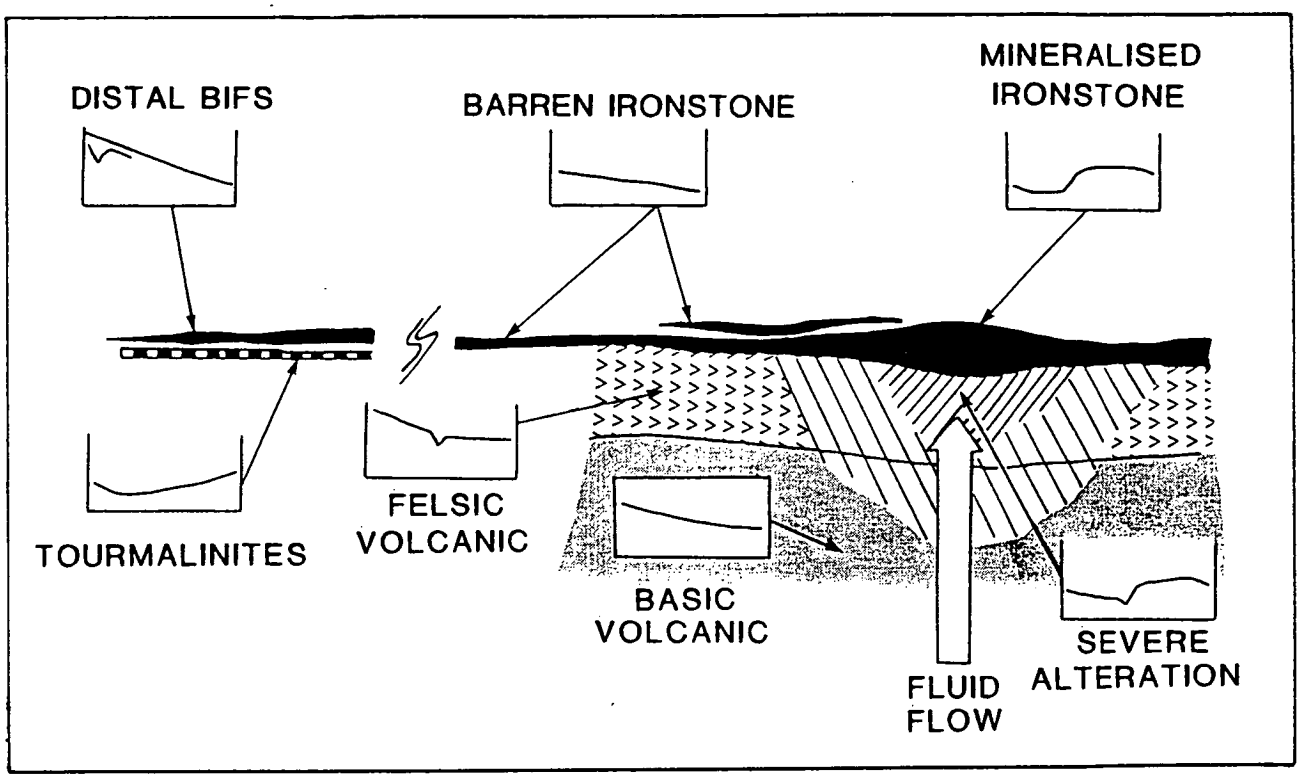

Figure 8.11 *A summary of the distribution of REE in the Starra hydrothermal system. HREE were contributed to the fluid during hydrothermal leaching, to be subsequently deposited in mineralised ironstone.*

(Fryer 1977) (Fig. 8.12) although the trait is not present in all samples. In the present day the oxidation of Ce^{3+} to Ce^{4+}, and the subsequent extraction of Ce^{4+} by Mn nodules, imparts a negative Ce anomaly to oxidised seawater. A fluctuating seawater component to the basin waters could explain the variable presence of Ce anomalies in the Starra BIFs.

In summary, an exhalative model is strongly advocated to explain Trough Tank REE patterns, and can also reasonably be adapted to account for the profiles of Starra ironstones, as depicted in Fig. 8.11. Specific circumstances at Starra were the extensive leaching of zircon and retention of LREE-enriched albite, imparting a distinctive HREE signature to mineralised proximal ironstones. LREE enrichment in cherty BIF was enhanced through scavenging by phosphates, and by sediment addition at the basin margin.

Tourmalinite Patterns

The interpretation of the tourmalinite REE patterns revolves around the controversial question of lanthanide aqueous/mineral partitioning discussed above. To resolve whether tourmaline has a fixed REE pattern, or instead reflects the chemistry of its source-fluid, the stratiform tourmaline analyses were compared to tourmalines from a completely different environment: the late stage fractionation and hydrothermal phases of granites (Fig. 8.12). It was found that the spectra differed from granite to granite, and were also different to those of the stratiform tourmalinites. Auriat Granite tourmaline (Arniaud et al. 1984) is strongly LREE - enriched with a very distinct negative Eu anomaly. Tourmaline from the tourmalinised granites of south-west England (Alderton et al. 1980) is concave-down with the apex at Sm-Tb, and has a well-developed positive Eu anomaly. These differences suggest that while there may be some crystallographic influence within tourmaline, it is the stability and abundance of the complexes in the fluid forming the tourmaline that is important. King (1988) found a similar diversity in a study of the REE contents of Archean shear-hosted tourmalines. Tourmaline fits a model of no net volume change of the crystallographic unit-cell (Khomyakov 1963), advanced for minerals with low REE contents, which allows the mineral to show a wide variation in REE pattern. The diverse range of cation sites in tourmaline also is favourable for trace element substitution over a wide ionic radii range. Tourmaline is therefore identified as a useful mineral for characterising the REE content of source-fluids in the many different tourmaline-forming environments (Henry & Guidotti 1985).

A gradual enrichment of HREE across individual tourmalinite profiles therefore suggests that the equilibrium fluid was also HREE enriched. Such enrichment typifies seawater and estuarine waters (Fig. 8.13), favoured at low temperatures by alkaline conditions, because of higher concentrations of REE-scavenging hydrogeno-carbonate complexes (Michard & Albarede 1986, Sanjuan et al. 1988). A lack of a Eu anomaly in the tourmalinites implies precipitation from oxidised waters, above the Eu^{2+}/Eu^{3+} stability transition. The lack of a Ce anomaly, a feature present in modern seawater, implies that the source fluid in equilibrium with the sediment was not seawater, but a brine with a high groundwater component. This is supported by the similarity of the tourmalinite patterns to the saline, alkaline, waters of the Gironde Estuary (Martin et al. 1976) (salinity = 0.42 ‰).

Therefore, the REE data is consistent with the geological interpretation presented in Chapter 9, that tourmalines grew from probable borate evaporite precursors during diagenesis, in equilibrium with an alkaline HCO^{3-}-rich pore-water. Alkaline connate water differed from the prevailing basin waters which deposited cherty BIF. This had a large seawater component, and was comparably less alkaline. In contrast, scavenging of HREE-enriched alkaline waters may be the explanation for the "dish" patterns of BIFs from the Hamersley Basin, Australia (Fig. 8.13), which are strikingly different to other Superior-type BIFs of a similar age (Graf 1978).

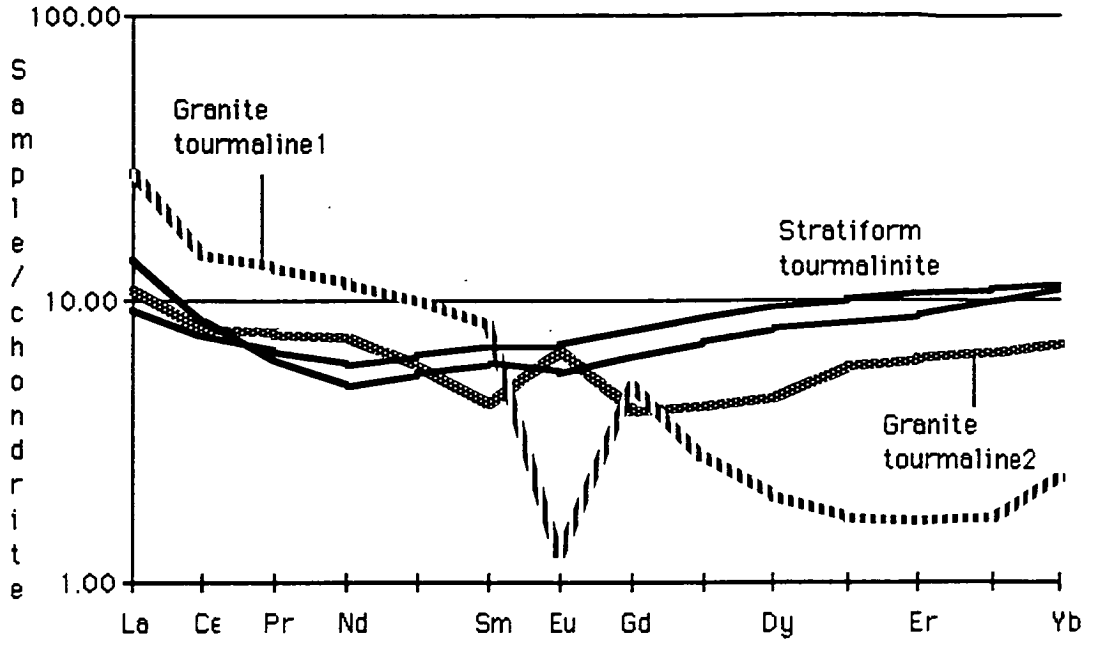

Figure 8.12 *A comparison of the REE patterns of Starra tourmalinites (black) and granitic tourmalines (1): Arniaud et al. (1984), (2): Alderton et al. (1980). Variable patterns are evidence that tourmaline REE levels are a function of fluid REE levels and REE complex stability, rather than lattice parameters. If this is accepted, then the REE patterns of tourmaline are a useful guide to the characteristics of the fluid.*

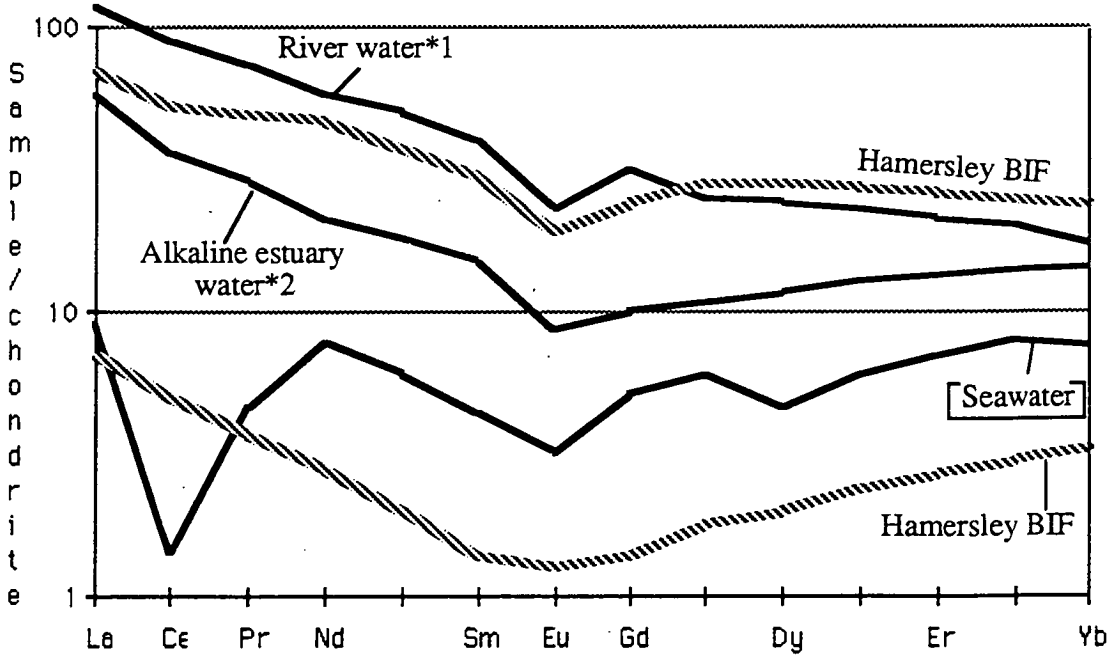

Figure 8.13 *A comparison of the REE distribution in some natural waters: seawater, river water ([1]Garonne - Dordogne river system; Martin et al. 1976), and alkaline estuary water ([2]Gironde estuary; Martin et al. 1976). All have been multiplied by 10^6 to show them on the diagram.. They are all significantly different — seawater has pronounced Ce, Eu and Dy anomalies, river water approximates an average Post-Archean shale pattern, whereas estuary water shows distinct HREE enrichment, inferred to be an effect of HCO_3^- complexing in alkaline conditions. The latter feature is invoked as the explanation for HREE-enrichment of Starra tourmalinites (Fig. 8.4, 8.12), and also for the unusual patterns of Hamersley iron formation (data from (Graf 1978)), shown (upper: HR15, lower: HR13Q).*

CHAPTER 9

TOURMALINITES AND TOURMALINE-BEARING IRON FORMATION OF THE SOUTHERN STAVELEY FORMATION

INTRODUCTION

Recent geochemical and isotopic studies of tourmaline from stratiform tourmaline-rich rocks, have shown them to be distinct from those formed during late-stage granitic activity (Slack 1982; Slack et al. 1984, Taylor & Slack 1984). The term "tourmalinite" has been used to describe conformable lithostratigraphic units with 15% or more tourmaline (Slack 1982). Many stratabound mineral deposits have associated tourmalinites, including Sullivan, British Columbia; Kidd Creek, Ontario; Broken Hill, New South Wales; the Golden Dyke Dome deposits, Northern Territory; and some massive sulphide deposits of the Appalachian-Caledonian orogen (Ethier & Campbell 1977; Plimer 1983, 1986; Taylor & Slack 1984, Lottermosser 1989). Some tourmalinites also occur in terrains apparently unrelated to sulphide mineralisation, including those in the Damara orogen, Namibia; Grenville Complex of St. Lawrence County, New York, U.S.A.; Houxianyu, Manchuria, China; and the Arzberg series of West Germany (Abraham et al. 1972, Brown & Ayuso 1985, Plimer 1987b, Schmidt-mumm et al. 1987). Tourmaline compositions of the latter group chemically overlap those associated with mineral deposits, leading to doubts concerning the significance of dravitic tourmaline in the search for stratabound ores.

Because stratiform tourmalinites occur mainly in metamorphosed rocks, and because no modern analogues of primary tourmalinite are known, it seems likely that some may have formed during diagenesis and metamorphism. This viewpoint is examined in the light of newly discovered tourmalinites which are stratigraphically equivalent to the Starra Cu-Au deposit (Davidson et al. 1988; Kary & Harley, in press), associated with evaporitic sediments of the Staveley Formation.

REGIONAL TOURMALINE OCCURRENCES

None of the localities listed below are analysed in detail, but form an important context for tourmaline-rich rocks in the Starra area.

Tourmaline-rich rocks are known in the Mt. Isa region from the Dugald River Pb-Zn ore sequence (Whitcher 1975, Muir 1981), as minor lenses in the Eastern Creek Volcanics (Plimer 1987b), and from many poorly documented stratiform settings associated with Pegmont-style Pb-Zn prospects in the Soldiers Cap Group (e.g., Pegmont, Annitra, Monokoff)(Plimer 1987b, Stephen Walters pers. comm. 1988). In addition, Stewart & Williams (1988) have in passing documented the presence of extensive tourmaline-filled breccias within pre-D2 faults in the Deighton Klippe, a D1-related fault-bound block in the Cloncurry area (Loosveld & Schreurs 1987).

Figure 9.1 *A detailed geological map of the area south of Starra, based in part on the mapping of Leishman (1983).*

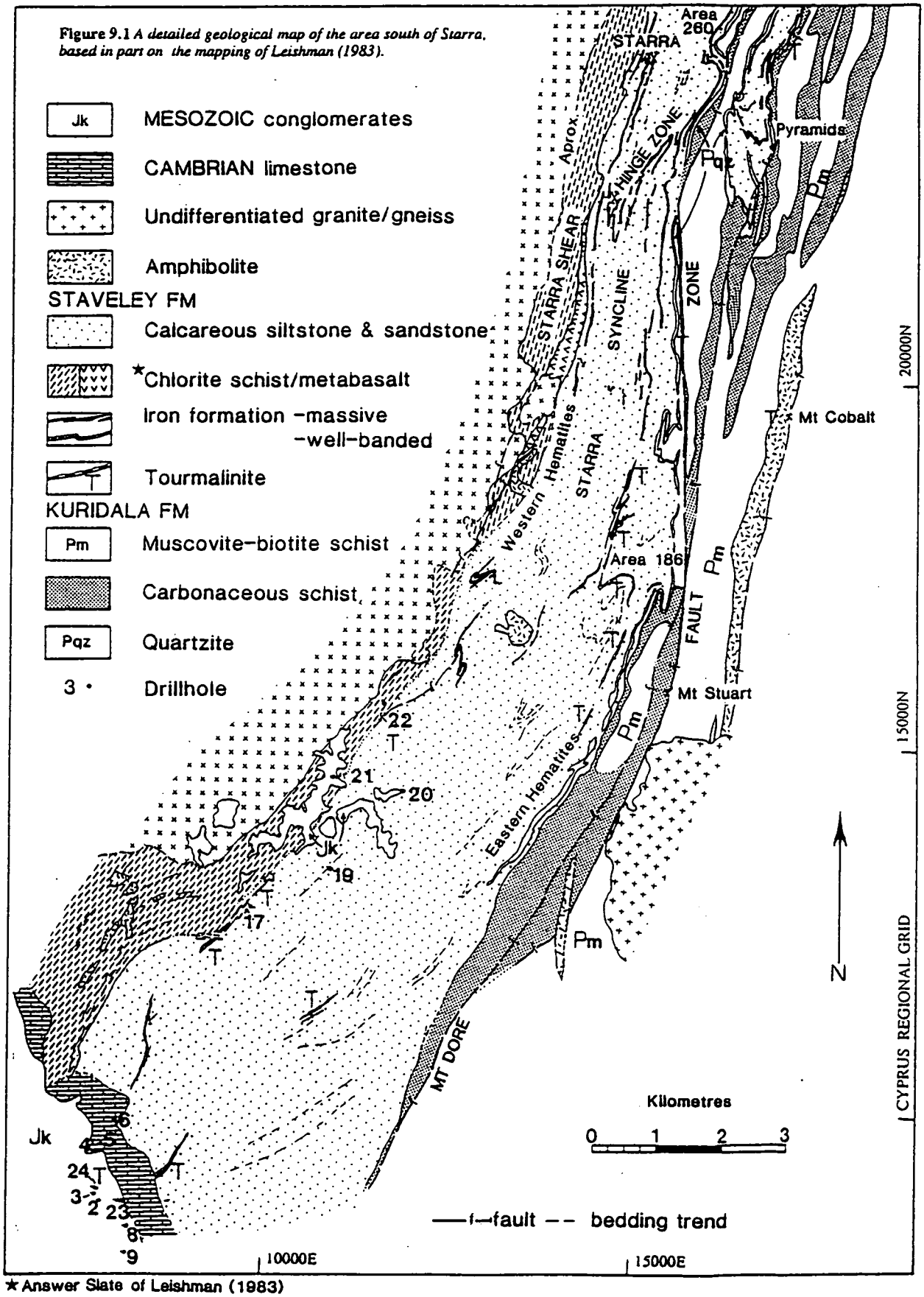

★ Answer Slate of Leishman (1983)

Fault-controlled tourmalinisation affects amphibolitic dolerites around the Mt Cobalt Co-As and New Hope W mines (Figs. 9.1 & 4.1), documented by Nisbet et al.(1983). Dravitic tourmaline replaced metamorphic biotite during a late metasomatic event. Nisbet et al. (1983) discount any genetic link between tourmaline and the Co-mineralisation, preferring to relate the boron enrichment to fluid expulsion from the Mt Williams Batholith.

Stratabound 1 – 5 m-thick tourmaline-quartz beds occur 25 km northwest of Starra at Limestone Creek (located on Fig. 4.1). The tourmalinites extend along strike from Starra-style hematite-lenses, and are folded by D2(MP). Petrographically tourmaline occurs as randomly oriented, ultrafine, prismatic grains set in a quartz matrix, suggestive of replacement. Compositionally these tourmalines show very little variation away from Fe/Fe+Mg = 0.34, i.e., dravitic.

THE DISTRIBUTION OF TOURMALINE-RICH ROCKS STUDIED IN THE STARRA AREA

Stratiform tourmaline: The main stratiform tourmalinite concentration in the Staveley Formation extends south of the Starra Au-Cu deposit for 20 km before disappearing beneath Cambrian and Mesozoic cover (Fig. 9.1). Most occur within the Starra Iron-formation Member, or immediately above it, although one notable locality is stratigraphically much higher, interbedded with calcareous sediments (12000N, 11000E; Fig. 9.1). The area south of Starra has not been exhaustively mapped, so tourmalinites may be more widespread than indicated on Fig. 9.1. However, close-scale mapping near the Starra gold deposit (Leishman, 1983) indicates that the closest stratiform tourmalinite is 4 km south of the known Au-Cu mineralisation, although stratiform chlorite schist and hangingwall metasediments can be appreciably tourmaline-enriched (Chapter 3).

Shear and Fault-related Tourmaline: The Mt. Dore Fault Zone (Beardsmore 1988) has several occurrences up to 25 m thick, in which S-C fabrics suggest emplacement in a left-lateral strike-slip regime, prior to the well-documented reverse motion of the fault (detailed on Fig. 4.2).

Metasomatic Tourmaline: Disseminated tourmaline adjacent to local veins are present in sandstone west of the Mt.Stuart Mine, strike-equivalent to iron formation. Locally-discordant quartz-tourmaline lenses occur close to iron-formation at Area 186 (Fig. 9.1).

Tourmaline-bearing granite, pegmatite and pegmatitic veins: These are related mainly to the Gin Creek Granite, and are noted along the length of the granite/gneiss outcrop. Several granite-related tourmaline-rich veins occur 250 m west of the Area 257 Au-Cu orebody.

The latter three tourmaline-types are evidence that boron was mobile or introduced at several times during the post-depositional history of the study area, and therefore a synsedimentary origin cannot automatically be assumed for the stratiform tourmalinites, despite their conformable appearance. For instance, pseudo-bedded tourmalinites associated with granites are documented by Appleby & Williams (1988), and have also been observed

by the author close to the margins of the Heemskirk Granite, Tasmania. The timing of tourmaline-growth in the Starra area is examined below.

MINERALOGY AND TEXTURES OF STARRA TOURMALINITES.

Stratiform Tourmalinite

Variation in the degree of metamorphism and deformation amongst samples has facilitated the study of the timing of tourmaline growth. Tourmalinites classed as stratiform are defined by a layered conformable character, in which tourmaline and associated minerals have been affected by the main S2(MP) cleavage, and hence predate it.

Sedimentary Structures.

The least recrystallised samples occur at Area 186 in the east of the area (Fig. 9.1), associated with cherty hematite iron formation, which extend along strike from massive hematitic ironstone. Tourmaline also occurs as mono-mineralic plane-laminated units 0.5 to 5 m-thick, in which internal layering is defined by variations in tourmaline grain-type and size. Observed sedimentary structures include cross-bedding and layer-truncation. Mono-mineralic tourmaline layers are 1mm to 5 cm thick, interbedded with quartz or microcline layers of similar width. In some samples tourmaline forms clusters rather than laminae.

Tourmaline in iron formation of Area 186 constitutes up to 25% of beds containing hematite, quartz, microcline and minor illite. A critical feature here are 0.1 – 2 mm long gypsum pseudomorphs scattered within the I.F. (Fig.9.2D), and larger (2-4 mm) nodules and radiating crusts above the beds, replaced by microcline. The pseudomorphs are identified as gypsum by comparison with gypsum crystals grown by Cody (1976) in smectite muds, which have interfacial angles of 47° and 54° measured on forms elongate parallel to crystallographic {001}. This form of gypsum occurs under saline conditions, whereas forms markedly flattened parallel to {001}(i.e., disks) indicate hypersaline conditions (Cody 1976). While some crystals have well-developed terminations at both ends, several crystals have only a single euhedral termination, and possess an internal cavity filled with fragmental quartz and ultrafine smectite. Layering is disturbed by compaction around these crystals. They are interpreted as selenite, a hollow gypsum form found growing at the sediment surface in sabkha brine pools (Walker et al.1977). These observations are evidence that gypsum grew displacively within Fe- and B-rich sediments both at the time of sedimentation and during early diagenesis, with gypsum pseudomorphs later reorienting into a weak cleavage defined by thin illite clumps.

Tourmaline only rarely occurs within gypsum pseudomorphs, but commonly clusters along the pseudomorph margins. It averages 12 μm length, as short, blocky, poorly-zoned crystals with pseudohexagonal sections, locally with a very small, optically-continuous bluish core. Tourmaline frequently contains a multitude of ultrafine hematite inclusions (smaller than hematite surrounding the tourmaline), implying that tourmaline growth accompanied hematite recrystallisation (Fig. 9.2B). The widespread exclusion of tourmaline from gypsum suggests it was not mobile during gypsum replacement by potassium feldspar

Figure 9.2

TOURMALINITES

Photomicrographs of typical tourmaline-bearing lithologies. Numbers in some plates refer to microprobe analyses available in Table 9.2.

A. *Cross-bedded stratiform granofelsic tourmalinite, highlighting the metamorphic nature of mineral boundaries. Tourmaline ranks more highly than quartz in the crystalloblastic series, but 120° triple-point boundaries between the two are a common feature here.(SG45).*

B. *Detail of "D". Fine-grained titaniferous hematite encloses tourmaline crystals (Tm). The tourmaline is a very early phase, enclosing very fine round inclusions of hematite.*

C. *Trigonal euhedral tourmaline which is attributed to metasomatism, growing across peak-metamorphic grain-boundaries. The grains are zoned, and have pseudohexagonal cores similar in form to those found in low-grade stratiform examples (SG35c).*

D. *Diagenetic gypsum crystals (gyp) elongate parallel to {001}, pseudomorphed by microcline, within a fine matrix of hematite, tourmaline and microcline (SG33).*

E. *The coarse, pervasive, randomly-oriented fabric of a metasomatic syn to post-metamorphic tourmalinite. The nodular texture suggests that tourmaline distribution was controlled by inhomogeneities in the original fabric, such as conglomerate pebbles or crystal pseudomorphs (SG18).*

F. *Tourmaline in granitic miarolytic cavities of the post-tectonic phase of the Gin Creek Granite. An early blue schorl phase (6) is altered by a late green dravitic tourmaline in most samples (7) (SG10).*

G. *A folded stratiform tourmalinite (2) is cut by a left-lateral fault into which remobilised tourmaline has migrated (1). The latter is distinctly iron-rich and calcium-poor. The major clear zone in the slide is a quartzite clast (SG45F).*

H. *Late tourmaline fault-fill within the Mt. Dore fault zone, projecting into a quartz- and potassium feldspar-filled cavity. Fluid inclusions in this material are saline, with daughter phases halite and possibly sylvite (SX13).*

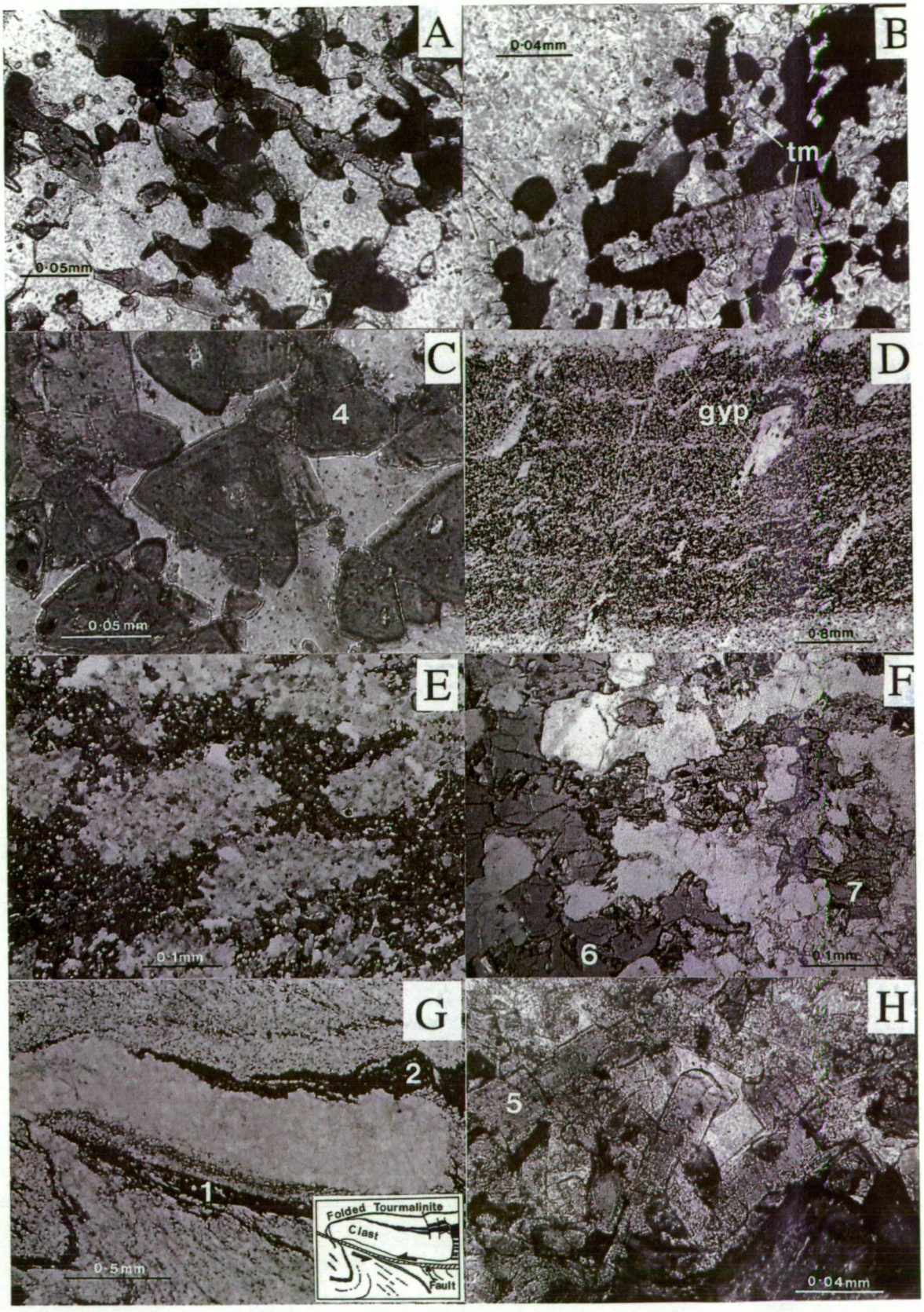
A
0·05mm
B
0·04mm
tm
C
4
0·05 mm
D
gyp
0·8mm
E
0·1mm
F
7
6
0·1mm
G
2
1
0·5mm
Folded Tourmalinite
Clast
Fault
H
5
0·04mm

(a relatively common feature of some evaporites, due to the migration of very soluble K-salts trapped within evaporites (Sonnenfeld 1984).

These observations are evidence that boron in BIF was linked genetically with the deposition of iron (tourmaline forms no more than 2% of the Fe-poor host-rocks), and that both Fe and B were deposited in an evaporitic saline setting, prior to deformation and metamorphism. While tourmaline may not have been the primary boron mineral, textural relationships indicate that its growth predated recrystallisation of all other minerals.

Morphology and changes due to recrystallisation.

Recrystallisation affects most tourmalinites to varying extents. It is manifested as a steady increase in the grain-size of tourmaline and quartz, with a particular increase in polygonal character of the latter. Grain-size of tourmaline increases broadly from 12 μm in the least recrystallised sample, to 100 μm in the most recrystallised, with an average of ~40 μm. This corresponds to an increase in metamorphic grade from illite to muscovite-biotite-epidote stable in calcareous pelitic rocks i.e., upper Greenschist facies.

Tourmaline morphology alters with metamorphic growth, with a decrease in the number of inclusions, and an increase in crystal-face definition (Fig. 9.2A). An observation reflecting the crystallisation conditions is the general change during growth, from pseudohexagonal forms to crystallographically-dominant trigonal forms in sections perpendicular to the c-axis, with preservation of the earlier inclusion-rich core shape (Fig. 9.2C). Zoning of crystals may or may not occur, and is not colour-consistent. In several recrystallised samples in which argillaceous and psammitic layers are interbedded, disseminated tourmaline is present preferentially in the psammitic beds. Within the muscovite-biotite-rich layers tourmaline shows no preference for an association with muscovite, and no reaction relationship; Muscovite crystallises around tourmaline with no visible change in the tourmaline colour or morphology.

These observations lead to the following conclusions:

a) Tourmaline grain-size increases during recrystallisation, suggesting that as tourmaline grows it equilibrates with the bulk rock and metamorphic fluid; and

b) Preservation of colour zoning, core inclusions, and previous core morphologies underline the refractory nature of tourmaline (Henry & Guidotti 1985), i.e., previously deposited layers of tourmaline do not readily exchange with subsequent layers during normal prograde metamorphism. Cores of crystals are therefore the most reliable areas for obtaining the original tourmaline chemistry (Henry & Guidotti 1985).

Deformational Remobilisation of Tourmaline

In stratiform tourmalinites which experienced strong shearing, tourmaline is found in thin faults with small shear movements (Fig. 9.2G), and defines lineations within the cleavage. Tourmaline in these sites is much coarser (100 μm) than adjacent conformable tourmaline (20 μm), and virtually inclusion-free. Whereas the stratiform tourmaline is pale to dark green, the fault-hosted crystals are well-zoned, from a corroded blue-grey core, through

dark-blue, to a grey-green rim, brown-pink in other sections. Multiply-twinned rutile is a constant accessory in the faults. Disseminated tourmaline within the muscovite-defined cleavage are well-zoned from deep green or blue cores to pale green rims, and are generally subhedral. The clear conclusion from these observations is that at sites of preferential stress tourmaline is dissolved during deformation, with the subsequent reprecipitation of tourmaline in adjacent veins.

Shear-related Tourmalines

Several major fault strands in the Mt. Dore Fault Zone contain thick tourmaline fill, and show well-developed phacoidal fabrics from which a sense of shear can be deduced. Tourmaline is coarse (50 – 400 μm), inclusion-free, strongly zoned from olive-green to yellow rims in orientations perpendicular to the c-axis (generally pyramidal in this section) (Fig. 9.2H). There is no consistent banding or fine layering. Breccia fragments within these fault zones are impregnated with tourmaline which is similar in colour and euhedral morphology to that in the fault-breccia matrix.

The matrix in these shear zones consists of quartz and abundant microcline, with accessory biotite and 2 – 3 mm diameter plates of rutile. In faults with a history of very late fluid introduction, quartz is often strain-free, typically containing large (10-30 μm) equant fluid inclusions either rich in CO_2, or highly saline. Thus, tourmalines within shears were deposited from salt/CO_2-bearing fluids, resulting in shapes and compositions which are distinct from bedded tourmaline.

Metasomatically-derived Tourmalinite.

Although some shear-related tourmalinites are metasomatically derived, other crudely-banded to massive, stratabound to stratiform, metasomatic tourmalinite was formed away from obvious shears. In several instances massive quartz-tourmaline also occurs as "blows" ~ 30 m in diameter on sheared D2(LP) fold hinges.

The following features of the metasomatic tourmalinite are considered characteristic at a meso and microscopic level:

a) A coarser grain-size than that of the surrounding rocks,

b) Tourmaline (up to 60% of the rock) together with coarse muscovite and rutile, cross-cut the regional cleavage and bedding,

c) Tourmaline replaces quartz and muscovite, resulting in a poikilitic character, frayed embayed margins (Fig. 9.2E), and a nodular fabric (1 – 4 mm diameter)

e) Tourmaline grains are light green to yellow pleochroic, and are well-zoned with pyramidal cross-sections (Fig. 9.2C).

Igneous Tourmaline

Tourmaline related to a late phase of the Gin Creek Granite occurs in pegmatites, in miarolytic clusters and in sporadic quartz-tourmaline veins extending at least 200 metres beyond the granite contact. Tourmaline-bearing granite is poorly cleaved.

Altered granite contains coarse (0.5 – 3 mm), poorly-zoned, deep-blue tourmaline. Crystals are subhedral, and may show alteration to a more dravitic green to pink variety around grain margins. In one section, deformed granite with a muscovite defining a spaced cleavage has been replaced by tourmaline, good microstructural evidence for the syn to post-deformational movement of some boron-rich fluids.

CHEMISTRY

Trace Elements

A limited number of samples were analysed by XRF methods (Appendix 2) to assess the bulk chemistry of tourmaline-rich rocks (Table 9.1). The small number of samples

	SG45F Strat. Tm. concent.	SG49 Strat. Tm'te	SG23 Strat. Tm'te	SG25G Tm.-BIF	SG35C Metasom. Tm'te	Tm. in VMS's *1	Tm. in granites *2
(%)							
SiO_2	37.21	70.32	79.63	44.94	55.29		
TiO_2	0.91	0.35	0.18	0.50	0.72		
Al_2O_3	31.97	7.66	8.67	4.50	17.29		
$Fe_2O_3^{tot}$	12.73	16.46	3.32	47.16	12.5		
MnO_2	0.02	0.02	0.02	0.02	0.11		
MgO	5.6	1.15	2.46	0.94	5.2		
CaO	0.18	0.19	0.47	0.18	1.2		
Na_2O	2.58	1.69	0.38	<0.3	1.12		
K_2O	0.06	0.16	0.31	0.38	0.09		
P_2O_5	<0.01	<0.01	0.01	0.03	0.01		
LOSS	3.0	1.58	1.51	0.82	2.2		
(ppm)							
Ba	67	177	516	870	189	10	n.d.
Sc	71	17	10	10	17	47	41
Cu	4	41	<2	<2	7	77	7
Pb	<2	2.3	4.3	<2	<2	114	n.d.
Zn	3	48	3	4	8	387	n.d.
Mo	<2	5	4	<2	<2	<3	n.d.
W	6	2	9	6	7	<100	n.d.
Rb	<2	26	10	16	2	<2	n.d.
Sr	69	42	58	44	121	98	16
As	2	3	3	<1	6	n.d.	n.d.
Nb	11.4	4.6	2.1	14	1.4	<10	n.d.
Zr	142	102	214	175	191	<10-340	n.d.
Y	18.3	5.6	17.2	24	34.7	<10	n.d.
Ni	634	32	26	22	67	<5	23
V	1389	270	63	121	160	195	28
Au	n.d.	n.d.	<0.02	n.d.	<0.02	n.d.	n.d.

Table 9.1 *Whole rockCompositions of selected tourmalinites, including one mineral concentrate, and some comparative analyses from known environments *1-Taylor & Slack (1984). *2-Power (1968). (n.d.: not determined, Strat. Tm'te = Stratiform tourmalinite.)*

analysed does not permit a rigorous statistical analysis of the populations; only one stratiform tourmaline concentrate was analysed (SG45F).The sample classified as "metasomatic" from

thin section observation (SG35C), showed only small whole rock chemical differences with those classified as stratiform (SG23/SG49). These differences include an enrichment in Mg, Mn, Ca and Y.

The main chemical features of the stratiform tourmalinite samples are strong enrichments in Ti, V, Sr, Sc, and Ni over BIF and the host sediments. Base-metals and Au concentrations are at very low levels in both the stratiform and metasomatic types. Tourmaline is an important repository for Y (18.3 ppm) and Zr (141.7 ppm), and where abundant probably controls the bulk levels of these elements.

Taylor & Slack (1984) provide one of the few syntheses of tourmaline trace element data which are available, indicating that massive sulphide tourmalines are enriched in V and Sr, and sporadically in Cu and Pb. In contrast igneous tourmalines (Power 1968, Taylor & Slack 1984) contain higher levels of Li, Mn, and possibly Zn. Starra tourmalines share a strong enrichment in V, Sc and Sr with those from massive sulphides deposits, but exhibit Ni enrichment in the concentrate beyond that found in any previous study of tourmaline from any setting. The Ni-enriched sample is notably part of a larger Cu-enriched sediment package.

MINERAL CHEMISTRY

Method

Compositions of tourmalines were obtained using a Jeol JX50A microprobe, for the elements summarised in Table 9.2 (and Appendix 7), using a set of natural silicate standards. In most instances spot analyses of tourmaline cores were averaged for individual grains, and some rims were analysed for comparison. Optical work described earlier suggests that tourmaline cores are the most reliable sample-points for the comparison of different grains.

Tourmaline is a mineral characterised by complex substitutions and is difficult to analyse because B_2O_3, Li_2O, and OH^- cannot be measured on the probe and make up 11–14% by weight. Ethier & Campbell (1977) also found that Na_2O was lost if the beam diameter was increased beyond 10 μm at 15 kV and 0.5 μA beam current. To alleviate problems encountered by other workers, oxide ratios have been used here as more meaningful indicators of compositional change in tourmaline.

The idealized tourmaline formula is

$$X\ Y_3\ Z_6\ (BO_3)_3\ (Si_6O_{27})\ (OH,F,Cl)_4$$

where $X = Na^+, Ca^{2+}, K^+$

$Y = Mg^{2+}, Fe^{2+}, Fe^{3+}, Mn^{2+}, Ti^{4+}, Al^{3+}$

$Z = Al^{3+}$, Mg^{2+} and Fe^{3+} ions may substitute here if Al^{3+} does not completely fill the Z-site.

Werding & Schreyer (1984) illustrate that although the ideal number of silica cations in tourmaline is 6.0, natural tourmalines show a variation between 5.6 and 6.2 because Na^+ and Al^{4+} may also substitute in this site.

Results

The samples were divided into the four groups distinguished by field and thin-section criteria, with typical compositions summarised in Table 9.2. In general, mineral chemistry does not wholly discriminate between the groups.

On the basis of Na:Ca and Mg:Fe ratios most of the samples are compositionally intermediate between dravite and schorl (Fig. 9.3). In particular the composition of tourmalines in granites and those within faults away from granites, are very similar (Mg# (mol %) = 0.32 – 0.68) ; metasomatic samples cluster between Mg# = 0.56 – 0.69, while stratiform samples show the greatest variation with MgO# = 0.26 – 0.82. Since conventional means of chemical discrimination (Fig.9.3) were relatively ineffective, the samples are plotted on binary and ternary diagram using ratios reflecting the occupancy of the three cation sites X, Y and Z (Figs. 9.4 & 9.5).

	Stratiform, hosted in BIF.	Stratiform SG45F(2)	Minor shear within SG45F(1)	Meta-somatic (4)	Shear-hosted (5)	Early tourm.(6) in granite	Late tourm. (7) in granite
SiO_2	38.76	40.82	36.59	36.07	36.24	35.42	37.73
TiO_2	0.16	0.31	0.25	0.56	0.75	0.54	0.54
Al_2O_3	32.18	32.19	32.35	30.57	30.45	34.68	32.64
MgO	9.19	7	4.41	7.57	9.08	11.12	7.24
FeO^{tot}	4.63	6.93	12.82	8.51	7.75	2.96	8.53
CaO	0.36	0.39	-	0.98	1.87	-	0.39
K_2O	1.06	-	-	-	-	-	-
Na_2O	2.03	1.97	2.59	2.15	1.59	1.93	2.56
SUM	88.37	89.62	89.00	86.42	88.41	86.64	89.63
Mg #	78.0	64.3	38.0	66.7	67.6	32.1	67.8

Table 9.2 *A compilation of tourmaline mineral chemistry for the four different genetic groups studied in the Starra area.*

These diagrams, although still not successful as discriminators, indicate that:

(1) Primary blue granitic tourmalines compositionally are within the elbaite-schorl series, with Al enrichment and Ca depletion (0 – 0.34 wt %), whereas the second generation of green tourmaline observed to alter blue granitic tourmaline is slightly more Ca-rich (0.3 – 0.63%); it is still aluminous compared to tourmalines from other settings (Table 9.2). A significant unusual feature of the later generation is its high Mg content, Mg# up to 0.56, whereas most lithium-poor igneous tourmalines have Mg# between 0.06 and 0.32 (Neiva 1974).

(2) Tourmalines in faults and shears at all scales have some of the chemical features of granites, but are more Ca- and Ti rich, and Al-poor. The SiO_2/Al_2O_3 and CaO/Na_2O ranges are similar to the fields of metasomatic and synsedimentary tourmalines, but the range of variation is not as large (Fig. 9.5). Analysis of sample SG45F (Table 9.2) has clarified the extent of compositional change which occurs during preferential tourmaline dissolution

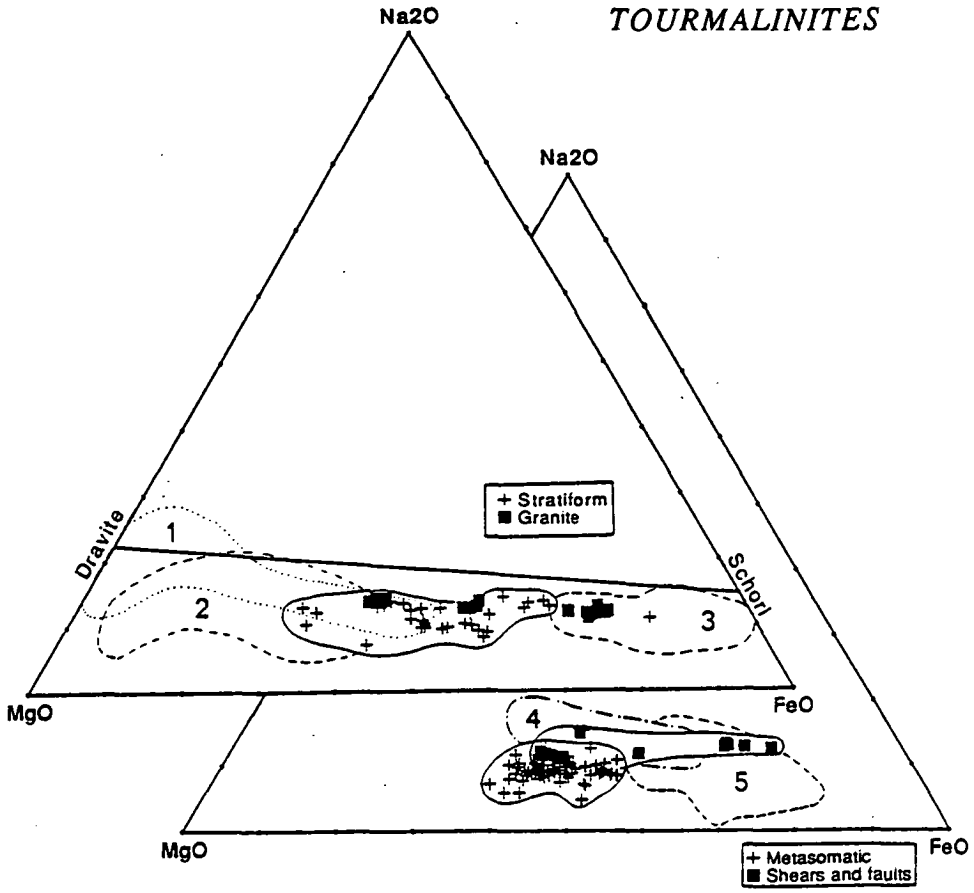

Figure 9.3 *A standard plot of weight percent Na_2O-MgO-FeO^{tot} showing the position of the four tourmaline groups of the Starra area, relative to some global tourmaline-types. Other fields shown are : 1. Proterozoic stratiform tourmalinite (Bone 1988). 2. Tourmalines in Phanerozoic Caledonian VMS deposits (Taylor & Slack 1984). 3. Granites and pegmatites (Neiva 1974). 4. Suite 3 Broken Hill tourmalinite, associated with magnetite quartz rocks. 5. Suite 4, Broken Hill tourmalinite, within the Pb-Zn-hosting sequence (Plimer 1983).*

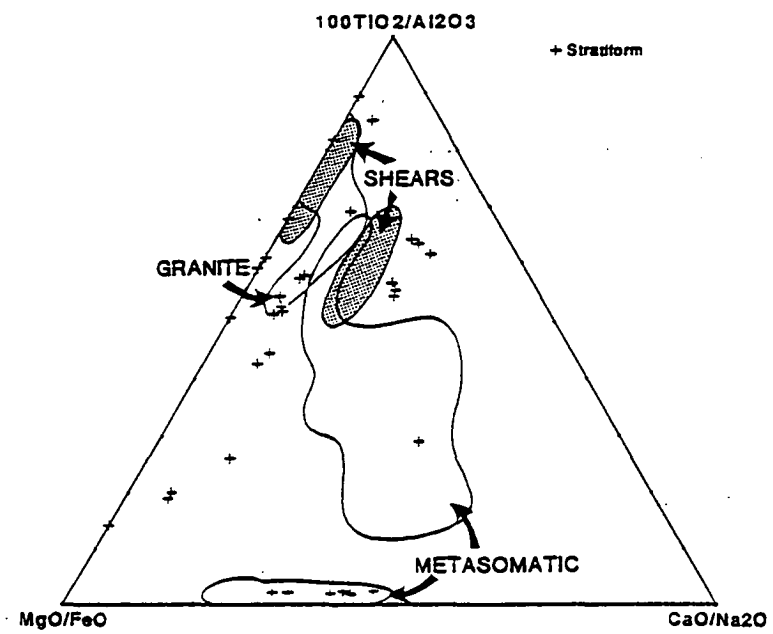

Figure 9.4 *MgO/FeO-CaO/Na_2O-100TiO_2/Al_2O_3 weight percent variation diagram, which ratios the elements from each tourmaline cation site, showing the distribution of the Starra tourmaline groups. The diagram is able to separate the wide fields of metasomatic and synsedimentary tourmalines. Tourmalines from the stratiform setting are plotted as points, whereas all other types are plotted as fields.*

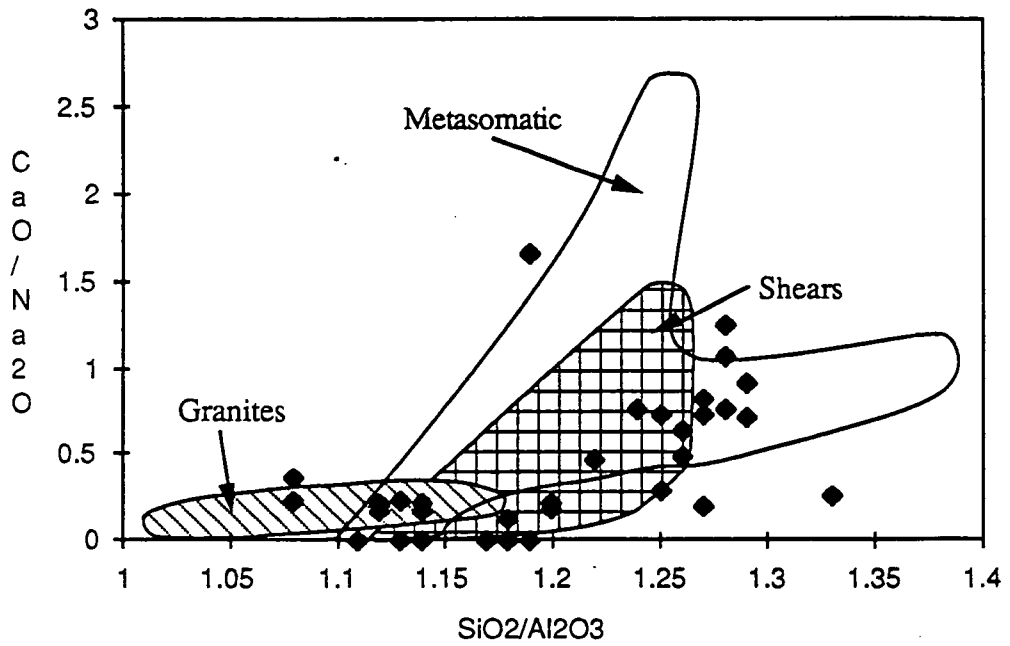

Figure 9.5 *A binary plot of CaO/Na_2O versus SiO_2/Al_2O_3. The higher Al and low Ca contents of granitic tourmaline is distinctive, but the other groups are not discriminated. Tourmaline grains from stratiform tourmalinites are indicated as points, not a field.*

under high deformational stress. Synsedimentary tourmaline has Mg# = 63.1 – 68.8, while intersecting shears have tourmaline cores with Mg# = 35.0 – 38.8, and rims around 30.0. TiO_2 contents of all grains are similar at about 0.45%.

(3) The characteristic feature of metasomatic tourmaline is a strong Ca enrichment, with some overlap into the fields of granite and shears (Figs.9.4 & 9.5). TiO_2 varies widely from 0.15 to 1.2 wt%, whereas the MgO/FeO ratio is restricted from 0.16 to 0.45 (Fig.9.3).

(4) Syn-sedimentary tourmalines show a wide chemical variation of Ti, Al, Mg and Fe, but are separated from the bulk of metasomatic tourmalines by their lower CaO/Na_2O ratios (Fig. 9.4). The highest MgO contents characterise synsedimentary tourmalines intergrown with BIF and evaporites. Such a pattern is also apparent from the data of Plimer (1983) in which he compared Broken Hill tourmalinites, equivalent to magnetite-quartz rocks, with tourmalinite in the overlying Pb-Zn-equivalent sequence. The former are appreciably more magnesian. It is a general feature of the co-crystallisation of many Fe-oxides and silicates that Mg partitions preferentially into the silicate phase (Bachinski 1976).

An important feature of the stratiform evaporite-bearing tourmalinites is the reflection of the diagenetic rather than the primary depositional environment in the mineral chemistry. Although Ca-evaporite minerals must have dominated the primary chemistry, the associated tourmalines contain 1.4 to 1.7 % K_2O, reflecting the potassic diagenetic regime under which gypsum was replaced by microcline. This is chemical evidence in favour of a minimum-early-diagenetic timing for tourmaline growth in these sediments, although geological evidence indicates that boron was initially deposited, presumably as a metastable borate, with iron at the sediment-water interface.

DISCUSSION: THE ORIGIN OF STARRA TOURMALINITES

Tourmaline and Boron in the Modern Environment

Stability range of Tourmaline

No systematic study has been made of the complete stability range of tourmaline, although some works, documented in Table 9.3, have tested the range of particular compositions. These workers have shown that tourmaline is refractory during metamorphism, with low pressure melting at 760° C (0.5 kb) and 865° C (2 kb); a theoretical stability of 100° to 600°C (0.2 – 1.5 kb) has been calculated (Govorov 1971). Tourmaline has been synthesised readily in NaCl-rich fluids by reaction with low-calcium minerals at 350° C and 2 kB (Frondel & Collette 1957), which include the likely reaction conditions for the formation of granite-related metasomatic tourmaline.

T° C	P (kB)	pH	Comments	Reference
SYNTHETIC TOURMALINES				
350-550	0.7-2.0	-	Stable in weakly acid to moderately alkaline solutions. Unstable in strongly alkaline solutions.	1
400-450	>1.0	8 - 8.6	Dravite	2
400-500	0.2-0.5	alkaline	Schorl and dravite	3
300-800	low	-	Alkali-free tourmaline	4
400-600	1.5-2.0	4	schorl	5
400-700	2.0-3.0	3-6	schorl	5
500-600	2.0-2.5	4	schorl	5
HYDROTHERMAL TOURMALINES				
200-250	Deep water	-	Sullivan alteration, marine fluids.	6
200-350	Deep water	acid to neutral	Black Hawk mine (VMS). sph., py., gal. intergrown with dravite. Conditions estimated by this author.	7

Table 9.3. *Some estimates of the formation conditions of natural and stratiform hydrothermal tourmalines.1 Frondel & Collette (1957); 2. Smith (1949); 3. Michel-Levy (1953); 4 Werding & Schreyer (1984); 5. Voskresenskaya & Barsukova (1971); 6. Beaty et al. (1988); 7. Taylor & Slack (1984).*

Surprisingly, the recent focus on stratiform tourmalinites associated with VMS deposits has yielded few natural formation-temperature estimates for tourmaline, but by comparison with similar sulphide assemblages in well-documented ores, a maximum range of 200 – 350° C is suggested. Beaty et al.(1988) have provided an oxygen isotope estimate for tourmaline associated with the Pb-Zn ores of Sullivan, of 200 – 250°C. At the Rum Jungle Pb-Zn deposit, shallow-water tourmalinites associated with evaporitically-derived magnesite have fluid inclusion temperatures in the range 100° to 250° C (Bone 1987).

Authigenic deposition of tourmaline is also in conflict with the above experimental data. Although authigenic tourmaline is uncommon, its occurrence paragenetically between silica and carbonate in some sandstone cement sequences, suggests a low temperature of formation (i.e., < 200° C). Formation temperatures of typical silica and carbonate cements in sandstones and carbonates indicate deposition commonly between 58° and 170° C (Roedder 1984, Klosterman 1981, Nahnybida et al. 1982). However, no temperature studies of tourmaline-bearing samples are known to the author. Documented occurrences (Gautier 1979, Ricketts 1981) suggest that boron-rich formation waters are a special diagenetic condition, with both authors invoking contributions of boron from buried granites, evaporite sequences or volcanic activity.

Boron Contents of Natural Waters

Boron is markedly concentrated in seawater (average 4.6 ppm) over river waters (1.4 – 58 ppb ; Drever 1982) because of its conservative behaviour, which has obvious implications for the origin of boron in marine versus lacustrine (non-marine) evaporites.

FLUID TYPE, LOCATION	B (PPM)	pH	T°C	Reference
Oilfield brine, average	8-108	-	50-200	1
Pacific M.O.R. Black Smoker.	4.6	-	250-400	2
Guymas Basin vents (sediment-hosted).	~9	-	-	2
Wairakei Hotsprings, N.Z. (volcanic hosted).	26-30	6.8	245	3
Thermal brine, Salton Sea, US	498	5.5	340	3
Red Sea, Atlantis 2 Deep	11	5.3	56	3
Ngawha field, N.Z.	1200	6.4-8	233	3
Osereyama Springs, Japan	343	7.3	100	3
Well 7, El Tatio, Chile.	210	7.31	255	3
Searles Lake, California	3225	alk.	<50	4
Owens Lake, California	626	alk.	<50	4

Table 9.4 *Chemistry and composition of some natural waters. (1. White 1957; 2. Plimer 1986; 3. Ellis 1979; 4. Ethier & Campbell 1979).*

Boron in hydrothermal systems concentrates relative to chlorine in fluids circulating through aquifers in sedimentary piles ((Ellis 1979, Bischoff et al. 1981, and Table 9.4) but shows great variability. It is probable that evolved high-level magmas may also contribute boron to hydrothermal waters, e.g., Naboko (1959). The majority of measured hydrothermal springs have a Cl/B ratio between 7 and 30 (Ellis 1979) i.e., lower than seawater, but in these situations boron remains conservative. The exceptions are waters such as the Ngawha geothermal field of New Zealand (1200 ppm B), and Searles Lake, California (3225 ppm B), which show very high levels of B without proportional Cl enrichment. At present the controls on B solubility in these settings are uncertain; B concentrations in

hydrothermal waters increase erratically with temperature, show little pH control, and although some waters carry sub-percent levels of B at high temperature (Table 9.4) no boron minerals occur at the vent site except in arid evaporitic settings (discussed below). This, and the low levels of B (close to sea-water values) in active sulphide-forming vent-waters of the mid-ocean ridges (Table 9.4), makes the formation of large concentrations of tourmaline associated with some massive sulphide deposits (Taylor & Slack 1984) all the more problematic. The specific conditions which favour borate deposition from low-B fluids are still not understood, but might be better appreciated by the study of sites such as the thermal springs of Lardells, Italy, where commercial borates are forming from fluids bearing only 35 ppm B.

In Search of Modern Tourmalinite

Several workers (Plimer 1987b, Ethier & Campbell 1979) have indicated that isochemical metamorphism of sediments with normal boron contents cannot produce tourmalinites, because their natural boron levels are too low. For instance, illite is the most B-rich mineral in average sediment, with concentrations of 100 – 2000 ppm B (Harder 1970), which is incorporated into lattice sites ~ 5000 years after the initial adsorption. Metamorphism of even pure illite therefore would produce only a few percent tourmaline. These authors did not consider that authigenic clays such as glauconite theoretically adsorb far more boron in evaporitic settings (Harder 1970), but specific whole-rock sampling of known evaporitic glauconite deposits (Moine et al. 1981) has thus far failed to show enrichment even in these beyond ~400 ppm B. Thus the metamorphism of average sediment is discounted as a viable origin for tourmalinite.

Marine and lacustrine evaporite settings also are unlikely environments for the formation of tourmalinites, despite the concentration of boron into evaporite bitterns (Sonnenfeld 1984). A review of data for many large evaporite sequences shows that borates only occur in the most evolved potash-magnesia facies, and that even here, the initial deposition of sylvite (KCl) is not accompanied by B incorporation. Osichkina (1978) states that a sequence may in fact lose almost all of its boron if only 2000 ppm of the original seawater left is lost. Hence, pore-water fluids of evaporite sequences are likely to be very B-rich. This is additionally so if the anhydrite to gypsum transition occurs during diagenesis, because ~ 100 ppm B in anhydrite is lost to the fluid (Holser 1979). The channelling of such a fluid during early metamorphism to favourable clay horizons could result in the formation of some tourmaline through continuous illite-fluid reactions (Reynolds 1965). Povondra and Novak (1986) document an analogous uvite-forming reaction in metaevaporites at higher metamorphic temperature (495° C), as:

$$10 \text{ phlogopite} + 24 \text{ calcite} + 3\ B_2O_3 + 20\ CO_2 =$$
$$2 \text{ uvite} + 18 \text{ quartz} + 22 \text{ dolomite} + 5\ K_2O + 6\ H_2O + 5\ O_2$$

Where borates occur abundantly with evaporites, most authors have appealed to a hydrothermal origin for the boron (e.g., Muessig 1966, Bernard & Kistler 1966, Ricketts

1981, Alonso 1988). This is because the borates are not associated with highly evolved evaporite minerals, but with lower-order minerals such as gypsum and halite, contravening the normal observed order in the precipitation path of a marine brine. In some cases the only evaporite present is borate. These modern deposits represent the only documented sequences on the globe containing the concentrations of boron found in ancient tourmalinites, and hence have great appeal from a uniformitarian perspective.

Borate deposits characterise evaporitic rift-settings with active volcanism. They occur either as mound spring deposits (Muessig 1966), or as stratiform accumulations in fault-controlled playa lakes, with areas of up to 100 km^2 (Muessig 1966, Helvaci 1978, Alonso et al. 1988). The Kramer borate deposit of California (110 m thick), had an active fault control evidenced by interfingering arkose and talus breccia (Bernard and Kistler 1966). An origin through the supply of boron-rich hydrothermal fluids to bodies of standing saline water is favoured, with the precipitation of borax triggered as lake temperatures decreased to 25° – 35°C (Christ et al. 1967). In some South American examples, Muessig (1966) documents anomalous levels of trace metals such as As and Sb, which are common to epithermal sinter deposits. Under low temperature diagenesis a host of secondary borates stabilise, dominated by ulexite ($NaCaB_5O_9.8H_2O$), colemanite ($Ca_2B_6O_{11}.5H_2O$), kernite ($Na_2B_4O_7.4H_2O$ — stable over 58.5° C), and borax ($Na_2B_4O_9.10H_2O$) (Helvaci 1978, Smith 1979). These secondary borates form nodules, reprecipitated crusts, displacive crystals and veins in the diagenetic fabric, intergrown with Na-Ca minerals (typical of alkaline lakes) such as trona, nahcolite and gaylussite (Smith 1979, Alonso 1988).

The behaviour of these assemblages during subsequent metamorphism is unknown above 100°C, but it is suggested here that reaction with clays and cation-rich diagenetic waters would produce prograde tourmaline. This is supported by the recent discovery of borax-pseudomorphs in stratiform tourmalinite from the Damara orogen, Namibia (Behr et al. 1987, Porada & Behr 1988).

Paragenesis of Boron in the Starra Sequence

While the distribution of lithologies is evidence for at least a semi-closed-basin origin for the environs of the Starra Au-Cu deposits, this is reinforced by widespread tourmalinite in an evaporitic setting. It is suggested that in this area boron was originally deposited as Na-Ca borates around the shallow margins of a fault-bound basin, partially open to the sea, at the same time as BIF deposition was occurring. An attractive source for the boron is the hydrothermal system proposed for the formation of the Starra Au-Cu deposits (Davidson et al. 1988). The footwall alteration zone below the Starra ironstones is severely depleted in K, Ba, Rb and B, all of which show enrichments in the interpreted distal marginal evaporitic sediments. The system is also the logical supply of Fe to the associated distal cherty BIFs, as previously discussed.

Burial resulted in the speculative conversion of borates to tourmaline, as well as the migration of boron-rich fluids into the sedimentary pile. The resulting stratiform tourmalines

did not have Mg:Fe ratios reflecting the bulk rock (e.g., the most magnesian examples occur in BIF), but like other Proterozoic tourmalinites were enriched in Fe compared to Phanerozoic tourmalines in massive sulphide deposits (Plimer 1987b).

Some of the borates were dissolved, and the resulting diagenetic fluids migrated to react with interstitial clays, forming discordant and strata-parallel tourmaline-rich zones. During low-grade metamorphism, boron would partition into the fluid-phase by conversion of illite to muscovite, and anhydrite to gypsum (Harder 1970). Low to medium-grade retrogression accompanying later deformation was also a period of boron mobility, with leaching of tourmaline at high-stress sites by NaCl-rich solutions, and the liberation of boron by muscovite breakdown (average 10 – 500 ppm B; Harder 1970) to chlorite (< 50ppm B). Detailed study of deformed tourmaline samples shows that the Fe, Al and Na in tourmaline partitioned into the metamorphic fluid, while Ca and Mg were preferentially retained.

Fluids from the late phase of the Gin Creek Granite are not favoured to form stratabound metasomatic tourmalinite, because there is no close spatial association between the two; rather, a basinal stratigraphic control is likely. Boron-rich metamorphic fluids may have in fact percolated into the granite, mixing with igneous fluids to form the unusual (relatively magnesian) tourmaline observed to alter earlier Fe-rich tourmaline and deformed muscovite.

The compositional range found in each group of tourmalines is attributed to formation under variable fluid to rock ratios. Stratiform and metasomatic tourmalines formed under low W/R conditions, while granite and shear-types crystallised from large open fluid systems and hence are relatively chemically homogeneous. Compositional similarities between the groups are attributed to the redistribution of some original sedimentary-diagenetic tourmaline into metamorphic and deformational sites by saline fluids.

CONCLUSIONS

1. Meso- and microscopic-scale sedimentary structures and a spatial association with one extensive horizon require that stratiform tourmalinite formed in a sedimentary evaporitic environment, probably during diagenesis. In one instance, the timing of tourmaline replacement of a synsedimentary borate precursor is constrained to early diagenesis.

2. In contradiction to the published experimental data implying immobility of tourmaline, boron is leached by saline fluids at high-stress sites during low-grade metamorphism and deformation. Where redeposited in veins and larger-scale shears, the Mg# in tourmaline alters from ~0.65 in primary tourmalinite to ~0.36 in redeposited metamorphic tourmaline. Other geochemical characteristics of remobilised tourmaline are an increase in Al, Na, and Fe, and a depletion in Ca and Mg.

3. Igneous and shear-hosted tourmalines are chemically similar and have a restricted compositional range, reflecting their formation from a fluid with a high fluid to rock ratio. Conversely, stratiform and metasomatic tourmalines show a large compositional range

typical of low W/R conditions, with metasomatic types discriminated on the basis of their high Ca content.

4. In keeping with other studies (Appel 1986, Bone 1987, Plimer 1987b, Beatty et al. 1988), the ultimate source of boron for stratiform and metasomatic tourmalinite is interpreted to be hydrothermal, but is specifically identified as the exhalative Starra magnetite Cu-Au deposits, (or a similar nearby vent-site), which have a footwall depleted in K, B, Ba and Rb. Thus evaporitic stratiform tourmalinite is a time-marker of mineralisation in the sequence.

5. Global stratiform tourmalinites can be divided into two diverse groups:

A. Evaporitic hydrothermally-sourced borate deposits, which are metamorphosed at low temperatures (100 – 300° C) to form tourmalinite. Deposits in the Damara orogen (Schmidt-Mumm et al. 1987), Rum Jungle (Bone 1987), Starra, and the Grenville province (Brown and Ayuso 1982) are grouped into this type, because of their association with shallow water sediments and evaporitic minerals or structures.

B. Deep water hydrothermal precipitates intimately associated with VMS deposits, in which tourmaline may be deposited directly from the hydrothermal fluid. Such deposits are enclosed by turbidites or black shales indicating relatively reducing conditions, and include the Appalachian-Caledonide massive sulphides (Taylor & Slack 1984) and the Sullivan orebody (Ethier & Campbell 1979, Beaty et al. 1988). They have no modern analogue, but probably characterise sediment-leached hydrothermal systems (Plimer 1987), because of the ready availability of boron in argillaceous sediment compared to basalt (Bischoff et al. 1981).

CHAPTER 10

CARBON/OXYGEN ISOTOPE STUDY OF THE STARRA AND TROUGH TANK IRONSTONES, AND THEIR HOST-ROCKS

INTRODUCTION

An isotopic study was carried out to determine the origin and affinities of the different carbonate generations at Starra and Trough Tank, and their significance to mineralisation. The main carbonate-types sampled in the study were:

(1) Regional and ore-adjacent synsedimentary Staveley Formation carbonate,

(2) Syn-tectonic veins and carbonate-filled shears in the Starra hangingwall,

(3) Disseminated carbonate forming part of the Trough Tank alteration, and

(4) Disseminated carbonate in Starra ore environment ironstones.

A fluid inclusion study helped to constrain the genesis of the syn-tectonic veins, but could not be extended to the other carbonate groups because of their metamorphosed nature.

TEXTURAL CHARACTER OF THE SELECTED SAMPLE-TYPES

Synsedimentary carbonate of the Staveley Formation

Calcareous lithologies are widespread in the Staveley Formation, a unit described by Blake et al.(1984) as "calcareous, ferruginous, siliceous and micaceous arenite, siltstone and phyllite". In general terms, excepting the immediate stratigraphy adjacent to the Starra Iron-formation Member (which is more variable), the carbonate content of the Staveley Formation increases from south to north in the Staveley Belt. South of the Hinge Zone, carbonate-absent feldspathic sandstones and siltstones dominate, whereas arenites in the Starra Syncline between Areas 222 and 276 are cemented by 5 – 10 % calcite (Fig. 10.1).The northern strike-equivalents of these rocks are flaggy cleaved calc-silicates and marbles. In isolated instances (e.g., 26800N, 16800E Amoco Regional Grid) these are strongly silicified, or altered adjacent to the Mt. Dore Granite (calc-silicate granofels of Leishman (1983); Fig. 10.1).

Within 500.m of the Western Hematites, thin-banded calc-silicate, chert and siltstone beds occur, a facies described more fully in Chapter 3. The prograde calc-silicate assemblage is generally quartz-albite-actinolite-calcite-epidote, indicating that an original calcareous component was reacted during metamorphism. This rock-type is hornfelsed at Area 257 Area by amphibolitic intrusives 100 – 150 m from the ironstone contact. The sediments immediately adjacent to ironstone at Area 257 consists of graded calcarenite beds (quartz-feldspar-carbonate) alternating with thin layers of biotite ± scapolite/cordierite. In unveined samples of the latter, the carbonate has a metamorphosed habit. For instance, calcite forms grains which parallel S2(MP), occurs as inclusions in quartz and plagioclase, and contains

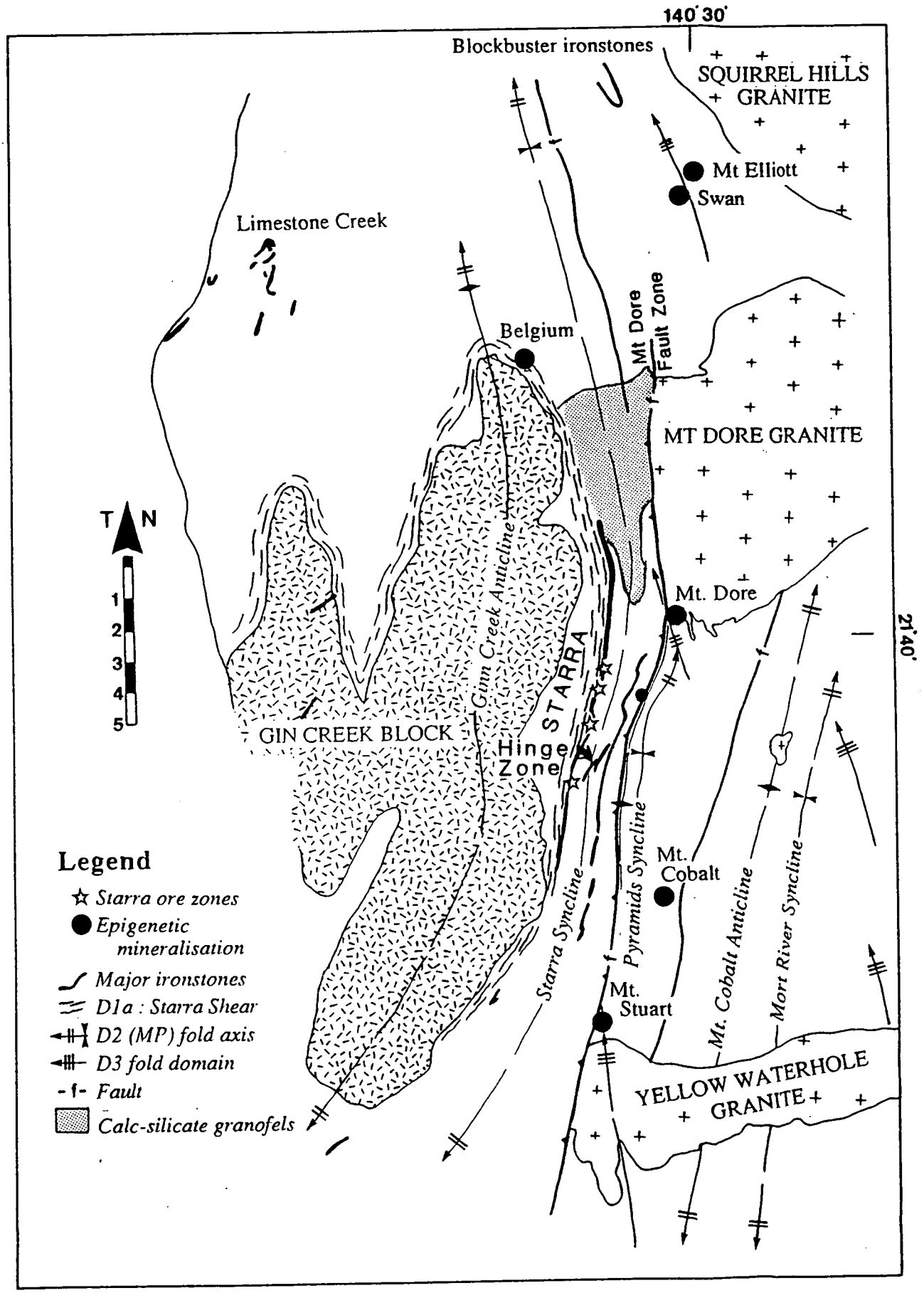

Figure 10.1 *Tectonic elements of the Starra region. The boundary of the Gin Creek Block includes the Double Crossing Metamorphics (Blake et al. 1984) and all Gin Creek Granite types.*

deformation lamellae. In graded calcareous samples the greatest calcite content correlates with the coarsest quartz at the base of each couplet (Fig. 4.6E). An early carbonate content is also implied for the calc-silicate interbeds, through such Greenschist facies reactions as (modified after Klein (1982)):

$$5Ca(Mg,Fe)(CO_3)_2 \textit{ (carbonate)} + 8SiO_2 + H_2O =$$

$$Ca_2(Mg,Fe)_5Si_8O_{22}(OH)_2 \textit{ (actinolite)} + 3CaCO_3 \textit{ (calcite)} + 7CO_2$$

Carbonate in Ironstone

Calcite and siderite are commonly disseminated in magnetite ironstone, but are rare in hematitic ironstone. Both occur as texturally-pre-metamorphic phases in contact with hematite and magnetite, displaying "baroque" recrystallisation, triple-point development, and undulose extinction (Fig.3.15). In more deformed samples, carbonate has migrated to low stress sites such as cracks in magnetites (which parallel carbonate tension-gashes in the hangingwall) and pressure-shadows. Siderite is a common phase in D2(MP) interboudin vein-networks in ironstone, together with magnetite, chalcopyrite and quartz. This carbonate was introduced or remobilised coevally or prior to D2 peak-metamorphism and deformation (see Chapter 4), whereas bedding-parallel carbonate bands may have formed at the sediment-water interface.

Metamorphic minerals, which might normally develop during metamorphism by the reaction of primary carbonate with iron-oxide, are not abundant. However, the magnetite porphyroblasts in barren hematitic ironstone (Figs. 3.9F & 3.15B) could well have formed by the complete reaction of siderite with hematite to form magnetite, which is a very common phenomenon in iron formations (Klein 1973). The simple thermal disassociation of hematite to form magnetite ($6Fe_2O_3 = 4Fe_3O_4 + O_2$) is unlikely during metamorphism because the diffusion rates required to remove O_2 are geologically unacceptable (Mel'nik 1982). A reductant is necessary, such as free carbon, CO, H_2, CH_4, carbonate, etc. The reaction of siderite + hematite to form magnetite has been documented at relatively low temperatures (La Berge 1973, Klein 1973) — 300° C at P_{CO2} min. =2 kB, enhanced in the presence of water. Excess carbonate is a feature of mineralised magnetite ironstone, and if the above inference is correct, has probably been preserved because of a relative lack of hematite. Carbonate-bearing ironstones in the sample-set all had Au > 0.6 ppm .

Hangingwall Veins and Shears

Distribution

A prominent set of D2(LP) (or younger) pervasive calcite veins cuts hangingwall metasediments, dolerite and some ironstones at a high angle to bedding. They are distinct from near-peak-metamorphic veins, which consist of quartz, biotite, actinolite ± calcite, and most commonly have near-bedding parallel attitudes, or radiate from interboudin neck-points related to D2(MP). The D2(LP) veins occur within 150 m of the Starra Shear (i.e., the

highly sheared rocks extending west from the ironstone), intensifying in number, width and length, towards the shear. At the greatest distance from the shear, dolerite and dolerite hornfels contain only a few semi-continuous veins. Further towards the shear, veins are only present in the calcareous arenites, not the interbedded phyllite, but at ~ 50 m all bed-types are veined. The vein intensity is highly variable, suggestive of strain variation. In subsidiary shears, which can be wholly-filled with banded carbonate paralleling the fault walls (Fig. 4.6F, left), carbonate veins are strongly folded, brecciated and rotated (Fig. 4.6F, middle), compatable with progressive vein development during shearing.

Strongly-carbonate-veined areas are not confined to mineralisation loci, but are documented along the the length of the hangingwall. They are best-correlated with calc-arenites (increasing in number and thickness towards the ironstone),which constituted a competent rock likely to deform brittly in the brittle-ductile conditions, producing a carbonate-rich pressure-solution phase capable of migrating into gash veins.

Vein Orientations

The main carbonate-vein generation cuts bedding at a high angle to both strike and dip, with only occasional conjugates (Fig. 4.6G). Less commonly veins of similar

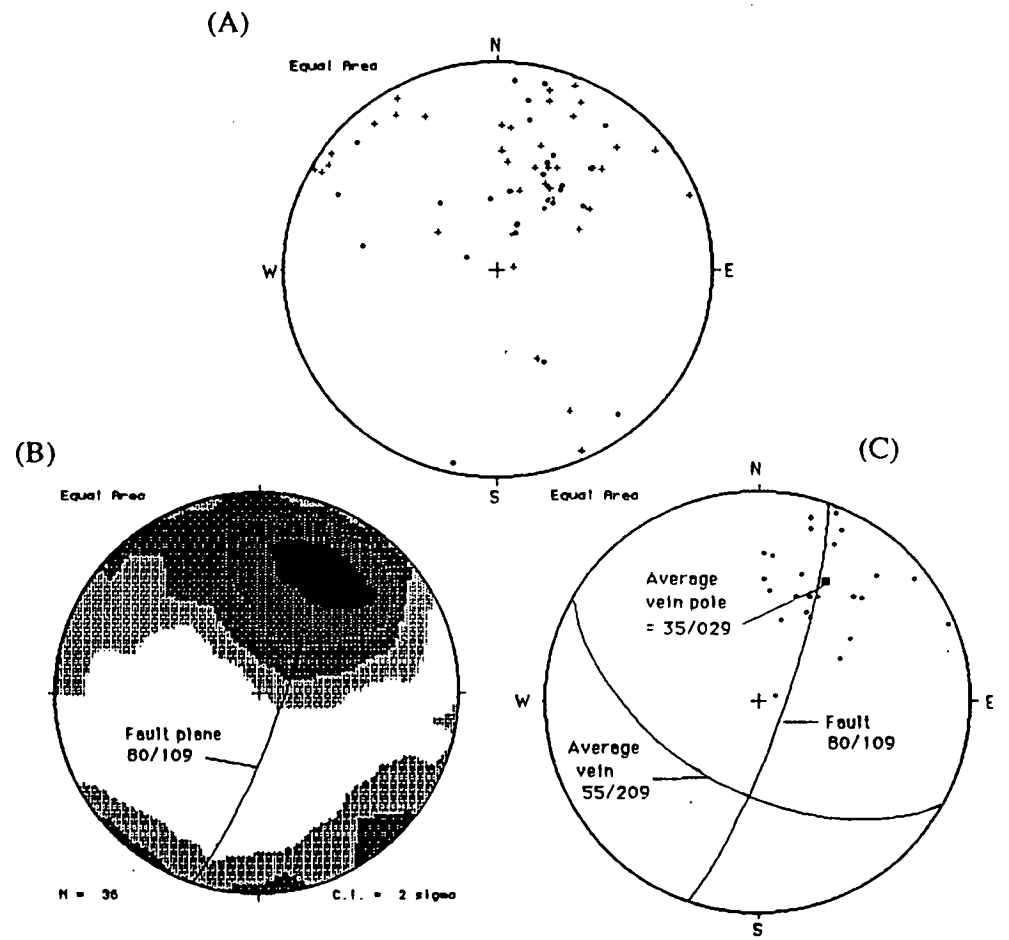

Figure 10.2A *An equal area plot of poles to veins from Areas 257 (crosses and 244 (dots).* **10.2B** *A contoured presentation of 10.2A.* **10.2C** *The data points from Area 257 used to define the average vein pole of 35°/029°.*

composition occur sub-parallel to bedding. Vein orientations were measured at surface in weathered drill-pad exposures at Areas 257 and 244, where they are replaced by kaolinite and chalcedony. The measurements are consistent between the two sites (Figs. 10.2A-C). The dominant vein set has an average dip of 55°/209° (95% confidence cone of 9°), whereas bedding and near-bedding-parallel veins dip steeply to the east and west (averaging 80°/324° and 85°/144° respectively). Several veins are virtually flat-lying at both sites, and have uncertain affinities.

Vein Composition, and Morphology

Vein orientation is least consistent close to the shear, because gapes which were created during transposition are calcite-filled. Where the orientation is consistent, veining is often present on a microstructural scale (as revealed by carbonate staining) (Fig. 4.6G). Most commonly veins average 2 – 5 cm long by ~ 0.5 cm wide. The margin of each is embayed rather than sharp, with the common development of fibre-chlorite and calcite perpendicular to the vein walls. Compositionally the veins are 95% carbonate, with minor amounts of green chlorite, quartz, and trace chalcopyrite, pyrite and pyrrhotite. The carbonate is mainly calcite containing liquid-vapour fluid inclusions (imparting a grainy appearance). Dolomitic calcite in some well-zoned veins occupies the vein-margins, in at least one case separated from late clear-calcite by a thin layer of euhedral siderite (Fig. 4.6H).

Ironstone carbonate (siderite and calcite) veins form clots and 1-10 mm wide short gashes, and are far less abundant (<5% of the rock) than veins in the hangingwall. Sulphides and oxides intersected by siderite veins are embayed and altered to more oxidised minerals (e.g., chalcopyrite to chalcocite, magnetite to hematite).

An important feature of the whole vein system is a lack of mineralogical or compositional zoning away from mineralisation.

Tectonic Implications of the Veins

The timing of the vein generation clearly post-dates both the kinematic and structural peaks of D2(MP), because veins cut the S2(MP) cleavage, cut porphyroblasts, and are dominated by chlorite rather than biotite. A late-D2(LP) timing is favoured because the veins transect phacoidal D2(LP) breccias (Fig. 4.6F, right), but are themselves sheared and brecciated in places. An origin as tensional veins (i.e., pinnate fractures and tension gashes) with a shear component is likely because the vein fibres have both pure tensional and simple shear features. The spatial distribution of the veins only in the near-fault area rules out an origin due to regional folding. Given that the veins relate to shearing, the simplest solution to the direction of fault movement is to assume that the attitude of the gash fractures are perpendicular to the axis of maximum extension describing the fault-induced strain. This assumption is based on the lack of vein conjugates, feather fractures, or conjugate en-

echelon crack arrays (e.g., Roering 1967) associated with the main vein generation. Hence the projection of the average pole to veins on to the fault plane can also be interpreted as the

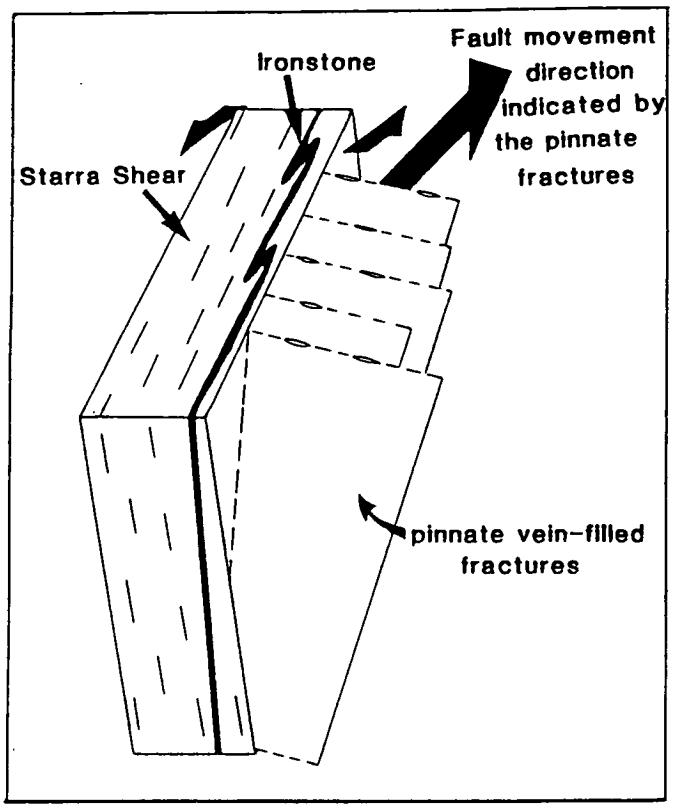

Figure 10.3 *A summary sketch of the vein orientation with respect to the Starra Shear .*

average line of motion, given that the acute angle between the fault plane and the gashes indicates the actual direction of motion (Hobbs et al. 1976, p. 296). In this case, motion is interpreted as east-block-north, moving on a line to the pole 35°/029° i.e., left lateral with a component of normal motion (Fig. 10.3).

Deducing the stresses which produced the fault motion is more difficult to quantify because the active stress system did not produce the movement surface. One factor is the unusually high angle of the pinnate fractures and gashes to the fault plane, approximately 80°, whereas the ideal angle is 45° for tension gashes and 60° for antithetic pinnate fractures (Hancock 1972). An explanation for this is the extensive layer slip and transposition within the shear, which causes the rotation of the effective maximum principle stress direction (Rickard and Rixon 1983). This change in the main stress direction is often recorded in the orientation of mineral fibres within veins, but no detailed analysis of these has been carried out here other than general comments made above. It is likely in general terms that this principle stress outside the shear-zone is south of that within the shear-zone, trending south-east/north-west, compatable with the generation of a sinistral shear-couple during D2(LP) on the north-trending Starra Shear.

In conclusion the calcite veins are interpreted as brittle-ductile pinnate fractures generated during sinistral motion on the Starra Shear, late in the D2(LP) deformation (summarised in Fig. 10.3).

CONDITIONS OF VEIN FORMATION: THE FLUID INCLUSION EVIDENCE

Approximately 70 fluid inclusions from five veins were measured to deduce the hydrothermal conditions which prevailed during calcite and quartz formation, with results tabulated in Appendix 9. The veins were sampled over the range of oxygen isotope variation in carbonate (~+10 to +25‰). Freezing measurements preceded heating runs to circumvent false readings caused by inclusion-stretching. Homogenisation temperatures were adjusted using calibration information from synthetic inclusions with a wide vapour homogenisation range. All of the measured carbonate veins come from hangingwall metasediments or from dolerite; attempts to find inclusions in ironstone carbonates were thwarted by recrystallisation fabrics which have destroyed primary inclusions.

The measured inclusions ranged from 5 – 60 μm, averaging ~12 μm in diameter. Most were obtained from "grainy" carbonate with well-developed growth-fibers. Inclusions have crystal cleavage-controlled form, are not generally aligned, and show no signs of necking; hence they are unlikely to be secondary (Fig. 4.6H, inset). A vapour volume of 5-10% is characteristic. Selvedge quartz contains fluid-inclusions with higher homogenisation temperatures than those of the host carbonate, and daughter minerals including halite (cubic, isotropic) and an opaque. This early quartz suggests that calcite was deposited from cooler fluids characterising waning hydrothermal activity, rather than at the hydrothermal peak.

Sample No.	$\delta^{13}C$	$\delta^{18}O$	Mean T_h (° C)	95% conf. range for Temp. (° C)	Av. Wt.% equiv. NaCl	$\delta^{18}O$ (fluid) free-water*1	$\delta^{18}O$ (fluid) NaCl-cor'd*2
D4	-3.73	10.47	143	26.4	4.0	-2.47	-2.47
St65	-3.10	18.51	200.8	53.6	18.88	9.18	12.23
St127	-2.74	18.31	170.5	31.9	15.35	7.28	7.88
St270A	-3.30	24.20	114.1	19.7	23.13	8.75	9.75
St270A qtz			333.9	24.7	51.23	-	-
St263A	-2.83	15.37	125.4	16.7	15.85	0.74	-0.82

Table 10.1 *A summary of the compositional and fluid inclusion data for vein specimens, including the calculated isotopic compositions of the fluids. * 1.Calculated from the calcite-water fractionation equation of Friedman & O'Neil (1977).*2. Corrected for salinity after Truesdell (1974).*

Eutectic Temperatures (T_e)

Where observed, the eutectic temperatures, i.e., the temperature of first melting of ice in the simple liquid-vapour inclusions, ranged between -40.4 and -8.4° C, with an average of -26.4° C. Many of these values are below the eutectics of H_2O-NaCl (-20.8° C), H_2O-KCl (-10.6° C), H_2O-NaCl-KCl (-22.9° C), and even H_2O-NaCl-$MgCl_2$ (-35.0° C). It is therefore likely that there is a significant amount of $CaCl_2$ (eutectic = -49.8° C, H_2O-NaCl-

$CaCl_2$ = -52.0° C) in the brines, although T_e values closer to -52.0° C were expected. Their absence is attributed to the difficulty in observing the exact onset of eutectic melting, exacerbated by small inclusion sizes and the notoriously poor optics of calcite.

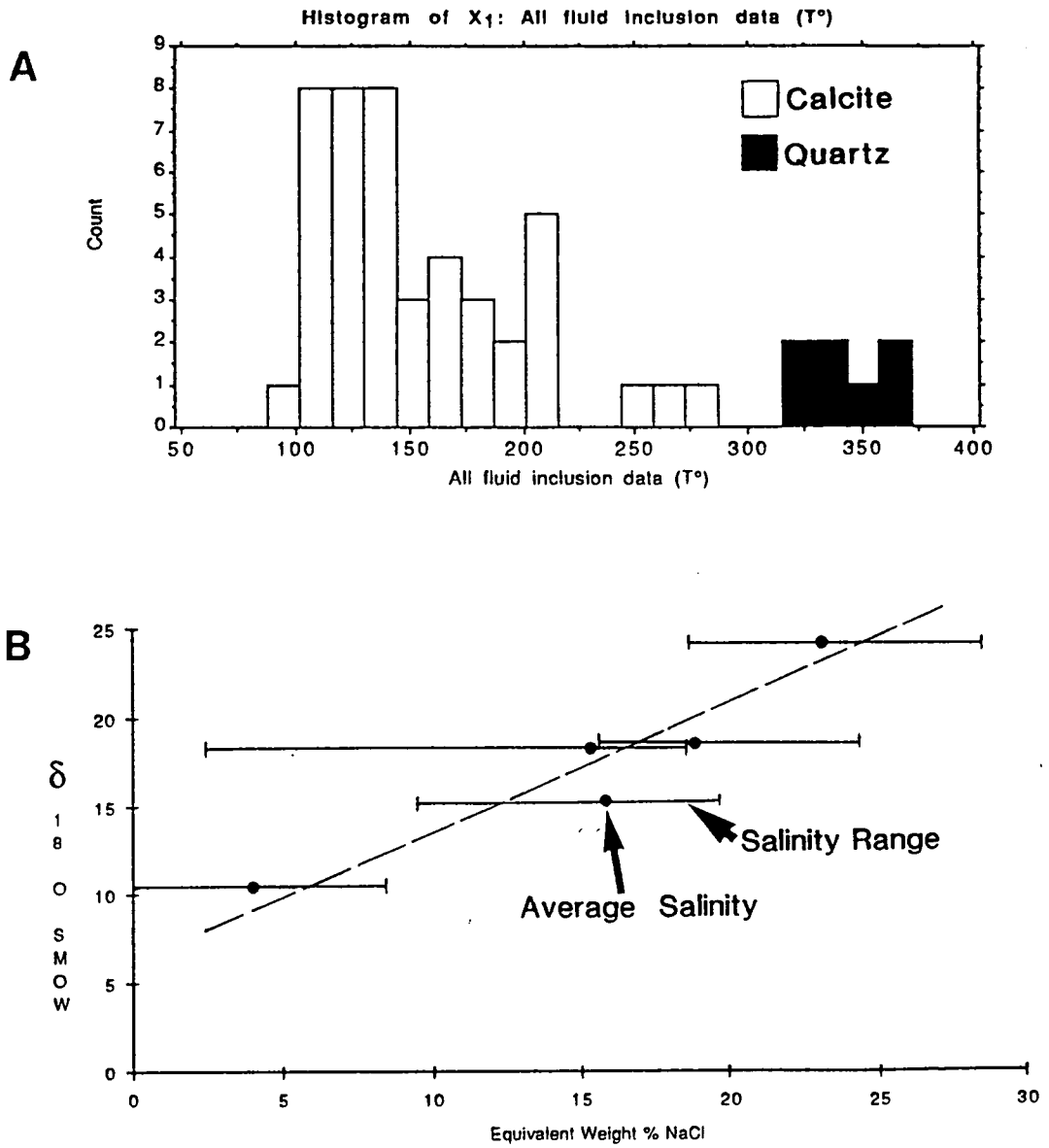

Figure 10.4A *A frequency distribution of homogenisation temperatures for all primary fluid inclusions in vein calcites.* **10.4B** *A plot of salinity in fluid inclusions versus the $\delta^{18}O$ -isotope composition of the host calcite.*

Ice Melting Temperatures (T_m)

Hydrohalite was observed to melt in one inclusion at -7.4° C, while ice melted at -14.9° C, in an inclusion with a maximum T_e of -24.9° C. However, most inclusions only exhibited ice-melting, from which salinity was deduced. Salinities ranged between 0 - 28 wt.% NaCl-equivalent for calcites in the five samples, and 50.5 - 52.0 % for quartz in the only sample analysed (determined by the temperature of halite dissolution; Table 10.1).

Within each sample the variation of primary salinity was 9 % on average. Notably secondary inclusions possessed a much smaller salinity range of only 3.6% (e.g., in St 263A calcite).

Homogenisation Temperatures (T_h)

An analysis of all liquid-vapour homogenisation temperatures of calcite for all veins reveals a skewed distribution with the bulk of trapping occurring between 100-145° C (not pressure corrected), trailing off towards a maximum of 285° C. A pressure-correction was not applied because the depth of formation of D2(LP) deformation is not well-constrained. Temperatures in paragenetically-earlier quartz form a distinct population ranging between 315 – 365° C. Within individual veins there is also a substantial variation in temperature reflecting prolonged crystallisation of carbonate, with ranges between 106 – 239° C (Table 10.1, Fig. 10.4A). This phenomenon was assessed in more detail in St 263A (Fig. 4.6H), a complex vein initially filled with poorly crystallised dolomitic calcite, then "baroque" dolomite (minimum crystallisation temperature of ~150° C) followed by a thin euhedral layer of pure siderite, and ultimately filled with clear calcite. The early phase had average T_h = 125.4° C, 15.9 % salinity; the baroque rim averaged 149.2° C, 23.2 % salinity, while the calcite centre was cut by secondary inclusions with T_h = 130.6° C, 22.4 % salinity (no primary inclusions were found in the latter). Siderite precipitation in this vein was therefore preceded by a temperature and salinity rise.

CARBON-OXYGEN ISOTOPE EVIDENCE

Sampling Strategy

Two populations were sampled: (1) veins, and (2) matrix carbonates within sediments/ironstones. Matrix-vein pairs were obtained from the same samples over a range of veining intensities, to assess isotopic exchange between the two. Calcites were mainly used in the metasediment samples, identified using an alizarin red S stain described by Dickson (1965). Siderite and calcite compositions were confirmed in some samples using a Jeol 50A microprobe.

Method

Calcite (25 mg) was drilled from vein samples and reacted with H_3PO_4 (phosphoric acid) at 25° C for a 24 hour period, using the method of McCrea (1950). The isotopic composition of C and O in the extracted CO_2 was obtained from a Micromass 602D stable-isotope mass spectrometer. Weights of matrix sample were obtained in proportion to the modal abundance of calcite. A review of previous analyses of the international standard Biggenden calcite gave a standard error for $\delta^{13}C$ of ±0.06 ‰, and ±0.1‰ for $\delta^{18}O$ for this machine; standards analysed with the samples were well within this precision.

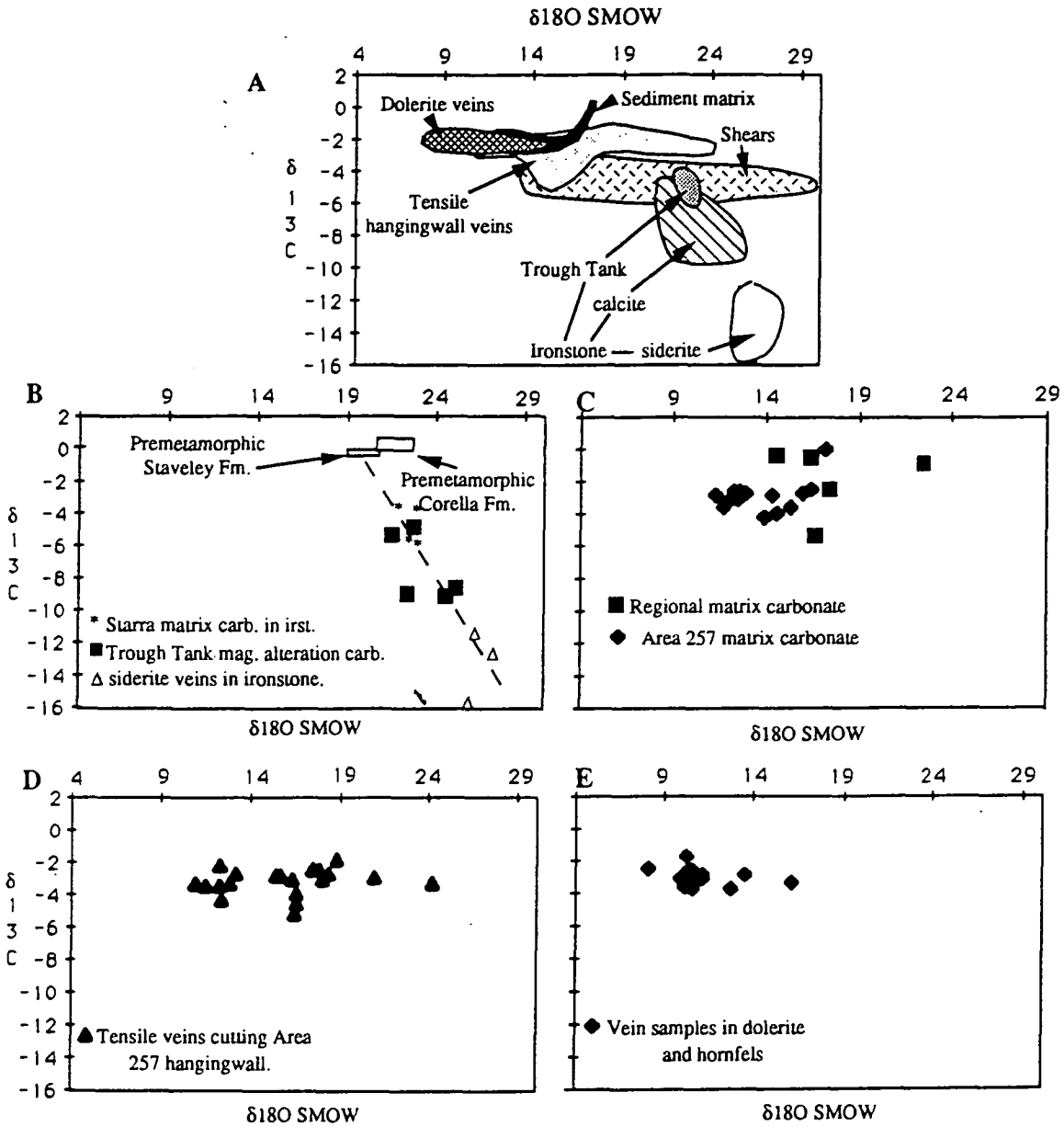

Figure 10.5 A *Carbon - Oxygen isotope fields of all Starra sample groups.* **10.5B** *Ironstone carbonates from Area 257, and Trough Tank silica alteration zones. The regression line has the equation δ18O = -4.76(δ13C) + 19.38, notably intersecting the field of premetamorphic Staveley Formation carbonate.* **10.5C** *Regional carbonate, compared to Area 257 matrix carbonate.* **10.5D.** *Veins in the Starra hangingwall metasediments.***10.5E** *Veins in hornfels and dolerite, generally > 70 m from the main Starra Shear.*

RESULTS

Regional Staveley Formation Carbonate

Five regional samples were obtained from dolomites and calcareous sandstones in the Staveley Formation from outside of the potential circulation of Starra hydrothermal fluids. The results varied between $\delta^{13}C$ = -5.26 – -0.38 ‰, $\delta^{18}O$ = +14.50 – +22.42 ‰, (average $\delta^{13}C$ = -1.48, $\delta^{18}O$ = +17.44) (Fig. 10.5C, data in Table 10.2) a spread suggesting that the original carbonate was heterogeneous, or exchanged light oxygen and carbon during diagenesis.

Hangingwall Matrix Carbonate

Twelve matrix carbonates in the hangingwall of the 257 orebody were analysed, summarised in Table 10.2. Two samples were also taken from Area 236, and from above the 222 orebody. All samples were unsheared, and in some instances sedimentary structures such as cross-bedding and grading are distinguishable.

The results overlap with those of regional matrix carbonate, but most Starra matrix samples have distinctly lighter oxygen, and slightly depleted carbon values (Fig. 10.5B) ($\delta^{18}O$ = +11.24 – +17.29 ‰, and $\delta^{13}C$ = -4.23 – +0.03 ‰). Within particular samples, the analysis of adjacent layers revealed variation beyond analytical precision. $\delta^{18}O$ varied by ± 0.6 ‰, and $\delta^{13}C$ by ±0.2 ‰.

Hangingwall Vein Carbonates

Two groups were extensively sampled (37 samples) : (1) veins which cut carbonate-bearing metasediment, and (2) those which cut hornfelsed metasediment and dolerite. The two groups overlap with the isotopic field of matrix carbonate (Fig. 10.5A), but dolerite and hornfels samples are $\delta^{18}O$ depleted (+8.01 – +16.00 ‰, average +10.27‰) compared to veins in sediment, which vary from +10.01 – +24.20 ‰, average +15.88 ‰.

Fluid inclusion data reported earlier was plotted against the isotopic character of some vein samples. The result (Fig.10.4B) was a linear relationship between salinity and $\delta^{18}O$, whereas temperature-$\delta^{18}O$ showed no consistent variation. The highest average salinity of 23.13 wt. % equivalent NaCl corresponds to $\delta^{18}O$ = +24.2 ‰ , and the lowest (4.0 %) to $\delta^{18}O$ = +10.47 ‰ (hosted by dolerite fartherest from the shear).

The average $\delta^{18}O$ fluid composition from which the vein calcites precipitated can be calculated, assuming isotopic equilibrium between the fluid and the precipitate. The calcite-water fractionation expression of O'Neil et al. (1969) was used, combined with the CO_2-H_2O fractionation factor at 25° C; (α = 1.0412; O'Neil et al. 1975), giving the expression of Friedman & O'Neil (1977):

$$10^3 \ln \alpha_{calcite\text{-}water} = 2.78(10^6 T^{-2}) - 2.89$$

where "$10^3 \ln \alpha$" approximates $\Delta_{calcite\text{-}water}$, and T is in degrees Kelvin. T values were assumed to equal the filling temperatures of fluid inclusions in calcites from which the isotopic samples were obtained. A correction for the isotopic effect of salinity has been made

Table 10.2 Isotopic data from calcites obtained from regional and immediate ore hangingwall metasediments

Sample	Area	Location	13C PDB	18O SMOW	13C PDB	Comment
St65	257	80-16/200	-2.41	16.29	-2.41	Scapolitic calcarenite
St66	257	80-16/225	-2.58	12.16	-2.58	Scapolitic metasediment
St121	257	85-129/161	-3.55	11.63	-3.55	Scapolitic metasediment
St127	257	85-137/175	-2.66	15.87	-2.66	Scapolitic metasediment
St163	257	77-26/165	-2.60	12.52	-2.60	Scapolitic metasediment
St177	257	85-137/205	-4.23	13.89	-4.23	Feldspathic metasediment
St193	257	81-19/174	-3.09	12.41	-3.09	Scapolitic metasediment
St193rpt.	257	81-19/174	-2.84	11.24	-2.84	Scapolitic metasediment
St204	257	80-16/249.5	-3.93	14.54	-3.93	Feldspathic metasediment
St219	236	85-113/103	-2.44	17.29	-2.44	Graded calcarenite
St251	257	78-3/75m	0.03	17.15	0.03	Cross-bedded calcarenite
St254	257	78-3/114m	-2.82	14.32	-2.82	Graded calcarenite
St256	257	78-3/127m	-2.64	12.86	-2.64	Graded calcarenite
LK12		Surface,Lst.Ck	-5.26	16.51	-5.26	Deformed marble in D1 mylonite.
St282A		Surface	-0.38	14.50	-0.38	Limestones 5 km north of Starra
St282B		Surface	-0.81	22.42	-0.81	Limestones 5 km north of Starra
St282A.2		Surface	-0.48	16.36	-0.48	Limestones 5 km north of Starra
M1-vein		Surface	-3.55	15.29	-3.55	Vein in regional Staveley Fm. marble
St245	222	86-200/32	-3.17	11.93	-3.17	Well-banded unveined scapolitic siltstone

Table 10.3 Trough Tank isotopic samples

Sample	Location	13C PDB	18O SMOW	Description
TT80A	HQ13/181.4n	-3.888	21.361	Dissem. dolomitic calcite in stratiform magnetite.
TT85C	HQ13/239m	-6.584	22.253	Cross-cutting magnetite in magnetite alteration zone
TT118A	HQ9/114.8	-4.351	22.739	Cross-cutting magnetite in magnetite alteration zone
TT118B	HQ9/116	-6.778	22.875	Cross-cutting magnetite in magnetite alteration zone
TT127	HQ9/180-181	-6.718	14.471	Fine-grained disseminated footwall carbonate

Table 10.4 Carbon-isotope data for the Starra ore environment.

Sample no.	Area	Drill-hole	18O SMOW	13C PDB	%VEIN /10cm	Av. vein width(cm)	Host rock	Vein-type	Carbonate	Accessories	Comments
VEINS ASSOCIATED WITH DOLERITE											
St48	257	80-15/153m	10.434	-3.298	5	1	hornfels	Brittle	Calcite		Some metasomatism evident
St108	257	85-129/109	11.121	-3.065	23	3	altered sedim.	Brittle	Calcite	-	Probably hornfelsed
St156		77-26/60m	10.319	-2.567	8	1	hornfels	Brittle	Calcite		-
St157		77-26/90m	8.01	-2.394	6	1	hornfels	Brittle	Calcite	chl.	-
St249	257	78-3/41.6	10.004	-3.536	0	0	dolerite	Brittle	Calcite	cpy	-
St250b	257	78-3/52m	10.295	-2.936	12	9	dolerite	Shear,metasom.	Calcite	chl., jasper	On intrusive margin
ST261A	257	71/53m	10.384	-2.626	10	1	albitised sed.	Brittle,metasom	Calcite		5m from dolerite contact.
St261B	257	71/47m	15.988	-3.38	20	10	dolerite	Shear,metasom.	Calcite	chl.,hem.	dolerite contact
St261C	257	71/48m	12.616	-3.644	4	5	dolerite	Brittle	Calcite	chl.,jasp.,cpy	In dolerite
St262	257	80-13/116	11.059	-2.82	25	25	hornfels	Brittle	Calcite	chl.,ferr. feld	-
St268	257	85-127/84.1	13.45	-2.83	4	4	dolerite	Brittle,zoned	Calcite	jasper	In dolerite
D4	251	underground	10.471	-3.733	50	30	dolerite	Brittle	Calcite	chl. trace	-
D5/1M	251	underground	10.167	-1.721	20	2	hornfels	Brittle	Calcite	-	1 metre from main dolerite body
D5/5M	251	underground	10.526	-2.568	8	2	hornfels	Brittle	Calcite	30% cpy	sediment hornfels
D5/10M	251	underground	9.845	-3.056	5	5	altered dolerite	Brittle	Calcite	cpy trace	thin dolerite ledge and altered sediment
VEINS ASSOCIATED WITH SKARN											
ST257B	257	78-2/82m	22.393	-10.147	5	2	coarse skarn	Shear, metasom.	Calcite	Scap.,chl.	-
VEINS IN SHEAR ZONES OR FAULTS											
St130	257	78-2/75m	20.054	-3.951	20	2	metasediment	Sheared	Calcite	-	-
St151	257	86-243/123	24.406	-6.423	12	2	Metased.	Sheared	Calcite	Ab. chl.	Retrogressed to chlorite
St252A	257	78-3/93m	29.407	-4.23	36	2	metasediment	Very sheared	Calcite	-	-
St269A	257	85-127/91	14.374	-3.917	22	10	Metasediment	Sheared	Calcite	chl.,cpy	Albitised
St276B	257	85-127/191	13.839	-5.317	75	13	Fault,m/mic	Shear zone	Calcite	–	-
VEINS and MATRIX IN IRONSTONE, MAGNETITE-RICH SEDIMENT											
St107	257	85-129/95.7	25.05	-8.514	20	2	Ironstone	Matrix	Calcite	Silica	Very siliceous well-bedded ironstone.
St115	257	85-129/135	27.451	-12.76	11	6	Ironstone	Brittle,remob.	Siderite	-	Magnetite-quartz mineralogy
St125	257	85-129/191	24.508	-9.075	3	3	Ironstone	Brittle	Calcite	-	Magnetite-Hematite
St128	257	78-2/90	22.327	-8.968	10	2	Ironstone	Matrix	Calcite		Magnetite-Hematite
St225	257	87-254/284	25.886	-11.551	5	2	Ironstone	Matrix	Siderite	-	Very late, incompletely-filled vughs
St264	257	80-13/140	14.777	-2.963	40	2	Sediment	Brittle	Caqlcite	-	
St270B	257	85-127/111	22.69	-4.79	20	18	Ironstone	Shear&brittle	Dolomite	hem.,chl,qtz	
St276C	257	85-127/193	21.496	-5.328	50	2	Ironstone	Brittle	Calcite	-	-
D8.3	251	underground	26.107	-15.566	0	0	Ironstone	In boudin	Siderite	cpy,py,mag	vein, filling vughs associated with D2
CROSS-CUTTING VEINS IN SEDIMENT											
St63	257	80-16/176.5	16.42	-5.147	23	1.5	Metasediment	Schistose/brit.	Calcite	-	-

Table 10.4 Carbon-isotope data for the Starra ore environment.

Table 10.4	Area	Drill-hole	18O SMOW	13C PDB	%VEIN	Av. vein	Host rock	Vein-type	Carbonate	Accessories	Comments
St65	257	80-16/200	17.907	-3.101	15	2.5	Metasediment	Brittle	Calcite	-	-
St66	257	80-16/225	17.723	-2.42	3	1.5	Metasediment	Brittle	Calcite	-	-
St91	257	80-17/100.5	12.159	-2.2	5	2	Metasediment	Brittle	Calcite	-	-
St120	257	85-129/156	11.512	-4.297	12	4	metasediment	Sheared	Calcite	mag.	-
St121	257	85-129/161	10.848	-3.371	10	1.5	Metasediment	Brittle	Calcite	-	Silicified
St127	257	85-137/175	18.305	-2.738	18	6	Metasediment	Brittle	Calcite	-	-
St163	257	77-26/188	14.566	1.401	6	3	Metasediment	Brittle	Calcite	-	
St187	257	81-19/110	12.306	-4.259	0	0	Metasediment	Brittle	Calcite	po,py,chl	A major vein, 1 metre thick
St193	257	81-19/174	12.225	-3.398	6	1	Metasediment	Brittle	calcite	-	Well-bedded
St204	257	80-16/250	16.476	-4.515	6	1.5	Metasediment	Brittle	Calcite	-	Feldspathic sediment
St219	236	85-113	18.809	-1.858	11	2	Metasediment	Brittle	siderite	-	
St251	257	78-3/75	16.224	-3.013	16	3	Metasediment	Brittle	Calcite	-	Jasperised
St253	257	78-3/104	20.906	-2.944	20	2	Metasediment	Brittle	Calcite		
St254	257	78-3/114	17.374	-2.481	4	3	Metasediment	Brittle	Calcite	-	-
St256	257	78-3/127	13.133	-2.696	10	3	Metasediment	Brittle	Calcite	-	
St257A	257	78-2/71	16.454	-3.961	14	3	Metasediment	Brittle	Calcite	-	Altered
St263A,inner	257	80-13/126	12.714	-3.286	45	45	Metasediment	Brittle-metas.	Calcite	chl.	Metasomatic
outer	257	80-13/126	15.366	-2.833	45	45	Metasediment	Brittle-metas.	Calcite	chl.	Metasomatic
St269c	257	85-127/95	15.574	-2.762	40	38	Altered sed.	Brittle-metas.	Calcite	chl.	Strongly metasomatised
ST270A	257	85-127/107	24.197	-3.302	8	8	Arenite	Brittle	Calcite	chl.	-
St276A	257	85-127/189	11.455	-3.482	15	3	Metasediment	Brittle	Calcite	20% chl.	-

in samples with NaCl >10% (Truesdell 1974). The corrected fluid estimates are presented in Table 10.1, showing a variation of $\delta^{18}O$ = -2.47‰ (corresponding to the lowest salinity inclusions), to +12.23 ‰ (higher salinity). The effect of dissolved salts has the greatest influence on the estimate for St 65 (Table 10.1), where at a temperature of 205° C, uncorrected for pressure as per previous discussion, a correction of 3.05 ‰ was added to the free-water estimate.

Hangingwall Shears

Five samples of shear-hosted carbonate were analysed from the hangingwall. Some of these shears can be confidently dated as prior to the main late calcite vein event, because their internal foliation is cut by tensile carbonate veins. One shear on section 11335N is considered near-contemporary with the veins because of its chlorite-calcite mineralogy.

The five sampled shears therefore represent fluid conduits active at different times during the development of the Starra Shear. Similar calcite-filled shears elsewhere in the Mount Isa Block are attributed to the infiltration of hypersaline fluids during metamorphism (Oliver and Wall 1987).

The isotopic results for this group are very scattered, but have generally lighter carbon than the other hangingwall groups ($\delta^{13}C$= -6.42 – -3.95 ‰), with a wide range of $\delta^{18}O$ (+13.84 – +29.41‰) (Fig. 10.5A). The lighter $\delta^{13}C$ values and the presence of peak metamorphic minerals such as actinolite, suggest that temperatures in these shears were hotter than in the tensile veins. The spread of oxygen values may therefore derive from either (1) heterogeneous fluids in the sequence, or (2) carbonate deposition over a wide temperature range, or a combination of these alternatives: a lack of a coupled C-O depletion trend mitigates against possibility (2) as the sole mechanism.

Ironstone Matrix and Vein Carbonate; Starra and Trough Tank

Eight ironstone carbonates were analysed from auriferous ironstone (grades between 0.6 – 11.26 g/t Au) at Starra (Table 10.4), and four from cross-cutting silica-magnetite alteration zones at Trough Tank (grades less than 1 g/t) (Table 10.3). No relationship between gold-grade and isotopic character is apparent. The results form a linear trend from $\delta^{13}C$ (-4.79), $\delta^{18}O$ (+22.69) to $\delta^{13}C$ (-9.08), $\delta^{18}O$ (+24.51), i.e., an unusual negative trend with a strong linear depletion of carbon. Three siderite vein samples from the Starra ironstone also lie on this trend, forming the light C-heavy O end of the group. Importantly, the four samples of magnesian calcite taken from Trough Tank also lie within the trend (Fig. 10.5B). This coincidence of values from two geographically-separated locations suggests that the controls on isotopic fractionation in the two orebodies were similar.

Isotopic Spatial Distribution at Area 257

An analysis of the distribution of isotopic vein and matrix values on three geological sections illustrates the complexity of the isotopic history (Fig. 10.6). Unfortunately whilst

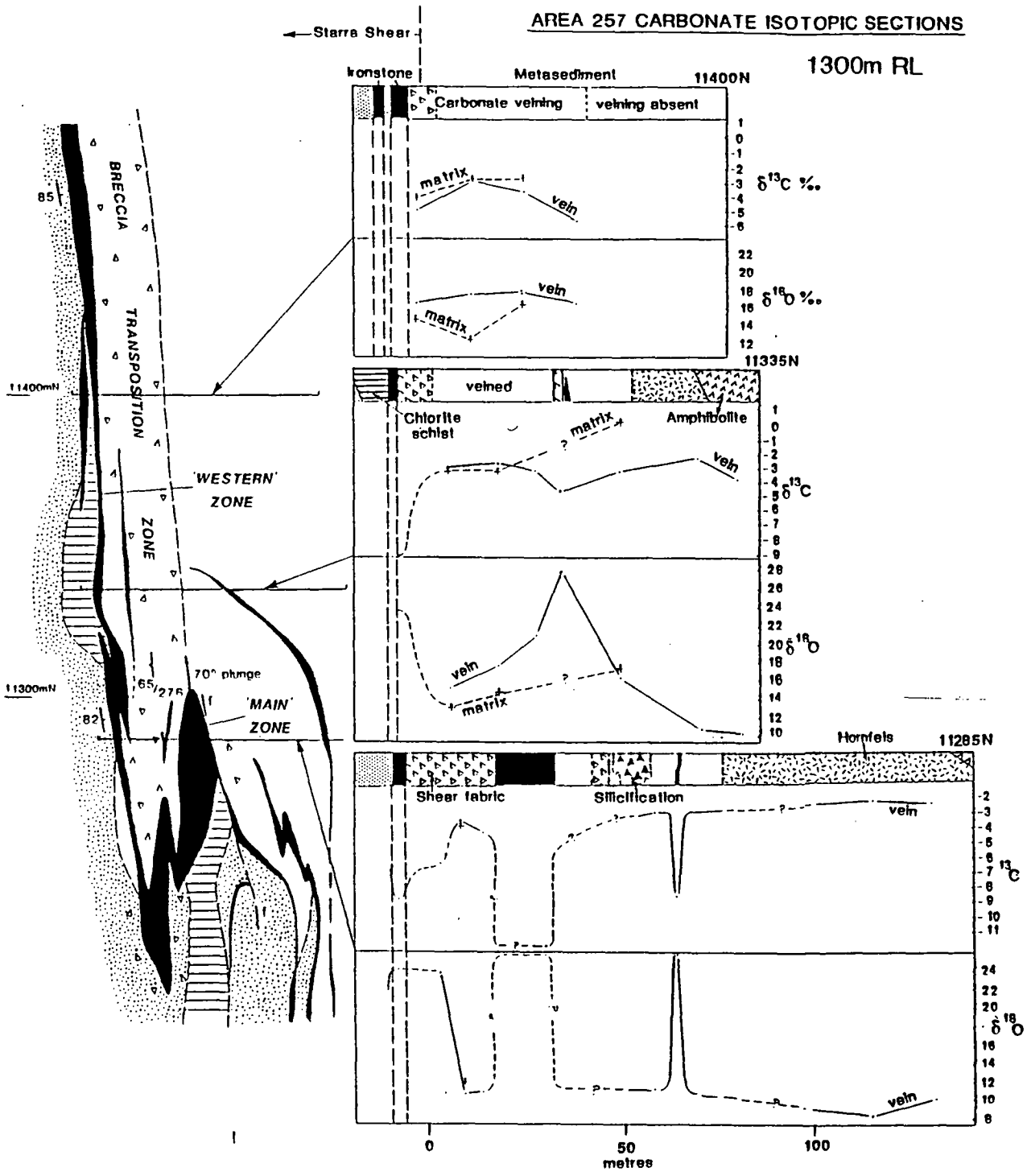

Figure 10.6 *Area 257 isotopic sections. The three sections sampled mainly hangingwall vein carbonates in the 257 orebody.*

the vein sampling is reasonably complete on these sections, the matrix values are not well-sampled because of the problem in obtaining unveined matrix close to the ore.

A striking feature of the sections is the general depletion of $\delta^{18}O$ in amphibolite and hornfels carbonate veins, resulting in a strip of light $\delta^{18}O$ beginning 80 – 150 m east of the 257 ironstone. As was reported earlier, these veins have low salinities and low to moderate temperatures. Oxygen in veins around the central portion of the orebody (11285N, Fig. 10.7) are also very depleted (+8 –+12‰) whereas the adjacent ironstones contain very heavy oxygen (+22 – +26‰). This is in contrast to sections north of the "Main Zone" (but still overlying auriferous ironstone) in which vein values normally exceed 16‰ $\delta^{18}O$.

Oxygen isotope values of the limited metasediment matrix data are depleted to +10 – +12‰ close to the ironstones, increasing stratigraphically upwards (+12.5 – +17.5 ‰) towards unaltered sedimentary values. $\delta^{13}C$ matrix values are in the range 0 to -4 ‰.

Complexities in interpretation are illustrated by the behaviour of vein oxygen around a shear on line 11335N (Fig.10.6). This section passes westward from amphibolite and hornfels, through 110 m of meta-arenite including an inferred D2(LP) anticline, before reaching ironstone. A narrow shear zone (Fig. 4.6H, left) east of the anticline was the focus of very heavy $\delta^{18}O$ fluids, resulting in a calcite value of near +30 ‰; values within 10 m of the shear in unsheared veins are also relatively heavy. The shear contains lighter $\delta^{13}C$ compared to other epigenetic carbonate on the section.

DISCUSSION

The Pre-metamorphic Isotopic Character of the Staveley Formation

The original isotopic values of synsedimentary carbonate in the Staveley and closely associated Corella Formations (1780-1750 Ma; Page 1983a) were estimated using typical devolatilisation equations to reverse the effects of metamorphism (Valley 1986). Oliver & Wall (1987) obtained a comprehensive sample-set from the Corella Formation (80 km north of Starra). A shallow marine, locally evaporitic environment was favoured by Blake et al. (1984), which resulted in widespread scapolite development during regional Amphibolite facies metamorphism (Ramsay and Davidson 1970). Carbonate which remained after silicate-quartz metamorphic reactions, had $\delta^{18}O$ (SMOW) between +18.2 – +20.8 ‰, and $\delta^{13}C$ between -1.6 – -0.6 ‰; metamorphic fluids had an estimated final $X_{CO2} = 0.6$ at 580° C and 3.5 kB.

Both the Staveley and Corella Formation data sets have been extrapolated back to obtain their initial average isotopic values, assuming a Rayleigh "continuous decarbonation" volatilisation model. The following equation from Broecker and Oversby (1971) has been applied to correct for the effect of metamorphism,

$$\delta_i = \delta_f - 1000(F^{(\alpha-1)} - 1)$$

where δ_i is the initial isotopic value, δ_f is the final value, F is the mole fraction of C and/or O remaining in the rock, and α is the fractionation factor (fluid-rock). Average fractionation factors appropriate to the metamorphic temperatures have been used (Valley 1986) i.e., ^{13}C

= 1.0022, and ^{18}O = 1.0060. The determination of F is relatively simple for $\delta^{18}O$, because the Calc-silicate Limit of 0.6 can be employed, which assumes that all CO_2 has been liberated from the rock, resulting in a maximum estimate. (In fact this is not the case: Oliver and Wall (1987) refer to calcite as an abundant rock component, and calcite is common in the Starra sediments). Limits of ^{18}O F = 0.6 - 0.8, and ^{13}C F=0.3 - 0.7— in the absence of exact data on the modal abundance of the metamorphic minerals—provide an estimated initial range of $\delta^{18}O$= +20.8 – +22.6 ‰, $\delta^{13}C$ = -0.32 – +1.54 for Corella calcite, and $\delta^{18}O$ = +18.78 – +23.50, $\delta^{13}C$ = -0.99 – -0.36 for Staveley Formation at Starra.

To gauge how reasonable these estimates are, they have been compared to unmetamorphosed Mid-Proterozoic carbonates from northern Australian and Canadian hypersaline dolomite sequences (Table 10.5). The calculated $\delta^{18}O$ estimates for the Corella and Staveley Formations are within the global ranges, whereas the $\delta^{13}C$ estimates are heavier, suggesting that the estimates of volatile carbon loss made above were too drastic.

Veizer and Hoefs (1976) demonstrated that global marine-carbonate $\delta^{18}O$ has shown secula variation, gradually decreasing towards the Archean, although the detailed variation

Source	Age	Stratigraphic Unit	Isotopic Composition $\delta^{13}C$‰	$\delta^{18}O$‰
(1)	1700-1600Ma	McArthur Group, McArthur Basin, N.T.	-2.0 to 0 av. -1.0	+17.2 – +25.6 av. +21.2
(2)			-4.9 – 0	+19.9 – +22.9
(3)			–2.2 – 0	+18.2 – +26.1
(4)	~1700 Ma	Reward Dolomite, McArthur Basin, N.T.	-3.0 – -0.2 av. -0.9	+19.8 – +24.7 av. +22.3
(5)	~1700 Ma	Lady Loretta Fm., N.W. Qld.	-2.4 – -1.6 av. -2.0	
(6)	~1600 Ma	Bungle Bungle Dolomite, W.A	-1.0 – -0.25	+19.85 –+24.78
	~1800 Ma	Earaheedy Gp., Canada	-2.41 – +1.0	+17.90 – +23.39
	~2000 Ma	Pethei Gp., associated with BIF Canada.	+1.25 – +1.62	+15.7 –+18.35
	~2000 Ma	Wyloo Gp., associated with BIF, W.Australia.	+0.35 – +0.99	+15.13 – +18.36
	~1720 Ma	**STAVELEY FM. ESTIMATE**	-0.99 – -0.36	+18.78 – +23.50
	1780 – 1750 Ma	**CORELLA FM. ESTIMATE**	-0.32 – +1.54	+20.80 – +22.60

Table 10.5 *Ranges of C-O isotopic data from relatively unmetamorphosed Proterozoic northern Australian and Canadian hypersaline dolomite sequences. (1) Smith and Croxford(1975) ; (2) Veizer and Hoefs(1976) ;(3) Rye and Williams; (4) Walker et al.(1983) ; (5) Carr and Smith(1977);(6) Schidlowski et al.(1983).*

is more complex, and its interpretation controversial (Muehlenbachs 1986). Ancient carbon on the other hand, has fluctuated only 2 ‰ about an average value of +1 ‰ (Schidlowski et al. 1983). Muir et al. (1985) consider that Veizer and Hoefs (1976) biased their Mid-

Proterozoic global data towards basins which subsequently have been interpreted as evaporitic or closed during sedimentation.This lead to error in the global marine estimate for the Mid-Proterozoic, towards heavier $\delta^{18}O$ isotopic compositions (~ 22‰). In line with modern isotopic variation, in which evaporitic dolomite is ~4‰ heavier than marine carbonate (Budai et al.1987), the average Proterozoic marine $\delta^{18}O$ value was ~18 ‰.

There is geological evidence that the Staveley Formation, like the near-contemporary McArthur and Mount Isa Groups, was deposited under hypersaline conditions. If a marine average of 18 ‰ is assumed for the Mid-Proterozoic, then the Staveley Formation estimate of average $\delta^{18}O$=+18.78 – +20.5 ‰, with a spread to values as high as ~+23.50 ‰ (calculated), corroborates some deposition in a hypersaline environment.

The Origin of Starra Metasediment and Dolerite Carbonate

Matrix carbonates from Area 257 are isotopically depleted relative to the unaltered regional carbonates, and as all of these rocks have experienced similar metamorphism, those from Area 257 must have exchanged carbon and oxygen beyond that expected through Rayleigh Distillation. Further complications are the individual isotopic effects of later deformation, intrusion, and hydrothermal activity. In the order of the most recent to the oldest, the events which had a likely effect on the Area 257 isotopic character were (1) D2(LP) veining, (2) D2 folding and shearing, (3) dolerite intrusion, (4) D1 deformation, (5) a possible early hydrothermal overprint associated with exhalation, one of the genetic ideas for ore formation (Davidson et al. 1988), and (6) carbonate sedimentation and diagenesis. The approach of this discussion is to examine the effects of the consecutively most recent events to determine if older events are still discernible.

A first test of the extent of the most recent shear and vein effects (1, above) is the isotopic homogeneity of the area. Many studies have shown that introduced fluids will modify host rock carbonate oxygen towards the fluid isotopic value, although host rock carbon exchanges more gradually. For instance, high temperature fluids on shears in the Mary Kathleen Fold Belt altered dolerites and calc-silicates to a narrow range of $\delta^{18}O_{carb.}$=+11.3 – +11.7‰, whilst $\delta^{13}C$ was altered to -7.2 – -3.8‰ (Oliver and Wall 1987). Rye and Williams (1981) also demonstrated exchange at the H.Y.C. orebody between detrital carbonate and hydrothermal fluids. The degree of convergence of the rock with the fluid isotopic value during wall-rock reaction is dependent on the fluid to rock ratio; for instance in the Salton Sea geothermal area, reacted waters have shifted towards the original rock $\delta^{18}O$ value by 13‰, whilst the reacted rocks have been depleted by 10‰, indicating a volume ratio of water to rock (W/R) of 1.15 (Clayton et al. 1968). The extent of convergence is also a function of temperature and porosity. For instance, in the Salton Sea example, 600 m of section retained its original signature because it was finer-grained and hence impervious to fluid penetration.

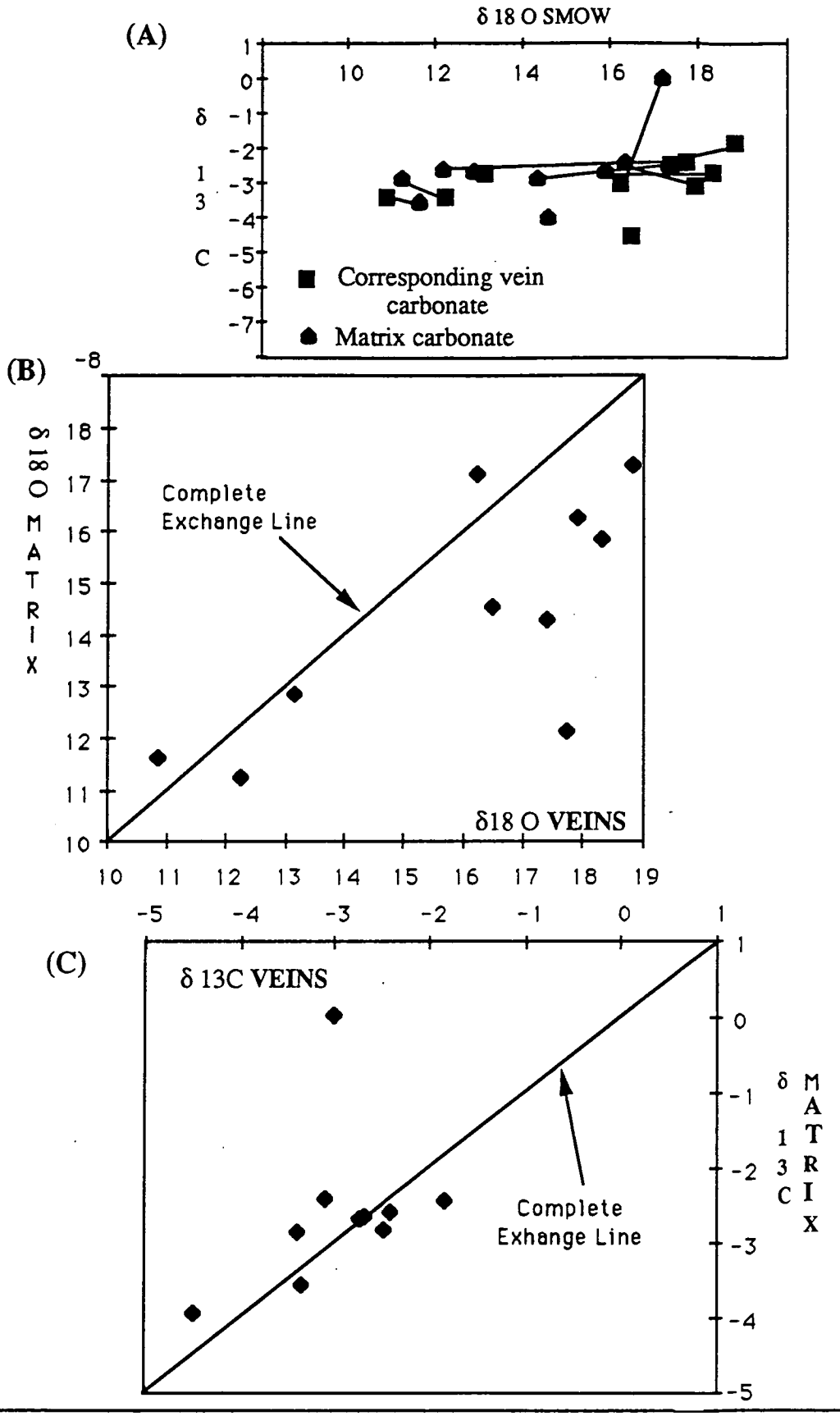

Figure 10.7A *"Equilibrium Diagrams" :'A' is a conventional C-O isotope plot of the matrix and corresponding veins from a given sample.* **10.7B** *δ18O of the vein is plotted against the matrix value: isotopic exchange was most complete if the values cluster on the diagonal line after fluid-rock reaction.* **10.7C** *Similarly for δ13C.*

To test the effect of isotopic fluid-rock exchange during the D2(LP) veining, 10 matrix/vein pairs were sampled across the sequence. Complete fluid-rock exchange was achieved between the vein fluid and the host-rock if the vein and matrix have the same value; the degree of divergence of the two is a measure of disequilibrium. The initial results (Fig. 10.7A) show that there is a wide $\delta^{18}O$ range (narrow $\delta^{13}C$), and that most veins are within 3 ‰ of the matrix; notably lighter $\delta^{18}O$ matrix values are closer to vein values than heavier matrix.

A method of representing the degree of exchange is to plot matrix versus corresponding vein values for each isotope (Figs. 10.7B & C). This type of diagram can be used to classify the degree and style of isotopic exchange, as illustrated in Fig.10.8(A-H). The observed pattern, a similarity between matrix and vein values across a wide $\delta^{18}O$ range, matches model E, i.e., the generation of small disconnected veins whose isotopic character reflects the local matrix $\delta^{18}O$, at low W/R. In this situation the spread in matrix values identifies a pre-existing rock range, such as the original sedimentary carbonate variation.

However, this simple model does not explain why, in some instances, similar isotopic values are found in veins which transect isotopically divergent rock-types. If the veins are simply reflecting the local host-rock values, then $\delta^{13}C$ vein values should, for instance, decrease as they approach hornfels/dolerite (see Fig. 10.6). Sediments typically exhibit substantial ^{13}C depletion close to mafic intrusions, (which should be reflected in the veins under the premise of Model E) because the isotopic exchange at magmatic temperatures (800 – 1200°C) is very efficient (Shieh and Taylor 1969, Valley 1986). In fact little or no ^{13}C change is observed. The $\delta^{13}C$ data does not support a model of local isotopic redistribution into veins during faulting and shearing.

A more complex model featuring the mixing of two fluid-types is dictated by the salinity-$\delta^{18}O$ correlation. In this model, a heavy $\delta^{18}O$ fluid (minimum ~+13 ‰) with NaCl-equiv. salinity ≥ 23 %), moved up the Starra Shear from a deeper source, with fluids (initial temperature ~350° C) depositing carbonate in the 100 – 220° C (uncorrected for pressure) range. The pervasion of this fluid away from shears is clearly demonstrated on line 11335N, Area 257 (Fig. 10.6). A second isotopically light ($\delta^{18}O$~-2.5‰ max.) low salinity (average 4%) fluid was encountered mainly in the more brittle hornfels and dolerite 100 m or more from the shear. Fluids of intermediate salinity were generated during the mixing of these two fluid-types. In this model the pervading fluids wholly controlled the isotopic value of the sedimentary carbonates, as in Model H, Fig. 10.8. This model adequately explains the salinity range, the salinity-$\delta^{18}O$ correlation, and the observed matrix-vein pair data.

The source of hot, heavy $\delta^{18}O$ waters is likely to be metamorphosed evaporitic sediments, such as the Staveley formation would provide. Fluids in this range also lie at the margin of the field of unaltered acid plutonic rocks (+7 – +12‰) but these would also have supplied carbon in the range -4 to -8 $\delta^{13}C$. $\delta^{18}O$ in the range +8 – +15‰ is characteristic of fluids coexisting with meta-igneous, and with siliciclastic rocks, whose fields converge with

increasing metamorphic grade (Taylor 1979). However, the high salinities and $CaCl_2$ content of the fluid favours a metasedimentary origin for the $\delta^{18}O$-enriched waters.

A source for the end-member isotopically-light fluid is likely to be altered Proterozoic meteoric or formation waters. The other sources invoked above are not likely to have fluids as light as -2‰, whereas such values are common for temperate to equatorial meteoric or evolved meteoric waters (Yurtsever & Gat 1981), which also have the required low salinities. Notably the end-member value excludes seawater or evaporated seawater, (0 – 10‰). The lack of major difference in $\delta^{13}C$ between the two fluid types is readily explained by the heavy, saline fluid being the dominant $\delta^{13}C$ source in equilibrium with metamorphosed calcareous sediment, whereas the light fluid supplied very little carbon to precipitated minerals. This explains the uniformity of $\delta^{13}C$ in veins and matrix across a wide $\delta^{18}O$ range.

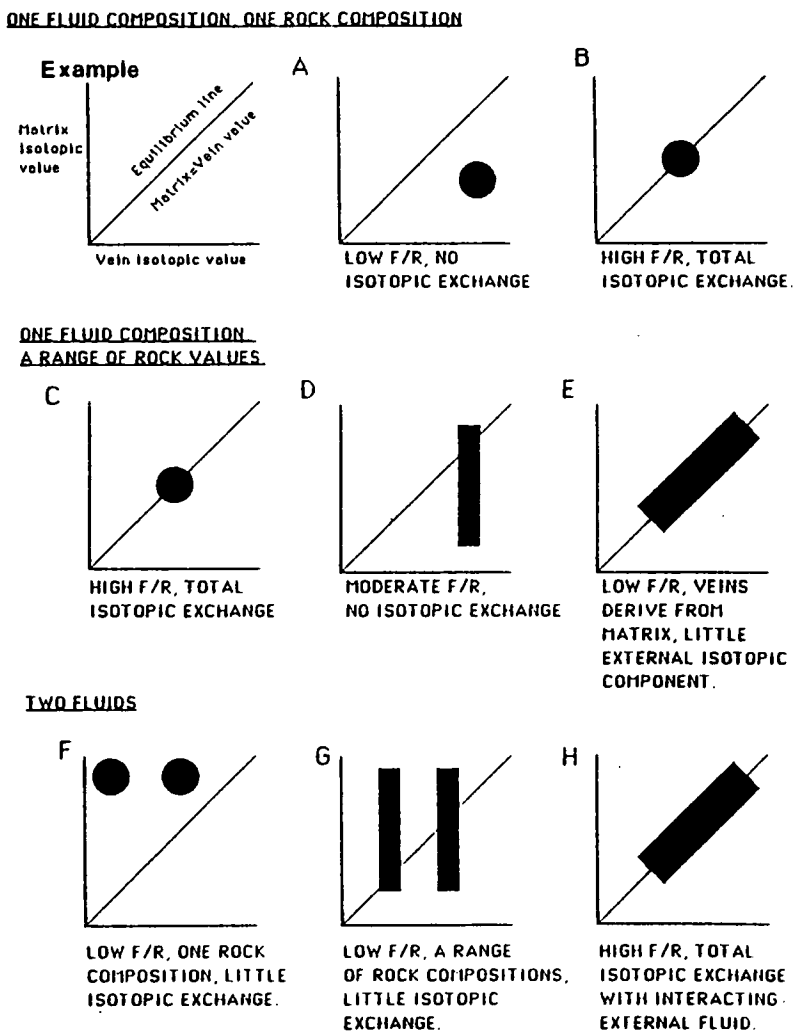

Figure 10.8 *Theoretical examples of degrees of equilibrium for one and two fluids, interacting with isotopically homogeneous and heterogeneous rocks. Some combinations produce similar results, e.g., if total exchange occurs between a fluid and a rock, the original isotopic variation in the rock will be close to the fluid value.*

In summary, a hydrologic model of a metamorphic fluid channelled upwards within the Starra Shear, mixing with downward percolating meteoric waters, is favoured to explain the isotopic and fluid inclusion data. These fluids reacted with rocks thoroughly at local scales altering matrix values towards the vein-fluid values, as predicted in Fig. 10.8, Model H. The matrix values therefore are mostly not original, and neither they nor the vein values can be used to determine the characteristics of earlier ore-forming hydrothermal systems, or sediment character. The characteristics of the late veins show similarities to other documented exhumed faults formed under brittle-ductile conditions (e.g., Parry et al. 1988), namely temperatures peaking at ~ 350°C, and a progressive reduction in salinity and temperature with age.

The Isotopic Character of Carbonate in Ironstones at Starra and Trough Tank

All Starra ironstone carbonates lie on a trend which diverges markedly from other matrix and vein data at the prospect (Figs. 10.5A & B), indicating that, unlike the hangingwall, ironstone carbonates have not been 'reset' by vein-fluid interaction during faulting. In particular they show no spread towards the light $\delta^{18}O$ which is characteristic of vein-matrix interaction. The field of ironstone carbonate does not coincide with the field of older shears, and hence predates these. It is concluded that the ironstone trend is a primary hydrothermal /sedimentary relic. The maintenance of the coupled O-C trend is evidence of the impermeability of the iron-formation through tectonothermal events, significantly corroborated by the coincidence of Trough Tank alteration-pipe data with the same trend. This is evidence for the involvement of a unique fluid-type which formed the stratiform Cu-Au oxide systems in the Staveley belt, and justifies the preliminary identification of a "target" C-O isotopic signature of use in identifying new companion systems.

Ironstone carbonates have negative carbon (-3.8 – -15.5‰ $\delta^{13}C$), and heavy oxygen (+21 – +27.5‰). Oxygen becomes lighter as carbon becomes heavier, with a modelled linear regression of $\delta^{18}O = -0.47(\delta^{13}C)+19.90$, or $\delta^{18}O = -0.48(\delta^{13}C)+19.84$ if the Trough Tank data is included. This notably intersects the average value of original Staveley Formation carbonate (Fig. 10.5B). This trend cannot be explained by the simple deposition of carbonate from a constant isotopic fluid over a range of temperatures, as this would produce a positively correlated O-C trend (Rye and Williams 1981, Peter 1986). The main possibilities which could explain the trend, exploit the response of carbon isotopes to varying temperature, pH and fO_2. They are:

(1) Changing fluid isotopic composition by the leaching of sedimentary carbonate by a light C/heavy O hydrothermal fluid.

(2) Progressive oxidation and cooling of an isotopically constant fluid during carbonate deposition, resulting in the deposition of lighter carbon and heavier oxygen.

(3) Progressive alkalisation during cooling of an isotopically constant fluid.

(4) Rayleigh Distillation in the metamorphic environment, in which the production of magnetite through the reaction of hematite and siderite lightens carbon, while oxygen is exchanged with an introduced heavier fluid.

Of these possibilities, (4) is a probable contributor, but is not the main factor because such a reaction could not produce the magnitude of C-isotopic change observed. Fyon et al. (1981) documented a change of only 1.5‰ in $\delta^{13}C$ during the production of 10 – 95% metamorphic magnetite in some Canadian BIFs. For progressive alkalisation (possibility 3) of the fluid to be a viable explanation, a pH shift of 5, up to pH=10, is needed to obtain the required 5‰ shift in the $\delta^{13}C$ composition, ignoring the effects of temperature (Ohmoto, 1972). This is not likely given the pH constraints on the hydrothermal fluid outlined in Chapter 12.

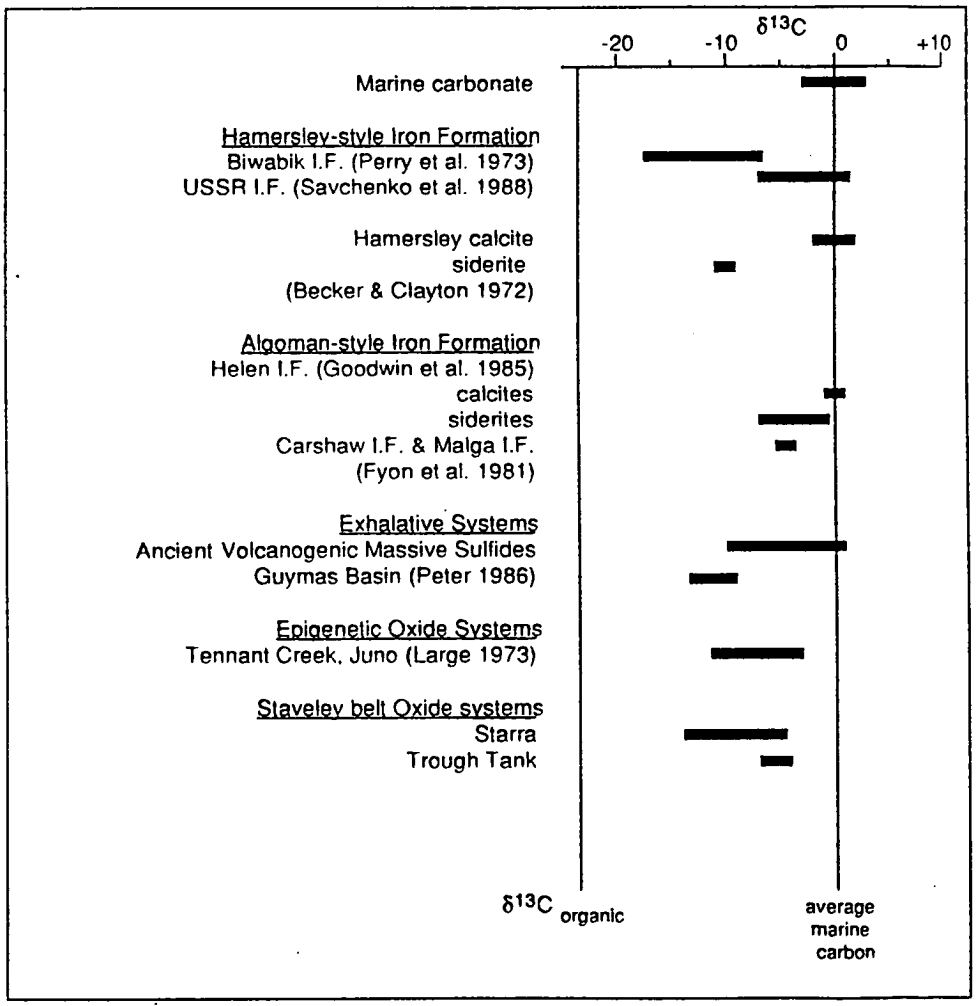

Figure 10.9 *Ranges of $\delta^{13}C$ in carbonates from known oxide- and sulphide-depositing chemical and hydrothermal systems.*

Possibility (1), and an influence of possibility (2), tentatively provide the best explanation for the unusual trend, because sedimentary Staveley Formation is readily identifiable as one end-member of the mixing trend. The other fluid end-member is difficult to estimate because no temperature constraint exists for ironstone carbonates at Starra. Using the calcite-water relationship of Friedman & O'Neill et al.(1977), and a possible temperature range of 50 – 350°C, the fluid must have been between $\delta^{18}O$ = +3.3 – +23.6‰, which excludes pure seawater (0‰) and meteoric waters.

The fluid end–member must also have had very light $\delta^{13}C$ in the range -15‰, likely to be organic in origin, although a juvenile contribution is also possible (i.e., $\delta^{13}C$ of volcanic gas is -12 – -8‰; Craig 1963). An end-member mix of 61% oxidised organic C ($\delta^{13}C$ av.= -25‰; Schidlowski et al. 1983) and 39% Staveley Formation sedimentary carbonate ($\delta^{13}C$ av.= -0.65‰) is calculated if juvenile CO_2 was not contributed to carbonate. The Starra/Trough Tank $\delta^{13}C$ range is similar to other Fe-oxide+ carbonate-depositing systems, such as the Hamersley and Algoman BIFs, and some modern exhalative systems. Fig. 10.9 illustrates that the range of ironstone $\delta^{13}C$ overlaps in many examples because of the common contribution of organic $\delta^{13}C$. Organic C is commonly oxidised during diagenesis or periods of low basin circulation in BIFs (Goodwin et al. 1983), resulting in the precipitation of light carbon (e.g., Becker and Clayton 1972). In the case of Starra, $\delta^{18}O$ values heavier than those in Proterozoic marine carbonate preclude a low temperature origin such as that invoked for Hamersley-BIF deposition.

Guymas Basin fluids provide a possible isotopic analog through which to view the Starra/Trough Tank isotopic values. These fluids leach a sedimented spreading ridge, extracting carbonate and organic $\delta^{13}C$ from the sediments, resulting in the deposition of strongly negative exhalative carbonate on the seafloor. At Starra, a ^{18}O-rich fluid could have leached organic-C-bearing marine carbonate in the hydrothermal aquifer, to obtain the unusual isotopic fluid features observed.

CONCLUSIONS

(1) Tensional veins which dominate the hangingwall of the Starra ironstones originated as pinnate fractures during sinistral transcurrent movements of the Starra Shear, late in D2(LP).

(2) Fluids circulating within the veins deposited quartz and chlorite between 315 and 365° C (uncorrected for pressure), and calcite in the range 106 – 285° C. Salinity varied between 0 and 27 wt. % equiv. NaCl, and was positively correlated with $\delta^{18}O$ in vein calcite. A model involving the introduction of saline metamorphic fluids along the Starra Shear, which mixed with low-$\delta^{18}O$ meteoric water in fractures away from the shear, is proposed to explain this data. The veins show little isotopic relationship to ore, and are generally barren.

(3) Equilibration between vein-fluids and matrix has destroyed pre-existing carbonate isotopic signatures in the hangingwall metasediments.

(4) Carbonate in ironstone and alteration pipes at Starra and Trough Tank lie on a distinctive trend which was unaffected by later veining and shearing. This trend, regardless of its origin, is identified as a "target" C-O signature for Cu-Au-magnetite ores in the Staveley Formation.

(5) The distinctive negative character of the O-C trend in ironstone is proposed to result from the mixing between leached components of ^{18}O-rich limestone and organic carbon. Deposition of carbonate during exhalation is favoured.

(6) Regional isotopic sampling of the Staveley Formation demonstrates that $\delta^{18}O$ is up to 5‰ heavier than that estimated for marine Mid-Proterozoic carbonate, consistent with the geological evidence for hypersaline sedimentary conditions in the basin.

CHAPTER 11

SULPHUR ISOTOPE VARIATION OF STARRA, TROUGH TANK, AND SOME CLONCURRY-STYLE Cu–Au DEPOSITS

INTRODUCTION

Previous sulphur isotopic studies in the Mount Isa Inlier have concentrated on the Western Succession (Chapter 2), with work on the Mount Isa Pb–Zn–Cu deposit (Solomon & Jensen 1965, Smith et al. 1978, Eldridge et al. 1985, and Andrew et al., in press), Lady Loretta Pb–Zn (Carr & Smith 1977), and vein/replacement Cu deposits such as Mammoth, Paradise Valley, Gunpowder Creek and Mount Kelly (Scott et al. 1985, Taylor & Scott 1976). In contrast, Eastern Succession mineralisation has been very sparsely sampled, with only a small number of values reported for the Mount Dore copper deposit (Scott 1986) and the stratiform BIF-hosted Pegmont Pb–Zn mineralisation (Vaughan & Stanton 1986).

In this study, sulphur isotope results from a spectrum of ore deposits in the Eastern Succession are reported. This includes a detailed study of the Starra and Trough Tank mineralisation, undertaken with the aim of determining the isotopic variation of sulphur in this new deposit type, and the source of sulphur. The other sampled deposits are historically mined epigenetic "Cloncurry" or "Selwyn"-style ores (Beardsmore 1988, Beardsmore et al. 1988), including the Answer (Cu–Au), Hampden (Au–Cu–Ag), Mount Elliott/Swan (Au–Cu), and Mount Cobalt (Co–Cu) deposits (Fig. 11.1). This aspect was intended as a reconnaissance study of the types of sulphur mobilised within shears during deformation of the Selwyn region. Fresh samples could often only be obtained from mine dumps, and this, together with small sample populations (3 to 7 samples per mine) justifies only preliminary conclusions.

SAMPLING AND MEASUREMENT

A total of 100 sulphide separates were obtained from the Starra ores and host rocks (53), Trough Tank (27) and four epigenetic Cu–Au deposits in the Selwyn region (20). Sulphides were extracted by drilling, after the preparation of polished blocks and inspection of sulphide phases for contaminant inclusions. Fine-grained pyrite in barren hematite ore was separated by S.Capp using froth flotation and magnetic techniques. SO_2 gas was extracted by the method of Robinson & Kusabe (1975), and analysed in a VG Micromass 602D spectrometer under the supervision of M. Power Sr. at the Central Science Laboratory of the University of Tasmania. The samples were calibrated against standard galena from Broken Hill ($\delta^{34}S$ = 3.2‰) and Tullah, Tasmania ($\delta^{34}S$ = 15.3‰), and the international sphalerite standards IAEA NZ1 and NBS 123 (1.83 and 4.34‰ respectively). Results for all of these standards were reproducible within 0.2‰, whereas sample replicates, subject to the

inhomogeneities of natural processes, varied between 0.21 and 0.41‰ in grains drilled side by side. Results are tabulated in Table 11.1.

RESULTS

Starra

Isotopic Variation

All Starra sulphides range between –7.06 and +3.95‰, average –0.74‰, have a skewed Normal distribution with a distinct mode at 0.5‰, a sharp cut-off at 4‰, and a negatively skewed tail (Fig. 11.2A, Table 11.2). Ironstone has a narrower range than disseminated footwall pyrite (Figs. 11.2B & C), and stratiform chlorite schist contains predominantly lighter sulphide, in the range $\delta^{34}S = -2.99$ to +0.9‰. There is no apparent zonation of $\delta^{34}S$ within the footwall or ironstone, or a relationship to gold grade (Fig. 11.3B). However, more systematic sampling is required to confirm this. Chalcopyrite and pyrite obtained from hangingwall veins, and from reaction skarns near the ironstone/ metasediment boundary, form a distinctly lighter part of the overall population (range –5.43 to –1.16‰, n = 8, average = –3.31‰; Fig. 11.2A).

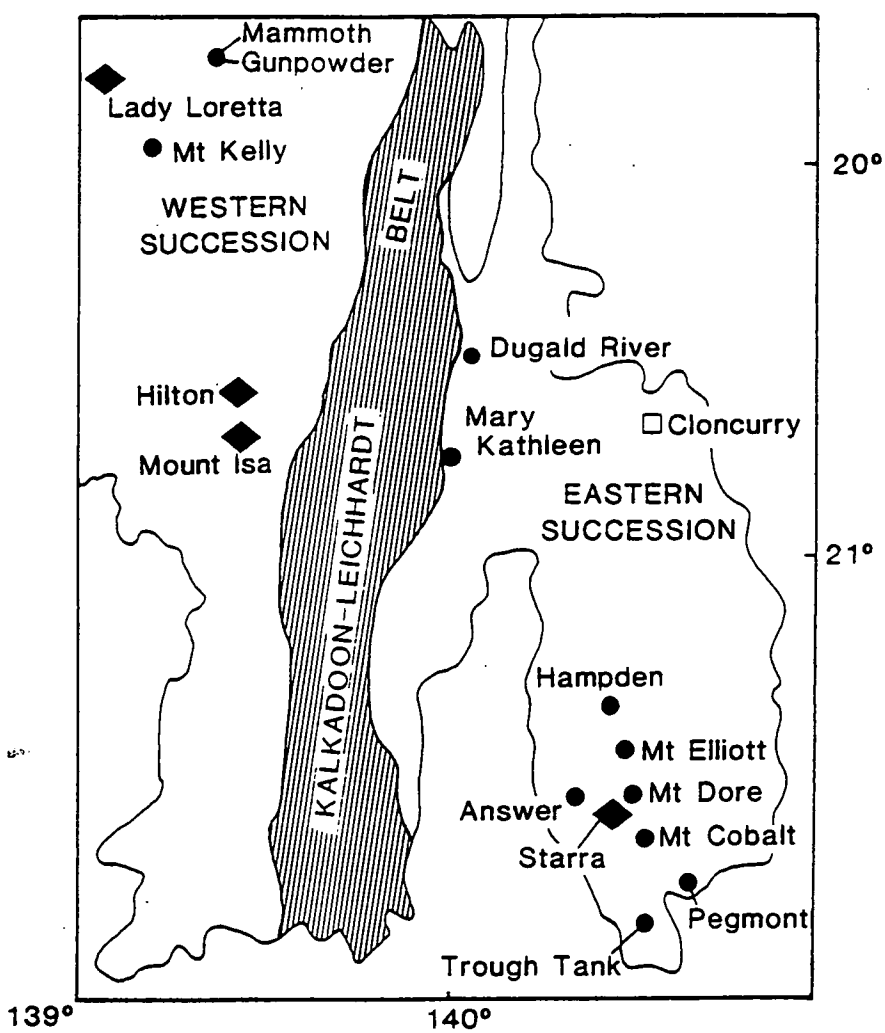

Fig. 11.1 *Location of sulphide occurences in the Mount Isa Inlier, most of which are discussed in the context of their sulphur isotope variation. Operating mines are shown as diamonds.*

Category	Sample No.	Mean ‰	S.D.	Range ‰
Starra				
All sulphides	53	–0.74	2.61	–7.06 to +3.95
All pyrite	35	+0.22	2.42	–5.43 to +3.95
All chalcopyrite	18	–2.30	1.86	–7.06 to +1.08
Ironstone pyrite	8	+0.92	1.91	–0.80 to +3.27
Ironstone chalcopyrite	9	–1.47	1.28	–3.81 to –0.02
Chlorite schist	4	–1.56	-	–2.99 to +0.9
Footwall pyrite	18	+0.85	2.39	–4.31 to +3.95
Footwall chalcopyrite	6	–3.69	-	–7.06 to –0.69
Vein and skarn pyrite	4	–3.03	-	–5.43 to –1.16
Vein and skarn cpy	5	–3.00	-	–5.25 to –1.64
Dolerite	2	+1.59	-	+1.08 to +2.17
Trough Tank				
All sulphides	27	+0.36	2.61	–6.05 to +5.93
Pyrite	16	+1.38	1.11	–2.38 to +5.93
Chalcopyrite	11	–1.11	2.33	–6.05 to +2.26
Hampden	5	+1.98	-	–2.99 to +3.65
Mount Elliott/Swan	7	–5.6	-	–6.45 to –4.85
Answer	4	+8.67	-	+8.41 to +8.85
Mount Cobalt	3	+4.53	-	+4.23 to +4.94

Table 11.2 *A summary of the statistical variation of $\delta^{34}S$‰ for all samples as a function of rock-type and prospect.*

Ironstone and footwall chalcopyrite (averages = –1.47 & –3.69‰) are lighter on average than pyrite from the same rocks (= +0.49 & +0.85‰) (Figs. 11.2B & C), which is the fractionation order expected if the two minerals were deposited in equilibrium. That this is only an approach to equilibrium is illustrated by the results of individual chalcopyrite-pyrite pairs (phases in contact, in inferred textural equilibrium), which although also always in the correct fractionation order, nevertheless supply geologically unreasonable temperatures for Cu and Au deposition (Huston & Large 1989). The isotopic thermometer used was

Py–Cpy $T = [(0.67 \pm 0.04) \times 1000] / \Delta^{0.5}$ ($\pm 35°$ C at 300° C)

where $\Delta = \delta^{34}S_{py} - \delta^{34}S_{cpy}$

(Ohmoto & Rye 1979)

Results obtained (86°, 113.8°, 134.0°, 227.8° and 500.6° C) corroborate the notoriously inaccurate reputation of the pyrite-chalcopyrite isotopic thermometer, which commonly indicates apparent disequilibrium, although pyrite and chalcopyrite are often demonstrably part of the same depositional system (Ohmoto & Rye 1979, Peter 1986).

Table 11.1 Sulfur isotopic data from the Cloncurry area. (Abbreviations: u.g.- underground)

Sample	∂34S cdt	mineral	location	rock-type	Hole
Ironstone — pyrite					
St57	3.15	pyrite	Starra/257	barren irst.	80-15/196.2m
St115	3.27	pyrite	Starra/257	min. irst.	85-129/135m
St116	-0.04	pyrite	Starra/257	min. irst.	85-129,140m
ST141	-0.47	pyrite	Starra/276	barren irst	85-121,157.5m
ST179	-0.80	pyrite	Starra/257	min. irst.	85-137,221m
St179/226.4m	1.10	pyrite	Starra/257	barren irst.	85-137,226.4m
St234A(pair)	0.42	pyrite	Starra/251	min. irst.	STQ253-210m
St237A(pair)	0.78	pyrite	Starra/257	min. irst.	STQ253,217m
Ironstone-cpy					
St117	-3.81	cpy	Starra 257	min. irst.	85-129,145m-boudin vein
St231	-0.71	cpy	Starra/257	min. irst.	STQ253,203.2m
St232A(pair)	-0.02	cpy	Starra/251	min. irst	STQ253,216.7m
St234B(pair)	-1.37	cpy	Starra/251	min.irst.	STQ253,210.3m
St236	-0.56	cpy	Starra/251	min.irst.	STQ253,221.6m
St237B(pair)	-2.87	cpy	Starra/251	min.irst.	STQ253,217m
D8.3	-2.33	cpy	Starra,251u.g	min.irst.	Boudin-vein in irst.
D9.1A	-0.89	cpy	Starra,251u.g	min.irst.	Boudin-vein in irst.
D9.1B	-0.75	cpy	Starra,251u.g	min.irst.	Boudin-vein in irst.
Footwall — pyrite					
ST46-core	-4.31	pyrite	Starra/257	footwall	STQ78-1,210m
St49	-0.02	pyrite	Starra/257	Footwall	STQ80-15/155-156m
St62-core	2.53	pyrite	Starra/257	Footwall	STQ80-15/239-245m
St101A-rim	2.79	pyrite	Starra/257	footwall	STQ80-17,167.3-173.3m
St101B-core	3.95	pyrite	Starra/257	footwall	STQ80-17,167.3-173.3m
St129V	-0.59	pyrite	Starra/257	footwall	STQ85-139
St144-core	1.18	pyrite	Starra/276	footwall	STQ85-121,161.0m
St171A-rim	1.33	pyrite	Starra/257	footwall	CRQ77-26,280m
St171B-core	3.41	pyrite	Starra/257	footwall	CRQ77-26,280m
St200A/250-core	1.78	pyrite	Starra/257	footwall	81-19/250m
St200B/250-rim	1.36	pyrite	Starra/257	footwall	81-19/250m
St200A/264-core	3.4	pyrite	Starra/257	footwall	81-19,264m
St200B/264-rim	2.95	pyrite	Starra/257	footwall	81-19,264m
St200A/289-core	-0.86	pyrite	Starra/257	footwall	81-19/289m
St200B/289-rim	-1.07	pyrite	Starra/257	footwall	81-19/289m
St200/310-rim	1.94	pyrite	Starra/257	footwall	81-19,310m
St210	-3.93	pyrite	Starra/244	footwall	79-2,95m
St212-core	-0.62	pyrite	Starra/244	footwall	79-2,127m
Footwall — cpy					
St56	-0.69	cpy	Starra/257	footwall	STQ80-15/195.25
D12.2	-7.06	cpy	Starra,251u.g	footwall	chlorite-hosted boudin-vein
Chlorite Schist— pyrite					
St222	-1.97	pyrite	Starra/236	irst-equivalent	STQ85-113,118m
St222.rpt	-2.18	pyrite	Starra/236	irst-equivalent	STQ85-113,118m
St223A(pair)	0.9	pyrite	Starra/236	irst-equivalent	STQ85-113,130m
Chlorite Schist— cpy					
St223B(pair)	-2.99	cpy	Starra 236	irst. equivalent	STQ85-113,130m
Hangingwall					
St187vPY	-5.43	pyrite	Starra/257	Carbonate vein	81-19,103m
St187vPYH	-5.76	pyrrhotite	Starra/257	Carbonate vein	81-19,103m
Skarn - pyrite					
St149	-3.02	pyrite	Starra/257	min. irst.	86-243,98-108m
St228A	-2.54	pyrite	Starra	chl-scap-mag	STQ86-254,270.8m
St229A(pair)	-1.16	pyrite	Starra/257	min. irst.	86-254,262.5m
Skarn - cpy					
St165	-1.64	cpy	Starra/257	chl-scap-mag	CRQ77-26,215m
St228B	-5.25	cpy	Starra/257	chl-scap-mag	STQ86-254,270.8m

Table 11.1 Sulfur isotopic data from the Cloncurry area. (Abbreviations: u.g.- underground)

St228B(pair)	-3.57	cpy	Starra/257	chl-scap-mag	STQ254,270.8m
St229B(pair)	-1.91	cpy	Starra/257	chl-scap-mag	STQ86-254,270.8m
77-26/206.5	-2.63	cpy	Starra/257	chl-scap-mag	CRQ77-26,206.5m
Dolerite					
ST249	1.08	cpy	Starra/257	dolerite edge	78-3,41.6m
ST250A	2.17	pyrite	Starra/257	dolerite	78-3,52m
Epigenetic Mines— Cloncurry District					
ST288A	8.41	pyrite	**Answer Mine**	Vein	
ST288B	8.77	pyrite	**Answer Mine**	Vein	
ST288C	8.66	pyrite	**Answer Mine**	Vein	
ST288D	8.85	pyrite	**Answer Mine**	Vein	
ST283A	2.52	pyrite	**Hampden**	Shear/vein	
ST283B	3.65	pyrite	**Hampden**	Shear/vein	
ST283C	3.42	pyrite	**Hampden**	Shear/vein	
ST283D	-2.99	pyrite	**Hampden**	Shear/vein	
ST283E	3.29	pyrite	**Hampden**	Shear/vein	
ST286A	4.43	cobaltite	**Mt. Cobalt**	Shear/vein	
ST286B	4.94	cobaltite	**Mt. Cobalt**	Shear/vein	
ST286C	4.23	cobaltite	**Mt. Cobalt**	Shear/vein	
ST281A	-6.44	chalcocite	**Swan/Elliot**	skarn	
ST281B	-4.15	chalcocite	**Swan/Elliot**	skarn	
ST285A	-6.45	chalcocite	**Swan/Elliot**	skarn	
ST285B	-5.08	pyrite	**Swan/Elliot**	skarn	
ST285D	-4.85	chalcocite	**Swan/Elliot**	skarn	
ST284C	-6.01	cpy	**Swan/Elliot**	skarn	
ST284E	-6.22	cpy	**Swan/Elliot**	skarn	
Trough Tank					
Ironstone-pyrite					
TT73	5.93	pyrite	Trough Tank	ironstone	TT13,132.2
Ironstone- Chalcopyrite					
TT101	-3.33	cpy	Trough Tank	ironstone	TT10,185.5
TT103	-1.17	cpy	Trough Tank	ironstone	TT10,205m
TT121B	0.24	cpy	Trough Tank	ironstone	HQ9,202.3m
TT132B	-6.05	cpy	Trough Tank	ironstone	HQ15,200m
Footwall alteration-pyrite					
C(pair)	1.14	pyrite	Trough Tank	alt'd irst	NQ2
TT17	-0.06	pyrite	Trough Tank	Massive mag. alt.	NQ3,91.5m
TT37	-2.38	pyrite	Trough Tank	alt'd irst	NQ6,113.5m
TT38A(pair)	-0.14	pyrite	Trough Tank	mag-py vn in BIF	NQ6,112.7m
TT39A(pair)	-1.85	pyrite	Trough Tank	Massive mag. alt.	NQ6,116.5
TT42A(pair)	-0.77	pyrite	Trough Tank	mag-py-cpy vn	NQ6,118.5m
TT44A(pair)	-0.32	pyrite	Trough Tank	mag-py-cpy vn	NQ6,119.8m
TT49	2.63	pyrite	Trough Tank	Massive mag alt.	NQ2,62.4m
TT50	1.01	pyrite	Trough Tank	mag-py in vn.	NQ2,66.23m
TT53	4.45	pyrite	Trough Tank	Silica alt.	NQ2,92.1m
TT57	2.51	pyrite	Trough Tank	dissem. py	NQ2,145.8m
TT64	0.11	pyrite	Trough Tank	Silica alt.	NQ4,134.4m
TT66	4.38	pyrite	Trough Tank	Silica alt.	NQ4,140.4m
TT68A	2.51	pyrite	Trough Tank	dissem. py	NQ2,108.6m
TT68B	2.92	pyrite	Trough Tank	dissem. py	NQ2,108.6m
Footwall alteration-chalcopyrite					
A	2.26	cpy	Trough Tank	vein in alt'd irst	NQ2
B(pair)	1.78	cpy	Trough Tank	vein in alt'd irst	NQ2
TT38B(pair)	-2.75	cpy	Trough Tank	Mag-py vn in BIF	NQ6,112.7m
TT39B(pair)	-1.02	cpy	Trough Tank	Massive mag. alt.	NQ6,116.5
TT42B(pair)	-0.87	cpy	Trough Tank	mag-py-cpy vn	NQ6,118.5m
TT44B(pair)	-0.64	cpy	Trough Tank	mag-py-cpy vn	NQ6,119.8m
TT121B.vn	-0.61	cpy	Trough Tank	vein in irst.	HQ9,202.3m
Miscellaneous					
STP18	-0.88	pyrite	Southern Grids	BIF-hosted	

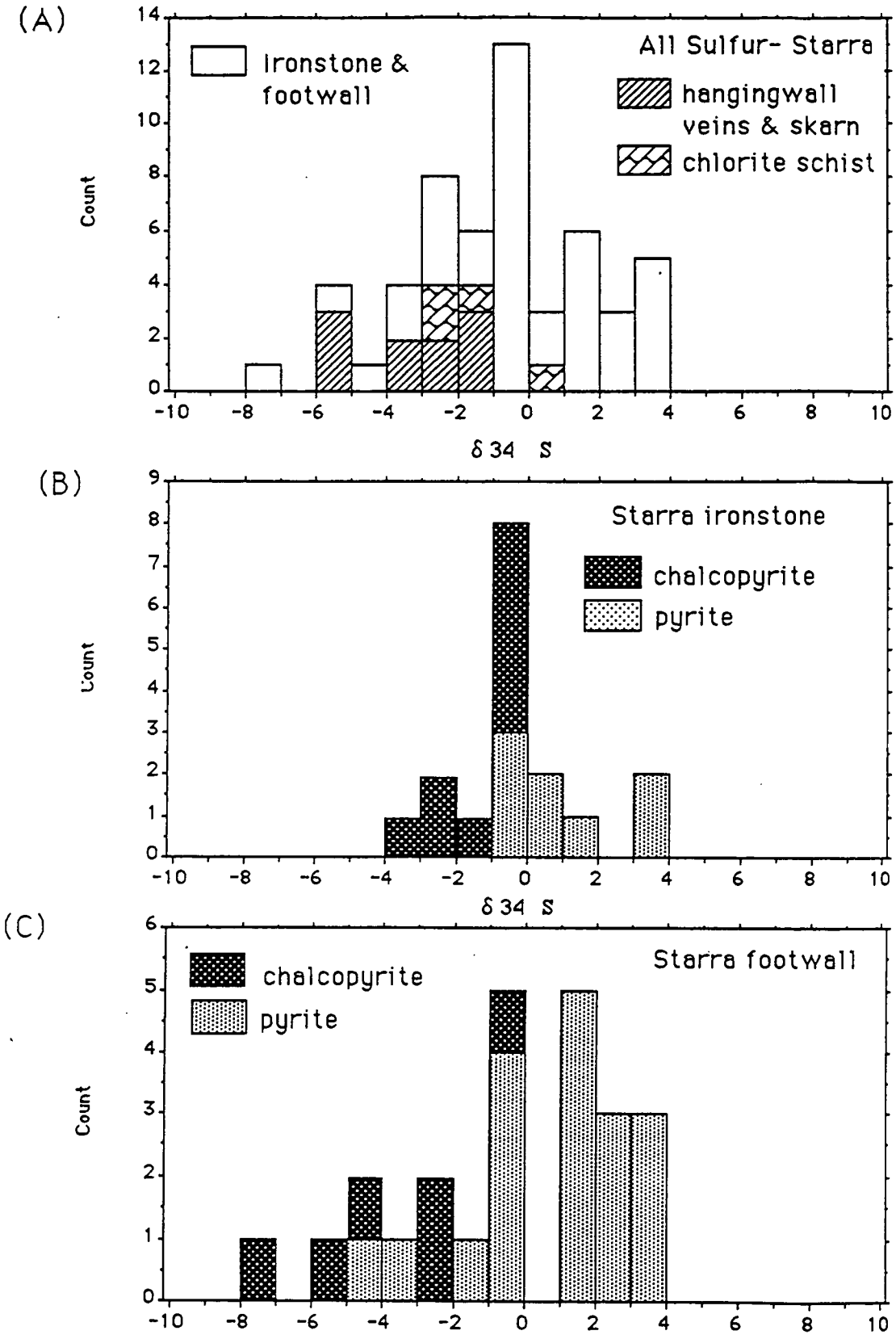

Figure 11.2A, B&C: Starra sulfur isotope distribution. The data is compiled in Table 11.1, summarised in Table 11.2.

Deformation Effects

The two main pyrite generations from the Starra feldspathic footwall were examined for isotopic disparities. These pyrites have inclusion-free euhedral rims, interpreted as a products of D2(MP) metamorphic recrystallisation, whereas the cores are corroded and poikilitic (Figs. 3.12G, 3.12H & 4.5H). A common lack of inclusion alignment within the pyrite cores favours the growth of this pyrite prior to any cleavage development. D2(LP) deformation has deformed both pyrite generations (e.g., Fig. 4.5C), but has added very little new sulphide to the footwall (discussed in greater detail in Chapters 3 and 4).

Pyrites with thick euhedral rims were drilled from single samples, composited, and compared to pyrite cores from the same sample. This analysis did not compare individual cores with individual rims, but compared a population of rims with a population of cores from the one sample. Rims proved to be consistently *lighter* by between 0.21 and 2.18‰ (average difference 0.86‰) than the corresponding cores, as illustrated in Figs. 11.3A & C. It is probable that chalcopyrite, commonly mobilised at Starra into pressure shadows and gash veins during deformation, also incorporated isotopically lighter sulphur.

Two hypotheses are available to explain the more negative sulphur values of the euhedral pyrite rims : either (1) the composition of the metamorphic fluid was isotopically-lighter than that which deposited the pyrite cores, or (2) the metamorphic fluid isotopic composition was the same as that which deposited the pyrite cores, but the euhedral rims were deposited at high enough f_{O2} to cause $\delta^{34}S_{H2S}$ to deviate from $\delta^{34}S_{fluid}$, a common feature of sulphide deposition close to the hematite-pyrite boundary (Fig. 11.7).
In fact, the present pyrite-rim/core sampling infers a specific $\delta^{34}S_{fluid}$ value, favouring alternative (1) above. In Fig. 11.3C, $\delta^{34}S_{rim}$ would converge with $\delta^{34}S_{core}$ at an estimated –3‰, whereas the heaviest core values (max. 4‰) display the greatest difference between core and rim. A second important feature is the systematic similarity of the shape of the rim profile to the core profile in across-strike isotopic sections (Fig. 11.3A). The simplest model which explains both of these observations, is that the rim pyrite obtained its sulphur both by recrystallisation of the older core pyrite, without isotopic fractionation, and also by the addition of new sulphur from a metamorphic fluid of constant $\delta^{34}S \sim -3$ ‰, lighter than the footwall pyrite average of +0.85‰. For the metamorphic assemblage pyrite-hematite to be stable, and exhibit no substantial fractionation away from the D2(MP) metamorphic fluid value during the growth of new pyrite, the oxidation state of the fluid must have been buffered to below ~ $\log f_{O2} = -26$, $T \geq 350°$ C, with ΣS between $10^{-3.0}$ and $10^{-2.5}$ ("B" on Fig. 11.7). The other area of pyrite-hematite stability would produce significant deviation of $\delta^{34}S_{H2S}$ from $\delta^{34}S_{fluid}$, shown as "A" on Fig. 11.7.

Several large D2(LP)? hangingwall carbonate veins, in which pyrrhotite replaces pyrite, deposited even lighter sulphur ($\delta^{34}S \sim -5.5$‰). This *reduced* assemblage would not permit deviation of $\delta^{34}S_{H2S}$ from $\delta^{34}S_{fluid}$, and emphasises that deformation-related sulphur resulted in part from the fluid assimilation of light sulphur, such as that associated with organic material (Ohmoto 1986).

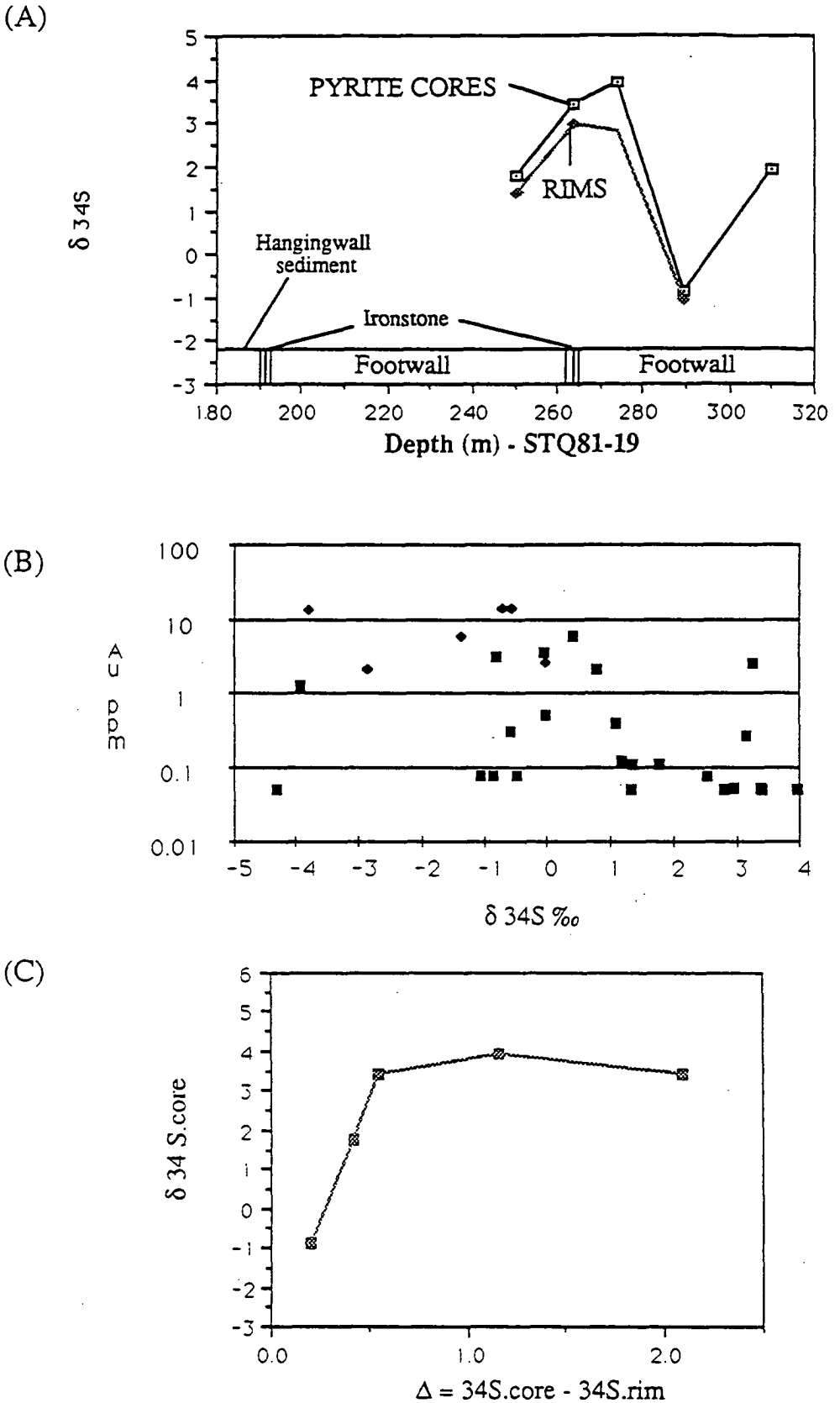

Figure 11.3 A *A sulfur isotope transect along STQ 81-19, Starra, Area 257, illustrating that there is no systematic variation at this location. However, pyrite overgrowths show a systematic variation to the pyrite core δ34S value.* **11.3B** *Plotting of gold-grade against δ 34S shows no dependency, using all available data.* **11.3C** *A detailed examination of pyrite core-overgrowth data at Starra shows that the isotopic difference between the two converges as the core value lightens (see text).Each point represents two analyses from one pyrite.*

Trough Tank

Sampling at Trough Tank concentrated on the discrete silica alteration zones containing coarse sulphides (22 samples), rather than the ironstone (5 samples), in which sulphides are commonly fine-grained and difficult to extract. A comparison between the two is therefore not meaningful. The overall sulphur variation is –6.05 to +5.93‰, averaging +0.36‰ (Table 11.2). Partial equilibrium is indicated by the lighter $\delta^{34}S$ composition for the chalcopyrite population (–1.11‰) than for pyrite (average +1.38‰), but the range of individual pair temperatures (139°, 360°, 462°, 911° and an impossible 1845° C) is geologically unacceptable for Au-Cu formation.

Pyrite, unlike the unimodal chalcopyrite distribution, is separated into two populations overall, one with a mode at –0.5‰, and the other with a mode at +2.5‰ (Fig. 11.4A). A possibly systematic relationship exists in the discrete pipe mineralisation between Au grade and $\delta^{34}S$, as shown in hole NQ6 (Fig. 11.5A). An 8 metre long transect revealed a $\delta^{34}S_{py}$ correlation in which gold deposition is associated with more negative $\delta^{34}S$, a fact also suggested in a plot of all data, regardless of its location (Fig. 11.5B). Further work is required to establish the validity of this relationship.

In summary, Trough Tank and Starra are linked by
(1) a similar isotopic range with a mean approximating 0‰, and
(2) $\delta^{34}S_{chalcopyrite} < \delta^{34}S_{pyrite}$, the correct order for equilibrium, although mineral-pairs in detail display disequilibrium.

Other Eastern Succession Ore Deposits

Answer Mine

Quartz-vein-hosted pyrite-chalcopyrite mineralisation lies in a shear zone entirely within the carbonaceous Answer Slate. The $\delta^{34}S$ variation of pyrite in four randomly picked dump-samples was very narrow, +8.41 to +8.85‰ (av. +8.67‰) (Fig. 11.4B). This suggests a single sulphur source with mineral precipitation under reduced conditions. The most likely source is local sediment sulphur extracted from the Answer Slate. Modern sediments containing biogenic pyrite in the range 0 to 10‰ are produced by "open system" bacterial sulphate reduction (Chambers 1982), although the bulk of anaerobic sulphate reduction produces "closed system" sulphides in the range -40 to -10‰. These values are directly comparable to Australian Mid-Proterozoic sediments, because seawater sulphate was similar to the present-day, $\delta^{34}S$ = 20 to 25 ‰ (Muir et al. 1985). The values are well outside the range of sulphides from mafic igneous sources.

Hampden Mine

The Hampden group of mines lie on a north-trending 60 m-wide shear zone, which juxtaposes carbonaceous black slate of the Kuridala Formation with metadolerite (Blake et al. 1984). The primary ore consists of chalcopyrite, marcasite and pyrite, but only pyrite

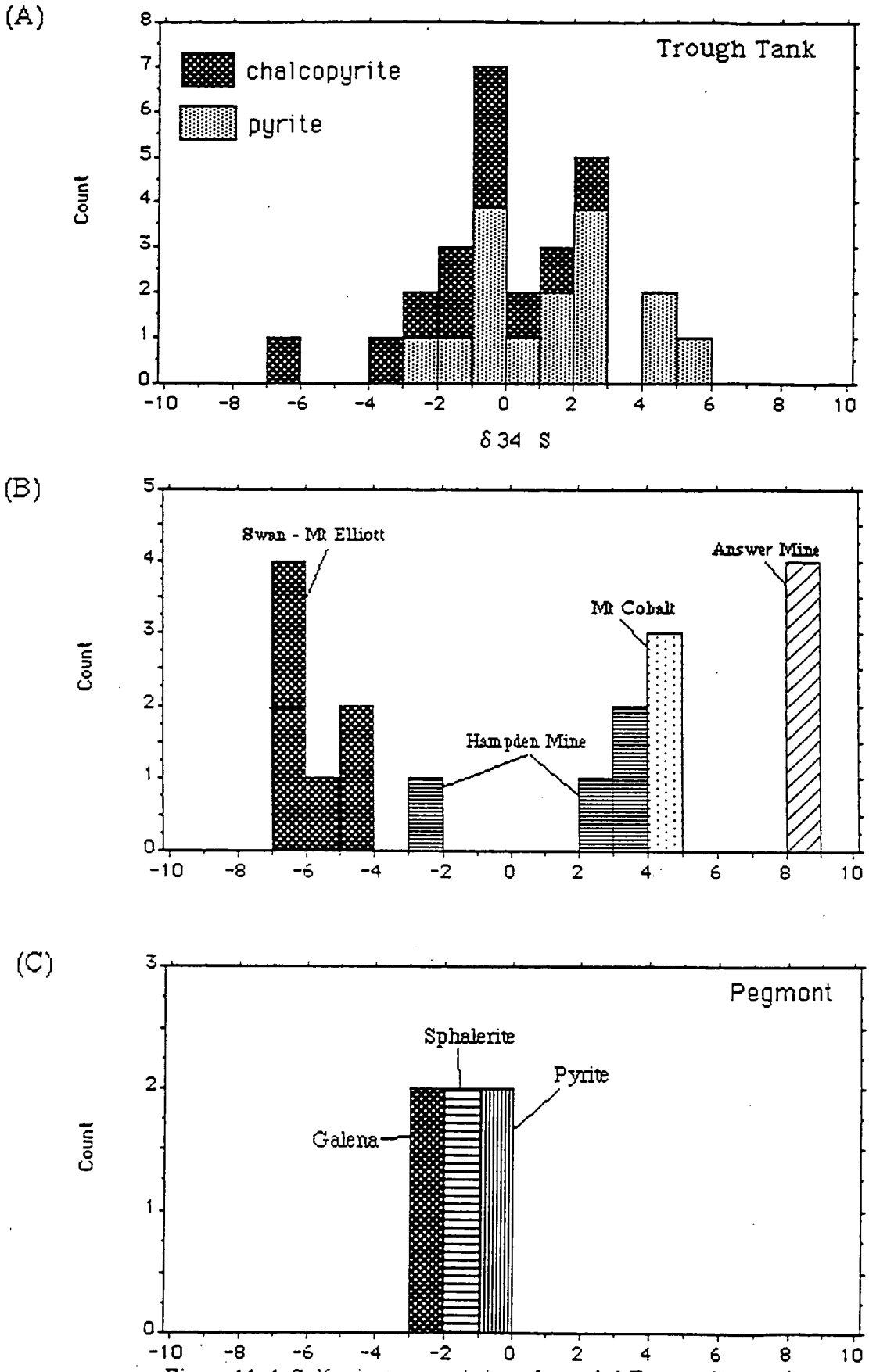

Figure 11.4 Sulfur isotope variation of sampled Eastern Succession ores.

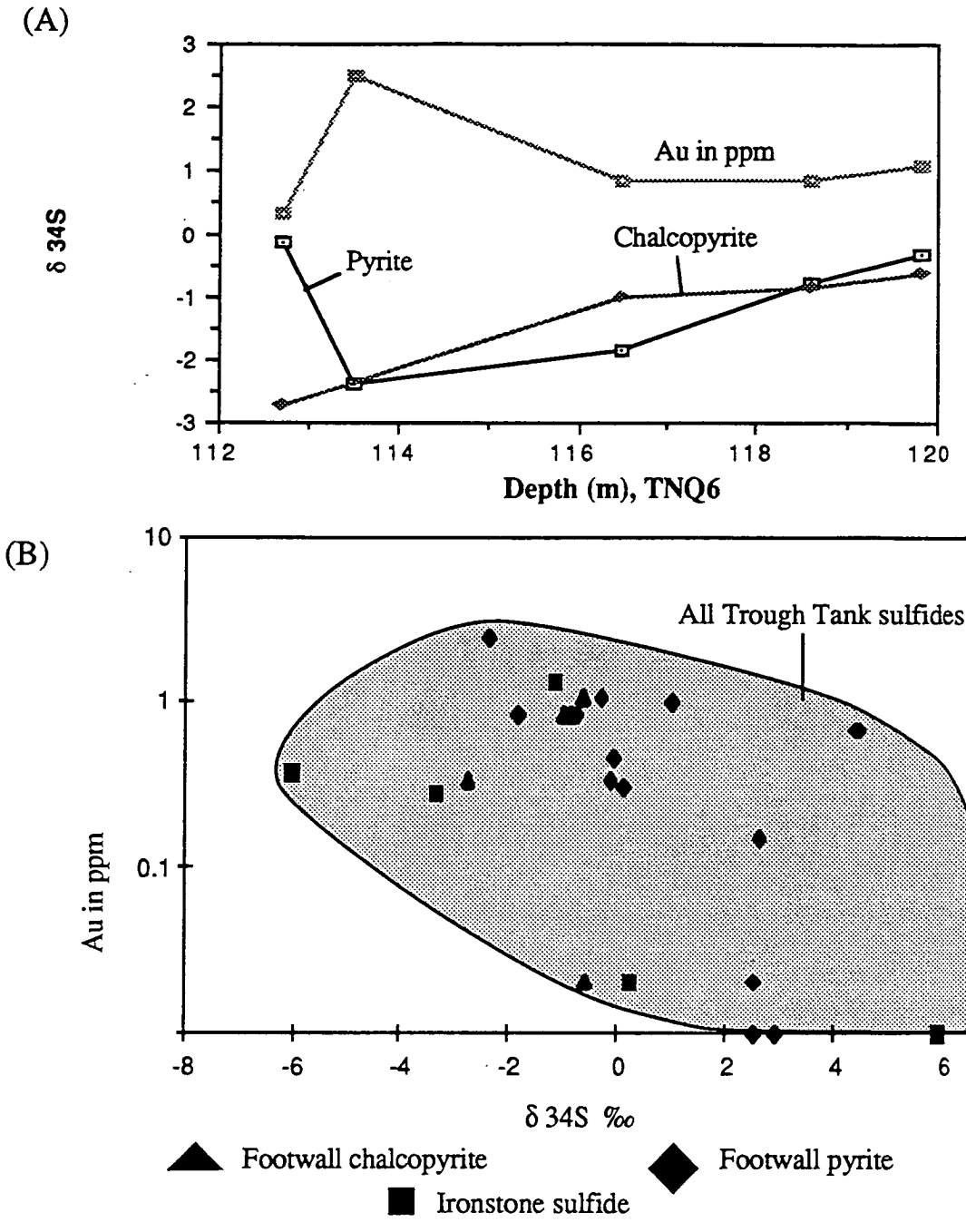

Figure 11.5A *At Trough Tank a discrete silica alteration zone in Hole TNQ6 shows some correlation of gold grade with sulfur isotopic character.* **5B** *A broad relationship is also suggested between Au and δ34S using all Trough Tank isotopic data, but this requires further testing through more detailed sampling.*

was sampled in this study. This deposit shows the greatest spread of all the sampled vein-style ores, $\delta^{34}S = -2.99$ to +3.65‰ (av. 1.98‰, n = 5), comparable to Starra. Many different sulphur sources can produce sulphur isotopes in this range (Ohmoto 1986).

Mount Cobalt

Nisbet et al. (1983) identified Mount Cobalt as a shear-controlled lode on the faulted contact between a metadolerite sill and metasediments of the Kuridala Fm. The main primary ore mineral in veins and shears is cobaltite (sampled in this study), with minor chalcopyrite,

galena, pyrite, sphalerite and scheelite. Nisbet et al. (1983) further suggest that Co-rich sediments in the region supplied metals to fluids driven from the dolerite. $\delta^{34}S$ values between +4.23 and 4.94‰ (Fig. 11.4B) tend to support this conclusion for sulphur also, as per the discussion of the Answer Mine sulphur source, because mafic igneous sulphur normally lies in the range –3 to +3‰, although departures are common (Ohmoto 1986).

Swan / Mount Elliott

The Mount Elliott lodes are localized en echelon within east-dipping NNW-trending reverse faults parallel to the Mt. Dore Fault Zone. The zone cuts carbonaceous Kuridala Formation sediments close to a metadolerite intrusion (Dimo 1975, Blake et al. 1984). It is related to the Swan Prospect ~800 m to the west, which has been diamond-drilled in some detail by Cyprus Minerals. Most of the 7 isotopic samples were obtained from chalcocite and pyrite veins in drillcore from Swan. A high oxidation state is suggested for this mineralisation by its association with abundant magnetite. This might explain the tight negative cluster (range –6.45 to –4.85‰, average –5.6‰; Fig. 11.4B), because sulphides in oxidised systems can display substantial negative fractionation from the $\delta^{34}S$ value of the fluid. However, such systems commonly show a wide isotopic range (Large 1975, Scott et al. 1985). In this instance the narrow negative range may therefore favour a thermally-degraded organic sulphur source, or dissolution of biogenic pyrite. Further analysis is required to separate these alternatives.

Mt. Dore

Beardsmore (1988) identified the Mt. Dore Cu deposit as the product of granitic fluids moving into gapes formed during shearing on the Mt. Dore fault. Vein and replacement pyrite-chalcopyrite-galena ores developed in a reverse fault breccia zone between granite and carbonaceous Kuridala Formation slates. Scott (1986) noted gross pyrite–chalcopyrite disequilibrium at Mt. Dore, similar to that of Western Succession Cu-replacement ores. Furthermore, he suggested that while the ore zone values of ~$\delta^{34}S$ = 2.9‰ permitted a granitic source for the sulphur, the low Cu content (150 ppm) of granitic pyrite indicated that the Cu was not granite-derived, but was more likely leached from the carbonaceous sediments. K. Scott (pers. comm. 1987) found that deep within the footwall Staveley Formation, pyrite had markedly variable values of 0.7, 4.4 and 12.0‰ in three samples, typical of biogenic sulphur.

Pegmont

This stratiform BIF-hosted Pb-Zn mineralisation is located ~30 km south-east of Starra within the Soldiers Cap Group. It is identified by Beardsmore et al. (1988) as older than other Pb-Zn deposits in the region because of its Pb-Pb isotopic signature. Workers agree that its mineral and chemical zonation link it closely to other Broken Hill-style exhalative sedimentary/volcanic ores, a conclusion borne out by the similarity of its sulphur isotopic signature to Broken Hill. Vaughan & Stanton (1986), in a preliminary study, found

that sphalerite, galena and pyrite ranged between $\delta^{34}S = -2.9$ to 0‰ (av. = –1.6‰, n = 6; Fig. 11.4C). Spry (1987) found that the isotopic range of the Broken Hill deposit ($\delta^{34}S = -3.3$ to +6.7‰) could best be explained by a magmatic sulphur (0‰) - seawater sulphate mix (15‰). The Pegmont isotopic signature is the best comparison for other potential exhalative ores in the Eastern Succession. An important feature is that the sulphides are in relative isotopic equilibrium, with $\delta^{34}S_{PbS} < \delta^{34}S_{ZnS} < \delta^{34}S_{FeS2}$.

DISCUSSION

A Comparison Of Sulphide Deposits in the Mount Isa Inlier

Western Succession

A consistent theme between the stratiform Pb-Zn ores (e.g. Mount Isa, Lady Loretta), and the epigenetic Cu ores of the Western Succession (e.g., Mount Isa, Mammoth, Paradise Valley) is the role that syngenetic/diagenetic pyrite played in localising metals during later hydrothermal events. This is evidenced in the Cu ores by pyrite-chalcopyrite disequilibrium (Scott et al. 1985, Andrew et al., in press). In the Pb-Zn ores it is implied by a spread of data between the earliest generation of pyrite (1.4 – 6‰ : Mount Isa; 3.9 – 4.7‰: Lady Loretta; –5.7 to –1.7‰ : Mammoth) and the most extreme products of the Pb–Zn mineralising events (frequently much heavier, in the range 6 – 25‰ for Mount Isa (Andrew et al. 1985) (Fig. 11.6).

In some instances diagenetic pyrite has very positive $\delta^{34}S$ values (20.8 – 50.8‰), interpreted as the product of extreme organic reduction of sulphate (Paradise Creek Formation, Gunpowder Creek Formation; Scott et al. 1985). North Australian mid-Proterozoic seawater had a value of ~20 - 25 ‰ (Muir et al. 1985). Diagenetic pyrite values greater than this are only possible in a closed system, for instance, by reducing sulphur from waters which have already experienced sulphate reduction. Partially-reduced sulphate migrates into pore spaces, where further reduction occurs, and so on. The opposite situation probably characterized the oxidised arenaceous sediments of the Mammoth area, where light $\delta^{34}S$ values (–5.7 to –1.7‰) in diagenetic pyrite are attributed to low degrees of organic reduction in a partially open system (Scott et al. 1985).

The most detailed and revealing study of isotopic variation in the Mount Isa Inlier has recently been completed by Andrew et al. (in press) for the Mount Isa Cu ores. These workers found that W/R ratios were important in determining the isotopic heterogeneity of sulphides in a multiple sulphur source model. At the centre of the hydrothermal system, at high W/R ratios, the Cu ores had a narrow $\delta^{34}S$ range (9 – 13‰), interpreted as the product of mixing between replaced Pb–Zn ores (5 – 21‰), diagenetic pyrite (1.4 – 6‰), and heavy sulphur carried by an invading Cu-rich fluid (>24‰). At the margins of the silica-dolomite alteration envelope, $\delta^{34}S_{cpy}$ varied far more widely than at the centre, between 1 and 30‰, even at petrographic scales (Eldridge et al. 1985). This was attributed to a variation in the degree of access of the invading fluid and the consequent sulphide replacement. The source of heavy sulphur ($\delta^{34}S > 24$‰) was identified as brine-leached evaporites,

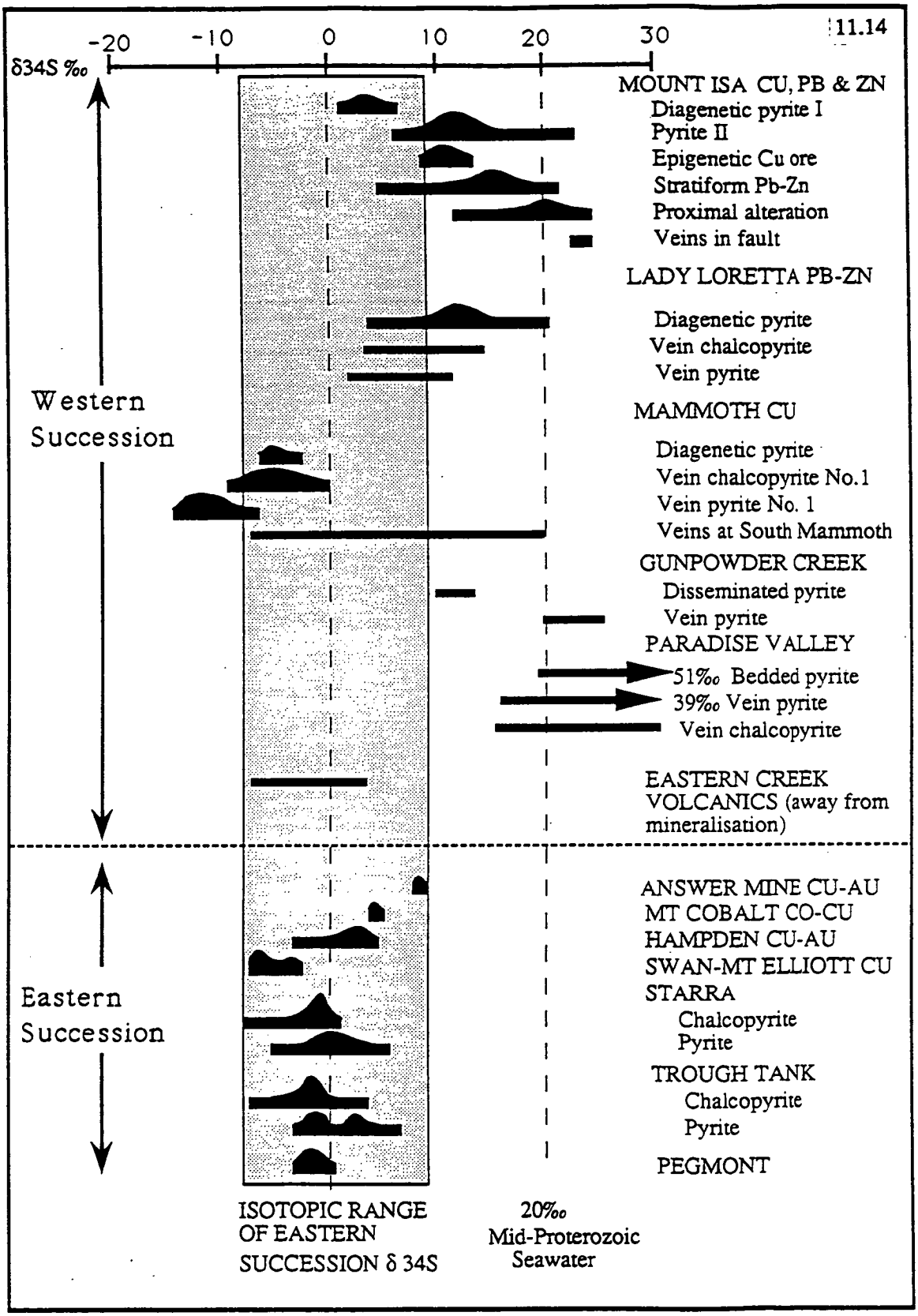

Figure 11.6 *A summary of the sulfur isotopic ranges of deposits within the Western Succession and the Eastern Succession of the Mount Isa Inlier. All Eastern Succession deposits occur in the range of -7- +8‰, whereas Western Succession deposits display a huge isotopic variation, attributed to a dissolved evaporite sulphate component or deposition from oxidised fluids. References used to compile the data are noted in the text.*

rather than seawater or wallrock sulphur from the footwall Eastern Creek Volcanics (regionally ~0‰; Andrew et al., (in press)). The detection of $CH_4 > CO_2$ in fluid inclusions implied that the mineralising fluid was highly reduced. Andrew et al. (in press) therefore formulated a model of distal leaching of evaporitic sulphate ($\delta^{34}S > 30‰$) by a circulating oxidised brine, from which sulphate was subsequently reduced by interaction with the footwall basalt (at the same time leaching Cu). Copper ores precipitated because of an interaction between this reduced fluid and the pre-existing pyritic Pb-Zn ore zone.

Variants of the above multiple-stage model can account for most Cu and Pb-Zn mineralisation in the Western Succession. Figure 11.6 illustrates that the range of sulphur isotope values for stratiform and epigenetic sulphides concentrates between 6 and 24‰, even higher for some fault-related epigenetic Cu ores, such as Esperanza and Paradise Valley (Scott et al. 1985). The exceptions to this range are ores which were deposited from hot oxidised fluids, which display large isotopic depletions, such as the Mammoth No. 1 and B orebodies ($\delta^{34}S = -18 - 0‰$; Scott et al. 1985). In the entire Western Succession, only diagenetic pyrite and primary sulphides in igneous rocks possess $\delta^{34}S$ values concentrating around 0‰.

Eastern Succession

All southern Eastern Succession prospects sampled in this paper (Mount Cobalt, Hampden, Answer Mine and Swan/ Mount Elliott), and values from Mt. Dore and Pegmont, are constrained in $\delta^{34}S$ between -7 and +8‰. This is in contrast to the enormous $\delta^{34}S$ variation of the Western Succession ores from the Mount Isa Group and Surprise Creek Formation. Deposits from other sulphate-dominated evaporite provinces, such as the McArthur Basin, also show a very broad $\delta^{34}S$ range, with some values much greater than the predicted Mid-Proterozoic seawater value (Muir et al. 1985). The isotopic range of sediment-sulphate in these basins indicates they were deposited from marine, rather than continental waters, which contain av. 10‰ sulphate (McKibben & Elders 1989). It follows therefore, that the southern Eastern Succession was not a marine sulphate-evaporite province, because its mineral deposits do not display the large, positively-skewed, isotopic range which typifies such provinces. This is in spite of the commonly saline nature of fluid inclusions (Davidson et al. 1988, Switzer 1987), the widespread presence of scapolite (Ramsay & Davidson 1972), and sporadically-documented evaporite crystal casts, which are evidence that at least halite-rich evaporites were once abundant in the Mary Kathleen Group. It is concluded on the basis of sulphur isotopes, that the southern Eastern Succession was a marine-halite or continental-sulphate, rather than a marine-sulphate evaporite province, during the deposition of the Mary Kathleen Group. The presently known time relationships between the Mount Isa/McNamara Groups (~1680 – 1600 Ma; Blake et al. 1983) and the Mary Kathleen Group (~1750 – 1700Ma), mean that these sulphate and halite provinces were not coeval.

As a general conclusion, this distinction between sulphate-rich and -poor evaporite basins may explain why large stratiform Pb-Zn deposits are to date confined to the younger sulphate-rich rocks of the Mount Isa Western Succession. These would have constituted an obvious abundant sulphur source to evolving diagenetic/metamorphic fluids. Following this logic, the Eastern Succession is a less-likely host for sedimentary Pb-Zn deposits. More detailed sampling of the numerous copper prospects scattered across the Mount Isa Inlier , and host-rock sulphur, could better define the sulphate and halite-dominant evaporite provinces.

A Summary of the Features of Cloncurry-style Cu-Au Deposits

Epigenetic Cloncurry-style Cu-Au deposits were derived from isotopically diverse fluids, within the range –7 to +8‰. Minor occurrences of this ore type are very common throughout the region, reflecting a common structural/chemical trap. Metamorphic/igneous fluids circulating around igneous bodies were fault-channelled to the pyritic carbonaceous shales in the Kuridala Formation and Answer Slate, where reduction resulted in sulphide precipitation. Those fluids which were dominated by magmatic sulphur produced sulphides closest to 0‰ (Mt. Dore, Hampden) but those displaying greater sediment-fluid interaction converged isotopically towards the average value of pyrite in shale (probably in the range –10 to +10‰, based on average values of the Mount Isa area). This produced deposits such as the Answer Mine and Mount Cobalt. "Cloncurry"-style ores differ from epigenetic Cu ores in the Western Succession by the common presence of igneous intrusives close to the ore. In respects of structural control, and replacement of pre-existing shale sulphide, they are similar.

Affinities of Starra/Trough Tank Mineralisation

Starra and Trough Tank have a similar isotopic average to that of the Pegmont exhalative Pb-Zn ores (~0‰). Most importantly, they differ from the epigenetic Mt. Dore and Western Succession ores (Scott 1986, Scott et al. 1985) in having $\delta^{34}S_{CuFeS2} < \delta^{34}S_{FeS2}$, which is the normal order for isotopic equilibrium. These features are inconsistent with any model involving chalcopyrite replacement of pre-existing sulphides (biogenic or otherwise), as proposed by Switzer et al. (1988), because under such a model pyrite and chalcopyrite should have approximately similar $\delta^{34}S$ values. The existing data suggests that sulphide deposition took place in a single mineralising event. A comparison with $\delta^{34}S$ estimates of fluids within the Answer, Mt. Cobalt and Mount Elliott shear systems indicates that none of these were acceptable sources for Starra/Trough Tank sulphur, although the Hampden sulphide range is overlapping.

Sulphur Isotopes of Oxidised Ore Deposits

Low sulphur, oxidised or very alkaline fluids substantially fractionate $\delta^{34}S$ in sulphides from the fluid $\delta^{34}S$ value, as indicated in Fig. 11.7. Ohmoto & Rye (1979) highlight skarn and porphyry copper deposits as common examples of this phenomena. In

some oxidised systems therefore, it is possible for a single fluid composition to give rise to a much larger isotopic range, from only small fO_2 changes (e.g, Juno, Tennant Creek; Large (1975), and Mammoth South; Scott et al. (1985)). Large isotopic ranges are not a feature of the Trough Tank or Starra ores. In contrast, acid, reduced hydrothermal systems show only small fractionations away from the fluid value, and in these instances the isotopic character of the mineral is more indicative of the fluid sulphur source. Such systems

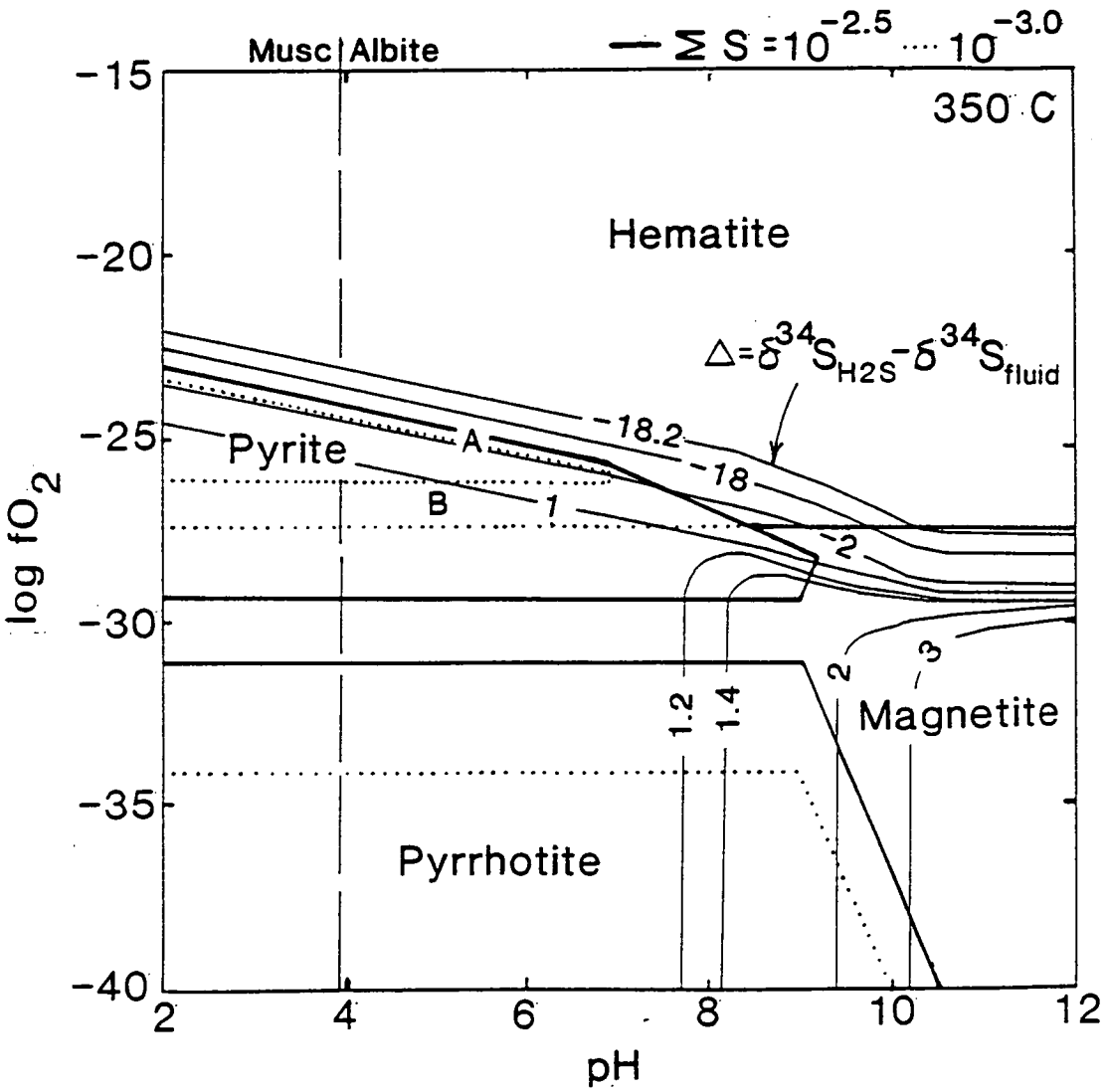

Figure 11.7 LogfO2 - *pH representation of the stability fields of minerals in the Fe - S - O system at 350° C, and variable total sulphur (shown). Also shown are sulphur isotope mineral/fluid contours, which notably change radically in the HSO_4^- and SO_4^{2-} fields. The probable conditions prevailing during the deposition of Starra footwall alteration and ironstone are shown. Points A and B are two possible positions for the fluid conditions prevailing during subsequent deformation: they are fixed with respect to fO_2 by the pyrite $\delta^{34}S$, but uncertain with regard to pH (see text).*

commonly stabilise pyrrhotite, pyrite or magnetite.

Sulphides in banded iron formations of the late Archean and Early Proterozoic have widely varying $\delta^{34}S$ values (for instance, Michipicoten I.F., Canadian shield, range: -10.5 to +10.1‰, average -1.3‰; Helen I.F.: -11.6 to +19.0‰) which is attributed to the activity of sulphur-reducing bacteria, and is proportional to organic carbon values (Mel'nik 1982, Goodwin et al. 1985). Where oxide facies BIF have $\delta^{34}S = 0 \pm 2$‰, for instance (Goodwin et al. 1985), the source is suggested to be juvenile sulphur, or "assimilatory" reduction from contemporary waters of the same isotopic value (Thode & Goodwin 1983). The latter origins are most likely for Starra sulphur from an empirical comparative viewpoint.

Sulphur Sources for Starra / Trough Tank

The best estimate of the isotopic range of the Starra/Trough Tank fluid is indicated by the least oxidised mineral assemblage, which occurs in mineralised mag-qtz-cpy±py ironstone, $\delta^{34}S = -2$ to +4‰.

Possible sulphur sources in the range –2 to +4‰ are

(1) Magmatic sulphur (including leached igneous rock sulphur).

(2) Inorganically reduced Mid-Proterozoic seawater sulphate (av. 20‰; Muir et al. 1987), at T ~ 300 to 350° C.

(3) Leached biogenic sedimentary sulphur.

These sources cannot be differentiated on the present data, although on the basis of the moderately large isotopic range, a magmatic source is less likely than the others. If sediment sulphur was involved, it was more negative than sulphur contributed to the Answer Mine and Mount Cobalt shears during subsequent deformation (–7 to +8‰). Nevertheless, some contribution from thermally degraded organic sulphur is suggested, because organic carbon was unequivocally contributed to Starra ironstone carbonates (Chapter 10).

A fourth intriguing alternative, accounting for $\delta^{34}S_{H2S} \sim 0$‰, was suggested by McKibben & Eldridge (1989) for vein sulphides in the sediment-filled, thermally-active, Salton Sea trough. The geological setting and the oxidised vein mineralogies make the findings relevant to this study. Detailed ion-probe analysis indicated that vein sulphides in the range -9 to +9‰ $\delta^{34}S$, av. ~ 0‰, derived their sulphide from a 50% reduction of sediment-anhydrite ($\delta^{34}S = 10$‰), at 300 to 320° C (resulting in $\delta^{34}S_{fluid\ H2S} \sim 0$‰, and $\delta^{34}S_{fluid\ SO4} \sim 20$‰). Fractionation during inorganic sulphate reduction at these temperatures in saline systems is the same as for seawater, ~ 19 to 20‰. The important feature of these observations is that the sulphur ultimately derived from continental evaporites; these have lower $\delta^{34}S$ than their marine counterparts (av. 10‰, versus 20‰ for modern marine waters). At Starra and Trough Tank, REE evidence (Chapter 8) indicates that marine waters were present during the deposition of some iron formations. Any contemporary sulphate evaporites would therefore have reflected the prevailing seawater isotopic signature. However, a buried continental evaporite succession may well have contributed sulphur, as discussed previously in a regional context.

In conclusion, the four possible sulphur sources above cannot be differentiated with the present data.

CONCLUSIONS

1. Starra and Trough Tank deposits (isotopic range –6 to +5‰, average ~0‰) differ isotopically from the stratiform Mount Isa Pb-Zn ores (6 –21‰), Western Succession epigenetic Cu ores (–20 to +51‰), and most Cloncurry-style epigenetic Cu ores (–7 to +8‰). Most of the latter ores require at least two sulphur sources to explain their isotopic character, whereas Starra sulphides predominantly formed in a single event, in conflict with the genetic model of Switzer et al. (1988).

2. Starra and Trough Tank $\delta^{34}S$ values are empirically most like the exhalative Pegmont mineralisation, and are the only ores in the Mount Isa Inlier concentrating around 0‰.

3. The $\delta^{34}S$ of sulphides in some ore deposits can be used to predict the types of evaporites which once existed in sedimentary provinces. This approach assumes that metamorphic fluids which dissolve the evaporites after burial, retain the isotopic features of these evaporites. The $\delta^{34}S$ of Mount Isa Inlier metamorphic fluids suggests that evaporite successions south of Cloncurry were marine-halite or continental-sulphate-dominated, whereas the Western Succession was a marine sulphate-halite province. The provinces were not contemporary. This observation may have important implications in the search for major Pb–Zn ores, as these derived much of their sulphur from the dissolution of sulphate evaporites (Andrew et al. in press).

4. Although the predeformational S-isotopic character is substantially preserved (-2 to +4‰), sulphides at Starra in reaction skarns, hangingwall veins, and as euhedral rims to primary pyrite porphyroblasts, are more negative than primary sulphides. The metamorphic fluid had a constant $\delta^{34}S$ value of ~–3.0‰ or lower, deduced from an analysis of pyrite grains.

5. An epigenetic or syngenetic origin for Starra cannot be differentiated using the sulphur-isotopic character alone. The possible sulphur sources, which cannot presently be distinguished, are magmatic sulphur, inorganic reduction of Proterozoic seawater sulphate, biogenic sediment sulphur, or continental evaporite sulphur.

CHAPTER 12

HYDROTHERMAL GEOCHEMISTRY AND ORE GENESIS

INTRODUCTION

The similarity of the Starra and Trough Tank mineral assemblages permits the formation of a general model to explain their chemistry, although some differences between the deposits require modifications to this model. At both prospects the paragenetic sequence is obscured by metamorphism and deformation, so that the bulk mineralogy has been used to infer the ore-fluid conditions. Fluid inclusions so useful for the determination of these conditions in less deformed ores have been destroyed, with the probable exception of tiny multi-phase examples in the least-strained portions of Area 222: thermometric analysis of these was not possible because of their small size, although their petrographic morphologies provide a guide to the ore-fluid composition.

In this chapter the constraints on ore genesis are summarised, together with their inferences for ore fluid composition. Two genetic hypotheses are discussed and evaluated using these constraints. Lastly, similar ores throughout the world are briefly reviewed, and a general model for the formation of stratabound BIF-hosted Cu-Au deposits is presented.

THE GEOLOGICAL AND GEOCHEMICAL CONSTRAINTS ON ORE GENESIS: A THESIS SUMMARY

At Starra, Au-Cu ore is hosted by massive and banded iron formations developed at the contact between an altered mafic and felsic volcaniclastic package (Harley and Mariposa Creek Members), and relatively unaltered calcareous metasediments. A chemical/sedimentary origin for the iron formations is supported by

(1) Their stratiform character over 610 sq. km.,

(2) Micro- and meso-scale banding preserved in some outcrops,

(3) Sedimentary reworking of iron formation clasts into polylithic debris flows above the main stratigraphic ironstone horizon at Area 222,

(4) Intergrowth of gypsum pseudomorphs with thinly bedded iron formation consistent with both diagenetic and synsedimentary growth,

(5) A lack of symmetric zoning, skarn mineralogies, or sudden terminations, which are typical of replacement iron ores.

The Starra sequence is strongly deformed, particularly in the footwall, which is part of the Starra Shear. Both the footwall and hangingwall accumulated by mass-flow processes below wavebase, in an elongate, oxidised, sub-basin bordered to the east and south by shallow evaporitic shelves. The basin margins contain ore-equivalent layers of massive Ba-enriched bedded hematite, chert-rich Hamersley-style BIF, breccia-bearing hematitic ironstone and synsedimentary tourmalinite, intercalated with anomalously potassic sediment.

Ore at Trough Tank, metamorphosed to upper Amphibolite facies, is hosted by well-banded oxide-facies iron formation (~ 70 % $Fe_2O_3^{tot}$) grading to poorly mineralised anthophyllite (meta-carbonate facies iron formation) schist, within a sequence of bedded feldspathic and pelitic sandstones, and massive feldspathic beds.

Evidence for a marine (rather than a lacustrine) setting is provided unequivocally by the REE concentrations in iron formations. Mineralised Trough Tank BIFs persistently possess a negative Ce anomaly, as do some distal Hamersley-style BIFs south of Starra. In modern waters, seawater is depleted in Ce relative to other REE, whereas river waters are not: inconsistent preservation of such an anomaly at Starra suggests mixing of fresh and marine waters, as would characterise, for instance, a partially land-locked basin.

The Starra footwall rocks are interpreted to be volcaniclastic rocks because of their chemical similarities with other Eastern Succession volcanics, particularly high field strength element-depleted varieties. In addition the least-altered samples contain Ti/Zr ratios (7 – 14) consistent with dacites or rhyodacites, distinct from the higher Ti/Zr ratios of overlying metasediments (17 – 25), (precluding the metasomatism of overlying sediment to form the footwall). The felsic footwall is not chemically cogenetic with the Gin Creek Granite, and its intrusive source was not observed in the Starra footwall, because of offset on the Starra Shear. Chemical study of the Trough Tank host rocks found that, despite their strong albite enrichment, a sedimentary origin was most likely, although some massive layers are interpreted to have a volcanic origin.

Footwall alteration was pervasive at Starra, but more focussed, zoned, and pipe-like at Trough Tank. In both, the alteration was characterised by enrichment of Fe, Na, Cu, Au ± Zn, and depletion of K, Mn, Ca, Zr, Nb, Ba and Sr. Ni, P, Mo and Co are specifically enriched in the Trough Tank footwall and ironstone, whereas W and Sn are enriched at Starra. Albite enrichment and associated K-Ba-Rb depletion are attributed to widespread low temperature, saline, alteration which may be unrelated to the mineralisation, although albite was also stable at high temperature. Disseminated pyrite and carbonate was a likely intermediate alteration stage because of its distribution at the edge of more intense disseminated and oxide-vein alteration. Much of this pyrite grew prior to thermo-tectonism, within semi-consolidated sediment. The most intense alteration was focussed at both deposits below the most gold-rich ironstones, resulting in severe silica replacement (with significant volume loss) at Trough Tank, and either chlorite ± mag-py or substantial mag-cpy ± hem ± py enrichment at Starra.

The Starra ore fluids were sufficiently oxidised to deposit magnetite, hematite and bornite prior to reaching the ironstone horizon, and capable of zircon dissolution, which resulted in widespread Zr and Nb loss, and enrichment of HREE (La/Yb* ~ 0.77) and Y in the Starra ironstone. Three deformed vein types are recognised, hosted by albite: hem-py-chl-musc, mag-hem-py-cpy-musc, and mag-cpy ± py ± hem ± rutile ± scheelite (this last most reflects the mineralogy of gold-rich ore).

Starra ore is zoned laterally from gold and quartz-rich, to gold and quartz-poor ironstone. Conversely at Trough Tank, the most siliceous and Au-rich rocks are footwall to,

or texturally overprint pre-existing Au-bearing BIF. Accompanying the Starra changes, a zonation is also observed from mag-cpy ± siderite, to mag-hem-cpy-py ± siderite, to hem-py assemblages. The sulphides and oxides possess metamorphic textures favouring their pre or early-D2(MP) origin. Isolated instances of pyrite replacement by chalcopyrite are associated with cataclastic pyrite deformation, with massive boudinage-related sulphide-quartz veins, and with metasomatic calc-silicate assemblages found hangingwall to mineralisation. Gold throughout the Starra ore is hosted mainly by chalcopyrite, but is also observed in pyrite, magnetite, quartz and siderite. Strong geochemical correlations exist between Au, Cu, Si, W, Sn, Y and Mn; anomalous W, Y and Sn extend beyond Au in any given ironstone.

Carbon isotopes in calcite, siderite and dolomite provide important constraints to the mineralisation. Siderite and calcite within ironstone shows no isotopic convergence with the fields of shears and veins from the Starra hangingwall. Starra and Trough Tank ore-related carbonates lie on the same distinctive unusual trend of increasing $\delta^{18}O$, coupled with decreasing $\delta^{13}C$. Values between -3.8 and -15.5 ‰ $\delta^{13}C$ require a contribution from oxidised organic carbon during the ironstone formation.

The sulphur isotopic range of Starra and Trough Tank are near identical, averaging ~ 0 ‰, and ranging from -6 to +5 ‰. This range is common to sulphur from Mid-Proterozoic magmatic, biogenic and continental evaporitic sulphate sources. Recrystallised pyrite rims at Starra are isotopically lighter than that of pyrite poikiloblast cores, to which they were added during D2(MP). In addition, Starra sulphides are isotopically different to those developed in nearby shears, such as the Answer and Mount Cobalt vein systems. They are similar to sulphur in the exhalative Pegmont Pb-Zn ores, 29 km south-east of Starra.

PHYSICO-CHEMICAL CONDITIONS OF STARRA/TROUGH TANK FLUIDS

Temperature: Constraints From the Assemblage Chalcopyrite-Gold

The chalcopyrite-gold association observed at Starra and Trough Tank provides the best temperature constraint for ore formation. Scheelite does not constrain the temperature range estimate, because it has a large stability range, 120° to >600° C (Higgins 1985, Davis & Williams-Jones 1985, Paterson 1987, Wollenberg et al. 1977, Ivanova 1988).

The available studies of the mobility of Au favour the dominance of either thio- or chloro-complexes in hydrothermal fluids (Seward 1973, Cole & Drummond 1986, Huston & Large 1989), with a possible contribution from less abundant species such as polysulphide, sulphite, bromide, ammide, telluride and carbonyl/carbonate complexes, depending on fluid composition (Kerrich & Fyfe 1981, Seward 1984, Wilde & Bloome 1988).

The predominant thio-complex is $Au(HS)_2^-$, which is most soluble in the pyrite field at < 300°C, particularly between 170° and 250° C. Huston & Large (1989) noted that the low solubility of $Au(HS)_2^-$ in the pyrrhotite, hematite and magnetite fields, and indicated that gold deposition may occur by decreasing the activity of reduced sulphur, through oxidation, sulphide precipitation, or by increasing alkalinity. Hydrothermal systems in which $Au(HS)_2^-$ transport is important commonly have an association of Zn-Pb-Ag ± As, Hg, Sb and W;

these include epithermal systems (Henley & Brown 1985, Cole & Drummond 1986), and a large number of volcanogenic massive sulphides (Hannington et al. 1986, Large et al. 1988).

$AuCl_2^-$ is the only important gold transporting complex in the magnetite and hematite fields, and therefore is the only viable species for gold transport in the Starra/Trough Tank fluids (its stability field for Starra conditions is shown on Fig. 12.10). $Au(HS)_2^-$ solubility is unlikely because of the very low sulphur content of the Au-bearing ores (2 – 5%). Huston & Large (1989) consider that where Au was transported as a chloride-complex, an association exists between Au-Cu ± Bi, Sn, and Mo. Gold is usually free-milling, or hosted by chalcopyrite, and a strong positive correlation between Cu and Au is evident (both are chloride-transported, with near-parallel solubility contours in the pyrite field). Examples are porphyry Cu-Au systems (Sillitoe 1979), igneous skarns (Einaudi et al. 1981), relatively oxidised high-temperature volcanogenic sulphide ores (Huston & Large 1989, Large et al. in press), and replacement Tennant Creek-style ores (Large 1975; Nguyen et al. 1988, Wedekind & Large, in press). The critical feature of $AuCl_2^-$ is its dominance over $Au(HS)_2^-$ above 300° C (and in very oxidised regions of the hematite field as low as 200° C). Au-

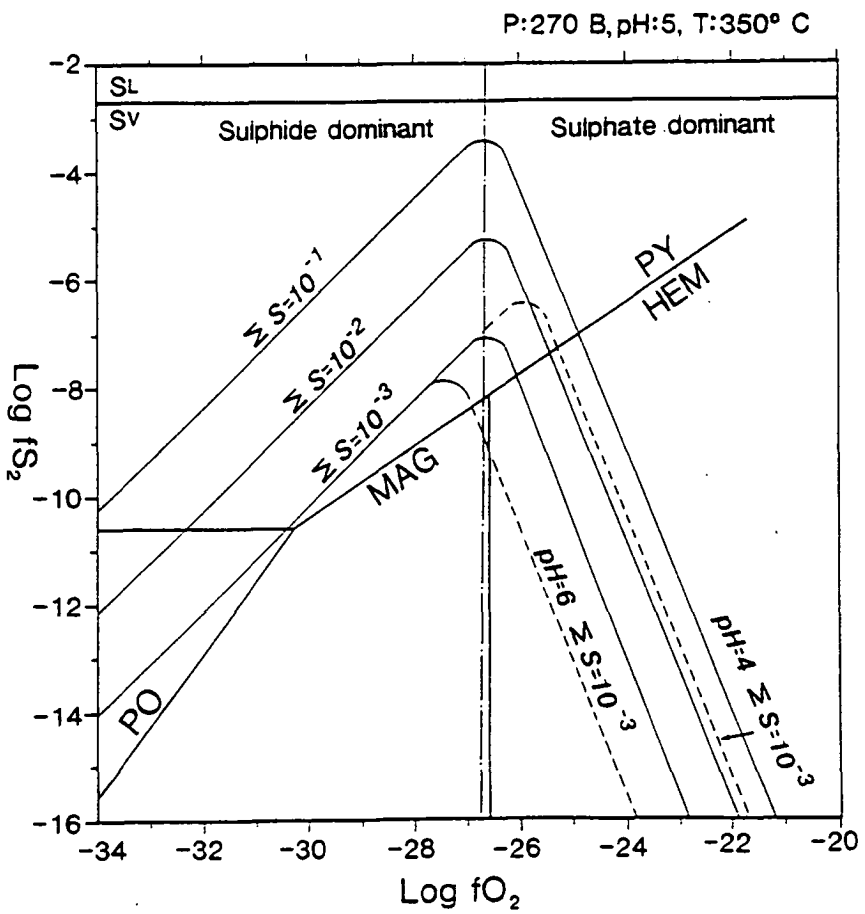

Figure 12.1 *A log fO_2 – log fS_2 diagram relevant at the conditions of 350° C, pH = 5, P = 270B. The intersection of ΣS contours (after Raymahashay & Holland 1969) with the magnetite-hematite-pyrite triple-point constrains ΣS to slightly greater than 10^{-3} M, using phase equilibria boundaries calculated from data in Barton et al. (1984) and Henley et al. (1984). The effect of changing pH is also shown for the $\Sigma S = 10^{-3}$ M contour.*

chloride transport is favoured by high salinities ($a_{Cl^-} > 10^0$), oxidised fluids, and low pH (< 4.5); gold deposition can be achieved by increasing pH or f_{S2}, or decreasing a_{Cl^-}, f_{O2}, or temperature (Huston & Large 1989). Chalcopyrite deposition is favoured in saline systems above 250° C, because Cu chloro-complexes exceed the solubility of Cu thio-complexes at this temperature (Walshe & Solomon 1981).

Thus the thermodynamics of joint chalcopyrite-gold deposition indicate formation temperatures for the Starra/ Trough Tank ores in the range 250° – 380° C. One possibility for the Cu-Au-absent assemblages, such as Type (1) hem-py-musc veins in the Starra footwall (Chapter 3), is that they formed at T < 250° C.

Sulphur Activity

Sulphur activity has been calculated for the Starra hydrothermal system using the mineral phase equilibria in Bowers et al. (1984), and the experimental data of Raymahashay & Holland (1969), plotted on an activity S_2 - activity O_2 diagram. Intuitively the amount of sulphur in the fluids, gauged by the very high ratio of oxides to sulphides, was probably low. The footwall vein assemblage mag-hem-py suggests Σa_S = ~ 10^{-3} M, given a pH of ~ 3.5 – 6, at 350° C (see "Constraints on pH") (Fig. 12.1). This value may increase $\Sigma a_S = 10^{-2.5}$ M if the assemblage formed at higher pH. Values as low as $\Sigma a_S = 10^{-4.0}$ M are unlikely because at 350° C the pyrite field would shrink to an unrealistically small area (Fig. 12.2A). $\Sigma a_S = 10^{-3.0}$ M has therefore been adopted to quantify other fluid parameters.

Constraints On pH

Albite-muscovite equilibria impose the best constraints on pH, but the lack of paragenetic control adds a large amount of uncertainty. As a general point, chloride-metal complexing at temperatures >200 ° C implies acid pH (Pottorf & Barnes 1983).

At 350° C a minimum pH of 3.91 is calculated for the muscovite/albite transition, using the conditions of 3.0 M NaCl, and 0.5 M KCl, parameters chosen to reflect the likely high ionic activity of the Starra brines if rock evaporite was present. The equilibria are listed in Appendix 10. Albite and chlorite are the stable alteration silicates. However, recrystallised muscovite (presumably after sericite) occurs on the margins and in the interiors of hem-mag-py±cpy veins, in contact with albite, but not in the dominantly albitic alteration matrix. In these veins, pH must have been less than 3.9, at T = 350° C. Muscovite is absent from the mag-cpy-py veins, suggesting that the peak ore fluids had pH > 3.9, or were undersaturated with respect to K. Hem-py-musc-albite veins, thought to have formed below 250° C, are calculated to have had a maximum pH of 5.1, at an arbitrary T = 200° C.

The solubilities of calcite and barite may also be useful guides to pH (Fig. 12.2A). The calculated stability of calcite is strongly dependent on the assumed $[Ca^{2+}]$. It is likely that sub-surface carbonate dissolution would have provided abundant Ca^{2+}, as is the case for the modern saline Salton Sea geothermal field fluids which contains ~ 0.7 M Ca^{2+} (Henley et al. 1984, McKibben & Elders 1985). $[Ca^{2+}]$ of between 0.01 and 0.50 M provide a minimum calcite stability limit of pH = 2.9 to 4.2 at 350° C. It is not surprising, given these low

solubilities, that minor carbonate is commonly associated with footwall alteration and auriferous ironstone.

Given the assumed conditions, the assemblage albite-muscovite in hematite-bearing veins indicates a local pH of ~4, which may have increased in the surrounding albite-bearing alteration zone.

Salinity

Salinities greater than 26.2 wt. % equivalent are documented in Chapter 3 for primary pre-metamorphic fluid inclusions at Area 222, which are intimately associated with hematite-quartz alteration. Unfortunately these have proved too small for thermometric work to date. Peak metamorphic (D2(MP)) inclusions at Starra are dominantly CO_2-rich, whereas retrogressive brittle-ductile and brittle-regime-associated inclusions are saline, up to 51 wt.% equiv. NaCl (see chapters 4 and 10). Furthermore, peak metamorphic fluid inclusions at Trough Tank include saline, as well as pure high-density CO_2 types. Hence, whether the ores at either location formed epigenetically or syngenetically, the ore fluids were probably saline, although the relative activities of the individual brine components may have varied.

Evaporite pseudomorphs in shallow water sediments, chlorine-bearing metamorphic minerals, and abundant hydrothermal albite (promoted by high Na^+/H^+; Fig. 12.2B) are all considered to be indirect evidence of high salinities during sedimentation, diagenesis, metamorphism and ore formation. A more specific strand of evidence supporting a high a_{Cl^-} during ore formation, is the domination of the ores by elements with enhanced solubilities in chloride-rich solutions. Those which complex directly with Cl^- are Au, Cu and Fe (Crerar & Barnes 1976, Kwak et al. 1986, Huston & Large 1989). More controversial is the effect of salinity on W solubility: do the high W levels at Starra imply high salinities? Bryzgalin (1976) and Foster (1977) experimentally found a strong correlation between salinity and W content in acid KCl and NaCl-rich fluids between 265° and 530° C (1 – 2 kb). Wesolowski et al. (1984) considered this correlation was due to an inhibition of polymerisation by NaCl at hydrothermal temperatures, rather than chloride complexing or ion-pairing. Most recently, Wood & Vlassopoulos (1989) proposed that high salinities favoured the ion-pair $NaHWO4^0$ (or a similar alkali complex) in the presence of either NaCl or NaOH. Thus, for the first time, the enormous range of depositional conditions attributed to tungstates can be understood in terms of tungsten speciation, particularly considering that WO_3 is also highly soluble in pure water (Wesolowski et al. 1984, Wood & Vlassopoulous 1989). The large solubility of WO_4^- reduces the problem of its presence in a particular system not to one of transport, but to an appropriate source and efficient trap. It follows that the anomalous W at Starra is not directly indicative of high salinity fluids, although this is a very likely possibility.

On the above evidence, a salinity of 3.0 M NaCl has been assumed in this study, because it is the highest salinity value for which there is abundant relevant thermodynamic data available. The actual fluid value may have been even higher.

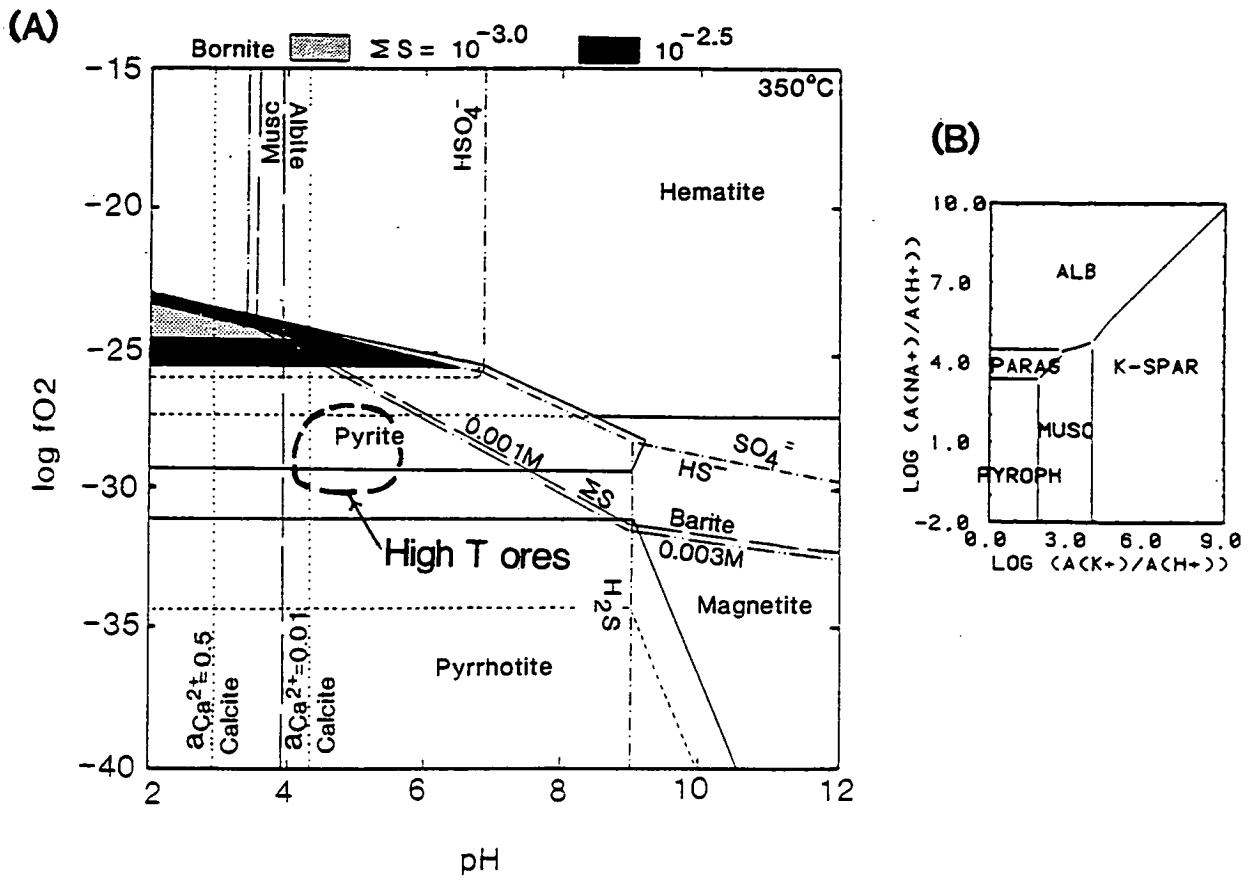

Figure 12.2A *LogfO2 - pH diagram indicating the stability of bornite at $\Sigma S = 10^{-2.5}$ and $10^{-3.0}$. Accessory bornite occurs in some footwall alteration assemblages and some Au-rich ironstones. The stability field of the sulfur species are also shown. (NaCl = 3M, K = 0.5M, Ca = 0.5M, $a_{\Sigma C} = 10^{-1.0}$ (which $[H_2CO_3]$ approximates in solution), $a_{\Sigma Ba} = 10^{-4.0}$ (as $BaCl^+$). The field of barite may be more limited than is shown on this diagram because of the greater stability of sulphate-alkali ion-pairs in brines (Henley et al. 1984). " High T ores" corresponds to magnetite-Au-Cu ores. (Fe-S-O phase boundaries: names apply to $\Sigma S = 10^{-2.5}$ M conditions, which are drawn as continuous lines; $\Sigma S = 10^{-3.0}$ M boundaries are dashed). 12.2B Equilibrium activity diagram in the system $HCl-H_2O-(Al_2O_3)-K_2O-Na_2O-SiO_2$, 300° C, 0.086 kbar, after Bowers et al. (1984).*

Oxidation State

The dominance of magnetite and hematite indicates that the Starra ironstones were deposited at high f_{O2}. The oxidation state has been determined on an f_{O2}-pH diagram in the Fe-Cu-S-O system at 350° C, using phase stabilities calculated from Bowers et al. (1984) and others, specified in Appendix 10.

Hem-mag-py-musc±cpy±bornite veins formed at 350° C, had an f_{O2} range of ~ -24 – -28 (Fig. 12.2A). The assemblage mag-cpy-albite±py which characterises the most gold-rich ironstone, and the underlying intense alteration, must have formed below the stability field of hematite at f_{O2} ~ -27.5 – -30: the absence of barite conforms to this range (Fig. 12.2A).

A Summary of the Ore Formation Conditions

Footwall veins and alteration at Starra formed under a spectrum of conditions, from high salinity fluids. Hem-py-musc veins, and pyrite porphyroblasts which commonly contain hematite blades, are interpreted as lower temperature products with T < 250° C, a_S ~ 10^-

$^{3.0}$, f_{O2} ~ -38 to -36. Similar constraints are suggested for proximal and distal barren hem-py ironstones. Mag-hem-py-cpy-musc veins were formed at T = >300° C, pH < 4 and f_{O2} ~ -24 to -28. The presence of only albite and chlorite in mag-cpy-scheelite ± py veins and ironstone, suggests that the precipitation of Au was accompanied by decreasing f_{O2}, and decreasing pH. Gold-rich mag-cpy ± py ironstones were formed at T >300° C, pH = > 4 and f_{O2} = -27.5 to -30 (Fig. 12.2A).

The stability of albite and scheelite in the ores is evidence that NaCl and $CaCl_2$ were important brine components. Au, Cu and Fe were likely to have been transported as chloride complexes, whereas W was present as $NaHWO4^0$, or a similar alkali ion-pair.

GENESIS

Several genetic hypotheses for Starra mineralisation have been proposed to date. Laing et al. (1988) and Switzer et al. (1988) have proposed the only detailed published model, a metamorphic/tectonic upgrading origin for ironstone, with later addition of Au and Cu to form the ore deposits. In this model, the mineralising event commenced during early D2(MP) with coarse foliation-parallel magnetite development. Au-rich, metamorphic, saline fluids were introduced into fold hinges and fractures, with Au-pyrite deposition occurring by magnetite-sulphidation. Chalcopyrite was introduced during D2, altering pyrite, filling fractures in magnetite and pyrite, and altering magnetite to hematite. Bedded ores were derived by fluid percolation from the hinge, thus forming "massive"(hinge-related) and "laminated" (limb-related) ores.

Alternative Hypotheses

Two models are proposed for testing. One is a modified structural-epigenetic model (incorporating features from Laing et al. (1988), Switzer et al. (1988) and aspects of epigenetic BIF ores (MacDonald 1983, Phillips et al. 1984, Gilligan & Foster 1987, Groves et al. 1987); the other is a syngenetic-volcanic model. The structural model of Laing et al. (1988) has been modified principally because of the strong evidence for a sedimentary origin for the ironstones, and because the folds on which several deposits are localised are considered in this thesis to be D2(LP) generation, not D2(MP).

A. Structural-metamorphic Hypothesis:

During D2(LP), transcurrent motion on the D1 shear generated open sinistral folds in hematitic BIF (Fig. 12.3), into which metamorphic fluids were focussed. Initially fluids were hinge-controlled. The fluid was in equilibrium with magnetite and pyrite (see previous discussion), depositing Au by the sulphidation of magnetite in the dilatant zones of existing iron formation. As shearing continued, brecciation corridors opened in transposed dextral fold limbs, and importantly, reverse-motion shear-fractures commenced to open and rotate to dilatancy. The latter provided a means to move metamorphic fluid across the shear zone to its eastern margin, and to deposit Au in both limb and hinge sites in the ironstone. Syn-shearing hydrothermal activity favoured the sulphidation process by continually exposing new magnetite grains to the invading fluids. The relevant reaction modified from Neall (1987) is:

$$3Au(HS)_2^- + Fe_3O_4 = 3Au^0 + 3FeS_2 + 3H_2O + 1/2O_2.$$

Static infiltration of fluids along brittle structures is not likely to be as effective as syn-shearing infiltration to form large orebodies, because of self-sealing of fluid conduits (Gilligan & Foster 1987).

This model attempts to explain the asymmetry of alteration by focussing fluids from west to east, depositing them against a north-south chemical and physical barrier.

B. Syngenetic Hypothesis:

A north-south, second-order, 50 km long rift or pull-apart graben developed in Kuridala Formation-time, initiating basaltic volcanism along its axis with the commencement of Staveley Formation deposition. Fault-bound margins shed shallow-water detritus into a locally deepened segment, where felsic pyroclastic volcanism and Fe-rich exhalation occurred. At the cessation of volcanism a hot saline fluid (estimated at >300° C based on the previous discussion) exhaled into a sulphur-poor, oxidising, saline basin, with the consequent deposition of magnetite-hematite-pyrite-chalcopyrite proximal to vent-sites, and hematite-pyrite distal to them (Fig. 12.4). Chlorite schist was produced both by low temperature exhalation and as an alteration facies. Quartz was deposited as a proximal component. Some exhaled products were carried as low temperature complexes to the shallow shelves of the basin, and deposited distally by solubility changes induced during evaporation.

During deformation the trough became a locus of shearing, with initial development of an extensional detachment zone as proposed by Laing et al. (1988). Very high grade ore pockets were formed by remobilisation into dilatant sites such as skarns, boudin-necks during D2(MP), and into low-angle reverse shear veins during D2(LP).

Discussion

It is felt that many of the features of the ore deposit style are inconsistent with the hypothesis of Laing et al. (1988), Switzer et al. (1988) or model A above. The important inconsistencies are:

(1) In the logic of these models, D2(LP) folds on which some orebodies are localised were instrumental in the ore formation. However, the ores are clearly remobilised into D2(MP) boudins and folds at Area 251, thus ore formation predated D2(LP).

(2) The plunges of the major orebodies are also inconsistent with their formation during D2(MP). Fig. 12.5 illustrates the expected location of ores if they formed from fluids circulating through D2(MP) dilatant zones. Shallow plunges would be predicted for these, with ores concentrating in D2(MP) hinges, on bedding/cleavage intersections, in boudin necklines, and in secondary fracture zones. In fact, the present distribution of ore is most consistent with emplacement prior to D2(MP), with some subsequent elongation in the D2(MP) maximum extension direction.

(3) The dominant textures are recrystallised intergrowths of pyrite, chalcopyrite and magnetite, implying these phases *predate* peak (D2(MP)) metamorphism, although this does not rule out structural introduction during early D1-D2(MP). Areas where *coarse* replacement textures occur are now known to be confined to D2(MP) zones of dilatancy, or D2(LP) tension gashes, or D2(MP) metasomatic hangingwall calc-silicates. Gold occurs not only in magnetite, pyrite and chalcopyrite, but also in quartz and hematite. In places these minerals form bedding-conformable layers indicative of an original sedimentation control, or faithful layer replacement.

(4) Some regional low to moderate-grade Au enrichment of iron formation occurs well away from shear zones (Chapter 6), which is difficult to explain with structural/metamorphic models. In addition, gold-BIF prospects such as Trough Tank and Blockbuster cannot presently be related to shear zones.

(5) Recent literature (Fyon et al. 1983, MacDonald 1983, Phillips et al. 1984, Groves et al. 1987; Saccocia 1987, Foster & Gilligan 1987, Lhotka & Nesbitt 1988, Perriam et al. 1988) has shown that finely laminated stratabound gold ore, once the foundation of an exhalative origin, can form by replacement, concentrating at the point of intersection of epigenetic veins with the BIF. Oxide-sulphide assemblage boundaries in this style are sharp. At Starra no sharp boundaries between different facies occur; instead a gradation exists between Au-rich and Au-poor ironstone. It seems difficult for Archean-style BIF-replacement to form the *disseminated* sulphides and gold that characterise low-S ironstone systems. For this to occur, a reduced epigenetic fluid must be invoked that by-passes numerous suitable oxide reactants before depositing at an isolated location in the BIF. Even in instances of fluid infiltration during shearing (Gilligan & Foster 1987), the resulting orebodies consist of massive sulphides close to an intersecting fluid conduit, with very limited adjacent disseminated sulphides. The task is likely to be even more difficult for the low sulphur fluid envisaged for Starra. This fluid is asked to by-pass both magnetite and hematite, both theoretically available for reduction, as well as high $Fe_2O_3^{tot}$ (14 – 18%) tholeiitic dolerites, emplaced prior to or during late-D2(MP) in the footwall. This problem also afflicts the amphibolite source proposal of Kary and Harley (in press).

(6) Coupled carbon-oxygen isotope trends in Starra and Trough Tank ironstones fall on the same unique line, which is markedly divergent to that of calcite deposited from deformational fluids in the Starra Shear, and cannot be linked genetically to them.

(7) Circumstantial evidence: Starra ironstone REE patterns are very different (low ΣREE, HREE enrichment) to those of clearly epigenetic magnetite bodies close by at Mount Elliott and Swan, approximately 20 km to the north (very high ΣREE, LREE-enriched). The sulphur isotopic character of the two stratiform ores also differs from sulphur within three shear-systems sampled north, west and east of Starra (Mt. Elliott, Answer, Mount Cobalt).

(8) Sulphur isotope values of chalcopyrite and pyrite favour their formation as part of one depositional system, rather than by the alteration of pyrite by Cu-bearing fluids to form chalcopyrite, as proposed in the structural model of Switzer et al. (1988).

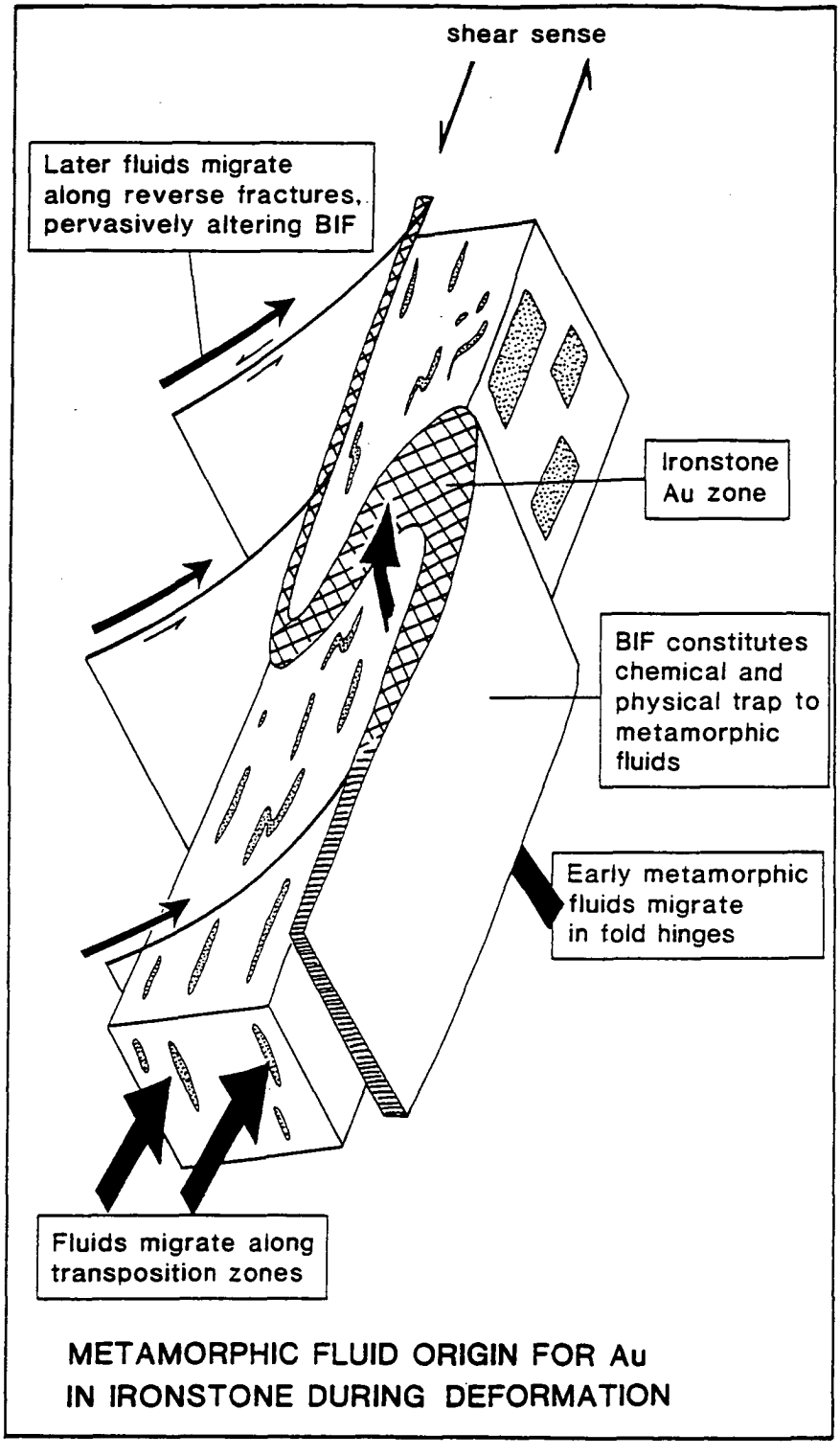

Figure 12.3 *A sketch of Model A, a structural-metamorphic model for ore deposit formation. Gold-rich solutions are introduced during the progressive shearing of D2(LP). The focussing of these solutions across the Starra shear is facilitated by the development of dilational reverse fractures, with deposition by magnetite/hematite sulphidation. Some disseminated sulphides in ironstone could form by the trapping of fluids on microfractures during continued shearing.*

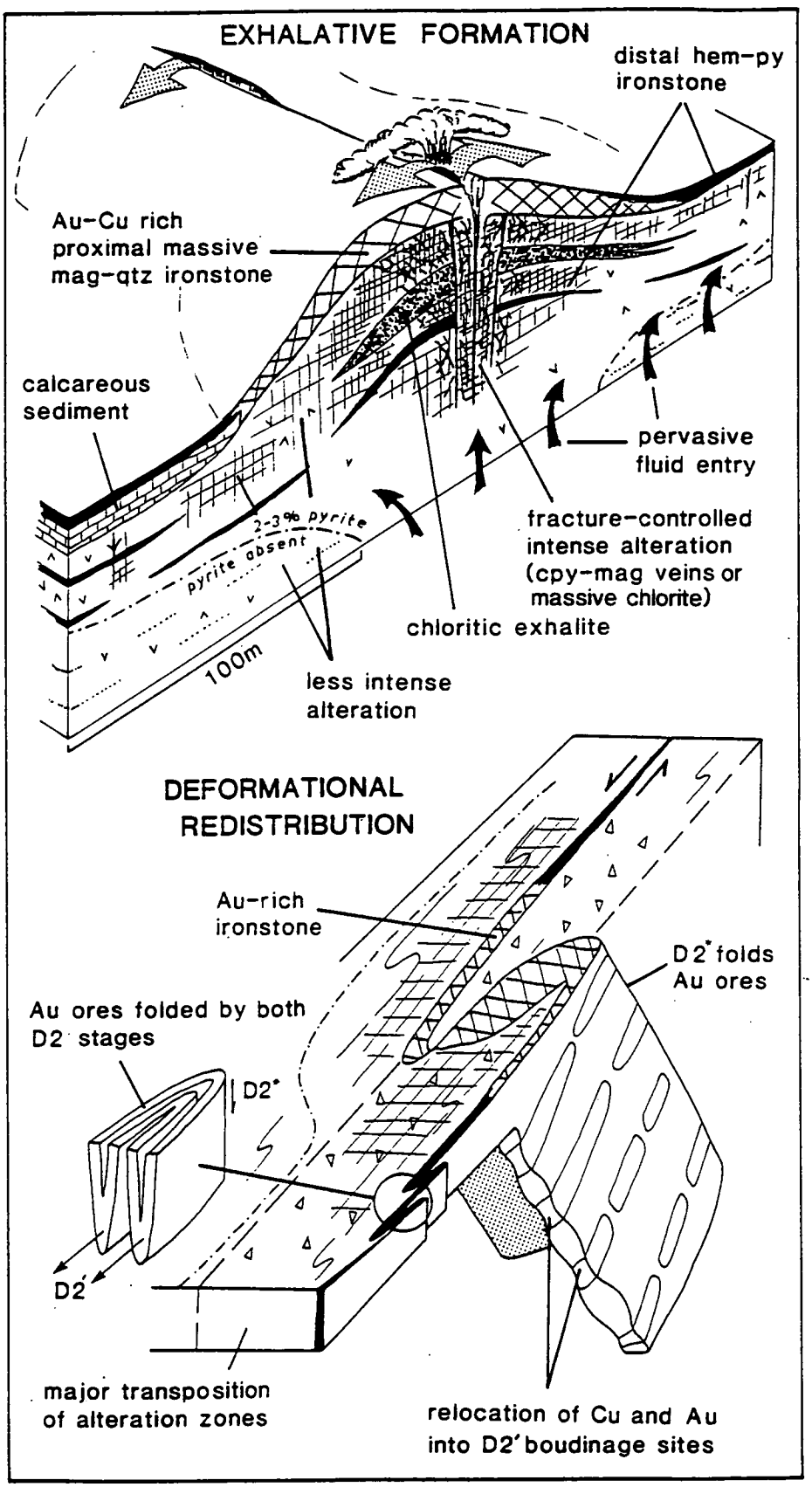

Figure 12.4 *Model B, in which ores are derived by exhalation of a hot, oxidised, saline fluid. Some sulphides are subsequently remobilised during D2(MP) and D2(LP) into boudin-necklines and reverse fractures. (D2' = D2(MP), D2* = D2(LP)).*

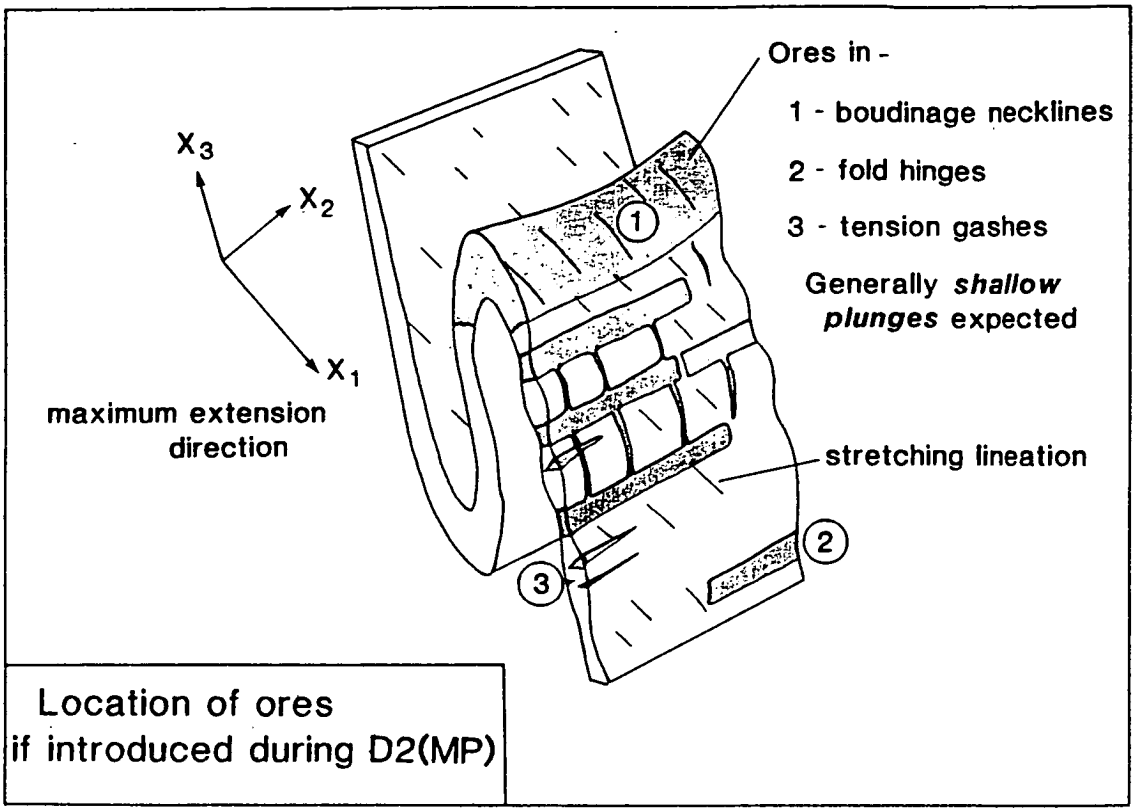

Figure 12.5 *A sketch of the hypothetical location of replacement sulphide-gold ore if it was deposited by metamorphic fluids in diliatant sites during D2(MP). Generally shallow plunges are predicted for these ores.*

(9) The tabular form of ironstone over large areas is unlike that of known magmatic/metamorphic replacement oxide ores. These tend to have an irregular interfingering form if located close to a magmatic contact (Kisvarsanyi & Proctor 1967, Forster et al. 1984, Rose et al. 1985, Ewers & Sun 1988), or spindle-shapes if hosted within folds or cleavage-bedding intersections, such as the Au-Cu-magnetite lodes of Tennant Creek (Large 1975, Large & Wedekind 1988, Wedekind & Large in press) or Mount Elliott, (Dimo 1975). The shear-hosted White Devil magnetite Cu-Au-Bi ores of Tennant Creek (Nguyen et al. 1988) are tabular within the shear, but in detail are gradational to chlorite schists and magnetite-quartz veins.

A syngenetic origin is preferred because it meets most of the criteria advanced by Groves et al. (1987). These are summarised below :

(1)*Predeformational character*: Sulphides and iron-formation are folded in the earliest recognisable deformation event (D2(MP)), although this evidence is not in itself definitive. An important piece of evidence are randomly oriented hematite and silicate inclusions in footwall pyrite cores, indicating that pyrite growth predated the formation of any foliation.

Long axes differ between the Starra ore-bodies; some are at odds to the expected structural controls of D2(MP) and D2(LP). The contoured Cu/Au ratios and Au metal factor in Trough Tank BIF also form sub-linear trends which are not aligned with the inferred D2 fold axis or stretching direction, as would be expected if these trends were deformationally-controlled.

(2) *High background gold*: Background Au values in distal BIFs are variable (1 – 1200 ppb) whereas, oxide facies BIFs invaded by epigenetic fluids described by Groves et al. (1987) and Fyon et al. (1983) are generally low, <2 ppb – 8 ppb. Regional metal enrichment is however a typical feature of exhalites.

(3) *Asymmetric alteration.* This is a common feature of proximal exhalative deposits, whereas wall-rock alteration in epigenetic BIF deposits surrounds the ore and is carbonate-dominated (Phillips & Groves 1984, and Groves et al.1987). Even under the premises of model 'A' some symmetrical magnetite-pyrite alteration would be expected in the hangingwall of the Starra Shear, but is not found.

(4) *Location at a volcanic-sedimentary interface*: The occurrence of gold-bearing ironstone at a volcanic-sedimentary interface may be more than coincidence. Sedimentary iron formations in the middle Proterozoic (1800 – 1200 Ma) are uncommon (James & Trendall 1982, Holland 1984), requiring special circumstances of an iron source or an Fe-concentrating mechanism. (This time-control may relate to the postulated rising of atmospheric oxygen to levels at which ferric iron was fixed at the earths surface (Borchert 1960, Garrels 1973, Holland 1984, Garrels 1987), although this concept has its opponents (Dimroth & Kimberley 1976, Palmer 1987)). The Eastern Succession is unique in the Mount Isa Inlier in hosting 3 major middle Proterozoic jaspilites: exhalative Pegmont-style BIFs (Stanton & Vaughan 1979), the Overhang Jaspilite, and the Starra Iron-formation Member. The isolation of each within much greater thicknesses of sediment compels a specific genetic circumstance, such as the maintenance of an iron supply. One logical source at Starra is exhalation of iron, and other metals, from the underlying volcanics and epiclastics, as has been postulated for many other iron ores associated with volcanism (Quade 1976, Krautner 1977, Appel 1982, Gross 1980, Simonson (1985, 1988), Sims & James 1987).

(5) *Zoning of mineralogy and geochemistry*: Ironstone zoning from magnetite-chalcopyrite-quartz, to hematite-magnetite-pyrite and ultimately to dominantly hematite, is compatible with the changing physico-chemical conditions expected around an exhalative vent.

(6) *Geochemical ratios*: Fyfe and Kerrich (1983) and Groves et al. (1987) suggest that bisulphide-dominated epigenetic fluids produce ores with low base-metal contents relative to Au, quoting Cu ppm/Au ppm = 4, Zn/Au = 24 for the Vubachikwe deposit in Zimbabwe. They have elevated As, Sb and/or Bi contents. By contrast, ore-grade sediments with a major volcanic-exhalative component have Cu/Au ratios in the thousands, attributed to chloride-complexing. The Area 251 orebody has a Cu/Au ratio of 5074. Orebody 257 has an average ratio of 1454, although Zn/Au for both are around 4; Trough Tank has very similar ratios. The high Cu/Au ratios in the Starra-Trough Tank deposits are unlikely to be a function of metamorphic grade, because one is upper Greenschist facies, whilst the other is upper Amphibolite grade (higher Cu/Au ratios characterise epigenetic deposits in higher metamorphic-grade domains; G.N. Phillips, pers. comm. 1988).

The presence of chalcopyrite and Au, and the relative absence of As, Sb and Bi, implies that chloride transport dominated the ore fluid (Huston & Large 1989; Large et al., in press), as is typical of volcanogenic massive sulphide systems.

(7) *The character of footwall alteration:* The oxidation state of footwall veins was similar to that of overlying auriferous ironstone. It follows that an epigenetic replacement model, invoking ironstone replacement by oxidation-reduction reactions with the vein fluids, is inappropriate. This is in contrast to Archean BIF-replacement deposits, in which the oxidation state of fluid and trap are very different (Phillips & Groves 1984, Foster & Gilligan 1987).

Similar mineralogies are, however, encountered in both the footwall stringer veins and exhalites of many VMS deposits (Franklin et al. 1981, Eldridge et al. 1983, Frater 1985).

A DETAILED SYNGENETIC ORE GENESIS MODEL

The Formation of Oxidised Precipitates on the Seafloor

A number of mechanisms have been proposed to form oxide precipitates on the seafloor during hydrothermal activity. These include low temperature (<150° C) exhalation producing hematite-quartz "tetsusekiei" mantles on Kuroko-style massive sulphides (Kalogeropoulous & Scott 1983), oxidation of sulphides in the water-column during plume fall-out in oxic waters (Lydon 1988), oxidation of sulphides at the sediment/water interface or during diagenesis (as observed in the Red Sea Deeps: Pottorf & Barnes 1983), bacterial fixation of oxides around low temperature vents (Juniper & Fouquet 1988), and exhalation of oxidised fluids (Large 1977, Frater 1983). These mechanisms represent an interplay between the oxidation state of the hydrothermal fluid, and the oxidation state of the water-column.

Above-seafloor oxidation mechanisms were unlikely for either Starra or Trough Tank, because vein oxides occur up to 100 m below the probable palaeo-seafloor. As discussed previously, these assemblages require deposition from oxidised fluids (e.g., Large 1977).

The features which the ore-forming fluid must principally explain are the transition laterally within ironstone from mag-cpy (Si/Fe ~ 0.27), to mag-hem-cpy-py, to hem ± py (Si/Fe ~ 0.08) assemblages, and the distal presence of massive hematite lenses which grade to cherty iron formation and tourmalinite. A further ore-feature is rapid deposition, which is required to explain the very low concentrations of clastically-concentrated elements such as Zr, TiO_2 and Al_2O_3 in ironstone (Chapter 6). To explain these features, the solubility of iron and silica was examined.

A Review of Iron Solubility

Theoretical and experimental studies of iron have shown it to be readily soluble as chloride complexes in many geological fluids. Fe^{2+} dominates in the range 50 – 200° C, $FeCl^+$ from 200 – 300° C, and $FeCl_2^0$ > 300° C (Barnes 1979, Hemley et al. 1986), although in the rare situation of Cl^--absent waters, hydroxy and organic complexes gain importance (Seward 1977, Crerar et al. 1985, Hennet at al. 1988); Fe^{3+} ions are only present in very

oxidised solutions (Barnes 1979). Iron solubility is mainly affected by temperature, pressure, pH and chloride content, with lesser but still significant influences of f_{O2} and f_{S2} (Crerar et al. 1985, Whitney et al. 1985, Hemley et al. 1986) (Fig.12.6). The distinct reduction of the solubility of $FeCl_2^0$ with increasing pressure lead Hemley et al. (1986) to conclude that ascending hydrothermal fluids were capable of scavenging Fe if cooling near-adiabatically. Theoretically and experimentally Fe is very soluble in hydrothermal fluids; Crerar et al. (1978) found that Fe solubility as a chloride complex increases dramatically beyond 250° C, transporting tens to thousands of ppm Fe. Very high Fe values in some modern saline hydrothermal systems support this. For instance, McKibben & Elders (1985) document 93 – 4200 ppm Fe in the saline geothermal waters of the Salton Sea.

At low temperatures (< 50° C), iron is soluble as Fe^{2+}, or as $Fe(OH)^+$ at alkaline pH. However, in the present day, f_{O2} is too high and pCO_2 too low to permit significant Fe^{2+} transport in the framework of the equilibria

$$FeCO_3 + H_2O + CO_2 = Fe^{2+} + 2HCO_3^- \quad \text{(Garrels 1987)}$$

with the result that the modern oceans do not contain appreciable Fe in solution. However, Whitney et al. (1985) observed that in high temperature aqueous experiments, Fe^{2+} remained in solution after quenching. They suggested this metastable behaviour would also occur in nature, and could explain the considerable distances separating source vents from some stratiform ferruginous cherts.

A Review of Silica Solubility

Under marine and most hydrothermal conditions, SiO_2 is soluble as monosilicic acid, $Si(OH)_4$ (Holland & Malinin 1979). The solubility of quartz at 25° C (1 bar) in seawater is 4.4 ppm, whereas amorphous silica is 56 ppm, and silica gel 114 ppm (Kastner 1979). In the modern seas, biogenic activity maintains general silica undersaturation, whereas Precambrian marine-waters likely had silica contents which were close to saturation, with the result that even slight evaporation would have lead to amorphous silica precipitation if feed-water values were close to the present-day (60 – 70 ppm; Garrels 1987).

Hydrothermal solutions which have interacted with typical continental crust in the range 150 to 350° C are close to quartz saturation, carrying 100 to 1500 ppm silica (Rimstidt & Barnes 1980). Ideal silica solubility is dependent on temperature and pressure, but virtually independent of pH (below pH = 8; Fournier (1983a)). Silica solubility is slightly enhanced by increases in ionic strength. These features have permitted the formulation of silica geothermometers based on the silica content of geothermal fluids (Truesdell 1976), also allowing the approximation of silica concentrations without consideration of other aqueous species. The temperature and pressure dependence of quartz solubility is illustrated in Fig. 12.7a. Below 1 kbar, an area of retrograde solubility has special implications for geothermal systems, because heating solutions that pass through this region will deposit quartz, reducing permeability (Kennedy 1980, Fournier & Potter 1982). The effect of added salt is to slightly increase the peak temperature of retrograde solubility, promoting more dissolved silica (Fig.

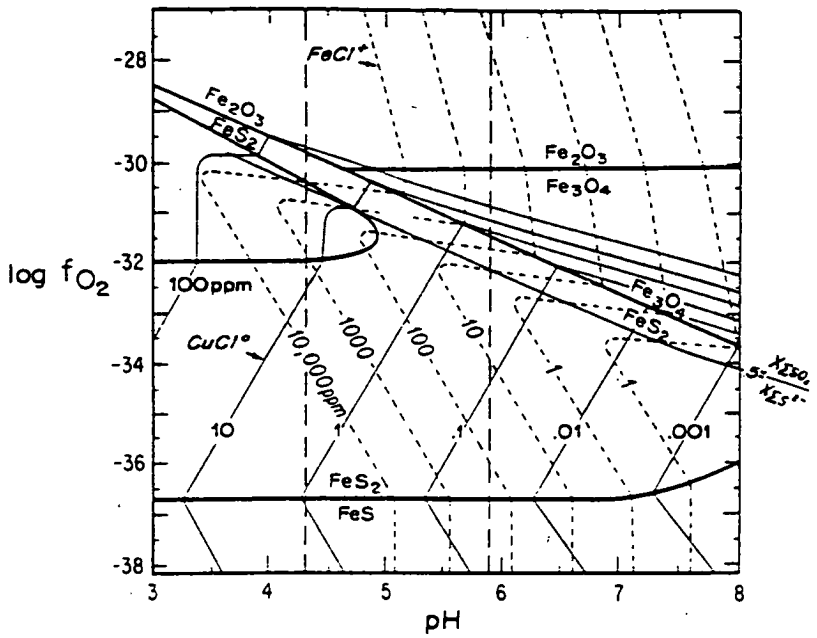

Figure 12.6 *An fO_2-pH diagram after Franklin et al. (1981), with mineral stability fields, and metal solubility contours for copper ($CuCl^0$-dominant species) and iron ($FeCl^+$ dominant species) at T = 300° C, m Cl^- = 0.25, m S = 0.05, aK^+ = 0.02. This diagram indicates the extreme solubility of iron under realistic geological conditions.*

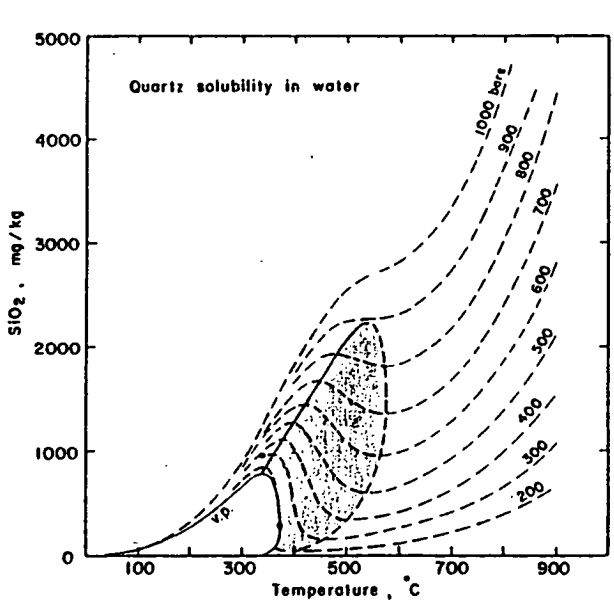

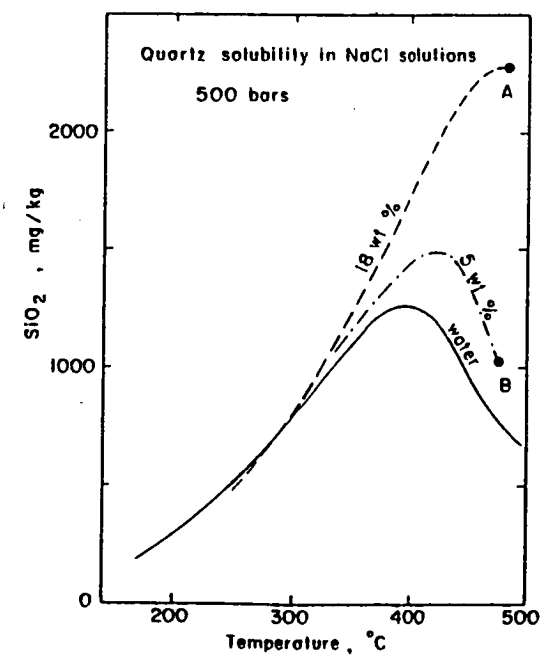

Figure 12.7a *Calculated solubility of quartz in water at the indicated pressures, after Fournier (1983). The shaded area emphasises the region of retrogade solubility.*
Figure 12.7b *A graphical presentation of the effect of salts on silica solubility. Salinity is an important factor above 300° C.*

12.7b). Boiling of such saline solutions would lead to rapid silica deposition, because although boiling increases the fluid salinity, this is insufficient to accommodate the tandem increase of SiO_2 partitioning into the fluid during the rapid exsolution of vapour (Fournier 1983a).

Whereas silica concentrations are predictable during rapid destabilising events, such as boiling, Rimstidt & Barnes (1980) have shown the importance of kinetic effects during simple cooling. SiO_2 precipitation increases in proportion to the available nucleation surface area, expressed as the ratio of surface area to the mass of SiO_2-bearing water. Where pluming hot fluids mix above the seafloor with cold seawater, the available surface area of other precipitating minerals is low, and dilution with undersaturated seawater is rapid, resulting in minimal silica precipitation. Ohmoto et al. (1983) suggest that low silica/sulphide ratios are good evidence that many massive sulphides formed from sulphides which precipitated above the seafloor during fluid-mixing, as well as constituting good evidence against boiling. In contrast, large amounts of silica are deposited in systems which are characterised by slow cooling and large available surface areas, such as the fractured stockworks below some VMS ores. Kalogeropoulos & Scott (1983) recognised that low temperature hematite-quartz "exhalites" must have formed by precipitation of silica on the many mineral surfaces within unconsolidated sediment and volcaniclastic debris. It follows that hydrothermal fluids dense enough to follow seafloor contours, such as Type I and II saline fluids of Sato (1972) (Fig. 12.9), and distal exhalites of Large (1977), are very likely to deposit more silica than turbulently-mixing fluids, such as Black Smoker ores.

A Model for the Concentration of Silica and Iron

This model is directed principally towards the features of the Starra ores. Differences with Trough Tank ores are dealt with separately.

Starra: Was Fluid Discharge Focussed or Dispersed?

Stringer-style oxide veinlets are pervasive in the Starra footwall, increasing in abundance towards the iron formation; major gold-bearing lodes are also associated with local intense chloritic alteration (Areas 257 and 244) or severe local iron-oxide alteration (Area 251; Fig. 12.8) The pervasive alteration is evidence of dispersed exhalation at many points, accompanied by focussed discharge beneath major ore bodies. Textural evidence was presented in chapter 3 for the growth of pyrite in unconsolidated sediment. A porous state of the altered medium could also account for the common bedding-parallel nature of stringer veinlets, and the disseminated pervasive nature of oxide alteration. Pervasive, layer-parallel sulphide growth is typical of the modern Salton Sea hydrothermal field in unconsolidated sediments (McKibben & Elders 1985), and stratabound sulphide deposits, such as Meggen, Rammelsberg, McArthur River and Mount Isa (Vokes 1969, Lambert 1976). In contrast, the presence of some consolidated rock during alteration is evidenced by brecciation in the intense oxide alteration zones below Area 251 (Fig. 12.8, Fig. 3.12D); these rocks may have

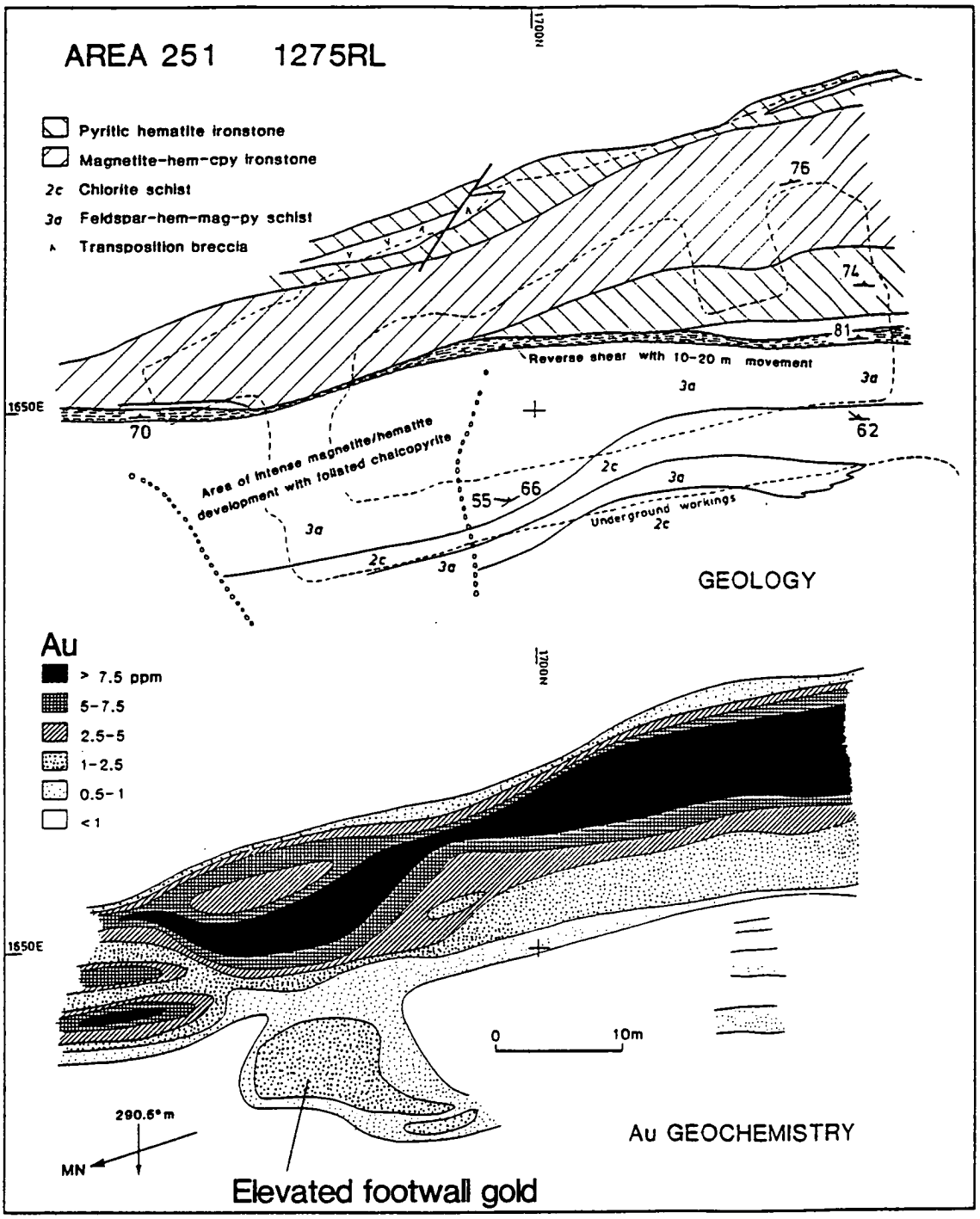

Figure 12.8 *Geology and geochemistry of underground development at Area 251, 1275 R.L. (relative level). The Au geochemical elevation in the footwall corresponds to a zone of intense oxide alteration. Au values were obtained from Cyprus Minerals 2m interval wallrock chip sampling. Locally subsequent sampling has indicated grades as high as 5 ppm in this area.*

originated as lavas within the felsic pyroclastic/epiclastic sequence. The chlorite alteration is attributed to elevated seawater-rock interaction in the stockwork, permitted by hydrothermal brecciation and seawater entrainment (Riverin & Hodgson 1980, Lydon & Galley 1986). Severely iron-oxide altered zones (Fig. 12.8) were similarly focussed discharge points, but were presumably sealed from the water column at an early stage by the deposition of hydrothermal precipitates.

Fluid Behaviour

The form of exhaled orebodies is controlled principally by fluid behaviour, and mode of discharge during exhalation, as argued by Sato (1972), Solomon & Walshe (1979), and Turner & Campbell (1987). This is mainly a function of fluid density: Sato (1972) suggested that very saline fluids (Type I) (Fig. 12.9) would remain more dense than seawater, and form density currents and brine pools, which result in thin, well-layered, tabular ores. (These could also form by dispersed hydrothermal discharge from many small vents, as is suggested for the Rosebery deposit of Tasmania by Huston (1988). Turner & Gustafson (1978) emphasised theoretical non-linear density-mixing for exhaled saline fluids, and thermohaline effects, which have since been demonstrated for Red Sea exhalation by Pottorf & Barnes (1983). More recently, Turner & Campbell (1987) have calculated that all fluids hotter than 300° C will be initially more buoyant than seawater, but if salinity is greater than ≈ 7% NaCl, will show a buoyancy reversal on mixing with seawater, forming Type II fluids of Sato (1972). Modern hydrothermal systems at mid-ocean ridges discharge in buoyant plumes conforming to Type III fluids of Sato (1972). Approximately 97% of the mineral load precipitates high in the plume during turbulent mixing, and is dispersed over a wide area. The remainder is incorporated into the sulphide mound, which owes its growth to the formation of anhydrite chimneys during the solubility decrease anhydrite experiences with heating to 130° C (Haymon & Kastner 1981). A small proportion of discharging fluid is trapped in the pores of the anhydrite wall, depositing sulphides across a steep temperature-pH gradient.

High-silica ironstone at Starra, which positively correlates with Au, precipitated closest to the vent at Starra. Following the logic of Ohmoto et al. (1983), their highly siliceous character is evidence that they did not form from a type III buoyantly-dispersing plume. At ≈ 350° C and high salinity, a type II reversing plume collapsing into a type I density current is most likely. A second possibility is the deposition of proximal silica by advective/conductive cooling in the outer part of a semi-mature oxide mound, sealing it, and therefore increasing intra-mound fluid-mixing. So-called seafloor "white smokers", precipitating barite, silica and pyrite, are thought to evolve in this way (Rona 1984, Peter 1986). While the latter alternative is attractive, its application is limited at Starra because no silica-rich footwall alteration occurs. Well-defined bands of quartz in the ironstone must have precipitated on the seafloor, rather than within a mound.

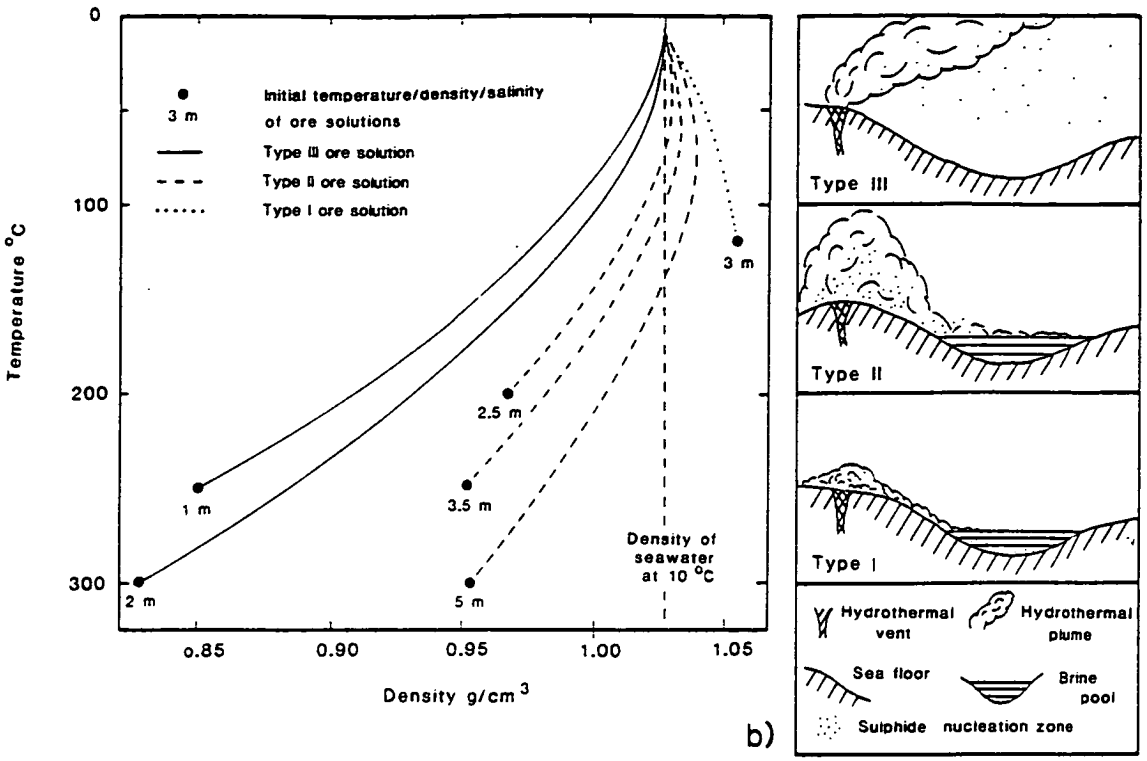

Figure 12.9 (left) *Density-temperature relationships of NaCl-rich hydrothermal solutions mixing with 10° C seawater, illustrating the behavior of Sato's (1972) three model fluids.* **(right)** *A schematic representation of the three fluid-types. The very saline Starra fluid is likely to have been a type 2 solution.*

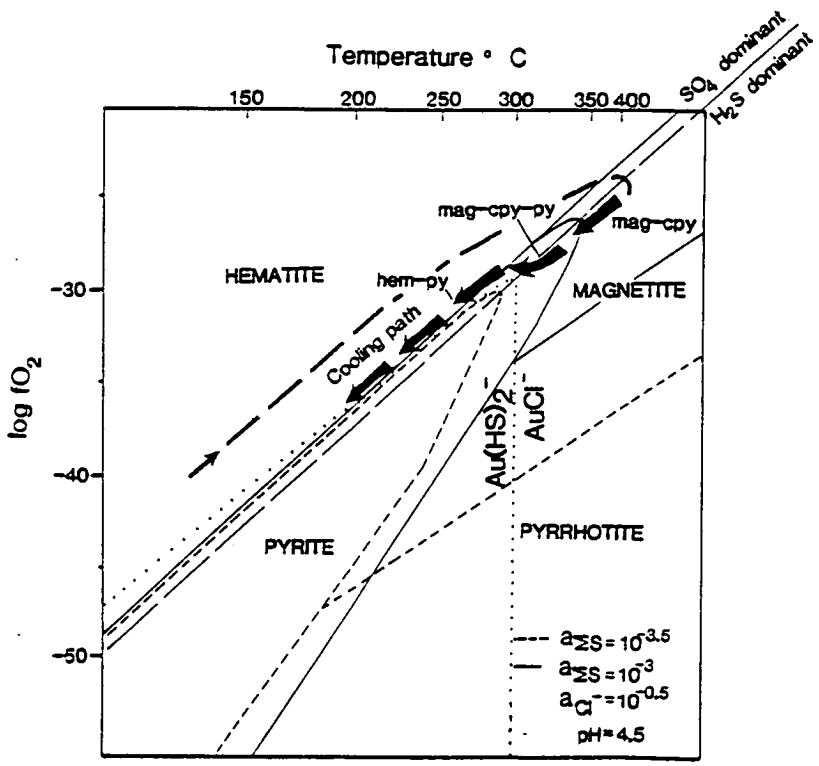

Figure 12.10 *A log fO_2 - temperature diagram illustrating the likely cooling path of the Starra fluids. This path has been used to calculate the metal solubility alternatives presented in Fig. 12.11.*

Iron/Silica Solubility Paths

On the basis of the previous discussion, two fluid paths were modeled to assess their effects on Fe and Si deposition. The methods of calculation are detailed in Appendix 12. Given the swarm of assumptions, this exercise was intended to be hypothetical, rather than reproduce the exact Si/Fe ratios of the ironstone. Both fluid paths were assumed to commence in the magnetite-chalcopyrite field, from single discharge points (Fig. 12.10) at 350° C, pH = 4.5.

The first path involves continuous linear-mixing of seawater (assumed at pH = 7, fO_2 = -64; Janecky & Seyfried 1984), as occurs in typical Type III fluid plume dispersal (Sato 1972), as a test of the conclusions of the previous discussion. This would result in a continuous increase in pH and fO_2 during cooling to move into the hematite field (A: Fig. 12.11). Even disregarding the aforementioned kinetic effects on silica precipitation, this path results in an accumulation of iron close to the vent, rather than silica.

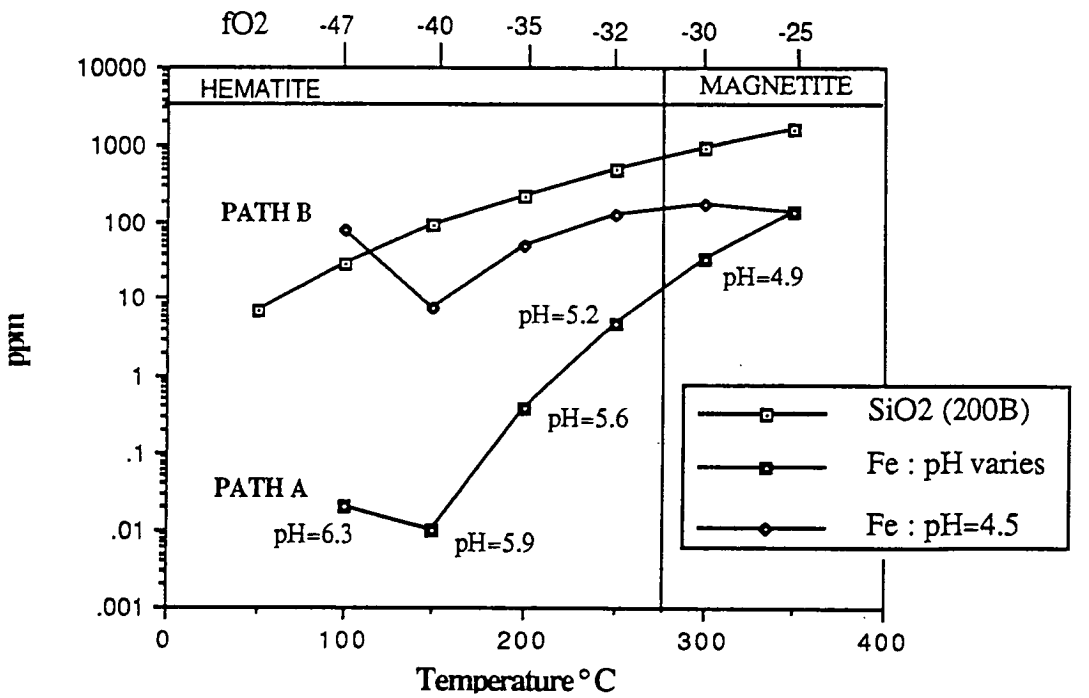

Figure 12.11 *Saturation paths for silica and iron under the specific conditions of NaCl = 3M, ΣS = 0.001M, and pressure = 200B. The diagram assumes Fe to be transported from the magnetite field into the hematite field as $FeCl_2^0$, $FeCl^+$ and Fe^{2+}. Silica transport is independent of pH on the diagram, whereas it is an important control on iron solubility. Path A models an ideal Fe-rich solution mixing linearly with cold seawater, hence regularly changing pH (Bouyantly dispersing plume discharge). Path B models an ideal Fe-rich solution which cools with no change in pH, such as a dense bottom-hugging brine. The relevant equilibria are documented in Appendix 12.1, with calculation methods in Appendix 12.2.*

The second path (B: Fig. 12.11) assumes that the fluid mixed with seawater in the 300 to 350° C range prior to collapsing on the vent as envisaged by Turner & Campbell (1987). It then cooled by conduction and slow mixing as a density current moving

downslope from the vent, maintaining a near-constant pH. This variation produces an initial decrease in silica solubility relative to iron, which could explain a ventward concentration of SiO_2. Silica would deposit when the collapsing plume contacted the sediment surface. It further predicts an area of retrograde Fe^{2+} solubility between 150 and 100° C, which would encourage the distal transport of iron.

The second path best explains the features of Starra ores, and is the more likely of the two options. It is envisaged that as the chemical sediment complex grew, rising fluids entered and reacted with it, for instance, by altering earlier hematite to magnetite, and pyrite to chalcopyrite. This could explain the common complete absence of pyrite in the magnetite-chalcopyrite zone.

Hematite lenses in the ore environment are envisaged to have formed at lower temperatures (50 – 150° C), where brines were ponded by topography, precipitating iron oxides during further cooling and slow mixing with the ambient oxidised waters. This process produced very thick but barren hematite lenses, such as those of Area 232, 244 and 276. The elevated W, Sn and Cu values in these rocks, compared to the distal barren lenses is attributed to their evolution from hotter fluids.

Distal hematite lenses, such as those of Area 186, and the Eastern Hematites, can also be explained in terms of path B (Fig. 12.11). Massive barren hematitic ironstones were deposited proximally around hot-spring vents in shallow sub-basins, at temperatures below those conducive of high gold and copper solubilities. Fe^{2+} is most soluble in saline fluids at 50 – 150° C (Fig. 12.11), favouring the accumulation of massive hematite lenses.

Modern seafloor studies recognise a group of low temperature iron oxide deposits which form by the bacterial oxidation of ferrous iron (Alt 1986). The hydrothermal fluids transport very little H_2S, therefore depositing only crystalline and amorphous iron oxides and opaline silica — not sulphides (Hekinian & Fouquet 1985).The chemistry of these deposits is similar that of Starra distal hematite lenses, as shown in Table 12.1.

	$Fe_2O_3^{tot}$	Fe/Si	Reference
Starra distal hematites	81.6 wt. %	12.8	This work
Oxide muds at 21° 30' S on the East Pacific Rise	65.8 wt. %	11.5	Juniper & Fouquet(1988)
Red Volcano seamount	71.5 wt. %	8.3	Alt(1986)
Core B,Santorini, Greece	47.9 wt. %*	8.6	Bostrom & Widenfalk (1984)

Table 12.1 *Average volatile-free iron and Fe/Si ratios for some modern seafloor oxide precipitates, compared to the average Starra distal hematite lens composition. (* not calculated on a volatile-free basis).*

Fluid and Metal Sources

Two types of fluid were present at the Starra mineralisation site. The first was the prevailing mid-Proterozoic waters occupying the free-standing water-column, and the second was the hot, metal-bearing, hydrothermal fluid. Hydrothermal solutions which are forming modern mid-ocean ridge Cu-Zn ores originate as seawater, chemically modified during fracture-controlled descent and subsequent fluid circulation close to a heat source. Oxygen isotopes from ironstone calcites, and the high salinities of Area 222 inclusions, suggests the circulating Starra fluid originated as evolved meteoric or marine water, with a connate contribution (chapter 10).

Abundant finely bedded hematite, and an absence of carbonaceous matter, provide evidence that the water column above the accumulating Staveley Formation was well-oxidised. Negative Ce anomalies in some southern Starra BIFs, and those at Trough Tank, are good evidence that conditions were marine. Salinities at the basin edge were locally high, but their effect on deeper water salinities is unknown. The best evidence for high salinities in the deeper water-column is the inferred diagenetic alteration of felsic volcanic detritus to Na-rich compositions, as discussed in chapter 5.

A circulation history, which buffered the fluid oxidation state to high f_{O2}, is suggested by the oxidised nature of lower temperature veins. The oxidation state of hydrothermal fluids is normally controlled by aquifer mineral reactions, for instance, oxidised seawater becomes highly reduced at mid-ocean ridges during basalt interaction by reaction between quartz, fayalite, magnetite and the fluid (QFM buffer: fO2 = -39.5 at 275° C; Large (1977)) (Humphris & Thompson 1978, Bischoff & Seyfried 1978, Mottl 1983). Oxidised epigenetic examples, such as the Tennant Creek hydrothermal fluids, maintained their high f_{O2} by reaction with hematite and magnetite-bearing turbidites and felsic volcanics (Large 1975). In a similar fashion, the oxidised sediments which typify the shallow-water evaporitic Mary Kathleen Group and upper Kuridala Formation, could have constituted efficient oxidising buffers. The presence of significant amounts of reduced basalt, ilmenite-bearing felsic volcanics or carbonaceous shale in the Starra footwall is discounted, because fluid reactions with these materials would have produced reduced rather than oxidised assemblages. The nature of the deep footwall at Starra can be inferred only in this way, because it has been removed by later tectonism. Other possible sources of oxidised fluids include highly fractionated alkaline granites (Forster et al. 1984, Wyborn 1988, Lyons 1988), or downward percolating basinal fluids (McKibben & Elders 1985, McKibben et al. 1988, Wilde and Bloom 1988).

The hypothetical fluid heating and cooling path is represented in Fig. 12.10. Heating (accompanied by leaching of iron and silica) followed a constant oxidised $\Sigma SO4/H_2S$ contour from 25 to 200° C in the hematite stability field. The $\Sigma SO_4^{2-}/H_2S$ ratio of the fluid then altered by (1)an increase in rate of reaction of the equation

$$SO4^{2-} + 2H^+ = H_2S + 2O_2 \text{ (Large 1977)},$$

in heating from 200° to 350° C, (2) anhydrite deposition during heating from T ≥ 150° C (Bischoff & Seyfried 1978), and (3) entrainment of deeper, more-reduced waters, evidenced by a component of oxidised organic carbon in ironstone calcite (Chapter 10).

McKibben et al. (1988) have proposed a model for the Salton Sea geothermal field which can be applied in a modified form at Starra (Fig. 12.12). An upwelling, reduced, metal-rich brine-diapir mixes with an overlying, oxidised, metal-poor fluid at an ascending interface. In this modification of the model, the lower fluid, in equilibrium with magnetite, breaches the sediment/water contact and deposits Au-rich ironstone. In the waning phase the system cools, the fluid interface subsides, drawing in cooler oxygenated waters, and forming late-stage hematitic veins. The hematite veins are most likely post-peak hydrothermal, because the pre-peak hematite veins would have been destroyed by the ascending brine diapir.

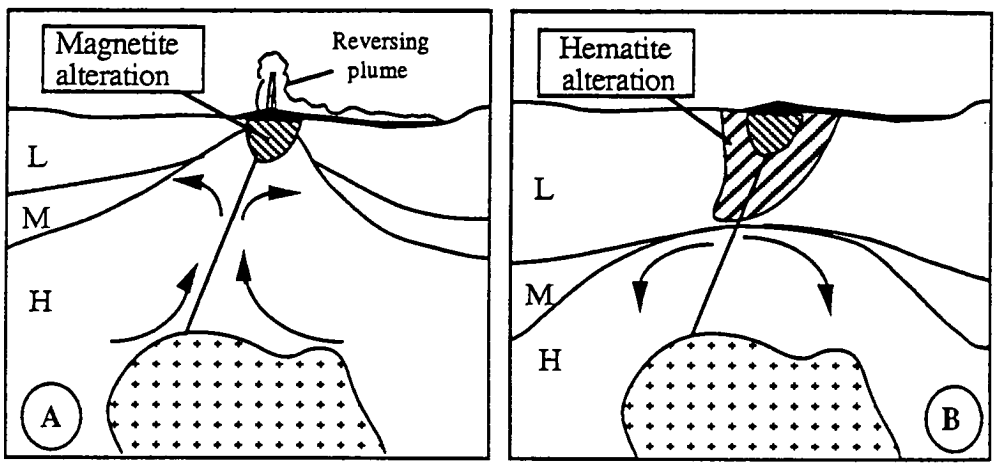

Figure 12.12 *A brine-diapir model for ore formation, modified from the uniformitarian approach of McKibben et al. (1988).* **(A)** *A brine diapir of hot saline fluid (H), driven by a rising pluton, ascends through a layer of intermediate-salinity fluid (M) to exhale magnetite-Cu-Au ore at the seafloor.* **(B)** *Upon cooling, the brine diapir descends, drawing in cooler oxidised waters (L) which form sub-surface hematite veins.*

The anomalous W and Sn in the ores could be explained by entrainment of magmatic fluids from the underlying heat source, or by alteration of W-rich detritus (Ririe 1989); the relative ease of W transport as an ion-pair has already been discussed. Cu enrichment is readily explained by leaching of typical oxidised shallow-water Mary Kathleen Group sediments, which are likely to contain elevated base metal background concentrations (e.g., Red Beds: Renfro (1974), Muir (1979)). Cu-enrichment throughout the region also may owe its origin to such a pre-concentration. However, even modest assumptions concerning average sediment Cu contents and degrees of leaching indicate that the Starra Cu tonnage can be accounted for by geologically reasonable depths of fluid circulation. The 8.8 X 10^{10} g of Cu in Area 251 can be produced by 10 % leaching of 11.7 km^3 of sandstone and shale containing average Cu contents (28 ppm, assumed density of 2.7 g/cc; Brownlow (1979)). This equates to a leaching cone with the formula $H = 11.2/R^2$, where H is the height of the cone in kilometres, and R is its basal radius (Fig. 12.13). A leaching cone of 2 km radius will

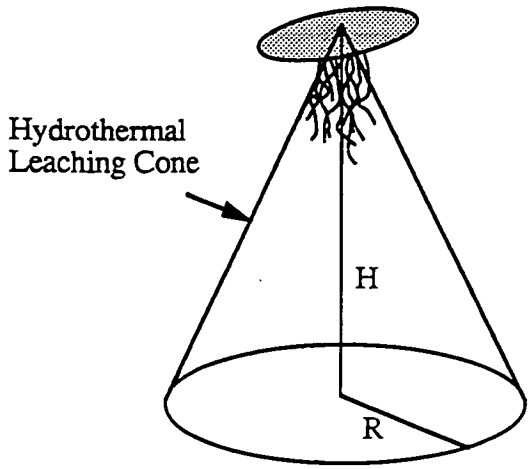

Figure 12.13 *A cone is one model for the shape of the hydrothermal leaching zone below a stratiform ore deposit, used here to model the volume of footwall alteration required to supply metals to the ores.*

extend to a depth of 2.8 km. A volume of ~18 km^3 is required to provide the 1.7 x 10^7 g of Au in Area 251, again assuming 10 % leaching of average terrigenous sediment (3.5 ppb; Boyle 1979) (leaching cone formula $H = 17.2/R^2$). Given that saline sediments have higher Au backgrounds than average sediments, (halite evaporites have an average of between 20.8 and 23.8 ppb Au; Boyle (1979)), and that these formed at least part of the footwall sequence to account for the high salinities, an even smaller volume would suffice. Thus for Starra ores, it is feasible to assume that Cu and Au were leached from the same sediment volume. These volume estimates could be better constrained by detailed analyses of appropriate Cloncurry-district lithologies.

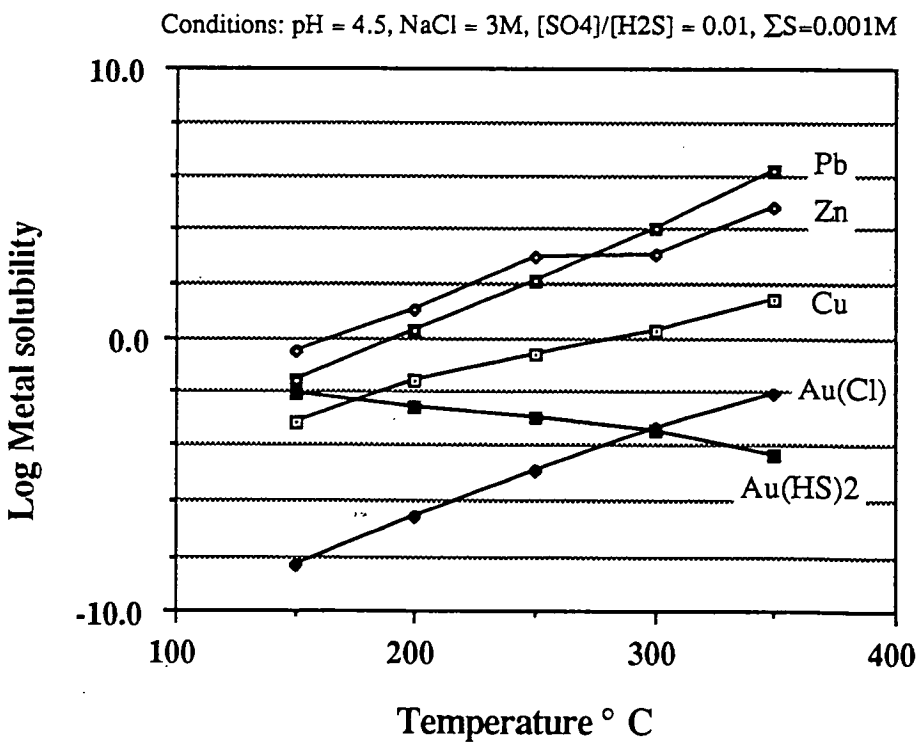

Figure 12.14 *Metal saturation curves for chloride-complexed Cu, Pb, Zn and Au, and for $Au(HS)_2$, derived using the program PLOTMETALS (Harold & Large 1987). The equilibria used are documented in Appendix 10.*

The Fate of Lead and Zinc

Lead and zinc occur at extremely low levels in Starra ironstone (average Area 257 ironstone: 1.0 ppm Pb, 2.9 ppm Zn), although isolated instances of Zn-enrichment occur in the footwall. The extreme depletion of Pb particularly poses a problem for future Pb-isotope analysis, because the isotopic composition is likely to be dominated by radiogenic decay products. It also poses a parodox, because the strongly-chloride-enriched Starra fluids must have been Pb-Zn-rich. This is illustrated by the Zn and Pb abundances of the analogous saline Salton Sea fluids (~ 350 ° C, 3M NaCl), which have been measured at an average 506 ppm Zn and 95 ppm Pb for the deep aquifer (McKibben et al. 1988). Even at these conditions, Salton Sea fluids are markedly Pb and Zn undersaturated (Fig. 12.14); saturation of 506 ppm Zn is only approached at ≈ 240° C ($\Sigma a_S = 10^{-3}$ M), whereas the average Salton Sea Cu value of 6 ppm is saturated at ≈ 330° C, using the solubility data of Walshe & Solomon (1981). These values provide reasonable clues as to the fate of Pb and Zn in Starra fluids. It is suggested that precipitation of chalcopyrite and pyrite in the magnetite ironstone over the range 330 – 260° C deposited 90 % of the Cu, overlapping with pyrite deposition, and in doing so removed all H_2S from the fluid prior to Pb and Zn saturation. The high oxidation state of the water column meant that no reduced sulphur was available on the seafloor. Pb and Zn which did deposit within the ironstone was scavenged by expanding isotherms within the accumulating exhalites, and dispersed into the water-column (zone-refining of Eldridge et al. (1983)).

Circumstantial verification of this mechanism exists at the Mobs Lease and Blockbuster prospects. These share the Au-Cu-W association of Starra (hence implying temperatures > 260° C), but also contain 75 – 1490 ppm Pb, and 115 – 1480 ppm Zn (unpublished Cyprus Minerals geochemical data). The hangingwall contains some graphitic shale, which suggests that reduced sulphur was available on the seafloor, and permitted precipitation of some Pb and Zn. Within a given ironstone, Pb and Zn enrichment is predicted to have been distal rather than proximal to ventward Cu-Au zones.

Pegmont-style Pb-Zn-Ag BIFs (Stanton & Vaughan 1979) may be viewed within the same framework. The relatively low temperature (<260° C) solutions from which they were deposited did not carry significant gold or copper, but Pb, Zn and Fe were highly soluble. Disseminated sulphides were deposited as a function of the availability of H_2S in anaerobic seafloor depressions, from fluids with initially high oxidation states. It is therefore probable that a chemical transition exists between Cu-Au±W±Co BIFs and Pb-Zn types. Chemical and physical transitions were dependent on the initial temperature of the fluid, and its H_2S-content, as shown in Fig. 12.15.

The Relationship between Depth, Salinity, and Fluid Boiling

The accepted proof of boiling within a hydrothermal system is the presence of heterogeneous liquid-vapour fluid inclusions with similar homogenisation temperatures; this proof is unavailable at Starra and Trough Tank. Secondary evidence is the generation of footwall breccia zones accompanied by metal and silica deposition; silica in particular attains

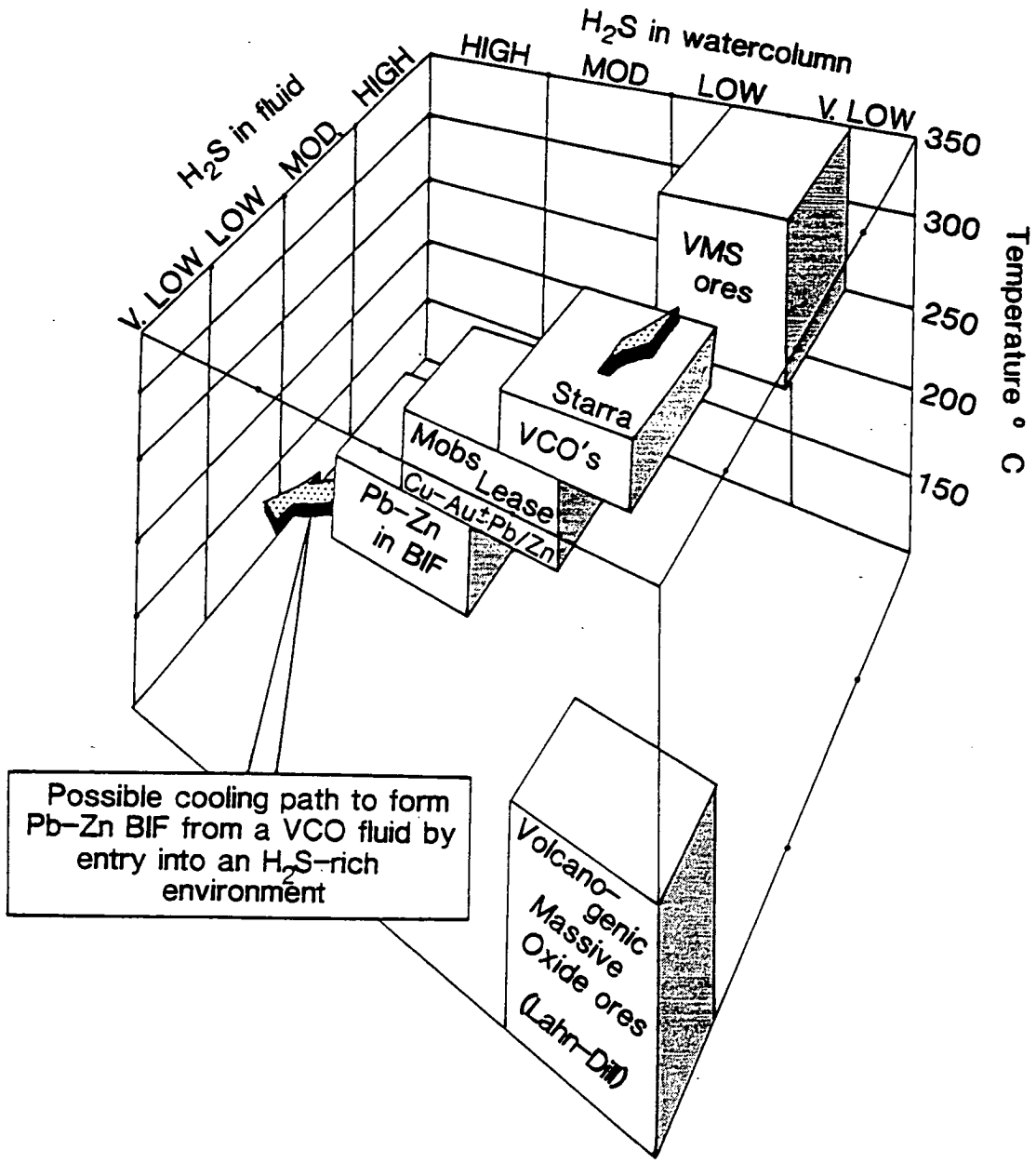

Figure 12.15 *A schematic representation of the variation of temperature, the amount of H_2S in a hydrothermal fluid, and the amount of H_2S in the watercolumn, for different ore-types. Black Smoker-style Volcanogenic Massive Sulphide ores form from H_2S-rich fluids entering H_2S-poor seawater at 250—350° C. In contrast, Starra and other Volcanogenic Copper-bearing Oxide ores formed from fluids low in H_2S, entering a low H_2S environment, at VMS temperatures. Increasing the available watercolumn H_2S to a dense migrating VCO fluid could produce Pb and Zn-enriched BIF (e.g., Pegmont); alternatively Pb-Zn-rich BIF could form from 200–250° C fluids at a vent site.*

saturation rapidly by boiling, as attested in numerous epithermal systems. At Starra, footwall hydrothermal brecciation is scant, although it may have been largely obscured by subsequent deformation. In addition, the majority of metals and silica were deposited on the the seafloor, rather than sub-surface, which indicated that any boiling occurred at higher temperatures than Au-Cu saturation. It is unlikely that the Starra continental rift-setting would have permitted water-depths sufficient to prevent boiling, despite the high salinities of Starra fluids. For instance, sub-critical and super-critical phase separation is now recognised in Red Sea saline hydrothermal solutions (≈ 2100 m; Ramboz et al. 1988), and other deep seafloor settings (Delaney (1982, 1985), Peter 1986). Using the boiling curves of Haas (1971), depths of between 670 and 1030 m would have been required to prevent the boiling of 300 to 350° C 25 wt. % equiv. NaCl solutions envisaged for Starra.

Trough Tank Fluids

In respect of the probable initial temperature, sulphur fugacity, salinity, and metal content, Trough Tank and Starra fluids were probably very similar, on the basis of their similar chemistry and alteration mineralogies. The scale of Trough Tank alteration is yet to be demonstrated to be as large as that of Starra. Its focussed, brecciated and silicified nature are a further contrast, as are the associated continuous and well-banded iron formations. On the basis of the previous discussion, the silica alteration zones are best interpreted as products of fluid-boiling, resulting in cooling of the solution through quartz, magnetite and metal precipitation. The result was the deposition of a larger proportion of sub-seafloor Au and Cu than is evident at Starra. The salinity and density of the remaining fluid was enhanced by vapour separation, emerging on to the seafloor as a type I or II fluid of Sato (1972) to form a brine-pool. Cu and Au varied systematically away from the vent in the well-banded iron formations, due to conductive cooling and fluid-mixing on the brine-water interface. With time, intensification of the hydrothermal system overprinted and redissolved some stratiform exhalites; three major hydrothermal pulses are required to explain the three main iron formation levels. The distinctive enrichment of Co and P, like the W at Starra, is best explained in terms of footwall preconcentration. Elevated Co hints at a large mafic body within the footwall, or Co-rich shales. Geochemical evidence has been presented favouring the leaching of P-rich sediments to explain elevated P in the ores (Chapter 5).

A high accumulation rate is suggested for Trough Tank by the lack of clastic elements within the ore-bands, despite their intercalation with coarse, graded and cross-bedded quartz and feldspar-rich metasediments. A high rate is required to prevent ore dilution by clastic sedimentary processes. The alternating magnetite and quartz mesobands are interpreted as products of single hydrothermal pulses, separated by the kinetic effects which hinder SiO_2 precipitation during cooling (Rimstidt & Barnes 1980).

The strong bedding-plane preference for Trough Tank alteration, resulting in extremely flattened funnel-shapes of the silica zones and layer-parallel veins, is attributed to the unconsolidated state of sediments during mineralisation. Presumably expansion of the boiling fluids was focussed along bedding, which constituted the weakest sub-surface

parting. True veins of magnetite and pyrite were probably only possible once areas of intense silica or feldspar cementation had lithified the sediment.

A COMPARISON WITH OTHER ORES: THE DEFINITION OF A NEW CLASS OF "VOLCANOGENIC COPPER-BEARING OXIDE" (VCO) DEPOSITS

A number of areas in the world contain exhalative copper-bearing (± gold) oxide ores of similar character to those at Starra/Trough Tank. These are summarised in Appendix 12. They are contained within mafic, intermediate and felsic volcano-sedimentary sequences, and are commonly metamorphosed and deformed. There is no clear time-control on the deposit-type. They most clearly represent a style transitional between barren volcanogenic massive oxide deposits, such as the Lahn-Dill and Teliuc-Ghelar sub-types (Quade 1976, Krautner 1979), Dunderlandsal, Langban (Freitsch 1979, Bostrom et al. 1979), and Santorini (Bostrom & Widenfalk 1984), and volcanogenic massive sulphide ores containing significant integral oxide-Cu zones, such as Golden Grove, Corbet, Orchan, Balcooma and Boksputs (Frater 1985, Knuckey & Watkins 1982, Large 1977, Geringer et al. 1987, Huston 1988). The Caledonian volcano-sedimentary rocks of Norway contain ores which cover this spectrum within a single belt (Waltham 1968, Nilsen 1978). Examples of deposits and prospects which are within the volcanogenic Cu-bearing oxide (VCO) class include Starra/Trough Tank, Big and Little Cadia, Copper Blow (Australia), Fosdalen (Norway), Pahtohavore, Saxberget, Ljusnarsberg (Sweden), Atikokan, Snakeweed Lake, Granduc, Pacand, Bousquet No. 4 lens (Canada), Salobo 3A (Brazil), and Athens Mine (Zimbabwe, Africa). A dominance of oxides, and the disseminated nature of the copper and iron sulphides, separate this ore-type from:

(a) silicate-carbonate-sulphide I.F. facies gold deposits, such as Homestake (Sawkins & Rye 1974), Morro Velho (Bernasconi 1988), The Granites (Ireland & Mayer 1984), Golden Dyke Dome (Nicholson 1982, Plimer 1986), Jardine (Hallager 1982), and the Salisgnes deposit of France (Bonnemaison et al. 1986), which have in common reduced sulphide assemblages, low iron oxide contents, and an As-Sb-Au-W ± Pb, Zn & Cu association. The features of theses ores could be accommodated by Au and metal-bisulphide transport in a reduced setting.

(b) replacement Au-BIF deposits, in which massive sulphides (po, py, aspy) are epigenetically concentrated around zones of structural permeability, within barren oxide facies iron formation. The similarity of the element association to "(a)" also suggests bisulphide gold-complexing (Phillips et al. 1984, Groves et al. 1987).

Unfortunately the fluid-types and physical conditions of formation of Volcanogenic Cu-bearing Oxide deposits are not well known, principally because of the effects of later deformation and metamorphism. However, Bajwah (1985) has recently characterised some parameters for the Big Cadia ores, which differ significantly in some respects to the inferred Starra conditions. Fluid inclusion and andesite vesicle evidence requires that Big Cadia ores formed at ~ 500 m water depth, between 140 and 320° C, from fluids with seawater salinities. The mound-like circular shape of the ore lens, the massive ore character, the

absence of distal exhalites, and low silica content, all suggest that the mineralisation was deposited from a buoyant plume by mixing with oxidised seawater, with no down-slope ore deposition. (A similar conclusion can be reached for barren massive oxide ores of the Lahn-Dill type of Europe (Quade 1976)). A concentration of chalcopyrite and pyrite towards the centre and base of the mound is evidence that much of the Cu and Au was added to the precipitate pile at its base, rather than at its top. Bajwah (1985) found that the early fluid was in equilibrium with hematite and epidote, but with time was replaced by a more reduced magnetite-sulphide assemblage.

The controlling parameters requisite for seafloor Cu-oxide deposition are $T \geq 260°$ C, high f_{O2}, $H_2S^{fluid} < \sim 10^{-2.5}$ M, similarly low H_2S levels for ambient waters, and pH ≤ 6 (to promote Cu solubility). While high salinities would promote this ore deposit style by increasing chloride/ion-pair metal solubilities, they are not mandatory. High salinities induce low pH, and stabilise albite relative to muscovite in the alteration. Salinity, water depth and mode of discharge are inter-related controls on the extent of individual deposits, and their silica contents.

CONCLUSIONS

Disparate structural/metamorphic and syngenetic models for Starra ore-genesis have been critically compared. The structural hypothesis involves the sulphidation of an existing iron formation by saline, retrogressional, metamorphic fluids in steeply-plunging D2(LP) fold-hinges. Progressive simple shearing of these folds generated transposition breccias, accompanied by the rotation of reverse shears to dilatancy, providing a means to move metamorphic fluid across the Starra Shear, depositing Au and Cu in the iron formation. The model cannot accommodate textural and megascopic evidence of the presence of ore sulphides during and prior to D2(LP) deformation, asymmetric alteration, regional low-grade Au-enrichment in iron formation away from folds and shears, the lack of similarity of the Starra ores to known Au-BIF replacement ores, strong isotopic evidence for predeformational carbonate in ironstone, and the existence of very similar ores away from shear zones at Trough Tank. Deformation has nevertheless played a clear role in upgrading sulphides and Au into interboudin pockets during D2(MP), and redistributing Cu and W locally into hangingwall metasomatic skarns.

A syngenetic model is preferred to explain Au-Cu mineralisation at Starra and Trough Tank. The heat source and plumbing system were provided by extensional faulting and acid-basic magmatism in a secondary rift or pull-apart basin; hydrothermal fluids equilibrated with oxidised halite-rich sediments, ascending through and pervasively altering an unconsolidated rhyodacitic pyroclastic/epiclastic pile. These saline exhaled fluids initially produced low temperature hematite-goethite ores, possibly precipitated with the aid of bacteria. A magnetite-dominant system evolved by the deepening of fluid circulation to include more reduced waters, or speculatively, by the ascent of a reduced high temperature brine diapir to the sea-sediment interface, modeled on the Salton Sea aquifer system (McKibben et al. 1988). In several areas, poddy breccia-hosting hematitic ironstone developed by fluid invasion of sub-

surface, porous, sedimentary conglomerates: at Area 222 these fluids carried Au and Cu, which may have deposited by decompression boiling. Syn-mineralisation fluid inclusions in these breccias are the best evidence in the area for the high salinities of the ore fluids.

At Areas 257 and 251, an ironstone zonation of mag-cpy-gold, to mag-hem-cpy-py ± gold, to hem ± py, accompanied by a steady decrease in silica content, is interpreted as the product of physico-chemical changes in a fluid as it moved away from a vent, overlying chloritic and oxide alteration. Fluid conditions of gold deposition were T = 260 – 380° C, pH = 3.9 – 6, $\log f_{O2}$ = -27.5 to -30, salinity ≥ 3 M NaCl; Au and Cu were transported as chloride complexes, whereas W was transported as $NaHWO4^0$ (Vlassopoulos & Wood 1987). The distribution of silica and gold also is evidence that any fluid-boiling did not cause sub-surface SiO_2 saturation, whereas this was very likely the case at Trough Tank.

A new stratabound mineralisation style is suggested, termed "Volcanogenic Copper-bearing Oxide" deposits, a variant of exhalative ores. The style is transitional between low temperature volcanogenic oxide deposits, such as the Lahn-Dill type (Quade 1976), and volcanogenic massive sulphide ores which contain integral stringer and basal magnetite-chalcopyrite zones. The description encompasses a significant number of deposits, distributed from the Early Archean to the Late Ordovician. Common denominators are an initially oxidised metal-bearing fluid, high $S_{oxidised}/S_{reduced}$ in the hydrothermal fluid and the overlying water-column, temperatures > 280° C and pH < 6. Oxidation of the fluid favours chloride-Au transport at even lower temperatures (Huston & Large 1989). Very low Pb and Zn abundances are attributed to scavenging of the available H_2S by chalcopyrite and pyrite, prior to Pb-Zn saturation, rather than to an original depletion of Pb and Zn in the fluid. This feature is the key to chemical transitions within exhalative BIFs of the Eastern Succession: Starra Au-Cu BIFs represent the hot H_2S-poor end-member, whereas cooling and migration of this brine to an H_2S-rich setting could evolve Pegmont-style Pb-Zn-rich BIF.

A contrasting deposit type occurs in the Tennant Creek field, Australia (Large 1975, Wedekind & Large in press) with similar mineralogy and geochemistry to Volcanogenic Copper-bearing Oxide deposits. These form lensoidal pipes, or elongate replacement bodies within shears (Nguyen et al. 1988), which are clearly bedding-transgressive, and can be used as a guide to the features of oxide-dominated structurally-controlled epigenetic deposits.

REFERENCES

Alderton D.H.M., Pearce J.A. & Potts P.J., 1980 Rare earth element mobility during granite alteration; evidence from southwest England. Earth Plan. Sci. Letts.; 49: 149-165.

Alonso R.N., Helvaci C., Sureda R.J. & Viramonte J.G., 1988 A new Tertiary borax deposit in the Andes. Mineral. Deposita 23: 299-305.

Alt J.C., 1986 A hydrothermal/bacterial iron deposit from a seamount near 21° N, EPR. EOS, Trans. Amer. Geophys. Union; 18: 526.

Amaro D., Ho S.E., Groves D.I., McNaughton N.J., Dahl Niels, Poll N.J. & Grigson M.W., 1988 The use of pyrite as an indicator of Archean gold mineralization processes: examples from Western Australia. In Bicentennial Gold '88 poster vol. 2, Geol. Soc. Aust Abstracts; 23: 414-418.

Andrew A.S, Heinrich C.A., Wilkins R.W.T. & Patterson D.J., In press Sulfur isotope systematics of copper ore formation at Mount Isa, Australia. Econ. Geol..

Anhaeusser C.R., 1976 The nature and distribution of Archaean gold mineralization in southern Africa. Minerals Sci. Eng. 8 (1); 46-84.

Appel P.W.U., 1979 Stratabound copper sulfides in a banded iron-formation and in basaltic tuffs in the early Precambrian Isua supracrustal belt, West Greenland. Econ. Geol.; 74: 45-52.

Appel P.W.U., 1983a Rare earth elements in the early Archaean Isua iron-formation, West. Greenland; 20: 243-258.

Appel P.W.U., 1983b Tourmalines in the Early Archaean Isua Supracrustal belt, West Greenland. J. of Geol.; 92: 599-612.

Appel P.W.U., 1986 Stratabound scheelite in the Archean Malene supracrustal belt, West Greenland. Min. Deposita; 21: 207-215.

Appleby A.-C. & Williams P.J., 1988 Epigenetic tourmalinite and arsenopyrite in the aureole of the Leinster batholith, SE Ireland. Mineral. Deposita 23: 247-255.

Arniaud D., Dupuy C. & Dostal J., 1984 Geochemistry of Auriat granite (Massif Central, France). Chem. Geol.; 45: 263-277.

Bachinski D.J., 1976 Metamorphism of cupriferous iron sulfide deposits, Notre Dame Bay, Newfoundland. Econ. Geol.; 71: 443-452.

Bajwah Z.U., 1985 Geology, geochemistry and genesis of the Big Cadia iron copper deposit, N.S.W. Unpublished Ph.D thesis, University of Newcastle, N.S.W., Australia; 412 p.

Bajwah Z. U., Seccombe P. & Offler R., 1987 Trace element distribution, Co:Ni ratios and genesis of the Big Cadia iron-copper deposit, New South Wales, Australia. Mineralium Deposita; 22: 292-300.

Baker J.H. & Hellingwerf R.H., 1988 Rare earth element geochemistry of W - Mo - (Au) skarns and granites from Western Bergslagen, Central Sweden. Mineral. and Petrol.; 39: 231-244.

Bandurkin P.A., 1961 Behavior of the rare earths in fluorine-bearing media. Geochemistry; 2: 159-167.

Barnard R. and Kistler R., 1966 Stratigraphic and structural evolution of the Kramer sodium borate orebody, Boron, California. Sec. Symp. on Salt., Ed. J. Rau. Ohio Geol. Soc.: 133-150.

Barnes H.L., 1979 Solubilities of ore minerals. In Barnes H.L. (ed.), Geochemistry of hydrothermal ore deposits, 2nd edition, Wiley & Sons, New York, 798 p.

Barnes R.G., 1975 Tibooburra-Wonominta block. In Markham N.L. & Basden H. (eds.). The mineral deposits of New South Wales, N.S.W. Geol. Surv., Sydney, 682 p.

Barnes R.G., 1980 Types of mineralization in the Broken Hill block and their relationship to stratigraphy. New South Wales Geol. Sur., Aust., Record 20 (1) : 33-70.

Barnes R.G., 1983 Stratiform and stratabound tungsten mineralisation in the Broken Hill block, N.S.W. Geol. Soc. Aust. J.; 30: 225-239.

Barnett E.S., Hutchinson R.W., Adamcik A. & Barnett R., 1982 Geology of the Agnico-Eagle gold deposit. In Hutchinson R.W., Spence C.D. & Franklin J.M. (Eds.), Precambrian sulphide deposits, H.S. Robinson memorial volume, Geological Association of Canada Special Paper 25; : 403 - 427.

Barrett T.J., Fralick P.W. & Jarvis I., 1988 Rare-earth-element geochemistry of some Archean iron formations north of Lake Superior, Ontario. Can. J. Earth Sci.; 25: 570-580.

Barrett T.J., Wares R.P. & Fox J.S., 1988 Two-stage hydrothermal formation of a Lower Proterozoic sediment-hosted massive sulfide deposit, northern Labrador Trough, Quebec. Can. Min.; 83: 871-888.

Barton P.B., 1984 Redox reactions in hydrothermal fluids. In Henley R.W., Truesdell A.H. & Barton P.B (eds.), Fluid-mineral equilibria in hydrothermal systems. Reviews in Econ. Geol.; 1: 99-114.

Beardsmore T.J., 1986 Aspects of the geology and mineralisation in the Selwyn region: a preliminary report. Unpublished report to Cyprus Minerals, Mount Isa, 155p.

Beardsmore T.J., 1988 The Selwyn-style Cu-Au deposits in the Mount Isa Block- a late orogenic, granite and deformation-related style. Ninth Australian Geological Convention Abstracts, Aust. Geol. Soc. Abs. 21: 55-56.

Beardsmore T.J., in prep. The Limestone Creek iron formation— product of syn-tectonic replacement in the middle Proterozoic of Northwestern Queensland. Submitted to J. Metamorph. Geol. Oct. 1989.

Beardsmore T.J., Newberry S. & Laing W.P., 1988 The Maronan Supergroup — an inferred early volcanosedimentary rift sequence in the Mt.Isa inlier, and its implications for ensialic rifting in the Middle Proterozoic of northwest Queensland. Precamb. Res.; 40/41: 487-509.

Beaty D., Hahn G.A. and Threlkeld W.A., 1988 Field, isotopic and chemical studies of tourmaline-bearing rocks in the Belt-Purcell Supergroup: genetic constraints and exploration significance for Sullivan-type ore deposits. Can. J. of E. Sci.; 25: 392-402.

Becker R. and Clayton R., 1972 Carbon isotopic evidence for the origin of BIF in Western Australia. Geochim. Cosmochim. Acta.; 36: 577-595.

Behr H.J. & Horn E.E., 1982 Fluid inclusion systems in metaplaya deposits and their relationships to mineralisation and tectonics. Chem. Geol.; 37: 173-189.

Berger B.R., 1988 Lithologic and tectonic setting of epithermal gold-siver deposits in western north America. In Bicentenniall Gold '88 extended oral abstracts, Geol. Soc. of Aust. Abs., Melbourne; 22: 154-160.

Berner R.A., 1971 Principles of chemical sedimentology. McGraw-Hill, New York, 240 p.

Bell T.H., 1983 Thrusting and duplex formation at Mount Isa, Queensland, Australia. Nature; 1983; 304: 493-497.

Bell T.H. & Duncan A.C., 1978 A rationalized and unified shorthand terminology for lineations and fold axes in tectonites. Tectonophysics; 47: T1-T5.

Bence A.E., 1983 Volcanogenic massive sulfides: rock/water interactions in basaltic systems and their effects on the distributions of the rare earth elements and selected first series transition elements [abs]. 4th International Symposium on water - rock interaction, Misasa, Japan: 48-49.

Bernard A.J., Dagalier G. & Soler E., 1982 The exhalative sediments linked to the volcanic exhalative massive sulphide deposits: a case study of European occurrences. In Ore Genesis. The State of the Art. (eds. Amstutz G.C., Goresy A. El, Frenzel G., Kluth A. & Zimmerman R.A.) Springer-Verlag: 553-564.

Bettess D.E., 1987 The structural evolution of the Deighton Thrust Nappe Complex, Mount Isa, Queensland. Abstract, International Conference on Deformation of Crustal rocks, Mount Buffalo, Australia: 41-42.

Bhatia M.R., 1983 Plate tectonics and geochemical composition of sandstones. J. Geol.; 1983; 91: 611-627.

Bhatia M.R. & Crook A.W., 1986 Trace element characteristics of graywackes and tectonic setting discrimination of sedimentary basins. Contrib. Mineral. Petrol.; 92: 181-193.

Birnbaum S.J. & Wireman J.W., 1985 Sulfide-reducing bacteria and silica solubility: a possible mechanism for evaporite diagenesis and silica precipitation in banded iron formations. Can. J. Earth Sci.; 22 : 1904-1909.

Bischoff J.L. & Seyfried W.E., 1978 Hydrothermal chemistry of seawater from 25° to 350° C. Am. J. Sci.; 278: 838-860.

Bischoff J.L., Radtke A.S. & Rosenbauer R.J., 1981 Hydrothermal alteration of greywacke by brine, and seawater roles of alteration and chloride complexing on metal solubization at 200° C and 350° C. Econ. Geol.; 76: 659-677.

Blake D.H., 1982 A review of the Corella Formation, Mount Isa Inlier, Queensland. BMR J. Aust. Geol. Geophys.; 7: 113-118.

Blake D.H., 1986 Middle Proterozoic evolution of the Mount Isa Inlier, north-western Queensland, Australia: a synthesis. Trans. Geol. Soc. Afr.; 89: 253-262.

Blake D.H., 1987 Geology of the Mount Isa Inlier and environs, Queensland and Northern Territory. Aust. Bureau Min. Res. Bull. 225. 83 p.; 1987.

Blake D.H. & Page R.W., 1988 Early Proterozoic migmatitic basement in the Kalkadoon -Leichhardt belt of the Mount Isa Inlier, northwestern Queensland. BMR J. Aust. Geol. Geophys.; 10: 323-328.

Blake D.H. & Stewart A., 1988 Block and possible terrane boundaries in the Mount Isa Inlier. BMR Research Newsletter 9, October : 2-3.

Blake D.H., Bultitude R.J. & Donchak P.J.T., 1981 Definitions of newly and revised Precambrian stratigraphic and intrusive rock units in the Duchess and Urandangi

1:250 000 Sheet areas, northwestern Queensland. Aust. Bur. Miner. Res., Rep. 233 (Microform MF164).

Blake D.H., Bultitude R.J. & Donchak P.J.T., 1982 Proterozoic intrusive breccia bodies near Duchess, northwestern Queensland. BMR Journal of Aust. Geol. & Geophys.; 7: 135-140.

Blake D.H., Bultitude R.J, Donchak P.J.T., Wyborn L.A.I. & Hone I., 1984 Geology of the Duchess-Urandangi region, Mt. Isa Inlier, Queensland. Aust. Bureau Min. Res. Bull.; 219.

Blake D.H, Etheridge M.A. Stewart A.J. & Williams P.W., 1987 Integrated studies of the tectonic history of the Mount Isa base-metal province, Queensland. BMR87: Yearbook of the Bureau of Mineral Resources, Canberra.: 100-101.

Blatt H., Middleton G. and Murray R., 1972 Origin of Sedimentary Rocks. Prentice-Hall.

Bone Y., 1987 The geological setting of tourmalinite at Rum Jungle, N.T., Australia — genetic and economic implications. Mineral. Deposita; 23: 34-41.

Bonnemaison M., Crouzet J., Thiercelin F. & Tollon F., 1986 Controls on exhalative gold deposits hosted by volcaniclastic sediments in the 'Schistes X', Salsigne gold district, Montagne Noire, Southern France. Proceedings of Gold '86 symposium, Toronto, 1986: 457-468.

Borchert H., 1972 Genesis of marine sedimentary iron ores. Trans. Inst. Mining. Metall.; 69B: 261-277.

Bostrom K. & Widenfalk L., 1984 The origin of iron-rich muds at the Kameni Islands, Santorini, Greece. Chem. Geol.;42: 203-218.

Bostrom K., Rydell H. & Joensuu O., 1979 Langban — an exhalative sedimentary deposit ? Econ. Geol.; 74: 1002-1011.

Bouma A.H., 1962 Sedimentology of some flysch deposits.Amsterdam, Elsevier.

Bowers T.S., Jackson K.J. & Helgeson H.C., 1984 Equilibrium activity diagrams for coexisting minerals and aqueous species at pressures and temperatures to 5 kb and 600° C. Springer-Verlag, Berlin, 397 p.

Boyle R.W., 1979 The geochemistry of gold and its deposits. Can. Geol. Surv. Bull. 280.

Brill B.A., 1988 Illite crystallinity, b_0 and Si content of K-white mica as indicators of metamorphic conditions in low-grade rocks at Cobar, New South Wales. Aust. J. Earth Sci.; 35: 295 - 303.

Broeker W.S. and Oversby V.M., 1971 Chemical Equilibria in the Earth. McGraw Hill, New York.

Brooker D., Craig J. & Rimstidt D., 1987 Ore metamorphism and pyrite porphyroblast development at the Cherokee Mine, Ducktown, Tennessee. Econ. Geol.; 82: 72-86.

Brooks J.H., Wilson I.H. & Sawers J.D., 1975 Minor copper deposits in the Mount Isa/Cloncurry district. In Knight C.L., Ed., Economic Geology of Australia and Papua New Guinea. 1. Metals. Mon. 5 Australas. Inst. Min. Metall.; 392-396.

Brownlow A.H., 1979 Geochemistry. Prentice-Hall, New Jersey, 498 p.

Brown E.C. and Ayuso R.A., 1985 Significance of tourmaline-rich rocks in the Grenville Complex of St. Lawrence County, New York. U.S.G.S. Bull. 1626.

Bryzgalin O.V., 1976 On the solubility of tungstic acid in aqueous salt solutions at high temperatures. Geochem. Intl.; 13: 155-159.

Bucher-Nurminen K., 1987 A recalibration of the chlorite-biotite-muscovite geobarometer. Contrib. Miner. Petrol.; 96: 519-522.

Budai J., Lohmann K., Wilson J., 1987 Dolomitisation of the Madison Group, Wyoming and Utah Overthrust Belt. AAPG Bull.; 71: 909-924.

Bultitude R. & Wyborn L.A.I., 1982 Distribution and geochemistry of volcanic rocks in the Duchess-Urandangi region, Queensland. BMR J. of Aust. Geol. & Geophys.; 7: 99-113.

Burg J.P. & Harris L.B., 1982 Tension fractures and boudinage oblique to the maximum extension direction: an analogy with Luders bands. Tectonophysics ; 83: 347-363.

Burkov V.V. & Podporina Y. K., 1967 Rare earths in granitoid residuium. Dokl. Acad. Sci. USSR; 177: 691-694.

Cameron E.M., 1989 Derivation of gold by oxidative metamorphism of a deep ductile shear zone: Part 2. Evidence for the Bamble Belt, south Norway. Journal of Geochem. Expl.; 31: 149-171.

Cameron E.M., 1989 Scouring of gold from the lower crust. Geology; 17: 26-29.

Campbell I.H., Lesher C.M., Coad P., Franklin J.M., Gorton M.P. & Thurston P.C., 1984 Rare-earth element mobility in alteration pipes below massive Cu-Zn sulfide deposits. Chem. Geol.;45: 181-202.

Carlson L., Halenius U. & Johansson L., 1988 Pahtohavare, a new copper deposit in the Kiruna Greenstone belt, Northern Sweden. Bicentennial Gold '88 extended oral abstracts, Geol. Soc. Aust. Abs. 23: 176-179.

Carr G. and Smith J., 1975 A comparative isotopic study of the Lady Loretta zinc-lead-silver deposit. Mineral. Dep.;10: 269-276.

Carter E.K., 1959 New stratigraphic units in the Precambrian of north-western Queensland. Qld. Govt. Min. J.; 60: 437-441.

Carter E.K., Brooks J.H. & Walker K.R., 1961 The Precambrian mineral belt of north-western Queensland. Bur. Min. Res., Australia, Bull. 51.

Casselman M.J. & Mioduszewska B.M., 1982 The Bathurst Norsemines sulphide deposits, Hackett River, N.W.T. In Hutchinson R.W., Spence C.D. & Franklin J.M. (Eds.), Precambrian sulphide deposits, H.S. Robinson memorial volume, Geological Association of Canada Special Paper 25: 365-403.

Chadwick B., Garrioch N.H.G., Ramakrishnan M. & Viswanatha M.N., 1986 Mineral composition, textures and deformation in Late Archean banded iron formation rich in magnesioriebeckite and aegerine, Bababudan, Karnataka, Southern India. J. Geol. Soc. India; 28: 189-200.

Chambers L.A., 1982 Sulphur isotope study of a modern intertidal environment, and the interpretation of ancient sulphides. Geochim. Cosmochim. Acta; 46: 721-728.

Chappell B.W. & White A.J.R., 1974 Two contrasting granite types. Pacific Geology; 8: 173-174.

Chevalier Y. & Dejou J., 1972 Observations sur l'alteration superficielle de la cordierite resultats avec ceux acquis dans les regions temperees humides. CR Acad. Sci., Paris. ser. D.: 275: 149-151.

Christ C.L., Truesdell A.H. and Erd R.C., 1967 Borate mineral assemblages in the system Na_2O-CaO-MgO-B_2O_3-H_2O. Geochim. Cosmochim. Acta; 31: 313-337.

Christiansen E., Sheridan M. & Burt D., 1986 The geology and geochemistry of Cenozoic topaz rhyolites from the Western United States. U.S. Geol. Surv. Prof. Paper 205.

Clayton R.N., Muffler L.J. and White D.E., 1968 Oxygen isotope study of calcite and silicates of the River Ranch No. 1 well, Salton Sea Geothermal field, California. Am. J. Sci.; 266: 968-979.

Cloud P.E. A working model for the primitive earth. Amer. J. Sci.; 1972; 272: 537-548.

Coats J.S., Fortey N.J., Gallagher M.J. & Grout A., 1984 Stratiform barium enrichment in the Dalradian of Scotland. Econ. Geol.; 79: 1585-1595.

Cobbold P.R. & Watkinson A.J., 1981 Bending anisotropy: a mechanical constraint on the orientation of fold axes in an anisotropic medium. Tectonophysics; 72: T1-T10.

Cody R.D., 1976 Growth and early diagenetic changes in artificial gypsum crystal grown within bentonite muds and gels. Geol. Soc. Am. Bull.; 87: 1163-1168.

Cole D.R. & Drummond S.E., 1986 The effect of transport and boiling on Ag/Au ratios in hydrothermal solutions: a preliminary assessment and implications for the formation of epithermal precious-metal ore deposits. J. Geochem. Expl.; 25: 45-80.

Colvine A.C., Andrews A.J., Cherry M.E., Durocher M.E., Fyon A.J., Lavigne M.J., MacDonald A.J., Marmont S., Poulsen K.H., Springer J.S. & Troop D.G., 1984 An integrated model for the origin of Archean lode gold deposits. Ontario Geol. Surv., Open File Rep., 5524, 98 p.

Coombs D.S., 1984 Sedimentary analcime rocks and sodium-rich gneisses. Min. Mag.; 34: 144.

Cox S.F., Etheridge M.A. & Hobbs B.E., 1981 The experimental ductile deformation of polycrystalline and single crystal pyrite. Econ. Geol.; 76: 2105-2017.

Copeland R.A., Frey F.A. & Wones D.R., 1971 Origin of clay minerals in a Mid-Atlantic Ridge sediment. Earth Planet. Sci. Lett.; 10: 186-192.

Cox K.G., Bell J.D. & Pankhurst R.J., 1979 The interpretation of igneous rocks. 450 p. Allen & Unwin press — London — Boston — Sydney.

Craig H.M., 1963 The isotope geochemistry of water and carbon in geothermal areas. In Tongiorgi, E., Ed., Nuclear Geology in Geothermal Areas: Consiglio Nazionale delle Richerche. Laboratorio di Geolgia Nucleare, Pisa : 17-53.

Crerar D.A. & Barnes H.L., 1976 Ore solution chemistry V. Solubilities of chalcopyrite and chalcocite assemblages in hydrothermal solution at 200° to 350° C. Econ. Geol.; 71: 772-794.

Crerar D.A., Susak H.J., Borcisk M. & Schwartz S., 1984 Solubility of the buffer assemblage pyrite + pyrrhotite + magnetite in NaCl solution from 200° C to 350° C. Geochim. Cosmochim. Acta; 42; 1427-1439.

Crerar D.A., Wood S., Brantly S. & Bocarsly A., 1985 Chemical controls on solubility of ore-forming minerals in hydrothermal solutions. Can. Mineral.; 23: 333-352.

Cullers R.L. & Graf J.L., 1984a Rare earth elements in igneous rocks of the continental crust: predominantly basic and ultrabasic rocks. In Henderson P. (Ed.) Rare earth

element geochemistry, Developments in Geochemistry 2, Elsevier - Amsterdam.; 237 - 275.

Cullers R.L. & Graf J.L., 1984b Rare earth elements in igneous rocks of the continental crust: intermediate and silicic rocks — ore petrogenesis. In Henderson P. (Ed.) Rare earth element geochemistry, Developments in Geochemistry 2, Elsevier - Amsterdam : 275-317.

Davidson G.J. & Dashlooty S.A., In press The Glyde Sub-basin: a pull-apart basin with associated acid volcanism, in the the mid-Proterozoic Barney Creek Formation, McArthur Basin, Northern Territory. Aust. J. Earth Sci..

Davidson G.J., Large R.R., Kary G. & Osborne R., 1988 The BIF hosted Starra and Trough Tank Au-Cu mineralisation: a new stratiform association from the Proterozoic Eastern Succession, Mt Isa, Australia. Bicentennial Gold '88, Extended Oral Abstracts Geol. Soc. of Australia Abstracts 22 : 85-90.

Davidson G.J., Large R.R., Kary G. & Osborne R., In press The deformed iron formation-hosted Starra and Trough Tank Au-Cu mineralization: a new association from the Proterozoic Eastern Succession of Mount Isa, Australia. In Keays R., Ramsay R. & Groves D. (Eds.) The geology of gold deposits: the perspective in 1988.

Davis W.J. & Williams-Jones A.E., 1987 A fluid inclusion study of the porphyry-greisen, tungsten-molybdenum deposit at Mount Pleasant, New Brunswick, Canada. Mineral. Deposita; 20; 94-101.

Deb M., 1979 Genesis and metamorphic evolution of two stratiform massive sulphide deposits at Ambaji-Deri, in the Precambrian of India. Min. Dep.; 14: 21-31.

Deer W.A., Howie R.A. & Zussman J., 1986 Rock-forming Minerals: Disilicates and ring silicates, 2nd. Ed. Longman, New York, 629 p.; 1B.

Delaney J.R. & Cosens B.A., 1982 Boiling and metal deposition in submarine hydrothermal systems. Marine Geol.; 16: 62-66.

Delaney J.R., McDuff R. & Lupton J.E., 1985 Evidence for supercritical two-phase separation in submarine hydrothermal systems (abs.). EOS, Trans. Am. Geophys. Union; 66: 402.

Delaney J.R., Mogk D.M. & Cosens B., 1982 Indirect evidence of boiling hydrothermal systems on the Mid-Atlantic ridge. American Geophysical Union EOS; 63: 472.

Dennen W.H. & Moore B.R., 1982 Chemical recognition of pre-metamorphic detrital sediments. Proc. IV Cong. Geol. Venezolana, Caracas, Venezuala.

Derrick G.M., 1974 Stratigraphic and palaeogeographic evolution and revolution in the Mount Isa area. In Recent technical and social advances in the north Australian mineral industry, Aust. Inst. Min. Met., NW Qld branch, Mount Isa, 177-187.

Derrick G.M., 1982 A Proterozoic rift zone at Mount Isa, Queensland, and implications for mineralisation. BMR J. Aust. Geol. Geophys.; 7: 81-92.

Derrick G.M., 1984 Conception, development and results of gold exploration in jaspilite and related rocks near Cloncurry N.W. Queensland ((abs.). Aust. Geol. Soc. Aust. Abstracts, Sydney; 12: 137.

Derrick G.M., Wilson I.H. & Hill R.M., 1976 Revision of stratigraphic nomenclature in the Precambrian of northwestern Queensland. IV. Malbon Group. Queensland Govt. Mining J.; 77: 601-604.

Derrick G.M., Wilson I.H. & Hill R., 1977 Revision of stratigraphic nomenclature in the preCambrian of northwestern Queensland.VI Mary Kathleen Group. Queensland Govt. Mining Journal.; 78: 15-23.

Derrick G.M., Wilson I.H. & Hill R.M., 1978 Revision of stratigraphic nomenclature in the Precambrian of northwestern Queensland. VIII. Igneous rocks. Queensland Govt. Min. J. ; 78: 151-156.

Derrick G.M., Wilson I.H. & Sweet I.P., 1980 The Quilarlar and Surprise Creek Formations - new Proterozoic units from the Mount Isa Inlier: their regional sedimentology and application to regional correlation. Bureau of Mineral Resources Journal of Australian Geology & Geophysics; 5: 215-223.

Dickson J., 1965 A modified staining technique for carbonates in thin section. Nature; 206: 587.

Dietrich R.V., 1968 Behavior of zirconium in certain artificial magma under diverse P-T conditions. Lithos; 1: 20-29.

Dimo G., 1975 Precambrian geology and copper mineralisation of the Mt. Elliot area, northwest Queensland. Unpub. Hons. thesis, University of Qld., Brisbane, Aust.

Dimroth E. & Kimberley M.M., 1976 Precambrian atmospheric oxygen: evidence in the sedimentary distributions of carbon, sulfur, uranium and iron. Can. J. Earth Sci.; 13.

Dougan T.W., 1976 Origin of trondhjemitic biotite-quartz-oligoclase gneisses from the Venezuelan Guyana shield. Precamb. Res.; 3: 317-342.

Drever J.I., 1974 Geochemical model for the origin of Precambrian banded iron formations. Geol. Soc. Amer. Bull.; 85: 1099-1106.

Drever J.I., 1982 The Geochemistry of Natural Waters. Prentice-Hall.

Drury S.A., 1974 Chemical changes during retrogressive metamorphism of Lewisian granulite facies rocks from Coll and Tiree. Scottish J. Geol.; 10: 237-256.

Dunnet D., 1976 Some aspects of the Panantarctic cratonic margin in Australia. Phil. Trans.Royal Soc. London, Series A; 280: 641-654.

Edmond J.M., Von Damm R.L., McDuff R.E. & Measures C.I., 1982 The chemistry of hot springs on the East Pacific Rise and their effluent dispersal. Nature; 297: 187-191.

Eldridge C.S., Barton P.B.Jr & Ohmoto H., 1983 Mineral textures and their bearing on the formation of the Kuroko orebodies. In Ohmoto H. & Skinner B.J. (Eds.), Kuroko and related volcanogenic massive sulphide depostis. Econ. Geol. Mon. 5: 241-281.

Eldridge C.S., Compston W., Williams I.S., Patterson D.J., Williams N., Both R.A. & Walshe J.L., 1985 Ion microprobe analyses of sulphur and lead isotopic compositions of sulphides from the Pb-Zn ore bodies at Mt. Isa, Queensland, Australia,. In Herbert H.K. (Ed.) Conference on stable isotopes and fluid processes in mineralization: Univ. of Queensland : 22-23.

Einaudi M.T., Meinert L.D. & Newberry R.J., 1981 Skarn deposits. In Skinner B.J. (Ed.) Economic Geology 75th Anniversary Volume: 317-391.

Ellis, A.J., 1979 Explored geothermal systems. In: Barnes, H.L. (ed) Geochemistry of hydrothermal ore deposits. Wiley, New York : 632-683.

Ellis D.J. & Wyborn L.A.I., 1984 Petrology and geochemistry of Proterozoic dolerites from the Mount Isa Inlier. Bureau of Mineral Resources Journal of Australian Geology & Geophysics; 9: 19-32.

Engel A.E.J., Engel C.G. & Havens R.G., 1965 Chemical characteristics of oceanic basalts and the upper mantle. Geol. Soc. Am. Bull.; 76: 719-734.

Eskola P., 1914 On the petrology of the Orijarvi region in southwestern Finland. Bulletin de la Commission Geologique de Finlande; 40: 1-279.

Etheridge M.A., 1987 Extensional structures in the Mount Isa Inlier. BMR Research Newsletter 6, April : 9-11.

Etheridge M.A., Rutland R.W.R. & Wyborn L.A.I., 1987 Orogenesis and tectonic processes in the early to middle Proterozoic of Northern Australia. In Kroner A. (Ed.) Precambrian Lithospheric Evolution. Geodynamics Series, 17, Am. Geophys. Union, Washington, D.C., p.131-147.

Ethier, V.G. and Campbell, F.A., 1977 Tourmaline concentrations in Proterozoic sediments of the southern Cordillera of Canada and their economic significance. Can. J. Earth Sci.; 14: 2348-2363.

Evensen N.M., Hamilton P.J. & O'Nions R.K., 1978 Rare-earth abundances in chondritic meteorites. Geochim. Cosmochim. Acta; 42: 223-236.

Ewart A., 1979 A review of the mineralogy and chemistry of Tertiary-Recent dacitic, latitic, rhyolitic, and related salic volcanic rocks. In Trondjheiites & related rocks. Elsevier; 1979: 13-103.

Ewart A., Taylor S. & Capp A., 1968 Trace and minor element geochemistry of the rhyolitic volcanic rocks, Central North Island, New Zealand. Cont. Min. Pet.; 18: 76-104.

Ewers G.R. & Sun S-S., 1988 Genesis of the Red Dome deposit, northeast Queensland. Bicentennial Gold '88, Melbourne, Aust.; Geol. Soc. extended oral abstracts vol. 22; 110-115.

Exley R.A., 1980 Microprobe studies of REE-rich accessory minerals; implications for Skye granite petrogenesis and REE mobility in hydrothermal systems. Earth Plan. Sci. Lett.; 48: 97-110.

Fabiana W.M.B., 1987 Controls to the gold-copper mineralization at the Athens Mine, Zimbabwe. In Viewing K.A.(ed.), Eighteenth Anual Rep., No. 66, Inst. Min. Research, Univ. Zimbabwe, 168p: 77-89.

Fairbridge R.W., 1983 Syndiagenesis-anadiagenesis-epidiagenesis: phases in lithogenesis. In Larsen G. & Chilinger G.V. (Eds.) Diagenesis in sediments and sedimentary rocks, 2 (Elsevier); Developments in sedimentology 25B: 17-115.

Ferry J.M. & Spear F.S., 1978 Experimental calibration of Fe and Mg partitioning between biotite and garnet. Contr. Mineral. & Petrol.; 66: 113-117.

Finlow-Bates T. & Stumpfl E.F., 1981 The behaviour of so-called immobile elements in hydrothermally altered rocks associated with volcanogenic submarine-exhalative ore deposits. Min. Deposita; 16: 319-328.

Fisher R.V. & Schmincke H.U., 1984 Pyroclastic Rocks. Springer-Verlag.;

Fisher N.H., 1945 The fineness of gold with special reference to the Morobe goldfield, New Guinea. Econ. Geol.; 40: 449-495.

Fleischer R. & Routhier P., 1973 The"consangiuneous" origin of a tourmaline-bearing gold deposit: Passagem de Mariana (Brazil). Econ. Geol.: 68: 11-22.

Floyd P.A. & Winchester J.A., 1975 Magma type and tectonic setting discrimination using immobile elements. Earth & Plan. Sci. Lett.; 27: 211-218.

Floyd P.A. & Winchester J.A., 1978 Identification and discrimination of altered and metamorphosed volcanic rocks using immobile elements. Chem. Geol.; 21: 291-306.

Flynn R.T. & Burnham C.W., 1978 An experimental determination of rare earth partition coefficients between a chloride containing vapour phase and silicate melts. Geochim. Cosmochim. Acta; 42: 685-701.

Fodor R., 1987 Low and high TiO2 flood basalts of southern Brazil: origin from picritic parentage and a common mantle source. Earth Plan. Sci. Lett.; 84: 423-430.

Folk R.L., 1962 Spectral subdivision of limestone types. In Ham W.E. (Ed.) Classification of carbonate rocks. Am. Assoc. Petrol. Geol. Mem.; 1: 62-84.

Fontes J.C., Fritz P., Gauthier J. & Kulbicki G., 1967 Mineraux argileux, elements-traces et compositions isotopiques ($^{18}O/^{16}O$ et $^{13}C/^{12}C$) dans les formations gypsiferes de l'Eocene superieur et de l'Ogliocene de Cormeilles-en-Parisis. Bulletin du Centre de Recherches de Pau; 1: 315-366.

Foster R.P., 1977 Solubility of scheelite in hydrothermal chloride solutions. Chem. Geol.; 20: 27-43.

Foster R.P., 1988 Archaean gold mineralisation in Zimbabwe: implications for metallogenesis and exploration. Bicentennial Gold '88 extended poster abstracts, Geol. Soc. Aust. Abs. 23; 1988: 62-73.

Foster R.P. & Gilligan J.M., 1987 Archaean iron-formation and gold mineralization in Zimbabwe. In Appel P.W.U. & La Berge G.L.(Eds.)Precambrian iron-formations, Theophrastus Publications, S.A., Athens, 674 p.; 635-674.

Fournier R.O., 1983a The behavior of silica in hydrothermal solutions. In Berger B.R. & Bethke P.M. (Eds.), Geology and geochemistry of epithermal systems. Reviews in Econ. Geol. 2: 45 - 61.

Fournier R.O., 1983b A method of calculating quartz solubilities in aqueous sodium chloride solutions. Geochim. Cosmochim. Acta; 47: 579-586.

Fournier R.O. & Potter R.W.(II)., 1982 An equation correlating the solubility of quartz in water from 25° to 900° C at pressures up to 10,000 bars. Geochim. Cosmochim. Acta; 46: 1969-1973.

Fournier R.O., Rosenbauer R.J. & Bischoff J.L., 1982 The solubility of quartz in aqueous sodium chloride solution at 350° C and 180 to 500 bars. Geochim. Cosmochim. Acta; 46: 1975-1978.

Franklin J.M., Sangster D.M. & Lydon J.W., 1981 Volcanic-associated massive sulfide deposits. 75th Anniversary Volume, Econ. Geol.; 485 - 628.

Frater K.M., 1983 Geology of the Golden Grove prospect, Western Australia: a volcanogenic massive sulfide-magnetite deposit. Econ. Geol.; 78: 875-919.

Frater K.M., 1985 Mineralization at the Golden Grove Cu-Zn deposit, Western Australia. I: Premetamorphic textures of the opaque minerals. Can. J. Earth Sci.; 22: 1-14.

Freitsch R., 1978 On the magmatic origin of iron ores of the Kiruna type. Econ. Geol.; 73: 478-485.

Freitsch R., 1982a On the chemical compostion of the ore breccia at Loussavaara, Northern Sweden. Mineral. Deposita; 17: 239-243.

Freitsch R., 1982b A model for the formation of iron, manganese and sulphide ores of central Sweden. Geol. Rund.; 71: 206-212.

Freitsch R., Papunen H. & Vokes F.M., 1979 The ore deposits in Finland, Norway, and Sweden — a review. Econ. Geol.; 74: 975-1001.

Freund J.E., 1976 Statistics, a first course.(2nd. edition). Prentice-Hall, New Jersey, 374p.

Freund R. The role of shear in rifting. In : Continental and Oceanic rifts. Ed. G. Palmason Geodynamics Series #8.; 1982.

Friedman I. & O'Neil J.R., 1977 Compilation of stable isotope fractionation factors of geochemical interest. U.S. Geol. Surv. Prof. Paper 440-KK, 12p.

Friesen R.G., Pierce G.A. & Weeks R.M., 1982 Geology of the Geco base metal deposit. In Hutchinson R.W., Spence C.D. & Franklin J.M. (Eds.), Precambrian sulphide deposits, H.S. Robinson memorial volume, Geological Association of Canada Special Paper 25: 343 - 365.

Frimmel H., Gotzinger M.A. & Papesch W., 1989 Isotope geochemistry (C, O, Sr) and fluid inclusion study of wolframite and scheelite bearing Fe-magnesite rocks, Eastern Alps. In 79th Annual meeting of the Geologische Vereinigung, Mineral deposits (abs.), Leoben, Austria; (29.).

Fripp R.E.P., 1976 Stratabound gold deposits in Archean Banded Iron-formation, Rhodesia. Econ. Geol.; 71: 58-75.

Fryer B.J., 1977 Rare earth evidence in iron-formations for changing Precambrian oxidation states. Geochim. Cosmochim. Acta; 41: 361-367.

Fryer B.J. & Hutchinson R.W. Generation of metal deposits on the sea floor. Can. J. Earth Sci.; 1976; 13: 126-135.

Fryer B.J. & Taylor R.P., 1987 Rare-earth element distributions in uraninites : implications for ore genesis. Chem. Geol.; 63: 101-109.

Fyon J.A., Crocket J.H., Schwarcz H.P., 1983 The Carshaw and Malga iron-formation hosted gold deposits of the Timmins area. In Colvine A.C.(Ed).The geology of gold in Ontario.; Ontario Geol. Surv. Misc. Paper 110: 98-110.

Fyon J.A., Crocket J.H., Schwarcz H.P., Kabir A. and Knyf M., 1981 Trace element and stable isotope geochemistry of auriferous iron formations in the Timmins area. Grant 49, Geoscience research program, summary of research, 1980-81. Pye E.G. (Ed.), Ontario Geological Survey, Miscellaneous Paper 98, 340 p. : 90-107.

Gair J.E., 1962 Geology and ore deposits of the Nova Lima and Rio Acima quadrangles, Minais Gerais, Brazil. U.S. Geol. Surv. Prof. Paper 341-A.

Garrels R.M., 1987 A model for the deposition of the microbanded Precambrian iron formations. Am. J. Sci.; 287: 81-106.

Garrels R.M., Perry E.A. Jr. & MacKenzie F.T., 1973 Genesis of Precambrian iron formations and the development of atmospheric oxygen. Econ. Geol.; 68: 1173-1179.

Garrett S., 1988 The geology and gold drainage geochemistry of the Lewis River Volcanics: Elliott Bay, Southwest Tasmania. Unpubl. Hons. Thesis, Geology Dept., University of Tasmania.:163 p.

Gates A.E., 1987 Shear zones: origin and mineralization. Geol. Soc. Am. Abs with programs; 19: 84-85.

Gautier D.L., 1979 Preliminary report of authigenic, euhedral tourmaline crystals in a productive gas reservoir of the Tiger Ridge field, north-central Montana. J. Sed. Pet.; 49: 911-916.

Gehrig M., Lentz H. & Stout M.Z., 1972 Thermodynamic properties of water-carbon dioxide-sodium chloride mixtures at high temperatures and pressures. In Timmerhaus K.D. & Barber M.S. (Eds.) High pressure science and technology 1, Physical properties and material synthesis, Plenum, New York; 539-542.

Geringer G.J.,Pretorious J. & Cilliers F.H., 1987 Stratabound copper-iron sulphide mineralisation in a Proterozoic front arc setting at Boksputs, Northwest Cape,South Africa — a possible Besshi-type deposit. Min. Dep.; 22: 81-89.

Ghosh S.K., 1988 Theory of chocolate tablet boudinage. J. Struct. Geol.; 10: 541-553.

Gibson H.L., Watkinson D.H. & Combe D.A., 1983 Silicification: hydrothermal alteration in an Archean geothermal system within the Amulet Rhyolite Formation, Noranda, Quebec. Econ. Geol.; 78: 954-971.

Gilligan J.M. & Foster R.P., 1987 Gold mineralization in iron formation: the importance of contrasting modes of deformation at Lennox mine, Zimbabwe. African Mining, Institution of Mining & Metall.; 127-138.

Glickson A.Y. & Derrick G.M., 1978 Geology and geochemistry of Middle Proterozoic basic volcanic belts, Mount Isa//Cloncurry, northwestern Queensland. Bureau of Mineral Resources, Australia, Record 1978/48 (unpubl.).

Glickson A.Y., Derrick G.M., Wilson I.H. & Hill R.M., 1976 Tectonic evolution and crustal setting of the middle Proterozoic Leichhardt River Fault Trough, Mount Isa region, northwestern Queensland. BMR J. Aust. Geol. Geophys.; 1: 115-129.

Gole M.J., 1981 Archean banded iron formations, Yilgarn Block, Western Australia. Econ. Geol.; 89: 169-183.

Gole M.J. & Klein C., 1981 Banded iron-formations through much of Precambrian time. Jour. Geol.; 89: 169-183.

Goodwin A.M., Thode H.G. and Chou C.-L., 1985 Chemostratigraphy and origin of the late Archean siderite-pyrite-rich Helen Iron Formation, Michipicoten Belt, Canada. Can. J. E. Sci.; 22: 72-84.

Govorov, I.N., 1971 Thermodynamic calculation and the interpretation of tourmaline systems. Chem. Abst.; 76: 129893s.

Graf R.L., 1977 Rare earth elements as hydrothermal tracers during the formation of massive sulfide deposits in volcanic rocks. Econ. Geol.; 72: 527 - 548.

Graf J.L., 1978 Rare earth elements, iron formations and sea water. Geochim. Cosmochim. Acta; 42: 1845-1850.

Grant J.A., 1986 The isocon diagram — a simple solution to Gresens' Equations for metasomatic alteration. Econ. Geol.; 81: 1976-1982.

Green G.R., Solomon M. & Walshe J.L., 1981 The formation of the volcanic-hosted massive sulfide ore deposit at Rosebery, Tasmania. Econ. Geol.; 76: 304-338.

Gresens R.L., 1967 Composition-volume relationships of metasomatism. Chem. Geol.; 2: 47-55.

Grip E., 1978 Sweden. In Bowie S.H.U. (Ed.), Mineral deposits of Europe, vol. 1, Northern Europe, Inst. Min. Metall. London.

Gross G.A., 1980 A classification of iron formations based on depositional environments. Canad. Miner.; 18: 215-222.

Groves D.I., Phillips N., Falconer L.J., Houstoun S.M., Ho S.E., Browning P., Dahl N. & McNaughton N.J., 1987 Evidence for an epigenetic origin for BIF-hosted gold deposits in greenstone belts of the Yilgarn Block, Western Australia. In "Recent Advances in understanding Precambrian gold deposits".; University of Western Australia, Publication 11.

Guidotti C.V. & Sassi F.P., 1976 Muscovite as a petrogenetic indicator mineral in pelitic schists. Neus Jahruch fur Mineralogie Abhadlungen; 127: 97-142.

Guiliani G., Chelletz A. & Mechiche M., 1987 Behavior of REE during thermal metamorphism and hydrothermal infiltration associated with skarn and vein type tungsten orebody in central Morocco. Chem. Geol.; 64: 279-294.

Gulson B.L., 1986 Lead isotopes in mineral exploration. Elsevier-Amsterdam. 245 p.

Guha J., Gauthier A., Vallee M., Descarreaux J. & Lange-Brard F., 1982 Gold mineralisation patterns at Doyon Mine (Silverstack), Bousquet, Quebec. In Hodder R.W. & Petruk W. (Eds.), Geology of Canadian gold deposits, C.I.M. special volume 24; 50-57.

Haas J.L., 1971 The effect of salinity on the maximum thermal gradient of a hydrothermal system at hydrostatic pressure. Econ. Geol.; 66: 940-946.

Hallager W.S., 1982 Geology of gold-bearing metasediments near Jardine. Gold '82: 191-218.

Halls C., Reinsbakken A., Ferriday I. & Haugen A., 1977 Geological setting of the Skorovas ore-body within the allochthonous volcanic stratigraphy of the Gnmersvik Nappe, central Norway. Geol. Soc. London, Spec. Publ.; 7: 128-151.

Hancock P.L., 1972 The analysis of en-echelon veins. Geol. Mag.; 109: 269-276.

Hannington M.D., Peter J.M. & Scott S.D., 1986 Gold in seafloor polymetallic sulfide deposits. Econ. Geol.; 81: 1867-1883.

Harder H., 1970 Boron content of sediments as a tool in facies analysis. Sedim. Geol.; 4: 153-175.

Haymon R.M. & Kastner M., 1981 Hot spring deposits on the East Pacific Rise at 21° N: preliminary description of mineralogy and genesis. Earth & Plan. Sci. Letts.; 53: 363-381.

Hekinian R. & Fouquet Y., 1985 Volcanism and metallogenesis of axial and off-axial structures on the East Pacific Rise near 13° N. Econ. Geol.; 80: 221-249.

Helgeson H.C., 1969 Thermodynamics of hydrothermal systems at elevated temperatures and pressures. Am. Jour. Sci.; 267: 729-804.

Helvaci C., 1978 A review of the mineralogy of the Turkish borate deposits. Mercian Geology; 6: 257-270.

Hemley J.J., Cygan G.L. & d'Angelo W.M., 1986 Effect of pressure on ore mineral solubilities under hydrothermal conditions. Geology; 14: 377-379.

Henley R.W., 1984 Chemical structure of geothermal systems. In Henley R.W., Truesdell A.H. & Barton P.B (eds.), Fluid-mineral equilibria in hydrothermal systems. Reviews in Econ. Geol.; 1: 9-27.

Henley R.W. & Brown K.L., 1985 A practical guide to the thermodynamics of geothermal fluids and hydrothermal ore dposits. In Berger B.R. & Bethke P.M. (Eds.), Geology and geochemistry of epithermal systems. Rev. Econ. Geol.; 2: 25-42.

Henley R.W., Truesdell A.H. & Barton P.B., 1984 Fluid-mineral equilibria in hydrothermal systems. Rev. in Econ. Geol. vol. 1, Soc. Econ. Geologists, 267 p.

Hennet R.J-C., Crerar D.A. & Schwartz J., 1988 Organic complexes in hydrothermal systems. Econ. Geol. ; 83: 742-764.

Henry D.J. and Guidotti C.V., 1985 Tourmaline as a petrogenetic indicator mineral: an example from the staurolite-grade metapelites of N.W. Maine. Am. Min.; 70: 1-15.

Herzig P.M., Becker K.P., Stoffers P., Backer H. & Blum N., 1989 The 'Cauliflower Garden' silica chimneys: a new variety of seafloor hydrothermal deposits. In 79th Annual meeting of the Geologische Vereinigung, Mineral deposits (abs.), Leoben, Austria; 5.

Hewitt D.A., 1973 The metamorphism of micaceous limestones from south-central Connecticut. Am. J. Sci.; 273A: 444-467.

Hey M.H., 1954 A new review of the chlorites. Min. Mag.; 30: 277.

Hobbs B.E., Means W.D. and Williams P.F., 1976 An outline of structural geology. Wiley and sons, New York-London-Sydney-Ontario.

Hodgson C.J., 1983 Preliminary report on a computer file of gold deposits of the Abitibi belt, Ontario. In Colvine A.C. (ed.), The geology of gold in Ontario: Ontario Geological Survey, Miscellaneous Paper 110: 11-37.

Holdaway M.J., 1971 Stability of andalusite and the aluminium silicate phase diagram. Am. J. Sci.; 271: 97-131.

Holland H.D., 1984 Chemical evolution of the atmosphere and oceans. Princeton University press, Princeton, 582 p.

Holland H.D. & Malinin S.D., 1979 On the solubility and occurrence of non-ore minerals. In Barnes H.L. (ed.), Geochemistry of hydrothermal ore deposits, 2nd edition: John-Wiley and sons, New York: 461-508.

Hollister L.S., Burruss R.C., Henry K.L. & Hendel E.M., 1979 Physical conditions during uplift of metamorphic terranes as recorded by fluid inclusions. Bull. Mineral.; 102: 555-561.

Holcombe R.J Pearson P.J. & Oliver N.H., 1987 The Mary Kathleen Fold belt, northwestern Queensland: geometry and timing of deformation. Abstract, International conference on the deformation of crustal rocks : 35-36.

Holm P.O., 1982 Non-recognition of continental tholeiites using the Ti-Y-Zr diagram. Cont. Min. & Pet.; 79: 308-310.

Hossack J.R., 1968 Pebble deformation and thrusting in the Bygdin area (southern Norway). Tectonophysics; 5: 315-339.

Hudson N.F.C. & Harte B., 1985 K_2O-poor, aluminous assemblages from the Buchan Dalradian, and the variety of orthoamphibole assemblages in aluminous bulk compositions in the amphibolite facies. Am. J. Sci.; 285: 224-266.

Humphris S.E., 1984 The mobility of the rare earth elements in the crust. In Henderson P (Ed.), Rare earth element geochemistry, Developments in Geochemistry 2, Elsevier - Amsterdam : 317-343.

Humphris S.E. & Thompson G., 1978 Hydrothermal alteration of oceanic basalts by seawater. Geochim. Cosmochim. Acta; 42: 107-125.

Huston D.L., 1989 Aspects of the structure and stratigraphy of the Balcooma volcanogenic massive sulfide deposit, northern Queensland. Unpub. University of Tasmania Ph.D thesis, 380 p.

Huston D.L. & Khin Zaw, 1988 Control on the fineness and grain-size of electrum in volcanogenic massive sulphide deposits. Unpubl. Final Rpt. to AMIRA project 84/P210, "Controls on gold and silver grades in volcanogenic sulphide deposits." University of Tasmania: 61-70.

Huston D.L. & Large R.R., 1989 A chemical model for the concentration of gold in volcanogenic massive sulphide deposits. Ore Deposit Reviews.; 4: 171-200.

Hutton L.J., Cavaney R.J. & Sweet I.P., 1981 New and revised stratigraphic units, Lawn Hill Platform, northwest Queensland. Qld. Govt. Min. J.; 82: 423-434.

Ireland T.J. & Mayer T.E., 1984 The geology and mineralisation of the Granites gold deposits, Northern Territory. Australian Inst. Min. Metall. Conference proceedings, Darwin, N.T., August 1984: 397-405.

Irvine T. & Baragar W., 1971 A guide to the chemical classification of the common volcanic rocks. Can. J. Earth Sci.; 8: 523-548.

Ivanova G.F., 1988 Geochemical conditions of formation of various composition wolfromates. Bull. Mineral.; 111: 97-103.

Jackson M.J., 1989 Sequence-stratigraphy, rifts, and tides at Mount Isa. BMR Research Newsletter 10, April : 8-11.

Jackson N.J., Drysdall A.R. & Stoeser D.B., 1985 Alkali granite-related Nb-Zr-REE-U-Th mineralisation in the Arabian Shield. In C. Halls, chairperson, High heat production (HHP) granites, hydrothermal circulation and ore genesis, p. 479-487. Inst. Min. & Metall., Cornwall, U.K.

James H.L., 1966 Chemistry of the iron-rich sedimentary rocks. U.S. Geol. Survey Prof. Paper 440-W.

James H.L. & Trendall A.F., 1982 Banded iron formation: distribution in time and paleoenvironmental significance. In Holland H.D. & Schidlowski M. (eds.) Mineral deposits and the evolution of the biosphere. Dahlem Konferenzen. Berlin: Springer-Verlag, Berlin : 199-217.

James R.S., Grieve R.A.F. & Paul L., 1978 The petrology of cordierite-anthophyllite gneisses and associated mafic and pelitic gneisses at Manitouwadge, Ontario. Am. J. Sci.; 278; (41-63.).

Janecky D.R. & Seyfried W.E., Jr., 1984 Formation of massive sulfide deposits on oceanic ridge crests: incremental reaction models from mixing between hydrothermal solutions and seawater. Geochem. Cosmochim. Acta; 48: 2723-2738.

Jaques A, Blake D & Donchak P., 1987 Regional metamorphism in the Selwyn Range area, northwest Queensland. Aust. BMR J of Geol. & Geophys.; 7: 181-196.

Johnson K.M. & McIntyre D.H., 1983 Disseminated gold-silver deposit in a rhyolite dome at the Sunbeam mine, Custer County, Idaho. Geol. Soc. Am. abs. with prog.; 15: 324-325.

Juniper S.K. & Fouquet Y., 1988 Filamentous iron-silica deposits from modern and ancient hydrothermal sites. Can. Min.; 83: 859-869.

Kalogeropoulos S.I., 1983 Chemistry, and role of zirconium in the formation of the Tsunokakezawa No. 1 orebody, Fukazawa Mine, Japan. Min. Deposita; 18: 535-541.

Kalogeropoulos S.I. & Scott S.D., 1983 Mineralogy and geochemistry of tuffaceous exhalites (Tetsusekiei) of the Fukazawa Mine, Hokuroku District, Japan. In Ohmoto H. & Skinner B.J. (Eds.), Kuroko and related volcanogenic massive sulphide deposits. Econ. Geol. Mon. 5 : 412-432.

Kary G. & Harley R., In press The Selwyn gold-copper project. Aust. Inst. Min. Metall. special volume on Australian ore deposits.

Kastner M., 1979 Silica polymorphs. In Burns R.G. (ed.), Marine minerals, Reviews in Mineralogy 6, Min. Soc. Am.; 99-107.

Kastner M. & Siever R., 1979 Low temperature feldspars in sedimentary rocks. Am. J. of Sci.; 45: 435-479.

Kennedy G.C., 1950 A portion of the system silica-water. Econ. Geol.; 45: 373-402.

Kerrich R. & Fryer B.J., 1979 Archaean precious-metal hydrothermal systems, Dome Mine, Abitibi Greenstone Belt II. REE and oxygen isotope relations. Can. J. Earth Sci.; 16: 440-458.

Kerrich R. & Fyfe W.S., 1981 The gold-carbonate association: source of CO_2, and CO_2 fixation reactions in Archaean lode deposits. Chem. Geol.; 33: 265-294.

Kerrich R., Fryer B.J., Milner K.J. & Peirce M.G., 1981 The geochemistry of gold-bearing chemical sediments, Dickenson Mine, Red Lake, Ontario: a reconnaissance study. Can. J. Earth Sci.; 18: 624-637.

Khomyakov A.P., 1963 Relation between content and composition of the rare earths in minerals. Geochemistry (U.S.S.R.); 2: 125-132.

Kimberley M.M., 1979 Geochemical distinctions among environmental types of iron formations. Chem. Geol.; 1979; 25: 185-212.

King R.W., 1988 Geochemical characteristics of tourmaline from Superior Province Archaean lode gold deposits: implications fro source regions and processes. Bicentennial Gold '88 extended oral abstracts, Geol. Soc. Aust. Abs. 23: 445-448.

Kirkham R.V., 1979 Copper in iron formation. In Current Research, Part B, Geol. Surv. of Canada. Paper 79-1B: 17-22.

Kisvarsanyi G. & Proctor P.D., 1967 Trace element content of magnetites and hematites, southeast Missouri iron metallogenic province, U.S.A. Econ. Geol.; 62: 449-471.

Klein C., 1973 Changes in mineral assemblages with metamorphism of some banded iron formations. Econ. Geol.; 1973; 68: 1075-1088.

Klein C., 1982 Amphiboles in iron formation. In Veblen D.R. & Ribbe H. (Eds.) Amphiboles: petrology and experimental phase relations. Min. Soc. America, Rev. In Min. 9B: 88-95.

Klosterman M.J., 1981 Applications of fluid inclusion techniques to burial diagenesis in carbonate rock sequences. Appl. Carb. Res. Prog. Tech. Ser. Contrib. (Louisiana State Univ.); 7.

Knuckey M.J. & Watkins J.J., 1982 The geology of the Corbet massive sulphide deposit, Noranda district, Quebec, Canada. In Hutchinson R.W., Spence C.D. &

Franklin J.M. (Eds.), Precambrian sulphide deposits, H.S. Robinson memorial volume, Geological Association of Canada Special Paper 25: 297-319.

Krautner H.G., 1977 Hydrothermal-sedimentary iron ores related to submarine volcanic rises: the Teliuc-Ghelar type as a carbonatic equivalent of the Lahn-Dill type. In Klemm D.D. & Schneider H.-J., Time- and stratabound ore deposits; Berlin, Springer-Verlag.

Kwak T.A.P., Brown W.M., Abersinghe P.B. & Tan Hing Teong, 1986 Fe solubilities in very saline hydrothermal fluids: their relation to zoning in some ore deposits. Econ. Geol.; 81: 447-465.

La Berge G.L., 1973 Possible biological origin of Precambrian iron-formations. Econ. Geol.; 68: 1098-1109.

Laing W.P. & Beardsmore T.J., 1986 Stratigraphic rationalisation of the eastern Mount Isa block, recognition of key correlations with the Georgetown and Broken Hill blocks in an Eastern Australian Proterozoic terrain, and their metallogenic implications. Abstr., Proceedings of the Eighth Australian Geological Convention, Adelaide, 16-22 February; 1986: 114-115.

Laing W.P., Rubenach M. & Switzer C.K., 1988 The Starra gold-copper deposit — syndeformational metamorphic mineralisation localised in a folded early regional zone of decollement. Ninth Aust. Geol. Soc. Conf. Abs., Brisbane, Qld. Geol. Soc. Aust. Abs. 21: 229.

Lambert I.B., 1976 The McArthur Zn-Pb-Ag deposit: features, metallogenesis and comparisons with some other stratiform ores. Handbook of stratabound and stratiform ore deposits. Wolf K.H. (Ed.) Amsterdam, Elsevier, 585 p.; 6: 535-585.

Lambert I.B. & Bubela B., 1970 Banded sulfide ores: the experimental production of monomineralic sulfide bands in sediments. Mineral. Deposita; 5: 97-102.

Lambert I.B., Donnelly T.H., Dunlop J.S.R. and Groves D.I., 1978 Stable isotope composition of early Archean sulphate deposits of probable evaporitic and volcanogenic origin. Nature; 276: 808-810.

Large R.R., 1975 Zonation of hydrothermal minerals at the Juno Mine, Tennant Creek goldfield, Central Australia. Econ. Geol.; 70: 1387-1413.

Large R.R., 1977 Chemical evolution and zonation of massive sulfide deposits in volcanic terrains. Econ. Geol.; 72: 549-572.

Large R.R., 1988 Development of an exploration model for gold-copper-bismuth ore deposits at Tennant Creek. Workshop Manual 2, University of Tasmania Gold-Copper project (Unpubl.): 95-104.

Large R.R. & Wedekind R., 1988 Geological controls on high grade gold mineralisation at Tennant Creek. Bicentennial Gold '88 extended oral abstracts, Geol. Soc. Aust. Abs. 22: 73-78.

Large R.R., Huston D.H., McGoldrick P., McArthur G. & Ruxton P., 1988 Gold distribution and genesis in Palaeozoic volcanogenic massive sulphide systems, Eastern Australia. Bicentennial Gold '88 extended oral abstracts, Geol. Soc. Aust. Abs. 22: 121-127.

Large R.R., Huston D.H., McGoldrick P., McArthur G. & Ruxton P., In press Gold distribution and genesis in Australian volcanogenic massive sulfide deposits, and their significance for gold transport models. In Keays R., Ramsay R. & Groves D. (Eds.) The geology of gold deposits: the perspective in 1988.; Econ. Geol. Mon. 6.

Large R.R., McGoldrick P.J., Berry R.F. & Young C.H., 1988 A tightly folded, gold-rich, massive sulfide deposit: Que River Mine, Tasmania. Econ. Geol.; 83: 681-694.

Lavreau J.J., 1973 New data about the Kilo-Mito gold deposits (Zaire). Mineral. Deposita; 8: 1-16.

Leishman J., 1983 Report on 1:25000, 1:5000 and 1:1000 geological mapping, Starra/Selwyn area, N.W. Qld. (Unpubl. Cyprus Minerals report).

Leonardos O.H. Jost H. Veiga A.T.C., 1988 Brazilian gold districts: how many are not associated with shear zones? Bicentennial Gold '88 extended oral abstracts, Geol. Soc. Aust. Abs. 23: 611-613.

Lhotka P.G. & Nesbitt B.E., 1988 Evidence for epigenetic Au mineralization in Archean silicate iron formation, Lupin Mine, Slave Province, Canada. Bicentennial Gold '88 extended oral abstracts, Geol. Soc. Aust. Abs. 23: 89-91.

Lister G.S. & Snoke A.W., 1984 S-C Mylonites. J. Struct. Geol.; 6: 617-638.

Loosveld R., 1989 The synchronism of crustal thickening and low-P facies metamorphism in the Mount Isa Inlier, Australia. Part 1: an example, the central Soldiers Cap Group belt. Tectonophysics; 158: 173-190.

Loosveld R. & G. Schreurs., 1987 Discovery of thrust klippen, northwest of Mary Kathleen, Mount Isa Inlier. Aust. J. Earth Sci.; 34: 387-402.

Lottermoser B.G., 1989 Rare earth elemnet study of exhalites within the Willyama Supergroup, Broken Hill Block, Australia. Mineral. Deposita; 24: 92-99.

Ludden J.N. & Thompson G., 1979 An evaluation of the behavior of the rare earth elements during weathering of sea floor basalt. Earth Planet. Sci. Lett.; 43: 85-92.

Luddington S., Desborough G. & Rostad O., 1980 Unique low-pressure hydrothermal alteration at Big Southern Butte, Snake River Plain, Idaho. Geol. Soc. Am Abs.;12: 279.

Lundberg B. & Smellie J.A.T., 1979 Painirova and Mertainen iron ores: two deposits of the Kiruna iron ore type in northern Sweden. Econ. Geol.; 24: 1131-1152.

Lydon J.W., 1988 Ore deposit model #14. Volcanogenic massive sulphide deposits. Part 2: genetic models. Geoscience Canada; 15: 43-65.

Lydon J.W. & Galley A., 1986 Chemical and mineralogical zonation of the Mathiati alteration pipe, Cyprus, and its genetic significance. In Gallagher M.J., Ixer R.A., Neary C.R. & Prichard H.M.(Eds.), Metallogeny of basic and ultrabasic rocks: Institution of Min. & Met., London : 49-68.

Lyons J.I., 1988 Volcanogenic iron oxide deposits, Cerro de Merado and vicinity, Durango, Mexico. Econ. Geol.; 83: 1886-1906.

MacDonald A.J., 1983 The iron formation-gold association: evidence from the Geraldton area. In Colvine A.C. (Ed.), The geology of gold in Ontario. Ontario Geol. Surv. Misc. Paper 110, 278 p.

Maclean W.H., 1988 Rare earth element mobility at constant inter-REE ratios in the alteration zone at the Phelps Dodge massive sulphide deposit, Matagami, Quebec. Mineral. Deposita; 23: 231-238.

Magnusson N.H., 1970 The origin of the iron ores in central Sweden and the history of their alterations. Sveriges Geol. Under-sokning, ser. C, 493 p.; 643.

Maiden K., 1986 Metamorphic features of stratiform gold ores in the Barberton Greenstone belt, Eastern Transvaal. Trans. S. Afr. Min. Soc.; 1986; 89: 325-338.

Maksimovic Z. & Roaldset E., 1976 Lanthanide elements in some Mediterranean karstic bauxite deposits. Trav. Com. Int. Etude Bauxites, Oxydes, Hydroxydes Alum.; 13: 199-220.

Mangan M., Craig J.R. & Rimstidt J.D., 1984 Submarine exhalative gold mineralisation at the London-Virginia Mine, Buckingham County, Virginia. Min. Deposita; 19: 227-236.

Markun C.D. & Randazzo A.F., 1988 Early silica cementation and subsequent diagenesis in arenites from four early Proterozoic iron formations of North America — discussion. J. Sed. Pet.; 58: 544-546.

Martin J.-M., Hogdahl O.T. & Philippot J.C., 1976 Rare earth element supply to the ocean. J. Geophys. Res.; 81: 3119-3124.

Mason D.J., 1981 On the origin and geology of the Little Cadia stratiform, iron-copper ores, near Orange NSW. BSc. (Hons.) thesis, University of Newcastle, 88 p.

Massone H. J. & Schreyer W., 1987 Phengite geobarometry based on the limiting assemblage with K-feldspar, phlogopite and quartz. Cont. Min. & Pet.; 96: 212-224.

Master S., Henry G. & Borg G., 1989 Geochemistry and mineralogy of banded iron-formation-hosted gold mineralization in the Gwanda greenstone belt, Zimbabwe — a discussion. Econ. Geol.; 84: 194-197.

Mathews A., 1976 Magnetite formation by reduction of hematite with iron under hydrothermal conditions. Am. Mineral.; 61: 927-932.

Mathias B.V. & Clarke G.J., 1975 Mount Isa copper and silver-lead-zinc orebodies — Isa and Hilton mines. In Knight C.L. (ed.), Econ. Geol. Aust. and Papua New Guinea. I — Metals. Aust. Inst. Min. Met. Monograph 5 : 377-382.

Mathieson N.A. & Hodgson C.J., 1984 Alteration, mineralization, and metamorphism in the area of the East South "C" ore zone, 24th level of the Dickenson mine, Red Lake, northwestern Ontario. Can. J. Earth Sci.; 21: 35-52.

Maus, H., 1979 Mineralization of the thermal water fissures of Wildbad. Chem. Abst.; 79; 68515h.

Maynard J.B., 1983 Geochemistry of sedimentary ore deposits.; 1983: Springer-Verlag.

Maynard J.B., Valloni R. & Yu H.-S., 1982 Composition of modern deep-sea sands from arc-related basins. In Leggett J.K. (ed.), Trench-forearc geology: sedimentation and tectonics on modern and ancient active plate margins. Geol Soc. London spec. publ.; 551-560.

McBirney A. & Murase T., 1971 Factors governing the formation of pyroclastic rocks. Bull. Volc.; 34: 372-384.

McClay K & Ellis P., 1984 Deformation of pyrite. Econ. Geol.; 79: 400-403.

McCrea T., 1950 The isotopic chemistry of carbonates and a paleotemperature scale. J. Chem. Phys.; 18: 849-857.

McKenzie D., 1978 Some remarks on the development of sedimentary basins. Earth Plan Sci. Lett.; 40: 25-32.

McKibben M.A. & Elders W.A., 1985 Fe-Zn-Cu-Pb mineralization in the Salton Sea geothermal system, Imperial Valley, California. Econ. Geol.; 80: 539-559.

McKibben M.A. & Eldridge C.S., 1989 Sulfur isotopic variations among mineral and aqueous species in the Salton Sea geothermal system: a SHRIMP ion microprobe and conventional study of active ore genesis in a sediment-hosted environment. Am. J. Sci.; 289: 661-707.

McKibben M.A., Andes J.P. Jr. & Williams A.E., 1988 Active ore formation at a brine interface in metamorphosed deltaic lacustrine sediments: the Salton Sea geothermal system, California. Econ. Geol.; 83: 511-523.

McKibben M.A., Williams A. & Okubo S., 1988 Metamorphosed plio-Pleistocene evaporites and the origins of hypersaline brines in the Salton Sea geothermal system, California; fluid inclusion evidence. Geochim. Cosmochim. Acta; 52: 1047-1056.

Mel'nik Y.P., 1982 Precambrian banded iron formations: physicochemical conditions of formation. Elsevier.

Menzies M., Blanchard D. & Jacobs J., 1977 Rare earth and trace element geochemistry of metabasalts from the Point Sal ophiolite, California. Earth Planet. Sci. Lett.; 37: 203-215.

Merrill R.B., Robertson J.K. & Wyllie P.J., 1970 Melting reactions in the systems $NaAlSi_3O_8$-$KAlSi_3O_8$-SiO_2-H_2O to 20 kilobars compared with results for other feldspar-quartz-H_2O and rock-H_2O systems. J. Geol.; 78: 558-69.

Meschede M., 1986 A method of discriminating between different types of mid-ocean ridge basalts and continental tholeiites with the Nb-Zr-Y diagram. Chem. Geol.; 56: 207-218.

Michard A. & Albarede F., 1986 The REE content of some hydrothermal fluids. Chem. Geol.; 55: 51-60.

Michel-Levy, M. C., 1953 Synthesis of minerals associated with contact metamorphism by granite. Soc. Francaise de Min. Cryst.; 76: 237-293.

Mineyev D.A., Dikov Yu. P. Sobolev B.P. & Borutskaya V.L., 1966 Differentiation of rare-earth elements under supercritical conditions. Geochem. Int.; 3: 357-359.

Moine B. & de la Roche H., 1968 Nouvelle approche du probleme de l'origine des amphibolites a partir de leur composition chimique. C.R.Acad.Sci. Paris; 267(2084-2088.).

Moine B., Sauvan P. & Jarousse J., 1981 Geochemistry of evaporite-bearing series: a tentative guide for the identification of metaevaporities. Contr. Min. Pet.; 76: 401-412.

Mookherjee A., 1971 Deformation of pyrite — a discussion. Econ. Geol.; 66: 200.

Moore R., 1964 Geology and ore deposits of the Gongo Socco and Rio Acima quadrangles, Minas Gerais, Brazil. U.S.G.S. Prof. Paper 341-D.

Morgan J.W. & Wandless G.A., 1980 Rare earth element distribution in some hydrothermal minerals: evidence for crystallographic control. Geochim. Cosmochim. Acta; 44: 973-980.

Morrison I., 1985 The Starra Au-Cu prospect, north-west Queensland: summary report. Unpublished report to James Cook University geology department, in fulfillment of GL 504, 19 p.

Mossman D.J. & Brown M.J., 1986 Stratiform barite in sabkha sediments, Walton-Cheverie, Nova Scotia. Econ. Geol.; 81: 2016-2024.

Mottl M.J., 1983 Metabasalts, axial hot springs, and the structure of hydrothermal systems at mid-ocean ridges. Geol. Soc. Am. Bull.; 94: 1161-180.

Muehlenbachs K., 1986 Alteration of the oceanic crust and 18O history of seawater. In Valley J.W., Yaylor H.P. Jr. & O'Neil J.R. (Eds.) Stable isotopes in high temperature geological processes. Min. Soc. Am., Revs. In Min. 16: 425-445.

Muessig S., 1966 Recent South American borate deposits. Sec. Symp. on Salt, Ed. J.Rau., North Ohio Geol. Soc.: 151-159.

Muir M.D., 1979 A sabkha model for the deposition of part of the Proterozoic McArthur Group of the Northern Territory, and its implication for mineralisation. BMR Journal of Aust. Geol. & Geophys.; 4: 149-162.

Muir M.D., 1981 Depositional environments of host rocks to northern Australian lead - zinc deposits, with special reference to McArthur River. Min. Assoc. Canada, Short Course Notes; Sediment-hosted stratiform Pb-Zn deposits.; 9: 141-174.

Muir M., Donnelly T., Wilkins R. and Armstrong K., 1987 Stable isotope, petrological and fluid inclusion studies of minor mineral deposits from the McArthur Basin, implications for the genesis of some sediment-hosted base-metal mineralisation from the N.T. Aust. J. of Earth Sci.; 32: 239-260.

Murphy B. & Hynes A., 1986 Contrasting secondary mobility of Ti, P, Zr, Nb and Y in two metabasaltic suites in the Appalachians. Can. J. Earth Sci.; 23: 1138-1144.

Naboko, S.I., 1959 Volcanic exhalations and products of their reactions as exemplified by Kamchatka-Kurile volcanoes. Bull. Volcanoligique, Series 2.; 20: 121-136.

Nagasawa H. & Suwa K., 1986 Rare-earth concentrations in 3.5-billion-year-old Onverwacht cherts: an indicator for early Precambrian crustal environments. Geochemical J.; 20: 253-260.

Nahnybida C.I., Hutcheon I and Kirker J., 1982 Diagenesis of the Nisku formation and the origin of late-stage cements. Can. Min.; 1982; 20: 129-140.

Neiva, A.M., 1974 Geochemistry of tourmaline (schorlite) from granites, aplites and pegmatites from northern Portugal. Geochim. Cosmochim. Acta; 38: 1307-17.

Nesbitt H.W., 1979 Mobility and fractionation of rare earth elements during weathering of a granodiorite. Nature; 279: 206-210.

Neudert M.K. & Russell R.E., 1982 Shallow water and hypersaline features from the Middle Proterozoic Mount Isa sequence, northern Australia. Nature; 293: 284-288.

Nguyen P.T., Booth S., James P.R. & Both R.A., 1988 The White Devil gold deposit, Tennant Creek, Northern Territory. Bicentennial Gold '88, Extended Oral Abstracts Geol. Soc. of Australia Abstracts vol. 22: 198-200.

Nicholson P.M., 1980 The geology and economic significance of the Golden Dyke Dome, Northern Territory. Proceedings of the international Uranium symposium on the Pine Creek Geosyncline: 319-334.

Niem A.R., 1977 Mississipian pyroclastic flow and ash-fall deposits in the deep-marine Ouachite flysch basin, Oklohoma and Arkansas. Bull. Geol. Soc. Am.; 88: 49-61.

Nilsen O., 1978 Caledonian sulphide deposits and minor iron-formations from the southern Trondheim region, Norway. Norges Geol. Undersokelse; 340: 35-85.

Nisbet, B.W., 1983 A brief study of the relationship between metamorphism, mineralisation and structure in the Selwyn region, Northwestern Queensland. Unpubl. BMR internal report.: 1983.

Nisbet B.W. & Joyce P., 1980 Squirrel Hills Zn-mineralisation, Mt. Isa belt, Qld. In Butt C.R.M. & Smith R.E. (Eds.) Conceptual models in exploration geochemistry 4, Assoc. of Explor. Geochemistry special publ. 8: 109-174.

Nisbet B.W., Devlin S. & Joyce P., 1983 Geology and mineralization at Mt. Cobalt, northwestern Queensland. Aust. Inst. Min. & Metall.; 287: 9-17.

Norrish K. & Hutton J.T., 1969 An accurate X-ray spectrographic method for the analysis of a wide range of geological samples. Geochim. Cosmochim. Acta; 33: 431-453.

Norrish K. & Chappell B.W., 1977 X-ray fluorescence spectrometry. In J. Zussman (Ed.), Physical methods in determinative mineralogy. Academic Press, London, 2nd ed.: 254-272.

Nutt T.H.C., 1982 Archaean gold mineralization in the Nando and Pinkun mines, Kadoma district, Zimbabwe. In Foster R.P.(ed.), Gold '82: The geology, geochemistry and genesis of gold deposits. Geol. Soc. of Zimbabwe Spec. Publ. 1: 261-284.

Nyvlt J.A., 1980 Aspects of metasomatic alteration, mineralisation and geochemistry at the SWAN copper prospect, northwest Queensland. Unpubl. Hons. Thesis, University of Sydney.

Oberthur T. & Saager R., 1986 Silver and mercury in gold particles from the Proterozoic Witwatersrand placer deposits of South Africa: metallogenic and geochemical implications. Econ. Geol.; 81: 20-31.

Oen I.S., Helmers H., Verschure R.H. & Wiklander U., 1982 Ore deposition in a Proterozoic incipient rift zone environment: a tentative model for the Filipstad-Grythyttan-Hjulsjo region, Bergslagen, Sweden. Geol. Runds.; 71: 182-194.

Ohmoto H., 1972 Systematics of sulfur and carbon isotopes in hydrothermal ore deposits. Econ. Geol.; 68: 1110-1125.

Ohmoto H., 1986 Stable isotope geochemistry of ore deposits. In Valley R.W., Taylor H.P. and O'Neil J.R. (eds.), Stable isotopes in high temperature geological processes. Reviews in Min.; 16: 491-556.

Ohmoto H. & Rye R.O., 1979 Isotopes of sulfur and carbon. In Barnes H.L. (Ed.) Geochemistry of hydrothermal ore deposits, 2nd. ed., Wiley - New York. 781p.

Ohmoto H., Mizukami M., Drummond S.E., Eldridge C.S., Pisutha-Arnond V. & Lenagh T.C., 1983 Chemical processes of Kuroko formation. In Ohmoto H. & Skinner B.J. (Eds.), Kuroko and related volcanogenic massive sulphide deposits. Econ. Geol. Mon. 5 : 570-604.

Ohtagaki T., Takahashi Y. & Obara K., 1974 Geology of the Hanawa mine, Akits Prefecture. Soc. Mining Geologist, Japan, Spec. Issue 6: 131-139.

Oliver N.H.S. and Wall V.J., 1987 A metamorphic plumbing system in Proterozoic calc-silicates, Queensland, Australia. Geology; 15(793-796.).

Oliver N.H.S. & Wall V.J., 1986 Scapolite paragenesis in calc-silicates at Mary Kathleen, N.E. Queensland: implications for metamorphic fluid evolution. Eighth Aust. Geol. Conv, Adelaide Abstracts; 15: 147-148.

O'Neil J.R., Clayton R.N. and Mayeda T.K., 1969 Oxygen isotope fractionation in divalent metal carbonates. J. Chem. Phys.; 51: 5547-5558.

O'Neil J.R., Adami L.H. & Epstein S., 1975 Revised value for the ^{18}O fracionation between CO_2 and H_2O at 25° C. J. Res. US Geol. Surv.; 3: 623-624.

Ophel M.A., 1980 Mineralogy and geochemistry of a copper-bearing breccia zone, Mt. Dore, northwest Queensland. Unpubl. Hons. thesis, University of Sydney.

Orridge G.R., 1980 25. The Pegmont Pb-Zn deposit, Mt. Isa belt, Qld. In Butt C.R.M. & Smith R.E. (Eds.) Conceptual models in exploration geochemistry 4, Assoc. of Explor. Geochemistry special publ. 8: 166-169.

Osichkina R.G., 1978 Rubidium and cesium in salt deposits of an Upper Jurassic evaporite formation in southern Central Asia as an index of the conditions of their formation. Geochem. Inst. (Engl. Trans.); 15(3): 168-173.

Otagaki T., Abe Y., Tsukada Y., Kimura A., Osada T. & Fukioka H., 1970 Geology and ore deposits of the Shakanai Mine (4) . On the occurrence of ore deposits and pyroclastic rocks near the ore bodies. Mining Geol.; 26: 315-327.

Owen J.V., 1988 Geochemical changes accompanying the mylonitization of diverse rock-types from the Grenville Front zone, eastern Labrador. Can. J. Earth Sci.; 25: 1472-1484.

Page R.W., 1983a Timing of superposed volcanism in the Proterozoic Mount Isa Inlier, Australia. Precamb. Res.; 21: 223-245.

Page R.W., 1983b Chronology of magmatism, skarn formation and uranium mineralisation, Mary Kathleen, Queensland, Australia. Econ. Geol.; 78: 833-853.

Page R.W. & Bell T. H., 1986 Isotopic and structural responses of granite to successive deformation and metamorphism. J. of Geol.; 94: 365-379.

Page R.W. & Williams I.S., 1988 Age of the Barramundi orogeny in northern Australia by means of ion microprobe and conventional U-Pb zircon studies. Precamb. Res.; 40/41: 21-36.

Palacios C.M., Hein U.F. & Dulski P., 1986 Behavior of rare earth elements during hydrothermal alteration at the Buena Esperanza copper-silver deposit, northern Chile. Earth Plan. Sci. Lett.; 80: 208-216.

Palmer J.A., Phillips G.N. & McCarthy T.S., 1987 The nature of the Precambrian atmosphere and its relevance to Archaean gold mineralization. In Ho S.E. & Groves D.I. (Eds.), Recent advances in understanding Precambrian gold deposits; geol. Dept. & Uni. Ext., University of W.A. Publ. 11: 341-355.

Parak T., 1975 Kiruna iron ores are not "intrusive-magmatic ores of the Kiruna type". Econ. Geol.; 70: 1242-1258.

Parak T., 1984 On the magmatic origin of iron ores of the Kiruna type — a discussion. Econ. Geol.; 79: 1945-1949.

Parak T., 1985 Phosphorous in different types of ore, sulfides in the iron deposits, and the type and origin of ores at Kiruna. Econ. Geol.; 80: 646-666.

Parry W.T., Wilson P.N. and Bruhn R.L., 1988 Pore fluid chemistry and chemical reactions on the Wasatch normal fault, Utah. Geochim. Cosmochim. Acta; 1988; 52: 2053-2063.

Passchier C.W., 1986 Alligator Syncline: evidence for extensional tectonics in the Proterozoic Mount Isa Inlier, Australia. Geology; 14: 1008-1011.

Passchier C.W. & Simpson C., 1986 Porphyroclast systems as kinematic indicators. J. Struct. Geol.; 8: 831-843.

Passchier C.W. & Williams P.R., In press Proterozoic extensional deformation in the Mount Isa Inlier, Queensland, Australia. Geol. Mag.

Paterson C.J., 1987 Controls on gold and tungsten mineralization in metamorphic-hydrothermal systems, Otago, New Zealand. Geological Association of Canada, Special Paper; 32: 25-39.

Pearce J.A. & Cann J.R., 1973 Tectonic setting of basic volcanic rocks determined using trace element analyses. Earth Plan. Sci. Lett.; 19: 290-300.

Perkins W.G., 1981 Mount Isa copper ore bodies — evidence against a sedimentary origin. BMR J. Aust. Geol. & Geoph.; 6: 331.

Perriam R.P.A., Hronsky J.M.A., Schmulian M.L., Simmonds J.R. & Goss B.J., 1988 Geology of the Lancefield gold deposit. Bicentennial Gold '88 extended poster abstracts, Geol. Soc. Aust. Abs. 23 : 107-112.

Perry E.C. Tan F.C., Jr., and Morey, G.B., 1973 Geology and stable isotope geochemistry of the Biwabik iron formation, Northern Minnesota. Econ. Geol.; 68: 1110-1125.

Peter J.M., 1986 Genesis of hydrothermal vent deposits in the southern trough of the Guymas Basin, Gulf of California: a mineralogical and chemical study. Unpubl. MsC. thesis, Univers. of Toronto.

Phillips G.N. & Groves D.I., 1983 The nature of Archean gold-bearing fluids as deduced from gold deposits in Western Australia. J. Geol. Soc. Aust.; 1983; 30: 25-40.

Phillips G.N., Groves D.I. & Martyn J.E., 1984 An epigenetic origin for Archean banded iron-formation hosted gold deposits. Sci. Comm. in Econ. Geol.; 79: 162-171.

Phillips G.N., Groves D.I., Neall F.B., Donnelly T.H. & Lambert I.B., 1986 Anomalous sulfur isotope compositions in the Golden Mile, Kalgoorlie. Econ. Geol. (Sci. Comm.); 81: 2008-2015.

Philpotts A.R., 1967 Origin of certain iron-titanium oxide and apatite rocks. Econ. Geol.; 62: 303-315.

Pietsch B.A. & Edgoose C.J., 1988 The stratigraphy , metamorphism and tectonics of the Early Proterozoic Litchfield Province and western Pine Creek Geosycline, Northern Territory. Precamb. Res.; 40/41: 565-588.

Plimer I.R., 1977 The origin of the albite-rich rocks enclosing the cobaltion-pyrite deposit at Thackaringa, N.S.W., Australia.; 12: 175-181.

Plimer I.R., 1983 The association of tourmaline-bearing rocks with mineralization at Broken Hill. N.S.W. Proc. Ann. Aus. Inst. Min. Met. Conf., Broken Hill; 157-176.

Plimer I.R., 1986 Tourmalinites from the Golden Dyke Dome, Northern Australia. Min. Dep.; 21: 263-270.

Plimer I.R., 1987a The association of tourmalinite with stratiform scheelite deposits. Mineral. Deposita; 22: 282-291.

Plimer I.R., 1987b Tourmalinites associated with Australian Proterozoic submarine exhalative ores. In: Friedrich, Schneider H-J, Herzig P (eds) Base metal sulfide deposits in volcanic and sedimentary environments. Springer, Berlin Heidelberg New York Tokyo.

Plumb K.A & Derrick G.M., 1975 Geology of the Proterozoic Rocks of the Kimberly o Mt Isa region. Knight C.L. (ed). Economic Geology of Australia and Papua New Guinea, Vol 1; 217-252.: Aust. Inst. Min.& Metall.

Plumb K.A., Derrick G.M., & Wilson I.H., 1980 PreCambrian geology of the McArthur River- Mt Isa region, Northern Australia. In Henderson R.A. & Stephenson P.J. (Eds.) The Geology and Geophysics of North Eastern Australia. Geol. Soc. Aust., Qld. Div., Brisbane.

Plyusnina L., 1982 Geothermometry and geobarometry of plagioclase-hornblende-bearing assemblages. Contrib. Min. & Pet.; 80: 140-146.

Pontifex I.R., 1986 Mineralogical report 4775, Starra project Mineralogical study Metallurgical hole No. 1 (STQ- 86 - 223) Area 251 (unpub.).

Porada H. & Behr H.J., 1988 Setting and sedimentary facies of late Proterozoic alkali lake (playa) deposits in the southern Damara belt of Namibia. Sed. Geol.; 58: 171-198.

Pottorf R.J. & Barnes H.J., 1983 Mineralogy, geochemistry, and ore genesis of hydrothermal sediments from the Atlantis II Deep, Red Sea. In Ohmoto H. & Skinner B.J. (Eds.), Kuroko and related volcanogenic massive sulphide deposits. Econ. Geol. Mon. 5: 198-223.

Povondra P. and Novak M., 1986 Tourmalines in metamorphosed carbonate rocks from western Moravia, Czechoslavakia. N. Jb. Miner. Mh.: 273-282.

Power G.M., 1968 Chemical variation in tourmalines form south-west England. Min. Mag.; 36: 1078-1089.

Prider R.T., 1940 Cordierite-anthophyllite rocks associated with spinel-hypersthenites from Toodyay, Western Australia. Geol. Mag.; 77: 364-382.

Quade H., 1976 Genetic problems and environmental features of volcano-sedimentary iron-ore deposits of the Lahn-Dill type. In "Handbook of Stratabound and Stratiform ore deposits." Ed. K.H.Wolfe, Elsevier.; (89-156).

Quinquis H., 1980 Schistes bleues et deformation progressive. Unpubished Thesis, University of Rennes, 145 p.

Raimbault L., 1985 Utilisation des spectres de terres rares des mineraux hydrothermaux (apatite, fluorine, scheelite, wolframite) pour la caracterisation des fluides mineralisateurs et l'identification des magma sources et des processus evolutifs. Bull. Mineral.; 108: 737-744.

Ramboz C., Oudin E. & Thisse Y., 1988 Geyser-type discharge in the Atlantis II Deep, Red Sea. Can. Min. 26: 765-787.

Ramdohr P., 1980 Ore minerals and their intergrowths (3rd. Ed.). Pergamon, Oxford press, 1174p.; 1980.

Ramsay S.R. and Davidson L.R., 1970 The origin of scapolite in regionally metamorphosed rocks, Mary Kathleen, Queensland, Australia. Cont. Min. Pet.; 25: 41-51.

Rankin P.C. & Childs C.W., 1976 Rare-earth elements in iron-manganese concretions from New Zealand soils. Chem. Geol.; 18: 55-64.

Ransom D.M., 1986 Structural environment of the Starra auriferous ironstone deposits,Selwyn region, northwest Queensland. Unpubl. report to Cyprus Minerals.

Raymahashay B.C. & Holland H.D., 1969 Redox reactions accompanying hydrothermal wall rock alteration. Econ. Geol.; 64: 291-305.

Reading H.G., 1980 Characteristics and recognition of strike-slip fault systems. In: Sedimentation in oblique-slip mobile zones. Spec. Publ. 4 I.A.S. Ed. P.F. Ballance and H. G. Reading.

Reed M.H., 1983 Seawater-basalt reaction and the origin of greenstones and related ore deposits. Econ. Geol.; 78: 466-485.

Reid A.M., le Roex A.P. & Minter W.E.L., 1988 Compositions of gold grains in the Vaal Placer, Klerksdorp, South Africa. Mineral. Deposita; 1988; 23: 211-217.

Reinhardt J., 1987 Cordierite-anthophyllite rocks from north-west Queensland, Australia: metamorphosed magnesian pelites. J. Metamorphic Geol.; 5: 451-472.

Reinhardt J. & Hamilton L.M., In press Retrograde kyanite in a low-pressure/high temperature metamorphic terrain (Mary Kathleen Fold Belt, Australia): implications for the P-T-t history. Geology.

Renfro A.R., 1974 Genesis of evaporite-associated stratiform metalliferous deposits — a sabkha process. Econ. Geol.; 69: 33-45.

Reynolds R.C., 1965 Geochemical behavior of boron during metamorphism of carbonate rocks. Geochim. Cosmochim. Acta; 29: 1101-1114.

Rice J.M. & Ferry J.M., 1982 Buffering, infiltration and the control of intensive variables during metamorphism. In Ferry J.M. (Ed.) Characterization of metamorphism through mineral equilibria. Rev. in Min., Min. Soc. America; 10: 263-324.

Richardson S.H., 1979 Chemical variation induced by flow differentiation in an extensive Karoo dolerite sheet, southern Namibia. Geochim. Cosmochim. Acta; 43: 1433-1441.

Rickard M.J. and Rixon L.K., 1983 Stress configurations in conjugate quartz-vein arrays. J. Struct. Geol.; 5: 573-578.

Ricketts B.D., 1981 Authigenic tourmaline from the middle Precambrian Belcher Group, Northwest Territories. Can. Pet. Geol.; 26: 543-550.

Ridley J., 1986 Parallel stretching lineations and fold axes oblique to a shear displacement direction — a model and observations. J. Struct. Geol.; 8: 647-653.

Rigg D.M. & Helmstaedt H., 1981 Relations between structures and gold mineralization in Campbell Red Lake and Dickenson mines, Red Lake area, Ontario. In Pye E.G. & Roberts R.G. (Eds.), Genesis of Archean, volcanic-hosted gold deposits: Ontario Geological Survey, Miscellaneous Paper 97; 111-127.

Rimstidt J.D. & Barnes H.L., 1980 The kinetics of silica-water reactions. Geochim. Cosmochim. Acta; 44: 1683-1699.

Ripley E.M. & Ohmoto H., 1977 Mineralogic, sulfur isotope, and fluid inclusion studies of the stratabound copper deposits at the Raul Mine, Peru. Econ. Geol.; 72: 1017-1041.

Ririe G.T., 1989 Evaporites and stratabound tungsten mineralization. Geology; 17: 139-143.

Riverin G. & Hodgson C.J., 1980 Wall-rock alteration at the Millenbach Cu-Zn mine, Noranda, Quebec. Econ. Geol.; 75: 424-444.

Robbins, C.R. and Yoder, H.S.,Jr., 1962 Stability relations of dravite, a tourmaline. Ann.Rpt., Director Geophysical Laboratory, Carnegie Inst. Year Book 61; 106-108.

Roberts D.E. & Hudson G.R., 1983 The Olympic Dam Copper - Uranium - Gold deposit, Roxby Downs, South Australia. Econ. Geol.; 78: 799-822.

Roberts R.G., 1987 Ore deposit models #11. Archean Lode gold deposits. Geoscience Canada; 14: 37-52.

Roberts R.G. & Reardon E.J., 1978 Alteration and ore-forming processes at Mattagami Lake mine, Quebec. Can. J. Earth Sci.; 15: 1-21.

Robertson A.H.F. & Fleet A.J., 1976 The origin of rare earths in metalliferous sediments of the Troodos Massif, Cyprus. Earth Planet. Sci. Lett.; 28: 385-394.

Robertson C.W., 1982 The role of pre-existing sulphides in copper-ore formation at Mount Isa, Queensland. BMR Journal of Aust. Geol. & Geophys.; 7: 119-125.

Robinson B.W. & Kusabe M., 1975 Quantitative preparation of SO_2, for $^{34}S/^{32}S$ analyses, from sulphides by combustion with cuprous oxide. Anal. Chem.; 1975; 47: 1179-1181.

Robinson P., Higgins N.C. & Jenner G.A., 1986 Determination of rare-earth elements, Yttrium and Scandium in rocks by an ion exchange-X-ray fluorescence technique. Chem. Geol.; 55: 121-137.

Roedder E., 1984 Fluid Inclusions. Reviews in Mineralogy, Vol. 12, Min. Soc. Am. 644 p.

Roering C., 1967 The geometrical significance of natural en-echelon crack arrays. Tectonophysics; 5(2): 107-123.

Rona P.A., 1984 Hydrothermal mineralization at seafloor spreading centres. Earth Science Revs.; 20: 1-104.

Rona P.A., 1988 Hydrothermal mineralization at oceanic ridges. Canadian Mineralogist; 26: 431-465.

Rose A.W., Herrick D.C. & Deines P., 1985 An oxygen and sulfur isotope study of skarn-type magnetite deposits of the Cornwall-type, Southeastern Pennsylvania. Econ. Geol.; 80: 418-444.

Rose W.J. & Morrison G.W., 1988 Classification of gold deposits, using the silver content (fineness) of gold. Bicentennial Gold '88 Extended Poster Abstracts, Australian Geol. Soc. Abstracts No. 23; 1988: 464-468.

Rubin J.N., Henry C.D. & Price J.G., 1989 Hydrothermal zircons and zircon overgrowths, Sierra Blanca Peaks, Texas. Am. Min.; 74: 865-869.

Ruhlin D.E. & Owen R.M., 1986 The rare earth element geochemistry of hydrothermal sediments from the East Pacific Rise: examination of a seawater scavenging mechanism. Geochim. Cosmochim. Acta; 50: 393-400.

Rui I., 1973 Structural control and wall rock alteration at Kilingdal mine, central Norwegian Caledonides. Econ. Geol.; 1973; 68: 859-883.

Rumble D.(III)., 1976 Oxide Minerals in metamorphic rocks. In Rumble D.(III) (Ed.) Oxide minerals; Reviews in mineralogy 3: R1-R23.

Russell M.J., 1975 Lithogeochemical environment of the Tynagh base-metal deposit, Ireland, and its bearing on ore deposition. Trans. Inst. Min. & Metall.; 84: B128-133.

Rust B.R. & Koster E.H., 1984 Coarse alluvial deposits. In Walker R.G.(Ed.) Facies Models (2nd. ed.) Geoscience Canada Reprint Series 1: 53-71.

Rye D.M. & Williams N., 1981 Studies of base metal sulphide deposits at McArthur River, N.T., Australia #3: The stable isotope geochemistry of the HYC, Ridge and Cooley deposits. Econ. Geol.; 76: 1-26.

Rye D.M., Doe B.D. & Delevaux M.H., 1974 Homestake gold mine, South Dakota: II. Lead isotopes, mineralization ages, and source of lead in ores of the northern Black Hills. Econ. Geol.; 69: 814-822.

Saager R. & Oberthur T., 1989 Geochemistry and mineralogy of banded iron-formation-hosted gold mineralization in the Gwanda greenstone belt, Zimbabwe — a reply. Econ. Geol.; 84: 197-198.

Saager R., Oberthur T. & Tomschi H.P., 1987 Geochemistry and mineralogy of banded iron-formation-hosted gold mineralization in the Gwanda greenstone belt, Zimbabwe. Econ. Geol.; 82: 2017-2032.

Saccocia P.J., 1987 Sulfidation of oxide facies iron formation: implications for gold mineralization in East-Central Minnesota. Abs. Geol. Soc. Am. Ann. Meeting, University of Colorado, N.E. section: p. 241.

Saif S., 1983 Petrographic and geochemical characteristics of iron-rich rocks and their significance in exploration for massive sulfide deposits, Bathurst, New Brunswick, Canada. J. Chem. Expl.; 19: 705-721.

Sanderson D.J., 1974 Patterns of boudinage and apparent stretching lineation developed in folded rocks. J. Geol.; 82: 651-661.

Sanjuan B. Michard A. & Michard G., 1988 Influence of the temperature of CO_2-rich springs on their aluminium and rare-earth element contents. Chem. Geol.; 68: 57-69.

Sassi F.P. & Scolari A., 1974 The b_0 value of the potassic white micas as a barometric indicator in low grade metamorphism of pelitic schists. Cont. Min. & Pet.; 45: 143-152.

Sato T., 1972 Behaviors of ore-forming solutions in seawater. Mining Geol.; 22: 31-42.

Savchenko L.T. and Zhukov F.I., 1988 Isotopic composition of sulfur, carbon and oxygen in the Precambrian iron formations of the European part of the USSR. Intern. Geol. Rev.; 30: 1349-1358.

Sawkins F.J. & Rye D.M., 1974 Relationship of Homestake-type gold deposits to iron-rich Precambrian sedimentary rocks. Trans. Inst. Min. Metall., section B; 76: B56 - B59.

Schemerhorn L.J.G., 1978 Epigenetic magnesium metasomatism or syngenetic chloritite metamorphism at Falun and Orijarvi. Trans. Inst. Min. & Metall., section B; 87: 162-167.

Schidlowski M., Hayes J. and Kaplan I., 1983 Isotopic inferences of ancient biochemistries: carbon, sulphur, hydrogen and nitrogen. In Schopf J.W. (Ed.), Earths Earliest Biosphere: its origin and evolution.; ch 7: 149-186.

Schmalz K., 1969 Deep water evaporite deposition: a genetic model. Bull. Am. Ass. Pet. Geol.; 53: 798-823.

Schmidt J.M., 1988 Mineral and whole rock compositions of seawater-dominated hydrothermal alteration at the Arctic volcanogenic massive sulfide prospect, Alaska. Econ. Geol.; 83: 822-843.

Schmidt-mumm A., Behr H-J. and Horn E.E., 1987 Fluid systems in metaplaya sequences in the Damara orogen (Namibia): evidence for sulfur-rich brines--general evolution and first results. Chem. Geol.; 61: 135-145.

Scholz C.H., 1988 The brittle-plastic transition and the depth of seismic faulting. Geologische Rundschau; 77/1: 319-328.

Schreyer W., 1977 Whiteschists: their compositions and pressure-temperature regimes based on experimental, field, and petrographic evidence. Tectonophysics; 43: 127-144.

Scott K.M., 1986 Geochemistry and mineralogy of metasediments, Mount Dore copper deposit. In Eighth Australian Geol. Conv., Geol. Soc. of Australia Abstracts No. 15, 175-176.

Scott K.M., Smith J.W., Sun S.-S., & Taylor G.F., 1985 Proterozoic copper deposits in NW Queensland, Australia. Mineral. Deposita; 20: 116-126.

Seccombe P.K., Spry P.G., Both R.A., Jones M.T., & Schiller J.C., 1985 Base metal mineralisation in the Kanmantoo Group, South Australia: a regional sulfur isotope study. Econ. Geol.; 80: 1824-1841.

Seifert F. & Schreyer W., 1970 Lower temperature stability limit of Mg cordierite in the range 1–7 kb water pressure: redetermination. Contr. Min. Petr.; 27: 225-38.

Seward T.M. 1973. Thio complexes of gold in hydrothermal ore solutions; Geochim. Cosmochim. Acta; 37: 379-399.

Seward T.M., 1977 Solubility of coexisting pyrite and pyrrhotite in the system NaHS-H_2S-NaCl-H_2O at elevated temperature and pressure. In Hodder A.P.W. (Ed.), Geochemistry 1977, N.Z. Dept. Sci. Ind. Res. Bull. 218, Wellington.

Seward T.M., 1984 The transport and deposition of gold in hydrothermal systems. In Foster R.P.(Ed.), Gold '82: The geology, geochemistry and genesis of gold deposits. Geol. Soc. of Zimbabwe Spec. Publ. 1 165-181.

Shaw D., 1972 The origin of the Apsley Gneiss, Ontario. Can. J. Earth Sci.; 9: 18.

Sheppard R.A. & Gude A.J., 1968 Distribution and genesis of authigenic silicate minerals in tuffs of Pleistocene Lake Tecopa, Inyo County, California. U.S. Geol. Surv. Prof. Paper 597: 38p.

Sheppard R.A. & Gude A.J., 1969 Diagenesis of tuffs in the Barstow Formation, Mud Hills, San Bernadino County, California. U.S. Geol. Surv. Prof. Paper 634: 35 p.

Sheppard R.A. & Gude A.J., 1973 Zeolites and associated authigenic silicate minerals in tuffaceous rocks of the Big Sandy Formation, Mohave County, Arizona. U.S. Geol. Surv. Prof. Paper 830.

Shieh G. and Taylor H.P., Jr., 1969 Oxygen and carbon isotope studies of contact metamorphism of carbonate rocks. J.Petrol.;10: 307-331.

Shirozo H., 1974 Clay minerals in altered wall rocks of the Kuroko-type deposits. Soc. Mining Geologists Japan, Spec.Issue 6; 303-311.

Sigurdsson H., Sparks R.S., Carey S. N. & Huang T.C., 1980 Volcanogenic sedimentation in the Lesser Antilles Arc. J. Geol.; 88: 523-540.

Sillitoe R.H., 1979 Some thoughts on gold-rich porphyry copper deposits. Mineral. Deposita; 14: 161-174.

Simonson B.M., 1987 Early silica cementation and subsequent diagenesis in arenites from four early Proterozoic iron formations of North America. J. Sed. Pet.; 57: 494-511.

Simonson B.M., 1988 Early silica cementation and subsequent diagenesis in arenites from four early Proterozoic iron formations of North America — reply. J. Sed. Pet.; 58: 547-549.

Sims P.K., 1972 Banded iron-formation in Vermilion district. In Sims P.K. & Morey G.B. (Eds.), Geology of Minnesota; a centennial volume: St. Paul, Minnesota Geol. Survey; 79-81.

Sims P.K. & James H.L., 1984 Banded iron-formations of Late Proterozoic age in the central eastern desert, Egypt: geology and tectonic setting. Econ. Geol.; 79: 1777-1784.

Sinha A. Krishna, Hewitt D.A. & Rimstidt D., 1986 Fluid interaction and element mobility in the development of ultramylonites. Geology; 14: 883-886.

Sisson V.B., Crawford M.L. & Thompson P.H. CO_2-brine immiscibility at high temperatures, evidence from calcareous metasedimentary rocks. Contrib. Mineral. Petrol.; 78: 371-378.

Slack J.F., 1982 Tourmaline in Appalachian-Caledonian massive sulphide deposits and its exploration significance. Trans. Inst. Min. Met.; B91: B81-89.

Slack J.F., Herriman N., Barnes R.G. & Plimer I.R., 1984 Stratiform tourmalinites in metamorphic terranes and their geologic significance. Geol.; 12: 713-716.

Smith D.C., 1971 A tourmaline-bearing eclogite from Sunnmoere, Norway. Norsk Geologisk Tidsskrift; 51: 141-147.

Smith F.G., 1949 Transport and deposition of the non-sulfide minerals, IV Tourmaline. Econ. Geol.; 44(186-192.).

Smith G.I., 1979 Subsurface stratigraphy and geochemistry of Late Quaternary evaporites, Searles Lake, California. US Geol. Surv. Prof. Paper 1043.

Smith J.W. and Croxford N.J.W., 1975 An isotopic investigation of the environment of deposition of the McArthur mineralisation. Mineral. Dep.; 10: 269-276.

Smith J.W., Burns M.S. & Croxford N.J.W., 1978 Stable isotope studies of the origins of mineralization at Mount Isa. I. Mineralium Deposita; 13: 369-381.

Smith W.D., 1969 Penecontemporaneous faulting and its likely significance in relation to Mount Isa ore deposition. Geol. Soc. Aust. Spec. Publ. 2 : 225-235.

Solomon M. & Walshe J.L., 1979 The formation of massive sulfide deposits on the sea floor. Econ. Geol.; 74: 797-813.

Solomon P.J. & Jensen M.L., 1965 Sulfur isotopic fractionation in nature with particular reference to Mount Isa, Queensland. Proc. 8th Common. Min. Metall. Congr.; 6: 1275-1285.

Sonnenfeld P., 1984 Brines and Evaporites. Orlando, Academic Press, 613 p.

Spear F.S., 1980 NaSi-CaAl exchange equilibrium between plagioclase and amphibole. Contr. Mineral. Petrol.; 72: 33-41.

Speer J.A., 1982 Zircon. Min. Soc. Am. Rev. In Min.; 5: 67-112.

Spry P.G., 1987 A sulphur isotope study of the Broken Hill deposit, New South Wales, Australia. Mineralium Deposita; 22: 109-115.

Stanton R.L., 1976a Petrochemical studies of the ore environment at Broken Hill, New South Wales: 1 — constitution of banded iron formation. Trans. Inst. Min. & Metall. (Sect. B); 85: B33-46.

Stanton R.L., 1976b Petrochemical studies of the ore environment at Broken Hill, New South Wales: 3 — banded iron formation and sulphide orebodies: constitutional and genetic ties. Trans. Inst. Min. & Metall. ; 85: B132-141.

Stanton R.L., 1976c Petrochemical studies of the ore environment at Broken Hill, New South Wales: 4— environmental synthesis. Trans. Inst. Min. & Metall.; 85: B221-233.

Stanton R.L., 1976d Petrochemical studies of the ore environment at Broken Hill, New South Wales: 2 — regional metamorphism of banded iron formations and their immediate associates. Trans. Inst. Min. & Metall. ; 85: B118-131.

Stanton R.L. & Vaughan J.P., 1979 Facies of ore formation : a preliminary account of the Pegmont deposit as an example of potential relations between small 'iron formations' and stratiform sulphide ores. Proc. Australas. Inst. Min. Met.; 270: 25-38.

Staudigel H., Frey F.A. & Hart S.A., 1979 Incompatible trace element geochemistry and $^{87}Sr/^{86}Sr$ in basalts and corresponding glasses and palagonite. In Donelly T., Franchetau J. et al. Initial reports of the deepsea drilling project, 51, 52, 53, part 2, U.S. govt. printing office, Washington, D.C.:1137-1144.

Stewart A. and Williams S., 1988 Early extension in the Mt. Isa Inlier, and a solution to the problem of the Deighton Quartzite outliers. Ninth Austr. Geol. Conf. Abstracts, Brisbane, Queensland. Aust. Geol. Soc. Abs. 21; 382-382.

Switzer C.K., 1987 Implications of high strain for regional structural geometry and control on gold mineralisation in the Selwyn region, northwestern Queensland. James Cook Univ. Hons. Thes. (unpubl.).

Switzer C.K., Laing W.P. & Rubenach M.J., 1988 The Proterozoic Starra Au+Cu ironstone deposit - syntectonic mineralisation in a folded early regional zone of decollement. Bicentennial Gold '88, Extended Abstracts Poster Progamme, vol 1, Geol. Soc. of Aust. Abs. No. 23; 212-214.

Taylor S.R. & McLennan S., 1985 The continental crust: its composition and evolution. Blackwell.

Taylor G.F. & Scott K.M., 1976 The geochemistry of ironstones and core samples from the Mount Kelly area, northwest Queensland. Unpubl. report, CSIRO Mineral Research Laboratories.

Taylor, B.E. and Slack, J.F., 1984 Tourmalines from Appalachian-Caledonian massive sulphide deposits: textural, chemical, and isotopic relationships. Econ. Geol.; 79: 1703-1726.

Taylor H.P., Jr., 1979 Oxygen and hydrogen isotope relationships in hydrothermal mineral deposits. In Barnes H.L.(Ed.), Geochemistry of ore deposits, 2nd ed., John Wiley.; 236-277.

Tchalenko J.S., 1968 The evolution of kink-bands and the development of compressive textures on sheared clays. Tectonophysics; 6: 159-174.

Thode H.G. & Goodwin A.M., 1983 Further sulfur and carbon isotope studies of late Archean iron-formations of the Canadian Shield and the rise of sulfate-reducing bacteria. Precambrian Res.; 20: 337-356.

Tomisaka, T., 1968 Synthesis of some end-members of the tourmaline group. Min. J.; 5: 355-364.

Tracy R.J., Rye D.M., Hewitt D.A. & Schiffries C.M., 1983 Petrologic and stable isotopic studies of fluid-rock interactions, south-central Connecticut.I. The role of infiltration in producing reaction assemblages in impure marbles. In Greenwood H.J. (Ed.), Studies in metamorphism and metasomatism, Am. J.of Sci.; 283A: 89-616.

Tremaine P.R., Massow R.V. & Shierman G.R., 1977 A calculation of Gibbs free energies for ferrous ions and solubility of magnetite in H_2O and D_2O to 300° C. Thermochim. Acta; 19: 287-300.

Trendall A.F., 1973a Iron formations of the Hamersley Group of Western Australia: type examples of varved Precambrian evaporites. In Genesis of Precambrian iron and manganese deposits, Proceedings of the Kiev Symposium, Unesco, Paris. Earth sciences 9; 257-269.

Trendall A.F., 1973b Precambrian iron formations of Australia. Econ. Geol.; 68: 1023-1034.

Truesdell A.H., 1976 Geochemical techniques in exploration. In Proceedings 2nd U.N. Symp. geothermal research, U.S. Govt. Printing Office, Washington D.C.: 53-79.

Truesdell A.H., 1974 Oxygen isotope activities and concentrations in aqueous salt solutions at elevated temperatures: consequences for isotope geochemistry. E. Plan.Sci. Lets.; 23: 387-396.

Turner J.S. & Gustafson L.B., 1978 The flow of hot saline solutions from vents in the sea floor; some implications for exhalative sulfide and other ore deposits. Econ. Geol.; 73: 1082-1100.

Turner F.J., 1981 Metamorphic petrology, (2nd. Ed.) Mcgraw-Hill-New York, 524 pp.

Turner J.S. & Campbell I.H., 1987 Temperature, density and buoyancy fluxes in "black smoker" plumes, and the criterion for bouyancy reversal. Earth & Plan. Sci. Lett.; 73: 85-92.

Tyndale-Biscoe R., 1940 The geology of the country around Gwanda. Southern Rhodesia Geol Surv. Bull.; 36. 204 p.

Vallance T.G., 1976 Mafic rock alteration and isochemical development of some cordierite-anthophyllite rocks. J. Petrol.; 8; (84-96.).

Valley J. and O'Neil J., 1981 $^{13}C/^{12}C$ exchange between calcite and graphite: a possible thermometer in Grenville Marbles. Geochim. Cosmochim. Acta; 45: 411-419.

Valley J.W., 1986 Stable isotope geochemistry of metamorphic rocks. In Reviews in Mineralogy, Mineral. Soc. of America.; 16: 445-486.

Valliant R.I. & Barnett R.L., 1982 Manganiferous garnet underlying the Bousquet gold orebody, Quebec: metamorphosed manganese sediment as a guide to ore. Can. J. Earth Sci.; 19: 993-1010.

Valliant R.I. & Hutchinson R.W., 1982 Stratigraphic distribution and genesis of gold deposits, Bousquet region, northwestern Quebec. In Hodder R.W. & Petruk W. (Eds.), Geology of Canadian gold deposits, C.I.M. special volume 24; 27-40.

Van der Molen I. & Roermund H.L.M., 1986 The pressure path of solid inclusion in minerals: the retention of coesite inclusions during uplift. Lithos; 19: 317-324.

Vaughan J.P. & Stanton R.L., 1986 Sedimentary and metamorphic factors in the development of the Pegmont stratiform Pb-Zn deposit, Queensland, Australia. Trans. Inst. Min. & Metall.; B95: 94-121.

Veizer J. and Hoefs J. The nature of O^{18}/O^{16} and C^{13}/C^{12} secular trends in sedimentary carbonate rocks. Geochim. Cosmochim. Acta; 40: 1387-1395.

Velde B., 1965 Phengite micas: synthesis, stability and natural occurrence. Am. J. Sci.; 262: 886-913.

Vial D.S., 1988 Geology of the Cuiaba gold mine, Quadrilatero Ferrifero, Minas Gerais, Brazil. Bicentennial Gold '88 extended poster abstracts, Geol. Soc. Aust. Abs. 23; : 134-137.

Vial D.S., Fusikawa R., Castro E.P.G. & Vieira M.M.H., 1988 The sulfide-tourmaline-quartz-vein gold deposit Passagem de Mariana, Minas Gerais, Brazil. Bicentennial Gold '88 extended oral abstracts, Geol. Soc. Aust. Abs. 22; 30-35.

Vidale R., 1969 Metasomatism in a chemical gradient and the formation of calc-silicate bands. Am. J. Sci.; 267: 857-874.

Visser J.N.J., 1985 Structural and textural criteria for the recognition of early diagenetic nodules in well-bedded iron-bearing sequences. Trans. geol. Soc. S. Afr.; 88: 179-182.

Vogt J. & Stumpfl E., 1987 Abra: A stratabound Pb-Cu-Ba mineralisation in the Bangemall Basin, W.A. Econ. Geol.; 82: 805-825.

Vokes F.M., 1969 A review of the metamorphism of sulfide deposits. Earth-Sci. Revs.; 5: 99-143.

Walford P.C. & Franklin J.M., 1982 The Anderson Lake mine, Snow Lake, Manitoba. In Hutchinson R.W., Spence C.D. & Franklin J.M. (Eds.), Precambrian sulphide deposits, H.S. Robinson memorial volume, Geological Association of Canada Special Paper 25; 481 - 525.

Walker R.G., 1984 Turbidites and associated coarse clastic deposits. In Walker R.G. (Ed.) Facies Models, Geoscience Canada, Reprint series 1, 2nd Ed.; 171-189.

Walker R.N., Muir M.D. , Diver W.L., Williams N, & Wilkins N., 1977 Evidence of major evaporite deposits in the Proterozoic McArthur Group, Northern Territory, Australia. Nature; 265: 526-9.

Wall L., 1986 Geochemical Orientation report on the results of stage 1. Cyprus Minerals (unpubl).

Waltham A.C., 1968 Classification and genesis of some massive sulphide deposits in Norway. Trans. Inst. Min & Metall., sect. B; 77: B153-161.

Walshe J.L. & Solomon M., 1981 An investigation into the environment of formation of the volcanic-hosted Mount Lyell copper deposits using geology, mineralogy, stable isotopes and a six-component solid solution model. Econ. Geol.; 76: 246-284.

Warren R.G. & Shaw R.D., 1985 Volcanogenic Cu-Pb-Zn bodies in granulites of the central Arunta Block, central Australia. J. Metam. Geol.; 3: 481-499.

Watkinson A.J. & Cobbold P.R., 1981 Axial direction of folds in rocks with linear/planar fabrics. J.Struct. Geol.; 3: 211-217.

Wedekind R. & Large R.R., In press Controls on high grade gold mineralization at Tennant Creek, Northern Territory, Australia. In Keays R., Ramsay R. & Groves D.(Eds.), The geology of gold deposits: the perspective in 1988; Econ. Geol. Mon. 6.

Weisbrod A., 1969 Caracteres geochimiques et origine des "schists amygdalaires" des Cevennes (Massif Central Francais). C.R. Acad. Sci. Paris; 268: 3018-3020.

Werding, G. and Schreyer, W. Alkali-free tourmaline in the system MgO-Al_2O_3-B_2O_3-SiO_2-H_2O. Geochim. Cosmochim. Acta; 45: 1331-1344.

Westhuizen W.A., Strydon D., Schoch A., Tordiffe E. & Beukes G., 1986 Petrochemical evidence on the probable origin of ferriferous metasediments in western Bushmanland. Min. Dep.; 21: 121-128.

Wesolowski D., Drummond S.E., Mesmer R.E. & Ohmoto H., 1984 Hydrolysis equilibria of tungsten (IV) in aqueous sodium chloride solutions to 300° C. Inorg. Chem.; 23: 1120-1132.

Whitcher I.G., 1975 Dugald River zinc-lead lode. In Economic Geol. of Aust and P.N.G. Ed. C.L.Knight, Aust. Inst. Min. & Met. Mon. 5 : 372-376.

White, D.E., 1957 Magmatic, connate and metamorphic waters. Geol. Soc. Am. Bull.; 68(1659-1682.).

Whitford D.J., Creelman R.A. & Ramsden A.R., 1984 Petrological, geochemical and mineragraphic studies at Que River and Hellyer. CSIRO Restricted Investigation report.; 1544R.

Whitford D.J., Korsch M.J., Porritt P.M. & Craven S.J., 1988 Rare-earth mobility around the volcanogenic polymetallic massive sulfide deposit at Que River, Tasmania, Australia. Chem. Geol.; 68: 105-121.

White D.E., 1981 Active geothermal systems and hydrothermal ore deposits. In Skinner B.J. (Ed.) Economic Geology Seventy-fifth Anniversary Volume.: 392-424.

Whitney P.R. & Olmsted J.F., 1988 Geochemistry and origin of albite gneisses, northeastern Adirondack Mountains, New York. Contrib. Mineral. Petrol.; 99: 476-484.

Whitney J.A., Hemley J.J. & Simon F.O., 1985 The concentration of iron in chloride solutions equilibrated with synthetic granitic compositions: the sulfur free system. Econ. Geol.; 80: 444-460.

Wilde A.R. & Bloom M.S., 1988 Transport and deposition of gold with uranium and platinum-group elements in unconformity-related uranium deposits. Bicentennial Gold '88 extended oral abstracts, Geol. Soc. Aust. Abs. 23; 325-330.

Williams P.R., 1989 Nature and timing of early extensional structures in the Mitakoodi Quartzite, Mount Isa Inlier, northwest Queensland. Aust. J. Earth Sci.; 36: 283-296.

Williams N., 1978 Studies of the base metal sulfide deposits at McArthur River, Northern Territory, Australia.1. The Cooley and Ridge deposits. Econ. Geol.; 73: 1005-1035.

Wilson I.H., 1983 Geochemical discrimination of acid volcanic units in the Mount Isa region, Queensland. BMR Journal of Aust. Geol. & Geophys.; 8: 109-119.

Wilson I.H., 1978 Volcanism on a Proterozoic continental margin in northwestern Queensland. Precamb. Res.; 7: 205-235.

Wilson I.H., Derrick G.M., Hill R.M., Duff B.A., Noon T.A. & Ellis D.J., 1977 Geology of the Prospector 1:100 000 Sheet area (6857), Queensland. Bur. Min. Res., Aust. Rec. 1977/4 (unpub.).

Winchester J.A. & Floyd P.A., 1978 Geochemical discrimination of different magma series and their differentiation products using immobile elements. Chem. Geol.; 20: 325-343.

Wollenberg H., Bowman H. & Asaro F., 1977 Geochemical studies at four northern Nevada hot-spring areas. University of California, Lawrence Berkeley Laboratory Report 6808, 70 p.

Woodall R., 1975 Gold in the Precambrian shield of Western Australia. In Knight C.L.(Ed.) Economic Geology of Australia and Papua New Guineau 1. Metals. Mon. 5, Australas. Inst. Min. & Metall. : 175-183. 1088 p.

Wood S.A. & Vlassopoulos D., 1986 Experimental determination of the hydrothermal solubility and speciation of tungsten at 500° C and 1 kbar. Geochim. Cosmochim. Acta; 1989; 53: 303-312.

Woods T.L., Roedder E. & Bethke P.M., 1982 Fluid inclusion data on samples from Creede, Colorado, in relation to mineral paragenesis. U.S.G.S. File 82-313.

Wright J.V. & Mutti E., 1981 The Dali Ash, Island of Rhodes, Greece: a problem in interpreting submarine volcanogenic sediments. Bull. Volcan.; 44: 153-167.

Wyborn L.A.I. & Page R.W., 1983 The Proterozoic Kalkadoon and Ewen Batholiths, Mount Isa Inlier, Queensland: source, chemistry, age, and metamorphism. BMR Journal of Aust. Geol. & Geophys.; 8: 53-71.

Wyborn L.A.I., Page R. & McCulloch M., 1988 Petrology, geochronology, and isotope geochemistry of the post-1820 Ma granites of the Mt. Isa Inlier: mechanisms for the generation of Proterozoic anorogenic granites. Precamb. Res.; 40/41: 509-543.

Wyborn L.A.I., Warren R.G., Page R.W. & Etheridge M.A., 1988 Metallogenic overview of the Proterozoic of Australia with special reference to gold, platinum and rare earths (abs.). Ninth Aust. Geol. Conv. Abs., Brisbane, Queensland. Geol. Soc. Abs. No. 21; 432-433.

Wyman D.A., Kerrich R. & Fryer B.J., 1986 Gold mineralization overprinting iron formation at the Agnico-Eagle deposit, Quebec, Canada: mineralogical , microstructural and geochemical evidence. In MacDonald A.J. (Ed.), Proc. of Gold '86, an international symposium on the geology of gold: Toronto, 1986. 517 p.; 108-123.

Yurtsever Y. & Gat J.R., 1981 Atmospheric waters. In Gat J.R. & Gonfiantini R. (eds.) Stable isotope hydrology: deuterium and oxygen-18 in the water cycle. Technical reports series # 210, International Atomic Energy Agency, Vienna : 103-142.

APPENDIX 1

FLUID INCLUSION MEASUREMENTS FROM SILICA ALTERATION ZONES AT TROUGH TANK.

Appendix 1. Fluid inclusion measurements from silica alteration zones, Trough Tank.

SAMPLE	Location	T(h)° C	T(e)ice	T(m)-ice	T(h)-NaCl	T(h)-all	#daught.	T(d'crep)	size:µm	Max.T run	T(nucl.)*	COMMENT
TT4,R1	NQ4,108.2m	148.2	-9.4	-9.4	-	-	2	400	15	400	-	Prograde
TT41	NQ6,117.7m	201	0	0	325.1	-	2	402	12	402	-	Prograde
TT22,R4	NQ3,114.2m	272.6	-	-	485	483.7	2	-	12	488	440.8	Prograde
TT64, R4	NQ4,134.4m	239.6	-	-	470	-	3	478	15	490	-	Prograde
TT22, R2	NQ3,114.2m	318.4	-	-	>443.8	-	4	443.8	20	440	380	Prograde
" "	NQ3,114.2m	320	-	-	-	-	4	-	20	440	-	Prograde
" "	NQ3,114.2m	352	-	-	-	-	4	-	20	440	-	Prograde
TT22, R10	NQ3,114.2m	193.3	-	-	413.5	421.5	4	472	20	472	-	Prograde
TT22, R8	NQ3,114.2m	271	-18	-18	-	-	4	405	20	405	310	Prograde
TT22, R6	NQ3,114.2m	322	-13.4	-13.4	360	416	4	-	15	445	360	Prograde
TT22, R9	NQ3,114.2m	280	-	-	440	440	4	450	10	450	450	Prograde
"	NQ3,114.2m	288	-	-	-	-	4	450	10	450	450	Prograde
"	NQ3,114.2m	466	-	-	-	-	4	450	10	450	450	Prograde
TT10A, R5	NQ4,135m	181.6	-70	-34	351	-	3	447	25	447	434	Prograde
TT38, R2	NQ6,112.7m	380	-10.8	23.7	-	-	3	399	15	399	-	Prograde
"	NQ6,112.7m	360.6	0	0	-	-	3	-	15	460	-	Prograde
"	NQ6,112.7m	434	0	0	-	-	3	-	15	460	-	Prograde
TT38, R8	NQ6,112.7m	387.9	-43.2	19.2	-	-	3	-	12	432	-	Prograde
TT50,R4	NQ2,66.3m	186.5	-	-	399.4	469.5	4	-	30	485	409.8	Prograde
"	NQ2,66.3m	213.5	-	-	-	-	4	-	30	485	-	Prograde
"	NQ2,66.3m	244.4	-	-	-	-	4	-	30	485	-	Prograde
TT38, R1	NQ6,112.7m	361	0	0	-	-	2	-	12	450	-	Prograde
TT38, R1	NQ6,112.7m	434	0	0	-	-	2	-	12	450	-	Prograde
TT50, R5	NQ2,66.3m	297	-12.5	-1.1	-	-	2	356	15	356	-	Prograde
TT41	NQ6,117.7m	242.5	0	0	479.9	-	2	490	10	490	456	Retrogressive
TT38, R1	NQ6,112.7m	345	-9.4	20.9	-	-	2	390	12	450	-	Retrogressive
TT22, R3	NQ3,114.2m	157	-4.8	6.9	-	-	2	160	10	160	-	Retrogressive
TT22, R5	NQ3,114.2m	186	-36.4	-6.3	-	-	2	-	30	190	-	Retrogressive
TT10A, R1	NQ4,135m	205	-69.7	-36.8	445.6	503.2	2	-	15	505	451	Retrogressive
TT10, R2	NQ4,135m	229.7	-	-	229.7	513.5	2	-	10	513.5	463	Retrogressive
TT22, R8	NQ3,114.2m	248	0	0	419	484.1	3	-	12	500	423	Retrogressive
TT22, R7	NQ3,114.2m	243.5	-	-	-	-	4	338	30	338	-	Retrogressive
TT38, R5	NQ6,112.7m	0	-	-	-	462	3	-	15	470	-	Retrogressive
TT64,R7	NQ4, 134.4m	225	-	-	-	-	4	356	15	356	-	Retrogressive
TT64, R3	NQ4, 134.4m	212.4	-	-	-	-	4	441	25	441	309	Retrogressive
TT64, R6	NQ4, 134.4m	223.4	-	-	365	-	3	371	15	475	390	Retrogressive
TT64, R6	NQ4, 134.4m	218.8	-	-	-	-	3	470	15	475	-	Retrogressive
TT64, R6	NQ4, 134.4m	243.3	-	-	-	-	3	470	15	475	-	Retrogressive
TT64, R6	NQ4, 134.4m	264	-	-	-	-	3	470	15	475	-	Retrogressive
TT64, R6	NQ4, 134.4m	262	-	-	-	-	3	470	15	475	-	Retrogressive
TT64, R6	NQ4, 134.4m	273.9	-	-	-	-	3	470	15	475	-	Retrogressive
TT64, R6	NQ4, 134.4m	277.8	-	-	-	-	3	470	15	475	-	Retrogressive
TT64, R2	NQ4, 134.4m	152	-	-	454	457	3	-	10	470	457	Retrogressive
*Temperature at which a new acicular daughter mineral formed, suspected to be gypsum on the basis of crystal form.												

APPENDIX 2

MAJOR AND TRACE ELEMENT ANALYSIS TECHNIQUES.

MAJOR AND TRACE ELEMENT ANALYTICAL TECHNIQUES

Sampling and Analytical Methods

All major rock-types were sampled for geochemistry. The average 2 kg drill-core samples were jaw-crushed to gravel size, and a 50 gm split was taken for grinding. A -200 mesh powder was obtained by grinding in a a chromium-steel mill, with a batch of 24 samples crushed as duplicates in a tungsten-carbide mill to specifically analyse Cr in appropriate lithologies. Most Starra major and trace element analyses were performed using a Philips PW1410 automated XRF at the University of Tasmania Geology Department. (Apart from 6 analyses, all Trough Tank samples were analysed commercially by Analabs of Brisbane). The Tasmanian University procedures were carried out under the guidance of department analyst Phil Robinson. Accuracy was monitored using in-house University of Tasmania standard rocks, as well as international standards. Table 1 is a compilation of precision estimates for some of these, compiled by S. Eggins.

All Au analyses were performed by commercial laboratories.

Major and Trace Element Analysis

Concentrations of major element oxides were determined by X-ray fluoresence spectrometry on fused glass discs (after Norrish & Hutton 1969). Ironstone samples were diluted with silica before fusion and standards for Fe and Si prepared using mixtures of specpure Fe_2O_3 and SiO_2. Loss on ignition (LOI) was determined by igniting samples overnight at 1000° C (to adjust for loss of volatiles such as S, H_2O and CO_2).

The trace elements Ba, Rb, Sr, Y, Nb, Zr, Cu, Pb, Zn, Ni, Cr, V, W, Sn, Co, Sb and As were analysed on pressed powder pills, using the method of Norrish & Chappell (1977). Inter-element corrections for overlapping lines were made where necessary. Mass absorption coefficients were calculated from the major element compositions; the high iron samples had very high mass absorption coefficients which imposed higher detection limits. Pure Fe_2O_3 is approximately 7 times the absorption coefficient of pure SiO_2 for many elements, which increases the detection limit of, for instance, Zn, from 1 to 3 ppm. To allow for these effects, background profile and machine contamination measurements were also made with specpure SiO_2, Fe_2O_3 and mixtures of both. The samples were also corrected for Ba interference in some instances, with the aid of Tasmanian dolerite standards containing 0.1 %, 0.5 %, 2 % and 10 % BaO.

Rare Earth Element Analysis

The rare earth elements La, Ce, Pr, Nd, Sm, Eu, Gd, Dy, Er and Yb were analysed in sixteen samples by an ion-exchange/X-ray fluorescence technique formulated by Robinson et al. (1986). Except for very low level samples (< 5 ppm), La, Ce and Nd

of these samples were checked by XRF methods on pressed powders. Values of Ce < 20 ppm (20.9 X chondrite) in the pressed powders were discarded as unreliable. An initial attempt to analyse samples through a commercial ICP process was thwarted by eratic or low levels of REEs in some samples.

The basic REE extraction method involved sample-decomposition using a sodium peroxide sinter, prior to an ion-exchange procedure to separate the REEs. The REEs were adsorbed on to ion-exchange papers, and their absolute levels determined by X-ray fluorescence. (Clean ion-exchange columns are essential to obtain low (< 5 ppm) La levels). Samples containing very low REE levels were run in duplicate, and the results averaged to achieve a smooth pattern. The quantity of sodium peroxide was doubled in high-Fe samples to achieve maximum breakdown of highly resistive magnetite-spinel phases. Two in-house standards were used for each batch of 10 samples.

Table 1. Precision estimates determined for multiple analyses (n) of Tasmania University standard rocks (TasBas, TasDol, 47805) and Ambae sample #68611.

	TasBas			47805 or TasDol			68611		
	(+1σ)	n	σ%	(+1σ)	n	σ%	(+1σ)	n	σ%
Major Elements									
SiO_2	45.98∓0.23	46	0.5						
TiO_2	2.40∓0.04	46	1.7						
Al_2O_3	14.60∓0.10	46	0.7						
Fe_2O_3	11.75∓0.09	46	0.8						
MnO	0.18∓0.01	46	5.1						
MgO	8.46∓0.11	46	1.3						
CaO	8.08∓0.06	46	0.8						
Na_2O	5.63∓0.12	46	2.1						
K_2O	1.94∓0.03	46	1.6						
P_2O_5	1.00∓0.03	46	2.6						
Trace Elements									
Rb	16.5∓0.7	27	4.2	3.9∓0.6[a]	12	15.4	11.3∓0.6	9	5.4
Ba	204∓3.0	8	1.5	388∓4.7[b]	10	1.2			
Sr	1025∓11.2	25	1.1	64.9∓1.0[a]	12	1.5	591∓3.1	10	0.5
La	43.4∓1.4	30	3.2				9.6∓1.3	6	14
Ce	89.0∓3.4	30	3.8				20.1∓2.0	6	10
Nd	41.2∓2.4	30	5.8				12.6∓0.6	6	4.4
Y	23.1∓0.6	27	2.6	3.4∓0.4[a]	12	11.8	17.7∓0.5	10	3.0
Zr	260∓4.3	27	1.7	34.6∓0.9[a]	12	2.6	44.7∓1.0	10	2.2
Sc	13.1∓0.5	8	3.8	25.0∓0.8[b]	10	3.2			
Nb	61.4∓1.2	27	2.0	2.7∓0.5[a]	12	18.5	1.4∓0.5	10	38
V	163∓2.3	26	1.4						
Cr	198∓4.1	26	2.1						
Ni	154∓2.0	26	1.3						
REE (analysed by ion exchange technique[c])									
La	43.2∓1.25	3	2.9						
Ce	89.1∓2.58	3	2.9						
Pr	10.34∓0.28	3	2.7						
Nd	41.8∓0.79	3	1.9						
Sm	8.15∓0.10	3	1.2						
Eu	2.61∓0.11	3	4.3						
Gd	7.01∓0.10	3	1.5						
Dy	4.89∓0.10	3	2.0						
Er	2.05∓0.15	3	7.2						
Yb	1.26∓0.06	3	4.6						

a. Analyses of standard 47805.
b. Analyses of standard TasDol.
c. Precision estimates after Robinson et al. (1986).

APPENDIX 3

HOST-ROCK MAJOR AND TRACE ELEMENT GEOCHEMISTRY:

3A.STARRA FELDSPATHIC MARIPOSA CREEK MEMBER (FOOTWALL)

3B. STARRA STAVELEY FORMATION HANGINGWALL METASEDIMENTS

3C. TROUGH TANK HOST-ROCKS

Appendix 3A. Starra footwall chemistry. (n.d.— not detected, - = not analysed).

	Location	AREA	SiO2	Al2O3	TiO2	Fe2O3	MgO	MnO	Na2O	K2O	CaO	P2O5	LOI
Least altered													
volc.st109	STQ85-129/119-120	257	73.13	9.89	0.28	2.04	1.07	0.04	5.47	0.08	3.88	0.15	3.57
volc.st204	STQ80-16/249.5 - 250	257	72.99	11.33	0.64	5.24	1.55	0.01	5.08	0.23	1.10	0.17	1.57
St138	STQ85-121/144.8-145.1	257	69.64	10.83	0.26	11.27	1.33	0.01	0.14	3.10	0.07	0.05	3.07
St152	STQ86 - 243/149.7 -150.7	257	67.31	12.51	0.42	10.15	1.87	0.02	5.81	0.38	0.98	0.14	1.09
Typical altered													
251D	Underground, 1275 R.L.	251	51.70	13.10	0.52	25.50	0.35	0.01	6.50	0.43	0.20	0.13	0.6
251E	Underground, 1275 R.L.	251	48.10	10.50	0.46	33.00	1.17	0.01	4.34	0.65	0.22	0.17	1.46
251F	Underground, 1275 R.L.	251	51.40	10.00	0.47	30.80	0.52	0.01	3.44	0.06	0.17	0.13	1.6
251G	Underground, 1275 R.L.	251	47.20	11.50	0.48	32.20	0.16	0.00	6.53	0.16	0.13	0.12	1.41
251H	Underground, 1275 R.L.	251	49.50	10.80	0.44	32.00	0.36	0.01	5.46	0.32	0.17	0.14	0.99
251I	Underground, 1275 R.L.	251	49.80	11.00	0.44	31.60	0.58	0.00	4.43	0.99	0.13	0.11	1.06
251J	Underground, 1275 R.L.	251	49.50	9.48	0.41	31.90	0.65	0.02	4.42	0.58	0.20	0.14	2.01
251K	Underground, 1275 R.L.	251	45.10	8.34	0.37	39.60	0.90	0.01	3.47	0.58	0.18	0.15	0.88
251L	Underground, 1275 R.L.	251	50.00	10.20	0.40	33.10	0.33	0.00	5.78	0.14	0.15	0.13	0.36
251M	Underground, 1275 R.L.	251	45.50	11.10	0.46	34.80	0.43	0.00	6.33	0.19	0.16	0.13	0.67
251N	Underground, 1275 R.L.	251	45.30	10.80	0.45	35.90	1.04	0.01	4.62	0.60	0.21	0.13	1.17
251O	Underground, 1275 R.L.	251	36.50	9.08	0.39	46.50	0.63	0.00	4.02	0.31	0.18	0.12	1.59
St44b	CRQ78 - 1/204.2m	257	51.27	9.99	0.40	31.32	0.30	0.01	6.05	0.11	0.10	0.12	0.44
St46	CRQ78 - 1/210-213 m	257	51.50	12.30	0.59	24.50	2.30	0.03	5.60	0.99	0.44	0.14	0.9
St62	STQ80 - 15/239 - 245 m	257	53.71	12.70	0.53	23.98	0.27	0.01	7.44	0.18	0.36	0.27	0.64
St142	STQ85 - 121/156 - 170 m	276	49.09	11.42	0.52	25.48	6.18	0.02	2.32	0.93	0.21	0.13	3.83
St198	STQ81 - 19/200 - 215 m	257	49.66	11.79	0.51	28.75	2.36	0.03	3.72	0.91	0.63	0.13	1.06
St218	STQ79 - 2/200 -211 m	244	56.11	10.43	0.39	26.13	0.13	0.01	5.99	0.18	0.26	0.11	0.28
St278	STQ80 - 8/44 - 61 m	257	41.40	9.01	0.35	41.20	2.24	0.01	2.25	0.83	0.16	0.12	2.4
St280	STQ80 - 8/108 - 126 m	257	52.70	10.80	0.46	27.60	0.96	0.01	5.93	0.13	0.25	0.16	0.96
Most Altered, 'pipe'-like alteration													
251A.pipe	Underground, 1275 R.L.	251	40.40	7.56	0.36	45.00	0.72	0.01	3.10	0.37	0.15	0.11	1.12
251B.pipe	Underground, 1275 R.L.	251	45.00	8.90	0.41	38.60	0.67	0.01	3.62	0.59	0.22	0.16	1.08
251C.pipe	Underground, 1275 R.L.	251	36.50	8.83	0.38	47.10	0.45	0.01	4.37	0.19	0.15	0.11	1.17

Appendix 3A. Starra footwall chemistry. (n.d.— not detected, - = not analysed).

	Total	Au	Cu	Pb	Zn	Ba	Ni	Rb	Sr	Zr	Y	Sn	W	Sc	V	Nb
Least altered																
volc.st109	99.60	n.d.	n.d.	n.d	n.d	6	4.6	n.d.	22.2	222	15	-	-	2.6	22.2	7.8
volc.st204	99.91	n.d.	8.6	n.d	n.d	26	13.6	6	35	274.9	26	-	-	8.6	53.1	14
St138	99.77	0.76	119.3	n.d.	1.8	113	15.8	194	6.7	157	63	-	-	11.6	34.1	3.7
St152	100.68	0.005	650.8	4	2.8	40	31.5	19.4	24.2	179	35	-	-	5.3	33.5	8.7
Typical altered																
251D	99.04	0.74	10500	n.d.	5	48	14	25	4	115	13	20	95	-	-	-
251E	100.08	0.085	740	n.d.	5	59	29	25	4	117	9	5	45	-	-	-
251F	98.59	0.07	575	n.d.	5	125	22	45	4	120	14	15	170	-	-	-
251G	99.90	0.01	515	n.d.	n.d.	18	19	0	4	123	12	10	35	-	-	-
251H	100.19	0.005	205	n.d.	n.d.	29	17	10	5	125	16	9	35	-	-	-
251I	100.14	0.002	130	n.d.	n.d.	65	19	45	6	119	9	20	130	-	-	-
251J	99.31	0.035	1560	n.d.	5	52	28	30	4	100	11	20	120	-	-	-
251K	99.57	0.005	695	n.d.	n.d.	34	15	25	4	116	9	10	35	-	-	-
251L	100.59	0.002	75	n.d.	5	13	12	0	5	128	10	15	30	-	-	-
251M	99.78	0.002	135	n.d.	n.d.	16	12	15	9	116	11	9	35	-	-	-
251N	100.22	0.015	85	n.d.	5	57	19	30	6	115	14	15	30	-	-	-
251O	99.32	0.72	6030	n.d.	5	25	28	10	n.d.	92	10	20	220	-	-	-
St44b	100.11	0.005	61.7	n.d.	n.d.	12	11	5.2	2.8	107.1	12	-	-	7	55.4	7.9
St46	99.29	0.005	50	n.d.	8	45	18	70	-	-	-	-	-	n.d.	n.d.	12
St62	100.09	0.005	30.5	0.3	0.3	11	15	7.4	5.8	146.3	11.6	-	-	6.5	74.3	11.9
St142	100.13	0.096	150.9	n.d.	11	74	81	43.3	4.2	153	20	-	-	12.5	76.1	11.9
St198	99.55	0.58	2983.7	n.d.	2.8	106	29.1	50.3	10	149.5	61	-	-	11.5	64.1	13
St218	100.02	0.005	130.7	n.d.	n.d.	12	12	10.6	3	148.4	10	-	-	6.5	67.2	6
St278	99.97	0.425	910	n.d.	5	96	20	20	7	110	15	15	-	-	-	-
St280	99.95	0.001	70	n.d.	5	10	22	6	5	117	13	9	-	-	-	-
Most Altered, 'pipe'-like alteration																
251A.pipe	98.89	1.08	8530	n.d.	5	28	15	8	3	91	11	25	210	-	-	-
251B.pipe	99.26	0.91	7660	n.d.	5	49	11	20	3	91	10	35	240	-	-	-
251C.pipe	99.26	5.07	6860	n.d.	5	15	16	9	3	96	14	40	350	-	-	-

Appendix 3A. Starra footwall chemistry. (n.d.— not detected, - = not analysed).

	As	Bi	La	Ce	Nd	Co	Ga	B	F	U	Th
Least altered											
volc.st109	5	18	12.2	24	10.2	-	-	-	-	2	7
volc.st204	7	n.d.	42.2	90	33.6	-	-	-	-	28.1	18.1
St138	3.9	n.d.	16.4	b.d.	17.3	-	-	-	-	9	9
St152	5	4	11.8	25.1	5.82	12.8	-	-	-	44	14.9
Typical altered											
251D	-	-	-	-	-	-	-	-	-	-	-
251E	-	-	-	-	-	-	-	-	-	-	-
251F	-	-	-	-	-	-	-	-	-	-	-
251G	-	-	-	-	-	-	-	-	-	-	-
251H	-	-	-	-	-	-	-	-	-	-	-
251I	-	-	-	-	-	-	-	-	-	-	-
251J	-	-	-	-	-	-	-	-	-	-	-
251K	-	-	-	-	-	-	-	-	-	-	-
251L	-	-	-	-	-	-	-	-	-	-	-
251M	-	-	-	-	-	-	-	-	-	-	-
251N	-	-	-	-	-	-	-	-	-	-	-
251O	-	-	-	-	-	-	-	-	-	-	-
St44b	n.d.	4	13.6	n.d.	3.6	-	-	-	-	9	10
St46	4	2	-	-	-	-	-	-	-	n.d.	n.d.
St62	0.6	0.7	-	20	-	26	18	160	600	11	17
St142	4	n.d.	5.3	n.d.	4.8	-	-	-	-	14	14.1
St198	1	n.d.	10.8	9.6	10.3	-	-	-	-	7	19.3
St218	1	n.d.	1	n.d.	5	-	-	-	-	10	13.9
St278	-	-	-	-	-	-	-	-	-	-	-
St280	-	-	-	-	-	-	-	-	-	-	-
Most Altered, 'pipe'-like alteration											
251A.pipe	-	-	5.9	12.8	6.23	-	-	-	-	-	-
251B.pipe	-	-	-	-	-	-	-	-	-	-	-
251C.pipe	-	-	-	-	-	-	-	-	-	-	-

Appendix 3B. Starra hangingwall geochemistry

sample	Location	Area	SiO2	TiO2	Al2O3	Fe2O3	MnO	MgO	CaO	Na2O	K2O	P2O5	LOI	Total	Au ppm
St24	CRQ78 - 1/72 -83 m	257	45.9	0.51	12	6.55	0.11	3.7	13.4	3.45	2.2	0.14	11.2		<0.05
St27	STQ78-1/82 -108 m	257	42.72	0.34	8.8	12.7	0.34	7.43	8.41	2.99	1.02	0.17	14.94	99.86	<0.05
St35	CRQ78 - 1/132-135 m	257	41.9	0.45	10.1	12.3	0.12	7.25	12.1	2.75	1.8	0.12	10.8		<0.05
St65	STQ80-16/200-225m	257	52.02	0.54	13.1	5.17	0.08	3.42	10.4	4.95	1.56	0.13	8.29	99.66	<0.05
St66	STQ80-16/225 -250 m	257	55.03	0.47	11.29	4.99	0.08	2.73	10.58	4.39	1.42	0.13	8.44	99.55	<0.05
St67	STQ80-16/250 -275 m	257	61.34	0.56	12.43	6.63	0.07	4.65	4.14	4.65	1.42	0.16	4.19	100.24	<0.05
St104	STQ85-129/83.2m	257	51.06	0.55	13.55	9.26	0.08	2.74	8.4	8.96	0.26	0.19	4.51	99.56	<0.05
St105	STQ85-129/90m	257	52.29	0.55	13.89	7.29	0.09	3.56	9.48	6.6	0.52	0.15	5.48	99.9	<0.05
St110	STQ85-129/124m	257	46.11	0.46	10.59	18.58	0.11	7.23	4.28	3.64	0.84	0.14	7.81	99.79	<0.05
St120	STQ85-129/156m	257	56.65	0.49	12.56	6.51	0.08	1.74	10.13	1.66	3.07	0.14	7.25	100.28	<0.05
St121	STQ85-129/161m	257	56.06	0.34	8.93	1.55	0.1	0.77	14.56	5.16	0.05	0.15	11.86	99.53	<0.05
St123	STQ85-129/170.1m	257	52.88	0.43	10.74	4	0.1	2.36	13.81	5.73	0.07	0.14	10.14	100.39	<0.05
St127.aren	STQ85-137/170-185m	257	55.11	0.45	11.56	4.33	0.1	3.83	10.24	4.06	1.93	0.15	8.34	100.1	<0.05
St127.scap	STQ85-137/170-185m	257	46.68	0.99	19.73	11.28	0.05	7.67	1.77	2.6	5.21	0.11	4.47	100.56	<0.05
St133.aren	STQ85-121/118m	257	56.82	0.52	13.81	5.51	0.09	2.96	6.73	8.11	0.53	0.18	5.3	100.56	<0.05
St133.scap	STQ85-121/118m	257	51.88	0.81	16.42	7.57	0.07	8.13	3.17	5.32	2.72	0.16	4.24	100.49	<0.05
St156	CRQ77-26/50 - 80 m	257	55.62	0.72	14.19	8.61	0.18	4.8	6.95	7.19	0.13	0.03	1.84	100.26	<0.05
St157	CRQ77-26/ 80-125 m	257	52.84	0.56	13.29	10.73	0.14	5.38	7.04	6.95	0.16	0.09	2.52	99.7	<0.05
St158	CRQ77-26/ 125-160 m	257	53.06	0.6	14.04	7.71	0.18	5.49	7.5	6.88	0.33	0.21	3.43	100.01	<0.05
St161	CRQ77-26/160-180 m	257	51.53	0.53	12.52	5.97	0.1	4.6	10.98	4.61	1.2	0.13	7.9	100.07	<0.05
St162	CRQ77-26/ 180 - 203 m	257	49.1	0.48	11.97	6.87	0.12	4.24	11.02	3.93	1.4	0.13	10.21	99.47	<0.05

Appendix 3B. Starra hangingwall geochemistry

sample	Cu	Pb	Zn	As	Bi	Co	Sb	W	Mo	Ga	Ba	Rb	Sr	Sc	V	Ni	Zr	Y
St24	20	10	10	9	<4	10	14	-	-	8	240	110	-	-	-	28	-	-
St27	25.3		9.7		-		-	25.4	<2	-	34	18.5	33.9	11	51.7	20.5	128.6	62.9
St35	760	20	12	8	12	18	8	-	-	12	85	100	-	-	-	22	-	-
St65	2.7	-	5.4	-	-	-	-	10.7	<2	-	168	84.2	72.2	13.7	96.8	41	166	24
St66	30.5	-	<2	-	-	-	-	7.9	<2	-	182	75.5	55	10.1	74.3	15	190	24
St67	19.6	-	11.2	-	-	-	-	15	<2	-	122	64	41.7	13.8	81.1	26	268	28
St104	98	-	11.3	-	-	-	-	19.4	9.3	-	35	4.2	36.5	13.4	96.4	31.5	164	21
St105	6.3	3	11	7	<2	-	-	5.8	<2	-	94	35.1	60.9	15.1	99	34.8	150.4	25.5
St110	9.7	<2	19	5	<2	-	-	31	<2	-	78	29.1	28.3	12.5	74	32	159	34
St120	132.4	<2	4.6	4	<2	-	-	2.1	<2	-	322	123.8	46	13.3	93.3	20.5	142	31.2
St121	5.2	<2	<2	4	<2	-	-	12	<2	-	3	<2	35.6	8.8	28.4	7	233	25
St123	11.4	<2	<2	5	<2	-	-	14	<2	-	10	<2	45.9	7.2	85	28.8	228	20
St127.aren	<2	3	7.2	4	<2	-	-	7.9	<2	-	169	93.3	48.4	11.7	68.7	23.6	168.5	18.4
St127.scap	14.5	2	38	3	<2	-	-	12.4	<2	-	707	242.7	67.7	36.1	218.3	179.2	221	28.4
St133.aren	<2	<2	7	5	<2	-	-	13.1	<2	-	34	29.4	49.8	12.8	82.1	30.5	169.5	23.2
St133.scap	<2	3	19.7	4	<2	-	-	8.2	<2	-	158	177.4	61.5	24.7	131.2	77	217	24
St156	15.4	<2	70	<3	<2	-	-	4.6	<2	-	59	4.1	75	18.8	103.2	38.9	156.5	27.5
St157	89.8	<2	50.2	<3	<2	-	-	10.5	<2	-	165	8.5	45.8	14.9	100.6	35.5	152.5	25.1
St158	2.4	3	51.9	8	<2	-	-	8.2	<2	-	114	19.9	77.1	19.4	105.3	35.6	161.9	30.6
St161	3.8	<2	11	<3	<2	-	-	22	<2	-	138	55.5	46.1	13.1	88.3	35	154.5	24.2
St162	113.5	<2	8	4	<2	-	-	11.4	<2	-	170	63	41.9	14.5	78.7	36.1	144.8	29.2

Appendix 3B. Starra hangingwall geochemistry

sample	Nb	La	Ce	Nd	U	Th	B	F	COMMENTS
St24	12	-	40	-	-	-	100	1500	fresh sediment
St27	8.8	-	-	-	11	12.6	-	-	fresh sediment
St35	10	-	30	-	-	-	140	600	fresh sediment
St65	12.6	24.4	51	21.7	8	13.6	-	-	fresh sediment
St66	11	30.6	66	26.4	4	12	-	-	fresh sediment
St67	13.3	39.5	83	32.5	14	15.5	-	-	fresh sediment
St104	14.4	-	-	-	6	17.9	-	-	fresh sediment
St105	13.2	38.1	80	29.5	6	15.4	-	-	alkali-altered
St110	10.8	29.4	66	27.1	11	13.3	-	-	Breccia
St120	12.6	30	55.9	22.8	4	13.1	-	-	fresh sediment
St121	10.2	43	91	35.1	10	11.8	-	-	calcite veined
St123	10.5	20.4	42	18.4	10	11.8	-	-	retextured
St127.aren	10.8	29.7	62.9	24.4	6	11	-	-	fresh sediment
St127.scap	24.2	25.7	45.4	17.2	11	26.2	-	-	fresh sediment
St133.aren	11.8	33.5	64.7	28.2	4	12.8	-	-	fresh sediment
St133.scap	17.9	45.6	106.5	41.5	7	22.3	-	-	fresh sediment
St156	13.5	57.6	114	42.1	4	14.2	-	-	alkali-altered
St157	11.5	-	-	-	7	14.2	-	-	alkali-altered
St158	14	37.6	82.8	35.7	8	16.5	-	-	alkali-altered
St161	12.3	-	-	-	8	15.6	-	-	fresh sediment
St162	11.9	-	-	-	8	15	-	-	fresh sediment

Appendix 3C. Major and trace element data for the Trough Tank host-rocks. All data is from split core.

	Location	SiO2	TiO2	Al2O3	Fe2O3	MnO	MgO	CaO	Na2O	K2O	P2O5	LOI	Total	Ni	Co	Sc	Cu	Pb	Zn
Silica± mag., cpy, py																			
tt12/60.5-61.6m	tt12	-	0.007	-	26.9	0.066	-	0.04	0.061	0.022	-	-	-	-	4350	-	12200	25	55
tt12/57.92-58.0m	tt12	-	0.012	-	50.9	0.028	-	0.42	0.162	0.127	-	-	-	-	770	-	23800	15	80
tt12/61.9-62.0m	tt12	-	0.001	-	6.91	0.009	-	0.168	0.04	0.013	-	-	-	-	680	-	6050	10	40
tt12/55.85-56.0m	tt12	-	0.013	-	19.3	0.03	-	1.41	0.075	0.064	-	-	-	-	185	-	3100	70	140
32	NQ4/135-141m	-	-	-	23.88	0.123	-	-	-	-	-	-	-	145	1194	-	10680	2	14
236607	NQ6/112.5-114.5	19.2	0.07	0.84	70.9	0.07	0.71	1.22	1.17	0.14	0.87	-0.24	94.95	2	125	10	15200	14	5
236609	NQ6/118.5-120.5m	36	0.03	1.18	47.4	0.04	0.29	0.5	3.9	0.15	0.33	3.9	93.72	85	1100	10	22500	12	24
236610	NQ6/120.5-121.7	31	0.04	1.17	52	0.05	1.05	0.21	0.16	0.24	0.16	3.6	89.68	120	1200	30	51500	16	20
236617	NQ4/134.4-135.4	51.3	0.06	0.74	38.9	0.15	0.43	0.55	0.01	0.22	0.37	2.95	95.68	50	430	30	8300	14	6
236618	NQ4/138.4-140	66.6	0.08	4.3	16	0.17	0.78	0.63	1.07	0.59	0.38	4.05	94.65	80	340	50	8950	14	5
TT111	HQ10/210.8-211.8	45.3	0.005	0.76	30.8	0.1	3.8	4.1	0.03	0.12	0.21	12.2	97.43	185	1140	10	10900	10	14
TT112	HQ10/216.8-217.8	42	0.005	0.12	52.1	0.06	0.22	0.2	0.1	0.005	0.07	1.82	96.7	96	610	10	11000	12	15
Mag-py-carb alteration																			
TT87	HQ19/88.67 - 89.67	63.5	0.31	12.4	15	0.08	0.37	0.47	4.8	0.39	0.06	2.46	99.84	48	230	-	530	10	7
TT95	HQ19/85 - 86m	66.3	0.55	15.2	2.16	0.05	1.01	2.32	7.6	0.14	0.13	2.52	97.98	8	185	-	14	8	5
TT127	HQ9/180 - 181 m	54.8	0.3	7.9	15.1	0.11	7.15	3.66	2.44	0.16	0.11	8.15	99.88	98	840	-	290	6	13
236611	NQ6/121.7 - 124.0 r	59.12	0.36	9.15	24.02	0.02	0.8	0.37	4.31	0.1	0.1	1.3	99.65	28.03	539.03	32.3	776	13	10
TT113	HQ10/228 - 229 m	33.8	0.22	6.75	53.5	0.05	0.52	0.49	4.4	0.07	0.11	0.22	100.1	82	370	-	380	14	22
TT115	HQ10/262 - 263 m	67.4	0.09	8.85	15.3	0.04	0.26	0.87	4.66	0.005	0.005	0.64	98.12	38	470	-	78	16	10
TT116	HQ10/276.7 - 277.6	72.7	0.1	10	7.3	0.03	0.99	0.74	5.1	0.005	0.02	1.68	98.67	30	290	-	24	18	8
Py-carb. alteration																			
TT96	HQ13/253 -254 m	71.5	0.28	7.15	4.74	0.04	0.19	6.05	4.58	0.02	0.06	5.85	100.5	22	680	-	34	10	3
TT97	HQ13/258 -259 m	74.9	0.27	6.65	6.05	0.05	0.73	3.66	4.06	0.005	0.06	1.91	98.35	14	250	-	17	10	5
TT98	HQ13/262 - 263 m	72.9	0.38	12	4.16	0.03	0.34	1.5	6.86	0.1	0.1	1.46	99.83	8	170	-	26	2	4
TT123	HQ9/132.7 - 133.7 r	67.9	0.5	14.7	4.56	0.04	0.65	1.75	7.2	0.26	0.13	1.99	99.68	18	220	-	26	10	6
TT124	HQ9/137.8 - 138.8m	71.7	0.45	12.1	3.78	0.04	0.73	1.62	6.5	0.03	0.11	2.04	99.1	12	105	-	17	6	5
TT125	HQ9/142.3 - 143.3m	72.8	0.26	8.5	4.62	0.04	0.11	5.15	4.58	0.005	0.07	4.34	100.5	12	440	-	9	14	5
TT126	HQ9/ 148.7 - 149.7r	63.4	0.21	7.45	14.7	0.08	1.16	2.58	3	0.27	0.08	4.66	97.59	32	370	-	13	6	7
236612	NQ6/128.2 - 128.7m	49.96	0.13	5.93	11.62	0.64	5.09	8.39	1.22	1.08	0.1	15.8	99.96	106	187	62	1072	20	15
TT114	HQ10/239.1 - 240.1	74.5	0.28	8.5	5.65	0.04	2.92	1.41	3.12	0.23	0.08	3.62	100.4	38	280	-	170	10	9
Weak py. alteration																			
TT138	NQ7/98.2 - 100.2 m	74.5	0.44	11.7	2.76	0.04	0.38	1.12	5.4	0.28	0.12	0.94	97.68	14	14	-	5	4	17
TT139	NQ7/102.2 - 104.2 r	79.3	0.33	9.95	1.97	0.04	0.58	1.25	5.25	0.03	0.08	1.13	99.91	12	10	-	1	8	5
TT140	NQ7/105.7 - 107.7 r	76.7	0.33	11.1	2.64	0.03	0.35	0.7	5.45	0.26	0.1	0.6	98.26	18	20	-	9	6	5
TT18	NQ3/94.1 -95.1m	55.27	0.64	21.12	5.37	0.01	3.78	0.59	8.49	2.39	0.21	1.3	99.17	78	107	24	8	13	12
Least altered																			
TT128	HQ19/224.2 - 225.2	60.2	0.5	17.2	3.4	0.08	1.65	3.62	7.95	0.44	0.17	3.84	99.05	20	125	-	8	2	5
TT137	NQ7/93.2 - 95.2 m	78.4	0.44	12.8	1.66	0.04	0.37	0.95	5.9	0.34	0.12	0.51	101.5	16	12	-	4	4	6
236616(LEAST ALTERED	NQ7/88.1 - 92.0 m	75.18	0.47	12.59	3.15	0.01	0.64	0.66	5.07	1.61	0.18	0.5	100.1	8.3	83.6	31.3	18	8	7
TT4	NQ4/ 108.2-109.2 m	68.63	0.5	14.59	3.26	0.01	2.62	1.01	7.49	1.21	0.14	0.6	100.1	62	10	17.9	49	10	7
TT60(236619)	NQ1/ 97.5 - 98.2 m	80.48	0.35	9.68	2.29	0.03	0.25	0.93	4.6	0.21	0.11	1.1	100	15	19	42	152	6	5
TT63(236622)	NQ1/ 162 - 170 m	71.89	0.54	12.78	2.58	0.03	2.51	1.43	5.23	1.06	0.13	1.8	99.98	38	2	31	32	9	10
TT129	HQ19/212.4 - 213.4	74.9	0.31	8.65	6.16	0.05	0.76	1.29	3.94	0.13	0.11	1.61	97.91	18	115	-	24	4	4
TT130	HQ19/200.1 - 201.1	72.9	0.44	11.6	5.1	0.03	0.88	0.64	6.2	0.06	0.11	1.2	99.16	30	320	-	15	6	6
TT134	HQ18/131 - 132 m	73.8	0.43	11.9	2.6	0.03	2.82	0.97	5.85	0.31	0.12	1.19	100	24	20	-	13	14	16
(nd : not detected; '-': not analysed)																			

Appendix 3C. Major and trace element data for the Trough Tank host-rocks. All data is from split core.

	Sn	W	Mo	As	Au	Rb	Ba	Sr	Nb	Zr	Y	Sb	S%	Bi	U	comments
Silica± mag., cpy, py																
tt12/60.5-61.6m	10	5	292	135	1.27	-	20	-	-	5	**nd**	0.5	14.4	15	nd	
tt12/57.92-58.0m	10	5	56	10	0.45	-	60	-	-	20	**nd**	0.5	6.53	5	nd	
tt12/61.9-62.0m	2.5	5	148	1	0.17	-	20	-	-	5	**nd**	0.5	5.44	2.5	nd	
tt12/55.85-56.0m	5	5	60	5	0.12	-	40	-	-	5	**nd**	0.5	0.1	2.5	nd	
32	16	5	48	24	0.28	-	5	-	-	-	**nd**	0.5	nd	24	12	
236607	2	5	12	2	1.62	40	25	4	4	12	8	nd	nd	135	nd	
236609	14	5	46	60	2.7	34	15	4	4	8	4	nd	nd	28	nd	
236610	22	5	60	30	0.95	50	10	7	3	2	2	nd	nd	2	nd	
236617	8	5	24	26	0.27	28	15	6	6	12	18	nd	nd	2	nd	
236618	8	5	30	18	0.15	24	80	8	6	10	18	nd	nd	8	nd	
TT111	-	-	-	-	0.19	34	5	10	1	74	38	nd	nd	-	nd	
TT112	-	-	-	-	0.14	22	5	8	4	2	4	nd	nd	-	nd	
Mag-py-carb alteration																
TT87	nd	nd	nd	nd	0.18	15	25	8	11	76	4					
TT95	nd	nd	nd	nd	0.005	2	15	24	19	155	46					
TT127	nd	nd	nd	nd	0.01	19	30	16	19	160	24					
236611	8.6	21.6	10.8	10.8	0.1	10.8	5	9.7	10.8	134.8	2					
TT113	0	0	0	0	0.01	16	5	11	6	70	8					
TT115	0	0	0	0	0.02	1	40	13	40	170	28					
TT116	0	0	0	0	0.02	1	30	12	46	185	42					
Py-carb. alteration																
TT96	-	-	-	-	0.02	1	10	28	12	130	6					
TT97	-	-	-	-	0.005	1	15	15	11	140	6					
TT98	-	-	-	-	0.01	1	15	22	20	180	38					
TT123	-	-	-	-	0.01	5	20	18	16	170	30					
TT124	-	-	-	-	0.01	1	10	15	16	290	38					Volcanic
TT125	-	-	-	-	0.005	1	5	28	10	150	4					
TT126	-	-	-	-	0.005	9	15	18	11	150	10					
236612	nd	nd	nd	12	0.005	62	44	25	8.7	106	25					
TT114	-	-	-	-	0.01	12	20	10	10	160	28					
Weak py. alteration																
TT138	-	-	-	-	0.02	12	15	14	13	220	32					
TT139	-	-	-	-	0.005	1	5	12	10	210	18					
TT140	-	-	-	-	0.005	15	25	18	11	210	28					
TT18	nd	1	1	1	0.005	162	459	36	17.4	134	21					anatexic fabric
Least altered																
TT128	-	-	-	-	0.01	12	25	20	15	185	24					Volcanic
TT137	-	-	-	-	0.005	5	50	18	14	220	18					Volcanic
236616	-	-	-	-	0.005	73	344.9	29	14.6	204	27					Volcanic
TT4	-	4.7	1	5	0.005	95	123	48	13.4	174	17					anatexic fabric
TT60(236619)	nd	nd	nd	nd	0.005	2	10	12	10.5	231	19					
TT63(236622)	nd	nd	nd	nd	0.005	51	43	23	12.8	224	32					
TT129	-	-	-	-	0.02	5	25	10	11	220	8					
TT130	-	-	-	-	0.005	1	10	15	15	175	52					
TT134	-	-	-	-	0.005	17	10	17	11	210	46					

APPENDIX 4

LINEAR CORRELATION COEFFICIENTS FOR MAJOR AND TRACE ELEMENTS

4A. Starra: Altered feldspathic Mariposa Creek Member

4B. Trough Tank: Pyrite alteration in host-rocks

4C. Trough Tank: Magnetite alteration in host-rocks

4D. Trough Tank: Magnetite alteration in host-rocks

4E. Starra: Ore environment ironstones

4F. Starra: Distal ironstones and BIFs

4G. Trough Tank: Oxide facies iron formations

Appendix 4A. Starra altered Mariposa Creek Member correlation co-efficients, n=24, 99% sig. level = 0.517

	Fe2O3	Au	SiO2	Al2O3	TiO2	MgO	MnO	Na2O	K2O	CaO	P2O5	LOI	Cu	Pb	Zn	Ba	Ni	Rb	Sr	Zr	Y	Sn
Fe2O3	1																					
Au	0.413	1																				
SiO2	-0.963	-0.396	1																			
Al2O3	-0.747	-0.344	0.581	1																		
TiO2	-0.192	-0.269	-0.032	0.673	1																	
MgO	-0.245	-0.094	0.089	0.192	0.26	1																
MnO	-0.393	-0.067	0.275	0.316	0.38	0.611	1															
Na2O	-0.093	-0.198	0.022	0.477	0.545	-0.453	-0.142	1														
K2O	-0.427	-0.003	0.456	0.092	-0.344	0.347	0.265	-0.705	1													
CaO	-0.499	-0.13	0.424	0.48	0.33	0.274	0.665	0.225	-0.065	1												
P2O5	-0.03	-0.232	-0.059	0.287	0.555	-0.079	0.044	0.535	-0.465	0.265	1											
LOI	-0.141	0.043	0.083	-0.091	-0.196	0.704	0.195	-0.758	0.598	-0.152	-0.315	1										
Cu	0.423	0.568	-0.426	-0.274	-0.08	-0.172	-0.83	-0.091	-121	-0.079	-1.05	-0.112	1									
Pb	-0.502	-0.092	0.503	0.318	-0.024	0.122	0.273	0.174	-0.07	0.808	0.091	-0.059	-0.097	1								
Zn	0.099	0.182	-0.22	-0.06	0.255	0.638	0.386	-0.347	0.086	0.056	-0.051	0.492	0.267	-0.065	1							
Ba	-0.236	-0.086	0.23	0.048	-0.072	0.428	0.311	-0.719	0.606	0.06	-0.311	0.609	-0.075	-0.053	0.287	1						
Ni	-0.189	-0.108	0.032	0.182	0.289	0.878	0.408	-0.324	0.139	0.206	0.005	0.714	-0.152	0.147	0.591	0.309	1					
Rb	-0.52	-0.013	0.552	0.169	-0.258	0.274	0.243	-0.64	0.945	-0.041	-0.461	0.534	-0.166	-0.06	0.082	0.656	0.092	1				
Sr	-0.532	-0.151	0.534	0.381	-0.061	0.159	0.287	0.074	0.066	0.748	0.036	0.001	-0.222	0.869	-0.203	0.146	0.131	0.053	1			
Zr	-0.455	-0.16	0.497	0.254	-0.236	0.119	-0.127	-0.07	0.109	0.247	0.005	0.187	-0.249	0.401	-0.337	0.16	0.269	0.085	0.615	1		
Y	-0.506	0.075	0.53	0.238	-0.262	0.281	0.39	-0.467	0.641	0.359	-0.353	0.369	-0.062	0.253	-0.103	0.555	0.177	0.646	0.502	0.569	1	
Sn	0.7	0.636	-0.64	-0.578	-0.273	-0.344	-0.424	-0.139	-0.23	-0.378	-0.135	-0.079	.6 88	-0.234	0.205	-0.105	-0.265	-0.281	-0.303	-0.351	-0.344	1
W	0.631	0.719	-0.577	-0.561	-0.238	-0.299	-0.283	-0.188	-0.206	-0.279	-0.148	-0.029	0.711	-0.165	0.206	-0.063	-0.154	-0.184	-0.328	-0.335	-0.253	0.893

Appendix 4B. Trough Tank pyrite alteration correlation coefficients, n=10, 99 % significance level = 0.765.

	A	B	C	D	E	F	G	H	I	J	K	L	M	N	O	P	Q	R	S	T	U	V
1		SiO2	TiO2	Al2O3	Fe2O3	MnO	Na2O	P2O5	Ba	Sr	Nb	Zr	Y	log(MgO)	log(CaO)	log(K2O)	log(LOI)	log(Ni)	log(Co)	log(Cu)	log(Zn)	log(Au)
2	SiO2	1																				
3	TiO2	0.353	1																			
4	Al2O3	0.193	0.959	1																		
5	Fe2O3	-0.632	-0.735	-0.621	1																	
6	MnO	-0.893	-0.546	-0.421	0.542	1																
7	Na2O	0.461	0.947	0.908	-0.766	-0.632	1															
8	P2O5	-0.321	0.724	0.846	-0.264	0.097	0.589	1														
9	Ba	-0.82	-0.382	-0.247	0.491	0.902	-0.531	0.262	1													
10	Sr	-0.32	-0.121	-0.069	-0.061	0.262	0.039	-0.06	-0.027	1												
11	Nb	0.25	0.853	0.868	-0.587	-0.427	0.906	0.672	-0.291	0.029	1											
12	Zr	0.39	0.549	0.5	-0.388	-0.423	0.54	0.363	-0.422	-0.422	0.487	1										
13	Y	-0.117	0.689	0.77	-0.399	0.02	0.562	0.862	0.214	-0.218	0.742	0.476	1									
14	log(MgO)	-0.591	-0.215	-0.138	0.472	0.61	-0.471	0.294	0.804	-0.492	-0.242	-0.134	0.365	1								
15	log(CaO)	-0.491	-0.637	-0.655	0.342	0.603	-0.578	-0.456	0.306	0.686	-0.613	-0.641	-0.613	-0.087	1							
16	log(K2O)	-0.704	-0.033	0.159	0.451	0.541	-0.206	0.56	0.748	-0.141	0.067	-0.174	0.508	0.751	-0.166	1						
17	log(LOI)	-0.733	-0.724	-0.646	0.604	0.782	-0.791	-0.266	0.59	0.424	-0.714	-0.576	-0.362	0.358	0.775	0.359	1					
18	log (Ni)	-0.688	-0.721	-0.634	0.73	0.771	-0.861	-0.19	0.778	-0.073	-0.739	-0.468	-0.256	0.674	0.457	0.577	0.835	1				
19	log (Co)	0.159	-0.457	-0.514	0.195	-0.181	-0.356	-0.697	-0.295	0.403	-0.519	-0.61	-0.796	-0.437	0.494	-0.306	0.38	0.174	1			
20	log (Cu)	-0.618	-0.488	-0.394	0.356	0.819	-0.627	0.037	0.893	-0.052	-0.424	-0.378	0.137	0.724	0.312	0.631	0.665	0.831	-0.134	1		
21	log (Zn)	-0.705	-0.456	-0.298	0.602	0.765	-0.653	0.183	0.836	-0.263	-0.505	-0.276	0.116	0.85	0.161	0.679	0.582	0.801	-0.271	0.757	1	
22	log (Au)	0.391	0.218	0.126	-0.393	-0.337	0.271	-0.073	-0.247	-0.021	0.227	0.263	0.076	-0.301	-0.218	-0.057	-0.158	-0.087	0.2	0.044	-0.483	1
23	log (Rb)	-0.78	-0.458	-0.293	0.678	0.755	-0.652	0.189	0.867	-0.157	-0.471	-0.418	0.09	0.834	0.192	0.833	0.674	0.886	-0.083	0.8	0.93	-0.283

Appendix 4C. Trough Tank magnetite alteration correlation coefficients, n=6, 99 % significance level = 0.917.

	A	B	C	D	E	F	G	H	I	J	K	L	M	N	O	P	Q	R	S	T	U	V	W
1		SiO2	TiO2	Al2O3	Fe2O3	MnO	MgO	Na2O	P2O5	Pb	Ba	Sr	Nb	Zr	Y	log(MgO)	log(CaO)	log(K2O)	log(LOI)	log(Ni)	log(Co)	log(Cu)	log(Zn)
2	SiO2	1																					
3	TiO2	0.338	1																				
4	Al2O3	0.679	0.116	1																			
5	Fe2O3	-0.94	0.187	-0.63	1																		
6	MnO	-0.201	0.347	0.024	-0.113	1																	
7	MgO	-0.115	0.303	-0.325	-0.213	0.752	1																
8	Na2O	0.333	-0.453	0.468	-0.022	-0.722	-0.942	1															
9	P2O5	-0.772	0.794	-0.446	0.594	0.37	0.455	-0.628	1														
10	Pb	0.286	-0.738	-0.001	0.019	-0.869	-0.745	0.817	-0.654	1													
11	Ba	0.68	-0.585	0.301	-0.745	0.297	0.224	-0.034	-0.733	0.04	1												
12	Sr	-0.013	-0.297	-0.591	-0.189	0.405	0.774	-0.704	0.031	-0.241	0.477	1											
13	Nb	0.738	-0.839	0.132	-0.653	-0.294	-0.069	0.302	-0.856	0.586	0.761	0.395	1										
14	Zr	0.67	-0.492	-0.073	-0.689	-0.186	0.311	-0.13	-0.509	0.274	0.614	0.634	0.837	1									
15	Y	0.53	-0.796	-0.075	-0.543	-0.059	0.215	0.046	-0.633	0.409	0.716	0.621	0.922	0.816	1								
16	log(MgO)	-0.104	0.338	-0.326	-0.195	0.577	0.946	-0.852	0.514	-0.623	0.047	0.688	-0.064	0.347	0.237	1							
17	log(CaO)	0.053	-0.07	-0.317	-0.341	0.715	0.914	-0.812	0.11	-0.545	0.554	0.911	0.251	0.491	0.498	0.791	1						
18	log(K2O)	-0.441	0.916	0.178	0.257	0.585	0.306	-0.435	0.759	-0.823	-0.468	-0.313	-0.884	-0.692	-0.787	0.272	-0.007	1					
19	log(LOI)	0.45	0.378	0.377	-0.715	0.626	0.734	-0.573	.10 4	-0.658	0.408	0.351	0.09	0.374	0.194	0.716	0.642	0.349	1				
20	log (Ni)	-0.701	0.231	-0.497	0.45	0.799	0.628	-0.704	0.596	-0.668	-0.059	0.46	-0.46	-0.379	-0.147	0.488	0.581	0.473	0.126	1			
21	log (Co)	-0.207	0.25	-0.641	0.016	0.287	0.739	-0.847	. 438	-0.471	0.022	0.753	-0.079	0.409	0.057	0.675	. 668	0.069	0.332	0.365	1		
22	log (Cu)	-0.556	0.907	-0.029	0.471	0.274	0.091	-0.345	0.778	-0.642	-0.654	-0.383	-0.949	-0.706	-0.952	0.05	-0.222	0.882	0.034	0.318	0.199	1	
23	log (Zn)	-0.915	0.047	-0.909	-0.284	0.103	0.208	-0.393	0.609	-0.116	-0.49	0.331	-0.435	-0.337	-0.206	0.191	0.142	0.102	-0.49	0.671	0.406	0.263	1
24	log (Au)	0.38	.4	0.817	0.485	-0.175	-0.445	0.411	-0.081	-0.077	-0.18	-.8 09	-0.287	-0.323	-0.556	-0.413	-0.598	0.425	0.169	-0.547	-0.46	0.437	-0.686
25	log (Rb)	-0.677	0.88	-0.133	0.678	0.555	0.382	-0.549	0.914	-0.797	-0.605	-. 162	-0.94	-0.7	-0.769	0.367	0.055	0.949	0.205	0.625	0.225	0.887	0.399
26																							
27																							

Appendix 4D. Trough Tank silica alteration correlation coefficients, n=12, 99 % significance level = 0.708.

	A	B	C	D	E	F	G	H	I	J	K	L	M	N	O	P	Q	R	S	T	U	V	W	X
1		SiO2	TiO2	Al2O3	Fe2O3	MnO	Na2O	P2O5	Pb	Ba	Sr	Nb	Zr	Y	log(MgO)	log(CaO)	log(K2O)	log(LOI)	log(Ni)	log(Co)	log(Cu)	log(Zn)	log(Sn)	log(Mo)
2	SiO2	1																						
3	TiO2	0.951	1																					
4	Al2O3	0.773	0.754	1																				
5	Fe2O3	-0.975	-0.925	-0.894	1																			
6	MnO	0.944	0.959	0.574	-0.86	1																		
7	Na2O	-0.235	-0.502	-0.011	0.143	-0.494	1																	
8	P2O5	0.771	0.558	0.383	-0.692	0.69	0.234	1																
9	Pb	-0.127	0.184	-0.002	0.117	0.061	-0.846	-0.678	1															
10	Ba	0.868	0.832	0.986	-0.957	0.692	-0.046	0.517	-0.061	1														
11	Sr	0.557	0.77	0.659	-0.602	0.604	-0.734	-0.095	0.717	0.642	1													
12	Nb	0.913	0.827	0.454	-0.805	0.937	-0.228	0.891	-0.272	0.599	0.293	1												
13	Zr	0.73	0.557	0.213	-0.6	0.737	0.052	0.965	-0.567	0.369	-0.09	0.926	1											
14	Y	0.921	0.89	0.469	-0.81	0.981	-0.395	0.794	-0.094	0.608	0.438	0.984	0.851	1										
15	log(MgO)	0.092	0.365	0.39	-0.177	0.154	-0.689	-563	0.906	0.307	0.875	-0.2	-0.555	-0.037	1									
16	log(CaO)	0.766	0.542	0.427	-0.705	0.657	0.299	0.996	-0.712	0.551	-0.106	0.861	0.938	0.757	-0.565	1								
17	log(K2O)	0.811	0.899	0.913	-0.88	0.737	-0.418	0.272	0.331	0.918	0.893	0.524	0.193	0.605	0.622	0.284	1							
18	log(LOI)	0.084	-0.006	0.653	-0.297	-0.229	0.572	-0.048	-0.231	0.542	0.105	-0.254	-0.306	-0.306	0.159	0.038	0.349	1						
19	log (Ni)	-0.528	-0.416	0.115	0.337	-0.655	0.155	-0.795	0.391	-0.055	0.155	-0.829	-0.924	-0.784	0.542	-0.739	0.02	0.645	1					
20	log (Co)	-0.966	-0.944	-0.597	0.886	-0.993	0.388	-0.768	0.055	-0.719	-0.532	-0.965	-0.795	-0.988	-0.06	-0.74	-0.716	0.176	0.683	1				
21	log (Cu)	-0.875	-0.753	-0.403	0.763	-0.883	0.115	-0.939	0.392	-0.552	-0.168	-0.991	-0.966	-0.952	0.326	-0.912	-0.433	0.245	862	0.924	1			
22	log (Zn)	-0.929	-0.954	-0.548	0.839	-0.999	0.528	-0.669	-0.092	-0.667	-0.613	-0.929	-0.725	-0.978	-0.17	-0.632	-0.728	0.264	0.659	0.988	0.872	1		
23	log(Sn)	-0.893	-0.775	-0.437	0.788	-0.895	0.123	-0.935	0.377	0.583	-0.199	-0.994	-0.956	-0.958	0.297	-0.91	-0.467	0.218	0.842	0.935	0.999	0.884	1	
24	log(Mo)	-0.805	-0.726	0.249	0.656	-0.888	0.278	-0.859	0.263	-0.409	-0.182	-0.975	-0.944	-0.96	0.285	-0.814	-0.36	0.451	0.925	0.909	0.974	0.887	0.969	1
25	log (Au)	-0.875	-0.973	-0.599	0.813	-0.96	0.675	-0.463	-0.33	-0.687	-0.794	-0.801	-0.52	-0.891	-0.421	-0.428	-0.829	0.212	0.467	0.923	0.715	0.965	0.733	0.742

Appendix 4E. Starra ore environment ironstones* correlation co-efficients, n=17, 99% sig. level = 0.606

	SiO2	TiO2	Al2O3	Fe2O3	MnO	MgO	CaO	Na2O	K2O	P2O5	Ba	Sc	Ni	V	Rb	Sr	Zr	Y	Nb	Bi	Cu	Pb	Zn	Au	W
SiO2	1																								
TiO2	0.108	1																							
Al2O3	0.388	0.808	1																						
Fe2O3	-0.965	-0.3	-0.602	1																					
MnO	-0.424	-0.465	-0.303	0.436	1																				
MgO	0.432	0.665	0.738	-0.554	-0.218	1																			
CaO	-0.545	-0.121	-0.079	0.479	0.617	0.074	1																		
Na2O	0.353	0.474	0.757	-0.533	-0.409	0.355	-0.095	1																	
K2O	0.192	0.735	0.878	-0.401	-0.27	0.47	0.051	0.739	1																
P2O5	0.195	0.785	0.72	-0.325	-0.456	0.548	-0.322	0.405	0.745	1															
Ba	-0.015	0.683	0.725	-0.174	-0.012	0.377	0.288	0.517	0.908	0.612	1														
Sc	0.654	0.673	0.726	-0.72	-0.545	0.724	-0.313	0.364	0.629	0.72	0.513	1													
Ni	0.543	0.364	0.55	-0.637	-0.149	0.622	-0.339	0.471	0.161	0.232	-0.028	0.289	1												
V	-0.143	0.85	0.67	-0.057	-0.369	0.354	0.031	0.386	0.785	0.69	0.735	0.495	-0.042	1											
Rb	0.369	0.691	0.937	-0.575	-0.258	0.497	-0.066	0.797	0.933	0.621	0.81	0.656	0.354	0.673	1										
Sr	-0.232	0.196	0.39	0.094	0.322	0.056	0.642	0.428	0.602	0.074	0.777	0.09	-0.257	0.338	0.563	1									
Zr	0.235	0.962	0.902	-0.431	-0.432	0.77	-0.125	0.562	0.741	0.756	0.653	0.736	0.502	0.757	0.77	0.229	1								
Y	0.596	-0.318	-0.217	-0.405	-0.099	0.18	-0.352	-0.391	-0.391	-0.062	-0.404	0.375	0.068	-0.544	-0.29	-0.419	-0.209	1							
Nb	0.314	0.226	0.461	-0.422	0.35	0.275	-0.176	0.227	0.222	0.098	0.207	0.109	0.687	0.052	0.439	0.054	0.327	-0.099	1						
Bi	0.289	-0.323	-0.067	-0.189	-0.11	0.086	-0.152	-0.131	-0.033	0.203	-0.221	0.265	-0.198	-0.216	-0.099	-0.222	-0.238	0.576	-0.352	1					
Cu	0.737	-0.417	-0.017	-0.617	0.145	0.016	-0.249	-0.071	-0.082	-0.124	-0.137	0.308	0.126	-0.486	0.063	-0.082	-0.28	0.742	0.257	0.538	1				
Pb	-0.281	0.23	0.114	0.199	0.118	0.509	0.301	-0.096	-0.138	0.063	-0.206	-0.126	0.396	0.102	-0.186	-0.296	0.249	-0.204	0.069	-0.047	-0.458	1			
Zn	-0.309	0.224	0.111	0.23	0.107	0.49	0.271	-0.089	-0.142	0.096	-0.217	-0.136	0.39	0.089	-0.194	-0.302	0.249	-0.196	0.047	-0.013	-0.477	0.994	1		
Au	0.508	-0.543	-0.279	-0.359	0.407	-0.15	-0.26	-0.342	-0.402	-0.362	-0.337	-0.034	0.181	-0.678	-0.216	-0.228	-0.442	0.662	0.451	0.2	0.851	-0.38	-0.397	1	
W	0.443	-0.42	-0.143	-0.331	-0.116	-0.109	-0.17	-0.133	-0.025	-0.034	-0.191	0.239	-0.317	-0.184	-0.042	-0.161	-0.375	0.512	-0.271	0.83	0.699	-0.333	-0.349	0.357	1
Mo	0.01	0.247	0.128	-0.073	-0.01	0.533	0.075	-0.072	-0.173	0.013	-0.286	-0.034	.5 71	0.062	-0.162	-0.484	0.254	-0.108	0.233	-0.143	-0.288	0.909	0.874	-0.188	-0.262
* "Ore environment ironstones" includes the Mineralised Proximal population and the Barren Proximal strike-equivalents.																									

Appendix 4F. Starra distal ironstones and BIFs correlation co-efficients, n=22, 99% sig. level = 0.537

	SiO2	TiO2	Al2O3	Fe2O3	MnO	MgO	CaO	Na2O	K2O	P2O5	Cu	Zn	Ba	Sc	Ni	V	Rb	Sr	W	Zr	Y	Nb
SiO2	1																					
TiO2	-0.037	1																				
Al2O3	0.431	0.701	1																			
Fe2O3	-0.845	-0.24	-0.802	1																		
MnO	0.029	-0.479	-0.12	-0.148	1																	
MgO	0.175	-0.438	0.079	-0.357	0.766	1																
CaO	0.168	-0.51	-0.052	-0.28	0.949	0.868	1															
Na2O	0.317	-0.202	0.216	-0.464	0.602	0.681	0.793	1														
K2O	0.33	0.749	0.968	-0.705	-0.213	-0.034	-0.16	0.14	1													
P2O5	0.19	-0.599	-0.052	-0.297	0.815	0.947	0.923	0.741	-0.149	1												
Cu	0.221	0.199	0.407	-0.393	0.162	0.083	0.091	0.086	0.321	0.019	1											
Zn	0.185	-0.566	-0.035	-0.289	0.832	0.817	0.849	0.522	-0.151	0.873	0.295	1										
Ba	0.157	0.429	0.445	-0.313	-0.08	-0.175	-0.178	-0.104	0.412	-0.275	0.934	-0.016	1									
Sc	-0.042	0.882	0.803	-0.352	-0.32	-0.264	-0.3	0.066	0.845	-0.386	0.221	-0.412	0.386	1								
Ni	0.305	0.253	0.651	-0.639	0.229	0.562	0.417	0.668	0.597	0.518	0.215	0.424	0.102	0.424	1							
V	-0.038	-0.328	-0.024	-0.064	0.167	0.546	0.349	0.368	-0.108	0.595	-0.154	0.512	-0.39	-0.205	0.588	1						
Rb	0.327	0.797	0.955	-0.677	-0.224	-0.138	-0.196	0.108	0.985	-0.231	0.35	-0.197	0.458	0.87	0.541	-0.186	1					
Sr	0.375	-0.274	-0.145	-0.066	-0.341	-0.435	-0.305	-0.245	-0.209	-0.298	0.022	-0.165	-0.001	-0.193	-0.369	-0.072	-0.155	1				
W	-0.351	0.818	0.556	-0.002	-0.324	-0.412	-0.437	-0.32	0.624	-0.502	0.065	-0.472	0.239	0.807	0.103	-0.236	0.672	-0.25	1			
Zr	0.029	0.772	0.251	0.005	-0.536	-0.594	-0.587	-0.331	0.311	-0.717	0.128	-0.643	0.401	0.451	-0.084	-0.517	0.388	-0.184	0.384	1		
Y	-0.144	0.699	0.449	-0.07	-0.367	-0.46	-0.471	-0.271	0.473	-0.578	0.71	-0.384	0.881	0.641	0.019	-0.438	0.534	-0.055	0.562	0.595	1	
Nb	0.199	0.864	0.644	-0.365	-0.392	-0.3	-0.4	-0.183	0.633	-0.503	0.131	-0.449	0.299	0.652	0.17	-0.328	0.663	-0.232	0.556	0.772	0.466	1

Appendix 4G. Trough Tank oxide facies BIFs correlation co-efficients, n=25, 99% sig. level = 0.487

	SiO2	TiO2	Fe2O3	Al2O3	CaO	MgO	Na2O	K2O	MnO	P2O5	Zn	Fe/Fe+Si	V	Sc	Rb	Y	log(Au)	log(Cu)	log(Co)	log(As)
SiO2	1																			
TiO2	0.159	1																		
Fe2O3	-0.971	-0.362	1																	
Al2O3	0.207	0.973	-0.409	1																
CaO	-0.287	0.173	0.165	0.193	1															
MgO	0.201	0.388	-0.304	0.317	0.003	1														
Na2O	0.212	0.969	-0.418	0.962	0.162	0.392	1													
K2O	0.18	0.958	-0.371	0.984	0.119	0.241	0.946	1												
MnO	-0.379	-0.725	0.464	-0.656	0.365	-0.24	-0.661	-0.728	1											
P2O5	-0.224	0.498	0.041	0.471	0.886	0.096	0.485	0.42	-0.013	1										
Zn	0.013	0.48	-0.176	0.52	0.501	0.079	0.604	0.458	0.023	0.671	1									
Fe/Fe+Si*	-0.997	-0.229	0.986	-0.277	0.259	-0.226	-0.285	-0.247	0.415	0.172	-0.067	1								
V	0.27	0.401	0.176	0.305	-0.048	0.773	0.296	0.289	0.332	0.064	-0.152	0.25	1							
Sc	-0.087	0.645	-0.057	0.566	0.132	0.265	0.534	0.595	-0.618	0.394	-0.034	0.045	0.442	1						
Rb	0.104	0.811	-0.274	0.842	-0.023	0.116	0.841	0.909	-0.706	0.307	0.375	-0.167	0.174	0.618	1					
Y	-0.202	0.355	0.056	0.393	0.617	-0.226	0.408	0.326	0.182	0.73	0.81	0.15	-0.315	0.049	0.272	1				
log(Au)	-0.15	-0.42	0.205	-0.271	0.016	-0.624	-0.262	-0.24	0.535	-0.117	0.329	0.161	-0.688	-0.627	-0.058	0.374	1			
log(Cu)	-0.051	-0.518	0.142	-0.376	-0.035	-0.734	-0.387	-0.362	0.569	-0.199	0.207	0.073	-0.83	-0.63	-0.207	0.35	0.949	1		
log(Co)	0.025	-0.572	0.076	-0.622	-0.24	-0.168	-0.483	-0.583	0.299	-0.29	-0.305	0.004	-0.394	-0.105	-0.259	-0.179	0.219	0.299	1	
log(As)	0.447	0.029	-0.474	. 10 9	-0.014	0.153	0.097	0.114	-0.074	-0.04	-0.148	-0.453	-0.189	0.33	0.295	-0.101	-0.018	0.028	0.458	1
* Oxides i.e., (Fe2O3/Fe2O3+SiO2) X 100																				

APPENDIX 5

MAJOR AND TRACE ELEMENT GEOCHEMISTRY OF IRONSTONES

5A. Starra: Mineralised and barren ironstones and BIFs

5B. Trough Tank: All iron formations

Appendix 5A. Starra mineralised and barren ironstones and BIF ('-' = not determined; oxides in %, trace elements in ppm).

Sample	SiO2	TiO2	Al2O3	Fe2O3	MnO	MgO	CaO	Na2O	K2O	P2O5	loss	Total	Cu	Pb	Zn	Au	Ba	Sc	Ni	V	Rb	Sr
Mineralised																						
ST30s	22	0.04	0.13	73.6	0.05	0.25	0.1	0.24	0.08	0.01	3	**99.5**	18800	4	10	3.94	10	-	2	-	38	-
ST30d	24	0.04	0.15	71	0.08	0.38	0.1	0.21	0.07	0.02	2.45	**98.5**	7030	2	5	1.94	5	-	4	-	36	-
ST77	31.61	0.18	1.11	66.73	0.02	1.09	0.06	0.15	0.07	0.03	-1.15	**100**	7800	<2	<2	4.8	12	6	20.2	21.1	2	2
ST107	41.35	0	26	33.89	0.14	0.28	12.1	0.32	0.1	0.01	9.7	**98.2**	5680	<2	<2	3.12	17	1.1	-	-	<2	8.9
ST115	25.23	0.04	0.32	72.86	0.1	0.2	0.04	0	0	0	-2.38	**99.9**	11300	<2	<2	11.26	7	2	26.9	8.9	2	2
ST116	28.41	0.04	0.22	68.56	0.02	0.14	0.06	1.54	0.06	0	1.33	**100**	5500	<2	<2	2.45	5	2	22.9	11.6	2	2
ST118	34.62	0.02	0.47	63.84	0.04	0.59	0	0	0.06	0.02	-0.98	**98.7**	16900	<2	<2	7.52	5	5	12.9	16.5	2	1.7
St277	27.5	0.06	0.93	70.4	0.03	0.3	-	0.08	0.04	<0.01	0.42	**99.8**	330	<5	5	0.49	55	-	<10	-	2	2
Barren, proximal																						
ST19	19.95	0.06	0.3	80.59	0.04	0.1	1.17	0.02	0.04	0.8	2.38	**101**	4250	27	26	0.33	7	1	9.7	120.8	2	6.1
ST22	15.8	0.07	0.35	81.5	0.04	0.39	0.1	0.23	0.08	0.03	0.5	**99.1**	1630	6	1	0.19	10	0	2	-	40	-
ST59	32.69	0.3	6.24	55.22	0.02	1.34	0.1	2.29	0.4	0.06	0.7	**99.4**	6000	<2	<2	0.3	26	7	28.4	52.8	16	3
ST75	12.62	0.16	0.16	87.16	0.04	0	0.08	0	0.15	0.04	-0.06	**100**	12	<2	<2	0.05	15	3	6	41.9	2	2
ST99	8.56	0.14	1.1	90.14	0.04	0.9	0.06	0.15	0.04	0.06	-1.44	**99.5**	1400	2	6	0.05	9	4	8.8	30.4	2	2
ST100	13.37	0.12	1.14	86.55	0.04	0.46	0.02	0.62	0.08	0.04	-1.64	**101**	540	5	6	0.05	8	3	18.6	22.5	2	2
ST124	7.98	0.12	0.14	91.48	0.04	0.16	0.12	0.15	0.08	0.1	-0.8	**99.5**	40	<2	<2	0.05	9	16	-	-	2	2
ST139	17.04	0.12	0.06	82.56	0.02	0	0.04	0.15	0.02	0	0.18	**100**	50	<2	<2	0.28	6	3	10	32.8	2	2
ST167	24.33	0.21	2.22	70.39	0.03	1.41	0.09	0.43	0.06	0.03	-0.09	**99.1**	42	16	14	0.18	5	4	34.5	32.5	2	1.2
ST196	8.106	0.08	0.56	91.26	0.1	0.64	1.19	0.24	0.1	0	-1.6	**101**	1546	7	6	0.25	15	2	8.9	25.6	2	3.1
Distal, barren & chert-rich																						
A7	57.52	0.17	3.83	34.81	0.01	0.02	0.09	0.22	0.15	0.12	2.76	**99.7**	11.6	<2	10	<0.01	244	5.6	8	130.2	7.9	236.4
SG22	53.18	0.47	6.55	36.46	0.03	0.38	0.04	0.07	2	0.07	1.34	**101**	4.3	5	2.2	0.03	675	7.4	13.1	86.5	93	40.3
SG25G	44.94	0.5	4.5	47.16	0.02	0.94	0.18	<0.3	0.38	<0.03	0.82	**99.4**	2	-	3.5	0.01	870	10	21.9	120.7	16	43.8
SG36F	53.39	0.62	14.37	20.65	0.03	0.88	0.04	<0.3	6.08	0.02	2.35	**98.4**	182.4	<2	10.9	<0.01	10551	15.3	37.8	65.2	252	71.8
SG36G	48.87	0.33	1.39	48.12	0.02	0.1	0.01	<0.3	0.27	0.06	0.59	**99.8**	37.4	<2	3	<0.01	3768	6	13	35.3	11	35.8
SG41B	53.84	0.69	16.32	17.73	0.01	0.67	0.16	0.68	8.86	0.08	1.12	**100**	4.7	3.4	2.3	<0.01	1551	18.8	58.1	99.9	351	23
SG45B	36.52	0.06	0.8	60.61	0.11	0.04	0.02	<0.3	0.05	0.03	1.73	**100**	810.7	<2	12	<0.01	842	5	-	-	<4	9.2
STP5/90	52.42	1.04	10.33	25.44	0.06	4.66	1.72	2.16	1.09	0.23	3.35	**103**	19	<2	19	<0.01	188	26	60	259	53	268
STP6/88	52.96	0.34	8.98	25.54	0.09	4.64	2	0.65	2.29	0.36	1.98	**99.8**	584	<2	34	0.02	1293	9.8	33	123	68	23.8
STP7/120	52.64	0.27	6.64	27.88	0.17	4.65	3.15	1.5	1.4	0.65	1.64	**101**	36	<2	26	0.02	1116	9.3	46	129.1	58.1	25
STP23/66	54.13	0.36	6.44	23.4	0.16	5.74	3.09	0.49	1.4	0.3	3.94	**99.5**	16	<2	25	<0.01	1840	6.4	25	99.2	42	19.4

Appendix 5A. Starra mineralised and barren ironstones and BIF ('-' = not determined; oxides in %, trace elements in ppm).

Sample	SiO2	TiO2	Al2O3	Fe2O3	MnO	MgO	CaO	Na2O	K2O	P2O5	loss	Total	Cu	Pb	Zn	Au	Ba	Sc	Ni	V	Rb	Sr
STP24/56	49.95	0.29	7.16	32.34	0.05	3.57	1.03	0.73	2.63	0.39	2.33	**101**	27	<2	12	0.01	968	8.1	27	130	59	12.8
STP24/80	49.39	0.34	7.81	32.68	0.07	3.77	0.87	0.09	2.73	0.37	2.34	**101**	10	<2	19	0.01	1043	8	33	141	75.3	14.9
STP24/92	49.42	0.22	5.16	34.56	0.16	3.45	2.29	0.53	1.22	0.49	1.87	**99.5**	74	<2	39	<0.01	2648	4.9	25	111	47	22.4
STP24/94	50.61	0.28	6.18	26.63	0.58	3.66	4.65	0.48	1.89	0.38	3.45	**98.8**	176	5.2	34	0.01	6946	6.7	47	98.4	61.7	42.3
STP24/112	50.5	0.56	7.87	29.11	0.19	4.16	3.2	1.17	1.58	0.36	1.93	**101**	25	-	37	0.02	2029	10.5	35	136	66.3	36.5
STP25/EOH	50.64	0.29	7.31	31.32	0.06	4.09	1.44	0.92	2.17	0.58	1.09	**99.9**	47	-	30	0.01	1086	7.1	70	316	63.1	25.2
distal, barren & chert-poor																						
SG27	5.3	0.12	0.16	94	0.02	<0.1	<0.02	<0.3	0.06	0.03	0.44	**100**	20.5	-	<2	0.1	104	4	2.6	44	<4	4
SG28	10.54	0.18	0.14	88.87	0.02	<0.1	<0.02	<0.3	0.02	<0.03	0.16	**99.9**	24.5	<2	7.3	<0.1	219	3	6.1	27.9	<4	<4
SG30	19.35	0.2	0.34	78.69	0.02	<0.1	<0.02	<0.3	0.04	0.06	0.74	**99.5**	16.9	-	6.2	0.2	133	5	6.8	40.1	20	22
SG67	26.59	0.4	2.31	68.24	0.04	0.14	0.02	<0.3	0.48	0.06	0.8	**99.3**	6.6	<2	4	<0.1	892	11	10	128.7	20	22
SG78	17.86	0.24	1.2	79.38	0.04	<0.1	0.04	<0.3	0.18	0.08	1.18	**100**	10.2	3.2	5.3	<0.1	907	5	6.9	56.8	11	29.1

Appendix 5A. Starra mineralised and barren ironstones and BIF ('-' = not determined; oxides in %, trace elements in ppm).

Sample	W	Mo	Zr	Y	Nb	Bi	As	La	Ce	Nd	U	Th	La/Y.chond.
ST30s	-	-	-	-	6	4	5	-	-	-	-	-	
ST30d	-	-	-	-	5	4	12	-	-	-	-	-	
ST77	44	22	48	92	1	1	-	13	20	11.1	9	<3	1.23
ST107	28.1	5	1.1	39.8	<1	0	-	7.9	20.9	11.1	4.8	<3	1.73
ST115	27	37	10	52	10	-	-	-	-	0	11	<3	-
ST116	158.3	36	5	27	1	1	-	0.81	1.85	1.08	3	<3	0.26
ST118	695.6	11	5	98	1	6	-	0.5	2	0.4	7	<3	0.04
St277	30	-	19	9	<10	-	-	-	-	0	-	-	-
													-
ST19	1	<3	4	14	1	4	-	25.4	37	21.8	5	<3	15.82
ST22	-	-	-	-	6	6	5	-	-	-	-	-	-
ST59	109.5	5	94	16	7	1	-	1	1	3	7	8	0.54
ST75	145.4	5	23	9	1	1	-	3.68	8.51	1.1	4	<3	3.56
ST99	24.7	<3	26	25	1	1	-	5.3	<3	<3	4	<3	1.85
ST100	11.5	6	35	43	1	3	-	3.1	<3	<3	<2	<3	0.63
ST124	68.3	<3	9	10	6	-	-	4.89	8.93	4.64	-	-	4.26
ST139	85.1	3	29	30	1	-	-	-	-	-	-	-	-
ST167	1	362	59	34	5	1	-	4	<3	<3	5	<3	1.03
ST196	61.2	68.2	18	15	1	1	-	4	<3	4.5	<2	<3	2.32
A7	3.1	2	34	7	3	6	<3	46	88	47.5	-	-	57.29
SG22	8.9	<2	145.7	15.6	12.1	4	<3	-	-	-	-	-	-
SG25G	5.9	<2	175	24	14	-	<3	35.2	50	22.2	-	-	12.79
SG36F	10.1	<2	149.6	71	12.7	5.1	5	161.3	59	105	-	-	19.81
SG36G	3	<2	158.3	30	5	<1	5	31.6	58	19.5	-	-	9.18
SG41B	12	<2	144.5	28.8	14.5	<1	2.3	23.5	23	15.9	-	-	7.11
SG45B	11.3	<3	10.2	<3	<2	5.2	<3	-	-	-	-	-	-
STP5/90	-	<2	85.3	20.6	6.3	<2	<3	-	-	-	-	-	-
STP6/88	<2	5	66.7	16.4	9.8	<2	<3	-	-	-	-	-	-
STP7/120	4.7	<2	46.4	9.7	4.2	<2	-	-	-	-	-	-	-
STP23/66	<2	<2	103.8	10.7	5.6	<2	-	-	-	-	-	-	-

Appendix 5A. Starra mineralised and barren ironstones and BIF ('-' = not determined; oxides in %, trace elements in ppm).

Sample	W	Mo	Zr	Y	Nb	Bi	As	La	Ce	Nd	U	Th	La/Y.chond.
STP24/56	4	<2	54.6	13.3	8	<2	4	-	-	-	-	-	-
STP24/80	6.9	<2	59.8	10.5	6.9	<2	-	-	-	-	-	-	-
STP24/92	4	2	54.8	11.5	6.2	<2	3	13.2	28.8	12.1	-	-	10.01
STP24/94	<3	4	98	14.3	7.2	<2	9	20.7	43.6	14.5	-	-	12.62
STP24/112	<3	-	105.2	17.6	8	<2	-	-	-	-	-	-	-
STP25/EOH	4	<2	56.9	11.2	4.7	<2	-	-	-	-	-	-	-
SG27	-	-	19	8	<2	<1	6	<3	<5	<3	-	-	3.27
SG28	3.3	<2	39	6	<2	<1	<3	3.3	<5	<3	-	-	4.79
SG30	2.1	6	68	32	4	-	-	6.6	<5	<3	-	-	1.80
SG67	11.5	<2	68	32	4	<1	10	17.8	23	7.6	-	-	4.85
SG78	3	<3	49	7	4	2.5	7.3	-	-	-	-	-	-

Appendix 5B, Trough Tank BIF geochemistry (oxides %, traces in ppm)

	SiO2%	TiO2%	Fe2O3%	Al2O3%	CaO%	MgO%	Na2O%	K2O%	MnO%	P2O5%	LOI%	Au	Cu	Co	Pb	Zn	Fe+Si*	Fe/Fe+Si*	V
HQ9/191.1m	35.91	0.05	53.46	1.42	0.66	3.28	0.1	0.22	0.04	0.45	2.26	0.08	6416	480	-	6	89.37	0.60	237
HQ18/156-158	67	0.01	28.7	0.19	0.95	1.88	0.1	0.01	0.07	0.5	0.01	0.005	32	60	16	20	95.7	0.30	-
HQ18/162-164	35.9	0.03	50.4	1	4.06	3.74	0.32	0.12	0.18	0.61	2.66	0.01	60	96	10	42	86.3	0.58	-
HQ18/166-168	69.7	0.09	3.14	15	1.27	0.77	5.15	2.68	0.06	0.4	1.53	0.01	12	18	10	11	72.84	0.04	-
TT122/HQ9,131	25.3	0.04	59.5	1.32	1.18	8.8	0.22	0.15	0.12	0.02	1.76	0.005	78	270	10	26	84.8	0.70	-
HQ9/197.4m	36.45	0.08	54.63	2.63	0.65	1.36	0.64	0.28	0.04	0.72	1.24	1.82	7950	210	-	31	91.08	0.60	50
HQ9/201.5m	14.8	0.02	82.39	0.28	0.19	2.26	0.03	0.05	0.05	0.12	-1.69	0.02	275	70	-	1	97.19	0.85	188
HQ14/126m	19.94	0.03	75.68	0.86	0.58	0.39	0.11	0.15	0.04	0.53	-0.25	0.15	3232	490	-	3	95.62	0.79	63
HQ14/146m	18.56	0.005	79.32	0.16	0.7	0.31	0.02	0.13	0.04	0.54	-1.52	2.04	4948	155	-	8	97.88	0.81	73
HQ14/152m	16.7	0.01	80.46	0.1	0.91	0.25	0.02	0.05	0.05	0.74	-1.69	0.77	8547	56	-	21	97.16	0.83	59
HQ14/158m	15.75	0.01	77.43	0.59	2.67	0.95	0.04	0.05	0.08	1.4	-0.75	1.3	8101	100	-	24	93.18	0.83	61
HQ15/192.5	61.47	0.005	35.34	0.23	0.51	1.44	0.01	0.05	0.04	0.29	0.29	0.05	1409	160	-	6	96.81	0.37	54
HQ15/195m	29.87	0.02	67.98	0.13	0.79	0.48	0.005	0.05	0.04	0.57	-1.59	0.04	1587	155	-	1	97.85	0.69	55
HQ15/198.2	23.27	0.02	74.91	0.13	0.93	0.26	0.02	0.05	0.05	0.64	-2.1	0.22	3524	125	-	13	98.18	0.76	53
HQ15/202.2	18	0.005	80.45	0.08	1.33	0.5	0.02	0.05	0.06	0.55	-2.26	0.29	3380	105	-	7	98.45	0.82	57
TNQ6/92.5	16.8	0.03	80.5	0.005	1.14	0.24	0.17	0.01	0.04	0.8	-0.97	0.85	7850	14	14	16	97.3	0.83	-
TNQ6/98.5	14.4	0.05	80.9	0.12	1.54	0.53	0.57	0.05	0.06	1.05	-0.48	0.13	1050	85	18	12	95.3	0.85	-
TNQ6/102.5	19.7	0.09	70.6	1.59	1.51	1.61	1.8	0.09	0.06	0.92	0.18	0.005	70	32	20	16	90.3	0.78	-
TNQ6/106.5	16.9	0.05	76.7	0.33	1.78	0.8	0.23	0.07	0.06	1.24	-1.18	0.19	3150	100	16	14	93.6	0.82	-
TNQ6/110.5	19.8	0.04	76	0.005	0.96	0.11	1.01	0.04	0.05	0.64	-1.94	0.34	1300	65	14	8	95.8	0.79	-
TNQ6/114.5	19.2	0.07	70.9	0.84	1.22	0.71	1.17	0.14	0.07	0.87	-0.24	1.62	15200	125	14	5	90.1	0.79	-
TNQ6/116.5	18.6	0.07	72	0.78	1.08	0.58	1.63	0.19	0.14	0.75	-0.06	0.87	12200	115	14	8	90.6	0.79	-
TT1/NQ4, 104.5	33.59	0.14	56.4	5.23	1.14	0.84	0.76	0.54	0.02	0.9	-0.23	0.09	1040	8	19	19.5	89.99	0.63	101
TT6/NQ4,117.4	23.16	0.12	66.07	3.14	1.82	2.15	0.64	0.34	0.02	1.48	0.66	0.001	26	65	<5	19	89.23	0.74	161
TT1 mag	7.18	0.08	91.16	0.7	1.07	0.24	<0.3	0.1	0.04	0.84	-1.46	-	622	-	10	22.3	98.34	0.93	181.8
TT1 qutz	75.28	0.27	9.83	8.64	0.1	0.1	5.48	0.12	0.01	0.11	0.25	-	10	-	11	13	85.11	0.12	141
TNQ7/75.25	24.19	0.05	69.63	1.18	1.9	0.48	0.67	0.03	0.05	1.3	-1.2	0.05	36	115	20	22	93.82	0.74	-
TNQ7/79.25	16.31	0.05	83.41	0.3	1.23	0.37	0.22	0.03	0.05	0.81	-2.15	0.04	26	115	18	14	99.72	0.84	-
TNQ7/83.25	23.54	0.04	73.47	1.26	1.18	0.51	0.93	0.03	0.04	0.85	-1.85	0.1	18	80	16	24	97.01	0.76	-
* calculated as oxides.																			

Appendix 5B, Trough Tank BIF geochemistry (oxides %, traces in ppm)

	Ni	Sc	W	Mo	Sn	Ba	Rb	Sr	Zr	Y	Nb	As	Comment
HQ9/191.1m	-	3	-	-	-	-	32	-	-	0.5	-	5	Anthophyllite Schist
A352318	30	-	-	-	-	25	8	10	<4	0.5	4	-	Anthophyllite Schist
A352322	48	-	-	-	-	<10	32	8	8	0.5	7	-	Anthophyllite Schist
A352324	8	-	-	-	-	90	115	22	16	18	13	-	Anthophyllite Schist
TT122	125	20	-	-	-	10	40	3	18	0.5	16	-	Anthophyllite Schist
HQ9/197.4m	-	1	-	-	-	-	52	-	-	26	-	5	Magnetite BIF, lower unit
HQ9/201.5m	-	2	-	-	-	-	<15	-	-	4	-	2	Magnetite BIF, lower unit
HQ14/126m	-	9	-	-	-	-	44	-	-	15	-	14	Magnetite BIF, lower unit
HQ14/146m	-	<1	-	-	-	-	40	-	-	10	-	3	Magnetite BIF, lower unit
HQ14/152m	-	<1	-	-	-	-	<15	-	-	21	-	<2	Magnetite BIF, lower unit
HQ14/158m	-	<1	-	-	-	-	<15	-	-	31	-	5	Magnetite BIF, lower unit
HQ15/192.5	-	1	-	-	-	-	<15	-	-	4	-	10	Magnetite BIF, lower unit
HQ15/195m	-	2	-	-	-	-	<15	-	-	16	-	3	Magnetite BIF, lower unit
HQ15/198.2	-	<1	-	-	-	-	<15	-	-	19	-	1	Magnetite BIF, lower unit
HQ15/202.2	-	<1	-	-	-	-	<15	-	-	9	-	3	Magnetite BIF, lower unit
TNQ6/92.5	<4	-	20	<4	12	25	36	12	<4	0.5	3	40	Magnetite BIF, upper unit
TNQ6/98.5	<4	-	<10	4	<4	25	40	8	4	6	4	16	Magnetite BIF, upper unit
TNQ6/102.5	20	-	<10	<4	<4	20	36	10	16	0.5	4	12	Magnetite BIF, upper unit
TNQ6/106.5	8	-	<10	14	4	<10	40	10	8	0.5	6	12	Magnetite BIF, upper unit
TNQ6/110.5	14	-	<10	8	12	10	38	5	4	0.5	5	8	Magnetite BIF, upper unit
TNQ6/114.5	<4	-	<10	12	<4	25	40	4	12	8	4	3	Magnetite BIF, upper unit
TNQ6/116.5	22	-	20	12	-	30	40	9	10	10	6	2	Magnetite BIF, upper unit
TT1	38	6	2.3	<2	-	27	69	13	47	22	5	<6	Magnetite BIF, upper unit
TT6	83.4	10	4.3	<2	-	17	47	24	37	17	3	<6	Magnetite BIF, upper unit
TT1 mag	25.5	7	7.9	4	-	14	<4	9.2	8	33	<2	<3	magnetite bands only
TT1 qutz	33	0.9	4.2	2	-	12	1.5	5.1	141.8	14.4	5.4	<6	quartz bands only
TNQ7/75.25	6	-	20	4	<4	<10	32	5	20	<4	6	12	Magnetite BIF, upper unit
TNQ7/79.25	6	-	<10	<4	<4	<10	28	5	<4	<4	4	<2	Magnetite BIF, upper unit
TNQ7/83.25	6	-	<10	6	10	<10	30	7	<4	<4	3	<2	Magnetite BIF, upper unit

APPENDIX 6

MAJOR AND TRACE ELEMENT GEOCHEMISTRY OF MAGNESIAN LITHOLOGIES

APPENDIX 6. Mafic compositions from the Starra and Trough Tank areas.* **

Sample	Area	Location	Comments	SiO2	TiO2	Al2O3	Fe2O3	MgO	MnO	Na2O	K2O	CaO	P2O5	LOI	Au	Cu	Pb	Zn
Stratiform chlorite schist																		
St45B	257	CRQ78-1,219.3m	footwall interbed	63.45	0.68	16.85	3.57	4.21	0.01	6.84	1.47	1.04	0.17	1.50	<0.05	10.7	2	6.3
St52	257	STQ80-15,163.8m	well-banded, chlorite schist	48.22	0.53	12.72	25.25	5.19	0.02	3.16	0.86	0.28	0.14	3.11	0.04	54.3	<2	8.3
St221	236	STQ85-113	Stratiform chloritite	43.02	0.39	8.27	31.04	7.92	0.11	0.21	1.12	2.66	0.09	5.05	0.43	129.6	3	42
St222	236	STQ85-113	Stratiform chloritite	43.76	0.42	9.60	30.13	9.24	0.06	0.28	1.12	1.84	0.13	3.57	0.12	918	<2	25
St223	236	STQ85-113	Stratiform chloritite	47.51	0.47	11.70	19.97	11.74	0.05	1.70	0.54	0.51	0.16	6.04	0.06	5162	<2	2.4
Lensoidal chlorite schist beneath ironstone																		
St54	257	STQ80-15,185.7m	Typical chlorite schist	50.97	0.47	10.75	24.80	6.01	0.03	1.03	1.24	0.64	0.16	3.49	0.11	77.5	<2	6.4
St153	257	STQ86-243, 154-158m	Chl.-f-mag. schist	46.86	0.60	14.43	12.66	14.79	0.04	1.31	1.58	0.76	0.14	6.48	-	17.6	<2	12
ST168	257	CRQ77-26,240-250m	Chl.-f-mag. schist	53.89	0.44	10.53	18.74	10.25	0.04	<0.3	0.20	0.28	0.14	4.74	<0.05	1120	<2	7
St208A	244	STQ79-9,72-76m	Typical chl. schist, py absent	47.82	0.41	9.87	23.42	7.98	0.12	<.3	1.15	2.41	0.13	6.01	1.04	557.2	3	17.1
St208B	244	STQ79-9,76-86m	Typical chl. schist, py present	44.38	0.44	10.38	27.94	6.78	0.10	1.07	1.61	2.03	0.17	5.48	0.17	1495	<2	10
Chloritic Answer Slate																		
St172	257	CRQ77-26,336-349m	Answer Slate	57.87	0.71	15.82	10.68	4.47	0.02	6.52	1.52	0.79	0.20	1.33	<0.05	5.6	<2	6
St199	257	STQ81-19,270-285m	Answer Slate	50.70	0.38	9.86	30.18	1.08	0.02	5.27	0.25	0.22	0.11	1.38	-	462	3	3.9
Answer 1	257	Surface	Answer Slate, chip samples	55.36	0.78	18.94	10.90	2.60	0.03	3.07	4.18	0.77	0.23	3.16	-	-	-	-
St202	257	STQ81-19, m	Answer Slate, "fresh"	48.01	1.96	13.12	11.74	13.85	0.03	0.83	6.37	0.50	0.31	2.03	-	838	8	14
Metamorphically chloritised footwall																		
St119	257	STQ85-129,150.9m	Chl.-alt'd core adj. to irst.	57.35	0.42	13.00	11.85	5.93	0.05	0.88	2.02	0.56	0.19	6.15	0.15	20.6	<3	24
Starra mafic volcanics																		
Sample	Area	Location	Comments	SiO2	TiO2	Al2O3	Fe2O3	MgO	MnO	Na2O	K2O	CaO	P2O5	LOI	Au	Cu	Pb	Zn
BW1	-	Mobs Lease	Amygdaloidal basalt	49.69	1.70	13.22	17.58	5.72	0.35	4.40	0.36	7.07	0.16	0.31	-	23	<2	70.6
STP5/EOH	-	Southern Grids	Actinolite plagioclase schist	55.02	1.25	15.69	14.05	6.15	0.09	2.84	1.76	3.36	0.07	2.55	-	47.1	-	30.2
STP5/96	-	Southern Grids	Actinolite plagioclase schist	52.78	1.36	13.70	13.90	5.60	0.11	3.24	1.67	4.55	0.17	1.82	-	54	3.5	32
STP8/40	-	Southern Grids	Actinolite plagioclase schist	49.93	1.17	13.87	15.26	7.41	0.20	1.90	1.68	6.10	0.10	2.20	-	84.7	-	67.1
STP17/96	-	Southern Grids	Actinolite plagioclase schist	51.69	0.82	14.07	12.50	6.15	0.07	4.17	1.95	6.37	0.10	1.46	-	141	-	26
STP23/100	-	Southern Grids	Actinolite plagioclase schist	47.84	0.60	14.55	13.95	8.78	0.26	2.61	2.00	6.74	0.08	2.77	-	66	-	54
STP25/84	-	Southern Grids	Actinolite plagioclase schist	50.38	0.95	15.01	14.72	8.20	0.11	1.33	1.81	1.55	0.08	5.52	-	9	-	62
Starra dolerites																		
St4	257	CRQ78-1,47m	Med. gr'd ophitic amphibolite	49.05	1.56	14.31	15.24	5.61	0.19	5.48	0.60	6.33	0.13	1.88	-	377.2	3	46
St145	257	STQ86-243,33.2m	Med. gr'd ophitic amphibolite	50.71	1.55	14.43	14.04	6.02	0.14	5.41	0.53	6.20	0.15	1.19	-	48	<2	45
St154	257	CRQ77-26,53.1m	Med. gr'd ophitic amphibolite	49.36	1.74	14.10	16.00	5.17	0.28	4.76	0.80	6.12	0.15	0.90	-	191.7	<2	103
Trough Tank basalt																		
236620		NQ1,156.2-157.2m	Med. gr'd massive amphibolite	48.00	1.73	12.00	16.90	5.90	0.25	1.88	0.79	9.64	0.15	1.70	<0.01	175	15	40
236621		NQ1,112-120m	Med. gr'd massive amphibolite	47.30	1.83	12.40	17.60	6.00	0.26	2.08	0.34	10.50	0.16	0.50	<0.01	120	12	36

* All samples were analysed at the University of Tasmania, except Trough Tank basalt, analysed by Comlabs, South Australia, Job reference COM872263.

**Gold values are averaged from Cyprus Minerals assays.

APPENDIX 6. Mafic compositions from the Starra and Trough Tank areas.* **

Sample	Ba	Rb	Sr	Zr	Y	Nb	W	Sc	V	Cr	Ni	As	Bi	U	Th	Ti/Zr	Al2O3/TiO2	Nb/Y
Stratiform chlorite schist																		
St45B	73	72.7	85.7	291.5	36	20.2	7.9	21.7	138	-	36	<3	<2	6	24.4	13.99	24.78	0.56
St52	142	25.5	7.3	137	20	11	-	12.4	162	-	150.4	<3	<2	7	15	23.19	24.00	0.55
St221	824	35.5	9.3	153.6	46.6	11.2	24.6	9.7	59	41	24	<3	<2	-	-	15.22	21.21	0.24
St222	610	56.9	18.1	111.2	37.5	8.1	38.8	8.9	57.2	38	64	<3	<2	7	16	22.64	22.86	0.22
St223	553	24.8	3.4	107.5	53.7	10.9	23	11.1	60.5	50	48	8	<2	-	-	26.21	24.89	0.20
Lensoidal chlorite schist beneath ironstone																		
St54	102	42.5	7.5	133.9	19.3	11.1	37.2	12.2	78.7	-	33.5	3	<2	-	-	21.04	22.87	0.58
St153	75	88.3	10.4	163	26	13.2	11.6	12.3	81.1	66	42	3	3	-	-	22.07	24.05	0.51
ST168	25	11.4	1.9	141.5	68	10.6	18.2	9.1	52	-	44	<3	<2	9	15	18.64	23.93	0.16
St208A	230	66.8	9.4	133.5	44.6	10	62.1	11.4	78	51	36	4	<2	-	-	18.41	24.07	0.22
St208B	244	81	14	132	54.3	10.1	80.8	11.2	62.4	48	39	8	2	-	-	19.98	23.59	0.19
Chloritic Answer Slate																		
St172	87	90.8	50.6	137.5	22.4	13.7	11.9	20	144.7	79	47	<3	<2	-	-	30.96	22.28	0.61
St199	14	13.1	3.6	121.9	17.2	8.2	55.3	5.7	64.5	-	30.5	<3	<2	-	-	18.69	25.95	0.48
Answer 1	-	135	63	144	33	16	-	-	-	-	-	-	-	-	-	32.47	24.28	0.48
St202	270	387.7	8.5	147.3	41.1	9.5	28.4	30.5	468	103	127	<3	<2	69	<2	79.77	6.69	0.23
Metamorphically chloritised footwall																		
St119	49	121	16.5	248.4	18.2	9.9	-	4.3	33.3	-	18.1	-	-	11	20	10.14	30.95	0.54
Starra mafic volcanics																		
Sample	Ba	Rb	Sr	Zr	Y	Nb	W	Sc	V	Cr	Ni	As	Bi	U	Th	Ti/Zr	Al2O3/TiO2	Nb/Y
BW1	108	14	86.1	107	41	5.6	-	47.3	540	43	49	-	-	<2	<2	95.25	7.78	0.14
STP5/EOH	387	86.5	49.1	87.3	21.4	4.6	-	49.1	315.5	-	70.4	-	-	-	-	85.84	12.55	0.21
STP5/96	332	82	62.2	119	30.9	7.4	11	45.1	364	-	51	<3	-	-	-	68.52	10.07	0.24
STP8/40	934	59.9	49.7	77.6	24.4	3.7	-	42	363	-	88	-	-	-	-	90.39	11.85	0.15
STP17/96	273	88.6	127.8	77.4	21.7	4.1	<2	34.4	255.8	-	111.5	-	-	-	-	63.52	17.16	0.19
STP23/100	708	81.2	65	39.9	13.3	2.2	-	34.4	221	-	121	-	-	-	-	90.15	24.25	0.17
STP25/84	474	69	23	76.6	25.6	4.4	14.4	34.1	259	-	113	-	-	-	-	74.35	15.80	0.17
Starra dolerites																		
St4	144	37.1	143.2	100.4	29.3	6.2	-	41.8	403.2	-	69.7	10	3	-	-	93.15	9.17	0.21
St145	233	18.1	133.1	111	32	7.5	6.5	40.5	425	43	53	5	<2	2	3	83.72	9.31	0.23
St154	353	36	216.5	110.2	33.3	7.6	3.7	42.8	448.8	39	49	10	<2	-	-	94.66	8.10	0.23
Trough Tank basalt																		
236620	155	38	115	115	28	9	10	70	-	24	22	7	-	-	-	90.19	6.94	0.32
236621	70	10	100	115	28	10	<10	90	-	24	30	6	-	-	-	95.4	6.78	0.36

APPENDIX 7

A. CHLORITE MINERAL CHEMISTRY

B. TOURMALINE MINERAL CHEMISTRY

Appendix 7. Selected microprobe chlorite compositions from the Starra ore environment.

Weight %	anal. No.	SiO2	TiO2	Al2O3	FeO	Fe2O3	MgO	CaO	K2O	Na2O	SO3	Sum	Anhydrous	SiO2	TiO2	Al2O3	FeO
Primary chlorites													cations on the				
St222,R1	13	31.32	-	15.69	19.07	-	21.05	-	-	-	-	87.13	basis of 14	3.186	-	1.879	1.622
St222,R3	14	31.99	-	14.8	17.13	-	23.36	-	-	-	-	87.28	oxygens.	3.214	-	1.754	1.44
St222,R3	15	31.99	-	15.25	18.32	-	22.94	0.15	-	-	-	88.65		3.185	-	1.789	1.525
St222,R6	17	30.5	-	16.92	22.6	-	19.81	-	-	-	-	89.83		3.065	-	2.004	1.899
Massive foliated chlorites																	
St131,RA	1	33.07	0.17	29.15	16.61	-	11.21	0.34	0.44	0.95	-	91.94		3.085	0.017	3.205	1.295
St131,RA	2	28.19	-	18.26	23.54	-	18.01	-	0.37	-	-	87.93		2.925	-	2.232	2.042
St153,R2	4	27.27	-	21.87	14.59	-	25.51	-	-	-	-	89.69		2.689	-	2.499	1.184
St153,R5	5	28.57	-	21.46	14	-	25.71	-	-	-	-	90.09		2.752	-	2.436	1.128
St153,R6	6	28.83	-	21.37	14.02	-	25.19	-	0.54	-	-	89.95		2.782	-	2.431	1.132
St153,R5	7	31.59	-	16.38	15.78	-	22.89	0.14	-	-	-	86.97		3.158	-	1.929	1.319
St221,R1	8	25.93	-	24.23	14.61	-	23.37	-	-	-	0.34	87.67		2.563	-	2.823	1.208
St221,R1	9	28.33	-	22.33	12.26	1.31	26.22	-	-	-	-	90.46		2.699	-	2.507	0.976
St221,R2	10	27.17	-	22.9	13.08	1.75	24.75	-	-	-	-	89.66		2.629	-	2.613	1.059
St221,R2	11	26.89	-	22.969	13.28	1.97	24.4	-	-	-	-	89.5		2.613	-	2.629	1.079
St221,R3	12	27.49	-	23.23	14.31	1.31	24.39	-	-	-	-	90.73		2.638	-	2.628	1.149
St222,R6	16	26.89	-	22.62	16.14	-	23.7	-	-	-	-	89.35		2.639	-	2.618	1.325
St222,R4	18	26.91	-	22.7	16.34	-	23.72	-	-	-	-	89.67		2.635	-	2.619	1.338
St222,R4	19	27	-	22.58	16.32	-	23.6	-	-	-	-	89.49		2.649	-	2.61	1.338
Chlorite after biotite																	
St202,R4	3	30.99	-	17.06	14.66	-	26.09	-	-	-		86.84		3.076	-	1.995	1.217
Chlorite in ironstone																	
St81,RA	20	25.34	-	23.84	13.39	-	23.05	-	0.18	-	0.32	86.24		2.548	-	2.828	1.126
St81,RA	21	26.7	-	27.53	14.62	-	24.16	-	0.11	-	0.36	92.57		2.4911	-	3.027	1.141
St115,R3	22	27.37	-	22.66	13.29	1.42	24.75	-	-	-	-	89.49		2.6533	-	2.589	1.078
St115,R3	23	27.64	-	21.55	12.23	1.78	25.44	-	-	-	-	88.64		2.696	-	2.478	0.997
St115,R6	24	27.26	-	21.91	12.88	2.18	24.81	-	-	-	-	89.04		2.659	-	2.52	1.051
Reaction skarn-related chlorite																	
St40c,R1	25	26.67	-	23.18	10.88	2.04	25.57	-	-	-	-	88.34		2.596	-	2.659	0.886
St40c,R1	26	26.46	-	22.94	10.67	2.68	25.52	-	-	-	-	88.28		2.582	-	2.638	0.871
St40c,R2	27	26.48	-	22.75	11.01	2.31	25.26	-	-	-	-	87.81		2.599	-	2.631	0.904
St40c,R2	28	25.94	-	22.99	9.36	3.44	25.84	-	-	-	-	87.58		2.544	-	2.657	0.767
St148,R5	29	27.22	-	21.88	15.97	1.3	22.92	-	-	-	-	89.29		2.681	-	2.54	1.316
St148,R5	30	26.76	-	21.51	14.89	2.15	23.1	-	-	-	-	88.41		2.659	-	2.519	1.238
Chlorite in hangingwall veins																	
St203,R2	31	28.21	-	20.77	11.88	-	25.86	0.35	-	-	-	87.08		2.781	-	2.414	0.979

Appendix 7. Selected microprobe chlorite compositions from the Starra ore environment.

	Fe2O3	MgO	CaO	K2O	Na2O	SO3	Sum
Primary chlorites							
St222,R1	-	3.189	-	-	-	-	10
St222,R3	-	3.499	-	-	-	-	10
St222,R3	-	3.405	0.016	-	-	-	10
St222,R6	-	2.966	-	-	-	-	10
Massive foliated chlorites							
St131,RA	-	1.558	0.034	0.052	0.172	-	10
St131,RA	-	2.785	-	0.049	-	-	10
St153,R2	-	3.688	-	-	-	-	10
St153,R5	-	3.692	-	-	-	-	10
St153,R6	-	3.623	-	0.067	-	-	10
St153,R5	-	3.41	0.015	-	-	-	10
St221,R1	-	3.443	-	-	-	0.024	10
St221,R1	0.094	3.723	-	-	-	-	10
St221,R2	0.128	3.571	-	-	-	-	10
St221,R2	0.144	3.534	-	-	-	-	10
St221,R3	0.095	3.489	-	-	-	-	10
St222,R6	-	3.468	-	-	-	-	10
St222,R4	-	3.462	-	-	-	-	10
St222,R4	-	3.449	-	-	-	-	10
Chlorite after biotite							10
St202,R4	-	3.86	-	-	-		10
Chlorite in ironstone							
St81,RA	-	3.454	-	0.023	-	0.023	10
St81,RA	-	3.359	-	0.013	-	0.024	10
St115,R3	0.104	3.576	-	-	-	-	10
St115,R3	0.131	3.699	-	-	-	-	10
St115,R6	0.159	3.609	-	-	-	-	10
Ironstone selvedge chlorite							
St40c,R1	0.149	3.71	-	-	-	-	10
St40c,R1	0.197	3.712	-	-	-	-	10
St40c,R2	0.171	3.695	-	-	-	-	10
St40c,R2	0.254	3.777	-	-	-	-	10
St148,R5	0.096	3.366	-	-	-	-	10
St148,R5	0.161	3.422	-	-	-	-	10
Chlotite in h'wall veins							
St203,R2	-	3.801	0.037	-	-	-	10

	stp24/92bif	stp24/92bif	stp24/92bif	sg33.r1,bif	sg33.r1,bif	sg33.r1,bif	sg33.r1,bif	sg33,r3,bif	SG25G,R1bif	SG25G,R3bif
SiO2	36.75	36.25	36.21	36.72	37.31	34.62	38.76	34.13	36.6	36.63
TiO2	0.36	0.21	0.48	0.37	0.17	0.24	0.16	0.34	0.01	0.01
Al2O3	31.16	30.51	30.05	30.77	32.7	31.93	32.18	30.26	28.43	29.92
MgO	7.67	6.88	8.08	9.28	8.19	8.71	9.19	8.11	9.51	8.74
FeO	9.02	10.32	8.51	7.18	4.32	4.88	4.63	6.29	10.01	8.64
CaO	0.3	0.01	0.51	2.06	0.24	0.68	0.36	0.53	1.49	1.01
K2O	-	-	-	1.02	1.56	0.5	1.06	0.47	-	-
Na2O	2.41	2.59	2.4	1.25	1.44	1.87	2.03	2.45	2.09	2.17
SUM	87.68	86.76	86.24	88.65	85.93	83.45	88.37	82.58	88.13	87.1
Mg No., mole	46.7	40	48.7	69.7	77.1	76.1	78	69.7	62.9	64.3

	SG25G,R4bif	SG25G,R4bif	SG25G,R4bif	SG45F,R4	SG45F,R4	SG45F,R5	SG45F,R8,CT	sg45F,massv	sg45F,massv	sg45F,massv
SiO2	35.92	36.11	37.84	36.95	37.49	37.68	36.62	37.04	36.77	36.75
TiO2	0.01	0.01	0.54	0	0.56	0.46	0.51	0.26	0.6	1.4
Al2O3	28.03	28.66	33.78	33.18	32.9	33.53	33.77	32.73	31.06	27.6
MgO	9.24	9.17	8.15	2.63	7.87	8.08	7.68	5.41	5.32	7.85
FeO	10.99	9.83	6.6	14.51	7.47	7.12	6.48	10.79	12.23	12.42
CaO	1.6	1.4	0.46	0	0.5	0.42	0.46	0	0	0.66
K2O	-	-	-	-	-	-	-	-	0.12	-
Na2O	2.1	2.19	2.16	2.12	2.35	2.42	2.13	2.31	2.75	2.66
SUM	87.87	87.34	89.54	89.4	89.14	89.7	87.65	88.54	88.84	89.35
Mg No., mole	60	62.4	68.8	24.4	65.3	66.9	67.9	47.2	43.7	53

	sg45F,massv	sg45F,massv	sg45F,massv	SG49	SG49,R2	SG49,R3core	SG49,R3	SG49, R4	SG49, R6	SG49
SiO2	36.82	37.16	37.14	34.89	35.25	35.53	36.04	35.44	35.7	35.88
TiO2	1.12	0.33	0.27	0.76	0.84	0.51	0.51	0.84	0.64	0.61
Al2O3	30.87	31.88	32.56	27.12	27.58	28.7	28.8	27.77	28.46	28.34
MgO	5.27	5.62	5.91	7.48	7.7	7.61	7.52	7.74	7.47	8.19
FeO	12.48	11.58	10.39	11.51	11.63	10.31	10.68	11.34	10.58	9.99
CaO	0.01	0	0	1.67	2.16	1.54	1.49	2.08	0.71	1.59
K2O	0.01	-	-	-	-	-	-	-	-	-
Na2O	2.62	2.66	2.7	1.84	1.74	2.05	2.04	1.96	2.44	1.94
SUM	89.17	89.22	88.96	85.26	86.9	86.26	87.09	87.18	86	86.53
Mg No., mole	43	46.4	50.4	53.7	54.1	56.8	55.7	54.9	55.7	59.4
			encl. by hem.	encl. by hem.					in cleavage	in cleavage

Tourmaline microprobe compositions from stratiform tourmalinites

	SG26,R5	rim	SG26,R5	rim	SG26,R5	SG26,R4	SG26,r4	SG26,R4	rim	SG26,R3	SG26,R3	SG45F,R2,ct	SG45F,R2,rm
SiO2	37.58	37.35	36.96	37.26	37.31	36.24	37.11	36.67	36.85	36.63	37.19	36.69	36.43
TiO2	0.91	0.79	0.74	0.71	0.17	0.75	0.59	0.62	0.85	1.71	0.86	0.37	0.69
Cr2O3	-	-	-	-	-	-	-	-	-	-	-	-	-
Al2O3	30.59	30.36	30.3	30.01	32.65	30.45	30.98	30.95	30.08	29.42	30.17	31.73	31.07
MgO	8.68	8.83	8.87	9.11	8.29	9.08	8.58	8.58	8.96	9.24	8.79	4.71	3.63
FeO	8.36	8.66	8.57	8.67	7.12	7.75	7.62	7.86	8.04	7.82	8.88	13.25	15.24
Na2O	1.99	2.2	2.23	2.2	2.12	1.87	2.11	2.14	2.04	1.64	2.08	2.65	2.74
CaO	1.52	1.35	1.26	1.43	0.7	1.59	1.21	1.2	1.31	2.07	1.42	0	0
K2O	-	-	-	-	-	-	-	-	-	-	-	-	-
SUM	89.62	89.54	88.93	89.39	88.36	88.41	88.2	88.01	88.12	88.52	89.4	89.39	89.79
Mg/Mg+Fe	64.9	64.5	64.8	65.2	67.5	67.6	66.7	66	66.5	67.8	63.8	38.8	29.8

	SG45F,R2,ct	SG45F,R3ct	SG49, R1	SG49, R1	SG45F,R3	SG26,R2	SG26,R2	SG26,RI	SG26,R1	SX13,R5	SX13,R5	SX13, R5	SX13,R4	SX13, R4
SiO2	36.61	36.59	35.22	36.18	37.13	36.89	36.82	38.4	37.22	37.95	37.89	35.85	35.75	36.62
TiO2	0.44	0.25	0.53	0	0.48	1.08	0.44	0.78	0.88	0.24	0.23	0.51	0.35	0.89
Cr2O3	-	-	-	-	-	-	-	-	-	-	-	-	-	-
Al2O3	32.11	32.35	28.09	31.58	31.58	30.33	29.72	31.45	28.87	32.88	33.26	29.34	32.18	29.37
MgO	4.08	4.41	7.03	7.31	4.33	9.08	10.2	9.22	9.18	7.12	7.16	8.38	5.18	12.38
FeO	13.53	12.82	10.9	7.95	12.49	7.73	7.64	8.04	8.98	5.57	5.51	6.9	9.76	1.99
Na2O	2.6	2.59	2.39	2.69	2.63	1.96	1.92	2.18	1.95	2.55	2.51	2.64	2.3	1.57
CaO	0	0	0.92	0	0	1.57	1.61	1.41	1.68	-	-	0.26	-	2.32
K2O	-	-	-	-	0.77	1.96	-	-	-	-	-	-	-	-
SUM	89.39	89	85.18	85.72	89.41	88.62	88.36	91.48	89.04	86.31	86.2	83.88	85.53	85.14
Mg/Mg+Fe	35	38	53.8	62.1	38.2	67.7	70.4	67.1	64.5	69.5	65.9	68.4	48.6	91.7

	SX13,R3core	SX13,R3rim	SX13,R3	SX13, R1
SiO2	36	36.13	36.28	36.56
TiO2	0.19	0.21	-	-
Cr2O3	0.98	0.28	0.7	-
Al2O3	30.21	30.14	29.92	31.45
MgO	7.71	9.2	7.79	8.68
FeO	7.5	5.71	7.58	5.7
Na2O	2.69	2.47	2.6	2.55
CaO	-	-	-	-
K2O	-	-	-	-
SUM	85.28	84.14	84.86	84.94
Mg/Mg+Fe	64.7	74.2	64.7	73.1

Tourmaline microprobe compositions from shears and veins

	SG18B,R1	SG18B,R3	SG18B,R5	SG2B	SG2B	SG2B	SG2B	SG2B	SG2B	SG2B	SG2B	SG21	SG21	SG21, R2	SG21, R2	SG21, R2	SG21,R2
SiO2	36.75	36.07	36.77	36.88	36.05	37.04	36.15	36.19	36.01	37.1	37.56	37.84	37.8	38.07	36.83	38.12	36.24
TiO2	0.67	0.56	0.28	0.55	0.51	-	0.48	0.38	0.48	0.36	0.61	0.19	0.17	-	0.22	0.18	0.18
Al2O3	30.32	30.57	31.98	29.88	29.1	33.06	30.35	29.73	28.63	31.25	30.81	28.72	28.53	30.34	27.21	27.76	27.46
FeO	7.89	7.57	7.16	8.46	7.93	7.77	7.7	7.69	8.55	8.3	8.88	11.68	11.39	8.13	12.12	11.31	11.33
MgO	8.91	8.51	8.31	9.59	11.06	7.14	9.76	9.88	9.24	8.6	8.06	9.45	9.29	9.59	9.33	9.32	9.08
CaO	1.07	0.98	0.53	1.74	1.61	1.66	1.68	1.71	1.67	2.06	2.26	1.76	1.58	0.91	1.77	1.78	1.67
K2O	-	-	-	-	-	-	-	-	-	-	-	-	-	-	-	0.13	0.13
Na2O	2.43	2.15	2.24	1.6	2.1	0.76	1.77	1.46	1.87	1.34	1.3	2.1	2.17	2.3	2.06	1.93	2.04
SUM	88.04	86.42	87.27	88.7	88.48	87.42	87.9	87.05	86.44	89.02	89.46	91.7	90.94	89.34	89.56	90.53	88.13
Mg/Mg+Fe	66.8	66.7	67.4	61.2	56.1	66	58.4	58.1	62.3	63.2	66.2	59.1	59.3	67.8	57.9	59.5	58.8

	SG21, R2	SG21, R2	SG21	SG21	SG24,R2	SG24,R3	SG24, R3	SG24, R3	SG24,R5	SG24, R5	SG24	SG24	SG24	SG24	SG24	SG23,R1core
SiO2	37.62	36.79	36.32	37.87	36.25	35.61	35.58	35.19	35.76	35.11	36.09	34.52	34.88	34.62	37.99	35.72
TiO2	-	0.23	-	0.2	0.29	0.37	0.31	0.13	0.1	0.26	0.37	0.4	0.37	0.39	0.48	0.56
Al2O3	29.91	27.21	28.37	30	27.28	28.56	29.38	27.77	29.31	27.66	28.22	26.81	26.39	26.11	25.34	34.85
FeO	9.41	11.83	11.17	9.33	9.23	8.39	7.51	8.1	6.96	7.97	9.25	9.51	9.65	10.22	8.87	6.81
MgO	9.52	9.23	9.12	8.31	9.24	9.38	9.05	9.7	9.15	9.12	9.36	9.25	9.22	8.87	8.8	5.9
CaO	1.21	1.72	1.63	1.46	1.62	1.75	1.22	1.75	1.16	1.58	1.75	1.81	1.64	1.74	1.87	0.49
K2O	-	-	-	-	-	-	-	-	-	-	-	-	-	-	-	-
Na2O	2.03	1.92	1.98	1.88	1.78	1.81	1.89	1.71	1.83	1.74	1.77	1.81	1.99	1.75	1.57	1.85
SUM	89.7	88.93	88.59	89.06	85.68	85.93	84.96	84.96	84.59	83.74	86.8	84.12	84.12	83.7	84.91	86.18
Mg/Mg+Fe	64.3	58.2	59.3	61.3	64.1	66.6	68.2	67.3	70.1	67.8	64.3	63.4	63	60.7	63.9	60.7

	SG23,rim	SG23,R2	SG23,R2	SG23,R3	SG23,R3core	SG23,rim	SG23,R4core	SG23,rim	SG23,R5	SG35C,R1	SG35C,R1	SG35C,R2	SG35C,R3	SG35C,R3
SiO2	36.15	35.74	35.85	35.75	35.87	35.84	35.6	35.98	35.93	35.54	35.65	34.59	36.34	35.82
TiO2	0.2	0.47	0.3	0.36	0.4	0.75	0.25	0.34	0.33	0.23	0.19	0.18	0.53	0.24
Al2O3	31.92	27.68	28.83	28.88	28.29	28.45	27.95	28.79	28.55	29.15	29.56	27.31	30.06	29.08
FeO	7.89	9.31	7.44	7.09	8.16	10.25	7.51	6.89	7.52	7.5	7.42	8.14	6.82	7.66
MgO	7.06	9.99	10.32	10.12	9.69	7.58	9.75	10.7	10.03	9.36	9.94	9.32	9.21	9.55
CaO	0	1.77	2.21	2.73	1.65	1.13	2.54	2.56	2.04	1.85	1.92	1.57	1.12	1.54
K2O	-	-	-	-	-	0.09	-	-	-	-	-	-	-	-
Na2O	2.75	1.88	1.52	1.07	1.99	2.16	1.07	1.34	1.88	1.68	1.63	1.72	2.12	1.84
SUM	85.97	86.82	86.48	86	86.04	86.54	84.65	86.6	86.27	85.32	86.31	82.82	86.2	85.71
Mg/Mg+Fe	61.5	65.6	71.2	71.8	67.9	56.9	69.8	73.4	70.4	69	70.5	67.1	70.6	69

Tourmaline microprobe compositions from metasomatic tourmalinites

	SG10D	SG10D,R1	SG10D,R2	SG10D, R3	SG10D,R3	SG10D,RD	SG10D, RE	SG10D, RE	SG10	SG10,R4	SG10,R5	SG10,R6	SG10,R6	SG10,R1	SG10,R2
SiO2	35.42	35.15	36.77	35.76	35.49	35.53	34.95	36.31	36.42	38.4	37.73	38.09	37.99	36.52	36.43
TiO2	0.54	0.56	0.72	0.35	0.29	0.4	0.35	0.46	0.45	0.52	0.54	0.63	0.75	0.2	0.36
Al2O3	34.68	33.92	28.95	34.82	34.47	31.44	34.08	31.19	33.87	32.99	32.64	33.19	32.9	35.34	33.98
FeO	11.12	11.37	10.31	11.56	11.14	9.72	11.28	9.76	12.17	7.27	7.24	6.95	6.71	12.1	12.87
MgO	2.96	3.51	6.89	3.32	3.35	6.6	3.61	6.67	4.5	8.62	8.53	8.56	8.78	3.34	4.14
CaO	-	-	-	0.12	-	0.39	0.14	0.37	0.5	0.45	0.39	0.49	0.54	0.33	0.34
K2O	-	-	-	-	-	-	-	-	-	-	-	-	-	-	-
Na2O	1.93	1.94	2.72	2.2	1.95	2.41	1.99	2.45	2.31	2.62	2.56	2.57	2.46	2.06	2.1
SUM	86.64	86.45	86.36	88.12	86.69	86.49	86.4	87.21	90.21	90.87	89.63	90.48	90.14	89.91	90.23
Mg/Mg+Fe	32.1	35.5	54.4	33.8	34.9	54.8	36.3	54.9	39.7	67.9	67.8	68.7	70	33	36.5
Colour	Blue	Blue	Blue	Blue	Blue	Blue	Blue	Blue	Blue	Green	Green	Green	Green	Blue	Blue

	SG10,R1	SG10,R1
SiO2	37.12	37.51
TiO2	0.1	0.27
Al2O3	32.63	32.8
FeO	9.62	7.08
MgO	7.12	8.54
CaO	0.63	0.39
K2O	-	-
Na2O	2.39	2.49
SUM	89.52	89.08
Mg/Mg+Fe	56.9	68.3
Colour	Blue	Green

Microprobe compositions of granitic tourmalines

APPENDIX 8

RARE EARTH ELEMENT GEOCHEMISTRY

Appendix 8. Rare earth element contents of Starra lithologies.

Sample	La	Ce	Pr	Nd	Sm	Eu	Gd	Dy	Er	Yb	Y	W	Sample type
BIFS & IRONSTONES													
Barren, well-banded, distal													
A7	46	88	-	47.5	6.69	1.55	4.04	2.73	1.33	0.4	7	3.1	surface
24/92	13.2	28.8	3.05	12.1	2.25	0.72	1.88	2.24	1.37	1.23	11.5	4	percussion
24/94	20.7	43.6	-	14.5	-	-	-	-	-	-	14.3	2	percussion
SG22(n=2)	82.1	91.9	-	32.6	-	-	-	-	-	-	15.6	8.9	surface
SG25G	35.2	50	-	22.2	-	-	-	-	-	-	24	5.9	surface
SG36F	161.3	59	-	105	-	-	-	-	-	-	71	10.1	surface
SG36G	31.6	58	-	19.5	-	-	-	-	-	-	30	2	surface
SG41B(n=2)	23.5	23	-	15.9	-	-	-	-	-	-	28.8	12	surface
Barren, massive, distal													
SG27	<3	<5	-	<3	-	-	-	-	-	-	8		surface
SG28	3.3	<5	-	<3	-	-	-	-	-	-	6	3.3	surface
SG30	6.6	<5	-	<3	-	-	-	-	-	-	32	2.1	surface
SG67	17.8	23	-	7.6	-	-	-	-	-	-	32	11.5	surface
Barren, massive, proximal													
St19	25.4	37	-	21.8	-	-	-	-	-	-	14	0.33	DDH
St75	3.68	8.51	1.1		1.64	-	1.76		1.03	0.99	9	145.4	DDH
St99	5.3	<3	-	5.3	-	-	-	-	-	-	25	24.7	DDH
St100	3.1	<3	-	<3	-	-	-	-	-	-	43	11.5	DDH
St124	4.89	8.93	-	4.64	1.3	0.4	1.37	1.64	1.05	1.11	10	68.3	DDH
Mineralised ironstones													
St59	<3	<5	-	3	-	-	-	-	-	-	16	109	DDH
St77	13	20	-	11.1	-	-	-	-	-	-	92	44	DDH
St116(257)	0.81	1.85	-	1.08	0.58	0.25	2.09	4.61	3.54	2.68	27	158.3	DDH
St118(257)	<0.5	2	0.4	3	2	0.4	6	11	8.5	6	98	695	DDH
St167	4	<3	-	<3	-	-	-	-	-	-	34	<3	DDH

Sample	La	Ce	Pr	Nd	Sm	Eu	Gd	Dy	Er	Yb	Y	W	Sample type
D9.3 (251)	1.51	3.54	0.44	1.93	0.48	<0.22	1.05	1.32	0.66	0.45	-		underground chip
Primary 257	3.7	9.9	1.2	3.9	1.1	0.3	1.5	2	1.2	1.1	11	130	Metallurgical composite
Area257oxidised	6.1	15	1.7	6.8	1.3	0.4	2.4	2.1	1.5	1.3	12	-	Metallurgical composite
Area257leached	42	110	12	42	5.6	1.7	6.8	4.9	2.6	3.3	28	-	Metallurgical composite
Primary 251	4.5	9.3	1.1	4.4	0.8	0.3	1.3	1.1	0.8	0.4	7.5	530	Metallurgical composite
Area251oxidised	11	23	2.5	9.8	1.3	0.4	2.1	1.9	1.1	0.9	9.1	-	Metallurgical composite
Area251leached	40	50	11	40	7.2	1.5	8.4	5.7	3	3	31	-	Metallurgical composite
Primary 244	11	29	3.2	14	-	0.55	4.7	5.7	-	3.7	39	170	Metallurgical composite
Primary 222	30	74	7.7	31	1.8	0.85	7.3	3.8	2.1	1.5	22	71	Metallurgical composite
OTHER LITHOLOGIES													
Tourmalinite													
SG43	3.41	7.11	0.9	4.2	1.59	0.6	2.37	3.63	2.61	2.79	-	-	Surface
SG45F	5.12	8.09	0.83	3.53	1.37	0.48	1.93	3.02	2.19	2.69	-	-	Surface
SG49	1.5	2.5	-	<3	-	-	1	2	1.5	2	-	-	Surface
SG35c.tm.qtz.shea	22.5	75.3	-	18	-	-	-	-	-	-	-	-	Surface
Starra Footwall													
St152.l.alt	11.8	25.1	2.97	12.8	2.82	0.45	3.27	4.5	3.29	3.41	-	-	DDH
St138.l.alt	16.4	-	-	17.3	-	-	-	-	-	-	-	-	DDH
St204.l.alt	42.2	90	-	33.6	-	-	-	-	-	-	-	-	DDH
St109.l.alt	13	24.9	2.88	11.6	2.53	0.4	2.16	2.11	1.37	1.42	-	-	DDH
GD110.v.alt	5.86	12.8	1.51	6.23	2.02	0.67	4.79	8.7	6.29	5.17	-	-	undergound chip
GD111.clast	10.4	20.2	2.31	9.12	2.62	0.65	4.29	6.94	4.54	4.23	-	-	undergound chip
St44B	13.6	<5	-	3.6	-	-	-	-	-	-	-	-	DDH
St142	5.3	-	-	4.8	-	-	-	-	-	-	-	-	DDH
St198	10.8	-	-	10.3	-	-	-	-	-	-	-	-	DDH
St218	<3	<5	-	5	-	-	-	-	-	-	-	-	DDH

Sample	La	Ce	Pr	Nd	Sm	Eu	Gd	Dy	Er	Yb	Y	W	Sample type
Footwall to distal ironstones													
SG1(n=2)	29.5	76.3	-	38.6	-	-	-	-	-	-	-	-	surface
SG29	12.4	16	-	5	-	-	-	-	-	-	-	-	surface
SG36C	82.5	74.5	-	61.9	-	-	-	-	-	-	-	-	surface
STP7/82	23.7	50	-	22.3	-	-	-	-	-	-	-	-	percussion
STP20/72	9	18	-	7.8	-	-	-	-	-	-	-	-	percussion
Chlorite schist													
St45B.chert	117.7	279	-	106.8	-	-	-	-	-	-	-	-	DDH
St54	6.6	-	-	8.2	-	-	-	-	-	-	-	-	DDH
St168	<3	<5	-	6	-	-	-	-	-	-	-	-	DDH
St208A(244)	16.3	30	-	15.5	-	-	-	-	-	-	-	-	DDH
St221	10.3	21.3	2.64	11.8	3.58	1.09	5.22	6.58	3.69	2.28	-	-	DDH
St222	<3	<5	-	6.1	-	-	-	-	-	-	-	-	DDH
St223	8.3	-	-	7.1	-	-	-	-	-	-	-	-	DDH
Basalt													
STP5/eoh	33	70	-	30.3	-	-	-	-	-	-	-	-	Percussion
STP5/96	24	43	-	21.6	-	-	-	-	-	-	-	-	Percussion
STP5/90	12.6	27.1	3.11	12.2	2.61	0.82	2.85	3.39	1.97	1.86	-	-	Percussion
Av.Answer Schist	37.2	84.6	-	31.3	-	-	-	-	-	-	-	-	Surface
BW1	5	-	-	9.2	-	-	-	-	-	-	-	-	Surface
St147.Answer	27.2	58	-	23.6	-	-	-	-	-	-	-	-	DDH
St172.Answer	26.1	59	-	27	-	-	-	-	-	-	-	-	DDH
Dolerite													
St145	22	-	-	12.6	-	-	-	-	-	-	-	-	DDH
St154	26.9	15.5	-	12	-	-	-	-	-	-	-	-	DDH

Appendix 8. Rare earth element contents of Starra lithologies.

Sample	La	Ce	Pr	Nd	Sm	Eu	Gd	Dy	Er	Yb	Y	W	Sample type
Footwall veins, and hangingwall skarn													
St95.vn	4.4	6.4	-	8.1	-	-	-	-	-	-	-	-	DDH
St129.skn	14	14.2	-	8.5	-	-	-	-	-	-	-	-	DDH
St129.matrix	8	11.2	-	6.8	-	-	-	-	-	-	-	-	DDH
SG79.shear	72.6	114	-	33.4	-	-	-	-	-	-	-	-	surface
St64.vn	8.6	17.2	-	6.8	-	-	-	-	-	-	-	-	DDH
St183.Fe breccia	3.6	-	-	4.3	-	-	-	-	-	-	-	-	DDH
St148.skn	112.2	49.5	-	51	-	-	-	-	-	-	-	-	DDH
St165.skn	38.8	16.7	-	23	-	-	-	-	-	-	-	-	DDH
St196.skn.irst	4	-	-	4.5	-	-	-	-	-	-	-	-	DDH

APPENDIX 9

FLUID INCLUSION MEASUREMENTS ON STARRA HANGINGWALL CARBONATE VEINS.

	Mineral	Inclusion type	Th	NaCl-Equiv%	Tm	Te	Tm-NaCl	NaCl-Equiv% Salinity	Freezing Temp
St65	Vein calcite	I-v	164	20.03	-16.5	-30.9		20.03	-65.3
			208	-				-	
St65	Vein calcite	I-v	-	20.11	-16.6	-23.3		20.11	-69.1
			207	-				-	
			173	-				-	
			201	-				-	
			204	-				-	
St65	Vein calcite	I-v	138	23.43	-21.1	-33.8		23.43	-64.4
			-	12.99	-9.1			12.99	
			197	-				-	
St65	Vein calcite	I-v	152	24.83	-23.2	-38.2		24.83	
			142	-				-	
			341	-				-	
St65	Vein calcite	I-v	-	15.55	-11.5			15.55	-60.5
			-	15.24	-11.2	-23.6		15.24	
			169	-				-	
			456	-				-	
St127	Vein calcite	I-v	-	19.87	-16.3	-37.5		19.87	-56.1
			253	-				-	
			272	-				-	
St127	Vein calcite	I-v	-	19.62	-16	-32		19.62	-58.6
			148	-				-	
St127	Vein calcite	I-v	125	10.99	-7.4	-16.2		10.99	-53.5
			215	-				-	
St127	Vein calcite	I-v	124	8.81	-5.7	-15.7		8.81	-56
			349	-				-	
St127	Vein calcite	I-v	142	10.86	-7.3	-18.9		10.86	-50.3
			174	-				-	
St127	Vein calcite	I-v	153	3.05	-1.8			3.05	-42.9
			129	-				-	
			140	-				-	
			171	-				-	
D4	Vein calcite	I-v	124	7.29	-4.6	-20.7		7.29	-47.5
			109	-				-	
			110	-				-	
D4	Vein calcite	I-v	179	0.87	-0.5			0.87	
			142	7.85	-5			7.85	-48.7
			-	4.01	-2.4	-8.4		4.01	

Appendix 9. Fluid inclusion measurements, Starra hangingwall carbonate veins.

	Mineral	Inclusion	Th	NaCl-Equiv%	Tm	Te	Tm-NaCl	NaCl-Equiv%	Freezing Temp
			116	-				-	
D4	Vein calcite	l-v	186	-	0			-	
			112	-				-	
			181	-				-	
			141	-				-	
			213	-				-	
St270A	Vein calcite	l-v	128	18.09	-14.2	-24.9		18.09	-64.5
	(grainy)		115	-				-	
			126	28.16	-28.4	-40.4		28.16	-66.6
			88	-				-	
			115	-				-	
	Quartz crystal	l-v-halite+opaque	273	-				-	
			341	-				-	
			360	-				-	
			354	-				-	
			362	-				-	
			321	50.46			445	50.46	
			319	-			0	-	
			342	52.01			460	52.01	
St263A	Calcite	l-v	117	-				-	
	(outer grainy)		103	19.79	-16.2			19.79	-69.7
			124	17.92	-14			17.92	
			140	8.67	-5.6			8.67	
			108	17.28	-13.3	-26		17.28	-75.7
			140	13.77	-9.8			13.77	-80
	Outer edge of		151	22.66	-20	-28.5		22.66	
	grainy calcite		148	23.56	-21.3			23.56	
			141	-				-	
	Calcite:secs.		125	22.16	-19.3	-28.4		22.16	-80.3
	(inner clear)	l-v	120	22.87	-20.3			22.87	
			102	-				-	
			130	-				-	
			136	22.52	-19.8	-28.9		22.52	
			-	22.59	-19.9			22.59	-58.2
			122	-				-	
			155	-				-	
ABBREVIATIONS: l: liquid; v: vapour; Tm= temperature of last melting of ice; Te = temperature of first ice melting									
Th = temperature of homogenisation to vapour									

APPENDIX 10

EQUILIBRIA USED TO CALCULATE PHASE STABILITIES

Equation	log K (350° C)	Ref.
$HSO_4^- = H^+ + SO_4^{2-}$	-6.9	1
$H_2S = HS^- + H^+$	(-8.98)	2
$HS^- + 2O_2 = SO_4^{2-} + H^+$	47.28	3
$H_2S + 2O_2 = SO_4^{2-} + 2H^+$	38.3	4
$H_2S + 2O_2 = HSO_4^- + H^+$	45.2	5
$2H_2S + O_2\ (g) = S_2\ (g) + 2H_2O$	(24.40)	6
$2FeS_2 + 2H_2O = 2FeS + 2HS^- + 2H^+ + O_2$	-52.98	3
$2FeS_2 + 2H_2O = 2FeS + 2H_2S + O_2$	(-35.02)	3
$6FeS + 6H_2O + O_2 = 2Fe_3O_4 + 6HS^- + 6H^+$	-37.78	3
$6FeS + 6H_2O + O_2 = 2Fe_3O_4 + 6H_2S$	16.1	3
$3FeS_2 + 6H_2O = Fe_3O_4 + 6H_2S + O_2$	-98.36	3
$3FeS_2 + 6H_2O = Fe_3O_4 + 6HS^- + 6H^+ + O_2$	(-44.48)	3
$3FeS_2 + 6H_2O + 11O_2 = Fe_3O_4 + 6SO_4^{2-} + 12H^+$	185.32	3
$4Fe_3O_4 + O_2 = 6Fe_2O_3$	27.44	3
$4FeS_2 + 8H_2O = 2Fe_2O_3 + H_2S + O_2$	(-50.16)	3
$4FeS_2 + 8H_2O + 15O_2 = 2Fe_2O_3 + 8SO_4^{2-} + 16H^+$	256.24	3
$4FeS_2 + 8H_2O + 15O_2 = 2Fe_2O_3 + 8HSO_4^- + 8H^+$	311.44	3
$KAl_2(AlSi_3O_{10})(OH)_2 + 6SiO_2 + 3Na^+ =$ $3NaAlSi_3O_8 + K+ + 2H^+$	-9.57	3
$CuFeS_2 + 7/8H^+ + 1/2H_2O =$ $Cu^+ + Fe^{2+} + 15/8HS^- + 1/8SO_4^{2-}$	-27.5	4
$5Cu^+ + Fe^{2+} + 31/8HS^- + 1/8SO_4^{2-} =$ $Cu_5FeS_4 + 23/8H^+ + 1/2H_2O$	66.33	4
$5CuFeS_2 + 2H_2S + O_2 = 2H_2O + Cu_5FeS_4 + 4FeS_2$	30.75	5
$5CuFeS_2 + 2H^+ + 2HSO_4^- = 3O_2 + 2H_2O + Cu_5FeS_4 + 4FeS_2$	-59.65	5
$CaCO_3 + H^+ = Ca^{2+} + HCO_3^-$	-4.33	4
$HCO_3^- + H^+ = H_2CO_3$	(8.85)	6
$BaCl^+ + H_2S + 2O_2 = BaSO_4 + 2H^+ + Cl^-$	59.15	7
$BaCl^+ + H_2S + 2O_2 = BaSO_4 + 2H^+ + Cl^-$	50.17	7

1.Barton (1984)
2.Helgeson (1969)
3.Huston & Large (1989)
4.Bowers et al. (1984)
5.Calculated from Bowers et al. (1984) and Barton (1984)
6. Henley et al. (1984)
7. after Huston & Large (1989)

APPENDIX 11

A BRIEF REVIEW OF STRATIFORM ORE DEPOSITS ASSOCIATED WITH SIGNIFICANT MAGNETITE OR HEMATITE

APPENDIX 11

Stratiform/stratabound magnetite/hematite - chalcopyrite ± gold association

Big Cadia, NSW, Australia
Age: Late Ordovician
Size: Historical production of 0.75 mt Fe, 5000 t Cu and 48 kg Au, at an average grade of 50 % Fe, 6 % Cu, 6 g/t Au.
Setting: The ore occurs at a local limestone break within meta-andesitic pyroclastics and lavas (middle Greenschist facies metamorphism). Footwall alteration includes sericite, chlorite and intense focussed epidote development. A smaller body known as Little Cadia occurs nearby (Mason 1981).
Ores: The ore forms a 600 X 250 X 40 m stratiform lens, banded at its top and massive at its base, containing magnetite (80 %) (pseudomorphing low temperature goethite and hematite)-hem-py-cpy ± bn, cc and covellite. A geochemical association of Cu-Au ± Co, Ni exists. Py and cpy are concentrated in the basal zone. Fluid inclusions indicate calcite and quartz depostion in the range 140 – 320° C, and seawater salinities.
Cited origin: Volcanogenic exhalative.
References: Bajwah (1985), Bajwah et al. (1987).

Norwegian Caledonian
Age: Palaeozoic

Fosdalen
Size: 25 mt @ 60.2 % magnetite, 3 % py and 0.2 % cpy
Setting: A continuous stratiform lens on the contact between greenschist facies acid and basic volcanics. Footwall alteration is notably absent.
Ores: Well-banded but recrystallised mag-qtz ± py, cpy.
Cited origin: Volcanogenic-exhalative
References: Waltham (1968), Frietsch et al. (1979).

Tverrfjellet
Size: 19 mt @ 1 % Cu, 1.2 % Zn and 0.2 % Pb.
Setting: The mag-py-cpy ore forms a large lens within a sphalerite-pyrite-chalcopyrite body. The agglomeratic acid volcanic-host is devoid of footwall alteration.
Ores: 39.6 % mag, 11.2 % py, 1.6 % cpy, 0.3 % po, 0.1 % sphal., forming a finely banded ore.
Cited origin: volcanogenic exhalative.
References: Waltham (1968), Nilsen (1978).

Aitik, Norrbotten, Sweden
Age: ~ 1600 Ma
Size: 150 mt @ 0.4 % Cu
Setting: Altered basic and intermediate volcanics; footwall alteration includes chalcopyrite veining, and formation of disseminated tourmaline, sericite and scapolite.
Ore: Cpy - py - mag - po veining.
Cited origin: The veins are considered to be "syngenetic within the sediments" (Freitsch et al. 1979).

Pahtohavore, Northern Sweden
Age: Proterozoic
Size: 2 mt @ 3.7 g/t Au, 4.3 % Cu
Setting: Basic lavas, pyroclastics and metasediments intruded by gabbroic sills.
Ores: Five ore-types are documented, including disseminated sulphides in "skarn" zones. The major ore-type is chert-hosted cpy-mag-Au associated with graphitic schist and scapolitic alteration.
Cited origin: Metasomatic/exhalative.
Reference: Carlson et al. (1988).

Willyama Complex, Broken Hill, NSW, Australia
Age: ~ 1820 Ma
Region: Poly-deformed, upper amphibolite to granulite peak metamorphism.

Grasmere Copper Mine, Wonominta Block
Size: 500 t historical production
Setting: 1 to 3 m wide finely-banded ironstone, 1000 m long, within chloritic slate.
Ores: Mag - qtz - py - cpy - po - cov

Copper Blow, Suite 3, Broken Hill Block
Size:700-1500 t historical production. Present resource: 0.94 mt @ 1.0 % Cu, 1.9 g/t Au
Setting: ~ 2 m wide ironstone, 1.5 km long, within biotite - albite schist.
Ore: Disseminated py-po-cpy within mag-qtz ironstone.
Other Prospects: Iron Blow, the Sisters and the Razorback all are qtz-mag ± py-cpy lenses stratigraphically below the main Broken Hill Pb-Zn horizon.
References: Barnes (1980, 1985).

Hallefors & Vena areas, Bergslagen region, Sweden
Age: 1900 - 1850 Ma
Size: Several lenses, typically a few metres thick with several kilometres of strikelength.
Setting: rift-related albitic volcanics form the footwall to the host evaporitic carbonate and pelitic host-rocks, which are overlain by fragmental acid pyroclastics. (Oen et al. 1982).
Ores: Magnetite, silicate and carbonate (manganiferous) facies iron formation at the top of the first volcanic cycle host chalcopyrite-rich mag-qtz deposits at Saxberget and Ljusnarsberg.
Cited origin: A volcano-sedimentary origin is widely recognised (Magnusson 1970, Frietsch 1975, Grip 1978). The Fe-oxide-Cu assemblage is considered a basin edge facies of iron formation.

Canadian Archean greenstone terranes
General comment (after Kirkham 1979): Cu-rich oxide facies iron formations in the Canadian greenstone belt occur preferentially towards the base of mafic volcanic sequences.

No. 4 lens, Bousquet, Canada
Size: uneconomic, a semi-continuous 10 - 15 cm thick lens
Setting: One of 9 deformed and metamorphosed mineralised zones within sericitised andesitic flows and rhyolitic ash-flow tuffs.
Ore: Stratiform mag-py-gold (up to 30 g/t) within a larger disseminated zone of Au-pyrite ore.
References: Valliant et al. (1982), Valliant & Barnett (1982).

Pacand Township
Size: 1 - 3 m wide X 4 km long oxide facies BIF
Ores: Banded Qtz-mag-py-cpy ± carb. Cu ~ 1 %.
Reference: Kirkham (1979).

Atikokan Iron Formation
Size: 10 - 80 m thick, sporadically along a 20 km strikelength. 21.8 mt @ 35 % Fe, 0.40 % Cu ± Ni, Co.
Setting: Deformation is intense.
Ore: Mag-po-py-cpy, with massive sulphide zones in places.
Reference: Kirkham (1979).

Snakeweed Lake
Size: 0.78 mt @ 1.10 % Cu and 14.7 g/t Ag
Setting: strongly deformed silicate-oxide-sulphide facies iron formation in mafic volcanics.
Ore: banded mag- amphibole - po - cpy

Reference: Kirkham (1979).

Granduc Mine, British Columbia
Size: 13 mt @ 1.27 % Cu
Setting: strong deformation
Ore: py-po-cpy-mag lenses, grading to dominantly magnetite BIF.
Reference: Kirkham (1979).

Salobo 3A, Carajas district, Brazil.
Age: Archean
Size: 455 mt @ 1.32 % Cu, 0.4 g/t Au.
Setting: Oxide-silicate facies iron formation ~ 3 km long occurs within amphibolite-grade "tonalitic gneiss", with a haloe of disseminated magnetite.
Ores: Mag-grunerite-cord-anth-albite-cpy-born-cc forms the mineralised horizon. High grade sections average 13 % Cu, 15 % Si, 53.5 % Fe, 0.8 % P, 0.3 % Mn.
References: Gair (1962), Moore (1964), B.Beeson pers. comm.(1986), Fiho et al. (1988).

Athens Mine, Zimbabwe
Age: Archean
Size: Unknown
Setting: Volcano-sedimentary package including basalts, komatiites and a basal sedimentary section.
Ores: Anthophyllite-rich rocks are overlain by iron formation zoned from po - cpy, to py - cpy, to py - mag.
Cited Genesis: "dominantly syngenetic" (Foster 1988).
References: Fabiana (1987), Foster (1988).

Isua Iron Formation, Greenland
Age: > 3.75 Ga
Size: 5 to 10 m wide iron formation developed sporadically over ~ 15 km of strike.
Setting: Para-amphibolite-hosted are metamorphosed to upper amphibolite facies.
Ores: Oxide, silicate, carbonate and sulphide facies are present; oxide facies contains minor py and cpy, although the best Cu grades are confined to the carbonate and sulphide facies (0.25 - 3.15 % Cu, 0.005 - 0.25 g/t Au ± Ni, Ag and Mo).
Cited genesis: Volcanogenic-exhalative
References: Appel (1979, 1982).

Unmineralised Volcanogenic Massive Oxide Deposits

This ore-type is considered transitional with Algoman oxide facies iron formation, of which there are many examples, differing mainly by the lack of chert banding so characteristic of the latter. The massive character, at times resulting in very high total Fe (see chapter 6), suggests iron deposition at rates which exceeded local sedimentation.

Ó

Teliuc-Ghelar-type, Central Europe
Age: Siluro-Devonian
Individual examples: Teliuc, Ghelar, Vadul, Dobrii, Ruschita (and ~ 15 smaller examples).
Size: 1 – 10 mt range.
Setting: Irregular podiform lenses occur on the flanks of former eruptive centres in altered submarine basic and intermediate volcanics.
Ores: Siderite-quartz dominates the ores, with abundant peripheral magnetite, chlorite, hematite, chert and pyrite. Mn and Ba are commonly strongly enriched.
Cited origin: Low temperature volcanogenic-exhalative deposited under reducing conditions.
Reference: Krautner (1979).

Lahn-Dill-type, Central Europe
Age: Upper Devonian.
Individual examples: Fortuna, Waldhausen, Lindenberg.
Size: 1 –100 mt range.
Setting: At the tops of former eruptive centres in altered basic volcanics (acid volcanics to a lesser degree), and locally within depressions, overlain by pelagic limestones, shales, or reef complexes.
Ores: Hematite, magnetite and quartz are the dominant components, with lesser siderite, iron chlorite, stilpnomelane and pyrite. Deposits are zoned from siliceous bases to calcareous tops and peripheries. Base metal levels are highly erratic, but are generally less than 2000 ppm for any of Cu, Pb, Zn, Co and Ni. Mn and P are present in the 0.05 – 0.2 % range.
Cited origin: Low temperature exhalation at the tops of submarine eruptive centres, in oxidised waters.
Reference: Quade (1976).

Dunderlandsal, Norway
Age: Palaeozoic
Size: Large — production rates of ~ 3.3 mt/year.
Ores: Massive hematite lenses, with peripheral magnetite.
Cited origin: shallow water chemical sedimentation of Fe sourced at a weathering surface.
Reference: Freitsch et al. (1979).

Langban, Sweden
Age: > 1800 Ma
Setting: A massive stratiform lens within limestone, immediately above basic volcanics.
Ores: 70 80 % hem, altering to magnetite at the ore periphery.Haussmannite is locally abundant. An association exists between Fe-Mn-Ba-Pb-Zn ± Cu (Base metals occur in proportion to Mn content, and hence may have resulted from scavenging).
Other cited but poorly documented examples: Pajsbeg, Harstigen, Sjogruvan, Nordmarken, Kesebol (Sweden), Franklin Furnace, Sterling Hill (New Jersey), Dzhail'man trough (Kazahkstan).
Reference: Bostrom et al. (1979).

Kiruna area, Sweden.
Age: 2.2 – 2.0 Ga
Size: total ~ 500 mt
Setting: Stratiform iron ores occur at stratigraphic changes within the volcano-sedimentary package. They form a transitional group to epigenetic apatite-rich iron ores, which have a more controversial origin.

References: Freitsch (1977), Parak (1985).

Vermillion District, northern Minnesota, USA
Age: 2750 – 2700 Ma
Size: Lenses 1 to 10 m thick with kilometre-scale strikelength.
Setting: Interbedded with metabasalt, felsic tuff, and minor epiclastics.
Ores: Massive to laminated magnetite and chert, locally specularitic.
Cited origin: Low temperature fumarolic activity.
Reference: Sims (1972)

Volcanogenic Massive Sulphides with BIF extensions

These are most commonly associated with Zn-Pb-Cu, rather than Cu-Zn ores (Franklin et al. 1981).

Bathurst district, Canada. Palaeozoic. — 7 of 30 known deposits are associated with BIF (Graf 1977, Franklin et al. 1981, Saif 1983).

Manitouwadge, Canadian Archean — Franklin et al. (1981).

Geco, Canadian Archean — Friesen et al. (1982).

Loccen, Norwegian Palaeozoic — Nilsen (1978).

Kvikne, Norwegian Palaeozoic — Nilsen (1978).

Skorovas, Norwegian Palaeozoic — Halls et al. (1978).

Kuroko ores, Miocene of Japan — examples with "Tetsusekiei" include Shakanai, Matsumine, Ohmaki, Fukazawa, Furotobe, Ainai, Kosaka, Hanawa and Wanibuchi (Ohtagaki et al. 1974, Kalogeropoulous & Scott 1983).

Volcanogenic Massive Sulphide Ores with Significant Oxide Zones

Magnettite is nost common in the stratiform base and stockwork of some Archean massive sulphides, but is generally absent form Kuroko and Cyprus-style ores (Large 1977).

Fukazawa, Hokuroko district, Japan
Age: Miocene
Size: ~1.5 mt Cu-Zn ore
Setting: Dacitic footwall; ores occur at a stratigraphic break marked by hem-qtz "tetsusekiei" 20 – 30 cm thick, interpreted as low temperature exhalites.
Ores: The typical basal py-cpy "yellow ore" is absent from this deposit, although the stringer system is well-developed. Hem-qtz occurs as part of this stringer, in thick veins cut by later, hotter, vein stages. The hematite is interpreted as part of the "tetsusekiei" which developed in response to the low temperature (< 150 ° C), incursion of sea-water below the seafloor.
References: Franklin et al (1981), Kalogeropoulos & Scott (1983).

Folldal, Rodhammer, Killingdal, Hjerkinn and Nordgruve: Norway
Age: Palaeozoic
Size: Each orebody is less than ~ 5 mt.
Setting: Footwall — submarine felsic volcanics and pyroclastics. Hangingwall — sediments and pyroclastics. The sulphur and pyrrhotite-rich ores are overlain by graphitic sediments, in moderate metamorphic grade rocks.
Ores: Py - mag - po ± sphal, cpy, gn. Early py is colliform. Ores are strictly conformable, well-banded, without footwall alteration.
Cited origin: Red Sea-style exhalation. In a spectrum of deposits the mineral assemblage reflects the oxidation state of the host-sediments.
Reference: Waltham (1968).

Heathe Steel B-1, New Brunswick, Canada
Age: Ordovician
Size: > 10 mt
Setting: One of 30 sulphide deposits in sediments close to a submarine felsic ash-flow sequence.
Reference: Large (1977).

Balcooma, Mt Windsor Volcanics, Queensland, Australia
Age: Cambro-Ordovician
Size: 3 mt @ 3 % Cu. Significant Pb-Zn in a separate pod.
Setting: Greywackes and felsic epiclastics.
Ores: Magnetite is disseminated throughout the Cu-ore, and also forms significant 10 to 15 m wide massive magnetite facies equivalents. The chlorite alteration contains disseminated magnetite.
Reference: Huston (1988).

Boksputs, Northern Cape, South Africa
Age: ~1.5 Ga
Size: ~ 1.7 mt Fe-Cu-Zn mineralisation (uneconomic).
Setting: Hosted within chlorite, amphibole and garnet-biotite gneiss.
Ores: Consists of 200 X 300 X 3 m discs of two associations — (1) Py-mag ± cpy (sph absent), and (2) Cpy-py-sph ± mag, po.
Cited origin: "Besshi"-style VMS ore.
Reference: Geringer et al. (1987).

Golden Grove, Western Australia
Age: 3.2 Ga
Size: 15 mt @ 3.4 % Cu, 0.1 % Zn, 0.1 g/t Au, and a separate resource of 1.7 mt @ 14 % Zn, 1.6 % Pb, 0.4 % Cu and 2.2 g/t Au.

etting: Submarine felsic volcanic footwall, and a hangingwall of chert and crystal tuff, widely intruded by dacite.
Ores: Stratiform lenses of massive sphal, po and py, overprinted by a second stage of hematite goethite and late magnetite (which dominates in some lenses).
ited genesis of the oxides: Post-depositional oxidation of sulphides, or precipitation from oxidised solutions with higher pH or temperature than the earlier fluids.
eferences: Frater (1983, 1985).

Corbet, Canada
Age: Archean
ize: 2.7 mt @ 2.9 % Cu, 2.0 % Zn, 20.5 g/t Ag and o.93 g/t Au.
etting: The footwall consists of sericitised mafic lavas, whereas the hangingwall consists of unaltered mafic lavas, volcaniclastics and rhyolites.
Ores: The ore is predominantly a typical Cu-Zn style, overlain by pyritic and siliceous exhalite. A lens of massive magnetite-chalcopyrite lies directly over the stringer-zone, interpreted as a product of ponding in a depression. No magnetite-stringers are documented.
Reference: Knuckey & Watkins (1982).

Anderson Lake, Canada
Age: Archean
Size: 3.3 mt @ 3.4 % Cu, 0.1 % Zn, 6.8 g/t Ag and 0.56 g/t Au.
Setting: Mineralisation occurs at the contact between sericitised schist and dacite, rhyolite and andesite flows. Alteration includes tourmaline veins.
Ores: The ore is a 500 m long lens of massive py-po-cpy. Magnetite occurs with the chloritic footwall alteration, and disseminated with pyrite and sphalerite as an ore-equivalent stratifer horizon.
Reference: Walford & Franklin (1982).

Orchan No. 3, Matagami District, Quebec
Age: Archean
Setting: Orchan, like Mattagami Lake, Norita and New Hosco (all magnetite bearing) occurs near the contact of felsic and intermediate volcanics.
Ores: Massive and banded Cu-Zn ore. Magnetite is a common component of the central and lower portions of the chloritic alteration, forming up to 30 % of massive ore. It is considered the first Fe-S-O mineral to have formed in the hydrothermal system.
Reference: Large (1977).

Syngenetic Gold Deposits With No Cu-oxide association

An epigenetic origin has also recently been proposed for many of these ores, as listed in Table 1.1.

Salsigne gold district, France (Cambro-Ordovician): Sulphide-rich (55%; ars, py, po) beds 2 – 10 m thick extend over 1 km within a turbiditic volcano-sedimentary sequence. Gold grades are very high (5 – 17 g/t), and are associated with traces of Cu, Bi, Ag, Zn, Pb, Sn and W. A sedimentary exhalative origin is indicated (Bonnemaison et al. 1986).

Passagem de Mariana, Brazil (Middle Proterozoic): Over 60 tonnes of gold have been extracted from a 5 m wide zone extending over 15 km. The ore is iron formation-hosted (qtz-carb-tm-ars) (Fleischer & Routhier 1973), although the entire zone has also been interpreted as a metasomatic shear zone (Vial et al. 1988). Similar zones associated with itabarite in the Brazilian Proterozoic include Morro Velho (~250 t), Raposos, Bicalho, Fama, Urubu and Saa Bento (Bernasconi 1988).

Golden Dyke Dome, Pine Creek Geosyncline, Australia (2.0 – 1.8 Ga): Au occurs in pelitic iron formation containing py, ars, cpy, po and tourmaline enclosed within meta-pelites and albitic meta-tuff. Sub-economic grades are distributed over ~ 3 km of strikelength, with some zones of higher grade (Nicholson 1980, Plimer 1986).

Granites-Tanami, Northern Territory, Australia (L. Prot.): Deformed carbonate/silicate facies iron formation, containing > 30 t of Au in 4 main zones. The ores are overlain by graphitic schist, but have very low sulphide contents (<0.5 %), in which cpy> py> po± ars ± sph. Total Fe is < 20 % (Ireland & Mayer 1984).

Nando & Pinkun, Zimbabwe (2.7 Ga): Disseminated Au and pyrite in pyroclastics, with a structural up-grade of Au in fold zones (Nutt 1983, Foster 1988).

Dickenson Mine, Ontario, Canada (~ 2.8 Ga). Au-Ag-Pd-As-Sb-B-W-rich ore occurs in banded ars-po chert conformably bound by altered mafic metavolcanics. The chemistry of the unit suggests the exhalation of metamorphic (CO_2-rich) hydrothermal fluids on to the sea-floor (Kerrich et al. 1981).

Jardine, South Dakota (2.95 – 2.7 Ga): Silicate/carbonate facies iron formation carrying 4,400 kg Au, 34.7 t W and 5722 t As (Hallager 1982).

Homestake, South Dakota, USA (Archean): Over 35 million ounces of gold have been produced from strongly poly-deformed carbonate facies iron-formation. Gold ore occurs as "spindle"-shaped bodies in fold hinges, suggesting structural up-grading (Sawkins & Rye 1974, Rye et al. 1974).

Agnico-Eagle, Canada (Archean): Disseminated gold and chert at a major stratigraphic break in sericitised felsic volcanics. ore zone is ~ 600 X 20 X 4.5 m (Barnett et al. 1982).

Dumagami - Bousquet - Doyon, Canada (Archean)— these ores all occur at the same horizon:

Dumagami (low deformation): 2.5 mt @ 3.4 g/t Au, 9.5 g/t Ag and 0.16 % Cu. This ore comprises a small massive sulphide body in subaqueous rhyolitic ashflows.

Bousquet (highly deformed and metamorphosed): nine lenses including ~ 1 mt @ 7.5 g/t Au, and 6.6 mt @ 2.0 g/t Au. The ore is mainly disseminated pyrite or small stratiform lenses.

Doyon (highly sheared): 4.45 mt @ 5.8 g/t Au, consisting of disseminated py in qtz-ser schist.

References: Valliant & Barnett (1982), Valliant & Hutchinson (1982), Guha et al. (1982).

APPENDIX 12

METHODS USED TO CALCULATE THE SOLUBILITY OF IRON AND SILICA IN 3 M NACL SOLUTION

PENDIX 12

hods Used to Calculate Iron and Silica Solubilities for Figure 12.11

The solubility of iron was calculated as Fe^{2+}, $FeCl^{+}$ and $FeCl_2^0$ in equilibrium magnetite and with hematite in the range 100 – 350° C. Solutions in equilibrium with te were not considered because of the low sulphur content of ironstone. The effective c strength of a 3M NaCl solution was corrected for the effects ion-pairing, which are d by Berner (1971) to markedly reduce the amount of chloride available for metal-plexing in saline brines, particularly with increasing temperature (Table 1). The nded Debye-Huckel expression (Henley et al. 1984) was employed to calculate the vities of Fe^{2+} and $FeCl^{+}$; the equilibrium and thermodynamic data for these ulations are presented in Appendix 10.

perature ° C	25	50	100	150	200	250	300	350
M NaCl)	2.553	2.601	2.604	2.560	2.392	2.273	1.932	1.6

Table 1 *Values of I (Ionic Strength) used in calculating ionic activities. (Unpublished data after D.Huston, University of Tasmania. 350 °C data was obtained by extrapolation of a fourth order polynomial).*

SiO_2 solubilities in equilibrium with quartz were calculated at 200 and 500 B for a NaCl solution over 50 to 350° C. This was determined using the pure water empirical tionship of Fournier & Potter (1982):

$$\log Ms = -4.66206 + 0.0034063T + 2179.7T^{-1} - 1.1292 \times 10^{6}T^{-2} + 1.3543 \times 10^{8}T^{-3} + (0.0014180T + 806.97T^{-1})\log\partial_w + 3.9465 \times T(\log\partial_w)^2$$

where T = temperature in Kelvin
∂_w = density of pure water in g/cm^3

The effect of increased ionic strength on quartz solubility was determined by roximating ∂w by ∂e, the Effective Density of water. This is expressed as

$$\partial_e = \partial \times F \times [1-(h \times M(NaCl)/55.51)]$$

where ∂ = density, F = weight fraction of water, $hNa^{+} = 0$
urnier 1982, Fournier et al. 1982).

Values obtained for ∂e were 0.66028 for 200 B, and ∂e = 0.68866 at 500 B.